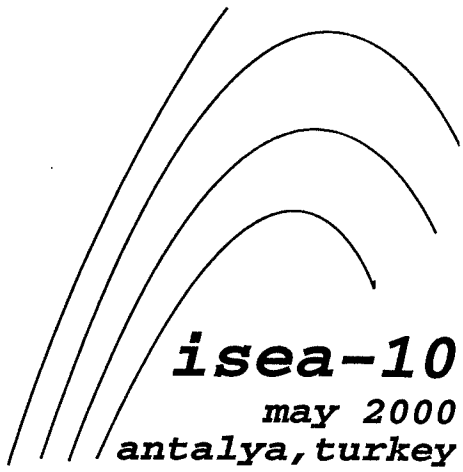


ABSTRACT NOTEBOOK

The Tenth International Symposium on Equatorial Aeronomy

Antalya Renaissance Resort, Antalya, Turkey
May 17-23, 2000

Sponsored by
AFOSR
EOARD
IAGA
NRL
NSF
ONR
SCOSTEP/EPIC
URSI

20040224 116

REPORT DOCUMENTATION PAGE

Form Approved OMB No. 0704-0188

naintaining the data needed, and completing and reviewing the collection of information. Send comments regarding this burden estimate or any other aspect of this collection of information, ncluding suggestions for reducing the burden, to Department of Defense, Washington Headquarters Services, Directorate for Information Operations and Reports (0704-0188), 1215 Jefferson Davis Highway, Suite 1204, Arlington, VA 22202-4302. Respondents should be aware that notwithstanding any other provision of law, no person shall be subject to any penalty for failing to comply with a collection of information if it does not display a currently valid OMB control number.
PLEASE DO NOT RETURN YOUR FORM TO THE ABOVE ADDRESS.

1. REPORT DATE *(DD-MM-YYYY)*	2. REPORT TYPE	3. DATES COVERED *(From – To)*
23-10-2003	Conference Proceedings	17 May 2000 - 23 May 2000

4. TITLE AND SUBTITLE

The Tenth International Symposium on Equatorial Aeronomy

5a. CONTRACT NUMBER
F61775-00-WF043

5b. GRANT NUMBER

5c. PROGRAM ELEMENT NUMBER

6. AUTHOR(S)

E. Kudeki, editor

5d. PROJECT NUMBER

5d. TASK NUMBER

5e. WORK UNIT NUMBER

7. PERFORMING ORGANIZATION NAME(S) AND ADDRESS(ES)

Hacettepe University
06532 Beytepe
Ankara
Turkey

8. PERFORMING ORGANIZATION REPORT NUMBER

N/A

9. SPONSORING/MONITORING AGENCY NAME(S) AND ADDRESS(ES)

EOARD
PSC 802 BOX 14
FPO 09499-0014

10. SPONSOR/MONITOR'S ACRONYM(S)

11. SPONSOR/MONITOR'S REPORT NUMBER(S)
CSP 00-5043

12. DISTRIBUTION/AVAILABILITY STATEMENT

Approved for public release; distribution is unlimited.

13. SUPPLEMENTARY NOTES

14. ABSTRACT

The Abstracts for The Tenth International Symposium on Equatorial Aeronomy, 17 May 2000 - 23 May 2000

This is a mulitdisciplinary conference. Topics include: Chemistry, dynamics, and thermodynamics of the low latitude neutral and ionized atmosphere, including ionospheric and thermospheric modeling, ionospheric (E- and F-region) plasma instabilities, effects of the turbulent ionosphere on EM wave propagation, prediction of spread-F events, and remote and in-situ dignostics of the low latitude upper atmosphere. The final papers are published as a special issue of *Journal of Atmospheric and Solar-Terrestrial Physics*, Aug-Sep 2002, Vol. 64, numbers 12-14.

15. SUBJECT TERMS
EOARD, Atmospheric Science

16. SECURITY CLASSIFICATION OF:			17. LIMITATION OF ABSTRACT	18, NUMBER OF PAGES	19a. NAME OF RESPONSIBLE PERSON
a. REPORT	b. ABSTRACT	c. THIS PAGE			INGRID J. WYSONG
UNCLAS	UNCLAS	UNCLAS	UL		19b. TELEPHONE NUMBER *(Include area code)* +44 (0)20 7514 4285

Best Available Copy

ABSTRACTS

The Tenth International Symposium on Equatorial Aeronomy

Antalya Renaissance Resort
Antalya, Turkey
May 17-23, 2000

Sponsored by:
Air Force Office of Scientific Research
European Office of Aerospace Research and Development
International Association of Geomagnetism and Aeronomy
Naval Research Laboratories
National Science Foundation
Office of Naval Research
Scientific Committee on Solar-Terrestrial Physics/EPIC
Union Radio Scientifique Internationale

The Tenth International Symposium on Equatorial Aeronomy

May 17-23, 2000
Antalya Renaissance Resort
Antalya, Turkey

Organizing Committee:

E. Kudeki, USA (chair)

C. Fesen, USA

J. LaBelle, USA

Program Committee:

Sa. Basu, USA

E. Blanc, France

J. Chau, Peru

B. Clemesha, Brazil

D. T. Farley, USA

B. G. Fejer, USA

S. Fukao, Japan

T. J. Fuller-Rowell, USA

S. A. Gonzales, USA

C. Haldoupis, Greece

C. Hanuise, France

R. Heelis, USA

D. L. Hysell, USA

M. C. Kelley, USA

R. Lieberman, USA

J. Roettger, Germany

G. H. Sastri, India

R. Sridharan, India

R. F. Woodman, Peru

H. C. Yeh, ROC

Local Organizing Committee:

F. Arikan, Hacettepe University

S. Cakir, Middle East Technical University

M. Safak, Hacettepe University

L. Sevgi, TUBITAK Marmara Research Center

Y. Tulunay, Istanbul Technical University

Scientific Program

May 17, Wednesday

Session 1: Opening and Tutorial Talks

Chair: Y. Tulunay

1. **9:00-9:40** (Invited) Gravity Wave Instability Dynamics and Mean-Flow Interactions in the Middle and Upper Atmosphere, **D. FRITTS.**
2. **9:40-10:20** (Invited) Tutorial On The Low Latitude Ionosphere, **D. N. ANDERSON.**

   10:20-10:40 Break

3. **10:40-11:20** (Invited) Donald T. Farley, Appleton Prize 1996: His contributions to Equatorial Aeronomy, **R. F. WOODMAN.**
4. **11:20-12:00** (Invited) Ronald Woodman's Contributions to Radio Science, **D. T. FARLEY.**

Session 2: Lower and middle atmosphere dynamics at low latitudes

Conveners: J. Chau, R. Lieberman, and J. Roettger

1. **13:30-13:55** (Invited) Introduction to El Nino Phenomena: A Peruvian Perspective, **R. F. WOODMAN.**
2. **13:55-14:10** In situ sensing of atmospheric properties in the boundary layer and lower troposphere at low latitudes, **B. B. BALSLEY and M. Jensen.**
3. **14:10-14:35** (Invited) Layered disturbances associated with low potential vorticity revealed by high-resolution radiosonde observation in Japan, **KAORU SATO and Timothy J. Dunkerton.**

4. **14:35-14:50** Jicamarca Radar Observations of Gravity Waves and the Diurnal Tide in the Troposphere and Lower Stratosphere, **DENNIS M. RIGGIN, Erhan Kudeki, Robert G. Stockwell, Zhaomei Feng, and Martin F. Sarango.**

5. **14:50-15:05** Lower and Middle Atmospheric Temperature & Studies Using Radiosonde, Lidar and UARS-HALOE Data over Chung Li, **J. B. NEE, W. N. Chen, and S. Thulasiraiuan.**

6. **15:05-15:30** (Invited) Observational Constraints on the Properties of Gravity Waves Generated by Tropical Convection, **M. JOAN ALEXANDER.**

7. **15:30-14:45** Acoustic Gravity Waves during 11 Aug 1999 Solar Eclipse in Troposphere/Mesosphere System, **M. LAL, C. Panneerseivani, K. U. Nair, S. Selvaraj, and R. Rajaram.**

15:45-16:05 Break

8. **16:05-16:20** Observations of momentum fluxes carried by AGWs in the mesosphere at Albuquerque, NM, **G. SWENSON, A. Liu, C. Gardner, L. Rumsey, and S. Hsia.**

9. **16:20-16:45** (Invited) Gravity Wave Interactions with Tides and Planetary Waves, **CHRISTIAN K. MEYER**

10. **16:45-17:00** Daytime mesopause temperature and its variabilities from low latitudes. **Alok Taori, R. SRIDHARAN, R. Narayanan, and N. K. Modi.**

11. **17:00-17:15** Tide-induced oscillations in the atmospheric sodium layer, **B. R. CLEMESHA, P. P. Batista, and D. M. Simonich**

12. **17:15-17:30** Simultaneous lidar observation of a sporadic sodium layer, a "wall" event in the OH and OI 5577 airglow images and the meteor winds, **P. P. BATISTA, B. R. Clemesha, D. M. Simonich, M. J. Taylor, H. Takahashi, D. Gobbi, and A. F. de Medeiros.**

13. **17:30-17:45** Lidar Measurements of Mesospheric Inversion at a Low Latitude (13.8*N, 79.2*E) : First Result, **V. SIVA KUMAR, Y. Bhavani Kumar, K. Raghunath and P. B. Rao, M. Krishnaiah, Kohei Mizutani, Tetsuo Aoki, Motoaki Yasui, and Toshikazu Itabe.**

14. **17:45-18:00** Seasonal variation of atomic oxygen over the equator derived from WINDII/UARS hydroxyl airglow observations, **R. P. LOWE and J. Russell.**

15. **18:00-18:25** (Invited) Ionospheric Effects of Lightning Discharges: Sprites, Elves, Runaway MeV Electron Beams, and Early/Fast Conductivity Changes, **U. S. INAN.**

May 18, Thursday

Session 3: Low Latitude Thermosphere

Conveners: T. Fuller-Rowell and R. Sridharan

1. **8:30-8:55** (Invited) Modeling the low latitude atmosphere and ionosphere, **C. G. FESEN.**

2. **8:55-9:10** Equatorial and Low latitude diurnal variations and Sq focus over the Indian Longitude, **S. Alex, B. D. Kadam, and K. Rao.**

3. **9:10-9:25** Whatever Happened to Superrotation? **HENRY RISHBETH.**

4. **9:25-9:40** Thermospheric wind climatology revealed with the MU radar, **S. FUKAO, S. Kawamura, Y. Otsuka, W. L. Oliver, and S. R. Zhang.**

5. **9:40-10:05** (Invited) The midnight Temperature Maximum (MTM) at Low Latitudes: A Status Report on Observations and Modeling, **M. COLERICO, M. Mendillo, and C. G. Fesen.**

6. **10:05-10:20** Equatorial Temperature Anomaly (ETA) in Solar Minimum, **R. Suhasini, R. RAGHAVARAO, H. G. Mayr, W. R. Hoegy, and L. E. Wharton.**

10:20-10:45 Break

7. **10:45-11:10** (Invited) The Equatorial Temperature and Wind Anomaly (ETWA), **R. RAGHAVARAO.**

8. **11:10-11:25** Plausible Explanation for the Equatorial Temperature and Wind Anomaly (ETWA) based on Chemical and Dynamical Processes, **Tarun Kumar Pant and R. SRIDHARAN.**

9. **11:25-11:40** Low-latitude thermospheric wind perturbations on the day side measured by WINDII during magnetic storms, **R. H. WIENS and G.G. Shepherd.**

10. **11:40-11:55** Geomagnetic forcing of the equatorial thermosphere-ionosphere system: a study of the disturbance interval 7-13 March 1994, **J. H. SASTRI, V. V. Somayajulu, K. B. Ramesh, H. N. R. Rao, and J. V. S. V. Rao.**

11. **11:55-12:10** Storm-Time Changes in Thermospheric Dynamics at Low Latitudes. **T. J. FULLER-ROWELL, M. C. Codrescu, A. D. Richmond, and G. H. Millward.**

12. **12:10:12:25** Emission rate and apparent temperature increases in the low-latitude day-side thermosphere during magnetic storms observed by WINDII, **R. H. WIENS, V. P . Bhatnagar and G. G. Shepherd.**

Session 4: Low Latitude Ionospheric Dynamics

Conveners: R. Heelis and H. C. Yeh

1. **14:00-14:30** (Invited) Low latitude Storm Time Ionospheric Electrodynamics **B. G. FEJER.**

2. **14:30-14:45** Spectral Analysis of Geomagnetic Data from Kandilli Observatory, Istanbul, **AYSE HUMEYRA BILGE and Yurdanur K. Tulunay.**

3. **14:45-15:00** A MU radar study on annual variations of the mid-latitude ionosphere, **S. FUKAO and S. Kawamura.**

4. **15:00-15:15** Spatially-Temporal Structure of Low-Latitude Ionosphere Obtained by Wavelet Analysis, **V. H. Depuev, N. M. Rotanova, A. H. DEPUEVA.**

5. **15:15-15:30** Penetration of auroral electric fields to the equator during a substorm, **T. KIKUCHI, R. Luhr, K. Schiegel, H. Tachihara, M. Shinohara, and T.-L. Kitamura.**

6. **15:30-15:45** Effect of the Field-aligned Currents on the Equatorial Ionosphere, **L. Z. SIZOVA and M. I. Pudovkin.**

15:45-16:05 Break

7. **16:05-16:20** ISR observations of the ionosphere over Arecibo: The effects of a solar eclipse and the effects of a small geomagnetic storm, **S. A. GONZALEZ, B. MacPherson, N. Aponte, M. Sulzer, M. Kelley, X. Pi, and C. Bailey.**

8. **16:20-16:30** Is there an Afternoon "Hole" in the Topside Equatorial Ionosphere? **D. T. FARLEY, W. E. Swartz, and J. L. Chau.**

9. **16:30-16:45** Field-aligned Ion Motions in the Topside Ionosphere, **R.A. HEELIS and S. Venkatraman.**

10. **16:45-17:00** Evening Enhancements in F-region Electron Temperature at Subtropical latitudes during summer in the Indian SROSS C2 RPA Data, **K. NIRANJAN, H. S. Sridhar, and P. V. S. Rama Rao.**

11. **17:00-17:15** Pre-seismic activity effects on the equatorial anomaly, **S. A. PULINETS, A. D. Legen'ka, and V. H. Depuev.**

12. **17:15-17:30** Variation of the F3 layer occurrence with the magnetic dip angle, **I. S. BATISTA, M. A. Abdu, A. M. Silva, P. F. Barbosa Neto, and J. MacDougall.**

13. **17:30-17:45** Appearance of F3 Layer over Waltair, **V. S. RAMA RAO, K. Niranjan, D. S. V. V. D. Prasad, P. Sri Ram, V. V. Somayajulu, and K. S. V. Subba Rao.**

14. **17:45-18:00** Diurnal, seasonal solar cycle and longitudinal studies of equatorial electrojet current based on rocket borne and ground based data, **H. Chandra, H. S. S. Sinha, and R.G. RASTOGI.**

May 19, Friday

Poster Session 1

Chair: C. Fesen

Session 2:

1. Correlative Study Between Geomagnetism and Surface Weather at Magnetic Equator and High Latitude, **M. LAL, K. U. Nair, C. Paneerselvam, P. Elango, C. Selvaraj, and R. Rajaram.**
2. Correlative Study between Geomagnetic and Weather Parameters at Magnetic Equator, **M. LAL B. Paramshivam, K. U. Nair, and R. Rajaram.**

Session 3:

1. Seasonal dependence of the response of the low latitude thermosphere for external forcings, **Tarun Kumar Pant and R. SRIDHARAN.**
2. All-sky nightglow imaging at Asmara, Eritrea, **R. H. WIENS and Samson Beyene.**

Session 4:

1. Joint ISR and spacecraft measurements in the ionosphere and plasmasphere using Arecibo and Jicamarea ISR together with GPS TEC and DMSP, **S. A. GONZALEZ, N. Aponte, B. MacPherson, M. Sulzer, R. Heelis, S. Venkataraman, and X. Pi.**
2. Some features of F3 layer observed with topside sounding, **V. H. Depuev and S. A. PULINETS.**
3. Solar flare and SSe effects in the electrojet region at different longitude sectors, abnormal induction effects in Indian longitudes, **R. G. RASTOGI.**
4. Variations of Critical Frequency foF2 at Midlatitudes During Great Geomagnetic Storms, **L. SIZOVA and R. Liperovskaya.**
5. The Time Delay in the Causal Analysis of Equatorial Ionospheric Processes, **L. SIZOVA.**
6. The Lunar Tide in the equatorial F region vertical ion drift velocity, **R. J. Stening and B. G. FEJER.**
7. Assertion and Prediction of Magnetic storms and Disturbances through IEC Parameters over Anomaly Crest Region, **M. DEVI, M. K. Barman and A. K. Barbara.**

May 20, Saturday

Session 5: Equatorial E-Region Irregularities

Conveners: E. Blanc and C. Hanuise

1. **8:30-8:55** (Invited) A review of equatorial E region irregularities from a broader perspective: anything new to discover, **J.-P. ST.-MAURICE**
2. **8:55-9:10** East-West Asymmetry in Type I Electrojet Echoes at Jicamarca, **J. L. CHAU, D. T. Farley, and Ben B. Balsley.**
3. **9:10-9:25** Electrodynamics of meteor trail evolution in the equatorial E-region ionosphere, **MEERS M. OPPENHEIM and Axel F. vom Endt.**
4. **9:25-9:50** (Invited) In-situ Observations in the Equatorial Ejectrojet: Outstanding Critical Problems, **R. PFAFF.**
5. **9:50-10:05** Coordinated study of ionospheric E region irregularities by rocket borne, ground based geomagnetic, Ionosonde, Ionspheric drift and Doppler radar data at the Indian electroject region, **R. G. RASTOGI.**
6. **10:05-10:30** (Invited) Gradient Drift Instabilities and Turbulence in the Daytime and Nighttime Equatorial Electrojet, **A. BHATTACHARJEE and S. Hu.**

10:30-10:45 Break

7. **10:45-11:00** Radar interferometric observations of the E- region irregularities over Gadanki, **P. B. Rao, A. K. PATRA, T. V. Chandrasekhar Sarma, V. K. Anandan, R. J. Doviak, and D. S. Zmic.**
8. **11:00-11:15** A new 50 MHz coherent back-scatter radar at the equatorial electrojet site, Sao Luiz, Brazil: some initial results, **M. A. ABDU, C. M. Denardini, J. H. A. Sobral, I. S. Batista, P. Muralikrishna, and R. R. de Paula.**
9. **11:15-11:40** (Invited) Plasma instabilities in the Equatorial Electrojet region, **R. RAGHAVARAO.**
10. **11:40-11:55** Lower E-region drifts as measured by partial reflection radar over magnetic equator, **T. K. RAMKUMAR, S. Gurubaran, and R. Rajaram.**
11. **11:55-12:10** Structural changes in tidal components in mesospheric winds as observed by the MF radar during counter electrojet events, **S. SRIDHARAN, S. Gurubaran, K. U. Nair, and R. Rajaram.**
12. **12:10-12:25** Short period oscillations of 2.8 m size Irregularities in the E region over Gadanki, **K. S. V. SUBBARAO, Sudha Ravindran, and K.S. Viswanathan.**

Session 6: Mid Latitude E-Region Irregularities

Conveners: S. Fukao and C. Haldoupis

13:40-13:45 Opening Comments: **C. Haldoupis**

1. **13:45-14:05** (Invited) Field-Aligned irregularities in the Midlatitude E Region: A Review, **R. TSUNODA.**
2. **14:05-14:20** Sporadic E Layers and Plasma Instabilities at Mid-Latitudes: Some experimental evidence, **J. Delloue, M. N. DE LA GRILLIERE, N. Cavaciuti, M. Six, and A. Bourdillon.**
3. **14:20-14:35** Non-local Theory of Mid-latitude E-region Plasma Instabilities, **J. M. Rosado-Roman, W. E. Swartz, D. T. FARLEY, and C. E. Seyler.**

4. **14:35-14:50** 50 MHz Continuous Wave Interferometry Observations from the Unstable Midlatitude E-Region Ionosphere, **CHRISTOS HALDOUPIS, Anastasios Karnburelis, Kristian Schlegel, and Alain Bourdillon.**

5. **14:50-15:10** (Invited) Recent results of MU radar observations of mid-latitude E region field-aligned irregularities, **T. OGAWA, K. Nozaki, M. Yamamoto, and S. Fukao.**

6. **15:10-15:25** Large scale E-region electric field structure due to gravity wave winds, **L. J. GELINAS, M. C. Kelley, M. F. Larsen, and D. Hysell.**

7. **15:25-15:35** Long Period Variations in Midlatitude E Region Coherent Radar Backscatter and Sporadic E Layers. Evidence for a Relation with Planetary Waves, **C. HALDOUPIS, M. Voiculescu, D. Pancheva, and S. Shalimov.**

8. **15:35-15:50** A New Mechanism for Midlatitude E Region Plasma Accumulation Driven by Planetary Wave Horizontal Wind Shears, **S. SHALIMOV, C. Haldoupis, M. Voilucescu, and K. Schlegel.**

9. **15:50-16:05** Inferred Vertical Ion Drifts associated with Intermediate Layers Observed by Arecibo Observatory, **G. D. Earle, R. L. BISHOP, and S. Collins.**

16:05-16:30 Break

10. **16:30-16:50** (Invited) Explaining Mid-latitude E-region Plasma Instabilities, **D. T. FARLEY.**

11. **16:50-17:05** Effects of Neutral Gas Motions on Midlatitude E Region Irregular Structure, **LUDMILA KAGAN.**

12. **17:05-17:20** High Resolution MU Radar observations of Large-Scale Waves in the Lower E-region, **S. FUKAO, P. B. Rao, M. Yamamoto, A. Uchida, and I. Hassenpflug.**

13. **17:20-17:35** 30 MHz radar interferometer observations of midlatitude E region irregularities, **D. L. HYSELL and J. D. Burcham.**

14. **17:35-17:55** (Invited) On the role of neutral wind shear instabilities in seeding quasi-periodic structures in sporadic E, **M. F. LARSEN.**

15. **17:55-18:10** Observations of E Region Field-aligned Irregularities just Outside the Equatorial Electrojet Region, **J. L. CHAU, R. F. Woodman, and L. A. Flores.**

16. **18:10-18:25** Coherent radar echoes from tidal ion layers in mid-latitude E-region, **J. Urbina, E. KUDEKI, and S. Franke.**

17. **18:25-18:40** Comprehensive In-situ, TMA Trail, and Ground-based Observations in the Lower Ionosphere in the Presence of Quasi-Periodic VHF Radar Echoes, **R. PFAFF, H. Freudenreich, M. Acuna, E. Kudeki, S. Franke, J. Urbina, M. Larsen, D. Hysell, J. Clemmons, G. Earle, R. Heelis, R. Bishop, and S. Bounds.**

18. **18:40-18:55** Effect of Ion Composition on the Shape of 1D Spectrum of Sporadic-E Plasma Irregularities Generated by Neutral Air Turbulence, **Y. Kyzyurov.**

18:55-19:00 Closing Comments: **S. Fukao.**

May 21, Sunday

Poster Session 2

Chair: J. LaBelle

Session 5:

1. VHF radar observations of field aligned irregularities at 85-95 km altitude over Gadanki, **A. K. PATRA, S. Sripathi, V. Sivakumar, and P. B. Rao.**
2. Studies on the low latitude off-electrojet field aligned E region irregularities as observed by the Gadanki MST radar, **A. K. PATRA, S. Sripathi, V. Sivakumar, P. B. Rao, and K. S. Viswanathan.**
3. Nonlocal Effects on Gradient Drift Instabilities in the Equatorial Electrojet, **S. HU and A. Bhattacharjee.**
4. A Possible Spectrum of Plasma Fluctuations Caused by Neutral Turbulence in the Equatorial Ionosphere, **Y. KYZYUROV.**
5. The Pohnpei Radar Observatory, **WARNER L. ECKLUND and Roland T. Tsunoda.**
6. Large Scale Structure in the Equatorial Electrojet, **FEI LU, D. T. Farley, and W. E. Swartz.**
7. Equatorial electrojet effects in the Sudden commencement, Disturbance daily and Storm time variations of geo-magnetic storms, **R. G. RASTOGI.**

8. Latitudinal Study of the Equatorial Electrojet Using a Ship-borne VHF radar: Prelirminary results, **R. F. WOODMAN, J. Briceho, J. L. Chau, and M. F. Sarango.**

Session 6:

1. Modulation of Sporadic E Layers by Gravity Waves at Mid-Latitudes: An experimental approach, **M. N. de la Grilliere and N. Cavaciuti.**

Session 7:

1. Ionospheric irregularity zonal velocities over Cachoeira Paulista, **E. R. DE PAULA, I. J. Kantor, J. H. A. Sobral, H. Takahashi, D. C. Santana, D. Gobbi, A. F. de Medeiros, L. A. T. Limiro, H. Kil, P. M. Kintner, and M. Taylor.**
2. DE-2 observations of morningside and eveningside plasma density depletions in the equatorial ionosphere, **M. PALMROTH, H. Laakso, B. G. Fejer, and R. F. Pfaff Jr.**
3. Interaction of two long wavelength modes in the nonlinear numerical model of equatorial spread F, **R. SEKAR, E. A. Kherani, P. B. Rao, and A. K. Patra.**
4. A Study of the Ionospheric Plasma Bubbles Climatology Over Brazil for a Period of 22 Years (1977-1998), **J. H. A. SOBRAL, M. A. Abdu, H. Takahashi, M. J. Taylor, E. R. De Paula, C. J. Zamlutti, and M. G. De Aquino.**

Session 8:

1. Satellite instrumentation to image Low-Latitude, Ionospheric irregularities and Radio wave scintillations, **P. A. BERNHARDT, J. D. Huba, C. A. Selcher, S. Basu, and K. M. Groves.**

Session 9:

1. Incoherent Scatter Measurements of Aurora-Like Ion Beam Distributions and Ionospheric Holes Produced by the Space Shuttle Flying over the Radars at Jicamarca, Kwajalein, and Arecibo, **P. A. BERNHARDT, M. P. Sulzer, E. Kudeki, R.F. Woodman, and R. Tsonuda.**
2. Reaction of Equatorial Ionosphere on Forthcoming Earthquake, **Y. RUZHIN, V. N. Oraevsky, and A. Depueva.**
3. Anomaly Preseismic Thunderstorm Activity as Source of HF Earthquake Precursors, **Y. RUZHIN, C. Nomicos, and F. Vallianatos.**

May 22, Monday

Session 7: F-Region Plasma Instabilities

Conveners: D. Hysell and J. Sobral

1. **8:00-8:15** Effects of molecular ions in the night-time equatorial F region irregularities, **E. A. Kherani and R. SEKAR.**
2. **8:15-8:30** First observations of an F-region turbulent up-welling coincident with severe E-region plasma and neutral perturbations, **WESLEY E. SWARTZ, Steve Collins, Michael C. Kelley, Erhan Kudeki, Steve Franke, Julio Urbina, Michael P. Sulzer, Sixto Gonzalez, and Nestor Aponte.**
3. **8:30-8:50** (Invited) Mesoscale structure in the mid-latitude Ionosphere: A review of Caribbean observations, **M. C. KELLEY.**
4. **8:50-9:05** Band-like structures of mid-latitude F-region field-aligned irregularities regularities (FAIs) observed with the MU radar, **S. FUKAO, M. Yamamoto, and A. Saito.**
5. **9:05-9:25** (Invited) Traveling Disturbances in the Nighttime Mid-latitude F-region Ionosphere, **A. SAITO and S. Fukao.**
6. **9:25-9:40** Equatorial and tropical latitude spread F study based on ionosonde, VHF backscatter radar and radio scintillation observations, **R. G. RASTOGI.**
7. **9:40-10:00** (Invited) Electric Field Effects on Equatorial F Region Plasma irregularities, **B . G. FEJER.**
8. **10:00-10:15** Radar observations of the nighttime equatorial ionosphere at two locations in the Indian region, **K. S. V. SUBBARAO, K. S. Viswanathan, A. K. Patra, and N. Ramachandran.**
9. **10:15-10:30** Quasiperiodic Echoes from Equatorial Field-aligned Irregularities Observed over Jicamarca, **R. F. WOODMAN and J. L. Chau.**

10:30-10:45 Break

10. **10:45-11:05** (Invited) Two-Dimensional Non-linear Modeling of Equatorial Spread F, **V. ECCLES.**

11. **11:05-11:20** Production of electric field perturbations by gravity wave winds in the E region through Hall conductivity suitable for initiating equatorial spread F, **SATYA PRAKASH.**

12. **11:20-11:40** (Invited) Equatorial Spread-F Irregularities Under Disturbed Geomagnetic Conditions, **J. H. SASTRI.**

13. **11:40-11:55** Results from the Guara Campaign High-Altitude Spread F Rocket Experiment, **JAMES LABELLE, and Joerg-Micha Jahn.**

14. **11:55-12:10** Changes in ionospheric height near the magnetic equator and onset of equatorial spread-F, **TAKASHI MARUYAMA, Kenro Nozaki, and Mamoru Yamamoto.**

15. **12:10-12:25** ROCSAT-1 satellite: Characterization of ion density and velocity structures in equatorial plasma bubbles, **H. C. YEH, S. Y. Su, J. M. Wu, L. F. Lee, S. C. Yang, H. L. Chen and K. Y. Chen.**

Session 8: Diagnostics, Effects, and Prediction of F-Region Irregularities

Conveners: S. Basu and J. H. Sastri

1. **14:00-14:20** (Invited) The Space Weather Program - Recent Advances, **SU. BASU, R. A. Behnke, and R. N. Robinson.**

2. **14:20-14:35** GPS and Ionospheric Equatorial Scintillations: A Curse and A Blessing, **P. M. KINTNER, H. Kil, B. Ledvina, F. Mota, and E. de Paula.**

3. **14:35-14:50** GPS scintillations near the equatorial anomaly region over the Indian sector, **S. RAY, A. DasGupta, A. Paul, and P. Banerjee.**

4. **14:50-15:05** Magnetic Storm Activity, GPS/DMSP Observations, and the Equatorial Region, **J. Aarons, M. MENDILLO, and P. Sultan.**

5. **15:05-15:20** Spread-F Dynamics from Scintillation Observations, **A. BHATTACHARYYA.**

6. **15:20-15:35** Equatorial Bubble Development and the Source of Satellite Scintillations, **G. S. SALES, B. Reinisch, V. Paznukhov, and D. Hysell.**

7. **15:35-15:55** (Invited) Equatorial Scintillations: Current Status and Future Plans, **S. BASU.**

15:55-16:15 Break

8. **16:15-16:35** (Invited) Spread F irregularities and drifts observed with the JULIA radar, **D. L. HYSELL and J. D. Burcham.**

9. **16:35-16:55** (Invited) Low-latitude ionospheric irregularities observed by the ROCSAT-1 satellite during the 22 October 1999 geomagnetic storm, **H. C. YEH, S. Y. Su, L. F. Lee, S. C. Yang, and C. F. Ho, and R. A. Heelis.**

10. **16:55-17:10** Equatorial Ionospheric Irregularity Diagnostics by the Dynasonde, **J. W. WRIGHT and N. A. Zabotin.**

11. **17:10-17:30** (Invited) OI 630.0 nm dayglow measurements as a means to forecast the nighttime Equatorial Spread-F, **D. PALLAMRAJU and S. Chakrabarti.**

12. **17:30-17:50** (Invited) Equatorial Spread F Variabilities and Predictive Capabilities Using Ground-Based Ionosondes, **M. A. ABDU.**

13. **17:50-18:05** Forecasting Scintillation Activity in the Equatorial Ionosphere, **D. N. ANDERSON and B. Reinisch.**

May 22, Tuesday

Session 9: New Developments in Observational Techniques

Conveners: B. Clemesha and S. Gonzales

1. **8:15-8:30** A new algorithm for computation of digital ionograms, **F. ARIKAN, O. Arkan, and S. Salous.**

2. **8:30-8:45** In-Situ Techniques for Aeronomy Using Ionization Gauges, **J. H. CLEMMONS, R. F. Pfaff, and M. F. Larsen.**

3. **8:45-9:00** Time and Frequency Domain Propagation Models in the Lower and Middle Atmosphere, **F. AKLEMAN and L. Sevgi.**

4. **9:00-9:20** (Invited) Daytime Observations of the Upper Atmosphere and Ionosphere using Passive and Lidar Techniques, **D. REES.**

5. **9:20-9:35** A high Resolution Imaging Spectrograph for Daytime Airglow Studies, **SUPRIYA CHAKRABARTI, Jeffrey Baumgardner and D. Pallamraju.**

6. **9:35-9:50** Simultaneous lidar and incoherent scatter radar observations of convective structures in the D- and lower E-region, **M. F. LARSEN, M. C. Kelley and S. Collins.**

7. **9:50-10:05** Low-Latitude Ionosphere Behavior before a few Strong Earthquakes, **A. DEPUEVA and N. Rotanova.**

8. **10:05-10:20** Comparison of Ionosphere TEC above Turkey during Solar Eclipse action and before two Strong Earthquakes at 1999, **V. N. Oraevsky, Y. RUZHIN, and I. I. Shagimuratov.**

10:20-10:35 Break

9. **10:35:10:55** (Invited) Illuminating the Physics Of the Upper Atmosphere With Optical Emissions Excited by High Power HF Pump Waves, **P. A. BERNHARDT, F. T. Djuth, C. A. Tepley, M. P. Sulzer, V. Frolov, L. M. Kagan, M. C. Kelley, Francisco Garcia, J. A. Gardner, A. L. Broadfoot.**

10. **10:55-11:15** (Invited) Ionospheric radiotomography by means of stochastic inversion, **T. NYGREN, M. Lehtinen, M. Markkanen, and E. D. Tereshchenko.**

11. **11:15-11:30** (Invited) Tomographic Studies of Aeronomic Phenomena Using Radio and UV Techniques, **F. KAMALABADI, G. Bust, K. Dymond, S. Gonzalez, P. Bernhardt, S. Chakrabarti, D. Cotton, A. Stephan, R. McCoy, S. Budzien, and S. Thonnard.**

    11:30 Introductory remarks by **S. A. Gonzales** on the controversy surrounding the effect of electron Coulomb collisions on the ISR signal spectrum.

12. **11:33-11:48** (Invited) Incoherent backscatter radar measurements at Jicamarca with a beam pointed perpendicular to B, **E. KUDEKI and R. F. Woodman.**

13. **11:48-12:08** (Invited) The effect of Electron Coulomb Collisions on the Jicamarca Incoherent Scatter Spectrum: Review of Theory and Comparisons with Experimental data, **MICHAEL P. SULZER, and Sixto A. Gonzalez.**

14. **12:08-12:23** Split-beam Studies of the Effect of Electron Collisions on ISR Spectra Near k perp B, **D. T. FARLEY, W. E. Swartz, J. L. Chau and R. F. Woodman.**

    12:23-12:30 Discussion on the effect of electron collisions

Session 10: Outstanding Scientific Issues and Future Challenges

Conveners: B. Fejer and M. Kelley

1. Multi-Instrument Studies of Low Latitude F-Region Plasma Irregularities, **B. G. FEJER.**

2. (Invited) An Overview of Low-Latitude Ionospheric Models, **J. D. HUBA.**

3. (Invited) Future Developments in Equatorial Aeronomy, **M. MENDILLO.**

4. "Living With a Star" and the "Tropical Coupler" Solar-Terrestrial Probe: New Programs at NASA that Explore Equatorial Ionospheric Physics, **R. PFAFF, Jr.**

Gravity Wave Instability Dynamics and Mean-Flow Interactions in the Middle and Upper Atmosphere

Dave Fritts
Colorado Research Associates/NWRA
3380 Mitchell Lane, Boulder CO 80301

This talk will review our current understanding of instability and turbulence dynamics accompanying gravity wave propagation and dissipation in the middle and upper atmosphere. High-resolution simulations are now probing the dynamics and morphology of turbulence due to gravity wave breaking and shear instability for the first time. These results provide insights into the impact of localized turbulence on wave amplitudes and coherence and permit quantitative tests of previous theories of mixing efficiency, turbulence structure, and isotropy and of the assumptions underlying experimental inferences of wave and turbulence quantities. Also discussed will be the implications of these gravity wave and turbulence dynamics for momentum transports and mean flow forcing due to wave dissipation and momentum flux divergence with increasing altitude.

TUTORIAL ON THE LOW LATITUDE IONOSPHERE

D. N. ANDERSON (CIRES/NOAA/SEC, Boulder, Colorado)

I. Introduction

The intent of this tutorial is to present a broad overview of the physical processes operating in the low latitude ionosphere and the theoretical models that have been developed to describe this region. While the emphasis of the talk will be on the F region between 200 and 800 km, the important processes occurring in the underlying E region and the overlying topside region will also be included, however, the plasmasphere, per se, will not be discussed. The paper is divided into four sections covering 1.) Physical processes, 2.) Theoretical models, 3.) Critical low latitude ground–based and satellite–borne sensor observations and 4.) Future directions.

II. Physical Processes

The important processes that determine the ambient ionized plasma distribution in the Earth's atmosphere can generally be grouped into three categories – production, loss and transport. I use the "ambient" because this discussion is limited to the large scale (tens of kilometers) thermal ionospheric population and not small–scale features. Whether or not transport is an important process will depend on the lifetime of the ion and electron density pairs. If the plasma can be transported over significant distances, either horizontally or vertically, within this lifetime then obviously transport plays an important role.

At low latitudes the primary source of production of ionization is solar extreme ultraviolet radiation. Higher energy solar photons (shorter wavelengths) can penetrate deeper into the neutral atmosphere before they lose a significant amount of their energy. The respective wavelength limits for ionization of N2, O and O2 are 79.6 nm, 91.1 nm and 102.6 nm. Another production source in the low and mid–latitude, nighttime region comes from scattered Ly α radiation at 121.6 nm. Because the energy of these photons is below the ionization potential of atomic oxygen, this radiation can only ionize NO which has an ionization potential corresponding to 134.0 nm. Ly α contributes to maintaining the nighttime ionospheric E region and not the F region.

Loss of ionization in the Earth's atmosphere can take place by one of two processes, either by dissociative recombination where an electron recombines with a molecular ion or by radiative recombination where an electron combines with an atomic ion. In the E region of the ionosphere where NO+ and O2+ are the major ions, dissociative recombination is the major loss process.

$$NO^+ + e \rightarrow N + O^*$$

$$O_2^+ + e \rightarrow O + O^*$$

where O* means the atomic oxygen is left in an excited state, which subsequently emits a photon as it transitions to the ground state. In the F region where O+ is the dominant ion one would think that the primary loss rate would be by radiative recombination

$$O^+ + e \rightarrow O + h\nu$$

However, this reaction is much slower than dissociative recombination because it is harder to satisfy both conservation of energy and momentum, simultaneously, since there is only one product of the reaction, namely atomic oxygen. Since this reaction is slow, O+ ions are lost primarily by ion–atom interchange

$$O+ + N2 \rightarrow NO+ + N$$

$$O+ + O2 \rightarrow O2+ + O$$

and subsequent dissociative recombination of NO+ and O2+. Because the rate limiting reaction is ion–atom interchange, the loss of O+ in the F region is governed by this reaction.

Ionospheric plasma transport mechanisms fall into two general categories, transport due to non–electromagnetic forces and those due to electromagnetic forces. The principal non–electromagnetic forces in the ionospheric F region above ~ 150 km include 1.) Collisions with neutral particles, 2.) Forces due to gravity and 3.) Plasma pressure gradient forces. In addition, because the ion–neutral collision frequency is less than the ion gyro–frequency around the Earth's magnetic field lines above these altitudes, it can be shown that only the component of these non–electromagnetic forces parallel to *B* are effective in producing plasma motion along the magnetic field lines. Electromagnetic forces, on the other hand, cause plasma motion perpendicular to *B*. This electric field may be generated in the ionospheric E region or F–region through dynamo action. The magnetic field lines can be considered equipotentials so that an electric field generated in the E region will affect F region plasma causing both ions and electrons to drift in the same direction with an $E \times B / B2$ drift velocity. A more detailed description of the E and F region dynamo mechanisms will be presented in the talk.

III. Theoretical Models

Solution of the time–dependent ion (O+) continuity equation (1) gives ion densities as a function of altitude, latitude and local time. The equation expresses the time–rate–of–change of the ion and electron density within a unit volume due to 1.) an ion production rate, Pi; 2.) a loss rate, Li; and 3.) the divergence of the plasma flux through the unit volume

$$\partial Ni/\partial t + \nabla \bullet (Ni\ Vi) = Pi - Li \qquad (1)$$

The plasma velocity, Vi, is found from the momentum equation given by equation (2).

$$Ni\ mi\ dVi/dt = Ni\ mi\ g - \nabla (Ni\ k\ Ti) + e\ Ni\ (E + Vi \times B) - Ni\ mi\ vin\ (Vi - U)$$
$$- Ni\ mi\ vij\ (Vi - Vj) - Ni\ mi\ vie\ (Vi - Ve) \qquad (2)$$

Plasma acceleration, dVi/dt, is given on the left hand side and various forces exerted on the O+ ions are provided by the terms on the right hand side. Respective forces on the

right hand side are 1.) gravity, 2.) pressure gradient forces, 3.) electromagnetic forces, 4.) collisions with neutrals, 5.) collisions with other ions and 6.) collisions with electrons. A similar momentum equation exists for electrons. An excellent review article by Moffett (1979) discusses the assumptions, approximations and manipulations needed to arrive at the two components of Vi parallel and perpendicular to *B*.

$$Vi\perp = E \times B / B \bullet B; \quad Vi\parallel = U\parallel + g\parallel / \nu in - [1/(Ni\ mi\ \nu in)]\ \nabla\parallel(Ni\ k\ Ti)$$

After some rearranging the plasma continuity equation can be written

$$\partial Ni/\partial t + Vi\perp \bullet \nabla Ni = Pi - Li - \nabla \bullet (Ni\ Vi\parallel) - Ni\ \nabla \bullet Vi\perp$$

The transformations necessary to solve this linear, second order partial differential equation, numerically can be found in the review paper by Moffett (1979). State–of–the–art, low latitude ionospheric models now couple the plasma continuity equation, the momentum equation with the plasma energy equation, the neutral atmosphere and the electrodynamics of the system, self–consistently (Schunk, 1996). A description of these coupled models and their success in realistically describing the low latitude ionosphere will be discussed.

IV. Observations

Probably the most significant low latitude measurement that has furthered our understanding of equatorial dynamics and density structure has been provided by the Jicamarca incoherent scatter radar (ISR) observations in Peru. Observations of the diurnal pattern of vertical E x B drifts over the last three solar cycles has allowed theoretical modelers to carry out extensive studies of the equatorial anomaly and its dependence on solar cycle and seasonal conditions. In the Pacific sector, the incoherent scatter radar on the Kwajalein Atoll has significantly contributed to our understanding of the onset of plasma instability processes with its ability to steer the antenna in different directions thereby viewing bottom–side and the topside ionosphere in both the East–West magnetic meridian plane.

A list of other ground–based sensors, which are important contributors to our understanding of the physical processes responsible for the low latitude ionospheric structure will be discussed. These would include (1) Bottom–side digital ionospheric sounders measuring electron density profiles as a function of local time, (2) All–sky optical imagers and Fabry–Perots observing the post–sunset structure of depleted flux–tubes and the meridional and zonal neutral wind velocities, respectively, (3) Dual frequency GPS receivers obtaining the slant total electron content (TEC) between the ground and the GPS satellites in view, (4) UHF and L–Band receivers viewing both geostationary and GPS satellites measuring the scintillation amplitude S4 index and the Doppler velocities of the depleted regions as they drift eastward after sunset, (5) Magnetometers measuring the changes in the horizontal (H) component of the Earth's magnetic field due to daytime currents flowing in the ionospheric E layer.
Observations by satellite–borne sensors are particularly important because they are not limited to land areas but can supply truly global information by also covering the ocean areas. Two low–inclination satellites, AE–E and San Marco, have provided in–situ

electron and ion density values at ionospheric heights around 400 km altitude and were particularly useful in measuring both the magnitude of the electron density reduction within the depleted flux–tubes after sunset and the vertical E x B drift velocities. The sun–synchronous, DMSP (Defense Meteorological Satellite Program) satellites at 840 km contain sensors that measure the in–situ ion and electron densities and temperatures and are particularly useful in observing the low latitude inter hemispheric asymmetries in electron density due to trans–equatorial meridional neutral winds. A relatively recent satellite sensor capable of measuring the magnitude of the equatorial anomaly is the dual frequency altimeter on TOPEX, an ocean observing, polar orbiting satellite that can extract the vertical TEC values below the satellite which orbits at 1300 km. Measuring the latitude of the crests of the equatorial anomaly provides information on the strength of the vertical E x B drift velocities over ocean areas. During the talk, a more detailed discussion of these observations and their importance and usefulness will be presented including the exciting new capability of obtaining electron density profiles from the GPS/Met sensor which flew on the MicroLab1 satellite in low Earth orbit (LEO) obtaining profiles using Earth limb occultation techniques.

V. Future Directions

Finally, I shall present a few of the exciting new directions the field of low latitude ionospheric physics seems to be taking us. From the modeling standpoint, a number of groups are beginning to develop global ionospheric data assimilation models using techniques that were pioneered forty years ago when atmospheric numerical weather models were first developed. The application of these methods to Space Weather models is in its infancy and the low latitude region is particularly challenging. The future observations that make data assimilation model development possible would include the far ultraviolet imagers soon to fly on DMSP satellites and the LEO constellation of GPS/Met type sensors proposed for COSMIC (Constellation Observing System for Meteorology, Ionosphere and Climate), a joint venture between the US and Taiwan. In addition, new ISR techniques will be discussed as well as new methods for forecasting equatorial scintillation activity on a day–to–day basis. These are certainly exciting times to be celebrating the 10^{th} anniversary of the International Symposium on Equatorial Aeronomy.

VI. References

Moffett, R. J., "The equatorial anomaly in the electron density distribution of the terrestrial F–region, *Fundamentals of Cosmic Physics, 4,* 313–391, 1979

Schunk, R. W., Solar–Terrestrial Energy Program: Handbook of Ionospheric Models, August, 1996

Donald T. Farley, Appleton Prize 1996: His contributions to Equatorial Aeronomy[1]

Ronald F. Woodman
Jicamarca Radio Observatory

On the 20th URSI General Assembly, Lille, 1996, Dr. Donald T. Farley was awarded the Appleton Prize. The Appleton Prize is awarded, every three years, to distinguished Scientists in the field of Ionospheric Physics by the Council of the Royal Society on the recommendations of the Board of Officers of URSI. This Symposium is an occasion to celebrate... because Don Farley is one of us. The citation of the award reads: "For contributions to the development of the incoherent scatter radar technique and to radar studies of ionospheric plasma instabilities". We could not agree more with the Council's decision. The occasion is especially relevant considering that most of his contributions have been associated with Equatorial Aeronomy.

We will celebrate and at the same time pay homage to Don by recalling the important contributions he has made to our field. This is not an easy task, considering that we would have to review close to 40 years of very productive work. In fact his first contribution to our field was his doctoral thesis, in 1960, where he made the first quantitative study of coupling between the equatorial *E* and *F* regions of the ionosphere along the almost equipotential magnetic field lines. This work is still often referred to in our community. It shows how this coupling weakens with decreasing scale size, and has special relevance in the stabilization of *F* region equatorial irregularities.

While at Cornell, Bill Gordon had published his famous paper on Incoherent Scatter. Soon after Don's graduation, he and John Dougherty publish several theoretical papers on the subject. Ken Bowls had experimentally proven that the magnitude and spectral shape of the incoherently scattered returns did not conform to the simple intuitive predictions of Gordon. Don's theory predicted, using plasma kinetic theory, the statistical characteristics of the echoes in a very precise and rigorous way.

The importance of the ion dynamics in defining the shape of the spectra had been shown experimentally by Ken Bowls. This led, in 1960, to the construction of the Jicamarca Incoherent Scatter Observatory, near Lima, Peru, where the (magnetically induced) ion gyro–resonances could be observed, and motivated Don to include the effects of the magnetic field in his theory. Don, later on, in 1967 publishes the first detection of this resonance: the proton gyroresonance in exact accordance with the theory. He had been the theorist at the Jicamarca Observatory since 1961, but his contributions, as we will see later, were not limited to plasma theory. In fact, he became his Director in 1964. In 1967 he joins Cornell, where we find him nowadays, but still with a very close connection to Jicamarca and, thus, to Equatorial Aeronomy. Don Farley has been for many years, and still is, the PI of the National Science Foundation Cooperative Agreement that supports most of the work at Jicamarca

The power of Incoherent Scatter radars stems from its ability to measure ionic composition and plasma (electron and ion) temperatures as a remote mass spectrometer. This requires that all physical process that could affect the shape of the spectrum of the radar echo returns be taken into account. Ion collision with the neutrals is an important effect in the lower ionosphere. Farley and Dougherty theory is adjusted to include such an effect. Later, it is realized that the free electrons and ions in the lower *F* region are not necessarily at the same temperature, despite the fact that they occupy the same volume. Farley incorporates in the theory the proper practical formulae that allow the quantitative measurements of both temperatures, and from their difference the amount of solar radiation energy being dump into them, and eventually transferred to the neutral gas in the background.

As I already mentioned, Farley's contribution to the incoherent scatter field is not limited to theoretical considerations. We can claim that most of the incoherent scatter radar techniques in use by the Jicamarca radar where developed by him, some times in collaboration with his students. Many have been implemented or are also used in other Incoherent Scatter radars. There are three *classical* papers in Radio Science 4, 1969, which are basic reading for any user of Jicamarca: his papers on incoherent scatter power, Faraday rotation and correlation techniques. These include the mathematical foundations necessary to invert the measurements into the state parameters of the plasma that the technique allows. The Faraday technique allows the absolute measurement of electron densities, independent of the radar parameters that describe the radar characteristics other than the direction of the antenna beam. The correlation techniques allow the determination of temperatures and composition. They now include the use of multiple pulses at non–redundant spacing, first suggested by him and which drastically improve

the correlation estimation efficiency. He was also first to suggest the use of Barker codes to improve the altitude resolution of the measurements without much loss in sensitivity.

His combined expert knowledge of theory and practical techniques has allow him, in collaboration with his students, to make important contributions in regards to the behavior of densities, composition and temperatures at the magnetic equator and other latitudes. This is, of course the reason why the incoherent scatter observatories where created and the reason we have, here at this symposium, an interest in them. We should also mention one important non–equatorial contribution of his: the measurement of counter–streaming velocities of the H^+ and O^+ ions along the magnetic field above Arecibo.

But radars are not limited to study incoherently scatter returns. The ionosphere is full of irregularities and instabilities capable to produce electron density fluctuations and hence very efficient scatters. In most cases the scattering crossections are so large that one does not require the large power and antenna sizes required by the former. The equatorial ionosphere is a very interesting example in this regard. Farley's name is associated with the two most known types of ionospheric irregularities: *E* region equatorial irregularities, related to the electrojet, and *F* region ones related with the equatorial Spread *F*. He, in collaboration with his students and colleagues, has made important contributions to both, from a theoretical and experimental point of view.

There are two types of irregularities present at the equatorial E–region. They are associated with two types of instabilities: two–stream and gradient–drift. Don was the first in presenting a proper kinetic theory that explains the physical mechanism responsible for the first. He did so in a paper in 1963 that became a *Current Content* 'Citation Classic' in 1981 and won a Dept. of Commerce award. The two–stream instability is now known as the Farley–Buneman instability (Buneman described the same instability using a fluid approach). The instability is a true universal type plasma instability that depends only on the local conditions described in a differential volume of the plasma. It occurs whenever the electron drift velocity with respect to that of the ions matches the ion acoustic velocity in a way that resembles the growth of an ocean wave whenever the wind matches the phase velocity of an ocean surface gravity wave. The gradient drift velocity is also driven by the relative drift of the electrons, but requires the existence of a transverse background plasma density gradient, since involves the convection of higher (lower) density plasma into regions of lower (higher) density.

F region equatorial irregularities where first reported by Booker in 1938 using the Huancayo ionosonde. Because of the "spread" nature of the echo traces it produces in an ionogram the phenomenon is known as equatorial Spread *F*. Since the early days of Jicamarca the same irregularities manifested themselves as very strong echoes in the radar, a nuisance that interfered with the Incoherent Scatter signals. Farley and colleagues wrote the first paper that made use of this "clutter" to infer properties of this signals and showed that all of the existing theories at the time (almost 40 years after their discovery) had problems: they did not conformed with the observed properties.

Again, as in the Incoherent–Scatter case, Don has made important contributions in the development of sophisticated radar techniques to observe the equatorial ionospheric irregularities. He was involved, with Mario Ierkic and Bela Fejer, in the development of the "frequency labeled" interferometer technique. It was first used to identify and track the vertical and transverse motion of "hot spots" in the instabilities of the *E* region. This was the first of the now more powerful imaging techniques, which are being used for the imaging of both E– and F–region structure of the irregularities.

Using very precise and careful interferometric experiments, in collaboration with Erhan Kudeki and Dave Hysell, he has measured the extremely high aspect sensitivities of *E* and *F* region irregularities. In the case of the *F* region, the aspect sensitivity was found to be of the order of 0.01 degrees! (A difficult experiment to perform) thereby ruling out some theories.

I have concentrated on his contributions of interest to the Equatorial Aeronomy community, but Don has been active in other latitudes as well. They can be easily identified by the title on the following partial list of a selected set of his more than 120 publications. I am sure the Equatorial Aeronomy community would appreciate to have this list handy. The list should also partially complement the many omissions made –-because of the limitations in time and space–- of other important contributions of his. It should also give proper credit to his collaborators. For a more complete list, I refer the reader to the Cornell web pages (http://www.ee.cornell.edu/faculty/Farley/Farley.html or http://www.jro.igp.gob.pe/farley.html)

Last but not least, Don is not only a good scientist but also a good athlete. Those in the Aeronomy community that jog or run can get good advice from Don on how to run, regardless of age, the Boston or the New York Marathon. In fact, one further contribution of his to the Jicamarca Observatory

is the development of the antenna periphery into a nice N* 1200–meter running course. The emphasis here is on the value of N.

Selected list of publications:

Farley, D.T., Jr., A theory of electrostatic fields in a horizontally stratified ionosphere subject to a vertical magnetic field, *J. Geophys. Res.*, 64, 1225--1233, 1959.

Farley, D.T., Jr., A theory of electrostatic fields in the ionosphere at nonpolar geomagnetic latitudes, *J. Geophys. Res.*, 65, 869--877, 1960.

Dougherty, J.P., and D.T. Farley, A theory of incoherent scattering of radio waves by a plasma, *Proc. Roy. Soc. London*, A, 259, 79--99, 1960.

Farley, D.T., J.P. Dougherty, and D.W. Barron, A theory of incoherent scattering of radio waves by a plasma, II. Scattering in a magnetic field, *Proc. Roy. Soc. London*, A, 263, 238--258, 1961.

Dougherty, J.P., and D.T. Farley, Jr., A theory of incoherent scattering of radio waves by a plasma, 3. Scattering in a partly ionized gas, *J. Geophys. Res.*, 68, 5473--5486, 1963.

Farley, D.T., Jr., A plasma instability resulting in field-aligned irregularities in the ionosphere, *J. Geophys. Res.*, 68, 6083--6097, 1963.

Farley, D.T., Jr., The effect of Coulomb collisions on incoherent scattering of radio waves by a plasma, *J. Geophys. Res.*, 69, 197--200, 1964.

Farley, D.T., Jr. A theory of incoherent scattering of radio waves by plasma 4. The effect of unequal ion and electron temperatures, *J. Geophys. Res.*, 71, 4091--4098, 1966.

Farley, D.T., Ionospheric temperature and composition measurements at the magnetic equator, Annales de Geophysique, 22, 448--453, 1966.

Farley, D.T., Proton gyro-resonance observed in incoherent scattering from the ionosphere, Phys. Fluids, 10, 1584--1586, 1967.

Farley, D.T., Incoherent scatter correlation function measurements, *Radio Sci.*, 4, 935--953, 1969.

Farley, D.T., Incoherent scattering at radio frequencies, *J. Atmos. Terr. Phys.*, 32, 693--704, 1970.

Farley, D.T., B.B. Balsley, R.F. Woodman, and J.P. McClure, Equatorial spread F: implications of VHF radar observations, *J. Geophys. Res.*, 75, 7199--7216, 1970.

Farley, D.T., Radio wave scattering from the ionosphere, Chapter 14 in Methods of Experimental Physics; Volume 9B (R. Lovberg and H. Greim, eds.), Academic Press, 1971.

Balsley, B.B., and D.T. Farley, Radar studies of the equatorial electrojet at three frequencies, *J. Geophys. Res.*, 76, 8341--8351, 1971.

Farley, D.T., Multiple pulse incoherent scatter correlation function measurements, *Radio Sci.*, 7, 661--666, 1972.

Ioannidis, G., and D.T. Farley, Incoherent scatter observations at Arecibo using compressed pulses, *Radio Sci.*, 7, 763--766, 1972.

Farley, D.T., and B.B. Balsley, Instabilities in the equatorial electrojet, *J. Geophys. Res.*, 78, 227--239, 1973.

Hagen, J.B., and D.T. Farley, Digital correlation techniques in radio science, *Radio Sci.*, 9, 775--784, 1973.

Fejer, B.G., D.T. Farley, B.B. Balsley, and R.F. Woodman, Vertical structure of the VHF backscattering region in the equatorial electrojet and the gradient-drift instability, *J. Geophys. Res.*, 80, 1313--1324, 1975.

Farley, D.T., and B.G. Fejer, The effect of the gradient drift term on type 1-electrojet irregularities, *J. Geophys. Res.*, 80, 3087--3090, 1975.

Vickrey, J.F., W.E. Swartz, and D.T. Farley, Incoherent scatter measurements of ion counter-streaming, *Geophys. Res. Lett.*, 3, 217--220, 1976.

Farley, D.T., B.G. Fejer, and B.B. Balsley, Radar observations of two-dimensional turbulence in the equatorial electrojet, 3. Nighttime observations of type 1 waves, *J. Geophys. Res.*, 83, 5625--5632, 1978.

Farley, D.T., H.M. Ierkic, and B.G. Fejer, Radar interferometry: A new technique for studying plasma turbulence in the ionosphere, *J. Geophys. Res.*, 86, 1467--1472, 1981.

Farley, D.T., H.M. Ierkic, and B.G. Fejer, The absolute scattering cross section at 50 MHz of equatorial electrojet irregularities, *J. Geophys. Res.*, 86, 1569--1575, 1981.

Farley, D.T., C. LaHoz, and B.G. Fejer, Studies of the self-focusing instability at Arecibo, *J. Geophys. Res.*, 88, 2093--2102, 1983.

Farley, D.T., Theory of equatorial electrojet plasma waves: New developments and current status, *J. Atmos. Terr. Phys.*, 47, 729--744, 1985.

Providakes, J., D.T. Farley, W.E. Swartz, and D. Riggin, Plasma irregularities associated with a morning auroral arc: Radar interferometer observations and theory, *J. Geophys. Res.*, 90, 7513--7523, 1985.

Fejer, B.G., J. Providakes, D.T. Farley, and W.E. Swartz, Auroral E region plasma waves and elevated electron temperatures, *J. Geophys. Res.*, 91, 13,583--13,592, 1986.

Farley, D.T., E. Bonelli, B.G. Fejer, and M.F. Larsen, The prereversal enhancement of the zonal electric field in the equatorial ionosphere, *J. Geophys. Res.*, 91, 13,723--13,728, 1986.

Kudeki, E., and D.T. Farley, Aspect sensitivity of equatorial electrojet irregularities and theoretical implications, *J. Geophys. Res.*, 94, 426--434, 1989.Farley, Donald, and Jason Providakes, The variation with Te and Ti of the velocity of unstable ionospheric two-stream waves, *J. Geophys. Res.*, 94, 15,415--15,420, 1989.

Sahr, J.D., D.T. Farley, W.E. Swartz, and J.F. Providakes, The altitude of type 3 auroral irregularities: Radar interferometer observations and implications, *J. Geophys. Res.*, 96, 17,805--17,811, 1991.

Farley, D.T., W.E. Swartz, D.L. Hysell, and C. Ronchi, High-resolution radar observations of daytime kilometer-scale wave structure in the equatorial electrojet, *J. Geophys. Res.*, 99, 299--307, 1994.

Farley, D.T., and D.L. Hysell, Radar measurements of very small aspect angles in the equatorial ionosphere, *J. Geophys. Res.*, 101, 5177--5184, 1996.

Farley, D.T., Theories of auroral electrojet instabilities, Proceedings of a Workshop held at the Max-Planck-Institut fur Aeronomie in Katlenburg-Lindau, Germany, 24--26 October 1995 (K. Schlegel, ed.), 111--114, Cuvillier Verlag, Gottingen, 1996.

Farley, D.T., Incoherent scatter radar probing, Chap. 14 (pp 415--439) in Modern Radio Science (H. Kohl, R. Ruster, and K. Schlegel, eds.), European Geophys. Society, Katlenburg-Lindau, FRG, 1996.

Haldoupis, C., D. T. Farley, and K. Schlegel, Type-1 echoes from the mid-latitude E-region ionosphere, *Ann. Geophys.*, 15, 908-917, 1997.

Aponte, N., W. E. Swartz, and D. T. Farley, Electron energy balance in the F-region above Jicamarca, *Geophys. Res. Lett* ., 104, 10,041--10,049, 1999.

Ronald Woodman's Contributions to Radio Science

D. T. FARLEY (School of Electrical Engineering, Cornell University, Ithaca, NY)

Woodman is an enormously creative scientist who has made major contributions to a wide range of topics related to radar probing of the upper atmosphere. In this review of his work I will try to touch on most of the highlights, with perhaps a little extra emphasis on topics of interest to this Symposium. Topics that I hope to cover in this talk include:

- **Incoherent scatter**. Woodman's 1967 Harvard PhD thesis was the first theory to explain exactly how ion–ion collisions affect the ion gyro–resonance. He developed a unique way of doing the numerical calculations that did not run into trouble for **k** nearly perpendicular to **B**. This work was never published in the open literature (!), but it is now being used again in some studies of the effect of *electron* collisions on the incoherent scatter spectrum near **k** perpendicular to **B**. This effect has been neglected in all routine analyses of IS spectra to date, but it may be important for observations at Jicamarca (as will be discussed in other talks at this Symposium). Woodman and Hagfors [1969] pioneered the extremely accurate measurements of plasma drift velocity at Jicamarca. Recent substantial refinements were made by Kudeki, Bhattacharyya, and Woodman [1998]. The technique permits us to measure ionospheric electric fields (via $\mathbf{V} = \mathbf{E} \times \mathbf{B}/B^2$) to an accuracy of better than 20 μV/m over a wide range of equatorial altitudes (and hence latitudes via field line mapping). These observations are the basis of most studies of low latitude ionospheric electrodynamics.
- **Equatorial spread–F (ESF)**. The 1976 paper by Woodman and LaHoz, and especially the 3–layer "bubble" diagram, provided the breakthrough idea for how the Rayleigh–Taylor instability generates the ESF "plumes" that are seen by radar and in–situ, and that are related to satellite signal scintillations. He made the first observa–tions of "explosive" ESF and its relation to lightning.
- **Radar interferometry and imaging**. Woodman pioneered the use of radar interfer–ometry in ionospheric studies, starting with a measurement in 1971 that very precisely determined the magnetic dip angle above Jicamarca. This same measure–ment, repeated from time to time, has allowed us to monitor the change in dip of a few tenths of a degree that have occurred since 1971. This technique and its more recent extensions to include Doppler sorting and multi–baseline radar imaging are now used by many in studies of E– and F–region plasma instabilities at the equator, in the auroral zone, and most recently even at mid–latitudes.
- **MST radar**. Woodman created the entire field of MST (mesosphere, stratosphere, troposphere) wind profile measurements with VHF radars with two 1974 papers. He recognized that the "clutter" echoes seen at short ranges with incoherent scatter radars were actually signals that could be utilized. A large network of wind profilers now exists throughout the world because of this insight. These profilers study mean winds, tides, and gravity waves and transport (especially in the mesosphere). Woodman and collaborators made the first direct radar measurements of vertical velocity in the neutral atmosphere. Another less obvious spinoff is research on PMSE (polar mesosphere summer echoes), which were first seen by such radars. Woodman has made many important contributions through the years to the

techniques used in MST work (e.g., pulse compression codes; see below) and to the analysis of MST data. One of particular interest is the idea of "post–statistics beam steering."

- **Pulse compression codes**. Woodman was the first to realize that complementary codes could provide a powerful pulse compression tool for observations in the stratosphere (where correlation times are long). He used 64–baud codes with the Arecibo 430 MHz radar, giving a compression ratio of 64:1 with no range sidelobes. He also used cyclic codes (1023:1) with the Arecibo S–band radar to study stratospheric turbulence and transport with an altitude resolution of 15 m. Complementary codes are now widely used at other radars. Woodman also applied these ideas to HF partial reflection measurements.
- **Antarctic PMSE**. Woodman developed the radar for, and led the Peruvian expedition that made, the first PMSE observations in the Southern Hemisphere. There is less PMSE in Antarctica than in the northern hemisphere, which suggests a temperature asymmetry that has global change implications. In 1998 he put a 50 MHz radar on a Peruvian ship to measure the latitude dependence of both PMSE and equatorial plasma instability echoes.

Other topics that should be mentioned include work on mid–latitude sporadic E and fundamental radar observing concepts, and there are certainly more. But perhaps as important as his written work is what he has *not* written, namely what he has contributed to others in conversations. Those who know Ron know that he loves to talk science–with anyone about almost anything. Whether it is ionospheric physics, RF electronics, electromagnetic theory, radar techniques, seismology, archeology in Peru, El Niño and its history in Peru, tree rings, radar data analysis, the formation of strange triangularly shaped rocks in the desert near Paracas, Peruvian politics, or the pros and cons of various email programs and why we should accept the inevitable and go with Microsoft–Ron always has something to say that is worth listening to, even if you don't agree with him. Many of us at this Symposium have had good ideas that arose out of conversations with Ron, ideas that we would not have had otherwise.

Some references

Below are a few selected references in abbreviated notation, organized roughly by topic.

Incoherent scatter:
Woodman, Harvard PhD thesis, 1967. (theory with magnetic field0
Woodman and Hagfors, JGR, 74, 1205, 1969. (measuring $\mathbf{V}_\perp$ accurately)
Woodman, JGR, 75, 6249, 1970. (equatorial vertical velocities and zonal **E** fields)
Woodman, JGR, 76, 178, 1971. (inclination of **B** using interferometry)
Kudeki et al., JGR, *104*, 28145, 1999. (better way to measure $\mathbf{V}_\perp$)

Equatorial spread F:
Woodman and La Hoz, JGR, 81, 5447, 1976. (observations, bubble idea)
Woodman and Kudeki, GRL, 11, 1165, 1984. (lightning and explosive ESF)
Hysell and Woodman, RS, 32, 2309, 1997. (imaging obs. of ESF)

MST radar:
Woodman and Guillen, J.Atmos.Sci., *31*, 491, 1974. ("clutter" is really signal)
Rastogi and Woodman, JATP, *36*, 1217, 1974. (mesosphere obs. at Jicamarca)
Harper and Woodman, JATP, *39*, 959, 1977. (more mesosphere obs at Jicamarca)
Woodman, JATP, *39*, 941. 1977. (equatorial mesospheric winds)
Sato and Woodman, JAS, *39*, 2539 and 2546, 1982. (winds, waves, turb. at Arecibo)
Woodman and Rastogi, GRL, *11*, 243, 1984. (eddy diffusion coefs. from radar obs.)

Pulse compression:
Woodman, RS, *15*, 417, 1980. (Arecibo 430 MHz stratospheric obs.)
Woodman, RS, *15*, 423, 1980. (Arecibo S–band stratospheric obs.)
Gonzales and Woodman, RS, *19*, 871, 1984. (HF probing of the mesosphere)
Sulzer and Woodman, RS, *20*, 337, 1984. (quasi–complementary codes)

PMSE:
Woodman et al., JGR, *104*, 22577, 1999. (first observations of PMSE in Antarctica)

Mid–latitude Es instabilities:
Woodman, Yamamoto, and Fukao, GRL, *7*, 1197, 1991. (gravity wave modulation)

Radar techniques:
Woodman, JGR, *96*, 7911, 1991. (general theory for atmospheric and ionospheric radars)
Woodman, RS, *32*, 2373, 1997. (coherent radar imaging)
Sato and Woodman, RS, *17*, 817, 1982. (spectral parameter estimation for CAT echoes)
Woodman, RS, *20*, 1185, 1985. (spectral moment estimation)
Kudeki and Woodman, RS, *25*, 591, 1990. (post statistics beam steering for MST)
Woodman, RS, *30*, 1459, 1995. (true velocity in full correlation analysis)

Introduction to El Niño Phenomena:

A Peruvian Perspective†

R. F. Woodman
Instituto Geofísico del Perú, Lima, February, 2000

The recent interest in El Niño Phenomenon stems from: 1) our better understanding of the physical processes involved, which in turn has made possible its early prediction, 2) the realization that it affects the climate at a global scale, and 3), its unusual recent intense episodes and their higher frequency of occurrence. The behavior of El Niño during the 1997-98 cycle was successfully predicted with six or more months in advance. From an equatorial eastern-Pacific point of view, more specifically from the long tradition and historical records available in Piura, Peru (~5°S, 79°W), the 1997-98 and the 1982-83 El Niño have been the strongest recorded in the last 470 years, i.e., since the Spanish foundation of the city.

Piura is the oldest post-Hispanic city in the whole South American continent and the most sensitive to El Niño related climatic variations. While the phenomena has only recently caught the attention of the world, its existence was well known by the local population. In fact, the name, El Niño (Christ Child), was coined by the fishermen of the area, with the believe that the warm waters associated with the phenomena came with the northern current which appeared around Christmas time. The author was born and brought up in Piura. This may explain of why an upper-atmospheric physicist has been invited to give a talk on the subject.

Climatologists have come to realize that, after the well known seasonal variations, the most important "predictable" climatic variations are the inter-annual ones related to El Niño. Its statistical signature can be observed far beyond the coastal areas around the equatorial Pacific and includes the effects on the climate of the Australian and whole American continent, the Asian monsoons and the frequency and intensity of hurricanes in the Caribbean, to mention a few .

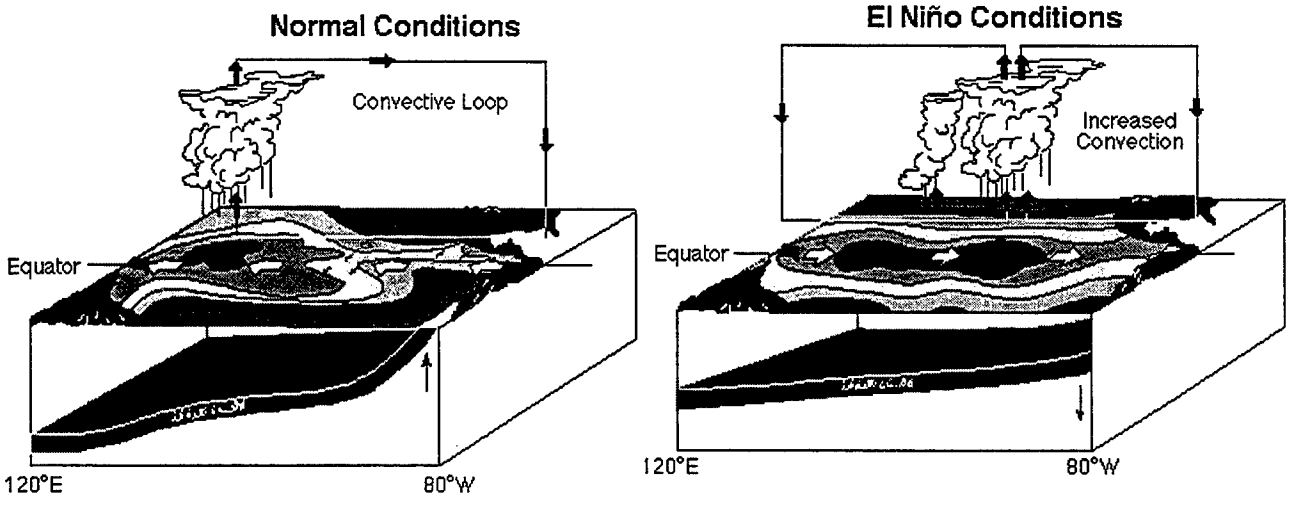


Figure 1. Schematic diagram of SST's during Normal and El Niño conditions

Tropospheric and oceanographic phenomena has not been included as a research topic of Equatorial Aeronomy nor of ISEA in particular. But, considering El Niño's current importance, both from a geophysical as well as political point of view, and because of its equatorial nature, the ISEA Organizing

Committee has considered appropriate to include an introduction in this symposium. In fact, I hope we will discuss in this opportunity the formal inclusion of this subject in future International Equatorial Symposia. I doubt there is already a better forum than ISEA to gather atmospheric scientists from equatorial countries, especially developing countries. And El Niño is indeed an equatorial phenomena. With no further justification, we should certainly start looking, as a research topic, for statistical signatures in the upper atmosphere that correlate with El Niño .

In this talk I will make a short introduction to El Niño- Southern Oscillation (ENSO) as a global phenomena and present more specific and regional features of the phenomena, namely its principal manifestations along coastal Peru.

Figure 1 shows a schematic diagram of Sea Surface Temperature (SST) in the Pacific Ocean under two conditions: during El Niño or ENSO's Warm-phase, and during Normal conditions, which does not deviate much from the Cold-phase, now known as La Niña. The normal situation can be easily accepted on physical grounds. The warmest SST's are in the equatorial region where the solar radiation is a maximum and where there is a convergence of the solar heated superficial waters. The surface winds play an important role in the SST distribution and they in turn are affected by this distribution in a coupled atmospheric-oceanic process. Warmer SST temperatures produce atmospheric convective instabilities and, thus, heavy rains. The associated water vapor condensation process deposit the solar energy in the atmosphere above the warmest sea surface, producing an atmospheric upwelling which is accompanied by a convergence of surface airs coming from north and south of the equator. The coriolis forces produce the large circulation cells in the north and south Pacific, with prevailing easterly winds in the equatorial belt. The convergent component of the winds produce convergence of warm waters, as mentioned before, and the easterly component sweep the warm waters from the eastern equatorial Pacific to the western Pacific where they accumulate. This explains the strong gradient in temperature along the equator increasing toward the west. Accompanying the warmer western SST there is a deepening of the thermocline (the surface that separates the warmer superficial waters from the cooler deep oceanic ones). One can say that there is a deep pool of warm waters in the western equatorial Pacific produced and maintained by the easterly equatorial winds. Above this warm pool we have the strongest vertical convection of the whole globe. It is also the region of highest precipitation and its maintain there by the positive feedback mechanism just described.

The above situation is not completely stable. There are fluctuations as in all weather processes. If the eastern winds weaken there is a shift of the location of highest SST and precipitation. The shift is dynamic with some inertia. The deep warm waters try to reach its static equilibrium level and propagate in

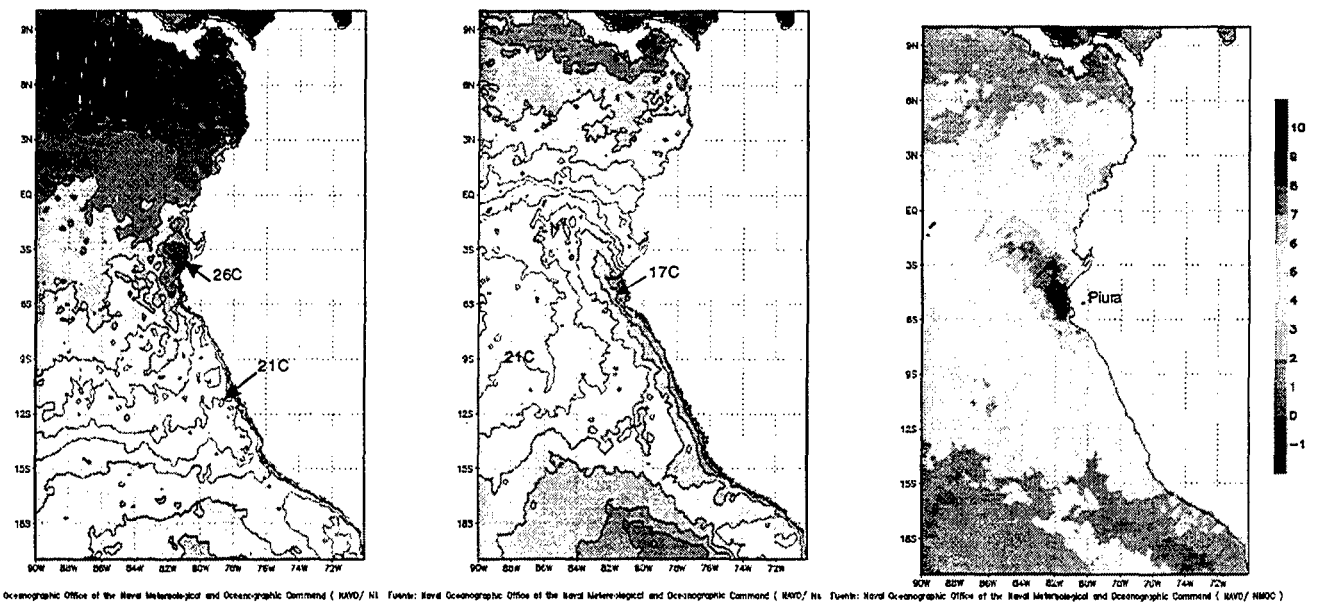


Figure2. a) SST's for the last week of November of 1997, b) the same for 1998, c) difference between the two previous conditions: El Niño minus La Niña

a (Kelvin) wave fashion towards the east, shifting the center of precipitation towards the east. The easterly wind weakens. When this disturbance is sufficiently strong the center of precipitation moves to the central Pacific, the warm waters reach by inertia the east coast, new precipitation cells form in the east and the easterly winds can even reverse in direction with a further positive feedback effect. A situation as the one depicted in Figure 1b develops, and we say we have El Niño conditions. The whole event takes about a year. When it comes to normality it usually overshoots into a extreme cold condition.

The large shift in the center of precipitation is an important energetic disturbance of the atmosphere as a whole and its effects propagate much beyond the equatorial Pacific region. These disturbances are responsible for the change in the climate in regions far away from the direct and more local influence of the SST of the equatorial Pacific. One of the large atmospheric manifestations of this disturbance was studied independently and was known as the Southern Oscillations (SO) and it is characterized by a few-year-scale deviations in the difference of the atmospheric pressure at Darwin and Tahiti. Now we know that this oscillation is a manifestation of the same global phenomena, and when we want to stress the global oceanic and atmospheric effects of El Niño (EN), we refer to it as ENSO.

As mentioned before, one of the most ---if not the most— sensitive regions in the whole world to El Niño is the northern coast of Peru southern coast of Ecuador, including the desert region around Piura, in particular. Figure 2a) shows the SST in front of Peru during the last week of November for the El Niño conditions of 1997 (temperatures became higher later, in the austral summer months) and the La Niña conditions of 1998 (panel b). The third panel shows the differences between these two states. I doubt there is any other region in the world where the temperature for the same time of the year can vary as much as shown in the depicted region. It shows differences of more than 9°C. More local thermometer measurements in the port of Paita, in front of the difference maximum, register differences as high as 12-13°C.

The effects of the variations in SST in front of the northern coast of Peru are dramatic. This region goes from being one of the driest desert regions of the world to precipitation regimes that are comparable with the wettest tropics. The average rainfall around Piura is 50mm a year, including normal El Niño events which occur every 5-7 years. During El Niño of 1982-83 it recorded close to 3000mm in the rainy season. It rained in three months more than the accumulated amount of 25 years. Never in its 470 years of written history had occurred rains as heavy and with such a long lasting duration. But in less than 15 years another equally devastating El Niño occurred: the 1997-98 event.

During normal years the coastal Peruvian SST are cold, 15 to 22°C, depending on latitude and season. These cold temperatures are a consequence of the upwelling of cold deep oceanic waters in front of the coast. The upwelling is a consequence of the prevailing winds which blow parallel to the coast from south to north. The wind stress is therefore also parallel to the wind direction, but the coriolis force produce a surface current response with an off-shore component. The divergence produced by this component forces the deep and cooler waters to replace the surface waters that have moved off-shore. As a consequence, the airs that cover the coast are cooled by their contact with these cool oceanic waters. They are humid and heavy. Aloft, we find warmer, drier and lighter airs which have not had any contact with the ocean. The contact between these two masses of air is almost discontinuous, producing a strong stabilizing temperature inversion with a temperature increase which can be as high as 15°C. This inversion prevents the convection necessary for rain to occur. As a consequence it does not rain and the Peruvian coast is a desert. On the other hand, the same (mineral rich) ocean upwelling responsible for this condition is the cause of the large fish population in front of the Peruvian shores, one of the riches fishing grounds in the world.

During El Niño conditions, warm equatorial waters from the west invade the Peruvian coast. In the northern coast they can reach 28-29°C with a thermocline as deep as 200 meters. Upwelling continues but the deep waters are warm as well (and nutrient poor). The atmospheric inversion layer disappears and the climatic conditions of these region does not differ much from normal maritime tropical conditions. Precipitation occurs at the same level of any tropical island. The mineral rich cold waters do not make it to the sunlight exposed surface, photosynthesis is poor, and the whole fish food chain collapses.

The dependence of precipitation on SST in front of the coast can be put in quantitative terms. Figure 3a shows the monthly average discharge of the Piura river. The Piura river basin includes the desert area around the city and the low western mountainous slopes of the Andes. In Figure 3b we show the accumulated monthly precipitation in the city of Piura. Both figures show the last eighteen years for which accurate SST satellite measurements are available. In the same figures we have plotted the result of a multivariable regression fits to the variation of SST in a selected number of points about 50 to 100km from

the coast. The month of the year has also been included as an input variable. The agreement is impressive. It is so good that suggests the use of the Piura river discharge or the precipitation over the city as a proxy index for the El Niño intensity, with the advantage that there are instrumental records for the last 75 years, and qualitative and semi-quantitative ones for the last 470 years.

Considering the success in predicting SST's in the equatorial Pacific several months in advance, the close correlation between this variable and precipitation opens the possibility of predicting the climate in the northern Peruvian coast with the same anticipation, a very difficult task in any other part of the world. Unfortunately, the important chain of oceanic and meteorological instruments displayed by the TOGA program stops at the Galapagos Is. and the fine structure of the upwelling is to fine for the coarse resolution of the current numerical predictive models. Thus, the performance of the models is not as good in this parts of the Pacific as they are in the 120-170°W longitudes. Scientific Peruvian institutions, the Instituto Geofísico del Perú included, are embarked in a project to correct these deficiencies and develop regional numerical models that would improve upon the global predictions of El Niño related SST deviations.

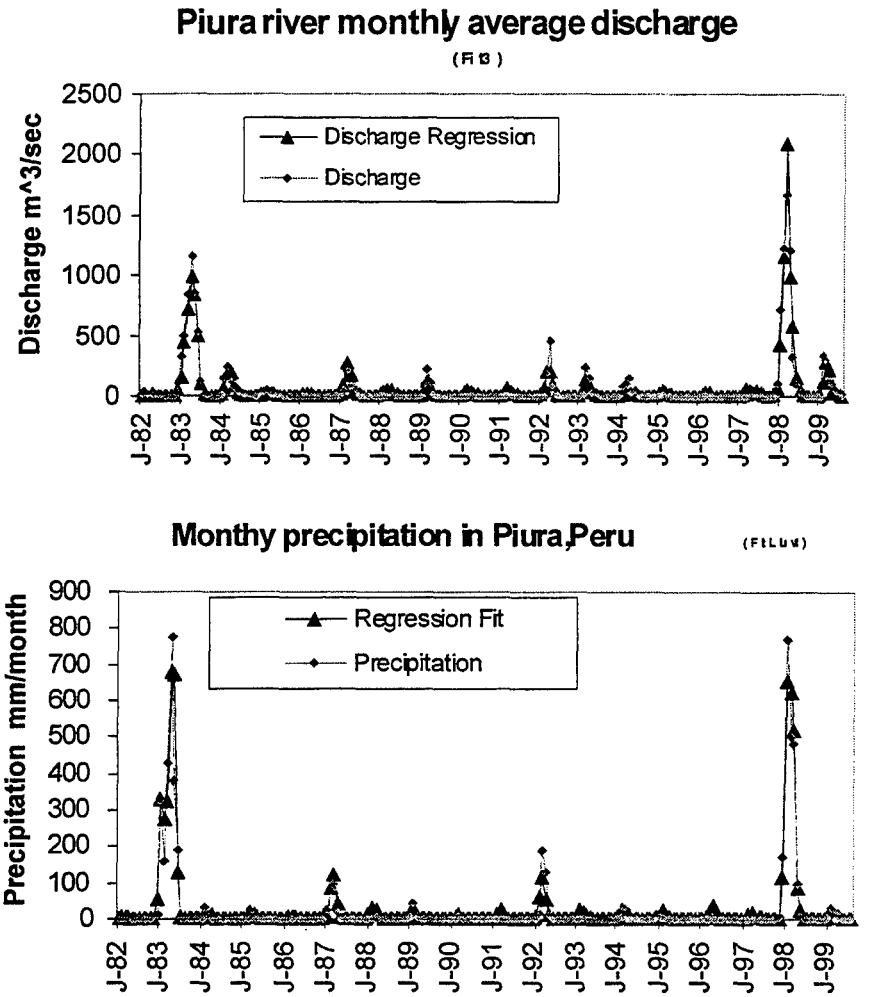


Figure 3a and b. As indicated

† Invited paper, International Symposium of Equatorial Aeronomy, Antalya, Turkey, 17-23 March, 2000

In situ sensing of atmospheric properties in the boundary layer and lower troposphere at low latitudes.

BEN B. BALSLEY, CIRES, University of Colorado, Boulder, CO 80309
Michael L. Jensen, CIRES, University of Colorado, Boulder, CO, 80309

Extended Abstract:

Long–term, continuous, high–resolution sampling of any quantity throughout the first few km of the atmosphere is difficult to accomplish anywhere in the world. It is particularly difficult to achieve at tropical latitudes. The factors that limit extensive measurements of atmospheric quantities in the tropics involve primarily the large expanses of inaccessible oceans and tropical forests. This limitation is further complicated by a general lack of usable facilities (i.e., research sites, small airports, weather stations, etc.) in the developing countries that largely comprise this region.

There is, on the other hand, a clear need for improved understanding of transport and dynamic properties in the tropical boundary layer and lower troposphere. The coupling of energy and chemical processes from the earth's surface to the free troposphere is achieved via mixing in the boundary layer and entrainment at the interface between top of the boundary layer and the lower troposphere. Thus, with increasing interest in global climate change––a phenomenon largely related to tropical processes––an enhanced understanding of these mixing/entrainment processes is vital.

Typically, in situ boundary layer measurements have been achieved through the use of instruments located on high towers, low–flying aircraft, and balloonsondes. Remote sensing of the region is accomplished using lidars, sodars, and boundary layer radars. Each of these technologies provides a unique set of measurements over a somewhat limited height range. One of the outstanding measurement problems, particularly for in situ sampling of both dynamic and chemical processes, is to obtain long–term data sets in the upper part of the region, e.g., between roughly 500–1500 m. The purpose of the present contribution is to outline the potential of so–called tethered lifting systems, or TLS, for obtaining these measurements.

The use of TLS (e.g., kites, balloons, and/or blimps) to measure many variables in the earth's lower atmosphere has a long, and an all but forgotten history. For example, between roughly 1885 and 1930 the lion's share of our knowledge of upper air temperature, humidity, and wind was obtained by lofting instruments beneath one or more tandemed kites. The last decade has seen a renaissance of this technology, which now incorporates state–of–the–art materials and high–tech instrumentation.

Briefly, TLS can be either land–based or ocean–based. On land, one needs only a relatively clear site that can support a small winching system energized by either a generator, a battery, or a gas engine. TLS operates equally well, or perhaps better, from the deck of a boat, provided that the operator has control of the speed and direction of the boat. Under reasonable wind conditions, the operator would use a parafoil kite (10 m^2 to 20 m^2) as a TLS platform. In the absence of sufficient winds, the use of a balloon or an aerodynamic–shaped blimp would be dictated. In either case, it is reasonable to expect that the TLS would lift a minimum payload of 10 kg to heights in excess of 1 km, and should remain there for hours to days. Vertical profiling is achieved in a number of ways. The simplest technique is to raise the TLS platform from ground to the desired height, then bring it down again, repeating the process as often as needed. An alternate method is to suspend instruments in series beneath the platform to achieve the desired height profile. A third technique involves the use of a wind–powered TRAM (Tethered Rover for Atmospheric Measurements) that travels up and down the tether under radio control, carrying the instrument payload.

Typical instrumentation for TLS measurements is limited primarily by weight: currently TLS can loft any instrument weighing less than about 5–10 kg, including batteries. Data can either be stored aboard or telemetered down to a ground station using high–frequency modems. To date, instruments lofted by TLS have made high–spatial–resolution measurements of wind, temperature, humidity, pressure, and high–time–resolution measurements of velocity and temperature fluctuations associated with atmospheric turbulence and wave and instability structures. Profiles of a large number of trace gas quantities have also been measured (e.g., CO, CO_2, ozone, methane, hydrogen, non–methane hydrocarbons, as well as carbon–13 and oxygen–18 ratios). Additional TLS–measured profiles include such esoteric quantities as supersonic bat calls and insect population densities.

We present here the basic concepts of TLS, touch briefly on the history of the technology, and outline a number of advantages of using TLS for atmospheric research in the tropics.

Layered disturbances associated with low potential vorticity revealed by high-resolution radiosonde observation in Japan

Kaoru Sato (National Institute of Polar Research, Kaga 1-9-10, Itabashi, Tokyo 173–8515, Japan. Email:kaoru@nipr.ac.jp) and Timothy J. Dunkerton (Northwest Research Associates, P.O.Box 3027, Bellevue, WA 98009, U.S.A.)

1 Introduction

Horizontal wind and temperature data obtained from operational high-resolution radiosonde observation over Japan have recently been available. By analyzing the data over 4 years, it is found that clear layered structure in horizontal winds appears frequently in winter at several stations simultaneously. The layered disturbances are dominant in the height region between 8 and 16 km corresponding to the tropical and midlatitude tropopauses, respectively. Using NCEP reanalysis data, the background field of layered disturbances is examined in detail and a backward trajectory analysis is made to see the origin of the disturbances.

2 Existence of layered disturbances

Figure 1a shows a time-height section of meridional winds v at Naha (26.2N, 127.7E) in the time period of 20 December, 1995 through 10 January, 1996. Dots show the tropopause levels estimated from vertical profiles of temperature by radiosondes. The tropopause is located at two levels, namely about 16 km (20–30 December and 3–10 January) and about 6 km (30 December to 3 January). Strong and shallow northward winds are observed below the upper tropopause level continuously from 25 December to 10 January. To see the layered structure more clearly, we extracted fluctuations using a bandpass filter with cutoff lengths of 1.5 and 6 km in the vertical and a lowpass filter with a cutoff length of 2 days in time, which hereafter we refer to v' component. The time-height section for v' at Naha is shown in Fig. 1b. The Layered structure is clear in the height region between the upper and lower tropopause and large positive v' values greater than 7m $s^{-1}$are seen around 13 km. Figures 1c and 1d show time-height sections of v' at Ishigakijima (24.3N, 124.2E) and Chichijima (27.1N, 142.2E) located at almost the same latitude as Naha. Similar layered disturbances are seen at both stations for almost the same time period. Judged from the similarity of the structure and the timing of occurrence, it is inferred that the layered disturbances observed at these three stations are due to the same event.

We made EOF analysis for v' time series at all 18 stations in Japan in winter of 4 years from 1995 through 1999, and found that there are two dominant EOF components. One component (EOF1) has large amplitudes in the latitude region of 30–40N and the other (EOF2) is to the south of 30N (Fig. 2). Hereafter we call EOF1 (EOF2) time periods for when EOF1 (EOF2) component takes large positive (larger than s.t.d.) values.

3 Background fields and source of layered disturbances

The background field is examined for each EOF time period using radiosonde data and NCEP reanalysis data. A difference between the two EOF periods is the position of the midlatitude jet, which is located slightly more poleward in EOF1 time periods than in EOF2 time periods. Another interesting and important feature is that Ertel's potential vorticity (PV) is very small and sometimes negative around 25N in EOF2 time periods. This fact suggests that the EOF2 disturbances are due to inertial instability. Phase difference between zonal and meridional wind components is also consistent with this inference. On the other hand, PV in EOF1 time periods is low but scarcely negative. Thus, the layered disturbances in EOF1 periods are probably due to neutral waves such as gravity waves.

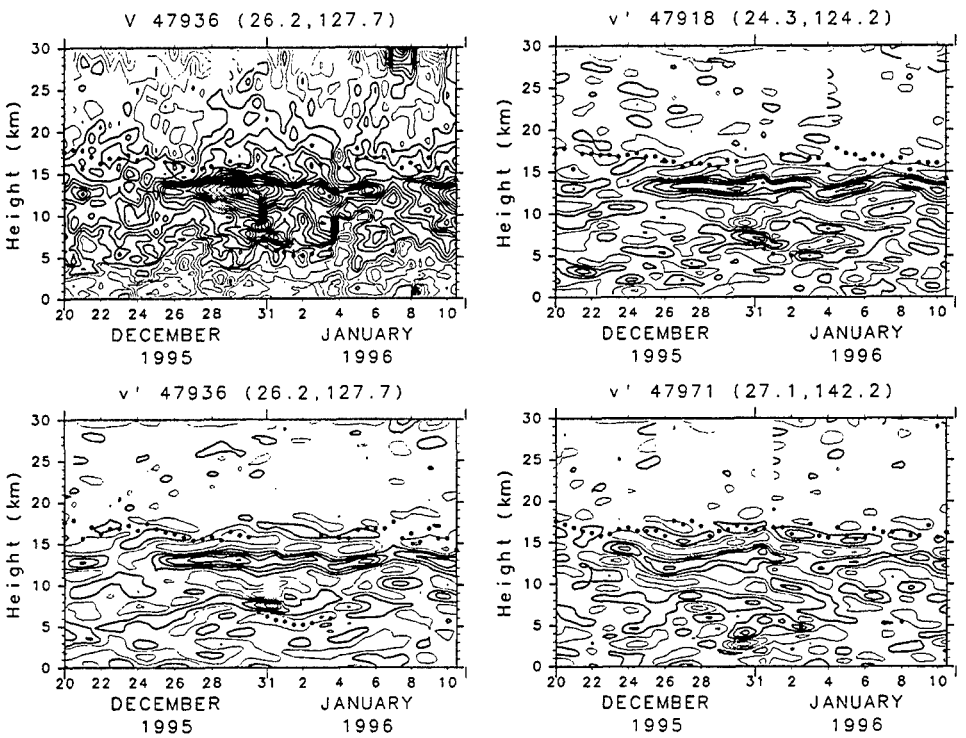


Figure 1: Time-height sections for the time period of December 20, 1995 to January 10, 1996 of (a) unfiltered meridional winds at Naha (26.2N, 127.7E), and layered disturbances at (b) Naha, (c) Ishigakijima (24.3N, 124.2E), and (d) Chichijima (27.1N, 142.2E). Contour intervals are 3m s^{-1}($\cdots$, -7.5, -4.5, -1.5, 1.5, 4.5, 7.5, $\cdots$) for (a) and 2m s^{-1}($\cdots$, -5, -3, -1, 1, 3, $\cdots$) for (b), (c) and (d). Thin (thick) contours show negative (positive) values. Dots indicate the tropopause levels.

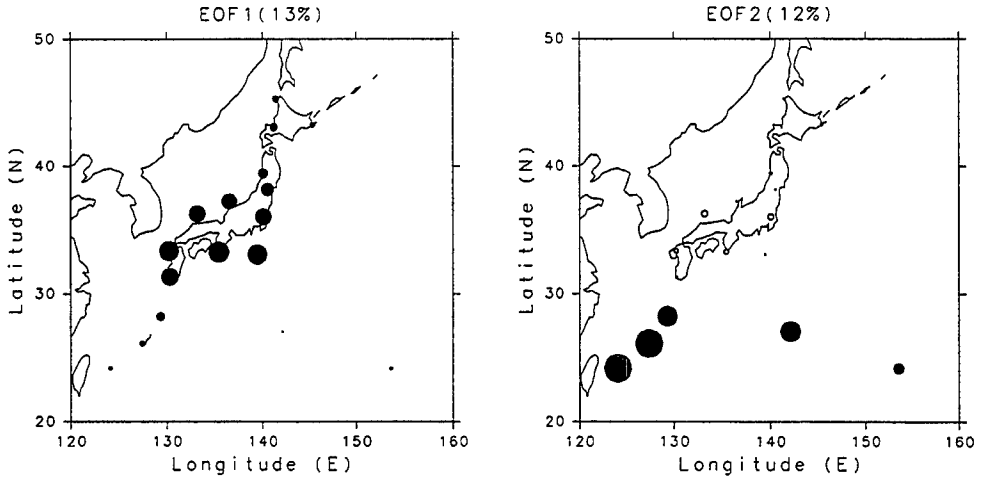


Figure 2: A pattern of (a) EOF1 and (2) EOF2 components. Positive and negative values are indicated by closed and open circles, respectively.

4 Origin of low potential vorticity air

Horizontal distribution of negative PV air is examined on a θ=345K surface (corresponding to an altitude of 10 km) where the layered disturbances are dominant. Figure 3 shows a contour map of the percentage of time when negative PV is observed in winter. It is seen that high percentage area in the northern hemisphere extends from the equator to higher latitudes in the South America to Indian Ocean (80W–80E) and intrudes to the subtropical region around 25N in 80–160E in East Asia.

To see the origin of the low potential vorticity around 25N to the south of Japan, a backward trajectory analysis was made. Figure 4a shows an example of results of trajectory analysis for the EOF2 time period as in Fig. 1. Only trajectories started at stations with large EOF2 values on 27 December 1995 are plotted. Intervals of dots at each trajectory show a time interval of 1 day. All trajectories can be traced back to the latitude region lower than 10N to the south of Japan in a few days.

Figure. 4b show PV (shading) and Montgomery stream function (contours) averaged for the time period of 20–27 December 1995. Lightly and darkly shaded are the regions with negative PV and PV smaller than 0.1 PVU, respectively. Low potential vorticity is observed around a latitude of 27N where stations with EOF2 disturbances are located. The PV values in this region are frequently negative during this time period. It should be noted that a dashed contour of stream function is almost zonal at longitudes of 120E–180E around 20N and is curved largely around 120E because of strong northward winds associated with Hadley circulation. The trajectories shown in Fig. 4a coincide roughly with this dashed stream function contour.

On the other hand, stations with EOF1 disturbances are located around the jet stream latitude (35N) and the trajectories are almost zonal and traced back to far westward (not shown).

Thus, it is concluded that the origins of air in which EOF1 and EOF2 disturbances are embeded are different. A statistical analysis of backward trajectories indicates that the former one is mostly in the midlatitude region far west of Japan, while the latter is mostly in the equatorial region south of Japan.

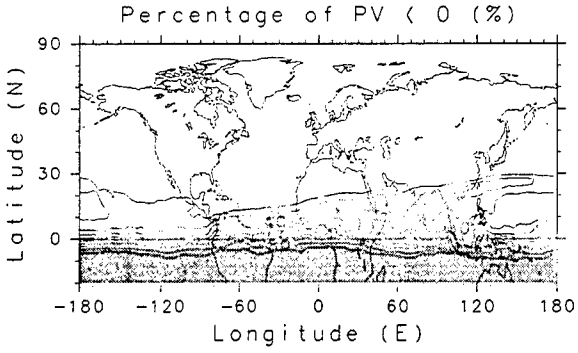


Figure 3: A contour map of the percentage of cases when potential vorticity is negative at each grid point in winter periods. Contour intervals are 10%. The regions with values greater than 20% are shaded.

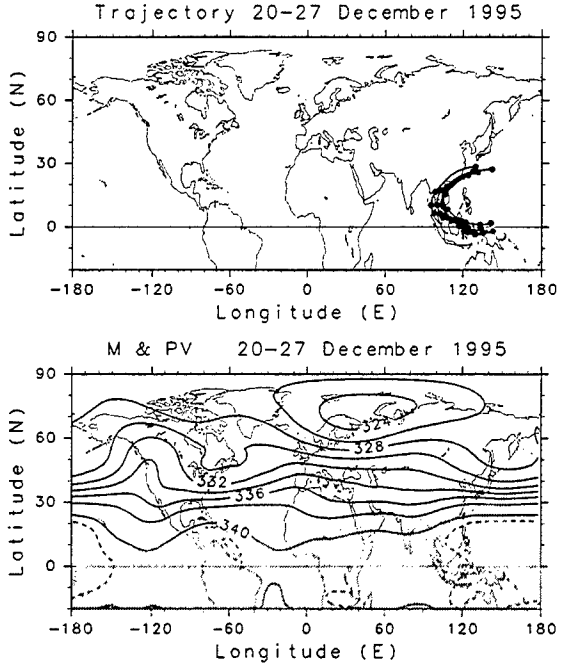


Figure 4: (a) Backward trajectories starting at EOF2 stations at 00Z 27 December, 1995. The distance between dots in each trajectory corresponds to 1 day. (b) A contour map of Montgomery stream function averaged for 20–27 December, 1995. Contour intervals are 10^3 m^2s^{-2}. Dashed curves are the contours of $340.5\times10^3 m^2s^{-2}$. Darkly (lightly) shaded are the region with negative potential vorticity (smaller than 0.1PVU)

Jicamarca Radar Observations of Gravity Waves and the Diurnal Tide in the Troposphere and Lower Stratosphere

Dennis M. Riggin[1], Erhan KUDEKI[2], Robert G. Stockwell[1], Zhaomei Feng[2], and Martin F. Sarango[3]

[1](Colorado Research Associates/NWRA, Boulder, Colorado.)
[2](Department of Electrical and Computer Engineering, University of Illinois, Urbana.)
[3](Instituto Geofisico del Perú, Jicamarca Radio Observatory, Lima, Perú.)

This paper presents Doppler wind measurements from a 10-day experiment in August 1998 with the mesosphere-stratosphere-troposphere (MST) radar at Jicamarca, Perú (11.95°S, 76.87°W). The radar was operated with four beams, 2.5° off vertical, pointing north, south, east and west. Horizontal and vertical winds were measured with 450 m height resolution over a height range of ~8–24 km. The main focus of this experiment was the measurement of momentum fluxes due to gravity waves. As shown in Figure 1, the measurements were made during a period of weak horizontal winds ($\lesssim$2 m s^{-1} up to 14 km), and stable conditions.

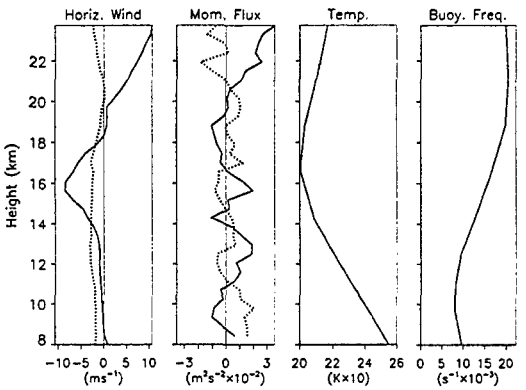


Figure 1: Profiles of eastward (solid line) and northward (dotted line) mean wind and momentum flux averaged over 10 days as computed from Jicamarca radar data. Profiles of temperature and buoyancy frequency as derived from NCEP/NCAR Reanalysis data.

The 10-day averaged zonal and meridional momentum fluxes ($u'w'$ and $v'w'$) in Figure 1 were computed from high-pass filtered (band edge of 36 hr) products of the u, v fields and the w field. The momentum flux profiles shown in Figure 1 are weak and fluctuate with altitude. Nonetheless, geophysical rather than statistical fluctuations appear to dominate since there is considerable height-to-height continuity in the momentum flux estimates. Also shown in Figure 1 are 10-day mean values of buoyancy frequency derived from NCEP/NCAR Reanalysis data. The buoyancy period was ~13 min at 10 km decreasing to ~5 min at 20 km. The tropopause was at ~16 km throughout the campaign, according to the Reanalysis data.

Power spectra of the horizontal and vertical wind fluctuations are shown in Figure 2. The buoyancy peaks in the vertical wind spectra are at $\sim 2\times10^{-8}$ m^{2}s^{-1}. This power spectral density is clearly above the noise level and corresponds to a velocity of ~0.003 m s^{-1} which gives an indication of the radar sensitivity. Since buoyancy waves are not seen at lower levels, their excitation may be associated with the higher static stability above the tropopause. At all heights the spectra also show peaks at periods of ~24 hr in the horizontal and vertical winds. Figure 3 shows spectral

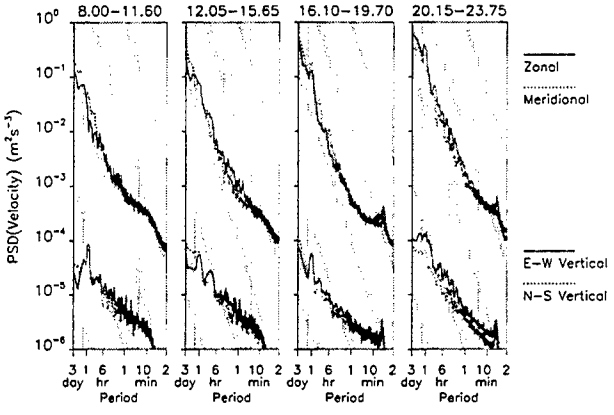


Figure 2: Power spectra of the zonal (solid) and meridional (dashed) winds and power spectra of vertical winds estimated from the sum of the east/west beams (solid) and north/south beams (dashed). Top labels denote height ranges in km.

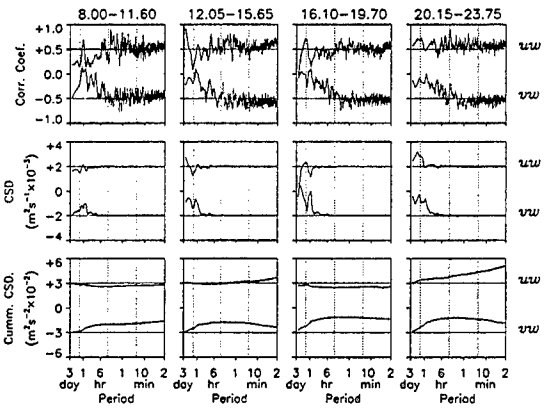


Figure 3: Top row: correlation coefficients between horizontal and vertical wind spectra. Middle panels: show spectral covariance. Bottom row: cummulative distribution of CSD. Spectra are offset from zero for visibility.

representations of spectral momentum flux in various forms. The middle row of panels shows the covariance spectral density (CSD) over four different height ranges. The cospectra and correlation coefficients are averaged over 9 heights and then smoothed with a running boxcar proportional to $f^{1/2}$ as was done in Figure 2. The top row of panels shows the signed correlation coefficients (r) between horizontal and vertical components, defined (e.g., for the zonal component) as

$$r(f) = \frac{< \mathrm{Re}\,(F_u(f)F_w^*(f)) >}{< |F_u(f)||F_w^*(f)| >} \tag{1}$$

Here, the asterisk denotes complex conjugate, "Re" means the real part, and the angular brackets indicate averaging, in this case averages over the nine heights. The correlation coefficients link the auto-spectra of Figure 2 to the cospectra of Figure 3. The $v'w'$ cospectra are dominated by a positive diurnal peak, corresponding to a northward flux. A much smaller negative peak is present in the $u'w'$ cospectra, corresponding to a westward flux. The diurnal peaks are generally more pronounced in the cospectra than in the corresponding autospectra, because the correlation coefficients are relatively high at the diurnal period. Although the CSD's appear to be completely dominated by low frequencies, higher frequencies contribute more to the momentum flux than might be suspected. This is shown by the cumulative CSD's in the bottom panels of Figure 3. At ranges of 12.05–15.65 km and 20.15–23.75 km, periods less than 10 min make a non-negligible contribution to the $u'w'$ momentum flux. Shear is nearly absent in the meridional mean wind profile (Figure 1) and the $v'w'$ cumulative CSD's change little with height. In contrast, the $u'w'$ cumulative CSD's change significantly with height. Although weak, the zonal wind shear appears sufficient to influence the gravity wave spectrum.

Below the tropopause (8.00–15.65 km), the horizontal component PSD peaks in Figure 2 are separated from the vertical component peaks by only $\sim$1000 $\mathrm{m^2 s^{-1}}$, corresponding to a ratio of

$\sim$30 in velocity. The frequency dependence of the horizontal velocity spectra is reasonably consistent with the canonical $f^{-5/3}$ gravity wave spectrum (c.f. grey diagonal stripes). However, the vertical spectra are nearly as steep and are inconsistent with the $f^{+1/3}$ canonical slope predicted in the absence of mean wind Doppler shifting [*Fritts and VanZandt,* 1987]. Doppler shifting does not explain the redness of the vertical wind spectra because the mean wind was weak. Instead we suggest that the vertical wind fluctuations were dominated by convective motions rather than gravity waves. Figure 4 shows these convective motions clearly. The winds in this Figure are

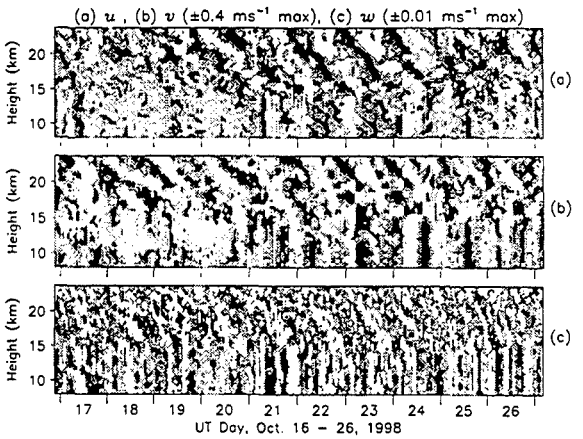


Figure 4: Hourly averaged zonal wind (a), meridional wind (b), and vertical wind (c) are shown high-pass filtered with a 36 hr band edge. The three level grey-scale saturates at $\pm 0.4\,\mathrm{m\,s^{-1}}$ for the horizontal wind components and $\pm 0.01\,\mathrm{m\,s^{-1}}$ for the vertical. Wind values below the negative saturation level (values above the positive saturation level) are denoted by black (white), respectively.

high-pass filtered with band edge at 36 hr (the same filter as used for the momentum fluxes in Figure 3). Below $\sim$16 km, there is no vertical phase variation in the motions. The alternating updrafts and downdrafts in the vertical wind component presumably correspond to convective motions with small horizontal scales. Coherent wave activity was mostly absent in the troposphere, although a wave with $\sim$8 hr period is visible at lower altitudes in the u-component during August 22–23 (see Figure 4(a)). Above the tropopause ($\sim$16 km), the tide is more coherent and begins propagating vertically.

Tidal signatures similar to those we observed at Jicamarca have been reported by *Tsuda et al.* [1995; 1997] from radiosonde observations at several western equatorial Pacific sites and by *Williams and Avery* [1996] from tropical Pacific wind profilers. The tidal wind over Jicamarca had peak amplitudes of $\sim 1\,\mathrm{m\,s^{-1}}$, increasing somewhat above the tropopause, consistent with the previous studies. The tidal phases reported from these other studies had a complicated and irregular vertical structure. These phase estimates were based on 24-hr period sinusoidal fits to the data. However, our observations at higher time resolution show little vertical phase variation for the dominant quasi-diurnal motions below the tropopause. Instead, the phase is irregular because the motions themselves are somewhat incoherent, i.e., the spectrum is broadly peaked around the diurnal period.

The conditions during the August 1998 10-day Jicamarca campaign were perhaps atypical of the tropical troposphere/lower stratosphere. During previous 10-day campaigns [e.g., *Riggin et al.,* 1997], the dominant motions in the troposphere and lower stratosphere were inertia-gravity waves. These waves had periods of 1.5–2.1 days, vertical wavelengths of $\sim$3–5 km and inferred horizontal scales of $\sim$500–1000 km. The more extensive radiosonde data records similarly show quite small ($\sim$2–3 km) vertical scales for inertia-gravity waves [*Tsuda et al.,* 1994; *Shimizu and*

Tsuda, 1997; *Vincent and Alexander,* 2000]. These wavelengths are much shorter than the tidal vertical wavelengths observed by us and by *Tsuda et al.* [1995; 1997] in the stratosphere. Inertia-gravity waves are usually observed to propagate throughout much of the troposphere and into the lower stratosphere without the abrupt change in vertical scale that we observed for the tidal motions.

Measurements were only made during daytime hours during earlier experiments at Jicamarca and these data gaps made tidal observations impossible. Therefore, the seasonal dependence of tidal amplitudes at Jicamarca is not yet known. However, the tidal amplitudes we observed are similar to amplitudes observed by *Tsuda et al.,* [1997], which were in turn consistent with a tidal model. There are few direct observations of the tide in the tropical lower stratosphere, because it is usually swamped by inertia-gravity waves, and also because radiosonde data records often lack sufficient time resolution. Compared to typical inertia-gravity waves, tidal amplitudes are weak in the lower stratosphere. However, the relative importance of the tide is likely to increase with height. The tide's larger horizontal phase speed and longer vertical wavelength makes it less susceptible to critical layer absorption and diffusive damping. In the absence of frontal activity or precipitating clouds (conditions which pertain to the Jicamarca campaign) the source spectrum corresponding to convective motions is probably fairly isotropic in the horizontal plane. The mean winds were too weak to do much filtering of the convectively excited waves. This may explain why the 10-day averaged momentum flux was observed to be so weak. Waves with periods longer than 6 hr were the main contributor to the momentum flux.

Acknowlegments. The help provided by the Jicamarca Radio Observatory staff is gratefully acknowledged. This research was supported by the National Science Foundation under grant ATM-9709030.

References

Fritts, D. C., and T. E. VanZandt, Effects of Doppler shifting on the frequency spectra of atmospheric gravity waves, *J. Geophys. Res., 92,* 9723–9732, 1987.

Riggin, D., D. C. Fritts, C. D. Fawcett, E. Kudeki, M. H. Hitchman, Radar observations of gravity waves over Jicamarca, Peru during the CADRE campaign, *J. Geophys. Res., , 102,* 26,263–26,281, 1997.

Shimizu, A., T. Tsuda, Characteristics of Kelvin and gravity waves observed with radiosondes over Indonesia, *J. Geophys. Res., 102,* 26,159–16,171, 1997.

Tsuda, T., Y. Murayama, H. Wiryosumarto, S. W. B. Harijono, and S. Kato, Radiosonde observations of equatorial atmosphere dynamics over Indonesia, 2, Characteristics of gravity waves *J. Geophys. Res., 99,* 10,507–10,516, 1994.

Tsuda, T., et al., A preliminary report on observations of equatorial atmosphere dynamics in Indonesia with radars and radiosondes, *J. Meteorol. Soc. Jpn., 73,* 393–406, 1995.

Tsuda, T., N. Nakamura, A. Shimizu, T. Yoshino, S. Woro, B. Harijono, T. Sribimawati, H. Wiryosumarto, Observations of diurnal oscillations with a meteor wind radar and radiosondes in Indonesia, *J. Geophys. Res., 102,* 26,217–26,224, 1997.

Vincent, R. A., M. J. Alexander, Gravity waves in the tropical lower stratosphere: An observational study of seasonal and interannual variability, Submitted to *J. Geophys. Res.,* 1999.

LOWER AND MIDDLE ATMOSPHERIC TEMPERATURE STUDIES USING RADIOSONDE, LIDAR AND UARS-HALOE DATA OVER CHUNG LI

J.B.NEE, W.N.Chen and S.Thulasiraman
Department of Physics, National Central University, Chung Li 32054, Taiwan

Abstract

The lower and middle atmospheric thermal structure is studied using the radiosonde and Nd:YAG lidar data. A good match between the lower limit of Lidar data and upper limit of radiosonde data is found. Comparison of Lidar temperature with UARS-HALOE data shows HALOE temperatures are less by about 5K at the stratopause and lower mesospheric region. Mesospheric inversion around 70 km is present in most of the Lidar temperature profile.

Introduction

The study of temperature structure of different atmospheric regions is important for understanding the atmospheric dynamics, which will be useful in climate studies. The lower atmospheric temperature structure is usually studied with a number of radiosonde stations around the world. The middle and upper atmospheric temperature structure can be studied using limited in-situ and remote sensing techniques. Studying middle and upper atmospheric temperature is bit complicated because of lack of techniques, since the balloons could reach only up to 35 km altitude levels and the Radars are blind in the 30-60 km region. In the past, the use of Sounding Rockets (Schmidlin, 1969) is the only way to get the middle atmospheric temperature information. Then with the introduction of LIDAR technique, the temperature profile of the middle atmosphere is obtained with good height and time resolution. The only drawback with this technique is that it is obtained at a single point and needs a clear sky weather condition. On the other hand, the use of satellites can provide good spatial and temporal coverage routinely with a reasonable height resolution, however, the uncertainties in the estimation should be understood clearly. The validation of satellite data using lidars around the globe will make the satellite data useful for the study of middle atmospheric dynamics on a global scale. The successful launch and operation of the Upper Atmospheric Research Satellite (UARS) and the HALOE payload provides a good database for the middle atmospheric temperatures.

Experiment and Methodology

In the present study, we have used the radiosonde, lidar and HALOE data in order to study the variations in the tropospheric, stratospheric and mesospheric temperatures. The radiosonde site is at Pan Chiao which is around 30 km from Chung Li. The LIDAR data used in the present study is from NCU Lidar being operated at the Physics Department, National Central University, Chung Li (25^0N, 121^0E), Taiwan. The Nd:YAG Lidar consists of a YAG laser at 532 nm (Spectra Physics, model GCR-4-30) operating at 30 Hz. The laser beam is steered into the vertical direction by a motor

controlled mirror mounted on an optical bench. The receiver consists of a 17.5 inch Newtonian type telescope. A photomultiplier tube with a narrow band interference filter (FWHM 3 nm) was employed as the detector. The photon counting signals were sent to a multichannel analyser (MCA, Stanford Instrument SR 430) for signal analysis. The results are then sent to a PC486 for storage and further analysis. The aerosol content above 30 km is negligible and the backscattered signal strength can be completely attributed to molecular atmosphere. The molecular density can be from the backscattered signal and the temperature profile can be computed assuming the atmosphere obeys the perfect gas law. The detailed information on the system is available Nee et al. (1995) and temperature retrieval is available in Hauchecorne and Chanin (1980).

HALOE uses the occultation of the Sun by the limb of the earth's atmosphere to measure vertical profiles of transmission in eight infrared bands. Transmission profiles measured in the 2.80 μm CO_2 band play an essential part in processing the HALOE measurements. Profiles of limb path atmospheric transmission in the 2.80 μm CO_2 band are obtained by ratioing the endoatmospheric signal profile to the exoatmospheric signal. Since the transmission is a ratio of two signals, which are measured using the same instrument optical-electrical path, the measurement is considered self-calibrating. The temperature and pressure retrieval starts at a level near 35 km and works in a bottom up procedure, similar to Mill and Drayson (1978), to altitudes where signal-to-noise limitations terminate the retrieval (about 85 km). A detailed description of the temperature retrieval procedure is given by Hervig et al. (1996).

Results and Discussion

A typical lower and middle atmospheric temperature profile using radiosonde and lidar data is shown in Figure 1. It can be seen that the overlapping region of measurements by radiosonde and lidar around 30 km matches well. This kind of matching is seen in almost all of the days when we have lidar data. HALOE makes limited latitude coverage measurements during the sunset and sunrise time. Thus the temperature profile over any particular location is limited to one or two profiles per month. The data when satellite passes over Taiwan is used for the comparison with Lidar data. The HALOE sunrise profile for 21 May 1993 is shown in Figure 2. The 0000 GMT (0800 LT) radiosonde data obtained at Pan Chiao is also plotted in the same figure. It can be seen that the uppermost radiosonde data and lowermost HALOE data matches well. This is expected, because the HALOE inferred profile makes a gradual transition from measured one to NMC from 45 to 35 km and below 35 km, it is strictly NMC.

For the intercomparison of the HALOE profile with the Nd:YAG Lidar profile, coincidence profiles were chosen for maximum spatial separations of 2^0 latitude, 20^0 longitude and time separation of 48 hours. Global circulations generally determine greater variability in latitude than in longitude and the stability of the stratosphere ensures that the time variations are slow. The coincidence criterion is therefore used with minimum latitude separations. Similar criteria is used by Hervig et al. (1996) to validate the HALOE data with Lidar and Rocket data. Figure 3 shows an example of the HALOE and Lidar profile comparisons. The radiosonde data of 4th November 1994, 00 00 GMT is

also plotted. It can be seen that the tropopause lies around 17.5 km and the radiosonde profile perfectly matches at the bottom of the HALOE and Lidar profiles within the error limits. The Lidar profile shows little deviation from the HALOE profile data in the upper stratosphere and lower mesospheric regions. The Lidar temperatures are more by 2K in the upper stratosphere and 5K more near stratopause and lower mesospheric regions. Hervig et al. (1996) also found similar kind of differences of 5K below 65 km in their comparisons. Another interesting point is that the stratopause is clearly shown by both HALOE and Lidar at the same altitude but with different temperatures. Also the mesospheric inversion is observed around 71 km by lidar and 73 km by HALOE. This kind of inversion is observed in many locations around the globe. The annual variation of the middle atmospheric temperature structure and the stratopause variations were also studied and the results will be presented.

Acknowledgement: We thank the National Space Program Office, Taiwan for providing financial assistance through NSC89-NSPO(3)-ISUAL-FA0901.

Reference:

Hauchecorne, A and M.L.Chanin, 1980. *Geophys. Res. Lett,* 7, 565-568.

Hervig, M.E., et al., 1996. *J. of Geophys. Res,* 101, 10277-10285.

Mill, J.D., and S.R. Drayson, 1978. A non linear technique for inverting limb absorption profiles, in *Remote sensing of the Atmosphere: Inversion Methods and Applications,* edited by A.L. Fymat and V.E. Zuev, Elsevier Sci., New York.

Nee, J.B., G.B.Wang, P.C.Lee and S.B.Lin, 1995. *Radio Science*, 30, 1167-1175.

Schmidlin, F.J., 1976. *Geophys. Res. Lett.,* 3, 173-176.

Figure 1. Temperature profile on 24 Apr'96

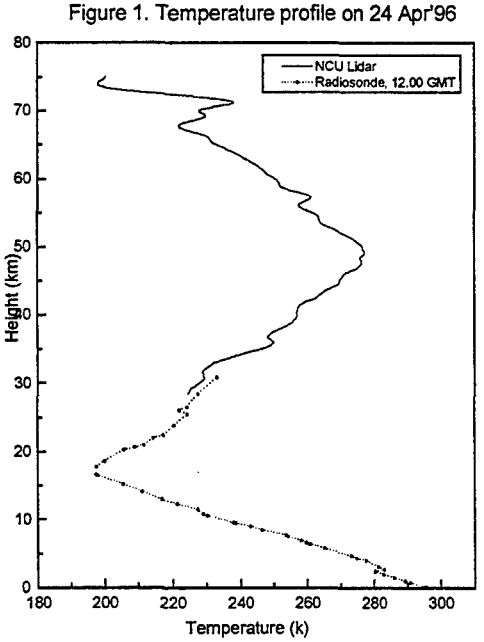


Fig.2 Temperature profile on 21 May 1993 using Radiosonde and HALOE d

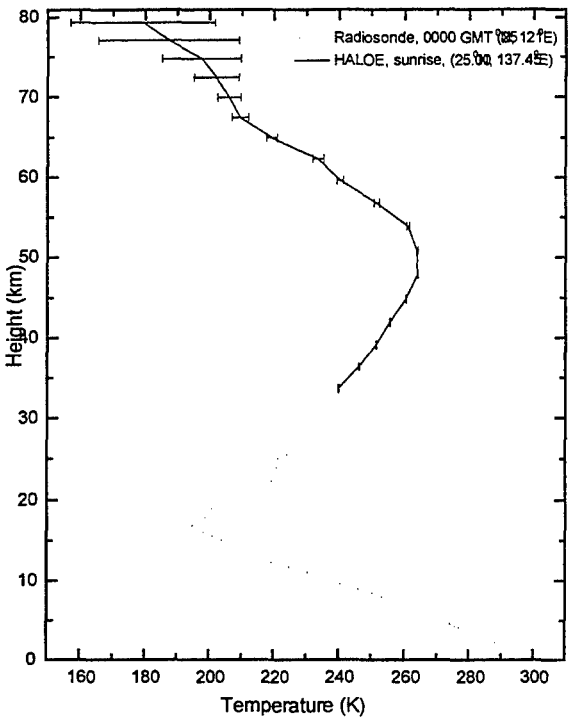
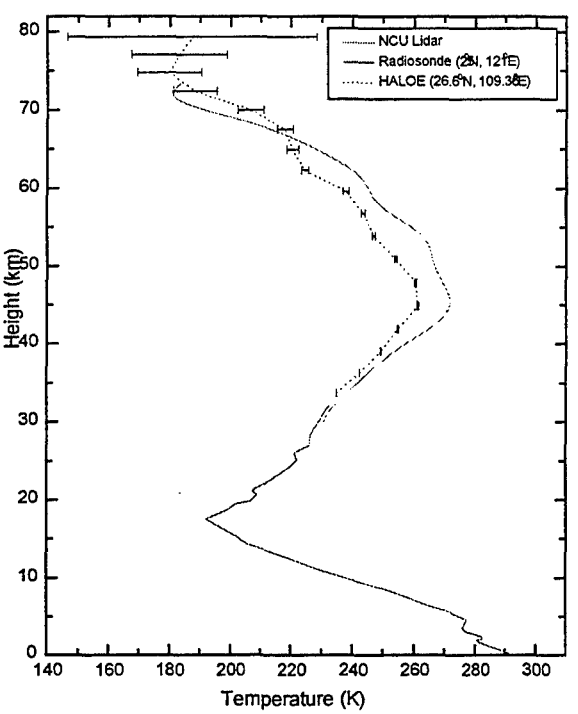


Figure 3. Comparison of temperatures from HALOE (4-11-94), Radiosonde (4-11-94) and NCU Lidar (3-11-94)



Observational Constraints on the Properties of Gravity Waves Generated by Tropical Convection

M. JOAN ALEXANDER (Colorado Research Associates, Boulder, CO)

Global circulation models (GCMs) of the middle and upper atmosphere must include the effects of gravity wave dissipation to produce realistic results. These waves have horizontal and vertical scales that are too small to resolve in GCMs so their effects must be parameterized. Gravity waves with high phase speeds are likely to be very important in the upper atmosphere, and convection is an important mechanism for generation of waves of this type. Key inputs for parameterization of the effects of gravity waves in GCMs are the momentum flux the waves carry, their phase speeds, the intermittency in their occurence, and knowledge of any anisotropy in wave propagation directions.

Several recent observational analyses and their interpretation in terms of these key properties will be the focus of the talk. The focus will be on waves observed in the lower stratosphere, close to the altitude where they are generated. At these altitudes, the background wind shear, which can dramatically alter the observable wave properties, will be minimized between the gravity wave source and the observation level. Observations from high resolution radiosondes, high altitude aircraft, and satellite will be shown and summarized to outline the existing constraints for parameterization of the effects of these waves in GCMs.

Each observation technique limits in some way the properties of the gravity waves that can be seen in the data. The satellite data that will be shown comes from the Microwave Limb Sounder (MLS) instrument flown on the Upper Atmosphere Research Satellite (UARS). These can only observe gravity waves with very long vertical wavelength (> 12 km) and horizontal wavelengths ~100-500 km. Such waves tend only to be visible in the stratosphere in certain latitude bands at certain seasons where the background winds are strong. One such region is in the subtropical summer latitude band between 5-25 degrees, where the longitudinal variations in gravity wave activity are found to closely follow the occurence of deep convective clouds. Model studies show this correlation is expected for the "deep heating" mechanism for gravity wave generation (Fig. 1). The MLS analysis is reported in McLandress et al. (2000).

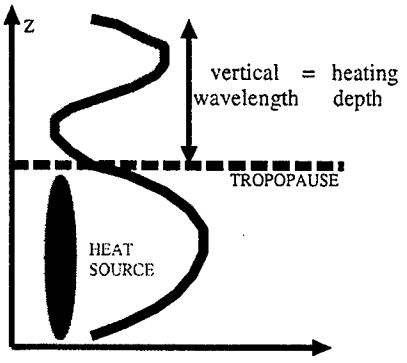


Figure 1: Schematic illustrating the deep heating mechanism for wave generation when stability in the stratosphere is twice that in the troposphere.

Observations from ER-2 aircraft in the lower stratosphere show similar relationships between deep convection and gravity waves for very short horizontal wavelength waves ~10-100 km. Unlike the satellite data, these can be used to infer gravity wave momentum flux. The fluxes inferred are large but the occurence of the waves is highly intermittent. These waves may be quite important to the momentum budgets of the middle andupper atmosphere. Analyses of these data are reported in Alexander et al. (2000).

Observations from radiosondes launched from Cocos Island in the tropical Indian Ocean (12S, 97E) will also be discussed. (Vincent and Alexander, 2000). A coordinated model study provided a means of inverting the stratospheric gravity wave properties in these data to infer the properties of the sources for the waves below. The inferred source is best described by the "transient mountain" mechanism described in Pfister et al. (1993). The waves in these observations are quite different from those observable in the other data. These have very low intrinsic frequencies, short vertical wavelengths (~2 km), and long horizontal wavelengths (~ 1000 km). These results are reported in Alexander and Vincent (2000). The results suggest that different generation mechanisms may be responsible for generating gravity waves with different properties. The simple mechanisms illustrated here obviously do not fully describe the complex nature of convection and the mechanisms for wave generation, but they are useful because each mechanism implies certain signatures in the gravity wave phase speed spectrum that will be needed to parameterize these waves in global models.

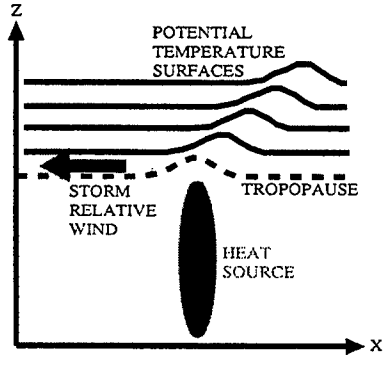


Figure 2: Schematic illustrating the "transient mountain" or "obstacle" mechanism for wave generation.

References:
Alexander, M.J., and R.A. Vincent, 2000: JGR (in review).
Alexander, M.J., J.H. Beres, and L. Pfister, 2000: JGR, (in review).
McLandress, C., M.J. Alexander, and D.L. Wu, 2000: JGR (accepted).
Vincent, R.A., and M.J. Alexander, 2000: JGR (in review).

ACOUSTIC GRAVITY WAVES DURING 11 AUG 1999 SOLAR ECLIPSE IN TROPOSPHERE/MESOSPHERE SYSTEM

M. Lal, C. Panneerselvam, K.U. Nair, S. Selvaraj, and R. Rajaram
Equatorial Geophysical Research Laboratory
Indian Institute of Geomagnetism
Krishnapuram, Tirunelveli – 627011, India
e–mail: egrl@vsnl.com

We have made an attempt to analyse the surface pressure data obtained by microbarograph, and ionospheric electron density variation by using Partial Reflection Radar at low latitude northern hemisphere, Tirunelveli (8.7 deg N, 77.8 deg E), India. The 11 August 1999 solar eclipse gave an opportunity to study the variation in atmospheric parameters. The surface pressure observed by the microbarograph reveal a decrease in surface pressure level by about 600 microbars during the maximum obscuration of the sun. The Partial Reflection Radar signal return from 88 km altitude shows the oscillations before the beginning of the eclipse, and it continues up to the maximum obscuration of the sun. Similar to the surface pressure decrease, ionospheric electron density variation also shows the significant decrease during the maximum obscuration of the sun. We have also measured surface humidity and temperature at this station. The surface temperature shows a decrease and humidity shows an increase, during the solar eclipse period. On the control days, the humidity after sunset has been found to almost constant, and its value was about 54%. The humidity values obtained on eclipse day is found to be 8% higher than the control day. Though the eclipse was partial at this site (~70%), we have found an increase in humidity of about 10% from the normal day. The temperature decrease has been found to be about 2–3 degree C on the eclipse day compared to the control days. We have also done the spectral analysis of surface pressure and ionospheric PR return signal from 88 km altitude region. We have found a prominent presence of acoustic gravity weaves of period about 3 minutes in the surface pressure as well as in the Partial Reflection Radar return signal. These waves might have been generated on the ground by the differential absorption of H2O and O3, whereas the acoustic gravity waves in the ionospheric altitude might have produced by the differential absorption of O2 molecule. The amplitude of the wave in the ionospheric region is very prominent compared to the amplitude of the wave obtaiend on the surface. The surface wave might have also propagated from ground to mesospheric altitudeand modulated the acoustic gravity waves. Apart from the acoustic gravity waves, ionospheric electron density variation also shows the presence of gravity wave of period 18 minute. This wave have observed after about one hour of maximum obscuration. Since the eclipse at this lcation was partial, the gravity wave of period 18 minute might have produced in the path of totality and propagated at this loaction. Similarly, surface pressure variation also shows the presence of gravity wave of period about 60 minutes. This wave is also very much prominent after about one hour of maximum obscuration of the sun.

Observations of momentum fluxes carried by AGWs in the mesosphere at Albuquerque, NM.

G. Swenson, A. Liu, C. Gardner, L. Rumsey and S. Hsia.

Momentum fluxes from quasi–monochromatic waves are characterized from brightness fluctuations in mesospheric airglows measured at Albuquerque, NM. Intrinsic characteristics of the waves have been deduced, in which lidar measurements of winds are used to correct for Doppler effects inherent in ground based measurements of observed waves. Na wind/temperature lidar measurements of wave induced vertical winds (w') provide new calibrations of wave magnitudes deduced from airglow measurements of the 'fast' waves which carry most of the momentum. Evidence for direct tidal filtering of meridional propagating waves will be presented along with statistical measurements of momentum fluxes in OH airglow and lidar wind and temperature.

Gravity Wave Interactions with Tides and Planetary Waves

Meyer, Christian K.
High Altitude Observatory
National Center for Atmospheric Research

Internal gravity waves can interact with and modify the behavior of global scale oscillations in the mesosphere and lower thermosphere. Seasonal variation of the diurnal propagating tide and the vertical extant and magnitude of 2- and 16-day planetary waves have been analyzed using a 2-D linear steady-state numerical model in conjunction with a hybrid gravity wave (GW) parameterization. The results compare favorably with observations of the global scale waves suggesting that wave-wave interactions can play an important role in this region.

Gravity wave interactions by the combined wave-mean wind field produces two distinct effects. Seasonal variation in gravity wave effects due to seasonal variation of the zonal mean zonal winds has the largest effect on the diurnal tide. Local time/longitudinal horizontal wind fields associated with planetary waves result in modulation of upward propagating internal gravity waves, providing an in-situ source of periodic forcing in the mesopause region. This forcing is shown to produce separate amplitude peaks in the PW horizontal wind fields in the lower thermosphere apart from the primary response in the mesosphere.

Daytime mesopause temperature and its variabilities from low latitudes.

ALOK TAORI[1], R. Sridharan[2], R. Narayanan[1] and N. K. Modi[1] .

1. Physical Research Laboratory, Ahmedabad -380 009, INDIA.
2. Space Physics Laboratory, VSSC, Trivandrum - 695 022, INDIA.

Mesopause region is the coldest and the least explored region in the Earth's upper atmosphere. Its thermal state defines the lower boundary conditions to the thermosphere and the exosphere higher above. Waves and associated processes, which are the main coupling agents between lower and upper atmospheres, deposit significant amount of heat and momentum in the mesopause region via filtering processes and modify the ambient conditions. This contributes nearly 20% of the total heat budget of the mesopause region. By studying the mesopause temperatures and their variabilities, one would be able to highlight many important aspects of the coupling processes.

OH band emissions are one of the most widely used emissions for the mesopause region studies, as their peak emission hight is centered around the mesopause (Mc Dade et al., 1987). The OH radicals are in local thermodynamical equilibrium with the ambient, and so also their rotational temperatures, derived from the ratio of two wuitable rotational lines of the same vibrational band, could be treated to be same as the mesopause temperatures (Sivjee, 1992). So far this method was used for the estimation of night time mesopause temperatures. With the advent of the multiwavelength daytime photometer (MWDPM) (Sridharan et al., 1998), which is capable of detecting three airglow emissions near simultaneously, even in the presence of high solar background, determination of daytime mesopause temperatures have become possible (Sridharan et al., 1999). This MWDPM was tuned to 7316 A nad 7402 A rotational lines of OH (8, 3) Meinel rotational vibrational band. Assuming

the OH radicals to follow Maxwell - Boltzmann distribution, rotational temperatures can be calculated using the following relation :-

$$T_{rot} = 362/\ln[3.44*I_{7316}/I_{7402}] \quad \text{--- (Meriwether, 1984)}$$

Where T_{rot} is the rotational temperature and I_λ is the intensity of emission line at wavelength λ.

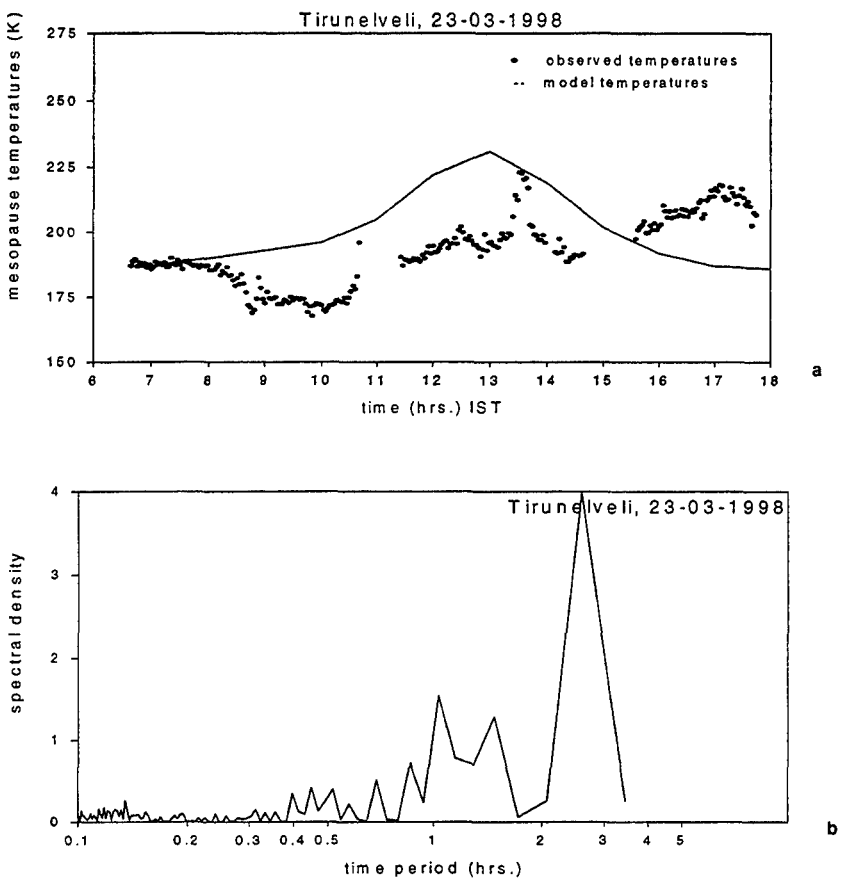


FIG. 1: mesopause temperature variabilities over Tirunelveli (a) on 23rd March 1998, and Fourier analysis of the same(b).

The MWDPM was operational from Tirunelveli (8.7N, 77.8E) and Kolhapur (16.8N, 74.2E) during March 1998 and January 1996, and daytime mesopause temperature variabilities are studied for the first time. These temperatures are compared with CIRA/ MSIS -90 model values [**fig. 1a, 2a**]. Further these variabilities are subjected to Fourier analysis to obtain the periodicities. Results of the above analysis revealed 20 min -2 hours periodicities to be dominant in the temperature variabilities [**fig 1b, 2b**]. Significant deviations to the line of 30 K from model temperatures, which are nearly 15% of the mean values, are also observed on several occasions.

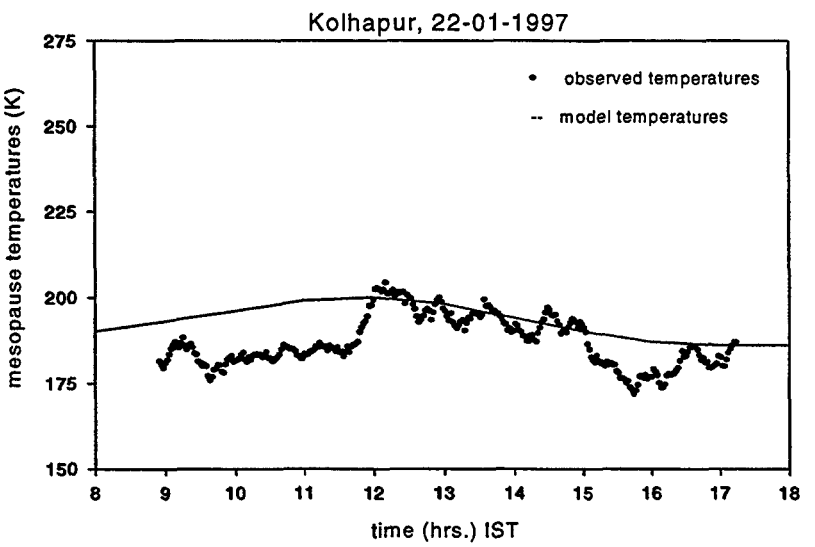


FIG. 2a : Mesopause temperature variabilities over Kolhapur on 22nd January.

Once shown by the present study, that mesopause temperatures are highly variable and there exist dominant periods in their variabilities, study of their possible impact on the neutral and electrodynamical processes (for

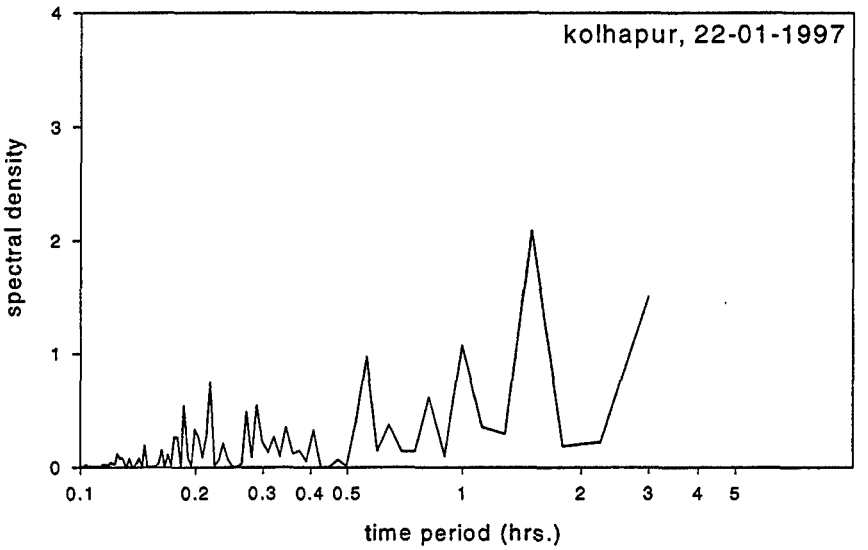


FIG. 2b : Fourier analysis of the temperature variabilities observed on 22nd January, over Kolhapur.

equatorial latitudes) becomes one of the most important aspects, which opens up a new topic of research.

References:

1# Mc Dade I. C. et al., 1987, Planet. Sp. Sci., 35, 1137 - 1147.

2# Meriwether J. W. Jr., 1984, MAP handbook, Vol. 13, 1 -18.

3# Sivjee G. G., 1992, Planet. Sp. Sci., 40, 23, 235 - 242.

4# Sridharan R. et al., 1998, Measurement Sci. and Tech., 9, 585 - 591.

5# Sridharan R. et al., 1999, J. Atmos. Sol. Terr. Phys., 61,15,1131-1142.

Tide-induced oscillations in the atmospheric sodium layer

B. R. CLEMESHA, P. P. Batista and D. M. Simonich

Instituto Nacional de Pesquisas Espaciais, CP 515, São José dos Campos, 12201-790 SP, Brazil

Introduction

At heights around the mesopause, solar-atmospheric tides should be expected have a significant influence on the vertical distribution of atmospheric constituents. Lidar measurements of meteor metals, mainly sodium and iron, have shown that the vertical distributions of these metals are influenced by atmospheric dynamics (see, for example, Shelton et al., 1980; Batista et al., 1985). Most studies of this sort have dealt with short period gravity waves, at least in part because of the difficulty of obtaining long runs of lidar data. Up until now, only two extensive sets of 24-hour lidar measurements have been reported. The first of these was made by the INPE lidar in 1984, and reported by Batista et al (1985). The second was made at Illinois between February 1996 and January 1998, and has been reported by States and Gardner (1999). In our 1985 paper we concluded that the diurnal and semi-diurnal oscillations which we observed in the atmospheric sodium layer were mainly induced by atmospheric tides, and we were unable to identify any unambiguous photochemical effects. States and Gardner (1999), on the other hand, find that "... *there is little evidence of direct tidal perturbations in Na density* ...", and conclude that the diurnal variations observed by them are provoked by photochemical effects. Thus the conclusions of States and Gardner (1999) are in direct opposition to those of Batista et al. (1985). Although the relative importance of tides and photochemistry might be different at different latitudes, it seems unlikely that tides should play a dominant role at 23° S and a negligible one at 44° N. The purpose of this paper is to present new 24-hour lidar measurements of atmospheric sodium, together with simultaneous meteor radar observations of horizontal winds.

Measurements

The INPE lidar, installed at São José dos Campos (23° S, 46° W), uses a flashlamp-pumped dye laser tuned to the sodium D2 line by 3 intra-cavity Fabry-Perot interferometers. The transmitted pulse is collimated by a 30 cm parabolic mirror, giving a beam-width of about 0.2 mR. The receiver uses a 76 cm collecting mirror with 3 photon-counting photomultiplier tubes, 2 of which measure the Rayleigh and resonant scattered signals, and the third of which registers the rotational Raman scattering from 15 to 35 km. Daytime measurements are made possible by including a narrow-band Fabry-Perot interferometer in the receiver path.

The meteor radar is a Genesis SkiYmet system, installed at Cachoeira Paulista (23° S, 45° W), 102 km to the NE of São José dos Campos. The radar operates automatically, 24 hours per day. The number of useful meteor detections per day is typically between 2000 and 4000, making it possible to obtain hourly wind values in 3 km bins from 82 to 100 km. When determining averages over many days it is possible to decrease the size of both time and height bins, and to extend the height range to 80 - 107 km.

During the southern winter of 1999 it was possible to obtain 24-hour lidar measurements over a total time period of 320 hours in 8 measurement campaigns, each of which covered several days. The distribution of measurements over the 24-hour period was not uniform, owing to frequent ground fog in the early morning hours and sporadic cloud cover during late afternoon, but the data obtained were sufficient to provide a reliable average daily variation of the vertical distribution of sodium concentration.

Results

In Figure 1 we show how the vertical distribution of atmospheric sodium varied over a period of 28 hours between 1500 GMT on July 12, 1999 and 1900 GMT on July 13, 1999. To remove rapid variations in height and time the data were filtered with a 1 hour cut-off in time and 2 km cut-off in height. In the figure the profiles are plotted at 30 min intervals, although the original data were taken at 5 min intervals, and the time scale is relative to zero hours on July 12. The horizontal sodium density scale is arbitrary, but the profiles have not been normalized to a constant abundance. Overlayed on the sodium density profiles are the meridional wind contours obtained from the meteor radar for the same time period. It is immediately obvious from Figure 1 that there is a close relationship between the meridional wind and the sodium concentration. This is particularly clear for the data from just before 36 hours to about 43 hours, where the main peak in sodium concentration falls from 91 km to 84 km, accompanied by the meridional wind contours. During the first 2 hours of this period the height of the sodium peak changes little, and the wind contours fall slowly. During the next 3 hours both the sodium peak and the wind contours fall rapidly, with the rate of fall flattening out again for the last 2 hours. Similar behavior can be seen during other time and height intervals.

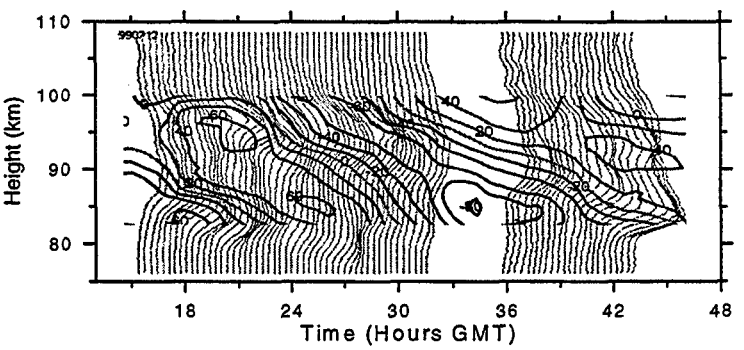


Fig. 1 Atmospheric Na and meridional winds for 12-13 July, 1999. The baseline position of each Na profile corresponds to the time of the profile; the Na density scale is arbitrary. Wind contours are labeled in units of m/s.

The data shown in Figure 1 enable us to conclude that there is a strong correlation between sodium concentration and the meridional wind. The purpose of this paper, however, is to investigate the mean diurnal variation of sodium, and to see whether it is related to tidal oscillations. With this aim in view we have plotted the average 24-hour sodium variation in the form of sodium isopleths in Figure 2, along with the average meridional wind. The meridional wind is shown in the form of a gray-scale contour map. To provide visual continuity two complete 24 hour cycles are shown in the figure. The sodium data plotted are the means of all data obtained during the winter of 1999, and the wind data have been averaged over all the days on which sodium data were obtained. The sodium isopleths show a vertical oscillation which is mainly semi-diurnal above the sodium peak, with an increasing diurnal component at lower heights, and the oscillation shows a downward phase propagation. The winds show a mainly diurnal oscillation at lower heights, with a semidiurnal component starting to appear above about 90 km. It is immediately obvious from Figure 2 that the downward phase propagation in the vertical oscillation of the sodium isopleths closely accompanies the phase propagation of the diurnal variation in the meridional wind velocity.

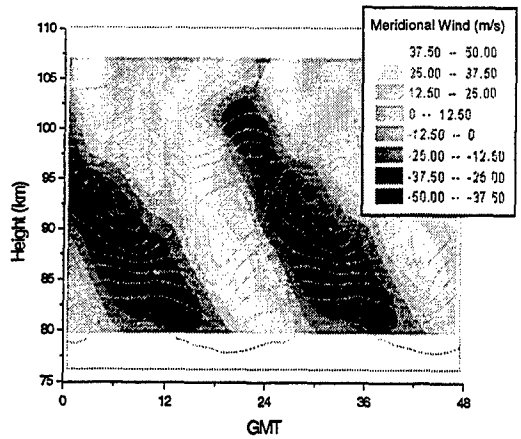


Fig. 2 Average Na density and meridional winds for winter 1999. Winds are shown as gray-scale levels, with white indicating northward winds, and the Na contours are in units of 3E9 m^{-3}.

If we assume that the sodium layer acts as a neutral tracer (i.e. we ignore any possible photochemical effects) and that horizontal gradients are small, then atmospheric waves will influence the sodium distribution both via their associated atmospheric density variations and through the associated vertical winds. It is easy to show that, except near the peak in sodium layer mixing ratio, it is the winds that exert the major effect. For a more general analysis of the effects of atmospheric waves on minor constituent layers see Dudis and Reber (1976) and Chiu and Ching (1978). The application of Dudis and Reber and Chiu and Ching's work to lidar observations of atmospheric gravity waves has been developed in a series of papers by the Illinois workers (see, for example, Shelton et al., 1980). Following Batista et al. (1985), for a wave period, T, we can write

$$\frac{\Delta n}{n_0} = \frac{\Delta N}{N_0} + \frac{iT}{2\pi}\left(\frac{1}{n_0}\frac{dn_0}{dz} - \frac{1}{N_0}\frac{dN_0}{dz}\right)W \qquad (1)$$

where $\Delta n/n_o$ is the fractional perturbation in sodium density, $\Delta N/N_o$ is the fractional perturbation in the density of the major atmospheric constituents, dn_o/dz is the vertical gradient in sodium density and dN_o/dz is the vertical gradient in the density of the major atmospheric constituents. If we analyze the time variation of sodium into diurnal and semidiurnal components having amplitudes A_{24} and A_{12}, plus a constant term A_o, we can write

$$n = A_o + A_{24}\cos(12(t-\phi_{24})/\pi) + A_{12}\cos(6(t-\phi_{12})/\pi) \qquad (2)$$

where ϕ_{24} and ϕ_{12} are the hours of maximum for the diurnal and semi-diurnal components respectively. Neglecting the density term $\Delta N/N_0$ in equation 1 we can write for the diurnal and semi-diurnal wind components respectively

$$W_{24} = \left(\frac{A_{24}\pi}{12n_0}\right)\Big/\left(\frac{1}{n_0}\frac{dn}{dz} + \frac{1}{H}\right) \qquad (3a)$$

$$W_{12} = \left(\frac{A_{12}\pi}{6n_0}\right)\Big/\left(\frac{1}{n_0}\frac{dn}{dz} + \frac{1}{H}\right) \qquad (3b)$$

where H is the atmospheric scale height and we have made the substitution

$$\frac{1}{H} = \frac{-1}{N_0}\frac{dN_0}{dz}$$

We have applied this analysis to our average 24-hour sodium variations by fitting 24- and 12-hour components at each height in a least mean squares sense, and then using equations 3a and 3b to compute the vertical wind. The results are shown in Figures 3a and 3b, where we show the amplitude and hour of maximum respectively. Below 90 km both the diurnal and semidiurnal components show velocities of less than 10 cm/s. Above 90 km the semidiurnal component grows rapidly in amplitude, reaching values of about 30 cm/s above 100 km, whereas the diurnal component is still only about 10 cm/s. Note that we are unable to determine velocities between 94 and 98 km because the approximation used is not valid in this region.

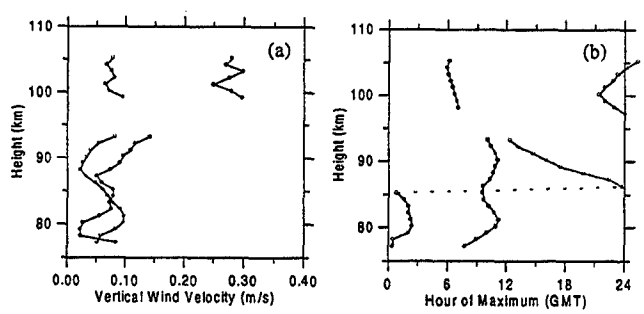


Fig. 3 Amplitude (a) and hour of maximum (b) of the vertical wind components derived from the mean daily variation in Na distribution. The diurnal component is shown by open circles, and the semi-diurnal component by filled circles.

The hour of maximum for the semidiurnal component varies smoothly with height, changing from 6 hours GMT at 105 km to almost 12 hours GMT at about 82 km. The phase of the diurnal component is much less regular, with a very rapid change in the hour of maximum from 12 hours at 94 km to 24 hours at 86 km.

Our ability to compare the sodium variations with the winds is limited by the fact that it is the vertical wind that is expected to influence the former, whereas it is the horizontal wind that is measured by the meteor radar (although it is theoretically possible to determine the vertical wind from the meteor radar data, the errors involved are so much larger than the vertical velocities as to render the results meaningless). We have attempted to remedy this situation to some extent by using Hagan et al's. (1995) Global Scale Wind Model (GSWM) to compute the vertical wind, and by validating the wind model by comparing it with the measured horizontal winds. Figures 4a and 4b show amplitude and phase of the meteor winds respectively. Open circles represent the diurnal component and filled circles the semidiurnal. In the same figures we show the GSWM winds computed for July at 24° S as broken lines for the diurnal component and dotted lines for the semi-diurnal. The agreement between computed and experimental winds is surprisingly good except for the diurnal amplitude. The phase of the measured diurnal wind is about 2 hours later than the model wind at all heights. The difference between the modeled and measured semidiurnal phases averaged over height is close to zero, and at no point is it greater than about 2 hours. The amplitude of the modeled semidiurnal component is very close to the measured wind at heights up to 95 km and, even above this height, the discrepancy is never greater than a factor of 2. Although the modeled and measured diurnal winds are in reasonable agreement up to about 95 km, above this height they diverge rapidly, the GSWM wind increasing rapidly with height where the measured wind decreases rapidly with height. Thus we can conclude that the GSWM does a reasonable job of modeling the wind at our location, except for the height variation of the diurnal amplitude, and we can use the modeled vertical wind to compare with our sodium measurements with some degree of confidence.

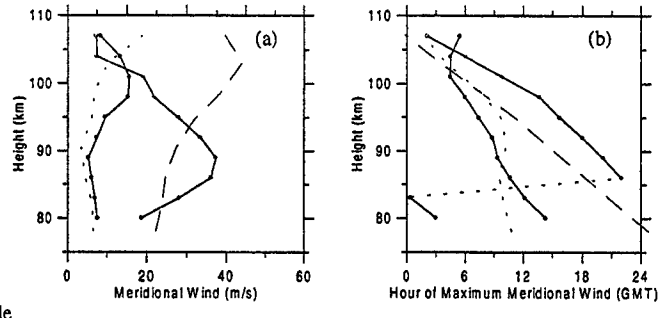


Fig. 4 Amplitude (a) and hour of maximum (b) of the meridional wind components. Open circles (diurnal component) and filled circles (semi-diurnal component) show the mean measured meteor winds for the times covered by the lidar measurements. The broken lines (diurnal component) and the dotted lines (semi-diurnal component) show the GSWM winds for 24° S July average.

The amplitude and phase of the modeled vertical winds are shown in Figures 5a and 5b respectively. These should be compared with the winds derived from the sodium measurements, shown in Figures 3a and 3b. The best agreement is in the semi-diurnal amplitude. Both the sodium layer and the GSWM semidiurnal vertical wind show very strong growth with height. The sodium layer-derived wind increases from about 2 cm/s at 80 km to 25-30 cm/s at 105 km. The model wind increases from 1 cm/s at 80 km to about 20 cm/s at 105 km. The semi-diurnal wind from the sodium measurements oscillates in the range 2-9 cm/s, as compared to 1-5 cm/s for the GSWM wind, neither showing any strong trend over the height range in question. The phase of the modeled wind is about 12 hours at 90 km, similar to that of the sodium layer derived wind, although the GSWM wind shows a more rapid and consistent progression with height. The phase of the sodium layer derived diurnal wind varies very rapidly with height, and bears no consistent relationship to the modeled wind. Thus, except for the phase of the diurnal wind, there is reasonable agreement between the GSWM vertical wind and the vertical winds derived by assuming that the average diurnal variation in the sodium layer is driven mainly by atmospheric tides.

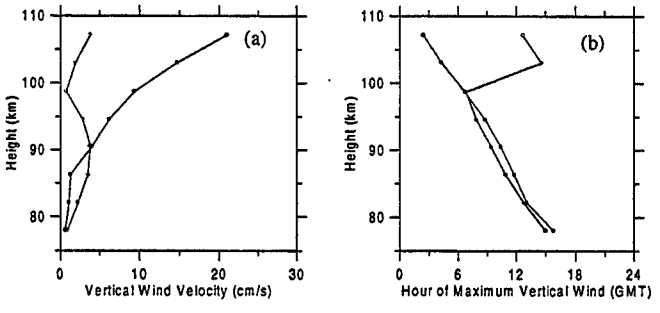


Fig. 5 Amplitude (a) and hour of maximum (b) for the GSWM vertical wind calculated for 24° S, July average. Open circles indicate the dirnal component and filled circles the semi-diurnal.

Conclusions

Simultaneous measurements of the atmospheric sodium layer and meteor winds, at locations separated by about 100 km, show that the observed diurnal and semidiurnal variations in sodium are closely related to tidal winds. We find general agreement between the vertical wind calculated from the sodium measurements, on the assumption that sodium acts as a conserved tracer, and Hagan et al's. (1995) Global Scale Winds Model. The fact that meridional winds derived from the GSWM are in general agreement with the measured meridional wind justifies the use of the model to determine the vertical wind. The agreement observed between the measured sodium layer variation, meteor winds and the GSWM provides very strong support for our earlier conclusion that atmospheric tides are responsible for the main diurnal and semidiurnal variations in the atmospheric sodium layer. This conclusion is diametrically opposite to that of States and Gardner (1999), who found "little evidence" for tidal effects in the sodium layer observed at Illinois.

Acknowledgements: This work was partially supported by the Conselho Nacional de Desenvolvimento Científico e Tecnológico - CNPq, the Fundação de Amparo à Pesquisa do Estado de São Paulo - FAPESP, and the Programa de Núcleos de Excelência - PRONEX. Numerical values for the model tides were taken from the GSWM homepage at http://www.hao.ucar.edu/public/research/tiso/gswm/gswm.html

References

Batista, P. P., B. R. Clemesha, D. M. Simonich and V. W. J. H. Kirchhoff, Tidal oscillations in the Atmospheric Sodium Layer, *J. Geophys. Res., 90*, 3881-3888, 1985.

Chiu, Y. T. and B. K. Ching, The response of atmospheric and lower ionospheric layer structures to gravity waves, *Geophys. Res. Lett., 5*, 539-542, 1978.

Dudis, J. J. and C. A. Reber, Composition effects in thermospheric gravity waves, *Geophys. Res. Lett., 3*, 727-730, 1976.

Hagan, M.E., J. M. Forbes, and F. Vial, On modeling migrating solar tides, *Geophys. Res. Lett., 22*, 893-896, 1995

Hagan, M. E., J. L., Chang, and S. K. Avery, GSWM estimates of non-migrating tidal effects, *J. Geophys. Res., 102,*, 16,439-16,452, 1997.

Hocking, W.K., and T. Thayaparan, "Simultaneous and co-located observation of winds and tides by MF and Meteor radars over London, Canada, (43N, 81W) during 1994-1996", Radio Sci., 32, 833-865, 1997.

Shelton, J. D., C. S. Gardner and C. F. Sechrist, Density response of the mesospheric sodium layer to gravity wave perturbations, *Geophys. Res. Lett., 7*, 1069-1072, 1980.

States, R. J. and C. S. Gardner, Structure of the mesospheric Na layer at 40 N latitude: Seasonal and diurnal variations, *J. Geophys. Res., 104*, 11783-11798, 1999.

Simultaneous lidar observation of a sporadic sodium layer, a "wall" event in the OH and OI 5577 airglow images and the meteor winds

P. P. BATISTA[1], B. R. Clemesha[1], D. M. Simonich[1], M. J. Taylor[2], H. Takahashi[1], D. Gobbi[1] and A. F. de Medeiros[1]

1)Instituto Nacional de Pesquisas Espaciais, CP 515, São José dos Campos, 12201-970, SP, Brazil
2) Space Dynamics Laboratory and Physics Department, Utah State University, Logan, Utah, USA

Introduction

The region of the upper mesosphere and lower thermosphere (MLT) from approximately 80 to 105 Km displays a large number of chemical and dynamical phenomena. In this region atmospheric tides have significant amplitudes, showing the propagation of many tidal modes with different vertical wavelengths and amplitudes. Also, superimposed on these tides, gravity waves are frequently present with oscillations from 5 min to ~10 h. Chemical processes originate neutral, ionized and emitting layers, which can be monitored by ground-based and satellite instruments, giving information about the chemical and dynamical processes occurring there. Meteoroids also ablate in this region, depositing extra-terrestrial material and also providing information about the winds present in the region. Additionally to the ever-present tides and gravity waves, rare and sporadic events, caused by unusual conditions occurring in the MLT region may also occur. Sporadic metal layers (Ns), which are enhancements over the regular metal layers with halfwidth of 1-2 Km, intensity from 2-10 times that of the regular layer and duration from minutes to hours (Batista et al., 1989, Hansen and vonZan, 1990) can be observed with lidars measuring the density of metals, mainly Na and Fe (Batista et al., 1989, Gardner et al., 1993). The origin of these metal layers is still a subject of research. A lot of information has been collected since the first observation of this kind of event in São José dos Campos, Brazil in the seventies (Clemesha et al., 1978). Today it is believed that these layers originate from the neutralization of ionized metals throughout a complex chemical scheme involving clustering (Cox and Plane, 1998) and the presence of suitable wind and temperature fields (Quian et al., 1998).

More recently, another singular mesospheric event was observed by imaging the optical emissions with an all sky CCD imager. Taylor et al. (1995) observed a sharp front in the infrared and visible nightglow emissions followed by several conspicuous wave crests progressing rapidly though the 180° image field of view. Few events of this kind have been reported in the literature (Swenson and Espy, 1995; Swenson et al., 1998; Batista et al., 2000). Explanation has been given in terms of a "bore wave" (Dewan and Picard), dispersion of long and short waves (Munasinghe et al., 1998) and large amplitude gravity wave (Swenson et all, 1998). Whatever is the cause of the events, it affects several atmospheric phenomena concurrently. It is therefore important that the mesosphere be observed by a set of instruments which gives simultaneous parameters like the wind and temperature , minor constituents concentrations and airglow.

In this work we report the observation of a sporadic sodium layer, measured by lidar at São José dos Campos (22.5° S, 46°W) on the night of July 13-14, 1999, followed by wall event, observed at Cachoeira Paulista (23°S, 45°W) in the OH NIR and OI 5577 CCD images and also by zenith-pointing tilting filter photometers. Winds were also measured at Cachoeira Paulista by meteor radar.

Instruments and Measurements

INPE's lidar operating at São José dos Campos (SJC) is the same as described by Clemesha, 1995. It uses a flashlamp-pumped dye laser tuned to the sodium D2 line by 3 intra-cavity Fabry-Perot interferometers. A 0.2 mR of bean-width is made possible by a 30-cm parabolic collimating mirror. The collecting system uses a 76 cm mirror and 3 photo-counting photomultiplier tubes, used for Rayleigh, resonant and Raman scattering. Daytime measurements are also possible with this system.

The airglow observatory at Cachoeira Paulista (CP) (102 km NE of SJC), routinely measures zenith mesospheric and thermospheric emissions of OH(6,2) and O2(0,1) (intensity and rotational temperature), NaD, OI557.7 nm and OI630.0 nm by means of a tilting filter multi-channel photometer.

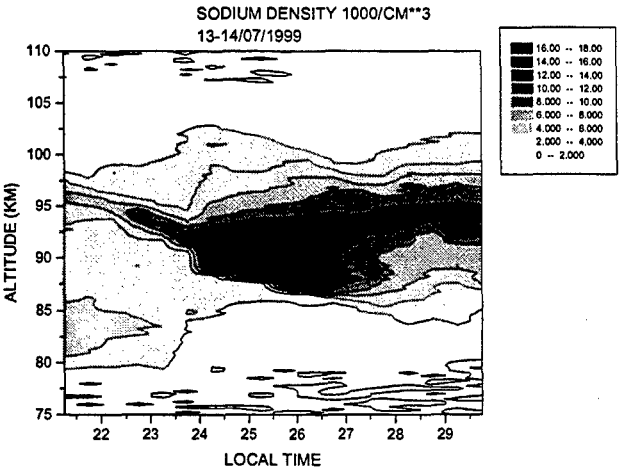


Fig. 1 Sodium density for the night 13-14 July, 1999. Gray-scale levels are given in 1000 cm^{-3}.

All sky images of the OI557.7, O2(0,1), OH near infrared from 715 to 930 nm, OI630.0 and background were also observed by a CCD imager in cooperation with the University of Utah with the same characteristics as described by Taylor et al., 1995.

The wind field was observed by a SkiYmet meteor radar system also operated at CP. The system collects typically between 3000 and 4000 useful echoes per day, making it possible to obtain hourly winds in 3-km bins from 82 to 100 km. Depending on the actual number of meteors, different choices of time end height resolution can be used.

From June 1 to August 13, 1999 during favorable new moon periods, a specific campaign was carried out in CP and SJC involving the above mentioned instruments. The measurements were not uniformly distributed throughout this period, owing to the presence of fog and clouds. But on 22 days, a total of 320 hours in 8 measurement sequences, most of them covering at least a 24-hour cycle of lidar measurement were obtained. During all of this period, wind measurements were obtained and during most of the nights, coincident airglow zenith and all sky images were obtained. In most of the measurement, Ns layers were present, but the most outstanding event with unusual behavior in all the data was observed in the night of 13-14 July, 1999.

Results

In Figure 1 we show the sodium isopleths and gray scale for the night of July 13-14, 1999 from 21:15 to 05:45 LT. Daytime measurements were obtained on July 13 from 9:00 to 17:00. When the daytime measurements stopped due to then presence of clouds at 17:00 the layer was very low with the peak maximum density at around 83 km. Cloudiness made it impossible to take measurements from 17:00 to 21:05. When measurements resumed at 21:08 the layer presented a small sporadic peak at 96 km and still maintained another peak at 84 km. The sporadic peak grew as it dropped to 92 km as the lower peak disappeared at around 23:45. At around this time the layer shape changed, with sodium almost disappearing below 85 km, and the sporadic peak fell and grew at the same time as the density increased at the topside of the layer. Noteworthy is the extremely steep density gradient at 88 km, that continued to decrease until around 03:00, when the layer started to return to a more normal shape.

In Figure 2 we show four individual profiles taken at 22:43, 23:43, 00:47 and 01:43. The steep density gradient at the bottom side and the rapid increase in the topside density of the layer is apparent.

From Figure 1 it can be seen that at around 23:45 a drastic change appears to have occurred in the mesosphere in order to cause so large a change in the sodium layer shape. At the same time an unusual situation also occurred in the airglow at Cachoeira Paulista, seen both by the imager and the zenith photometer. In Plate 1 we show a sequence of all sky images for the OI557.7 nm emission. In all the images N is up and W on the left and the time (UT : LT+3 h) is indicated in each image. A very clear line dividing the sky into bright and dark areas is seen, propagating from NE to SW at ~70 m/s. The OH NIR measured with a wide band filter (from 715 to 930 nm) with a notch at the O2(0,1) band at 865.0 nm is also shown for the same period of time in Plate 2. The OH shows widespread band structure, but also a less defined structure with high and low brightness regions, but with the dark region propagating to NNE at ~70 m/s. The zenith photometer also measured the OI557.7, OI630.0 and NaD intensities, and the OH(6,2) and O2(0,1) intensities and rotational temperatures in CP. In Figure 3 we show these intensities from 21:00 to 03:00 for July 13-14. Outstanding is the rapid decrease of the OH(6,2) intensity at around 23:45. A rapid fall of intensity is also apparent in the NaD, but surprisingly the E-region component of the OI557.7 do not show any noticeable change, although the O2 rotational temperature (volume emission weighted temperature at ~94 Km) shows a very large increase from 23:00 to 24:00 (~40K).

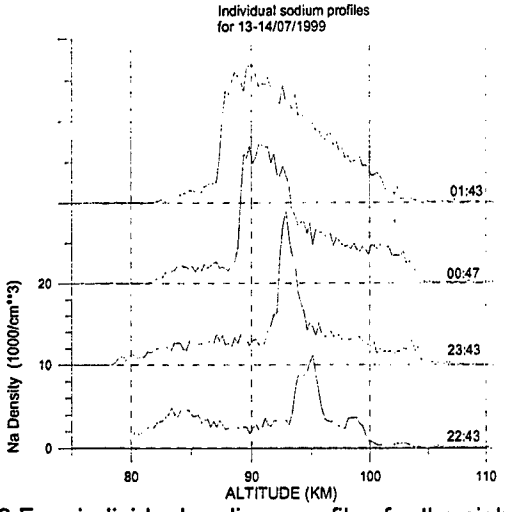


Fig. 2 Four individual sodium profiles for the night of 13-14 July, 1999, Profile times are shown at

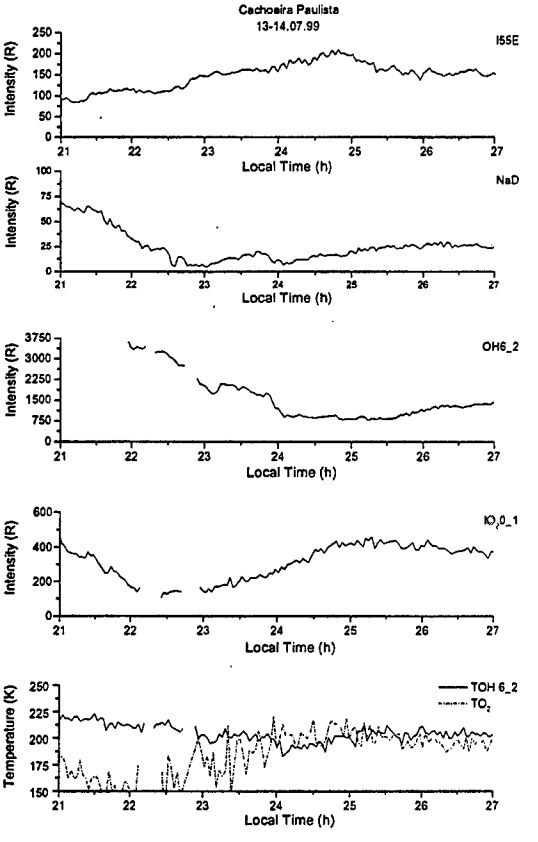


Fig. 3 Zenith nightglow intensities for OI(55.7 nm), NaD(589.0 nm), OH(6,2) and O2(0,0), and rotational temperatures for the OH(6,2) and O2(0,0) (from top to down).

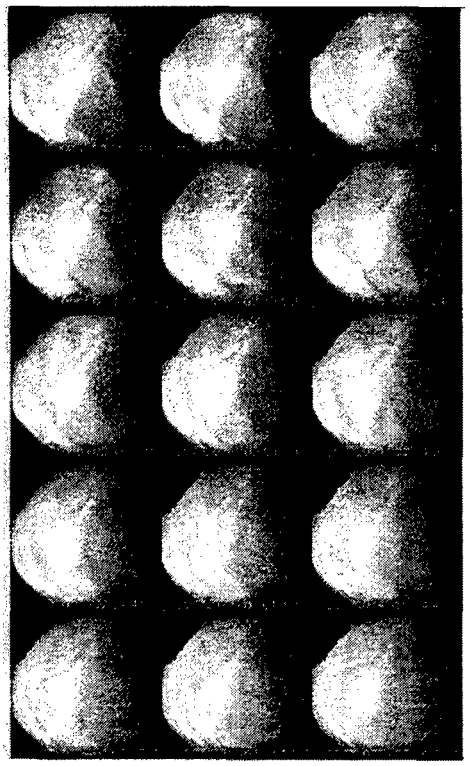


Plate 1. Sequence of OI(557.7 nm) all sky images for 13- 14 July,1999 from 02:25:34 UT to 03:15:31UT.

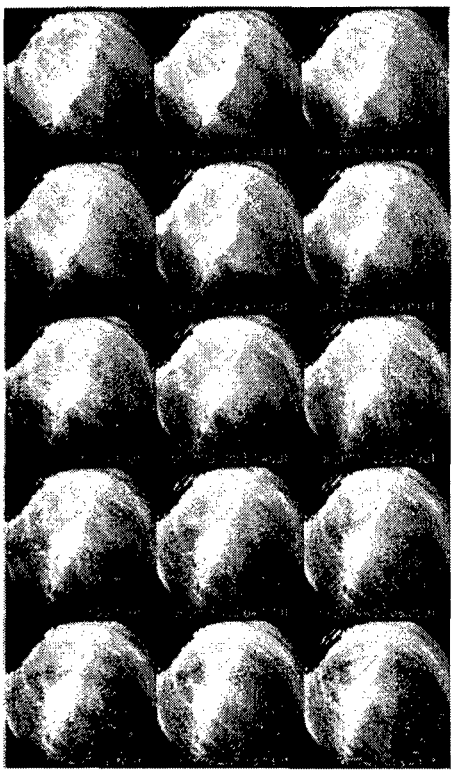
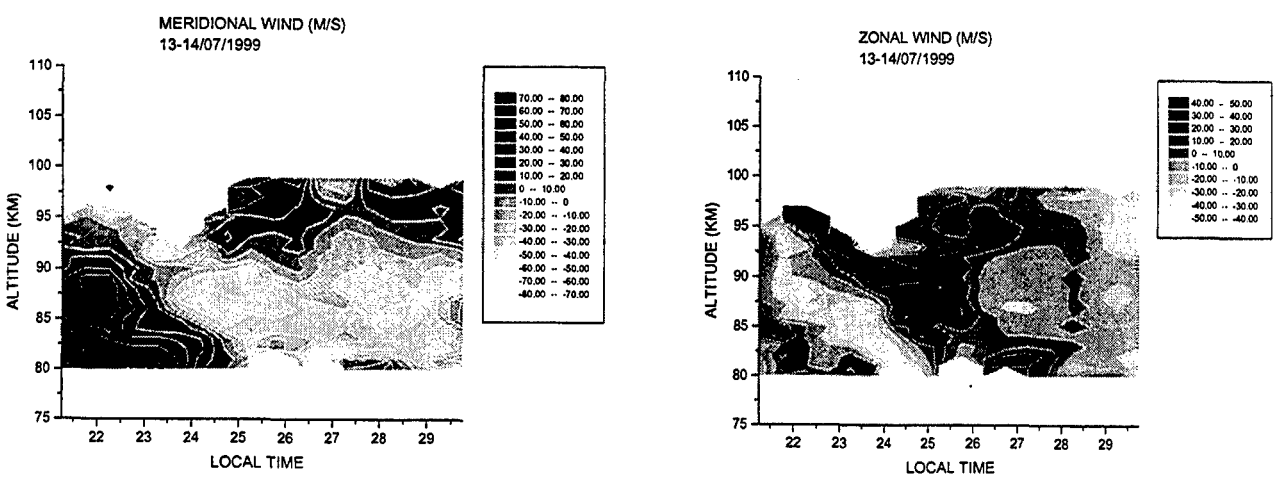


Plate 2. Sequence of OH NIR all sky images for 13-14 July, 1999 from 02:28:46 UT to 03:18:44 UT.

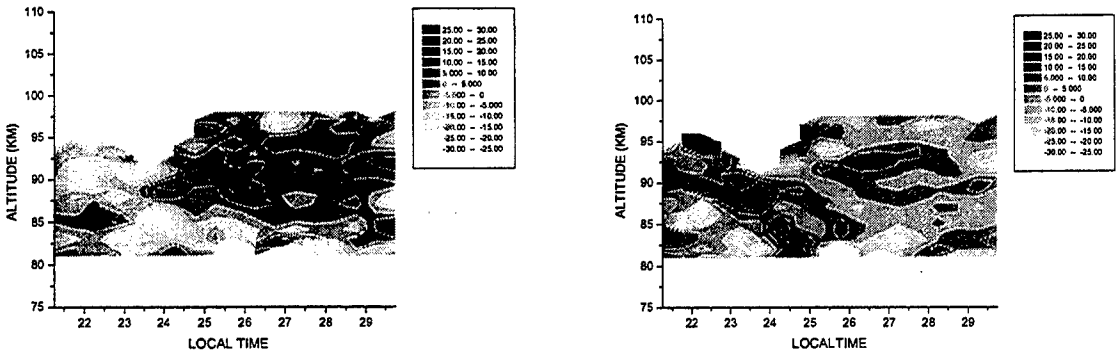
The meridional and zonal wind structure measured by the meteor radar at CP is shown in Figure 4. Values are shown in gray scale contour maps from 21:00 on July 13 to 6:00 on July 14. The meteor data were binned in intervals of 3-km in height and 90 minutes in time, and winds were computed at intervals of 1 km and 1 hr. It is noted that from 21:00 to 01:00 a strong wind shear is present both in the meridional and zonal winds with the phase propagating from ~97 km to 80 km during this time. Considering 87 km as the center of the OH layer, the total wind at 23:45 at this height is 40.7 m/s towards 28.6^0 from S to SW. Note that this direction is almost opposite to that of the OH front. This is consistent with the "bore" hypothesis put forward by Dewan and Pickard, 1998. Unfortunately at the OI layer height wind values are not available between 23:00 and 01:00.

The vertical shear of the horizontal wind for this night is shown in the Figure 5. Strong wind shear is observed both in the meridional and zonal winds. Despite the smaller height coverage for the derivative, the coincidence of high positive meridional wind shear with the steep vertical sodium gradient is noteworthy (compare Fig. 5(a) with Fig. 1). Correlation between vertical shear and Nas has been noted by Quian et al., 1998 and Miyagawa et al., 1999, although not in all the events studied. In the case of events studied by Quian et al., 1998 the maximum total shear is close to the instability limit of 42 m/s/km. In our case the values are smaller ~20 m/s/km, similar to Miyagawa's values.



a) b)

Fig. 4 Northward wind (a) and Westward wind (b) as a function of height and time for 13-14/07/1999.



a) b)

Fig 5 Vertical shear of the meridional wind (a) and zonal wind (b) for the night of 13-14/07/1999.

Summary and discussion

The data depicted in the previous figures and plates show that a very rare event (the propagation of a front of high and low brightness airglow emissions), and a more frequent event (sporadic sodium layer) occurred at around the same time at nearly the same location. In order to know whether these events are interconnected the wind structure dominant in the region was examined. Although the vertical propagation of phase shown by the wind structure and the vertical shear in the meridional wind are very well correlated with the appearance and vertical displacement of the sporadic peak, this wind is mainly tidal in nature, and similar structures appear on other nights without anything special in sodium and airglow. What appears to be different on this night is the temperature enhancement in the O2 (0,0) layer height. This temperature enhancement and the velocity and direction of propagation of the front suggest that the event is of the same nature as that described by Taylor et al., 1995, but with the difference that the fronts in OH and OI propagate in different directions. Compared with other sporadic layers observed at our site, the event of the July 13-14 night differ from the majority of others (see Batista et al., 1989, Clemesha et al., 1996) in the sense that, following the downward motion of the sporadic layer at 23:45, the density starts to grow on the topside at the same time as the steep gradient appears at the bottom side of the sporadic layer, and the lower sodium almost disappears. The temperature enhancement above 90 km could be responsible for the sodium density increase, and might also be associated with the conditions leading to the airglow events.

Acknowledgements: This work was partially supported by the Conselho Nacional de Desenvolvimento Científico e Tecnológico-CNPq, the Fundação de Amparo à Pesquisa do Estado de São Paulo-FAPESP, and the Programa de Núcleos de Excelência-PRONEX.

References

Batista, P. P., B. R. Clemesha, I. S. Batista and D. M. Simonich, Characteristics of the sporadic sodium layers observed at 23 degrees S, J. Geophys. Res., 94, 15349-15358, 1989.

Batista, P. P., H. Takahashi, D. Gobbi, A. F. de Medeiros, First Airglow All Sky images at 23^{0}S, Adv. Space Res., 2000, in press.

Clemesha, B. R., V. W. J. H. Kirchhoff, D. M. Simonich and H. Takahashi, Evidence of an Extraterrestrial Source for the Mesospheric Sodium Layer, Geophys. Res. Lett., 5, 873-876, 1978.

Clemesha, B. R., Sporadic neutral metal layers in the mesosphere and lower thermosphere, Journal of Atmospheric and Terrestrial Physics, 57, 725-736, 1995.

Clemesha, B. R., Batista, P. P. and D. M. Simonich, Formation of sporadic sodium layers, J. Geophys. Res., 101,19701-19706,1996.

Cox, R. M. and J. M. C. Plane, An ion-molecule mechanism for the formation of neutral sporadic Na layers, J. Geophys. Res., 103, 6349-6359, 1998.

Dewan, E. M. and R. H. Picard, Mesospheric bores, J. Geophys. Res., 103, 6295-6306, 1998.

Gardner, C. S., T. J. Kane, D. C. Senft, J. Quian and G. C. Papen, Simultaneous observations of sporadic E, Na, Fe, and Ca+ layers at Urbana, Illinois: three case studies, J. Geophys. Res., 98, 16865-16873, 1993.

Hansen, G. and U. v. Zahn, Sudden sodium layers in polar latitudes, Journal of Atmospheric and Terrestrial Physics, 52, 585-608, 1990.

Miyagawa, H., T. Nakamura, T. Tsuda, M. Abo, C. Nagasawa, T. D. Kawahara, K. Kobayashi, T. Kitahara, and A. Nomura, Observations of mesospheric sporadic sodium layers with th UM radar and sodium lidars, Eath, Planet and Space,51, 758-797, 1999.

Munasinghe, G., H. Hur, T. Y. Huang, A. Bhattachryya and T. F. Tuan, Application of the dispersion formula to long-and short-period gravity waves: Comparisons with ALOHA-93 data and an analytical model, J. Geophys. Res., 103, 6467-6481, 1998.

Qian, J., Y. Gu and C. S. Gardner, Characteristics of the sporadic Na lyers observed during the airborne lidar and observations of Hawaiian airglow/airborne noctilucent cloud campaigns, J. Geophys. Res., 103, 6333-6348, 19

Swenson, G. R., and P. J. Espy, Observations of 2-dimensional airglow structure and Na density from the ALOHA, October 9, 1993 'storm flight', Geophys. Res. Lett., 22, 28-2848, 1995.

Swenson, G. R., J. Qian, J. M. C. Plane, P. J. Espy, M. J. Taylor, D. N. Turnbull and R. P. Lowe, Dynamical and chemical aspects of the mesospheric Na "wall" event on October 9, 1993 during the Airborne Lidar and Observations of Hawaiian Airglow (ALOHA) campaign, J. Geophys. Res., 103, 6361-6380, 1998.

Taylor, M. J., D. N. Turnbull and R. P. Lowe, Spectrometric and imaging measurements of a spectacular gravity wave event observed during the ALOHAH-93 campaign, Geophys. Res. Lett., 22, 2849-2852, 1995.

Lidar Measurements of Mesospheric Inversion at a Low Latitude (13.8*N, 79.2*E) : First Result

V. SIVA KUMAR, Y. Bhavani Kumar, K. Raghunath and P.B. Rao,
National MST Radar Facility, P.B.No. 123, Tirupati – 517 502, India
e–mail:nmrf@isro.ernet.in
M. Krishnaiah,
Department of Physics, S.V.University, Tirupati– 517 502. India
Kohei Mizutani, Tetsuo Aoki, Motoaki Yasui and Toshikazu Itabe
Communication Research Laboratory, 4–2–1, Nukai Kitamachi, Koganei, Tokyo 184–8795, Japan.

1. Introduction :

Gravity wave activities are playing major role through momentum and energy transport and its deposition in the large–scale dynamics and thermal budget of the Middle atmosphere. Gravity waves in the middle atmosphere have been studied by investigating density and temperature fluctuations observed with Rayleigh lidars at many locations, but mainly in middle and high latitudes, such as Haute Provence (OHP), France (44*N, 6*E)1 , Biscarosse (BIS) (44*N, 1*E), France2, Tsukuba(36*N, 140*E), Canada3, Eureka, Canada(80*N, 86*W)4 and Urbana (40*N, 88*W), Illinois5. Rayleigh Lidar offers the unique ability to make continuous measurements of temperature (or density) mesoscale fluctuations in the altitude range 30 to 80 km with high resolution. A strong temperature inversion is often observed in the mesospheric height 70–80 km during our observation period, which could persist several days are likely to be induced by gravity wave breaking6–8 and by due to the release of heat9. A new probe to the atmosphere Lidar system has recently been established at National MST Radar Facility (NMRF), Gadanki (13.8*N, 79.2* E) under an Indo–Japanese collaboration programme. The Lidar and the co–located Mesosphere–Stratosphere–Troposphere (MST) Radar constitute a unique combination for conducting high–resolution studies on the structure and dynamics of the middle atmosphere. The present study is based on the Lidar data collected over 64 nights during Mar'98–June'99. For the first time, the mesospheric temperature inversion at low latitude (13.8*N, 79.2*E) and the role of gravity wave breaking in generating this inversion is examined.

2. Lidar System Description:

The Rayleigh Lidar system used, employs an Nd:YAG Laser with a pulse repetition of frequency of 20 Hz and a mean power of 11 W at 532 nm. The receiver makes use of 0.76m–dia mirror in a Newtonian type configuration, which provides a 1–mrad field of view, about 10 times larger than that of the transmitted beam. To extend the dynamic range of the detector, Indo–Japanese–Lidar(IJL) system uses a beam splitter (90 & 10%) to direct the

incoming radiation to two different photomultiplier tubes of dissimilar gains. The 10% channel (low sensitive – designated as U) is intended to collect the signals from the lower altitudes, whereas the 90% channel (high sensitive – designated as R) for higher altitudes. The PMTs operated in photon counting mode with the output pulses being fed to pulse discriminators and a PC based photon counting system operating with a real–time multi–channel scalar (MCS) software provides photon count profile with a range resolution of 300 m. The initial photon integration extends over a total of 5000 laser pulses, corresponding to a sampling time of 250 sec. The detailed Technical description of the IJL system has been presented by Bhavanikumar10 .

3. Methods of Analysis:

The method of analysis adopted for determination of temperature profile from the Rayleigh channel data of the Lidar follows closely that given by Chanin and Hauchecorne11. In the height range where Mie contribution is negligible (35–80 km), the recorded signal intensity, corrected for the range and atmospheric transmission, is proportional to the molecular number density. Using the number density taken from an appropriate model (US–76) for the height of 50km where the signal–to–noise ratio is fairly high, the constant of proportionality is evaluated and thereby the density profile *(Zi) is derived. Taking the pressure (P) at the top of the height range (90–km) from the atmospheric model, the pressure profile is computed using the measured density profile, assuming the atmosphere to be in hydrostatic equilibrium. Adopting the perfect gas law, the temperature T (Zi) is computed using the expression given by

$$T(Zi) = \frac{Mg(Zi)\,dz.}{R\,\mathrm{Log}(1+X)} \quad , \quad \text{Where} \quad X = \frac{*(ZI)\,g(Zi)\,dz}{P(Zi + dz/2)}$$

Any uncertainty in the pressure at the top of the profile would contribute to temperature uncertainty that falls rapidly with decreasing altitude.

4. Results and Discussion :

The temperature profiles, obtained by Rayleigh Lidar frequently exhibit a strong temperature inversion with 20 to 40° K at mesospheric heights. A sample result observed in the month of May–1998 for different nights is as shown in Figure 1(a–b). Figure 1(a) shows a typical example of observed temperature inversion at 75 km and the temperature difference is found to be 20* K with respect to Model (USRO–1976) on 8–9 May 1998. At the same instant there is no inversion found on 21–22 May 1998 and the measured temperature profile is closely following the model (Figure 1(b)). This implies that the phenomena are highly temporal. Similar observations were reported by Hauchecorne12, Leblanc13, An Leblanc and Hauchecorne14, This was attributed due to the gravity wave breaking at these altitudes12,14. Meriwether and Mlynczak9 independently carried out the analysis on mesospheric temperature inversions

and gave an explanation in terms of chemical heating caused by the sudden change in ozone concentration. In our observations, this inversion always persisted above 70 km, sometimes two minima were observed at ~5 km apart.

A statistical analysis has been carried out for the above study by using the database collected over 64 nights of observations during Mar'98 to June'99. Figure 2 shows that the histogram indicating the height of occurrence of mesospheric temperature inversion. It is found from that the height of occurrence is maximum at 76–79 km and the minimum occurrence around 70–75 km.. But the mid–latitude observations of inversion were reported below 70 km12. The observed inversion always associated with reduction in the density12. We observed strong inversions of the order of 20 – 40 °K with respect to model (USRO –1976), The maximum of the order of 33* K is found and minimum around 5* K by taking into consideration of standard deviation (Figure 3). Figure 4. represents the probability of occurrence with respect to seasonal, shows that in summer the percentage of occurrence is found to be 68, at spring to be 50 and the least during winter about 43. But at midlatitude the observation is found to be maximum during winter than in summer12. The observed temperature inversion at mesospheric heights were found with minimum persistency of 30 min to more than 7 hrs indicating that the phenomenon is highly temporal. The major role of gravity wave activity on these phenomena is on going. A rare case we have examined the strong turbulence at this height, with the help of co–located MST Radar operating at 53 MHz.

5. Conclusion :

The Rayleigh Lidar operated at Gadanki (13.8*N, 79.2*E) has been used to retrieve the temperature profiles for the period March'98 to June'99. The most of an interesting feature of the temperature profiles is the inversion observed in the height range of 70–80 km. This is found to occur mostly around 76–79 km and the deviation relative to the model temperature is as much as 33*K. The inversion is found to be most significant during summer and least conspicuous during winter. The role of gravity wave breaking in generating the inversion is examined and results on the evolution of the gravity wave spectra to indicate that gravity wave breaking is significant factor for the observed mesospheric inversion. In addition to this the release of heat due to exothermic chemical reaction may be a cause for this inversion where the role of gravity wave activity is minimum.

6. References :

1. Wilson R., M.L.,Chanin and A. Hauchecorne, J.Geohys. Res., 96 (1991),5153.
2. Wilson R., M.L.,Chanin and A. Hauchecorne, J.Geohys. Res., 96 (1991),5169.
3. Whiteway J.A., and A.I. Carswell, J.Geophs, Res., 100 (1995), 14113.
4. Whiteway A.A., and A.L.. Carswell, J.geophy., Res., 51 (1994), 3122.
5. Gardner C.S., M.S.Miller and C.H.Liu., J. Atmos. Sci., 46 (1989), 1838.

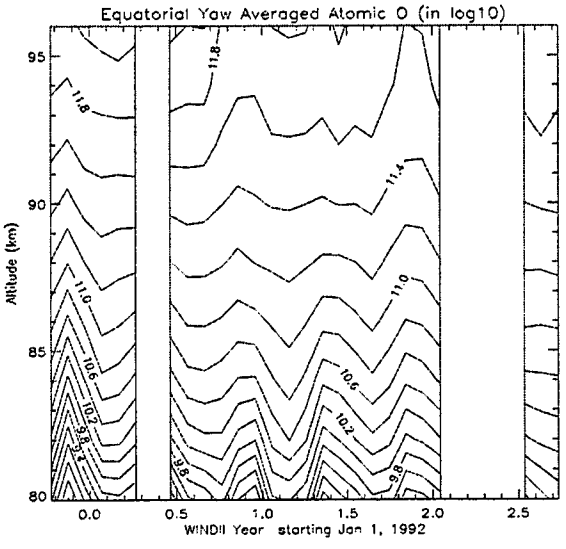
6. Hauchecorne A., M.L.Chanin, and R. Wilson, Geophys. Res. Lett., 14 (1987), 933.
7. Hauchecorne A., and A. Maillard, Geophys. Res. Lett., 17 (1990), 2197.
8. Chanin M.L., and A. Hauchecorne, Indian Journal of Radio and Space Physics, 20 (1991),1.
9. Meriwether W.J., and M.G.Mlynczak., J. Geophys. Res., 100 (1995) 1379.
10. Bhavani kumar Y., K. Raghunath, V, Siva kumar, P.B. Rao, A.R. Jain, Kohei Mizutani,
Tetsuo Aoki, Motoaki Yasui and Toshikazu Itabe Proceedings. IRSI (Radar Symposium
India–99, 14–17 December 1999, Bangalore, India).
11.Chanin M.L., and A. Hauchecorne, MAP, 13 (1986),87.
12. Hauchecorne A., Chanin.M.L. and Wilson.R, Geophys. Res. Lett (USA), 14 (1987) 933.
13. Leblanc T., Hauchecorne.A, Chanin.M.L., Taylor.F.W., Rodgers C.D., and Livesy.N, Geophys. Res. Lett (USA), 22 (1995) 1485.
14. Leblanc T., and Hauchecorne.A., J.Geophys, Res (USA), 102 (1997) 19,471.

Seasonal Variation of Atomic Oxygen over the Equator derived from WINDII/UARS Hydroxyl Airglow Observations

R.P. Lowe and Jason Russell, Department of Physics and Astronomy, The University of Western Ontario, London, Canada

The hydroxyl airglow occurs in the 80 to 95 km region in the region below the peak of the atomic oxygen distribution. Its height profile is determined by the product of the atomic oxygen density with the neutral density squared, if quenching is neglected . As a result the height profile can be used to infer the atomic oxygen distribution with little uncertainty.

The WINDII instrument on UARS measured the hydroxyl airglow height profile from late 1991 early 1995 on a regular basis. Over two million measurements were made, many of them over the equator. During a yaw period of 36 days, the observations covered all local times during the hours of darkness. For the purposes of this study, the data from a complete yaw period were averaged to minimize the effects of diurnal variation. The resulting hydroxyl profiles show that the peak emission at he equator is typically near 86 km but shows a strong semi-annaul oscillation which lowers the height of the peak by nearly 3 km near equinox.



These profiles have been used to derive the atomic oxygen profile making reasonable assumptions about the effect of quenching. The resulting height distribution of [O] is shown in the attached figure. All of the data used in this analysis was taken within 2.5 degrees of the equator. The blank regions correspond to periods when insufficient data were available due to technical difficulties with the satellite.

In addition to the semi-annual variation, the figure illustrates what appears to be a significant dependence on solar activity which decreased throughout the period studied. The effect appears to be different below 88 km than it is above.

Ionospheric Effects of Lightning Discharges: Sprites, Elves, Runaway MeV Electron Beams, and Early/Fast Conductivity Changes

U. S. INAN (Space, Telecommunications, and Radioscience Laboratory, Packard Bldg. Rm.355, 350 Serra Street, Stanford University, Stanford, CA 94305-9515)

INTRODUCTION

A fascinating menagerie of complex phenomena have been uncovered during the past decade that collectively indicate that tropospheric thunderstorms and lightning discharges are strongly coupled (electrodynamically) to the overlaying upper atmospheric regions, ranging from the mesosphere to the lower ionosphere and extending to the radiation belts. The mesospheric and lower ionospheric effects of lightning typically occur at $L <\sim 3$, including middle- and low-latitudes, and extending to equatorial regions.

Lightning phenomena at cloud altitudes (<20 km) affect the upper atmosphere at altitudes >40 km either via the release of intense electromagnetic pulses (EMPs) and/or the production of intense quasi-static electric (QE) fields at mesospheric altitudes. Lightning involves rapid removal of charge built-up within the thundercloud, either by intracloud discharges involving charge motion and neutralization within the cloud or by cloud-to-ground (CG) discharges which move charge to the ground. An average lightning discharge radiates an EMP of ~20 GW peak power, which propagates though the ionosphere and couples into the radiation belts, heating and ionizing the former and precipitating trapped energetic electrons from the latter. In addition, lightning discharges often produce intense transient QE fields of up to ~1 kV/m at 40–80 km altitudes, which for positive CG discharges is directed downwards, and which can thus avalanche accelerate upward-driven runaway MeV electron beams. In the context of the latter, it is startling to realize that the total transient potential drop between 20 to 80 km altitude is ~100 MeV for large positive CG discharges, amounting to a gigantic particle accelerator at high altitudes above thunderstorms. The potential global importance of these lightning-driven electrodynamic stresses of the upper atmosphere are underscored by the fact that up to ~2000 thunderstorms are active on the surface of the Earth at any time, with ~40–100 lightning discharges occurring every second [*Volland*, 1984; *Christian et al.*, 1999].

We provide a brief background and a discussion of recent results realized in the context of work carried out by the author and his students and associates. This paper is by no means a comprehensive review of the subject, which is simply not possible in the time or space available. Recent results concerning lightning-induced electron precipitation (LEP) from the inner radiation belt and slot regions [*Lauben et al.*, 1999; *Johnson et al.*, 1999b] are also not discussed, although they suggest that the LEP process may be an important (albeit indirect) means by which thunderstorms and lightning affect the lower ionosphere (as well as the inner radiation belt) on a global scale.

SPRITES AND ELVES

The earliest suggestion of possible upper atmospheric effects of lightning discharges was put forth by *Wilson* [1925], who remarkably predicted that lightning would lead to sparking of air at high altitudes (>40 km), upward acceleration of MeV electron beams, and g-radiation, simply because the air density falls of faster in altitude (exponential with scale height of 6 km) than the Coulomb field of the charge removed by lightning (inverse square of distance). Based on results realized in the past decade, it is now known that high altitude air indeed sparks in a manner of ways in response to charge removal at cloud levels, leading to optical emissions with complex temporal, spectral (color), and spatial structure over the altitude range 40 to 90 km, classified (based on various properties, but largely on temporal duration and altitude range), as sprites, elves and blue jets.

Sprites are large luminous discharges which appear in the altitude range of ~40 km to 90 km above large thunderstorms [e.g., *Sentman et al.*, 1995]. The basic physical mechanism of sprites is believed to be the heating of ambient electrons in the mesosphere and lower ionosphere by the intense QE fields which temporarily (for a few to tens of milliseconds) exist at high altitudes following intense lightning flashes [*Pasko et al.*, 1997]. Recent telescopic measurements [*Gerken et al.*, 2000] reveal the existence of highly complex fine structure in sprites, with transverse scales ranging from ~200 m to <40 m, generally consistent with theoretical predictions of streamer structure [*Pasko et al.*, 1998], but also exhibiting a broader variety and spatial scales than expected. The presence of branching tree-like shapes and well defined but isolated columns, and the fact that specific columnar regions are selectively excited by successive discharges and re-brighten, indicate the presence of persistent ionization [*Gerken et al.*, 2000].

Other new results concerning sprites include the observation of sprites produced by negative CG flashes [*Barrington-Leigh et al.*, 1999] and the development of a new fractal-based model of sprite fine structure and altitude extent [*Pasko et al.*, 2000]. The former is important because it indicates that runaway MeV electron beams do not play an important role in the production of sprites, although such beams are undoubtedly driven by the same intense QE fields and produce terrestrial γ-ray flashes (see below). The latter development allows us to understand the production of sprites by lightning discharges which remove comparatively small amount of charge [*Cummer and Inan*, 1997].

Elves are optical emissions [e.g., *Inan et al.*, 1997] which last much shorter (<1 ms) than sprites, and are typically limited to 80-95 km altitude, being produced by the heating, ionization, and optical emissions due to the EMPs radiated by both positive and negative lightning discharges [*Barrington-Leigh and Inan*, 1999]. Recent comparisons of theoretical modeling with high-speed video measurements have clarified the distinction between sprites and elves, showing that the disk-shaped diffuse flashes sometimes observed to precede sprite electrical breakdown are produced by QE heating and ionization rather than by EMP heating, and would better be viewed as 'sprite haloes' rather than elves [*Barrington-Leigh et al.*, 2000].

TERRESTRIAL γ-RAY FLASHES AND RUNAWAY MEV ELECTRON BEAMS

The observation of ~1 ms bursts of γ-rays (with photon energy extending above 1 MeV) originating in the Earth's atmosphere, associated with lightning discharges [*Inan et al.*, 1996a], indicates bremsstrahlung radiation from >1 MeV electrons, consistent with highly quantitative recent modeling [e.g., *Lehtinen et al.*, 1999a].

Quantitative modeling of sprites in comparison with experimental data [*Pasko et al.*, 1997] confirm the existence above thunderstorms of intense quasi-static electric fields as mentioned above. These fields are sufficient to produce runaway electron beams via avalanche acceleration [*Taranenko and Roussel-Dupré*, 1996; *Lehtinen et al.*, 1996; 1997; *Roussel-Dupré and Gurevich*, 1996], leading to the emission of bremsstrahlung γ-ray flashes [*Lehtinen et al.*, 1999a], of intensity consistent with BATSE observations. Quantitative models of the γ-ray production mechanism indicate a runaway beam of 100 keV to 10 MeV electrons radiating γ rays at 60-70 km altitudes [*Lehtinen et al.*, 1999a]. Since the upper atmosphere above 70 km is essentially a thin target for electrons of energy >500 keV, most of these particles must escape upward along the field lines into the radiation belt region, constituting an injected beam of total fluence predicted to be 10^6-10^7 el/cm^2 [*Lehtinen et al.*, 1999a; 2000a]. For cloud-to-ground discharges, the estimated transverse scale of the beam is ~10–20 km, while for horizontal intra-cloud discharges the scale is estimated to be as large as ~100 km [*Lehtinen et al.*, 1997; 1999a].

If even ~10% [*Lehtinen et al.*, 2000a] of the electrons are precipitated in the geomagnetically conjugate region, γ-ray fluxes exceeding those produced during beam formation (in the original hemisphere), as well as intense optical emissions would be produced [*Lehtinen et al.*, 1999b, 2000b]. The portion of injected relativistic electrons trapped due to pitch angle scattering by Langmuir waves (generated via beam-plasma instabilities) [*Lehtinen et al.*, 2000a] forms eastward drifting 'curtains' of trapped MeV

electrons. Even if only ~0.01% of typical lightning discharges produce γ-rays (and thus MeV electron beams) this process may be an important source of >1 MeV electrons in the inner belt.

EARLY/FAST CONDUCTIVITY CHANGES

The earliest evidence of direct modification of the overhead ionosphere by lightning discharges was in the form of early/fast subionospheric VLF events [e.g., *Inan et al.*, 1988], indicating rapid (<20 ms) changes in lower ionospheric conductivity occurring simultaneously (within <20 ms) with individual lightning discharges. The precise physical mechanism of these events is still under debate [*Inan et al.*, 1996b; *Dowden et al.*, 1996], but new results have been steadily emerging. VLF holographic measurements have conclusively shown that the transverse extent of the disturbed ionospheric regions is ~90 km [*Johnson et al.*, 1999] and that the recovery time of these events are distinctly different [*Sampath et al.*, 2000] from those of another class of subionospheric VLF events that are produced by lightning-induced electron precipitation bursts. The relatively large lateral extent of the disturbances indicate that these events are not likely to be produced via scattering of VLF waves by individual sprite columns, typically ~30 km in extent. More accurate measurements of the spatial shape of ionospheric disturbances underlying early/fast events are currently being implemented.

While early/fast events have been known to be associated with lightning discharges, the particular nature of lightning events that lead to these events have not been known, until a recent observation reported by *Johnson et al.* [2000]. Based on these new results, it appears that early/fast events are produced by those cloud-to-ground lightning discharges which are accompanied by a complex of intracloud horizontal discharges, which are evidenced at VLF as clusters of radio atmospherics. This new finding may shed light into the mechanism of production of these fast conductivity changes, and may also lead to a better understanding of the nature of lightning flashes which lead to sprites. In this connection, it is important to note that previous suggestions of possible contributions to sprite production by horizontal lightning activity [*Bell et al.*, 1998; *Cummer and Stanley*, 1999].

REFERENCES

1. Barrington-Leigh, C. P. and U. S. Inan, Elves triggered by positive and negative lightning discharges, *Geophys. Res. Lett., 26*, 683, 1999.
2. Barrington-Leigh, C. P., U. S. Inan, M. Stanley, and S. A. Cummer, Sprites triggered by negative lightning discharges, *Geophys. Res. Lett.,26*, 3605-3608, 1999.
3. Barrington-Leigh, C. P., U. S. Inan, and M. Stanley, Identification of Sprites and Elves with Broadband Imagery and Array Photometry, (in review), *J. Geophys. Res.*, 2000.
4. Bell, T. F., S. C. Reising, and U. S. Inan, Intense Continuing Currents Following Positive Cloud-to-Ground Lightning Associated with Red Sprites, *Geophys. Res. Lett., 25,* 1285, 1998.
5. Christian, H. J., R. J. Blakeslee, D. J. Boccippio, W. L. Boeck, D. E. Buechler, K. T. Driscoll, S. J. Goodman, J. M. Hall, W. J. Koshak, D. M. Mach, and M. F. Stewart, Global frequency and distribution of lightning as observed by the Optical Transient Detector (OTD), *Preprints, 11th Int. Conf. on Atmos. Electr.*, ed. H. J. Christian, NASA/CP-1999-209261, Guntersville, AL, 726-729, June 7-11, 1999.
6. Cummer, S. A. and U. S. Inan, Measurement of charge transfer in sprite-producing lightning using ELF radio atmospherics, *Geophys. Res.lett., 24*, 1731, 1997.
7. Cummer, S. A. and M. Stanley, Submillisecond resolution lightning currents and sprite development: observations and implications, *Geophys. Res.lett., 26*, 3205-3208, 2000.
8. Dowden, R. L., Comment on 'VLF Signatures of ionospheric disturbances associated with sprites' by Inan et al., *Geophys. Res. Lett., 23*, 3421, 1996.

9. Gerken, E. A., U. S. Inan, and C. P. Barrington-Leigh, Telescopic Imaging of Sprites, (in review), *Geophys. Res. Lett.*, 2000.

10. Inan, U. S., D. C. Shafer, W. Y. Yip, and R. E. Orville, Subionospheric VLF signatures of nighttime D-region perturbations in the vicinity of lightning discharges, *J. Geophys. Res., 93,* 11455, 1988.

11. Inan, U. S., C. Barrington-Leigh, S. Hansen, V. S. Glukhov, and T. F. Bell, Rapid Lateral Expansion of Optical Iuminosity in Lightning-Induced Ionospheric Flashes Referred to as 'Elves', *Geophys. Res. Lett., 24,* 583, 1997.

12. Inan, U. S., S. C. Reising, G. J. Fishman, and J. M. Horack, On the association of terrestrial gamma-ray bursts with lightning discharges vand sprites, *Geophys. Res. Lett., 23,* 1017, 1996a.

13. Inan, U. S., T. F. Bell, and V. P. Pasko, Reply to Comment by R. L. Dowden et al. on "VLF signatures of ionospheric disturbances associated with sprites", *Geophys. Res. Lett., 23,* 3423, 1996b.

14. Johnson, M. P., U. S. Inan, S. J. Lev-Tov, and T. F. Bell, Scattering Pattern of Lightning-Induced Ionospheric Disturbances Associated with Early/Fast VLF Events, *Geophys. Res. Lett., 26,* 2363, 1999a.

15. Johnson M. P., U. S. Inan, and D. S. Lauben, Subionospheric VLF observations of oblique (nonducted) whistler-induced electron precipitation, *Geophys. Res. Lett.,26,* 3569-3572, 1999b.

16. Johnson, M. P. and U. S. Inan, Sferic clusters associated with early/fast VLF events, *Geophys. Res. Lett.,* in press, 2000.

17. Lauben, D. S., U. S. Inan, and T. F. Bell, Poleward-displaced electron precipitation from lightning-generated oblique whistlers, *Geophys. Res. Lett., 26,* 2633-2636, 1999.

18. Lehtinen, N. G., T. F. Bell, and U. S. Inan, Monte Carlo simulation of runaway MeV electron breakdown with application to red sprites and terrestrial gamma ray flashes, *J. Geophys. Res., 104,* 24699, 1999a.

19. Lehtinen, N. G., U. S. Inan and T. F. Bell, Nonuniform Runaway Electron Avalanche above Thunderstorms and Effects in the Conjugate Hemisphere, *Eos Trans. AGU, 80 (46),* Fall Meet. Suppl., F225, 1999b.

20. Lehtinen, N. G., U. S. Inan and T. F. Bell, Trapped energetic electron curtains produced by thunderstorm driven relativistic runaway electrons, *Geophys. Res. Lett.,* in press, 2000a.

21. Lehtinen, N. G., U. S. Inan, and T. F. Bell, Effects of Thunderstorm Driven Runaway Electrons in the Conjugate Hemisphere: Purple Sprites and Ionization Enhancements, (in review), *J. Geophys. Res.*, 2000b.

22. Pasko, V. P., U. S. Inan, T. F. Bell, and Y. N. Taranenko, Sprites produced by quasi-electrostatic heating and ionization in the lower ionosphere, *J. Geophys. Res., 102,* 4529, 1997.

23. Pasko, V.P., U.S. Inan, T.F. Bell, Spatial structure of sprites, *Geophys. Res. Lett., 25,* 2123-2126, 1998.

24. Pasko, V.P., U.S. Inan, T.F. Bell, Fractal structure of sprites, *Geophys. Res. Lett.,* , in press, 2000.

25. Roussel-Dupré, R. A., and A. V. Gurevich, On runaway breakdown and upward propagating discharges, *J. Geophys. Res., 101,* 2297, 1996.

26. Sampath, H., U. S. Inan, and M. P. Johnson, Recovery signatures and occurrence properties of lightning-associated subionospheric VLF perturbations, *J. Geophys. Res.,105,* 183-191, 2000.

27. Sentman, D. D., E. M. Wescott, D. L. Osborne, D. L. Hampton, and M. J. Heavner, Preliminary results from the Sprites94 campaign: Red Sprites, *Geophys. Res. Lett., 22,* 1205, 1995.

28. Taranenko, Y. N., and R. A. Roussel-Dupré, High altitude discharges and gamma-ray flashes: a manifestation of runaway air breakdown, *Geophys. Res. Lett., 23,* 571, 1996.

29. Volland H., *Atmospheric Electrodynamics*, Springer- Verlag, New York, 1984.

30. Wilson, C. T. R., The electric field of a thundercloud and some of its effects, *Proc. Phys. Soc. London, 37,* 32D, 1925.

CORRELATIVE STUDY BETWEEN GEOMAGNETISM AND SURFACE WEATHER AT MAGNETIC EQUATOR AND HIGH LATITUDE

M. LAL(EGRL, Indian Institute of Geomagnetism, Krishnapuram, Tirunelveli–627011, India), B. Paramshivam(EGRL, IIG, Krishnapuram, Tirunelveli–627011), K.U. Nair(EGRL, IIG, krishnapuram, Tirunelveli –627011, India) , C. Paneerselvam(EGRL, IIG, krishnapuram, Tirunelveli–627011) , P. Elango(EGRL, Krishnapuram, Tirunelveli–627011, India), C. Selvaraj (Krishnapuram, Maharajangar, Tirunelveli–627011, India), and R. Rajaram (Indian Institute of Geomagnetism, Colaba, Mumbai–5, India)

INTRODUCTION

The variability's of the solar wind and high energy charged particle fluxes from an important channel of solar activity influence on the earth's atmosphere. There are many different component of this channel. Among these often interrelated phenomena are the variability of solar wind speed, interplanetary magnetic fields, Ap index, Kp index, Dst index, coronal mass ejection, solar flares, magnetospheric substorms; and geomagnetic storms. The effect of these phenomena are interconnected with each other. The majority of the effects of solar wind variability manifest themselves through geomagnetic storms, magnetospheric substorms and changes of geomagnetic activity. Geomagnetic storms are believed to cause the largest global atmospheric effects among all the above phenomena.

We have made an attempt to study the coupling between solar and earth's atmosphere, for the low latitude as well as high latitude region. In this process, we have utilized surface pressure, earth's magnetic filed, D–region electron density variation, Interplanetary magnetic filed, Dst Index, Kp index, Ap index, and solar wind at the geomagnetic equator. Similarly we have used surface pressure, earth's magnetic field and other solar component as explained above for the high latitude station. The effects generated by solar wind variability and high energy charged particles are well developed and fairly well understood in the lower lying layers and in the neutral middle atmosphere, particularly in the stratosphere (Lastovica, 1988). Effects in the troposphere are a topic of long – lasting controversial discussions.

The aim of this paper is to give a brief contemporary description of the effects of geomagnetic storms on the lower ionosphere, and lower atmosphere at geomagnetic equator and high latitude region. We have also tried to study the correlation between geomagnetic equator and high latitude magnetic filed variation. The surface pressure variability between low and high latitude has also been studied in the present work. This is done in the next two sections. The paper is based mainly on experimental findings and correlation's, since the mechanism responsible are mostly highly uncertain or unknown, except for those acting in the lower ionosphere.

LOW LATITUDE COUPLING

The data utilized in the present study are for the month of September 1999. This month happen to be very geomagnetically active period. During this period, a recurrent high speed coronal hole wind arrived at the earth on September 12, triggering a long interval of elevated magnetic activity. A major magnetic storm (near real–time Kyoto Dst reaching ~ –177 nT), followed on September 22–23, triggered by the arrival of an interplanetary shock and solar ejecta with associated southward IMF Bz reaching –20 nT. We have some of the instrument at geomagnetic equator installed by our institute, which can give surface pressure variation, earth's magnetic field component such as H, D, and Z, and mesospheric electron density variation by using Partial Reflection Radar. This study has been mainly for near geomagnetic equator. The horizontal component of magnetic field (ΔH) in the equatorial region is very significant. The electron density variation has been analyzed between 84 and 98 km altitude at the interval of 2 km. The electron density variation for 88 km altitude region has been compared with the ΔH. It has been observed that the electron density during nighttime is about 1% of the daytime values. The ΔH values shows the solar variability, i.e., maximum in the noontime and minimum during midnight. The effect of geomagnetic storm has been observed in the ΔH component of magnetic field. The Dst index on 12th September increases up to –60 nT. There is another pronounced geomagnetic storm observed on 23rd September 1999. During this period, the Dst index increases upto –110 nT. The effect of increased Dst index is clearly seen in the ΔH component of the magnetic field. But the rate of increase of Dst index is not same as the rate of increase of ΔH during geomagnetic storm period. It is difficult for us at present state to estimate the physical mechanism. The ΔH component found to be deviated from the normal diurnal variation during afternoon period. It has been found that the ΔH decreases during afternoon. The decrease in ΔH is significantly large by increasing the magnitude of geomagnetic storm. We have tried to compare the magnetic field component with the electron density variation obtained in the mesospheric region. The electron density obtained at 88 km shows pronounced increase during storm period. It has been observed that, by increasing the geomagnetic storm activity, the electron density increases, whereas ΔH component of magnetic filed decreases significantly. This may be due to the drift of electron from higher altitude (~110 km) to the lower altitude region, i.e., mesospheric region. This phenomenon has been observed at 88 km as well as at 94 km altitude. The surface pressure measured at geomagnetic equator does not show large correlation coefficient with the magnetic filed variation, whereas it shows pronounced positive correlation with the solar wind component. It is essential to look for the physical mechanism which reappear at the tropospheric altitude, which is a long lasting discussion.

HIGH LATITUDE COUPLING

We have also tried to study the solar terrestrial coupling at higher latitude station, Masco, Russia. In this regard, we have utilized surface pressure variation, all the component of earth's magnetic field, and solar wind to study the coupling mechanism within these parameters. The horizontal (ΔH) and vertical (ΔZ) component of magnetic field, for the September 1999, has been analyzed in the present work. The ΔH and ΔZ component shows the negative correlation with each other for almost all the time of the day. Though, the magnetic field intensity is large in the local noontime, the sudden enhancement in ΔH and ΔZ has been observed even in the nighttime. The signature of geomagnetic storm has been seen at local midnight with the variation of magnetic field by about 250 nT. This kind of signature has not been observed at the magnetic equator during geomagnetic storm. The correlation between solar wind variation and magnetic field component has been made. Unlike the magnetic equator, the high latitude magnetic component is found to be having negative correlation with solar wind variation. On the other hand, the solar wind speed and surface pressure variation measured at high latitude station, Masco, Russia, shows very good positive correlation. But the signature of geomagnetic storm is difficult to find in the surface pressure record. We have analyzed the data for very short time interval. These kind of feature can be very well study by using long period data which is the scope of future study.

ACKNOWLEDGEMENT

Authors are thankful to Department of Science & Technology, India for providing financial support for this project. We are also thankful to Dr. Vodin, IZMIRAN, Russia and Dr. A. Belov, Masco, Russia for providing geomagnetic and surface pressure data respectively. Authors are thankful to Director, Indian Institute of Geomagnetism , Mumbai, India for his encouragement.

REFERENCES

J. Lastovica, Geomagnetic Storms : their origin, mechanism and ionospheric/atmospheric effects, JASTP, **58,** May 1996.

Solar – Geophysical Data prompt reports, NOAA, November 1999.

Hitchman, A.P., F.E.M. Lilley, & W.H. Campbell, The quite daily variation in the total magnetic field : global curves, Geophys. Res. Letts., **25,** no. 11, p. 2007–2010, June 1, 1998.

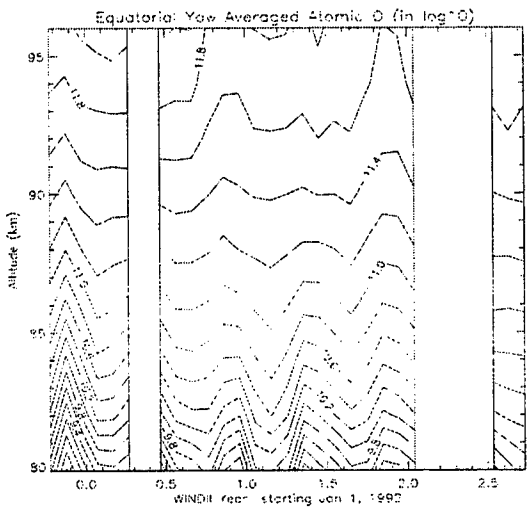
Tsurutani, B.T., W.D. Gonzalez, Y. Kamide, & J.K. Arballa, Magnetic storm, Geophysical Monogram Series, 1997.

Seasonal Variation of Atomic Oxygen over the Equator derived from WINDII/UARS Hydroxyl Airglow Observations

R.P. Lowe and Jason Russell, Department of Physics and Astronomy, The University of Western Ontario, London, Canada

The hydroxyl airglow occurs in the 80 to 95 km region in the region below the peak of the atomic oxygen distribution. Its height profile is determined by the product of the atomic oxygen density with the neutral density squared, if quenching is neglected . As a result the height profile can be used to infer the atomic oxygen distribution with little uncertainty.

The WINDII instrument on UARS measured the hydroxyl airglow height profile from late 1991 early 1995 on a regular basis. Over two million measurements were made, many of them over the equator. During a yaw period of 36 days, the observations covered all local times during the hours of darkness. For the purposes of this study, the data from a complete yaw period were averaged to minimize the effects of diurnal variation. The resulting hydroxyl profiles show that the peak emission at he equator is typically near 86 km but shows a strong semi-annaul oscillation which lowers the height of the peak by nearly 3 km near equinox.



These profiles have been used to derive the atomic oxygen profile making reasonable assumptions about the effect of quenching. The resulting height distribution of [O] is shown in the attached figure. All of the data used in this analysis was taken within 2.5 degrees of the equator. The blank regions correspond to periods when insufficient data were available due to technical difficulties with the satellite.

In addition to the semi-annual variation, the figure illustrates what appears to be a significant dependence on solar activity which decreased throughout the period studied. The effect appears to be different below 88 km than it is above.

CORRELATIVE STUDY BETWEEN GEOMAGNETIC AND WEATHER PARAMETERS AT MAGNETIC EQUATOR

M. Lal, B. Paramshivam, K.U. Nair, and R. Rajaram
Equatorial Geophysical Research Laboratory
Indian Institute of Geomagnetism,
Krishnapuram BO, Maharajanagar PO,
Tirunelveli – 627011, India
e–mail: egrl@vsnl.com

SUMMARY

An attempt has been made to study the coupling between earth's magnetic field, Kp index, ionospheric electron density, and surface pressure variation at low latitude northern hemispheric region, at magnetic equator (8.7°N, 77.8°E), Tirunelveli, India. The first four month of year 1997 data has been utilized for this purpose and we tried to find the correlation between these parameters. The magnetic field variation has been obtained by using ground–based magnetometer. The surface pressure variation has been obtained from Microbarograph. The ionospheric electron density has been obtained from the ionosonde operated at Kodikanal (10°N, 77°E), India. The local midnight data has been utilized for the present study. By using the local midnight data, the unwanted variation occurred during daytime has been minimized. The correlation coefficient has been obtained between Kp index and horizontal component of magnetic field, F–region electron density and horizontal component of magnetic field, and between surface pressure variation and horizontal component of magnetic field at the magnetic equator. The Kp index and horizontal component of the magnetic field shows maximum negative correlation coefficient of value –0.45, without and timelag. The surface pressure variation and horizontal component of the magnetic field shows the positive correlation of maximum value +0.47, without any timelag. Similarly, the Kp index and surface pressure variation shows maximum negative correlation coefficient of value –0.56, without any timelag. The correlation coefficient between Kp index and horizontal component of magnetic field shows the decrease in correlation coefficient by increase in timelag. We have also made an attempt to find the correlation coefficient between F–region electron density obtained at 10°N, and horizontal component of magnetic field at 8°N. It has been found that the maximum correlation coefficient has been obtained at the timelag of 12 days and its value is +0.47. This shows that the effect of electron density present at about 300 km altitude and 10°N, has been observed at the delay of about 12 days at 100 km altitude and at 8°N. Thus the diffusion of ion property has been estimated in great details and will be presented.

INTRODUCTION

This work is based mainly on experimental findings and correlation's, since the mechanism responsible are mostly highly unknown. The result is an original, so far not published, magnetic field and ionospheric electron density variations for the low latitude northern hemispheric region and also at the magnetic equator. Many papers that treat extraterrestrial effects on weather parameter changes in the troposphere and stratosphere seek the source of these changes in solar activity. However, as shown as early in the 1970s, not only solar activity, but also geomagnetic activity can be the factor which, under certain conditions, might influence the behaviour of the lower atmosphere.

Our observatory is located almost at the magnetic equator. There are several kind of instrumentation available to study the coupling between lower and upper atmospheric region. For example, ground–based magnetometer for the continuous measurements of earth's magnetic field, Partial Reflection Radar for the measurements of mesospheric wind as well as signal strength which can be interpreted as electron density variation between 70 and 100 km altitude region, Air–earth current measurements at the surface, surface pressure variation by using Microbarograph, VHF scintillation recorder to study the ionospheric irregularities. These measurements along with geomagnetic parameters available in the Internet are being utilized to study the coupling between lower, middle and upper atmosphere.

The solar wind –related phenomena and high–energy particle bombardment of the atmosphere play a role primarily at high latitudes. Some of these phenomena, e.g., geomagnetic storms or cosmic ray flux variability, also act at lower latitude, even if there effects are much weaker at low latitude region. We have made an attempt to study the coupling between geomagnetic and surface weather parameter at magnetic equator.

RESULTS

We have made an attempt to find the correlation coefficient between Kp index and horizontal component of the magnetic field by using the data described earlier. The Kp index and horizontal component of the magnetic field shows the maximum negative correlation coefficient of value –0.45, without any timelag. On the other hand, it shows the maximum positive correlation coefficient of value +0.20 at the time lag of 9 days. The negative correlation coefficient obtained between Kp and ΔH is very much prominent compared to the positive correlation coefficient obtained at the geomagnetic equator. The surface pressure variation and ΔH shows the positive correlation of maximum value +0.47, without ant timelag. Similarly, the Kp index and surface pressure variation shows maximum negative correlation coefficient of value –0.56, without ant timelag. There is a long–lived controversy as to geomagnetic phenomena effects in the troposphere.

CONCLUSION

The present study is done to find the correlation between geomagnetic and weather parameters at the magnetic equator. The data utilized for the present study are magnetic field, F–region electron density, Kp index and surface pressure for the month of January – April 1997. The maximum correlation coefficient between Kp index and ΔH found to be –0.45 without ant time lag. The surface pressure and ΔH shows maximum correlation coefficient of value +0.47 without any time lag. Similarly, the Kp index and surface pressure shows maximum correlation coefficient of –0.56 without any time lag. The F–region electron density at 10.2°N and ΔH at 8.7°N shows maximum positive correlation coefficient +0.47 at the delay of 12 days. This may be due to leakage of energy from one region to another region. These studied can be utilized for weather prediction on short and long–term time scale, after establishing correlation between various parameters.

ACKNOWLEDGEMENT

This work has been supported by Department of Science and Technology, India. Authors are thankful to Dr. P.L. Malhotra, NPL, New Delhi for providing ionosonde data. Authors are also thankful to Director, IIG, Prof. G.S. Lakhina for his encouragement at various steps.

Modeling the low latitude atmosphere and ionosphere

C G Fesen
Center for Space Sciences, U. of Texas at Dallas
POB 830688 MS FO22
Richardson, TX 75083-0688; fesen@tides.utdallas.edu

The earth's equatorial atmosphere and ionosphere is a region rich in physics and phenomenology such as the Appleton Ionization Anomaly, the Equatorial Wind and Temperature Anomaly, and the Midnight Temperature Anomaly. Partly because of this complexity, due in part to ion-neutral coupling, the low latitude atmosphere remains a challenge to understand and to model. Compounding the problem is the relative scarcity of data, particularly simultaneous observations of a variety of parameters.

Numerical models now solve the equations for the coupled thermosphere and ionosphere, including electrodynamics; recent simulations have been successfully capturing the pre-reversal enhancement in the vertical ion velocities that occurs shortly after sunset. This represents a major modeling advance. But before the models can be used to investigate the physics of the region, it's appropriate to ask how well they are doing in reproducing the atmosphere and ionosphere.

This paper will show comparisons between the National Center for Atmospheric Research thermosphere/ionosphere/electrodynamic general circulation model, the TIEGCM, and empirical models and observations of the low latitude upper atmosphere and ionosphere. The TIEGCM is also used in a series of numerical experiments to evaluate the influence of the model drivers on the low latitude atmosphere and ionosphere: these include the specification of the upper and lower boundary conditions and the high latitude energy and momentum sources.

The TIEGCM self-consistently calculates the coupled thermosphere and ionosphere, including electric potential, fields, and currents along with the ion and neutral densities, temperatures, and velocities. The vertical coordinate is log pressure with 29 levels spaced at 2 grid points per scale height; the altitudes extend roughly from 100 to $\geq$ 500 km. Latitude and longitude resolution is 5° by 5°. The model contains a realistic geomagnetic field, IGRF 1985.0, with offset geographic and geomagnetic poles.

Some of the adjustable parameters in the model are: the high latitude forcings, which parameterize the energy and momentum sources associated with magnetospheric convection and particle precipitation; the waves from the lower atmosphere that perturb the lower boundary of the model; and the fluxes of energy and constituents at the model boundaries.

The high latitude forcings are difficult to represent in a global model with coarse resolution in latitude and longitude, at least in terms of small scale auroral features.

With sufficient data, detailed forcings can be inferred through assimilative approaches such as AMIE but time and data requirements currently preclude its implementation in every model simulation. The high latitude forcings are very important to the global energy budget, significantly impacting the modeled neutral temperatures and composition.

The formulation of the lower boundary condition in the model allows it to be used for numerical experiments to investigate the effects of a variety of waves generated in the lower atmosphere which penetrate into the thermosphere. The model includes the diurnal 1,1 mode and the semidiurnal 2,2, 2,3, 2,4, 2,5, and 2,6 modes which are adjustable parameters. The tides at the lower boundary have been found to be particularly important for simulating the observed ion drifts in the zonal and vertical directions. The nighttime electron densities in the E region were found to play a key role in development of the pre-reversal enhancement in the low latitude vertical ion drifts.

Until recently, the effect of the upper boundary conditions in the model have been relatively unexplored. Investigations currently underway indicate that the O^+ fluxes at the model upper boundary (near 400–800 km, depending on solar cycle) can strongly affect the low latitude ionosphere, including the representation of n_max and h_max.

In all the simulations reported here, geomagnetically quiet conditions were imposed; the total hemispheric power of precipitating auroral electrons was 16 GW and a cross–polar–cap potential was 45 kV. Simulations were performed for March, June, and December for solar 10.7–cm levels of 85, 150, and 200 corresponding to solar cycle minimum, medium, and maximum conditions.

Comparisons were made to the empirical neutral atmosphere model MSIS and the empirical ionosphere model IRI-90. These were used to test and refine the model forcings until good agreement was obtained for global and zonal means (or for latitude/longitude at fixed UTs). This helps ensure a realistic background atmosphere and ionosphere is simulated in the TIEGCM. Good to excellent agreement is now achieved with global and zonal means, as illustrated in Figure 1. Comparisons were also made to datasets collected at Jicamarca, Peru by a variety of instruments, many of which were participating in MISETA campaigns.

Results of the sensitivity studies, which adjusted the model inputs described above, will be discussed. Among the most significant results is the importance of the E region semidiurnal 2,2 tidal wave in determining the magnitude and phase of the daytime F region vertical and zonal ion drifts. This is illustrated in Figure 2 which shows the ion drifts near 400 km for three different specifications of the 2,2 mode at the model lower boundary: no tide, a nominal amplitude consistent with climatological observations, and a larger amplitude consistent with more recent satellite data. In the model, the 2,2 amplitude is the most important factor in reproducing the observed daytime drifts. At night, in the model, the electron density in the E region is the most important factor in reproducing the pre-reversal enhancement in the vertical ion drifts.

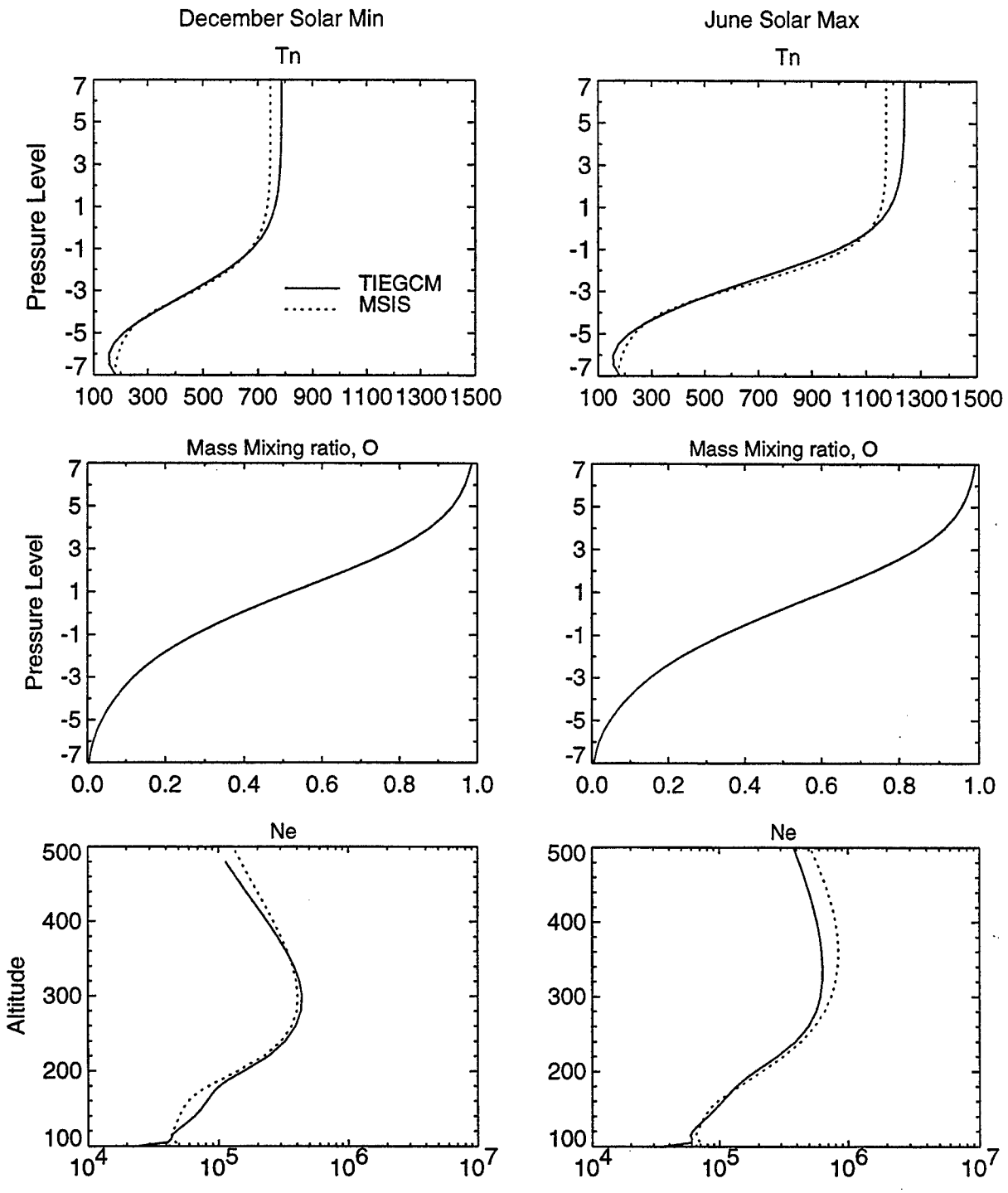


Figure 1. Comparison of global means from TIEGCM and MSIS for December solar minimum (left) and June solar maximum (right); neutral temperatures (top), O mass mixing ratio (middle) and electron density (bottom).

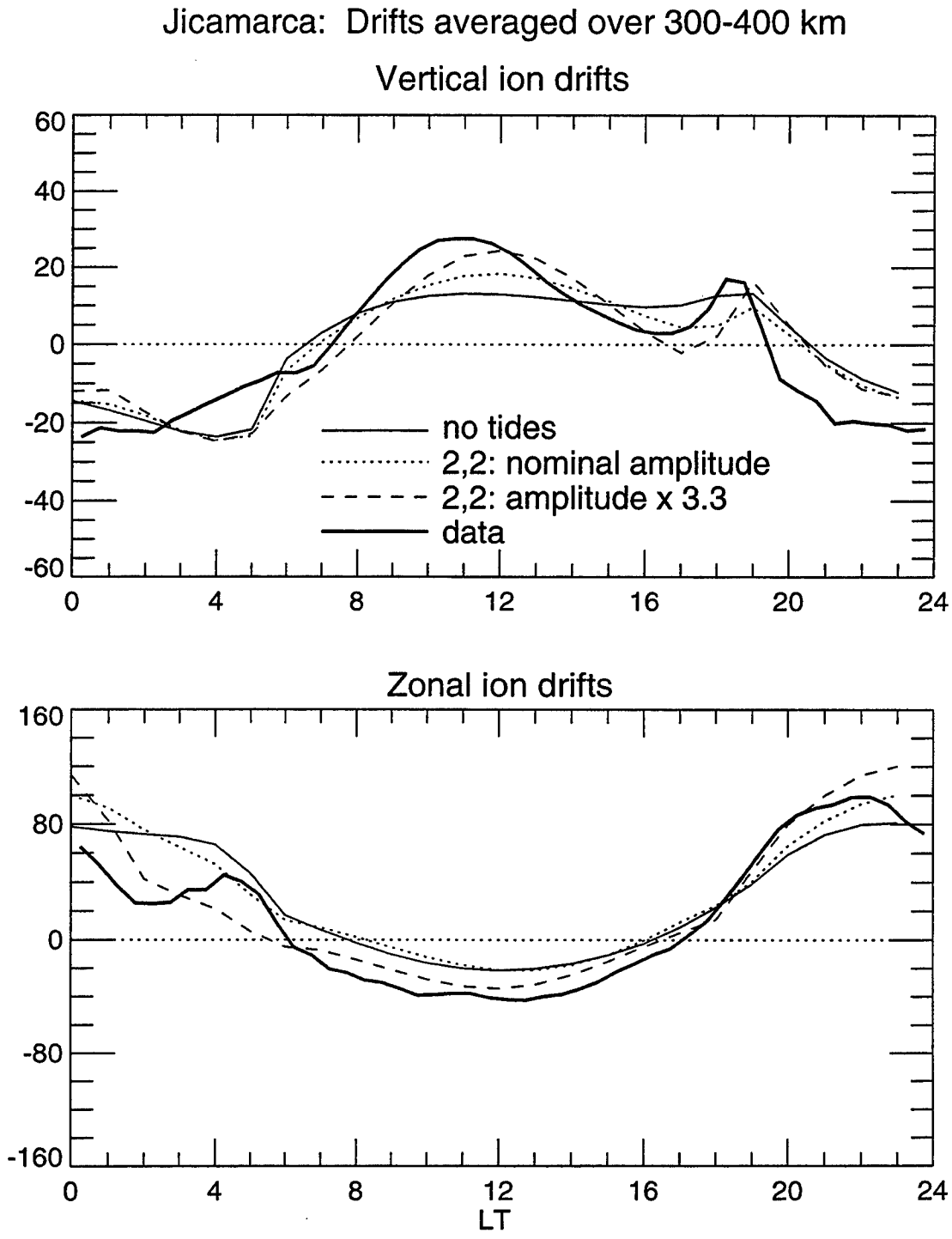


Figure 2. Ion drifts modeled at Jicamarca and averaged over 300 to 400 km for equinox solar cycle minimum. Different curves show results of imposing different tidal 2,2 forcing at the model lower boundary. Thick curve shows averaged Jicamarca data.

Equatorial and Low latitude diurnal variations and Sq focus over the Indian Longitude

S.Alex, B.D.Kadam and DR.K.Rao
Indian Institute of Geomagnetism, Colaba,
MUMBAI 400 005, INDIA

Ionospheric wind dynamo theory postulates the role of the wind induced ionisation currents, which contribute mainly to the predominantly smooth diurnal variations in the earth's magnetic field. The horizontal configuration of the earth's magnetic field over the equator is known to influence the magnitude of variation in the north south component (H) of the magnetic field at the equator to a large extent. However, irregular variations in the diurnal pattern during quiet days are of considerable interest in understanding the changing dynamics of the ionosphere.
Day to day variability in the diurnal signatures in the variations of the north –south (H) and east –west (D) components of the magnetic field over a sequence of consecutive quiet days are examined at locations encompassing equator to the latitude of sq focus in the Indian longitude zone. Proportionality in the latitudinal progression in the amplitude of the (Sq+electrojet) with reference to that over the equatorial latitudes is used to infer the distortions in the day to day Sq current system. Inequalities governing the day to day signatures are brought out utilizing the method of Principal Component Analysis. The present investigation cites the role of the asymmetric tidal winds in modifying the Sq current system.

Contact e–mail: salex@iig.iigm.res.in

WHATEVER HAPPENED TO SUPERROTATION?

HENRY RISHBETH

Department of Physics & Astronomy, University of Southampton, Southampton SO17 1RL, UK

In the sixties, it was deduced from observations of satellite orbits that the thermosphere rotates about 20% faster than the Earth; i.e., there is a prevailing west–to–east wind of order 100 m/s. In the seventies, this superrotation was 'explained' as a consequence of the day–to–night variation of ion drag at low latitudes, which arises from the strong nighttime polarization fields generated by the F–layer dynamo. In the eighties, satellite–borne instruments measured prevailing zonal winds of only about 20 m/s at low latitudes. In the nineties, global coupled thermosphere–ionosphere models indicate similar prevailing wind speeds. Can all these be reconciled?

The paper briefly reviews the theory and the observations. The agreement between the thermospheric models and the wind measurements implies that the zonal momentum balance is correctly represented in the models. It is also clear that the local–time variation of neutral air pressure is not the simple day/night variation assumed in the early F–layer dynamo' calculations. It seems that the discrepancy with the interpretation of the satellite orbital data still remains.

Thermospheric wind climatology revealed with the MU radar

S. FUKAO, and S. Kawamura (Radio Science Center for Space and Atmosphere, Kyoto University, Uji, Kyoto 611-0011, Japan), Y. Otsuka (Solar-Terrestrial Environment Laboratory, Nagoya University, 3-13 Honohara, Toyokawa, Aichi 442-8507, Japan), W. L. Oliver, and S.-R. Zhang (Center for Space Physics and Department of Electrical and Computer Engineering, Boston University, Boston, Massachusetts)

The MU radar at Shigaraki (34.85°N, 136.10°E) in Japan has measured ionospheric drift in the F-region monthly since September 1986. The component of this drift parallel to the magnetic field direction is interpreted in terms of the horizontal component of the neutral wind (thermospheric wind) along the magnetic meridian and reported as climatological averages in the form of time-of-day variations for several combinations of seasonal and solar-activity conditions. Comparisons are also made with the horizontal wind model (HWM) and with winds measured at Saint Santin and Millstone Hill.

The dominant feature revealed with the MU radar is its mean diurnal variation of northward flow by day and southward flow by night, with the nighttime wind smoothly approaching to and receding from a midnight maximum while the daytime wind tends to show two peaks, a strong one in the early daylight hours and weak one in the afternoon-evening. HWM shows the same unimodal nighttime and bimodal daytime behavior, but the HWM pattern is shifted about two hours later in time. The amplitude of the diurnal harmonic decreases from 78 m/s at solar minimum to 45 m/s at solar maximum while HWM shows a corresponding increase from 53 to 62 m/s. The diurnal amplitude is remarkably stable with season but is superposed on a steady DC wind of 41 m/s southward in summer, 15 m/s northward in winter, and midway between these limits at the equinoxes. HWM shows a symmetric pattern of 30 m/s southward in summer and 30 m/s northward in winter.

Ion drag appears to mainly regulate wind speed, and the seasonal wind patterns have profound effect upon the seasonal behavior of the ionosphere.

The Midnight Temperature Maximum (MTM) at Low Latitudes : A Status Report on Observations and Modeling

M . COLERICO and M. Mendillo
Center for Space Physics and Department of Electrical and Computer Engineering
Boston University, Boston, MA

C. G. Fesen
W. B. Hanson Center for Space Sciences
University of Texas at Dallas, Richardson, TX

We will discuss the current status of observation and modeling of the Midnight Temperature Maximum (MTM). The first *in–situ* measurements of the MTM were made by the Neutral Atmospheric Temperature Experiment (NATE) instrument on board the Atmospheric Explorer–E (AE–E) satellite (Spencer et al., 1979), which revealed an increase in the low latitude thermospheric neutral temperature at approximately local midnight. Examination of simultaneous thermospheric wind measurements indicated a correlation between the MTM feature and a reversal/abatement in the meridional neutral winds from equatorward to poleward. Zonal neutral wind measurements made by the Dynamics Explorer satellite indicated abatements at low latitudes near local midnight which were attributed to the passage of an MTM (Herrero et al., 1985). Herrero and Spencer [1982] determined the seasonal variations of the MTM through seasonal temperature maps of the AE–E data set. Their results indicated that the MTM occurs earlier and more pronounced in the summer hemisphere than the winter hemisphere. During equinox months, the MTM is generally symmetric about the geographic equator.

MTM ionospheric signatures have also been studied using ground–based instruments such as photometers (Greenspan, 1966), ionosondes (Nelson and Cogger, 1971) and radars (Behnke and Harper, 1973). Interpreting scanning photometer observations, Herrero and Meriwether [1980] attributed the modification of the meridional neutral winds, seen in the AE–E data, to a pressure bulge related to the MTM. This reversal/abatement in the meridional winds from equatorward to poleward would serve to lower the F–region and produce an enhancement in 6300 Å emission. Colerico et al. [1996] were the first to use an all–sky imaging system to study the 6300 Å airglow signature of the MTM. In 1993, as part of the NSF/CEDAR program in Multi–Instrumented Studies of Atmospheric Regions (MISETA), an all–sky imaging system was installed in Arequipa, Peru (16.2°S, 71.35°W). Since its installation, regular observations have been made of a region of enhanced 6300 Å airglow having an apparent north to south propagation through the field of view (FOV) of the imager at local midnight (5 UT). The occurrence rate of this 6300 Å airglow feature is highest during equinox seasons. Using coincident meridional and zonal neutral wind measurements made by a Fabry–Perot interferometer (FPI), collocated with the imager in Arequipa, Colerico et al. [1996] reported that this observed "brightness wave" (BW) of 6300 Å airglow emission had the same neutral wind pattern as AE–E found with the passage of an MTM. They concluded that the modification of the meridional neutral winds to poleward directions would serve to blow plasma down the field lines to altitude regions of higher chemical loss and produce an enhanced amount of 6300 Å airglow. With the MTM feature fixed in local time, the apparent north to south propagation of this feature would be due to the MTM's geographical orientation and Earth's rotation underneath it.

All–sky imaging observations of the "brightness wave" play an important role in the study of the day–to–day variability in latitude/longitude extent, geographic orientation, and relative magnitude of the MTM feature. Figure 1 shows a meridional intensity scan of data taken on the night of October 08, 1996. The BW event associated with the MTM enters the FOV of the imager from the north at 6:00 UT (1:00 LT) and

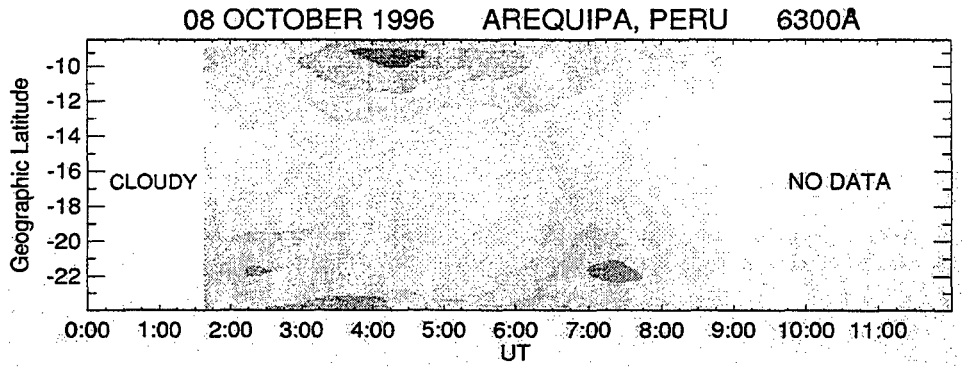


Figure 1. Observations of typical Brightness Wave features in the pre– and post–midnight periods.

exits to the south at 7:30 UT (2:30 LT). Notice the MTM related BW is accompanied by an additional enhanced 6300 Å feature propagating through the imager's FOV from south to north at 2:00 UT (21:00 LT). Colerico et al [1996] referred to this feature as a pre–midnight brightness wave (PMBW). Both features move through the FOV of the Arequipa imager to and from latitudes not within its range (–8° S to –24°S). The recent addition of a second imager at El Leoncito, Argentina (31.8°S, 69.3°W), south of Arequipa, will extend the southern latitude coverage to which their progression can be tracked .

The MTM phenomenon has been modeled extensively using the Thermosphere–Ionosphere–Electrodynamical General Circulation Model (TIEGCM). TIEGCM models the MTM through upward propagating semidiuranal tides (Fesen, 1996) which have been tuned to mimic UARS wind observations, such as those reported in McLandress et al. [1996]. Currently, TIEGCM can produce a midnight thermospheric temperature enhancement, but the magnitude of its MTM is significantly smaller than measurements made by the FPI. Fesen et al. [1996] suggest that the seasonal variation in the MTM may be due to interaction between the (2,2) and (2,3) semidiurnal tidal modes, since in the summer, the two modes may serve to reinforce each other, whereas in winter they made counteract each other. We will report on recent modeling efforts made of the BW associated with the MTM feature using output TIEGCM parameters as inputs to an airglow modeling code developed at Boston University. These parameters include values for T_n, T_i, T_e, N_e, O, O_2, and N_2. Figure 2 illustrates TIEGCM/airglow model 6300 Å calculations for the same geophysical conditions as in October 1996. The model results are presented in the same format as Figure 1 to aid in comparisons between the observations and model results. While the models were successful in producing the south to north propagating PMBW feature observed in Figure 1, they could not reproduce the BW feature that we associate with the MTM. Upon inspection of additional TIEGCM outputs, such as V_p, N_{max}, and h_{max}, we see that the PMBW is produced in response to

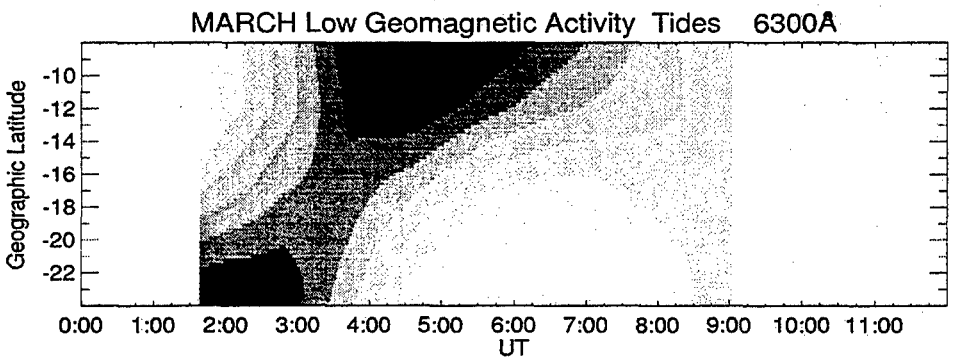


Figure 2. Model results of 6300 Å airglow from TIEGCM parameters.

typical equatorial dynamics. Before sunset, the fountain effect seen in the vertical plasma drifts (V_p) moves plasma upward at the equator and diffuses it down the magnetic field lines to lower altitudes at higher latitudes. A south to north gradient in V_p occurs shortly after the fountain effect is "turned off" and results in a similar gradient in h_{max} such that it reaches lower altitudes sooner in the south than in the north. This allows the plasma to the south to reach altitudes where it can dissociatively recombine and produce 6300 Å emission sooner than in the north, producing the PMBW 6300 Å airglow signature. One explanation for the explicit lack of a midnight BW in the model calculations may be that the magnitude of the MTM produced by the TIEGCM model was not sufficient to modify the winds needed to move plasma down to regions of higher chemical loss.

Though much progress has been made in our understanding of the MTM phenomenon and its effects on thermospheric dynamics, there is still more work to be done. With the addition of new diagnostic techniques, such as the ROCSAT Ionospheric Plasma and Electrodynamics Instrument (IPEI), thermospheric parameters measured by Incoherent Scatter Radars (ISRs), and imaging data over a larger latitudinal range, we may gain additional insights into the generation of this feature.

Equatorial Temperature Anomaly (ETA) in Solar Minimum

R. Suhasini,1,2 R. RAGHAVARAO,1,2 H. G. Mayr,2 W. R. Hoegy 2 and L. E. Wharton 2
1. Nitya Laboratories Ltd., Bhavanam Estate, Plot 15, Somajiguda, Hyderabad 500 082, India.
2. NASA/Goddard Space Flight Center, Greenbelt, MD 20771, USA.

We show evidence for the occurrence of the Equatorial Temperature Anomaly (ETA) in solar minimum period by analyzing the temperature data from the Neutral Atmospheric Temperature Experiment (NATE), onboard the AE–E satellite, measured when it was in circular orbit at a height of about 255 km. The data collected in the African and Asian longitudes from November 19, 1976 to February 4, 1977 were chosen for the analysis and in that period the data were collected mostly in the southern hemisphere and hence during a summer season.
The ETA formation is similar to and collocated with EIA (Equatorial Ionospheric Anomaly) as reported earlier during a solar maximum period (Raghavarao et al., 1991) with a minimum at the dip equator and maxima on either side of it. The maxima and minimum of ETA are collocated with the maxima and minimum of EIA respectively. The daytime behavior of ETA formation is about the same as that of EIA. Both form in the forenoon hours and intensify quickly reaching their respective peak values in the after noon. The ETA attains its strength whenever the EIA becomes strong. Thus the EIA is the primary cause of ETA.
The diurnal variation of ETA is found to be significantly different from its behavior in solar maximum. In solar minimum period, ETA develops around 1000 LST and attains its maximum strength of about 100K in the early afternoon around 1400 LST. In contrast, in solar maximum period it is known to start around 0930 LST, be present for the most part of the daytime and attains its peak value of about 120K quite late around 2000 LST (Raghavarao et al, 1998).
During the pre–midnight time (2100 LST), while the EIA is nonexistent, the temperature distribution with dip latitude forms a reverse sinusoidal shape revealing a maximum at the dip equator, which is a signature of the Midnight Temperature Maximum (MTM), and a broad minimum in the region of the day time crest where the post–sunset cooling is also faster than at the dip equator. And while the background temperatures decrease during the night, that sinusoidal pattern remains nearly the same until early morning hours (0400 LST). The results thus indicate that in solar minimum period, the ETA formation and its early intensification in the daytime controls the MTM occurrence and its intensity during the following nighttime.

References:
Raghavarao, R., R. Suhasini, W. R. Hoegy,.H. G. Mayr, and L. E. Wharton, Local time variation of equatorial temperature and zonal wind anomaly (ETWA), J. Atmos. & Solar–Terr. Phys., 60, 631–642, 1998.

Raghavarao, R., L. E. Wharton, N. W. Spencer, H. G. Mayr, and L. H. Brace, An equatorial temperature and wind anomaly (ETWA), Geophys. Res. Lett., 18, 1193–1196, 1991.

The Equatorial Temperature and Wind Anomaly (ETWA)

R.RAGHAVARAO, Nitya Laboratories Ltd., 202 ,Harita,
Bhavanam Estate, Plot 15, Somajiguda, Hyderabad
500 082, India

It is known that during solar maximum (Smax) period the neutral temperature (T) and the zonal winds (Z) at F region altitudes in the low – latitude thermosphere reveal an anomalous distribution with the geomagnetic dip latitude. The temperature variation shows a prominent minimum at the dip equator with maxima on either side of it. This is named as Equatorial Temperature Anomaly (ETA). On the other hand, the zonal winds exhibit a prominent maximum at the dip equator with minima on either side of it. This feature is named as Equatorial Zonal wind Anomaly (EZA). Both the anomalies when studied together were named earlier as the Equatorial Temperature and zonal wind Anomaly (ETWA) (Raghavarao et al., 1991).It should be noticed that neither the MSIS–86 model (Hedin,1987) for the temperatures nor the HWM–90 model (Hedin et al,1991) for the zonal winds describe the observed diurnal variations in 'T', 'Z', 'DT', 'DZ' in the Smax period.

The prominent features of ETWA are the collocation of the maxima in temperature and minima in the zonal winds with the crests of EIA and the reverse over its trough. Raghavarao et al., (1998)described the behaviour of the local (solar) time (LST) variation of ETWA phenomenon during Smax period. The diurnal variation in the strength of ETWA defined by the differences in the wind velocities (DZ) and temperatures (DT) at the crests and trough showed that both maximise (DZ=110m/sec and DT=120K) at ~2000 LST when the EIA strength (ratio of the ionization densities at crest and trough) is known to maximise in solar maximum period .

The largest zonal winds are also observed at 2000 LST over the dip equator. When compared to the wind amplitude of diurnal tide at trough, its amplitude at the crest is decreased by about 6%. Winds of semidiurnal tidal origin are weak everywhere in the region. There are high frequency tidal winds (3–4 hour period) of significant magnitudes around 2000 LST generated probably by the momentum coupling betweenthe tides of lower frequencies and the background ionosphere. Thus the observational evidence in Smax period showed that the development of Equatorial Temperature Anomaly (ETA) critically depends both on the development and intensification of the EIA crests and the Zonal winds which favoured the ion drag hypothesis (Hedin and Mayr, 1973) for heating near the EIA crests.

Further, DE–2 observations reveal that the latitudinal width of the temperature crests increase with the strength of ETA. The seasonal changes in the LST variations of T, Z, DT and DZ during Smax period could not be seperated with the available DE–2 data. Because of the solar flux dependence

of temperature direct comparison of tidal oscillations in temperature could not be related with those in zonal winds. Hence the ion drag hypothesis could not be verified.

The temperature crest intensities and hence the excess pressures maximise around 1900–2000 LST, when usually the Equatorial Spread–F(ESF) is known to get triggered. One of the important measurements made from the WATS instrument on the DE–2 satellite is the measurement of vertical winds. Downward vertical winds were observed at the equator around 2000–2100 LST (Raghavarao et al,1993) and it was shown that such winds could be responsible for the more frequent occurrence of ESF during Smax and its day to day variability (Raghavarao et al, 1992, 1999). A new circulatory wind system in the meridional plane engendered by the pressure crests on either side of the dip equator was suggested as the reason for the observed vertical winds. Fuller–Rowell et al (1997) too confirm through model calculationsthat such vertical winds could be present. It requires further experimental verification,as there were inadequacies in the desired levels of accuracy and the knowledge for measuring the satellite attitude of DE–2.

An analysis of temperature data from NATE experiment on board AE–E satellite shows that the ETA development during solar minimum (Smin) period and in particular, its local time (LST) variation is distinctly different from Smax Period. Both ETA and EIA build their intensities from 0930LST onwards and attain their respective maximum intensities rather quickly at 1400LST to nearly the same levels (about 100 degrees K at ETA crests) of their intensities as in Smax at 2000 LST. The intensities however are variable with seasons– summer and equinox. After 1400 LST the intensities of both ETA and EIA disappear rather abruptly in Smin period. The quick build–up of the intensities can perhaps be explained by the faster rise of the eastward electric fields in the forenoons during Smin than in Smax(Fejer,1981)..Abrupt disappearance of both the phenomena calls for the need for further measurements. There were no simultaneous zonal and vertical

wind measurements from AE–E unlike from DE–2.

The possible link between processes that are responsible for the generation of ETWA /ETA,with the other equatorial geophysical processes like the midnight temperature maximum is another interesting aspect. Although the data
sampling of temperature around midnight hours by the WATS instrument on board the DE–2 was not adequate, it appears that the Midnight Temperature Maximum (MTM) rarely occurs during Smax period. It is known to be frequent in solar minimum period (Spencer et al, 1979).The signature of MTM during the two seasons of our present study(Suhasini et al,2000) on the daytime ETA phenomenon indicate that the night time MTM occurrence and its intensity are linked or perhaps controlled by the ETA occurrence and its intensity on the previous day times. If this is consistent in all the four seasons in Smin (under analysis) it can be concluded that the day to day variability in

the EIA and hence ETA intensity and the time (LST) of occurrence of their respective maxima control the MTM occurrence and its intensity. There are two more phenomena in the equatorial ionosphere frequent in their occurrence in Smin than in Smax. They are, the 'Ionisation Ledge' formations at Hmax altitudes near the equator which move into the topside ionosphere (Raghavarao
and Sivaraman, 1974) and also the Counter Electrojet in the E – region it is known
that both, although well seperated in height ,occur on the same days (Sharma

and Raghavarao, 1990). It is important to investigate how the ionization ledge
formation is associated with the ETA development.

It is well known that the electric fields and winds play a central role in generating EIA and that inturn plays a vital role in the development of ETA through ion drag (Hedin and Mayr, 1973) and chemical heating (Fuller–Rowell et al. 1997). Pant and Sridharan (2000) showed, by an analysis of the wind and temperature data from DE–2, that both the ion drag and chemical heating processes are equally important to explain the observations. It is quite likely that once ETA strengthens beyond a limit and depending on the rate of energy input, either a new circulatory wind system, similar to the one suggested by Raghavarao et al, (1993) starts or the two crests of ETA become sources of gravity waves, similar to the auroral regions when significant energy inputs occur from the magnetosphere.

There are basically two theories currently in vogue for the ETA formation. Hedin and Mayr (1973) suggested the ion drag on the neutral motion, while Fuller–Rowell et al (1997) showed that the chemical heating as the source. Neither one is verified with appropriate measurements. With all the anomalies in the neutral atmospheric densities, temperatures, zonal winds and detection of significant vertical winds, unenvisaged a few years ago, now provide an opportunity for us to understand and possibly solve the well–defined but unsolved problems of the coupled ionosphere–thermosphere system by a well–coordinated accurate measurements by the satellite–borne and ground–based instruments.

References:

Fejer B.G., Equtorial Ionospheric electric fields : a review
J.Atmos.Terr.Phys.43,377–386,1981

Fuller–Rowell, T. J.,M. V. Cordrescu, B. G. Fejer, W. Barer, F. Marcos and D. N. Anderson, Dynamics of the low – latitude thermosphere,: Quiet and disturbed conditions, J. Atmos. Solar–Terr. Phys.,59,1533–1540,1997.

Hedin, A. E., MSIS – 86 Model, J. G. R., 92, 4649–4662, 1987.

Hedin, A. E., M. A. Biondi, et. al.,Revised global model of thermosphere winds using satellite and ground based observations, J. G. R., 96, 7657–7688, 1991.

Hedin, A. E. and H. G. Mayr, Magnetic control of the near equatorial neutral thermosphere, J. G. R, 78, 1688–1691, 1973.

Pant T. K., and R. Sridharan, Plausible explanation for the equatorialtemperature and wind anomaly (ETWA) based on chemical and dynamical processes, to be published in J. Atmos. Solar–Terr. Phys., 2000

Raghavarao, R., W. R. Hoegy, N. W. Spencer,and L. E. Wharton, Neutral temperature anomaly in the equatorial thermosphere, Geophys. Res. Lett., 20, 1023–1026, 1993.

Raghavarao, R.,Wharton, L. E. N. W. Spencer, H. G. Mayr, and L. H. Brace, An Equatorial Temperature and Wind Anomaly (ETWA),Geophys. Res. Lett.,18, 1193–1196,1991.

Raghavarao, R., R. Sekar and R. Suhasini, Nonlinear numerical simulationof equatorial spread–F – Effects of winds and electric fields, Advances Space Res.,12, (6), 227–230, 1992.

Raghavarao R., M.R.Sivaraman., Ionization legesin the equatorial ionosphere, Nature (London),249,331–332,1974

Raghavarao, R.,R. Suhasini, W. R. Hoegy, H. G. Mayr, and L. E. Wharton, Local time variation of equatorial temperature and zonal wind anomaly (ETWA), J. Atmos. Solar–Terr. Phys.,60, 631–642, 1998.

Raghavarao,R., R. Suhasini, H. G. Mayr, W. R. Hoegy and L. E. Wharton, Equatorial Spread–F (ESF) and vertical winds, J. Atmos. Solar–Terr. Phys.,61, 607–617

Sharma P, And R. Raghavarao., simultaneous occurrences of ionization ledges and counter electrojet in the equatorila ionosphere: observational evidence and its implications, Can.J.Phys. 67,166–172,1989

Spencer, N. W., G. R. Carignan, H. G. Mayr, H. B. Nieman, R. F. Theis, and L. E. Wharton, The Midnight Temperature Maximum in the earth's Equatorial Thermosphere, Geophys. Res. Lett., 6, 444–446, 1979.

Suhasini R , R. Raghavarao, H.g.Mayr, W.R .Hogey, and L.E.Wharton, Equatorial temperature anomaly(ETA) in Solar minimum, Proc. Of ISEA X , Turkey, 2000

PLAUSIBLE EXPLANATION FOR THE EQUATORIAL TEMPERATURE AND WIND ANOMALY (ETWA) BASED ON CHEMICAL AND DYNAMICAL PROCESSES

tarun kumar pant[1] and R. SRIDHARAN[2]

1. Physical Research Laboratory, Ahmedabad 380 009, India

email: tarun@prl.ernet.in

2. Space Physics Laboratory, Thiruvananthapuram 695 025, India

email: spl_vssc@vssc.org

In the low latitude F-region, the diffusion and plasma drifts are the dominating processes which compete with drag effects and chemistry to take control of the overall behaviour of the thermosphere ionosphere system (TIS). As a result of these plasma neutral interactions within TIS, several large scale dynamical processes get initiated. The most prominent of these processes over low and equatorial latitudes are the Equatorial Ionisation Anomaly (EIA) and Equatorial Temperature And Wind Anomaly (ETWA) [Appleton 1946; Raghavarao et al. 1991]. *Raghavarao et al.* [1991] using DE-2 satellite data, discovered an important effect where they found that the latitudinal distribution of thermospheric temperatures and zonal winds also showed a close linkage with the EIA. This new effect was referred to as the Equatorial Temperature and Wind Anomaly (ETWA). Since its discovery, there has been no satisfactory theory/mechanism which could explain the ETWA in totality.

However, in recent times, two schools of thought regarding the causative mechanisms of ETWA have emerged. One, favoured by *Raghavarao et al.* [1993] where they propose that the latitude variation of ion-drag associated with EIA, can explain all the observed features of ETWA, which includes the observed vertical wind structure. The other is initiated by *Fuller-Rowell et al.* [1997], where chemical heating is invoked to explain the

observed temperature and vertical wind field variations. In the present paper, it has been emphasised that both the above mentioned mechanisms operate and are important for the generation of the ETWA. Both these processes have been quantified and used successfully to explain the anomalous temperature feature associated with ETWA. The quantification schemes developed are dicussed in the sections to follow.

I. QUANTIFICATION OF ETWA

A. Contribution Due to Chemical Heating

It is the two stage recombination reaction of O^+ during nighttime and is exothermic in nature. This provides the source of chemical heating in the region of the ionisation crests, contributing to ETWA. The kinetic heating rates for the reactions involving the ground state species are the highest for molecular dissociative recombination reactions involving primarily ${O_2}^+$ at F-region altitudes.

$$O^+ + O_2 \Longrightarrow {O_2}^+ + O \tag{1}$$

Followed by the molecular dissociative recombination reactions

$${O_2}^+ + e \Longrightarrow O^*(^1D) + O(^3P) + energy \tag{2}$$

$$O^*(^1D) \Longrightarrow O(^3P) + (h\nu)_{6300\mathring{A}} + E \tag{3}$$

Under equilibrium conditions, the rate of production of $O(^1D)$ would be equal to the rate of the chemical energy (P_{ch}) released in the system. 'P_{ch}' is proportional to the electron density N_e and the available ${O_2}^+$ ions

$$P_{ch} \propto [{O_2}^+][N_e] \tag{4}$$

Since the dissociative recombination reaction is faster than the charge exchange reaction, the overall reaction rate is governed by the slower. It means, for a given F-region densities the availability of $[{O_2}^+]$ states will depend upon the efficiency of charge exchange reaction or the density of $[O_2]$ in the first reaction(1).

$$[O_2^+] \propto [O_2] \tag{5}$$

or in other words, we have

$$P_{ch} \propto [O_2][N_e] \tag{6}$$

Therefore, the chemical heating in upper thermosphere at any time, at any place, is expected to be proportional to the product of O_2 and the electron density N_e. For the estimation and quantification of chemical heating in the ETWA, only those satellite passes over low latitudes were considered which were in the nighttime when the F-region dynamo renders the 'ion-drag' to be negligible. The deviations (ΔT_n) of the observed temperature from the model were calculated alongwith the corresponding product of O_2 and electron density. A linear relation was obtained between the two, which can be used for calculating ΔT_n for a given product of O_2 and electron density at any given time. Using the linear relation, the temperature rise due to chemical heating (ΔT_{ch}) was estimated for all the DE-2 passes used in the present study.

B. Contribution of Ion-drag

The ion-drag couples the momentum of neutral and ionised species through ion-neutral collisions. During daytime any polarization field or wind driven current in the F-region gets short circuited by the currents flowing along the field lines to the electrically conducting E-layer. Therefore, no polarization field would be developed in the F-region. In other words, the F region dynamo would be inactive. Due to the absence of the F-region dynamo, there is a significant amount of relative motion between the ions and the neutral species during daytime. As a result the ion-drag becomes significant. Hence, only during the daytime, ion drag would play a significant role by abating the zonal wind flow. The loss of momentum in this process would then appear as enhanced temperature at the crests. At the same time, in the (EIA) trough region, the ion-drag is very little because of very low ionisation density there. Taking a clue from the above, the product of the change of zonal wind velocity (Δ Z) and ionisation density (Δ Ne) at the crests with respect to the dip equator (trough) at anytime is taken to be the measure of the 'ion-drag'.

After accounting for the chemical heating contribution, a linear relation was established between the observed heating due to the ion-drag effect alone and the proposed $\Delta Z \times \Delta$ Ne product. Using these two relations, the extent of temperature anomaly in ETWA can be quantified for any time if the thermospheric wind, composition and ionospheric densities are known.

REFERENCES

Anderson, D. N.,and R. G. Roble, 1974. The effect of vertical $\vec{E} \times \vec{B}$ ionospheric drifts on F-region neutral winds in the low-latitude thermosphere, Journal of Geophysical Research, 34, 5231-5236.

Fuller-Rowell, T. J., M. V. Codrescu, B. G. Fejer, W. Barer, F. Marcos and D. N. Anderson, 1997. Dynamics of the low-latitude thermosphere: quiet and disturbed conditions, Journal of Atmospheric and Terrestrial Physics, 59, 1533-1540.

Raghavarao, R., L. E. Wharton, N. W. Spencer, H. G. Mayr and L. H. Brace, 1991. An equatorial temperature and wind anomaly (ETWA), Geophysical Research Letter, 18, 1193-1196.

Raghavarao, R., L. E. Wharton, N. W. Spencer and Hoegy W. R., 1993. Neutral temperature anomaly in the equatorial thermosphere-A source of vertical winds, Geophysical Research Letter, 20, 1023-1026.

Low-latitude thermospheric wind perturbations on the day side measured by WINDII during magnetic storms

R. H. Wiens(1) and G.G. Shepherd

CRESS, York University, Toronto, Ontario, Canada

The response of neutral thermospheric winds to geomagnetic storms is an important aspect of "space weather." Changes in the wind pattern above the magnetic dip equator during these storms have been measured using ground-based interferometers by way of the O(1D) nightglow emission at 630 nm, but such measurements are possible only at night. WINDII, the WIND Imaging Interferometer aboard UARS, regularly measured winds up to 270 km using its O(1S) 558 nm green line channel on its dayside transits of the tropics, providing a data set unequalled for studying storm-induced perturbations of tropical dayside winds.

During the 1992-93 period, when WINDII measured the green line several days each week, at least four days of green line measurement coincided with days on which the Kp index reached 7o or more. These days were selected for comparison with surrounding days of lesser magnetic activity, specifically with regard to meridional and zonal wind components. Comparison days were chosen to be a day or two before and after the storm day so that the Sun-orbit geometries were similar for all days within any of the four comparison sets. Three of the storm sets entailed dip equator crossings between 0700 and 1000 LST (local solar time), our morning crossings, and the other entailed afternoon crossings from 1300-1500 LST. Averages of the winds measured at 250 and 150 km were computed over the Africa-India longitude sector between dip latitudes of 30°S and 30°N in 10-deg latitude bins.

Strong equatorward forcing was found to occur on the storm days compared with the days of lesser magnetic activity in both the morning and afternoon sectors, with average differences of 66 m/s at 250 km and 34 m/s at 150 km. During the storm days zonal mean winds showed an average westward forcing of 30 m/s at both 250 and 150 km in the morning sector, but the afternoon case suggests a small eastward forcing at 250 km with no distinct effect at 150 km. These results are compared with and complement those of an earlier study using data from Dynamics Explorer, DE-2.

(1)Present address: Department of Physics, University of Asmara, Asmara, Eritrea

Geomagnetic forcing of the equatorial thermosphere–ionosphere system: a study of the disturbance interval 7–13 March 1994

J. H. SASTRI (Indian Institute of Astrophysics, Bangalore, India), V. V. Somayajulu (Space Physics Laboratory, VSSC, Trivandrum, India), K. B. Ramesh, H. N. R. Rao, and J. V. S. V. Rao (Indian Institute of Astrophysics, Bangalore, India)

We present salient features of the behavior of the thermosphere–ionosphere system (TIS) in the Indian equatorial region during the prolonged disturbance period of 7–13 March 1994. A multi–experiment (FPI, ionosonde and HF Doppler radar) database is used for the study. The pressure–scanned Fabry–Perot Interferometer (FPI) is operated at Kavalur Observatory (12.5 N, 78.5 E geographic; dip 9.5 N) to measure the thermospheric temperature (zenith) from observations of 630nm night airglow line emission. The ionosondes are at Trivandrum (8.6 N, 77 E geographic; dip 0.6 S), Kodaikanal (10.2 N, 77.5 E geographic; dip 4 N) and Sriharikota (13.7 N, 80.2 E geographic; dip 10.5 N). h'F data from the ionosonde network are used to estimate the meridional thermospheric wind for the nighttime period following the method of Krishnamurthy et al [1990]. The HF Doppler radar is operated at Kodaikanal (10.2 N, 77.5 E geographic; dip 4 N) to measure the F–region vertical plasma drift with high time resolution and sensitivity over the evening–nighttime period.

The average nighttime (1930–0430 LT) thermospheric temperature, <Tn> over Kavalur varied from 701 k to 914 k on individual nights of the disturbance period. There is no evidence for any persistent change in <Tn> on disturbed nights compared to quiet nights. <Tn> is nevertheless reduced on three nights (8, 11 and 13 March 1994) corresponding to the recovery phase of Dst index. The agreement between the measured and MSIS model Tn is found to be better on disturbed nights rather than on quiet nights.

The nighttime pattern of meridional winds showed several interesting features on some nights which include strong surges in equatorward winds and quasi–periodic wind oscillations with period of about 3 hr, with a corresponding feature in Tn. The F–region vertical plasma drift pattern at Kodaikanal close to the magnetic equator revealed unambiguous effects of short–lived (2–3 hrs) electric field perturbations on some of the disturbed nights. These and other results are compared with earlier work and discussed in the light of current understanding of the disturbance–time behavior of the equatorial TI system.

Storm-Time Changes in Thermospheric Dynamics at Low Latitudes

T.J. FULLER-ROWELL, M.C. Codrescu (Space Environment Center, 325 Broadway, Boulder, CO 80303, USA)
A.D. Richmond (HAO/NCAR, P.O. Box 3000, Boulder, CO 80307, USA)
G.H. Millward (Atmospheric Physics Laboratory, University College London, UK)

Abstract

A three-dimensional coupled model of the thermosphere, ionosphere, plasmasphere and electrodynamics (CTIPE; Fuller-Rowell et al., 1996, Millward et al., 1996) has been used to investigate the dynamic and electrodynamic response at low latitudes during a geomagnetic storm. It has been a challenge for quiet-time model simulations to reproduce a consistent, and strong, pre-reversal enhancement of the vertical ion drift at the magnetic equator. In CTIPE the problem was resolved by increasing the E-region resolution in the longitude direction in order to resolve the steep ionospheric gradient across the terminator. The plasmasphere, with a resolution of 18° longitude, is sufficient to capture the observed local-time structure at higher altitudes, but a much higher latitude resolution is required. A total of 70 flux tubes are used to achieve a resolution better than 1° latitude and a grid spacing of 20km in altitude in the equatorial F-region. By using a 5° longitude resolution in the E region the electrodynamic solver in CTIPE is able to produce a robust pre-reversal enhancement and a realistic equatorial ionization anomaly. The model simulations at quiet-time reproduce the steep latitudinal gradients observed by the Dynamics Explorer satellite in winds, temperature, and ion density.

The success of the model in reproducing the dynamic and electrodynamic features at low latitudes during quiet times gives confidence in the storm-time simulation results. During a geomagnetic disturbance the first signature at low latitudes is the arrival of the penetration electric field. This magnetospheric electric field component is not generated self-consistently by CTIPE so needs to be imposed empirically. The response of the low latitude electron density, and dynamics, at low latitudes to this short-lived change in the electric field is expected to be modest.

To investigate the storm-time changes to the dynamics and electron density structure at low latitude two simulations were performed, one with self-consistent electrodynamics and one without. The two storms were characterized by a 12-hour enhancement of the high latitude convective electric field and auroral precipitation. Both were performed at equinox at a moderately high level of solar activity, and the penetration electric field was explicitly excluded.

Without self-consistent electrodynamics, the first change at low latitude was the arrival of a large-scale gravity wave driven by the sudden increase in energy input at high latitudes. These waves arrive at the equator from both polar regions about 3 hours after storm commencement. The change in electron density structure is modest and the weak coupling by the Coriolis force at low latitude drives little change in the zonal winds. The development of the global circulation forces downwelling at low latitudes that drives a small change in the neutral composition. The ratio of atomic oxygen to molecular nitrogen increases slightly producing a small positive phase in the ionosphere.

With self–consistent electrodynamics, large changes in the electron density structure were produced at low latitudes. The simulation confirmed the theory proposed by Blanc and Richmond (1980). The development of storm–time equatorward winds drives an equatorward Hall current and causes a positive charge build up at the equator. The poleward electric field balances the wind driven current and also drives an eastward Hall current that causes positive charge build–up at the dusk terminator and negative charge at dawn. The disturbance dynamo drives a downward plasma drift during the day and upward at night in opposition to the quiet–day field. The redistribution of plasma changes ion drag and allows the zonal wind to change, in dramatic contrast to the simulation were the electrodynamics was keep constant.

The surprising result was the speed with which the electrodynamic changes were manifest at low latitudes. The first change was seen after only 2 hours, about 1 hours before the first gravity wave arrived. The explanation appears to be that the midlatitude storm–time winds, that are forced in the very early stages of the storm by the gravity wave surges, drive an F–region dynamo. The winds begin to redistribute charge around the global circuit and alter the charge distribution at the magnetic equator. The results illustrated very clearly the dominant control of electrodynamics on the low latitude dynamics and ionospheric structure during geomagnetic disturbances.

Blanc, M and A.D. Richmond, The ionospheric disturbance dynamo. J. Geophys. Res. 85, 1669, 1980.
Fuller–Rowell T.J., D. Rees, S. Quegan, R.J. Moffett, M.V. Codrescu, and G.H. Millward, A coupled thermosphere ionosphere model (CTIM). Handbook of Ionospheric Models, STEP Report, editor R.W. Schunk , 1996.
Millward, G.H., R.J. Moffett, S. Quegan, and T.J. Fuller–Rowell, A coupled thermosphere ionosphere plasmasphere model (CTIP).). Handbook of Ionospheric Models, STEP Report, editor R.W. Schunk , 1996.

Emission rate and apparent temperature increases in the low–latitude day–side thermosphere during magnetic storms observed by WINDII

R.H. Wiens,

Department of Physics, University of Asmara, Asmara, Eritrea

and
V.P. Bhatnagar and G.G. Shepherd

CRESS, York University, Toronto, Canada

The heating effects of magnetic storms in the low–latitude thermosphere have been studied using the emission rate and Doppler broadening of the O(1D) auroral red line at 630 nm measured with ground–based instruments. Such measurements can only be made at night, but a limb–viewing satellite interferometer like WINDII can make them on the day side as well. During the 1992–93 period several cases of large magnetic storm with Kp reaching 7o or more coincided with WINDII gathering reliable data to altitudes as high as 275 km through its O(1S) green line filter at 558 nm. On these special occasions data were also acquired in the same way for nearby days of lesser magnetic activity for comparison. Enhancements were found in the emission rate, the apparent temperature, and the scale height of the emission rate during the more disturbed days

The emission rate was found to be enhanced by typically 30% on the disturbed days at 250 km. The slow precession of UARS gives local time differences of equator crossing of only 20 min/day, ensuring that the comparison days gave similar solar insolation histories. The scale height of the emission rate, found by fitting an exponential to the emission rate profiles at 180 and 250 km , were enhanced by about 5 km on disturbed days. Apparent temperatures increased by 56 K, and we estimate that this is equivalent to a real temperature enhancement of 174 K at 250 km, consistent with in situ measurements made with mass spectrometers. We show that the enhancements reported here for all three measured parameters are consistent with a theoretical picture based on auroral heating of the thermosphere during magnetic storms, even at equatorial latitudes.

1 Work done while author was with CRESS, York University, Toronto, Canada

Seasonal dependence of the response of the low latitude thermosphere for external forcings

tarun kumar pant[1] and R. SRIDHARAN[2]

1. Physical Research Laboratory, Ahmedabad - 380 009, India

email: tarun@prl.ernet.in

2. Space Physics Laboratory, Thiruvananthapuram- 695022, India

email: r_sridharan@vssc.org

Consequences of intense energy inputs to the earth's upper atmosphere during geomagnetic storms or the 'space weather disturbances' and the response of the thermosphere-ionosphere system (TIS) to various forcings generated thereby has become quite an important aspect of space research in recent years. In general, these consequences in terms of the changes brought about are global in nature and it has been very difficult to describe the exact physics behind these changes. It had been shown by *Prolss* [1980] and *Maeda et al.* [1989] that the upper atmospheric temperature could get modified to a very large extent at all latitudes during the storms. Moreover, it had been shown that the storm time meridional wind circulation, travelling atmospheric disturbances or gravity waves, and ring current associated particle precipitation are the important processes to cause abovesaid modifications in thermospheric temperatures. It is also established that the time taken by the different processes have their own characteristic time delays in producing the effects in upper atmosphere. In addition to the above, the time delayed response of equatorial and low latitude thermosphere to geomagnetic forcing has been shown by using satellite and ground based data [*Burns and Killeen* 1992; *Pant and Sridharan* 1998]. However, not much is known about the time response of low latitude thermosphere to various geomagnetic forcings during both storms and quiet times.A systematic investigation was carried out addressing to these aspects using the DE-2 satellite data and

the results, obtained using the measured temperatures, highlight the time-response characteristics of the thermosphere-ionosphere system to geomagnetic forcings of different strengths and also its seasonal dependence.

I. DATA ANALYSIS AND RESULTS

Pant and Sridharan [1998] on the basis of a case study using ground based high resolution spectrometer data, clearly established that the low latitude thermosphere i.e. $\sim 20^{\circ}$ dip latitude takes about 14-16 hours to respond to the forcings during a magnetic storm. To arrive at the above conclusion, time delayed cross correlations were established between deviations of observed F-region temperatures (ΔT_n) from the model (MSIS) [*Hedin* 1991] and the time rate of change of the ring current index D_{st}. It was shown unambiguously that the D_{st} variations act as a precursor to the variabilities in the neutral temperatures. This study was a clear indication of low latitude upper atmospheric system showing a characteristic time delay in responding to the external geomagnetic forcings. To investigate seasonal dependence of this time delay, if any, a detailed time delayed correlation analysis using the rate of change of D_{st} and the deviations of WATS measured temperatures from the MSIS model was carried out following the approach adopted by *Pant and Sridharan* [1998], for a dip latitude of 20°. While doing so no distinction has been made between magnetically disturbed and quiet periods. The data base covered different seasons throughout the year 1982-83. Though the time resolution of the D_{st} index is rather coarse, i.e. 1h, still the obtained correlation coefficients were high i.e. 0.8 and more for individual nights. In fact it was found that the estimated time delays corresponding to different days belonging to particular month were in the same range and these delays varied from month to month. In other words, it turned out to be that the thermosphere has, seasonally, a characteristic time delay or 'response time' showing the least delay ($\sim$10h) during summer and responding after 18-20h during the winter months. The seasonal changes are superposed over the changes dependent on the solar activity which reflects in the

form of a skewness in the seasonal variability. Corresponding to the response times for each month, an attempt to linearly model the $\frac{d(D_{st})}{dt}$ and ΔT_n was made and taken as representing that particular month. It is interesting to note that the gradients thus obtained, in other words the sensitivity of the thermosphere for any change in D_{st} remains more or less the same throughout the year, while only the corresponding intercepts undergo significant systematic seasonal variations . From the above results, it turns out that while the response sensitivity of the thermosphere remains the same for any change in D_{st} round the year, it is the background conditions due to the other processes that seem to introduce the observed seasonal variations.

REFERENCES

Burns, A. G., and T. L. Killeen, 1992 The equatorial neutral thermosphere response to geomagnetic forcing, Geophysical Research Letter, 10, 977-980.

Hedin, A. E., 1991 Extension of the MSIS thermosphere model into the middle and lower atmosphere, Journal of Geophysical Research, 96, 1159-1264.

Maeda S., T. J. Fuller Rowell and D. S. Evans, 1989 Zonally averaged dynamical and compositional response of the thermosphere to Auroral activity during Sept. 18-24, 1984; Journal of Geophysical Research, 94, 16869-16883.

Pant, T. K. and R. Sridharan, 1998 A case study of the low latitude thermosphere during geomagnetic storms and its new representation by improved MSIS model, Annales Geophysicae, 13, 1513-1518.

Prolss, G. W., 1980 Magnetic storm associated perturbations of the upper atmosphere: Recent results obtained by satellite-borne gas analysers, Reviews Of Geophysics And Space

Physics, 18, 183-202.

All–sky nightglow imaging at Asmara, Eritrea

R.H. Wiens and Samson Beyene

Dept. of Physics, University of Asmara, Asmara, Eritrea

YASAC, the York All–Sky Airglow Camera, was recently installed at Asmara (15.5° N, 38.2° E, geographic and 9°N dip) for the purpose of monitoring nightglow dynamics at a low–latitude station throughout the current solar maximum period. Emissions monitored include the O(1D) auroral red line at 630 nm for middle thermosphere and the O(1S) auroral green line and OH (6–1) band for lower thermosphere and upper mesosphere observations. Additional filters provide capability for background continuum and cloud correction. Exposure times are on the order of 30 s, giving O(1S) and OH measurements at least once every 5 min and O(1D) measurements once every 15 min. Although the average behavior of these target emissions has been studied extensively by instruments aboard the UARS satellite during the past decade, these space–based statistical results need to be complemented by ground–based data if we are to have a firm understanding of night–to–night and longitudinal variability.

By virtue of its 9° dip latitude, Asmara lies midway between the equatorial minimum and the maximum of the intertropical arc system associated with the EIA, the equatorial ionization anomaly. The intensity of the arc is known to depend directly upon the meridional wind , and the average thermospheric wind pattern is fairly well established. Our intent is to investigate the night–to–night variability of the pattern and that of the midnight temperature maximum. The many clear nights here should allow us to compile occurrence and morphology information on equatorial spread–F from a hitherto unexplored longitude sector.

Asmara is on a plateau at an altitude of 2400 m just 120 km west of the Red Sea.. Prevailing easterly winds during the summer may orographically produce internal gravity waves, the characteristics of which will be regularly compiled on the basis of the O(1S) and OH data. In the winter these winds become westerlies, but tropospheric storms over the Red Sea at this time may also generate waves that will be monitored. The same data set will inform us about tidal variability in the 80–100 km region and about free oscillations with periods of two and five days, known to occur at such a tropical latitude.

Examples of images taken and of preliminary data are presented and an invitation is extended to others working at similar latitudes to collaborate on longitudinal variability studies, particularly in West Africa and India, or through satellite programs. Such collaboration would parallel the goals and methods of the PSMOS (Planetary Scale Mesospheric Observing System) program already started in northern middle latitudes.

Low latitude Storm Time Ionospheric Electrodynamics

B. G. FEJER (Center for Atmospheric and Space Sciences, Utah State University, Logan, UT 84222–4405, USA)

The frequent occurrence of large ionospheric electric field and thermospheric neutral wind perturbations during magnetically disturbed conditions has been known for over four decades. In the last few years, it was realized that the complex electrodynamic response of the low latitude ionosphere to sudden changes in magnetospheric convection and to enhanced energy input into the high latitude ionosphere can only be understood by accounting for storm time dependent effects.

Studies of extensive Jicamarca radar measurements have shown that most of the plasma drift perturbations associated with magnetic activity can be explained as due to the effects of prompt penetration and ionospheric disturbance dynamo electric fields. Empirical equatorial, low– and mid–latitude prompt penetration electric fields are in excellent agreement with results from the Rice Convection Model (RCM). The derived disturbance dynamo electric field pattern is in good agreement with the results from Blanc–Richmond ionospheric disturbance model at the equator, but not at higher latitudes.

The basic characteristics of the *average* ionospheric disturbance drift patterns are now reasonably well understood. However, there are a large number of effects which can modify these electric field patterns. Recent numerical simulations using the RCM indicate that both the initial time response and steady state leakage of high latitude electric fields to lower latitudes is solar cycle dependent, and that prompt penetration effects seem to be highly affected by the reconfiguration of the Earth's magnetic filed following sudden changes in geomagnetic activity. In addition, there is evidence that the shielding of the mid– and low latitude ionosphere from high latitude electric fields undergoes large changes. Finally, convection enhancements and substorms could produce clearly different electric field perturbation patterns. Several of these effects are being studied using the recently upgraded RCM which now has self consistent magnetic field and particle precipitation models, a realistic ionospheric model, and a more powerful potential finder.

The variability of dynamo electric fields driven by storm time driven winds is also not well understood. The ionospheric disturbance dynamo patterns, which at the equator exhibit large seasonal and solar cycle effects, should be strongly dependent on the longitudinal sector where the bulk of the high latitude energy deposition takes place. Traveling atmospheric disturbances (TADs) and changes in the ionospheric conductivity due to changes in the ion composition are also common features of the mid– and low–latitude ionosphere during and after magnetically active times, but their effects on the generation of disturbance electric fields have not been determined. In fact, the general area of thermospheric neutral wind and plasma drift coupling during geomagnetic disturbances is still poorly understood.

In this talk, will discuss the recent progress on the response of equatorial and low latitude ionospheric electric fields to magnetospheric disturbances. We will also describe future numerical simulations and experimental studies which necessary to improve the understanding of these complex processes.

SPECTRAL ANALYSIS OF GEOMAGNETIC DATA FROM KANDILLI OBSERVATORY, ISTANBUL

Ayşe Hümeyra Bilge, *Department of Mathematics, Istanbul Technical University, 80626 Maslak, Istanbul, TURKEY,*
e-mail: bilge@itu.edu.tr

Yurdanur K. Tulunay, *Faculty of Aeronautics and Astronautics, Istanbul Technical University, 80626 Maslak, Istanbul, TURKEY*

Abstract: The geomagnetic field variation spectra for periods larger than 2 hours are analysed using the data obtained at the Kandilli Observatory in Istanbul, Turkey. Among the deterministic components, only the harmonics of the solar daily variation (S_i) and the second harmonic of the lunar daily variation (L_2) were observed. The seasonal dependence of the D component is analysed; the first harmonic of the solar daily variation (S_1) has maximum power in summer, decreasing symmetrically towards the winter, the second harmonic (S_2) has equal power in spring, summer and fall, while the third harmonic (S_3) has maximal power in spring and fall.

1. INTRODUCTION

In this work we study the geomagnetic field data obtained at the Kandilli Observatory in Istanbul, Turkey for the years 1973-1977, using spectral analysis. The coordinates of the Kandilli Observatory are given below.

$$\phi = 41°03.8\ \mathrm{N}, \quad \lambda = 29°03.7\ \mathrm{E}, \quad h = 130m \quad \Phi = 38°5, \quad \Lambda = 107°5,$$

where h is the elevation, $\{\phi, \lambda\}$ are geographical latitudes and longitudes and $\{\Phi, \Lambda\}$ are corresponding geomagnetic coordinates at 1976. The geomagnetic observation department in Kandilli has been in operation since 1947. The hourly mean values of D, H and Z components are regularly published in the observatory yearbook in which are also described instruments and data acquisition.

In our analysis we used the hourly mean values of the D, H and Z components for the years 1973-1977. Hence our analysis is necessarily directed to the study of the periodicities larger than the Nyquist frequency, 2 hours.

The short term variations of the geomgnetic field are mainly due to the changes in the atmospherical current systems and the best known "quite day" variations are the the solar daily variation S with 24 hour period and the lunar daily variation L with 24 hour 50 minute period.

The S variation is dominant and it can be seen from the magnetograms as an increase in the field intensity during the daylight hours. This variation is far from a regular sine curve even for quite days, there is an increase in the amplitude from winter to summer and its shape depends also on the latitude. The amplitude of L variation is around $1/10$ of S variation and it is usually masked by the latter (for example MITRA, 1952, Section 7.2). From time domain averaging techniqes, it is known that the main constituant of the L variation is a semi-diurnal component very close to a regular sine curve. Further details of the classical time domain methods for the analysis of the solar and lunar daily variations are described for example in MITRA (1952).

In the frequency analysis we applied the Fast Fourier Transform (FFT) to zero mean data. In our analysis we used either $N = 2^m$ (m integer) data points with a 4-term Blackman-Harris window (HARRIS, 1978), or a data length which is a multiple of the first harmonic of the solar daily variation (S_1) or of the second harmonic of the lunar daily variation (L_2) without windowing.

Preliminary investigations showed that the harmonics of the solar daily variation were dominant, and the analysis was directed to the study of any seasonal dependence of these variations and to separating the deterministic from the random variations.

2. ANALYSIS OF THE KANDILLI DATA

2.1. Spectral Analysis.

A clear resolution of the S harmonics is obtained by using FFT with $8784 = 366 \times 24$ data points. The power specta for 1976 (chosen as it is a magnetically quiet year in the period 1973-1977) shows the S_i harmonics for $i = 1, \ldots 4$; S_5 and even S_6 are also visible. The L_2 variation is observable, but it can not be distinguished from neighboring peaks of similar power. In order to confirm that the observed peak really corresponds to the L_2 variation, we obtained the power spectra for 6 overlapping intervals each of length 5960 data points (which corresponds to an exact multiple of the L_2 periodicity), shifted by 500 data points. In the average of these spectra the peak corresponding to the L_2 periodicity is enhanced, while other peaks previously of similar power are smeared out.

In order to decide which periodicities are deterministic, we worked with 58 monthly observation periods (excluding the first and the last months of the total observation period) for the D component as its variations were observed to be more accentuated.

2.2. Separation of determistic and random variations.

We consider the power spectra for the D components for 58 monthly samples. The number of occurences of peaks in the frequency spectrum of the samples are plotted as a histogram. In this analysis the S_1 periodicity occurs at frequency points corresponding to 24.09, 24.23 and 24.38 hours in respectively 15, 39 and 3 samples. We assume that there is a ± 1 frequency point uncertainity in the determination of a peak, i.e. a peak that occurs at the $n+1$'th or $n-1$'th frequency point in the power spectrum, will be considered as having occurred at the n'th point. Thus as S_1 peak occurs on 57 out of 58 samples we say that the "percentage of occurrence" of S_1 is %98. With

similar considerations we obtain the following table

Harmonic	L_1	S_1	L_2	S_2	S_3	S_4	S_5	S_6
Percentage of occurence (%)	0	98	50	98	79	69	41	17

Hence we clearly conclude that only the S_i, $i = 1, \ldots, 4$ are observed. The 50% occurrence of L_2, together with the enhanced peak in the averaged spectrum allows us to claim that L_2 also is observed via spectral analysis.

2.3. Seasonal dependence of the solar daily variation.

A qualitative analysis of the seasonal mean values of the D, H and Z components showed that the daily variation is confined mostly to the daylight hours. As the shape is far from a regular sine curve, it is expected to observe strong higher harmonics in the frequency analysis. The seasonal dependence of the solar daily variation is observed in all three components but mostly in the D component. During summer, the daily variations have larger amplitudes for all components.

The power spectra of the D variation for 5 years were analyzed. The variation of the amplitudes of the S_i for $i = 1 \ldots 3$ harmonics are obtained. The S_1 harmonic reaches its maximum at the 6th and 7th months and its power decreases symmetrically towards winter. The S_2 harmonic has more or less equal power during spring, summer and fall but it decreases again towards winter. The S_3 and S_4 harmonics are accentuated only during spring and fall. The power of the S_4 harmonic is considerably less than the others and it is almost uneffective in summer. The seasonal variation of the remaining periodicities is minor.

3. DISCUSSION AND CONCLUSIONS.

The main objective of this work is to introduce the geomagnetism community to the data from Kandilli observatory. We presented the diurnal and seasonal behaviour of the Kandilli D, H and Z data set for a relatively magnetically quiet period with particular attention to D. The S_i harmonics for $i = 1, 2, 3$ were clearly distinguishable, and we obtained the seasonal dependence of these harmonics using the spectra of one-month observation periods over five years. The enhancement of the S_1 variation in summer is well known, but to our knowledge the seasonal dependence of S_2 and S_3 and the observation that the higher harmonics are more effective in spring and fall is new. The seasonal variation of diurnal variations is also studied recently in RASTOGI (1993) using time domain methods. As our time domain analysis is only qualitative, we can only say that the D and H fields have concurrent midday *extrema* (except for winter), and this observation agrees with Rastogi's findings.

The power spectra and the histogram study revealed a number of low power peaks including the L_2 variation. Among these we claim to have "observed" the L_2 variation because it was enhanced in the averaged spectra using a total observation period which is an exact multiple of the L_2 period. One needs further investigation in order to decide whether other peaks of similar power are deterministic or not. In this context we mention that a quasi 2-day periodicity has been studied in TAKEDA and YAMADA (1989).

We conclude with two remarks concerning future directions for research. Firstly, the location of the Kandilli observatory is interesting for the change of phases of the average pressure at high

latitudes in the troposphere and a correlation between meteorological pressures and the strength of the geomagnetic activity has been observed (TULUNAY, KING and SLATER, 1988; KING, 1974). Secondly, the observatory is located near the Bosphosus, where a high speed southward current system is dominant. However the effects of such shallow (80-90 meter) current systems are expected to be reflected to higher frequencies (about 2.5 minutes) than those invertigated here. Thus the available magnetogram data is not suitable for this purpose and studies in this direction might necessitate new expriments.

Acknowledgements. The authors would like to thank the Kandilli Observatory administration for their kind permission in using the magnetic field data. This work was partially supported by the Scientific and Technological Research Council of Turkey, ÇAG 35.

REFERENCES

F.J. Harris, (1978): "On the use of windows for harmonic analysis with the Discrete Fourier Transform", *Proc. IEEE*, **66**, 51-83.

J.W.King, (1974): "Weather and Earth's magnetic field", *Nature*, **247**, No.5437, 131-134.

S.K. Mitra, (1952): *The Upper Atmosphere*, Chapter 7, (The Asiatic Soc. Monograph Series), Vol. V.

R.G. Rastogi, (1993): " Remarkable solar-cycle and seasonal dependenceof the diurnal geomagnetic D-variations at equatorial electrojet station, Kodaikanal", *Journal of Geomagnetism and Geoelectricity*, **45**, 657-668.

M. Takeda and Y. Yamada, (1989): " Quasi 2-day period variation of the geomagnetic field", *Journal of Geomagnetism and Geoelectricity*, **41**, 469-478.

Y.K. Tulunay, J.W. King and A.J. Slater, (1988): "Solar influences on the pressure diffference between $30^{o}N$ and $40^{o}N$ on the$30^{o}E$ meridian", *Bulletin of the Technical University of Istanbul*, **41**, 621-632.

A MU radar based study on annual variations of the mid-latitude ionosphere

S. FUKAO, and S. Kawamura (Radio Science Center for Space and Atmosphere, Kyoto University, Uji, Kyoto 611-0011, Japan), Y. Otsuka, and N. Balan (Solar-Terrestrial Environment Laboratory, Nagoya University, 3-13 Honohara, Toyokawa, Aichi 442-8507, Japan)

A review of the annual variations of the mid-latitude ionosphere, which focuses on the physical mechanisms causing the well-known seasonal anomaly and equinoctial asymmetry, is presented based on the observations by the MU radar at Shigaraki (34.85°N, 136.10°E) in Japan. The electron density, electron and ion temperatures, field-perpendicular plasma velocity, and meridional neutral wind velocity obtained by the MU radar in the 200–600 km altitude range during 1986–1996 are analyzed to study the altitude dependence of the seasonal variations of the ionosphere during different local time intervals with particular emphasis on the seasonal anomaly and equinoctial asymmetry.

The relative importance of the chemical and dynamical processes causing the anomaly and asymmetry is investigated. The observations show that the equinoctial asymmetry with the electron density in March equinox exceeding that in September equinox exists near the ionospheric peak and above at all local times. There is, however, a weak opposite asymmetry in the bottom side ionosphere during daytime. The seasonal anomaly with the daytime electron density in winter being greater than that in summer has an upper altitude limit of about 400 km. Although the anomaly and asymmetry involve both chemical and dynamical processes, the dynamical process predominates in the asymmetry while the chemical process predominates in the anomaly.

SPATIALLY-TEMPORAL STRUCTURE OF LOW-LATITUDE IONOSPHERE OBTAINED BY WAVELET ANALYSIS

V.H. Depuev, N.M. Rotanova, A.H. DEPUEVA (Institute of Terrestrial Magnetism, Ionosphere and Radio Wave Propagation, Troitsk, Moscow Reg., Russia, 142190)

During several past decades of regular ionospheric observations an extensive database was created. In our opinion it is of particular interest to reanalyse it by means of a modern technique appeared recently. Sufficient progress in different geophysical processes modelling in a nearest future is likely to be obtained due to the wavelet transform. The method advantages in the retrospective analysis of ionospheric data seems to be very promising now.

The aim of the presented work is to test this method applicability for the exposure of F-region critical frequency (foF2) spatially - temporal variations.

The database

Bottomside and topside vertical sounding data measured in the American longitudinal sector were analysed. There are hourly foF2 values from 1958 through 1985 for Huancayo and, besides, foF2 records onboard Alouette-1 satellite obtained at the American chain of receiving stations during August, 1963. The former was used for temporal ionosphere variability illustration, the latter – for spatial one.

Huancayo is a point located in a close proximity from the zero magnetic field inclination. We have chosen this station namely because of its most representative data set. For simplification of the procedure, the foF2 parameter is used due to its own distinctive feature of continuous data (in comparison with, say, foE rows having principal nocturnal gaps). The whole bottomside database consists of ≈8000 points. Below we'll only present midday and midnight behavior, analysed rows being not more than 500 values.

The satellite orbit inclination was 80.5°, therefore we can assume the meridional foF2 N-S sections that have been analysed. Any record duration was somewhat lesser than 1 hour. Analysed rows consist of not less than 150 values.

Gaps in records were filled with CCIR model values calculated for really observed heliogeophysical conditions.

The method used

Wavelet transform is the popular modern method of various geophysical processes analysis. Due to very important feature of wavelets called "time-frequency localization" one can study the one-dimensional signal peculiarities in both physical (coordinates and time) and frequency (frequency an time) domains, the permission staying constant independently on scale. As a basis, the solitone-like functions (mother wavelets) are used which are translated and dilatated during the processing procedure. In a matter of fact, the varying window is realized, which narrows for a small-scale characteristic evaluation and widens for a large-scale characteristic of the signal evaluation. The method discription is available in [1].

F2-layer critical frequency rows are the set of quasi-periodic signals, periods being from several tens years through some hours (sometimes up to a few minutes when so called continuous

one – by ionogram registration rate. There are a number of possibilities of such a signal analysis but wavelet transform has a certain advantages. It is suitable: it allows avoid additional preliminary operations, such as filtering, smoothing, and trend removal. It allows avoid spurious periodicities originated because of the relatively short row length as compared with maximum concidered period. At last, it allows study the thin signal structure with the same accuracy as those of larger-scale.

In order to apply the method for the real signal we have to use the discrete wavelet transform:

$$W(a,b) = a^{-1/2} \int_{-\infty}^{\infty} f(t)\tilde{\psi}[(t-b)/a]dt,$$

where f(t) – the initial one-dimensional temporal row, $\psi[(t-b)/a]$ - a wavelet's family, constructed by dilatation a and translation b coefficients changes. In our case we have used MHAT wavelet as a mother's one: $\psi(t) = (1 - t^2) \exp(-t^2/2)$. It is necessary to note that t in our case denotes time, so coefficient a is time scale also.

As a result of wavelet transform of the one-dimensional row one obtains two-dimensional amplitudes W(a,b). W(a,b) spatial distribution - wavelet coefficient spectra - characterizes the time evolution of different scale components relative contribution. It is a surface in a three-dimensional space and it can be presented as a projection on the ab-plane at the form of isolines. The characeristic temporal scale d appeares as a result of the wavelet analysis (it means an average duration making the main contribution to the power of the considered process) and it practically equal to $d = a\pi/\omega_\psi$. The ω_ψ value is calculated analytically and equal to 1.41 for the MHAT wavelet.

Results and discussion

For example, in fig. 1a the initial row of Huancayo foF2 values for midday conditions are presented. In fig. 1 b wavelet-transform coefficient modules reduced to zero average are presented. Along the ordinate axis the period T = 2d (in months for convinience) is marked. Six foF2 extremes are clearly seen. They correspond to T= 132 month (or 11-year) period. foF2 maxima are observed during high solar activity, foF2 minima – during low solar activity. In another words, by means of wavelet transform the well-known foF2 variation corresponding to 11-year solar cycle (usually approximated as $(foF2)^2 \approx (1 + 0.02\ R)$, R – an average Zurich sunspot number) is easily identified. At the magnetic equator the aforesaid phenomenon is caused not only by solar radiation and thermospheric parameters variabilities as it is for moderate latitudes, but also by circular electric field variation.

It is necessary to note that foF2 maxima are delayed by ≈1-2 years relatively to corresponding R maxima (1957, 1968, 1979). It is consistent with the recent idea that the foF2 follows rather solar burst activity than R or $F_{10.7}$ maxima.

The comparison between midday and midnight results confirms that foF2 dependence on solar activity is stronger for the daytime conditions.

In the same manner we can identify annual and even semiannual (1973-74) variation for noon (see fig. 1 c,d , the same as in fig. 1b, but on a large scale). For nocturnal conditions there is rather semiannual than annual periodicity. Sometimes so called quasi-biannual variation is clearly seen. This phenomenon is poorly studied, especially at the equatorial latitudes. Promising results could be obtained by means of not mentioned here wavelet analysis possibilities.

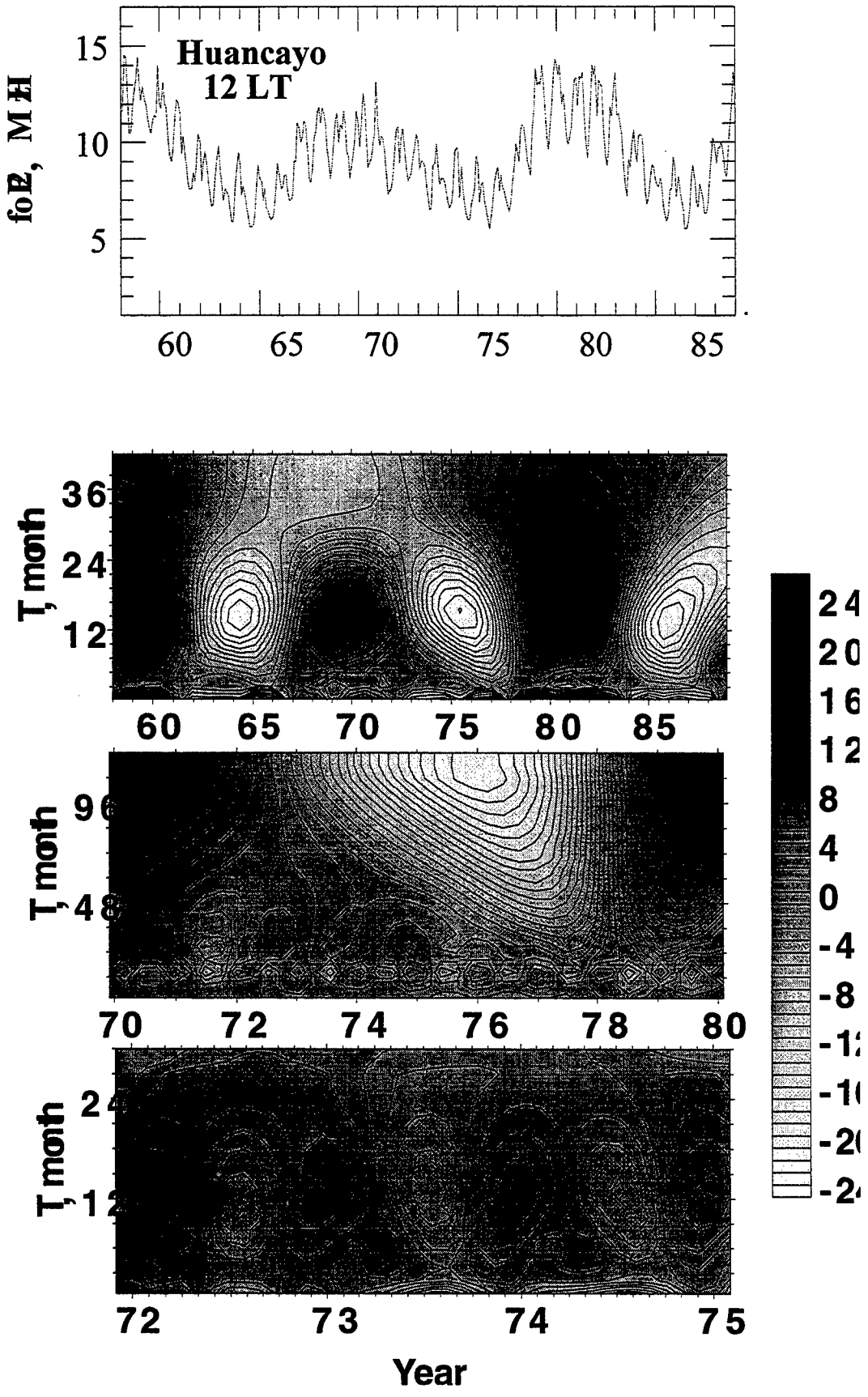

Huancayo
12 LT
foE, MHz
15
10
5
60
65
70
75
80
85
T, month
36
24
12
96
48
24
12
72
73
74
75
Year
24
20
16
12
8
4
0
-4
-8

Fig. 1

As it is well known, the seasonal anomaly in the equatorial daytime F-region is absent. Our results confirm this conclusion. (At low and middle latitudes it is caused by the sufficient decrease of the $[O] / ([O_2] + [N_2])$ ratio in summer relatively to winter conditions due to thermospheric circulation).

The 27-day foF2 variation corresponding to this observed in sunspot number is confirmed also. 27 days is the minimum distinguished period in our initial row analysis. But there are no principal difficulties for smaller scale period analysis by the method, so it may be used as the universal instrument for the time-frequency analysis of longterm ionospheric data sets.

The wavelet transform of the topside foF2 rows clearly identifies the large-scale spatial structure of the ionosphere like the main ionospheric trough and equatorial anomaly. Unfortunately, to distinguish less than some hundred km is impossible because of a small ionogram registration rate.

Because of the limited volume of the abstract, we are not in position to present some more figures. The detailed results of our work will be available in [2].

Conclusions

Our experience of wavelet analysis application shows that the method allows mark out characteristics of the peak electron density variations of different temporal and spatial scales. The possibility to obtain already known (solar-cycle, annual, seasonal, etc.) temporal periodicities is confirmed. The large-scale spatial peculiarities are distinguishable as well. There is a good reason to study interaction between different scale variations. The method advantages seems very prospective in further studies inluding phase, local extremes, power coefficients etc. evaluations.

References

1. Daubechies J. Ten Lectures on Wavelets, CBMS Ser. Appl. Math. 1992. V.61. Society for Industrial and Applied Mathematics. Philadelfia. 135 p.
2. Depuev V.H., Rotanova N.M., Depueva A.H. Wavelet transform application for spatially-temporal ionosphere characteristic studies. Geomagnetism i aeronomia. 2000. In press.

Penetration of auroral electric fields to the equator during a substorm

T. Kikuchi[1], H. Lühr[2], K. Schlegel[3], H. Tachihara[4], M. Shinohara[4], and T.-I. Kitamura[4]

[1] Communications Research Laboratory, Koganei, Tokyo 184, Japan
(Fax: 81-423-27-6676, e-mail: kikuchi@crl.go.jp)

[2] GeoForschungsZentrum Potsdam, D-14473 Potsdam, Germany

[3] Max-Planck Institut für Aeronomie, D-37191 Katlenburg-Lindau, Germany

[4] Department of Earth and Planetary Sciences, Kyushu University, 33 Hakozaki, Fukuoka 812-81, Japan

We have studied the negative magnetic bay associated with the substorm that occurred on April 20, 1993, and have found that it is markedly enhanced at the daytime dip equator, coherent with that at afternoon subauroral latitudes (Figure 1). The amplitude of the negative bay decreases monotonously with the latitude, but it is amplified at the dip equator by a factor of 2.5 compared to the low-latitude negative bay. This latitudinal profile implies that in addition to the 3-D current system in the magnetosphere, DP ionospheric currents originating in the polar ionosphere contribute greatly to negative bays. Penetration of the convection electric field and the effect of a shielding electric field due to Region-2 field-aligned currents (R2 FACs) are examined based on EISCAT and IMAGE magnetometer observations made in the afternoon sector. The northward electric field at EISCAT (66° corrected geomagnetic latitude) is well correlated with the magnetic field X-component at Nurmijärvi (56° cgmlat) during the pre-substorm period, but the coherency breaks down during the substorm cycle. By assuming that the R2 FACs intensify the northward electric field at EISCAT, but reduce it at Nurmijärvi, we demonstrate that the R2 FACs grow concurrently – although delay by some 17 min - with the convection electric field (Figure 2). Our analytical results indicate that the convection electric field decreases abruptly during the substorm and that the shielding electric field overcomes the convection electric field at around the peak of the negative bay due to its delayed reaction. The equatorial negative bay is thus due to an over-shielding effect caused by the electric field associated with the R2 FACs. We note that the equatorial currents are connected to magnetospheric source currents through the R1 and R2 FACs (Figure 3).

Reference

Kikuchi, T., H. Lühr, T. Kitamura, O. Saka, and K. Schlegel, Direct penetration of the polar electric field to the equator during a DP2 event as detected by the auroral and equatorial magnetometer chains and the EISCAT radar, J. Geophys. Res., 101, pp. 17161-17173, 1996.

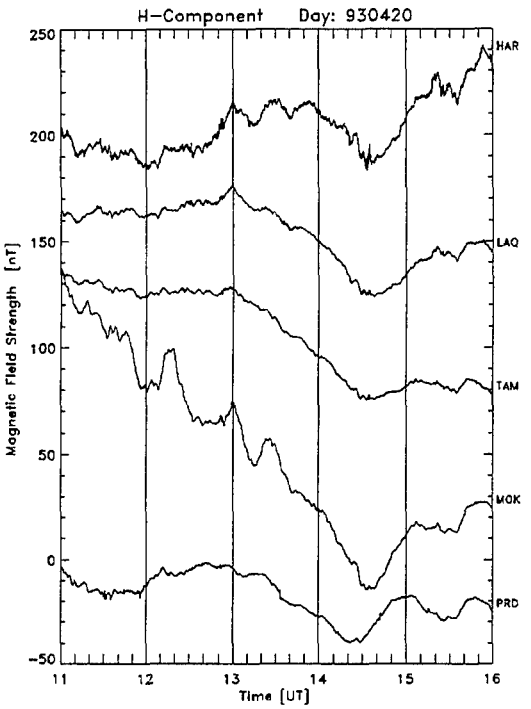


Figure 1
H-component of magnetic field at European mid-latitude (HAR, LAQ) and African low- (TAM) and equatorial- (MOK) latitude magnetometer stations located near the meridian of EISCAT, and at the equatorial station (PRD) in Sri Lanka. The DP2 event is apparent only at the dayside dip equator (MOK), while the negative magnetic bay appears at all latitudes but is enhanced at MOK.

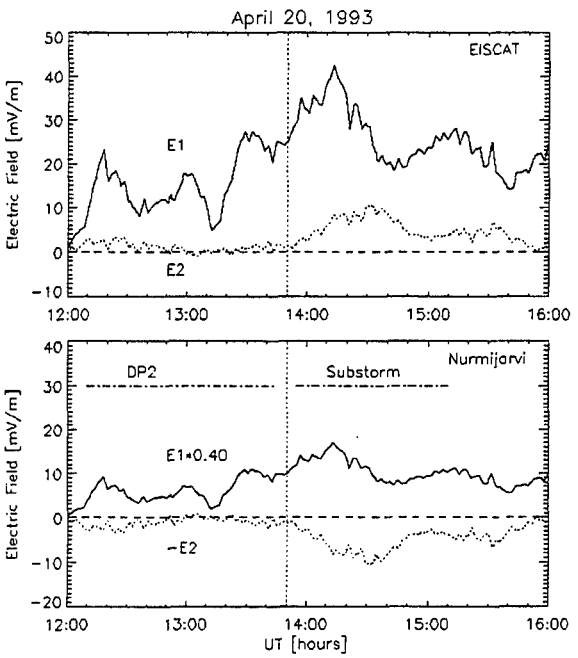


Figure 2
Estimated electric fields associated with the R1 and R2 FACs at EISCAT (E1, E2) and at Nurmijärvi (0.4E1, -E2) during DP2 and substorm events, deduced from electric field measured by EISCAT and from the magnetic field X-component at Nurmijärvi. E2 develops in response to E1, but is delayed by 17 min, resulting in E2 dominating around the peak of the negative bay (1430 UT).

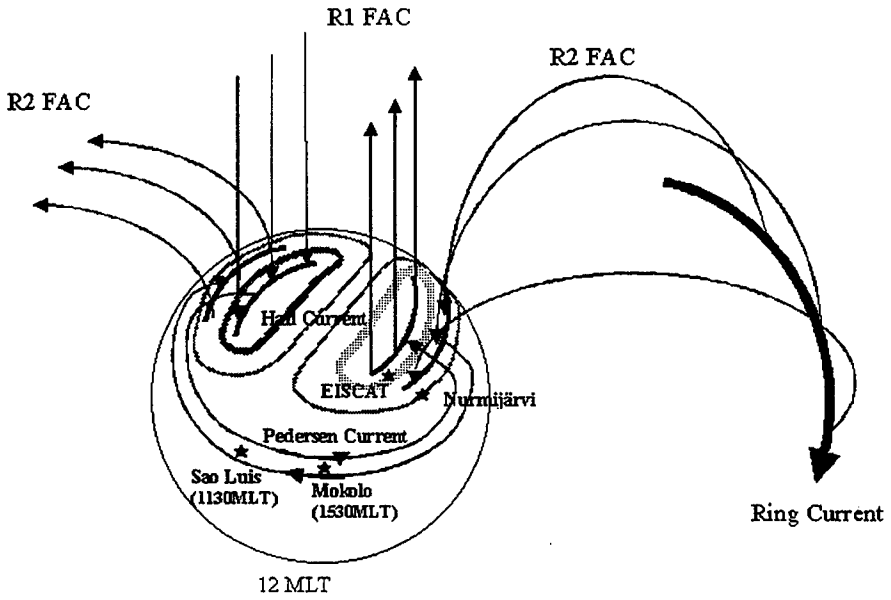


Figure 3
Schematic picture of R1 and R2 FACs with locations of EISCAT, Nurmijärvi, and equatorial (Sao Luis and Mokolo) stations. The R2 FACs enhance the northward electric field at EISCAT, but reduce this component at the Nurmijärvi and equatorial stations. The electric fields drive ionospheric Hall currents at high latitudes and Pedersen currents at the dip equator. The equatorial Pedersen currents are connected to the R1 and R2 FACs.

EFFECT OF THE FIELD-ALIGNED CURRENTS ON THE EQUATORIAL IONOSPHERE

L.Z. SIZOVA (Institute of Terrestrial Magnetism and Radio Wave Propagation Russian Academy of Sciences; 142190, Moscow region, IZMIRAN, Troitsk, Russia), M.I. Pudovkin (Institute of Physics, University of St. Petersburg, St. Petersburg 198904, Russia)

INTRODUCTION

During magnetic storms the equatorial ionosphere described by the various parameters (foF2, Vz etc) is defined to a significant degree by the state of the solar wind flowing around the Earth's magnetosphere. Numerous works present empirical relations between the solar and geomagnetic activity indexes and the equatorial ionosphere characteristics. There are certain relations between the equatorial ionosphere characteristics, solar wind parameters and polar magnetic field observations. This suggests that during magnetic storms the electric field from the solar wind can penetrate to the polar regions and to equatorial ionosphere (Pudovkin et.al., 1975, Fejer, 1991). The possibility of penetration was theoretically found and shown that the contribution of high latitude sources to low latitude electric fields and currents during quiet-time periods is comparable with dynamo fields. In connection with this Fejer (1991) pointed out that the understanding of the electric fields and plasma drifts during magnetically disturbed times is considerably less detailed. This results from measurement difficulties and from the high degree of complexity of the high latitude processes that control the electric field penetration to lower latitudes. This paper continues the investigations mentioned above and study the effect of the Bz-component of the interplanetary magnetic field on the equatorial ionosphere. A possible mechanism of electric field penetration to equatorial ionosphere during magnetically disturbed times is discussed.

ANALYSIS OF THE EQUATORIAL IONOSPHERE CHARACTERISTICS

The H-magnetograms and the f-plots at Huancayo, the F region vertical plasma drifts at Jicamarca (Balsley and Woodman, 1971, Fejer et al., 1979, Gonzales et al., 1979), solar wind data (King 1977) were used for our analysis. The variations of the critical frequency foF2 during magnetic storms and disturbances have been examined first. Abrupt breaks of foF2 as well as more long duration variations near 10 hours were noted. Sometimes more than one event per day have been observed. The intensity of foF2 variations can also be distinguished. The foF2 variations during main phase and recovery phase of magnetic storms are observed. There are very few papers concerning the problem of short duration foF2 variations associated with IMF effect and no acceptable explanations for these variations at equator. Because of this, in our study the analysis of foF2 events was supplemented by the equatorial magnetograms, the drifts velocities and by IMF Bz-component. The results of comparison have demonstrated that the Bz-component of the IMF is most suitable when describing the foF2 and F-region zonal electric field.

In Fig. 1 the H-component of magnetic field and the critical frequency foF2 at Huancayo, the vertical drift velocity Vz of the F region at Jicamarca, the hourly average of IMF Bz values are presented for three magnetic storms. The H and foF2 variations for quiet day are plotted in Fig. 1 by dashed lines. The large magnetic storm on 8 March 1970 is shown in Fig. 1(a). Two decreases and an increase of foF2 are observed during this storm. The decreases are consistent with southward Bz. The first decrease of foF2 with minimum at 15UT is associated with the substorm (see H-component) and the second decrease near 20UT is associated with the main phase of the magnetic storm. During these decreases foF2 peaked at about 9 MHz. The increase of the foF2 to 14 MHz is consistent with counterelectrojet (negative values of the Vz and the H) and assotiated with turning IMF Bz to the north.

Two magnetic storms 16 October 1970 and 13 September 1972 are shown in Fig. 1 (b, c). The counterelectrojet events associated with the reversal of the IMF Bz-component direction to the

north is observed between 19 UT and 21UT. The changes of the drift velocity during these events are remarkably similar. The increases of foF2 are the result of the downward drift of the plasma due to the reversal of the IMF Bz.

By this means the analysis of the southward IMF Bz effect on the equatorial ionosphere showed that the vertical drift velocity at daytime is increased and foF2 is decreased. The reverse of the IMF Bz–component from south to north implies to decreasing of the vertical drift velocity. The F region could then be fed with electrons from altitude above it and as result the increase of foF2 could be observed. Thus, the IMF Bz, the H–component of the geomagnetic field, the critical frequency foF2, and the F–region vertical plasma drifts at daytime are interrelated.

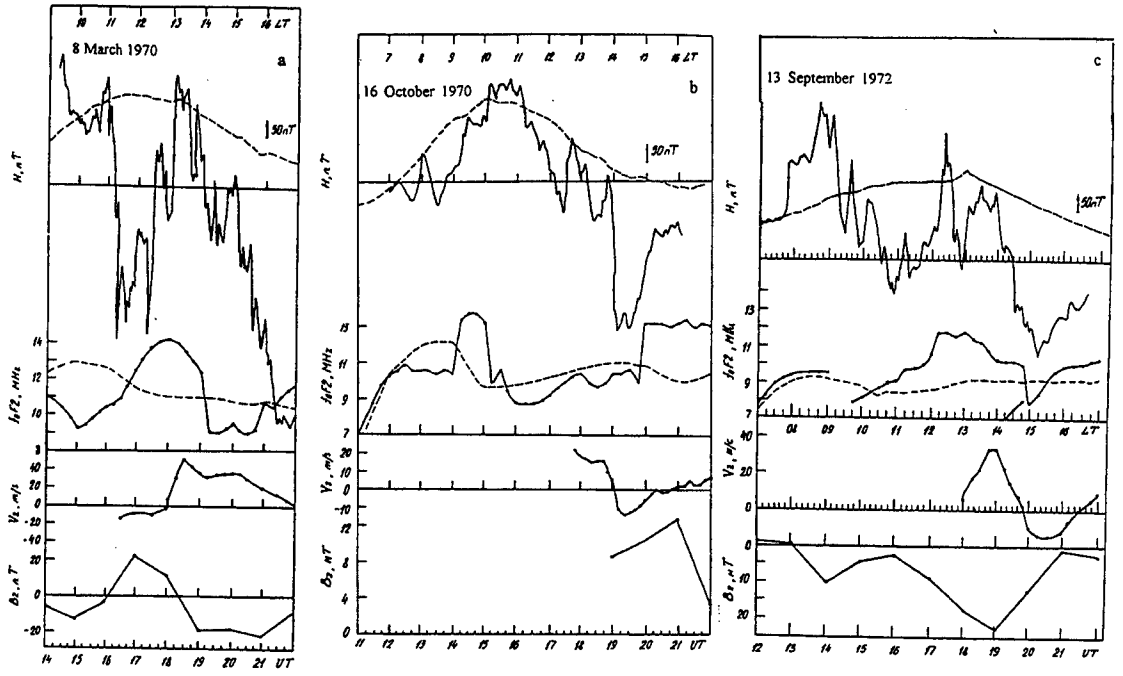


Fig.1. The H–component of the geomagnetic field, the foF2 variations at Huancayo (dashed lines are the quiet day variations), the vertical drift velocity Vz at Jicamarca, the Bz–component of the IMF during the geomagnetic storms 8 March 1970 (a), 16 October 1970 (b), 13 September 1972 (c).

CONTRIBUTION OF THE FIELD–ALIGNED CURRENTS TO EQUATORIAL ELECTROJET

In the present view, interaction between solar wind, magnetosphere and ionosphere effected by way of field–aligned currents. Model calculations of penetration of the high latitude field–aligned currents to quatorial ionosphere were carried by Zakharov et al (1989), Denisenko and Zamay (1992). These models can explain the general form equatorial electric field variations during quiet–time periods, but are still unable to account for several aspects of the experimental data because of the complexity of the high latitude and magnetospheric processes involved. For example, the relationship between the magnitude of a substorm and the value of the disturbance equatorial electric field is controversial (Fejer, 1986; 1992, Denisenko and Zamay, 1992).

We made attempt to understand the physical mechanism of the relationship between solar wind electric field, equatorial ionoshperic electric field, and foF2 variations during magnetic storms (Sizova et al, 1998; Sizova and Pudovkin, 2000). The influence of IMF Bz turnings on the equatorial ionosphere we explane in terms of the field–aligned currents. Zanetti and Potemra (1986) were made comparisons between Birkeland and ionospheric current systems were made. It

has been shown that the IMF produces Region 1 (R1) and Region 2 (R2) Birkeland and auroral electrojet current systems. The effects on these magnrtospheric–ionospheric currents systems when the IMF has a large northward component have been also considered in recent studies. Pudovkin (1975) suggested that disterbances of the equatorial ionospheric electric fields are the result of polar electric field penetration to the equator during magnetospheric substorms. Kikuchi et. al. (1996) using the auroral and equatorial magnetometer chains and the EISCAT radar had shown the equatorward penetration of the DP 2 magnetic fluctuations. From the above reasoning it is clear that the contribution of the field–aligned currents to equatorial ionosphere can be conceived of as Fig. 2. By our present view the field–aligned currents of the Region 1 (DP) which form during Bz<0 close across the ionosphere including the equatorial electrojet region. This process increases the daytime electric field (Fig.1). As the result the additional upward plasma drift velocity carries ions away from the equatorial F2–layer and we can see of foF2 decriasing and incriasing of the H–component of geomagnetic field. As the result of convection The field–aligned currents of the Region II (DP–3) as the result of convection are appeard during Bz>0. They also close partly across the equatorial ionosphere and decrease the drift velocity. As the result we see foF2 increasing and the H–component decreasing (counterelectrojet). The model of the field–aligned currents of the Region I and II closing across equatorial ionosphere in the daytime is presented on Fig. 2. The superposition of electric fields–produced by the aligned currents in the Region I and II is supposed to cause observed disturbances of the ionospheric parameters at equator.

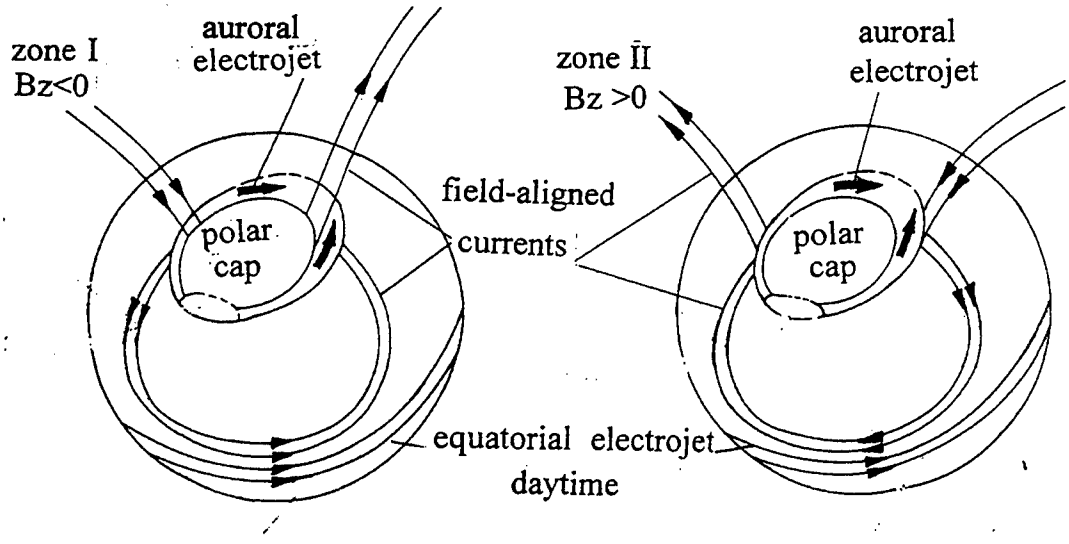


Fig. 2. The model of the field–aligned currents of the Region 1 and 2 (zone I and zone II) closing across the equatorial ionosphere in the daytime.

CONCLUSIONS

The daytime characteristics of the equatorial ionosphere during magnetic storms are investigated. It is shown that the IMF Bz, the H–component of the geomagnetic field, the critical frequency foF2, and the F–region vertical plasma drifts are interrelated. The H–component, the critical frequency foF2, and the F region plasma drifts variations at the magnetic equator are explained on the basis of effect of equatorward penetration of the field–aligned currents. The counterelectrojet, foF2 increasing, and Vz decreasing during magnetic storms at equator are associated with effect of the

Region 1 field–aligned currents (Bz>0). The additional increases in the H–component and Vz and corresponding foF2 decreases are assotiated with the Region 2 field–aligned currents (Bz<0).

REFFERENCES

Balsley B.B.and Woodman R.F. Ionospheric drifts velocity measurements at Jicamarca, Peru (Iuly 1967 – March 1970), Report UAG–17, Boulder 1971.

DenisenkoV.V.and Zamay S.S. Electric fields in the equatorial ionosphere. Planet. Spase Sci., 1992, 40, 941.

Fejer B.G., Gonzales C.A.and Farley D.T. Equatorial electric fields during magnetically disturbed conditions, J.Geophys.Res, 1979, 84, 5797.

Fejer B.G. Low latitude electrodynamic plasma drifts: a review. J. Atmos. Terr. Phys, 1992, 53, 677.

Gonzales C.A., Kelley M.C., Fejer B.G., Vickrey J.F. and Woodman R.F.Equatorial electric fields during magnetically disturbed conditions 2. Implications of simultaneous auroral and equatorial measurements, J. Geophys. Res, 1979, 84, 5803.

King Y.H. Interplanetary medium data book. Appendix. 1977

Kikuchi T., Luhr H., Kitamura T., Saka O. and Schlegel K. Direct penetration of the polar electric field to equator during a DP event as detected by the auroral and equatorial magnetometer chains and the EISCAT radar. J. Geophys. Res., 1996, 101, 17161.

Pudovkin M.I., Raspopov O.M. and Kleymenova N.G. Disturbances of earth electric fields. St. Petersburg. LGU. 220.

Sizova L.Z., Zelenova T.I. and Pudovkin M.I. Disturbances of the equatoral ionosphere parameters associated with the Bz–component of the interplanetary magnetic field, in Abstracts of the 2nd international conference " Problems of geospase" 1998,.89.

Sizova L.Z., Pudovkin M.I. Disturbances of the daytime equatorial ionosphere assotiated with the Bz–comonent of interplanetary magnetic field. Geomagn. Aeron. (Russian Edition). 40, 2000, 271.

Zakharov Y.Y., Nikitin M.A. and Smirnov O.A. The response of low–latitude fields to the action of magnetospheric source. Zakharov Y.Y., Nikitin M.A. and Smirnov D.A., The response of low–latitude fields to the action of magnetospheric source, Geomagn. Aeron. (Russian Edition), 29, 1989, 344.

Zanetti L.J. and Potemra T.A. The relationship of Birkeland and ionospheric current systems to the interplanetary magnetic field. in: Solar wind – magnetosphere coupling, Tokyo, 1986, 547.

ISR observations of the ionosphere over Arecibo: The effects of a solar eclipse, and the effects of a small geomagnetic storm.

S. A. GONZALEZ(Arecibo Observatory)
B. MacPherson(Arecibo Observatory)
N. Aponte(Arecibo Observatory)
M. Sulzer(Arecibo Observatory) M. Kelley(Cornell)
X. Pi (JPL) G. Bailey(Univ. Shefield)

In the first part of this presentation we will describe the effects of the solar eclipse of February, 1998 on the topside ionosphere over Arecibo. The response of the topside ionosphere to the eclipse is characterized by a descent in the O^+-H^+ transition altitude which falls by 200 km during the eclipse, as a result of the contraction of the plasma due to reduced plasma temperatures. The electron temperature was found to have decreased by 600degK at 400 km. This decrease was smaller with increasing altitude and we show this is the result of the lesser degree of obscuration of the solar disk at latitudes north of Arecibo. In addition the heating effects of conjugate point photoelectrons are shown to play a significant role in the electron energy balance during the eclipse. Finally the ion temperatures are examined and it will be shown that while the O^+ temperature exhibits very little response to the eclipse, the H^+ temperature decreases in response to the reduced T_e.

In the second part we will show an example of how disturbance dynamo electric fields can cause the equatorial anomaly to advect northward over Puerto Rico. On February 17-18, 1999 the Arecibo radar made observations during an event in which the electron density rose to daytime values near midnight. Arecibo was operated in the beam swinging mode, which made it possible to track the location and motion of these enhancements. For this event, the peaks in the density were observed predominantly south east of Arecibo while the ions sustained a northward-eastward motion due to an

eastward-southward storm dynamo electric field. TEC maps from GPS for this night confirmed that the density enhancements were due to a poleward expansion of the equatorial anomaly.

Is there an Afternoon "Hole" in the Topside Equatorial Ionosphere?

D. T. FARLEY, W. E. Swartz (both at School of Electrical Engineering, Cornell University, Ithaca, NY), and J. L. Chau (Jicamarca Radio Observatory, Lima, Peru)

Huba et al., in the January 15, 2000 issue of GRL, described modeling work that predicted that interhemispheric flow in the topside ionosphere, during a solstice period and for fairly high solar activity (F10.7 = 180), should produce a minimum in the electron density at an altitude somewhere in the vicinity of 2000 km. This paper discusses very recent measurements made at Jicamarca to test this idea. We alternated between two measurements. The first had a pulse length and height resolution of 15 km, and produced absolute density profiles (power profiles normalized with Faraday rotation data in the F region) up to about 1000 km. The second used a pulse length of 200 km (1.33 ms) and gave relative electron density (power profiles only) from about 500 km up to above 3500 km. The two profiles were fit together in the overlapping region in the topside ionosphere to give a complete density profile.

We obtained results on 14 and 15 February 2000, the abstract deadline, and so we have not had time to do much data analysis yet! A very crude look at the data from the 14th shows no obvious sign of the hole predicted in the paper of Huba et al. We have not yet removed obvious satellite echoes from the data, however, and have not looked at all at the data from the 15th. We should have more definite conclusions by the time of the Symposium.

Reference:

Huba, J. D., G. Joyce, and J. A. Fedder, The formation of an electron hole in the topside equatorial ionosphere, *J. Geophys. Res., 27*, 181–184, 2000.

FIELD–ALIGNED ION MOTIONS IN THE TOPSIDE IONOSPHERE

R.A. HEELIS (William B. Hanson Center for Space Sciences,University of Texas at Dallas, PO Box 830688, Richardson, TX 75083–0688, USA) and S. Venkatraman (William B. Hanson Center for Space Sciences,University of Texas at Dallas, PO Box 830688, Richardson, TX 75083–0688, USA)

The plasma temperature, composition, and density in the topside low–latitude ionosphere are strongly influenced by ExB drifts and field–aligned motions in the topside ionosphere. Here we describe the field–aligned motions of O+ ions observed at low latitudes near 800 km altitude by the DMSP spacecraft. These field–aligned drifts result from the combined effects of ExB drifts, F–region neutral winds and ion chemistry. They are dependent on plasma pressure gradients in the topside ionosphere, which are in turn modulated by the presence of the field–aligned motions. Thus a complex feedback process needs to be incorporated in the interpretation of the measurements. We describe the longitude and seasonal dependence of these drifts, and add additional information from previous measurements from the Atmosphere Explorer satellite, to understand the important factors controlling their behavior. The relationship between these field–aligned motions and previously observed adiabatic heating and cooling effects in the topside are also included in the data interpretation.

Evening Enhancements in F–region Electron Temperature at Subtropical latitudes during summer in the Indian SROSS C2 RPA Data

K. NIRANJAN, H.S. Sridhar and P.V.S. Rama Rao
Department of Physics, Andhra University, Visakhapatnam 530 003 INDIA
e–mail: niranjankandula@hotmail.com

Early information on the spatial and temporal variations of electron temperatures at low latitudes are mostly based on model calculations derived by solving the time dependent equations of continuity, momentum and energy balance for the various ionic species and electrons. With the advent of rockets and satellites a good experiential data base is generated on the spatial and temporal characteristics of electron and ion temperatures, electron densities and the densities of the various ionic species at F–region peak altitudes. There have been reports on various anomalous features in the temporal and spatial variations of the electron and ion temperatures at various locations that are not reflected in the model calculations. Such features have been interpreted based on the atmospheric energetics and dynamics related to the specific observations. Here we an anomalous feature in Electron Temperature observed at low latitudes during solar minimum periods.

Ionospheric F– region Electron temperatures (T_e) derived from the RPA payload aboard the Indian SROSS C2 satellite show characteristic enhancements in the sub–tropical latitudes around 15–20 Deg N in the evening hours centred around 18 hrs IST during June Solstice months of the low sunspot period 1995–96. During equinoctial months, this evening increase in electron temperature is smaller and earlier in time. During winter months this feature is not seen. These enhancements show a latitudinal differences with early sharp peaks at higher latitudes (23° N). Such distinct enhancements are not seen at latitudes beyond 10° N towards the equator during equinoctial months. There is no specific dependence of the T_e on the solar and geomagnetic activity. The observed features seem to depend on the equatorial plasma dynamics.

Pre-seismic activity effects on the equatorial anomaly

S. A. PULINETS, A. D. Legen'ka and V. H. Depuev
(Institute of Terrestrial Magnetism, Ionosphere and Radiowave Propagation,
Troitsk, Moscow Region, 142190, Russia, e-mail: pulse@izmiran.rssi.ru)

Introduction

It was demonstrated recently that one of the sources of day-to-day variability of the ionosphere is seismic activity [*Pulinets, 1998*]. Even more, the variability in the ionosphere starts to be observed few days before the strong earthquakes over the anticipated epicenter area and occupies the region within the ionosphere near 20° in latitude and longitude. It could be manifested in the form of negative or positive deviations from undisturbed level of *foF2*. It was revealed that the sign of deviation depends on the local time [*Pulinets et al., 1998*]. The ionosphere modification takes place on all heights of the ionosphere up to magnetosphere [*Pulinets et al., 1999a*] and leads to height scale changes, what in the case of seismic activity is due to ion compositions changes [*Pulinets et al., 1999b*]. The present paper is intended to study in more detail the pre-seismic effects in the vicinity of the equatorial anomaly where some effects were reported also [.

Experimental data

We used the data of topside sounding from Intercosmos-19 satellite (1979-1981) [*Pulinets, 1989*]. The parameters of an orbit (inclination of 74°, rotation period ~100 minutes) provided that the local time of intersection by the satellite of equatorial plane during several sequential orbits was practically the same. It allowed for fixed LT to obtain the quasi-meridional cuts of an ionosphere, displaced from each other by ~25 degrees of a longitude. In a data set considered, the vertical sounding was accomplished every 64 seconds. During this time the satellite was displaced along an orbit by ~3.6 degrees of a latitude. We selected several cases of strong earthquakes in the Pacific area for different local times to reveal the possible dependence on the local time, which was detected for the middle latitudes. The topside vertical profiles were calculated also.

Results and discussion

One can see on Fig. 1 and 2 examples of latitudinal cross-sections of the equatorial anomaly obtained several hours before two earthquakes: 20.03.79 and 16.07.80. Both of them took place close to the equator: 7.5 N and 3.2 S respectively. Fig.1 represents the passes scaled for two local times corresponding to daytime and nighttime parts of the trajectory (14 LT and 02 LT), but for the same longitudinal interval. They demonstrate the equatorial anomaly dynamics with time approaching to the earthquake. The reference curve (circles) represents the anomaly shape in undisturbed conditions. One can see that at daytime conditions the anomaly develops (crest-to-trough relation grows) while in nighttime conditions the trough is filled by plasma if we are closer to the earthquake moment. It is more evidently demonstrated on Fig.2 when the satellite crossed the anomaly at 04 LT. On the pass, closest in time to the earthquake, the anomaly practically disappears. So, as in middle latitudes the ionosphere behavior during preparatory stage of the earthquake depends on the local time. The difference looks like instead of simple positive and negative deviations of the critical frequency we observe the variations of equatorial anomaly development. This implies that the main role in the observed variations is played by electric field [*Pulinets et al., 2000*] the direction of which

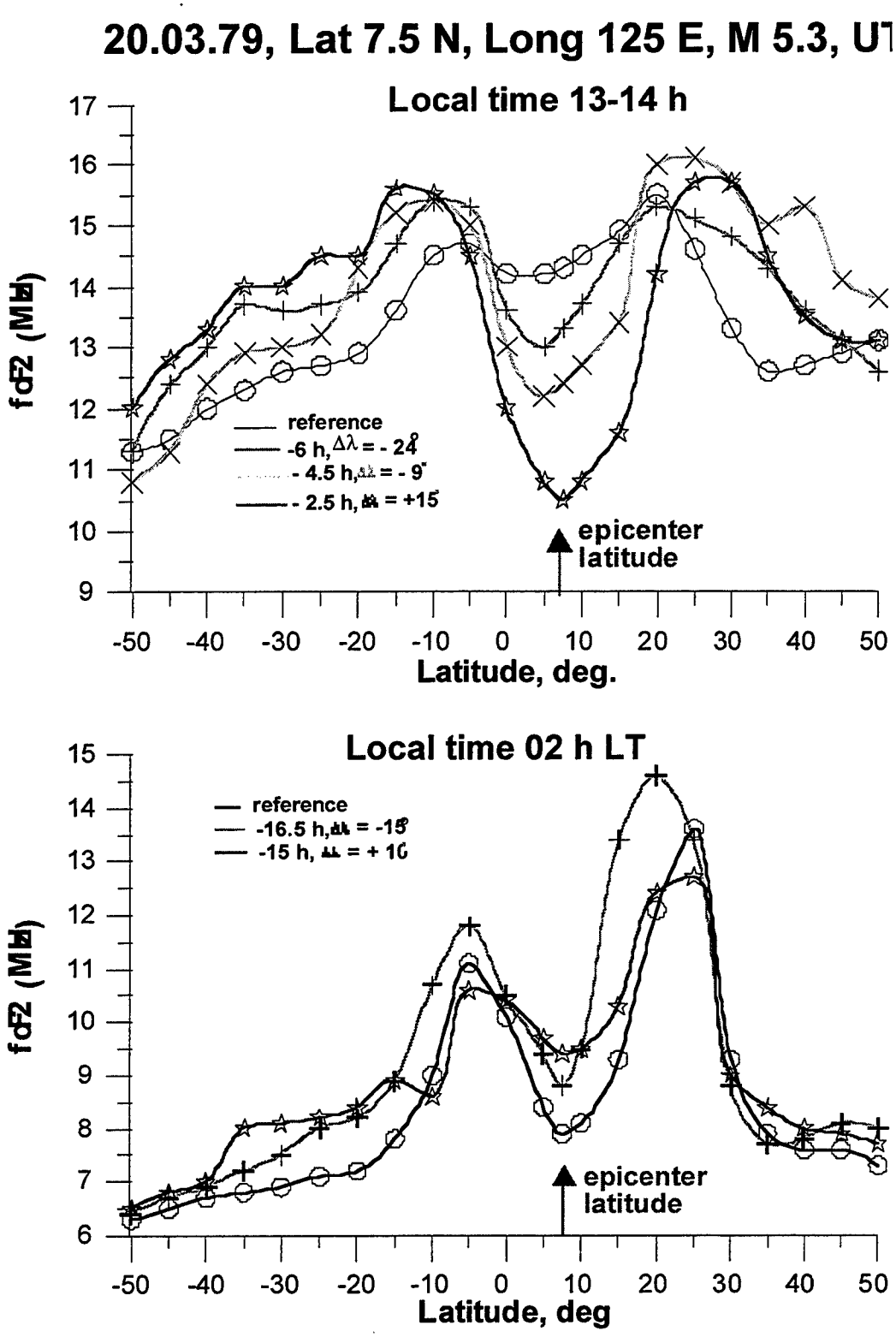


Fig.1 Variations of equatorial anomaly shape during earthquake preparatory phase

changes with the local time. The topside vertical profiles and *HmF2* variations over the anticipated earthquake epicenter area are considered also. The increase of height scale as well as *HmF2* is marked. Nevertheless some data do not permit to make the final conclusion on the local time dependence of equatorial anomaly only. It could be connected also with time in advance before the main shock. This question is under study now and needs more statistical data to clarify situation.

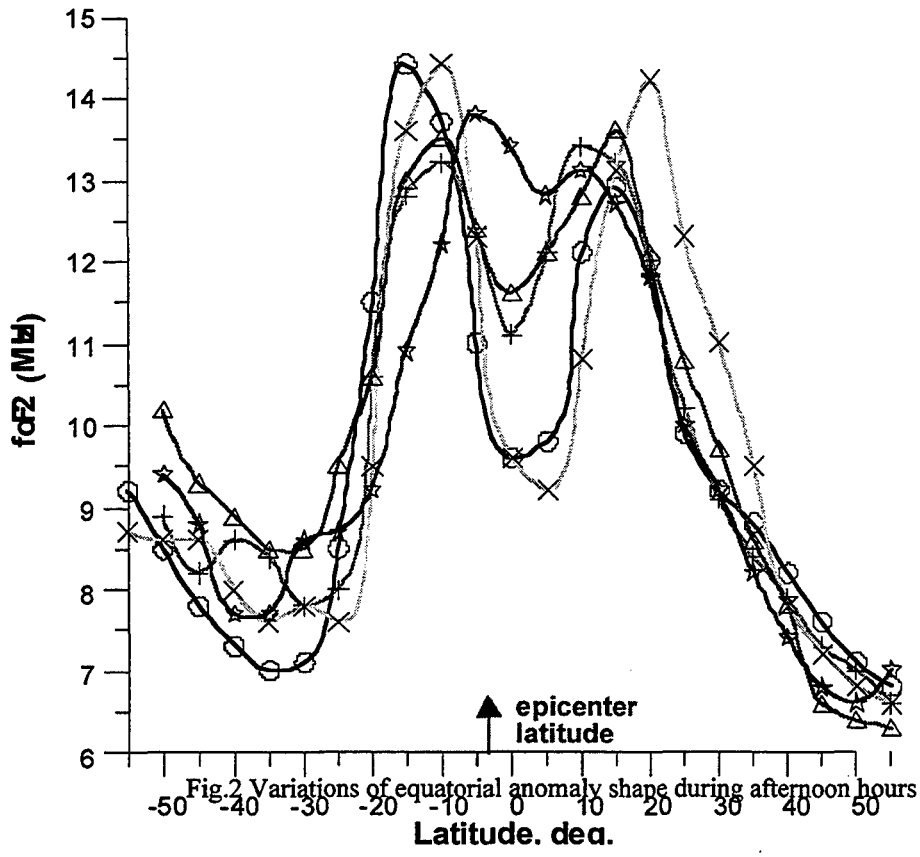


Fig.2 Variations of equatorial anomaly shape during afternoon hours

References

Depueva A.Kh, Yu.Ya. Ruzhin, Seismoionospheric fountain-effect as analogue of active space experiment, Adv. Space Res., *15*, 1995, No12, p.(12)151

Pulinets, S.A., Prospects of topside sounding, in WITS Handbook, 2, SCOSTEP publications, Urbana, 1989, p.99

Pulinets, S.A., Seismic activity as a source of the ionospheric variability, Adv. Space Res., *22*, 1998, No 6, p.903

Pulinets, S.A., Legen'ka A.D., Zelenova T.I., Dependence of the seismo-ionospheric variations in the F-layer maximum on the local time, Geomagnetism i Aeronomiya, *38*, No3 1998, p.188

Pulinets S.A., K.A.Boyarchuk, V.V.Hegai, D.R.Shklyar, Ground-Atmosphere-Ionosphere-Magnetosphere Coupling Conception Including Seismic Activity, *XXVI URSI General Assembly, Toronto, 13-21 Aug. 1999, Abstracts*, p.747

Pulinets S.A., V.Kh.Depuev, T.V.Gaivoronskaya, Ionospheric Variability Induced by Seismic Activity, *International Reference Ionosphere Workshop (IRI'99), 9-12 Aug. 1999, Lowell Mas., Abstracts*, P. 3A-9

Pulinets S. A., K.A.Boyarchuk, V.V.Hegai, V.P.Kim and A.M.Lomonosov, Quasielectrostatic Model of Atmosphere-Thermosphere-Ionosphere Coupling, *Adv. Space Res.*, **25**, 2000, in press

Variation of the F_3 layer occurrence with the magnetic dip angle

I. S. BATISTA (INPE, São José dos Campos, SP, Brazil), M. A. Abdu, A. M. Silva, P. F. Barbosa Neto and J. MacDougall (University of Western Ontario, London, Canada)

Abstract

Recent studies using model calculation and ionospheric observations have revealed the existence of an additional layer in the topside equatorial ionosphere, that was called the F_3 layer. The observations using bottomside ionograms from locations close to the magnetic equator in Brazilian region have shown that the occurrence of the layer is very high in the December solstice (local summer), less frequent in the June solstice (local winter) and very low in the equinoxes. In this work we use 25 years of data to investigate how the layer occurrence varies with the magnetic dip angle.

Introduction

Recent theoretical studies revealed the existence of an additional layer above the F_2 peak, called F_3 layer (Balan and Bailey, 1995; Balan et al., 1997; Jenkins et al., 1997). Ionospheric data from Fortaleza (4° S, 38° W, dip angle –12°), Brazil, and theoretical simulation using SUPIM (Sheffield University Plasmasphere Ionosphere Model) were used to study the physical mechanism and frequency of occurrence of the layer (Balan et al., 1998, 1999; Batista et al., 2000) and its variability over the Brazilian region (Balan et al., 2000). The present paper reports a detailed statistics of occurrence of the layer recorded at Fortaleza from 1975 to 1999, in which period the magnetic dip angle of the location has varied from 2.5° S to 11.7° S.

Observations

Ionospheric data have been recorded over the Brazilian location Fortaleza since 1975. From 1975 to 1993 a C4 ionosonde was recording ionograms at 15 min. intervals and from 1994 to 1999 the data were recorded by a digital ionosonde (CADI – Canadian Advanced Digital Ionosonde) at 5 min. intervals. Over the Brazilian region the geomagnetic equator is drifting northward at a very high rate. Due to this drift the geomagnetic dip angle over Fortaleza varied from 2.5° S in 1975 to 11.7° S in 1999 (a rate of –26.2 min/year). The long time series of ionospheric data registered at that location gives us the opportunity to study the dependence of ionospheric parameters with the geomagnetic position of the station.

In this study we have used the months of January and August as representative of December solstice (local summer) and June solstice (local winter), respectively, based on the statistics made for all months of the year 1995 (Balan et al., 1998).

The two upper panel in Figure 1 show the number of days with F_3 layer present on the ionograms, for the months included in this work and the third panel shows the variation of the magnetic dip angle over Fortaleza during the studied period. The vertical dashed lines indicate lack of data. Also shown in the figure (lower panel) is the solar flux variation at 10.7 cm (F10.7).

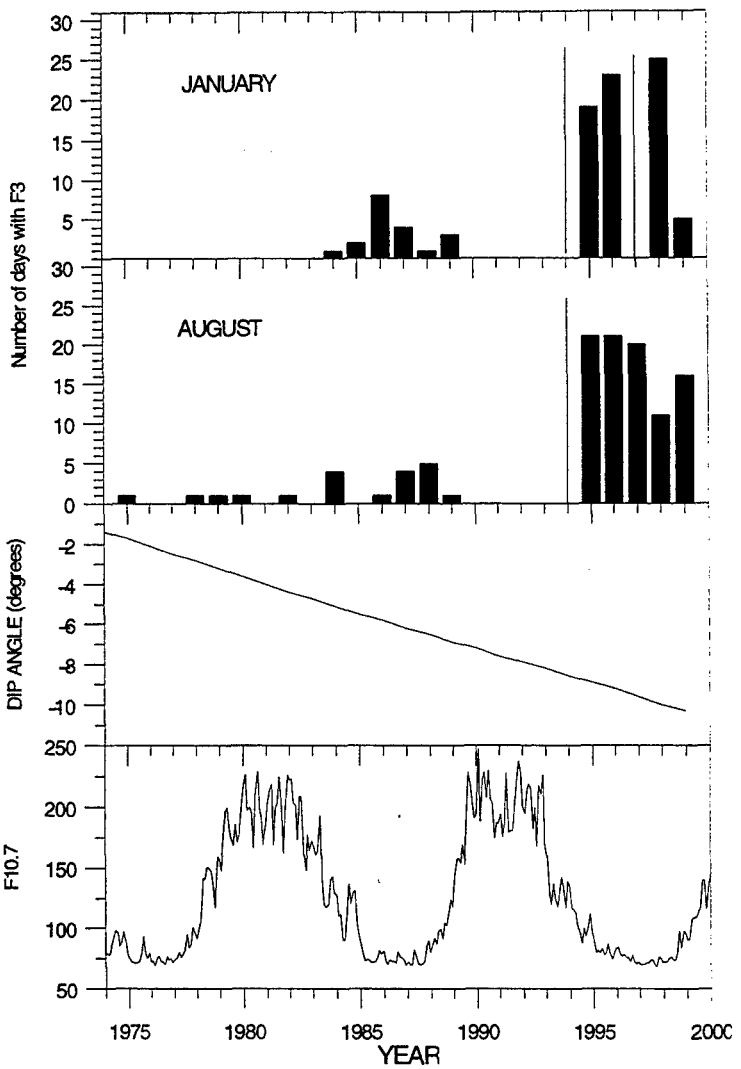


Figure 1 – Occurrence of F3 layer over Fortaleza and magnetic dip angle of the location during the two most recent solar cicles

As Figure 1 shows, the F_3 occurrence is very rare for dip angle between –2° and –4°; the occurrence then increases with increasing dip angle, and it is modulated by the solar activity. In fact very few F_3 layer occurs during the high solar activity periods (1979–1983 and 1990–1993). The three low solar activity periods shown on Figure 1 will be denoted by L1, L2 and L3. Table 1 shows the dip angle at Fortaleza for the three periods, and the corresponding mean occurrence of the F_3 layer for each period.

Table 1 – Occurrence of F_3 layer as a function of dip angle and time period

Period	Years	Dip Angle	Days/month	
			January	August
L1	1975–1978	$-4° < I < -2°$	0	1.0
L2	1984–1989	$-8° < I < -6°$	3.8	2.5
L3	1995–1999	$-12° < I < -10°$	18.0	17.6

We can see that the occurrence of the layer increased from ~0 days/month in period L1, to ~18 days/month in period L3, while the dip angle changed from 2° S to 12° S in the same period.

Discussion

Balan et al. (1998) discussed the physical mechanism for the formation of the F_3 layer and the location and latitude extent of the layer in different seasons at low solar activity. The layer forms during the morning–noon period at the equatorial region where the combined effects of the upward **ExB** drift and the magnetic meridional neutral wind provides vertically upward plasma velocity at altitudes near and above the F_2 peak. The morning F_2 peak drifts upward due to this velocity and form the F_3 layer, while the normal F_2 layer develops at lower altitudes through the usual photochemical and dynamical processes of the equatorial region. After the two layers become distinct, the F_3 layer peak (N_mF_3) density remains greater than the F_2 peak density (N_mF_2) for a period of time. During this period, both the F_3 and the F_2 can be recorded by ground based ionosondes as has been done at Fortaleza.

Very few F_3 layer occurs during the high solar activity periods (1979–1983 and 1990–1993) because the morning–noon ionosphere becomes broad and intense with increasing solar activity, while the corresponding driving mechanism for the F3 layer formation (drift and wind) remains more or less constant (Balan et al., 1998). Thus the upward force arising from drift and wind becomes insufficient to raise the morning F_2 peak to the topside altitude to form an F_3 layer during solar maximum.

Model calculations performed for low solar activity period using SUPIM, considering **ExB** drift velocities measured at Jicamarca and the neutral wind velocities calculated from HWM90 (Balan et al., 1998), has predicted that the F_3 layer, at the longitude of Fortaleza, will be centered at around 4° S (mag. lat.) in December solstice, and 6° N at June solstice, with latitude extents of about 10° and 14°, respectively.

Our results show that the layer can be observed at 12° S dip angle (6° S mag. lat.), during both December and June solstices. This shows that the model calculations are consistent with observations for December solstice but they disagree for the June solstice. In fact our results show a similar behavior during both solstices. The occurrence of the layer increases away from magnetic equator, and it is modulated by the solar activity. This behavior is not predicted by the simulation of Balan et al. (1998), probably due to the great difference that exist between HWM90 and real winds, as already pointed out by Batista et al. (1996) and Souza et al. (2000).

In conclusion, the F3 layer is a very common feature of the daytime equatorial ionosphere during low solar activity periods at the Brazilian longitude of Fortaleza (38° W) at locations having dip angle between 10° S and 12° S, during both December and June solstices. More realistic input parameters such as **ExB** drift and neutral winds are needed, in order to correctly simulate that behavior.

References

Balan, N., and G. J. Bailey, Equatorial plasma fountain and its effects: Possibility of an additional layer, *J. Geophys. Res., 100,* 21241, 1995.

Balan, N., G. J. Bailey, M. A. Abdu, K. I. Oyama, P. G. Richards, J. MacDougall, and I. S. Batista, Equatorial plasma fountain and its effects over three locations: Evidence for an additional layer, the F3 layer, *J. Geophys. Res., 102,* 2047, 1997.

Balan, N.; Batista, I. S.; Abdu, M. A.; MacDougall, J.; Bailey, G. J. Physical mechanism and statistics of occurrence of na additional layer in the equatorial ionosphere, *J. Geophys. Res., 103,* 29169, 1998.

Balan, N. Batista, I. S.; Abdu, M. A.; Sobral, J. H. A.; MacDougall, J.; Bailey, G. J. Occurrence of na additional layer in the ionosphere over Fortaleza, *Adv. Space Res., 11,* 1481, 1999.

Balan, N.; Batista, I. S.; Abdu, M. A.; Bailey, G. J.; MacDougall, J.; Sobral, J. H. A. Variability of na additional layer in the equatorial ionosphere over Fortaleza, *J. Geophys. Res., in press,* 2000.

Batista, I. S.; Medeiros, R. T.; Abdu, M. A.; Souza, J. R.; Bailey, G. J.; de Paula, E. R. Equatorial ionospheric vertical plasma drift model over the Brazilian region, *J. Geophys. Res., 101,* 10887, 1996.

Batista, I. S.; Balan, N.; Abdu, M. A.; MacDougall, J.; Barbosa Neto, P. F. F_3 layer observations at low and equatorial latitudes in Brazil, *Geofisica International, in press,* 2000.

Jenkins, B.; G. J. Bailey; M. A. Abdu; I. S. Batista, and N. Balan, Observations and model calculations of an additional layer in the topside ionosphere above Fortaleza, Brazil, *Ann. Geophys., 15,* 753, 1997.

Souza, J. R.; Abdu, M. A.; Batista, I. S.; Bailey, G. J. Determination of vertical plasma drift and meridional wind using SUPIM and ionospheric data at equatorial and low latitudes in Brazil: Summer solar minimum and maximum conditions. *J. Geophys. Res., in press,* 2000.

Appearance of F_3 Layer over Waltair

P V S RAMA RAO, K Niranjan, D S V V D Prasad, P Sri Ram
Dept of Physics, Andhra University, Visakhapatnam 530 003

V V Somayajulu & K S V Subba Rao
Space Physics Laboratory, VSSC, Trivandrum 695 022.

The ionograms obtained over Waltair during daytime hours normally show the presence of E, F_1 and F_2 layers. On some days, the F–region is found to be stratified into three layers, of which a new layer is observed and identified as F_3–layer. A study has been carried out on the presence of the F_3–layer using the ionograms from three different locations namely, Waltair(Dip 20°N), SHAR(Dip 10° N) and Trivandrum (Dip 0.6°N) during 1997 and 1998 and the results are presented.

The F_3– layer appeared frequently during the years 1997 & 1998 on more than 100 days in each year. The second stratification of the F– layer (from which F_3– layer is identified) starts during the morning hours (08:30 hrs LT) and extends upto 15:00 hrs LT over Waltair. The duration of the occurrence of F_3 layer is found to vary between half–an–hour to 5 hours. On some occasions, the F_3 layer first occurs in the morning hours (between 0900 to 1200 hrs LT) and reappears during the afternoon hours. This feature is found to be more probable during summer months and its occurrence does not show any dependence on the Solar and geomagnetic activities. Though this additional stratification was observed both at Trivandrum and SHAR on few days, interdependence of their occurrence at the three locations does not seem to exist.

The height of the F_2 layer rises abruptly by about 50 to 100 km when the F_3 layer starts to form, while the critical frequency of the F_2– layer (foF_2) decreases by 1–2 MHz. The altitude of the F_3 layer is found to vary between 400 and 550 km(while that of the F_2 layer varies between 350 and 450 km). On many occasions the critical frequency of F_3 layer (foF_3) increases by 1 to 2 MHz, whereas the foF_2 decreases by 1 to 2 MHz.

The appearance of second stratification in the F–region initially did not show much of a variation in the critical frequency i.e., the foF_3 values are almost similar to the foF_2 values just before the formation of F_3–layer , followed by a sudden change in the F_2–layer (increase in height and decrease in its critical frequency). This suggests that the appearance of F_3–layer may be due to an internal re–distribution of plasma as a function of altitude due to the counter play of the plasma transport by electrodynamic drift and neutral winds. While there is no variation in the virtual height of F–layer (h' F), the virtual heights of F_2 and F_3– layers (h' F_2 and h' F_3) show an increase. In light of the above observations, a detailed study on F_3–layer over Waltair is in progress.

Acknowledgements: This work was supported by the DST, Govt of India.

Diurnal, seasonal, solar cycle and longitudinal studies of equatorial electrojet current based on rocket borne and ground based data.

Chandra H, H S S Sinha and R.G.RASTOGI, Physical Research Laboratory,Ahmedabad 380009,India.

The change in the H field at ground due to the ionospheric current should naturally be proportional to the magnitude of the current, calibrating the measurements of ionospheric current by means of rocket borne proton precession magnetometers with H at the nearly magnetic observatory it was found that an eastward current of 10 Amp/km^2 produces a change of H equal to 98 nT in the Indian zone and 119 nT in the American zone. The height of peak current has found to be care about 2 km. higher in the American region with rocket to its location in Indian region. Using the MSIS 1986 model, typical electron density profile around noontime at an equatorial station and the appropriate value of B equal to 40009nT for Indian and 27148nT for the American sector it was found that the location of the peak in the Cowling conductivity peak comes out at 102 km. over the American and 100.6 km over the Indian sector. Thus the difference in the altitude of the peak current in the two sectors seems to be the results of different profiles of the collision and gyrofrequencies of the ions and electrons in the two sectors.

If the caliration between the ionospheric current measured by rocket instruments and H from ground observations are assumed to be true for different epochs then the long series of geomagnetic data at Huaucayo and Kodaikanal can be converted into corresponding currents (J). Combining these computed current values (J) with the observed peak electron density in the E layer (NmE) one can compute the electron drift velocity in the E region.

It has been found that the solar cycle variation of electrojet current is primarily due to the corresponding variation of the NmE and not due to the variation of electric field. The solar cycle variation of drift velocity is very small.

The two equinoctial maximum in the seasonal variation of the electrojet current persist even after correcting for the variation of NmE or of solar zenith angle.

The diurnal variation of the electrojet current is shown to be the combined effect of the electrojet field peaking at 09–10 LT and of NmE peaking at 12 LT.

The dominating role of electric field on the equatorial electrojet current is stressed here.

Joint ISR and spacecraft measurements in the ionosphere and plasmasphere using Arecibo and Jicamarca ISR together with GPS TEC and DMSP.

S. A. GONZALEZ(Arecibo Observatory)
N. Aponte(Arecibo Observatory)
B. MacPherson(Arecibo Observatory)
M. Sulzer(Arecibo Observatory) R. Heelis(UT Dallas)
S. Venkataraman(UT Dallas) X. Pi (JPL)

In the first part of this presentation we will describe joint measurements of TEC in the low latitude ionosphere and plasmasphere using GPS TEC and Arecibo electron density profiles. The results will show that if we have a detailed knowledge of the O^+-H^+ transition altitude then we can confidently extrapolate the incoherent scatter radar densities to higher altitudes in order to make an estimate of the vertical TEC. This technique provides an independent means of validating models used to eliminate receiver and satellite biases that are inherent in extracting GPS TEC measurements. The results will show that the plasmaspheric contribution to the vertical TEC over Arecibo is larger than previous studies have found, and that this contribution has a large seasonal variation. These variations can be explained by considering the seasonal changes in the relative O^+ and H^+ ion densities, which highlights the need to take proper account of the light ions at low and mid-latitudes when using models to interpret TEC data.

In the second part we will discuss how chain measurements of the low latitude topside ionosphere using the Arecibo and Jicamarca ISR's can be used together with DMSP fly-by's to obtain snapshots of the density, temperature and dynamical structure of the low latitude plasmasphere.

Some features of F3 layer observed with topside sounding

V. H. Depuev, and S. A. PULINETS (Institute of Terrestrial Magnetism, Ionosphere and Radio Wave Propagation. Troitsk Moscow Region, 142092 Russia, e-mail: pulse@izmiran.rssi.ru)

Introduction

The specificity of thermospheric wind action, electrodynamic drift and diffusion onto the plasma above geomagnetic equator creates a series of essential peculiarities of an equatorial ionosphere. One of them is the occurrence of layers of additional ionization above the main maximum. For the first time possibility of existence of a F3-layer was shown in [*Balan et el., 1995*] on a basis of Sheffield University Plasmasphere-Ionosphere Model (SUPIM). The computer modeling of an ionosphere above the Jicamarca radar was carried out for equinox quiet magnetic conditions of moderate solar activity. Later similar calculations were carried out for three geographical points (Jicamarca, Trivandrum and Fortaleza) for high solar activity [*Balan et el., 1997*]. At the same paper the indirect experimental confirmation of a F3-layer existence were reported (based on an essential modification of hourly values of peak height hmF2). The real layer of additional ionization was registered on vertical sounding ionograms at Fortaleza ionospheric station [*Jenkins et al., 1997*] at near noon hours, when the critical frequency foF3 on short time exceeded the foF2. In the given paper the topside sounding ionograms from the Intercosmos-19 satellite are used for study of spatially - temporal features of a F3-layer.

Input data

The activity period of Intercosmos-19 satellite (1979-1981) falls into the phase of high solar activity [*Pulinets, 1989*]. The parameters of an orbit (inclination of 74°, rotation period ~100 minutes) provided that the local time of intersection by the satellite of equatorial plane during several sequential orbits was practically the same. It allowed for fixed LT to obtain the quasi-meridional cuts of an ionosphere, displaced from each other by ~25 degrees of a longitude. In a data set considered, the vertical sounding was accomplished every 64 seconds. During this time the satellite was displaced along an orbit by ~3.6 degrees of a latitude. The ionograms obtained in mainly nonperturbed equinox conditions were selected for the analysis. Only several cases of F3-layer existence of were registered.

Results and discussion

The layer of additional ionization begins to be exhibited at $I \sim \pm 10°$ as considerable distortions of O, and X-traces on ionograms of vertical sounding close to a main maximum. While approaching to magnetic equator the peak height of a layer increases, the foF3 decreases and becomes easily defined

on the ionograms as well expressed group delay. The example of an ionogram with a well developed F3-layer is shown on the fig. 1.

Intercosmos-19 May 19, 1980 1.5 N 163 E 0420 LT

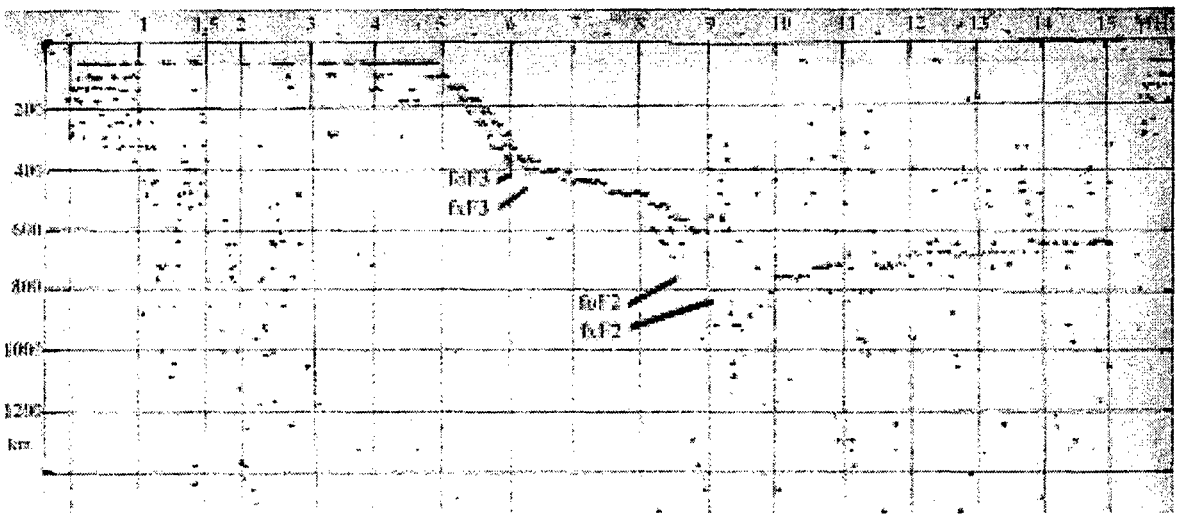


Fig.1.

At fig. 2a the latitudinal variation of critical frequencies of a F-layer, obtained on March 26, 1979 for a longitude 165° E is presented. The satellite intersected the magnetic equator in local noon. The F3-layer was observed in conditions of weakly developed equatorial anomaly (crest-to-through ratio was small), the crests are apart by ~ ±25° of magnetic inclination. The sequence of profiles of an electron concentration scaled above geomagnetic equator, is presented in a fig. 2b. The F3-layer is exhibited practically symmetrically in relation to the magnetic equator. The behavior of a maximum of a layer
depending on I can be traced on an essential modification of virtual height. The true height hmF3 varies from ~670 km at I=-6.5 and +9.5 up to ~730 km at I=1.5.

The F3-layer is observed usually on ionograms of 1-2 sequential passes of the satellite. It let us to assume, that its appearance has a restricted longitudinal scale which is not exceeding 50-60 degrees. However, the cases of the much greater longitudinal expansion of F3-layer were registered in magnetically disturbed conditions.

Though the additional ionization in F-layer is observed usually at noon hours, when the zonal electric field on equator has a local maximum, the cases of the distinctly expressed layer F3 were observed in night-time (0000 LT) and pre-dawn (0430 LT) hours.

The F3-layer features established from the data of topside sounding are in good correspondence with predicted earlier on a basis of computer modeling properties [*Balan et al., 1995*] and confirm, as a whole, offered mechanism of formation of a layer of additional ionization above geomagnetic equator.

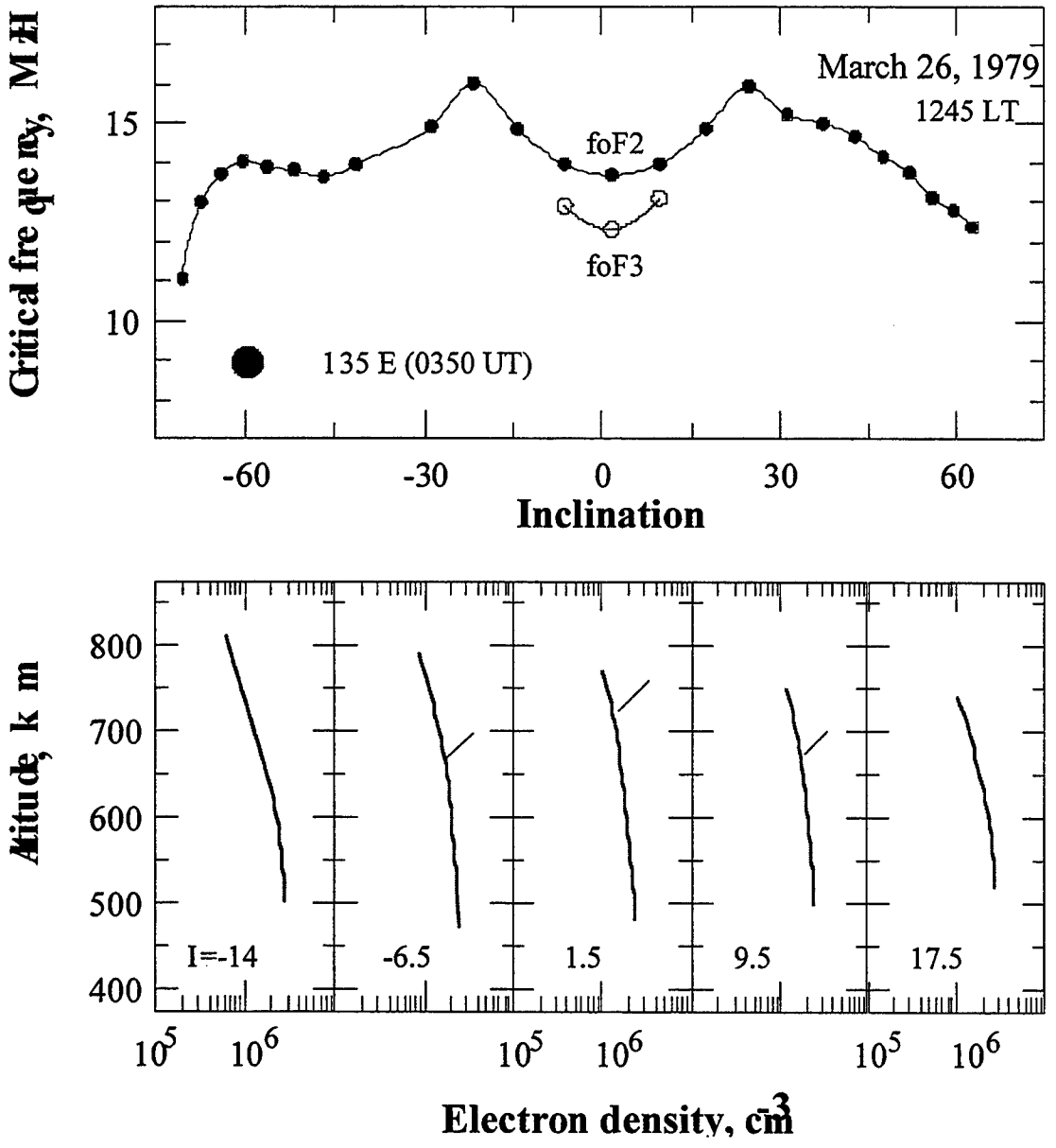


Fig.2.

Conclusions

The data of vertical sounding from the Intercosmos-19 satellite were used for an establishment of spatial-temporal characteristics of F3-layer of an equatorial ionosphere in magnetically quiet equinox conditions on the phase of high solar activity. A few cases of the layer appearance were detected. F3-layer was observed in a narrow longitude sectors (about 60 degrees) along the magnetic equator. Its intensity has a maximum just above the magnetic equator and decreased poleward within ± 10 degrees dip.

References

1. Balan, N. and G.J.Bailey, Equatorial plasma fountain and its effects: Possibility of an additional layer, J.Geophys. Res., *100*, 21421, 1995.

2. Balan, N., G.J.Bailey, M.A.Abdu, K.I.Oyama, P.G.Richards, J.MacDougall, I.S.Batista, Equatorial plasma fountain and its effects over three locations: Evidence for an additional layer, the F3 layer, J. Geophys. Res., *102*, 2047, 1997.

3. Jenkins, B., G.J.Bailey, M.A.Abdu, I.S.Batista, N.Balan, Observations and model calculations of an additional layer in the topside ionosphere above Fortaleza, Brasil, Ann. Geophysicae, *15*, 753, 1997.

4. Pulinets, S.A., Prospects of topside sounding, in WITS Handbook, 2, SCOSTEP publications, p.99, Urbana, 1989.

Solar flare and SSc effects in the electrojet region at different longitude sectors, abnormal induction effects in Indian longitudes.

RASTOGI R.G., Physical Research Laboratory,Ahmedabad,380009, India.

The effect of the solar flare on the dynamo region of the ionosphere has been generally considered to be the temporary extention of the current. Thus the sfe vector would generally be parallel to the preflare Sq vector. At low letitudes the sfe in H increases with the decreasing dip latidue and is maximum over the magnetic equator. The studies of H andY fields at Annamalainagar and Huancayo shows that the changes due to solar flare in these compononts is analogous to the preflare conditions. Thus it is concluded that the solar daily varitions of the Y field at equatorial stations is due to the corresponding meridional current in the dynamo region and not due to any transequatorial current.

A study of the solar flare effacts in H,Y andZ fields at all equatorial electrojet stations operating during the IGY–IGC period confirmed the midday maximaum in sfe amplitude in H at any of the stations. The sfe in Z field was found to be abnormally large at Trivandrum inspite of the station being only 0.3 deg south of the magnetic equators.The ratio of Δ z/Δ H was on the average about 1.34

Analysing the crocket effect on H,Y,Z at the latitudeinal chain of station in India it is found that the sfe (Z) is always positive at Trivandrum but at Annamalainagar it is mostly negative but in some cases of strong events Δ Z is seen to be strongly positive event at Annamalainagar.

This phenomenon is interpreted as due to abnormal electromagnetic induction in the subsurface conducting layer in the Palk Strait between India and Srilanka.Even the simple calculations indicate that the induction due to overhead electrojet current is not enough to explain the observed facts.

The negetive Δ Z due to solar flares at Annamalainagar were found not be releted to the intensity of solar flare but were correlated with the sharpness of the flare onset.The flares with small rise time produced positive Δ Z whereas slow but strong flares produced negetive Δ Zas excepted at an station situated at the northen fringe of the equatorial electrojet.This suggests that the conductor in the sea south of India is very near the surface may be at the seabed itself.Further it is also suggested that there is an accumulation of induced currents in this narrow conducting region from the currents over wider latitudes north and south of the equator.

VARIATIONS OF CRITICAL FREQUENCY foF2 AT MIDLATITUDES DURING GREAT GEOMAGNETIC STORMS

SIZOVA L. (1), Liperovskaya R. (2)

(1,2) Institute of Terrestrial Magnetism, Ionosphere and Radio wave Propogation, 142190, Moscow Region, Troitsk, Russia. E–mail: lsizova@izmiran.rssi.ru

Simultaneous variations of ionospheric critical frequency foF2 and the H–component of the geomagnetic field at middle latitudes are compared with solar wind data during several great magnetic storms. Dependence of foF2 variations from latitude and from Bz–component of IMF is found. Based on these facts we made attempt to understand the causes foF2 variations. For this purpose we extended our equatorial model of the field–aligned currents on midlatitudes. It is shown that the field aligned currents from region 1 and 2 can penetrate to midlatitudes during great magnetic storms and produced strong foF2 variations there.

THE TIME DELAY IN THE CAUSAL ANALYSIS OF EQUATORIAL IONOSPHERIC PROCESSES

L. SIZOVA (Institute of Terrestrial Magnetism and Radio Wave Propagation Russian Academy of Sciences, 142190, Moscow region, IZMIRAN, Troitsk, Russia, lsizova@izmiran.rssi.ru)

INTRODUCTION

The ionosphere response to the solar wind flowing around the Earth in a variety of complex ways. In the present view interaction between solar wind, magnetosphere and ionosphere are effected by the way of field–aligned currents (Zanetty and Potemra 1986). Model calculations carried out by Zakharov et al (1989), Denisenko and Zamay (1992) showed that the contribution of the field–aligned currents to low latitude electric fields and currents during quiet–time periods is comparable with that given by dynamo fields. The daytime characteristics of the equatorial F2–layer in connection with field–aligned currents during magnetic storms have investigated by Sizova et al. (1998), Sizova and Pudovkin (2000). It is shown that the IMF Bz, the H–component of the geomagnetic field, the critical frequency, and the F–region vertical plasma drifts are interrelated. The decrease in the H–component and in the equatorial electric field at the magnetic equator (counterelectrojet), that cause the foF2 increasing during magnetic storms are associated with the appearance there of the additional westward electric field produced by the field–aligned currents of the Region II (Bz>0). The increase in the H–component and in the equatorial electric field that cause the corresponding foF2 decrease are associated with the field–aligned currents of the Region I (Bz<0). By this means variations of the equatorial ionosphere electric fields, foF2 variations during disturbance periods are very complex and only a comprehensive analysis opens a clue to the relationships between solar wind and ionosphere. The time delay problems in the causal analysis of equatorial ionospheric processes are very important for predicting the short–term ionospheric characteristics, associated the field–aligned currents dynamics.
The response time of magnetosphere and ionosphere the solar wind effect were studied in numerous works. The response time of AE with respect to a southward Bz has been determined by correlation analysis by Rostoker et al. (1972) and Meng et al (1973) as 30–50 min and 10–90 min, respectively. These times are consistent with Arnoldy's (1971) an hour delay. Magnetospheric response as reflected in Dst to a change in Bz as determined by Burton et al (1975) is an average value of 25 min., there being a variation from 0 to 40 min. This is similar to the AE response time, though somewhat smaller. The magnetoshperic electric field penetrates to the equatorial ionosphere through the polar ionosphere almost instantaneously within the time resolution of 25 s as were determined by Kikuchi et al (1996). The purpose of this paper is to determine the response time of the critical frequency foF2 to a change in equatorial electric field.

THE CRITICAL FREQUENCY RESPONSE TO EQUATORIAL ELECTRIC FIELD VARIATIONS.

The H–magnetograms and the f–plots at Huancayo, the F region vertical plasma drifts at Jicamarca (Fejer et al., 1979), solar wind data (King 1977) were used for our analysis.
Figure 1 is an example of the foF2 variations at equator during two geomagnetic storms. The H–component of magnetic field and the critical frequency foF2 at Huancayo, the vertical drift velocity Vz at Jicamarca, the hourly average of IMF Bz values are shown. Dashed lines present the quiet day's data. The large magnetic storm on 8 March 1970 (Fig. 1, b) will be discussed first, because it is the simplest one containing all of the features. This great magnetic storm was followed by a disturbance of the equatorial ionosphere. Two decreases and an increase of foF2 are observed during the storm. The decreases are consistent with southward Bz. The first decrease of foF2 (14–

16 UT) is associated with the substorm (see H–component). The second decrease (18–22 UT) is associated with the main phase of the magnetic storm. The increase of the foF2 is consistent with counterelectrojet (negative values of Vz) and associate with northward Bz.

Thus, the IMF Bz, the H–component of the geomagnetic field, the critical frequency foF2, and the F–region vertical plasma drifts at daytime are interrelated during this magnetic storm.

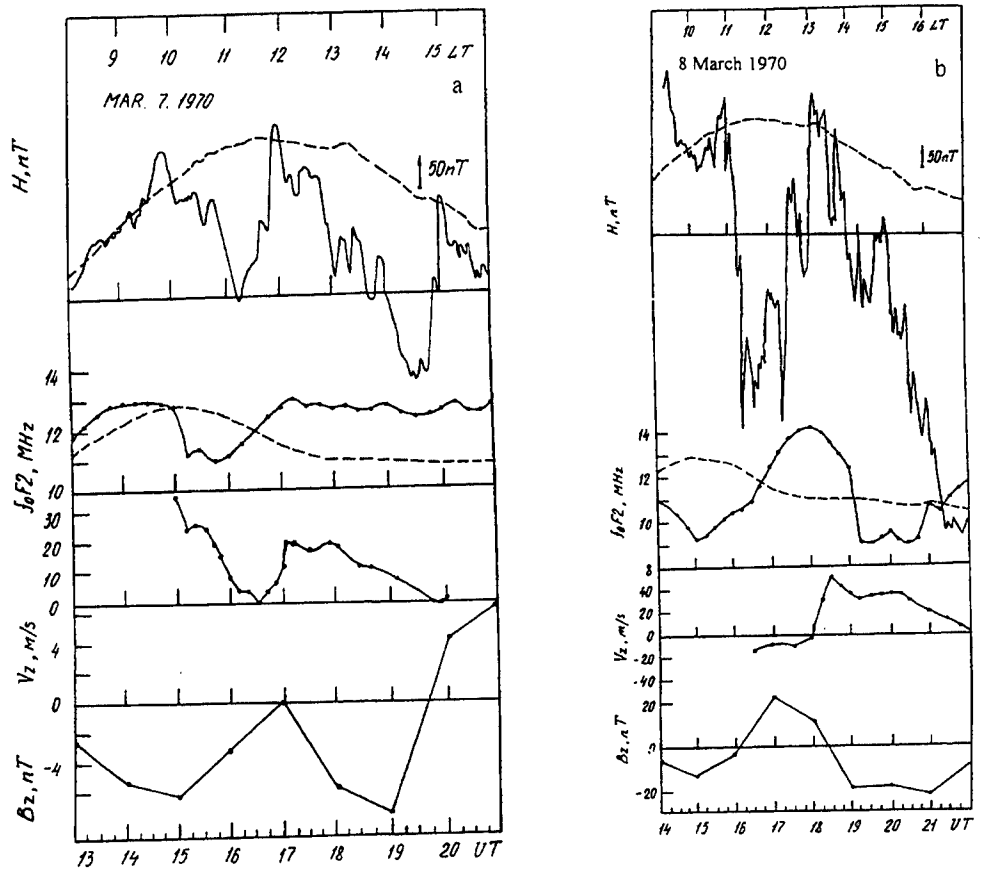


Fig. 1. The H–component of magnetic field, the foF2 variations at Huancayo (dashed lines are the quiet day variations), the vertical drift velocity Vz at Jicamarca, the Bz–component of the IMF during magnetic storms 7 and 8 March 1970.

Fig. 1 (a) shows the foF2 and Vz variations during small magnetic storm 7 March 1970 that was associated with IMF Bz. We can not to see so clear relationship between presented parameters for the ionospheric events during the 7 March 1970 storm. The decrease of foF2 (15–16 UT) does not support our point of view about the field–aligned currents penetration associated with Region I. Let us introduce the time lag an hour for foF2, by assuming that foF2 variations will be observed after increasing of the equatorial electric field. In this case, minimum of foF2 is shift from 16 UT to 15 UT and the minimum of foF2 will be coincides with the maximum of Vz during Bz<0. The correlation will be better if we input the time lag for 8 March foF2 events also. We point out that intensity of these storms is very different and equatorial electric fields for 8 March storm is nearly twice as large as that for 7 March. It is obvious that the direct relationship between the magnitude of substorm and value of the disturbance equatorial electric field have take place.

CONCLUSION

Response of the critical frequency foF2 on electric field variations during magnetic storms is analysed. The time lag has to be taken into account when causal analysis of ionospheric processes is carried out.

It is shown that the critical frequency foF2 starts to drop about an hour after the enhancement of the convection of the equatorial electric field caused by the IMF Bz<0. Variations of the foF2 intensity depend from the IMF Bz and the equatorial electric field magnitude. The electric fields from Region I and Region II penetrate to equatorial ionosphere almost instantaneously and correlated with the H–component of geomagnetic field. The time lag between IMF Bz, equatorial electric field and foF2 makes possible to predict IMF Bz associated variations of foF2 practically for 1,5 hours forward, taking into account time delay of the polar electric field to the IMF Bz.

REFERENCES

Arnoldy R. L. Signature in the interplanetary medium for substorms. J. Geophys. Res. 1971. 76. 5189

Burton R.K., McPherron R.L. and Russel C.T. An empirical relationship between interplanetary conditions and Dst. J. Geophys. Res. 1975. 80. 4204.

Denisenko V.V.and Zamay S.S. Electric fields in the equatorial ionosphere. Planet. Spase Sci. 1992. 40. 941.

Fejer B.G., Gonzales C.A., and Farley D.T. Equatorial electric fields during magnetically disturbed conditions. J.Geophys.Res. 1979. 84.5797.

Fejer B.G. Equatorial ionospheric electric fields associated with magnetospheric disturbances. In: Solar wind–magnetosphere coupling. Tokyo. 1986. 519.

King Y.H. Interplanetary medium data book. Appendix. (1977)

Kikuchi T., Luhr H., Kitamura T., Saka O. and Schlegel K. Direct penetration of the polar electric field to the equator during a DP2 event as detected by the auroral and equatorial magnetometer chains and the EISCAT radar. J. Geophys. Res.1996. 101. 17161.

Sizova L.Z., Zelenova T.I. and Pudovkin M.I., Disturbances of the equatorial ionosphere parameters associated with the Bz–component of the interplanetary magnetic field, in Abstracts of the 2nd international conference " Problems of geospase".1998. 89.

Sizova L. Z., Pudovkin M.I. Variations of the equatorial ionosphere characteristics associated with IMF Bz.

Geomagn. Aeron. (Russian Edition). 2000. 40. 271.

Zakharov Y.Y., Nikitin M.A. and Smirnov D.A. The response of low–latitude fields to the action of magnetospheric source. Geomagn. Aeron. (Russian Edition). 1989. 29. 344.

Zanetty L.J. and Potemra T.A. The relationship of Birkeland and ionospheric current systems to the IMF. In: Solar wind–magnetosphere coupling. Tokyo. 1986. 563.

The Lunar Tide in the equatorial F region vertical ion drift velocity

Robert J. Stening
University of New South Wales, Sydney, Australia
BELA G. FEJER
Utah State University, Logan, Utah

Introduction

The vertical ion drift velocity has been measured at the Jicamarca Observatory, near Lima in Peru (12°S, 76.9°W, dip latitude 1°N), using the 50-MHz radar, since 1968 (Woodman, 1970). A dataset of 25364 measurements has been built up spanning the time between April 1968 to April 1992. We shall use these data to extract the lunar tide using the method of Malin and Schlapp (1980).

An earlier analysis of electron drift velocity data was carried out by Tarpley and Balsley (1972). They used data collected at 10 minute intervals on eighty days between 1967 and 1970. They obtained amplitudes of the lunar semidiurnal tide of around 50 ms^{-1} while much smaller amplitudes were found during the May to August period. Their largest amplitude was 91 ms^{-1} for daytime data during the October to March period. There was some variation of phase with season and between day and night. These east-west electron drift data in the E region vary very similarly to the F region vertical drifts being considered here. An example is given by Balsley (1973) of their similar behaviour. The E region drift amplitudes are about 20 times the vertical drift amplitudes. While the E region east-west drifts depend on the E region vertical electric field, the F region drifts depend on the east-west electric field which has been shown to have little variation with latitude (or height) in the vicinity of the magnetic equator. The ratio of the amplitudes of the two drift measurements will therefore be equal to the ratio of these electric field strengths. This ratio in turn has been shown by Richmond (1973) to depend, under certain assumptions, on the ratio of the Hall conductivity to the Pedersen conductivity, both integrated along a magnetic field line.

The method of analysis used in the present work is the least squares fitting procedure described by Malin and Schlapp (1980). The data are randomly assigned to ten sets and each set is independently analysed for a mean, a solar diurnal tide, a solar semidiurnal tide and a lunar semidiurnal tide by least squares fitting. The ten results are put together for a mean and a standard deviation. The raw data used here may have several values within one hour and these may be considered to be not statistically independent of each other. After assignment to the ten different sets it is expected that this problem is overcome. One test was made in which the data were assigned to the sets one after the other so that no set had more than one value from the same hour and the results from this test were not significantly different from the random assignment procedure. The benefit of this analysis method is that a reasonably reliable estimate of error is obtained.

Results

The variation with season of the lunar tide in the drifts, using all data, is displayed in Fig. 1. Here, to improve the statistical significance, two months data

The error bars are one standard deviation. The first features to notice are that the amplitudes have magnitudes of about 4 ms^{-1}, that they are largest during the January to March period and they only reach about 1 ms^{-1} from July to November. There is some seasonal variation of phase ranging from 7-8 h in January to April, about 10 h from May to July and 5-6 h in August to November.

For further investigation the data were broken down into solar maximum and minimum periods and daytime and nighttime (Figs.2,3). A rough division was made assigning 1973-1978 and 1983-1987 as solar minimum years and the rest as solar maximum. Hours from 12 to 22 UT (7-17 LT) were taken as daytime and the rest as nighttime.

The largest amplitude reached is just over 6 ms^{-1}. Particularly at solar minimum the summer (December-March) amplitudes are smaller at night than in the day. During solar maximum nighttime there is a reversal of phase between summer and winter (Fig. 2). The seasonal variation of phase is smaller during daytime. Note that little attention should be paid to phase values when their associated amplitudes are very small.

The present phase results for the drifts are compared with those earlier obtained by Tarpley and Balsley (1972) in the Table below.

	Tarpley and Balsley	This work
Jan-Feb	9	8
May-June	11	10
Sept-Oct	10	5
Nov-Dec	8	7

Agreement is good except in September-October. The 10 h value from Tarpley and Balsley probably emphasises the daytime phase while our average results are closer to the nighttime phase. The phase of the lunar semidiurnal tide in the horizontal component of the magnetic field, H, at Huancayo ranges from 8 lunar hours in summer to 10 h in winter. These phases also agree with the present results, as expected. We have also examined the behaviour of the lunar tide in hmF2 at Huancayo by using tabulated values of M(3000)F2 and relating these to hmF2 by the formula of Shimazaki(1957). The phase of the lunar modulation of this height is expected to be similar to that of the vertical drift. Data from 1964-65 (solar minimum) during daytime gave phases of about 9 h in summer and 10-11 h in winter. This is good agreement. At nighttime the lunar tide in hmF2 is small and not well determined. Around midnight in summer 1964-65 phases of 11-12 h were obtained while in 1970-71 phase of 1-2 h in summer and 3-4 h in July-October were derived. The latter are getting close to some of the values in Fig. 2. The lunar tide in the F region has been modelled using the TIGCM (Stening et al, 1998). The modelled time of maximum of the drift was about 10 lunar hours in September and the time of maximum of hmF2 was up to 2 hours later than this in the model. This is probably partly due to the influence of the lunar tide in the neutral wind parallel to the magnetic field. This may have amplitudes up to three times those of the vertical drift velocities and so would give an appreciable vertical component for observatories situated at a latitude slightly off the magnetic dip equator. This model did not yield any significant variation of phase between day and night.

An analysis of Huancayo M(3000)F2 for 1978-79 in July gives a diurnal variation of lunar phase with a daytime phase of 8 h and a midnight phase of 13.7 h. If we subtract 2 h as suggested by the model analysis, we get 11.7 h and this is the same as the vertical drift result in Fig. 2. Furthermore the Huancayo result shows two separate maxima in the amplitude during the day with different phases: this adds some confidence that there is a real difference beween day and night. In a similar

Best Available Copy

and Winch (1987) previously reported a nighttime lunar tide in ΔH at this station which was out of phase with the daytime tide. An explanation for this phase difference is not yet available. It should be remembered that the magnetic dip equator at Jicamarca is quite far south of the geographic equator and therefore the behaviour of the lunar dynamo fields in this vicinity is likely to be fairly complex.

References

Malin, S.R.C., and D.M. Schlapp, Geomagnetic lunar analysis by least squares, Geophys. J.R. Astron. Soc., 60, 409-418, 1980.

Shimazaki, T., Dynamical structure of the ionospheric F2 layer, J. Radio Res. Labs. Japan 4, 309-332, 1957.

R.J. Stening and D.E. Winch, The lunar geomagnetic tide at night, Geophys J R astr Soc 88, 461-476, 1987.

Stening, R.J., J.M. Forbes, M.E. Hagan and A.D. Richmond, Experiments with a lunar tidal model, J Geophys Res. 102, 13,465-13,471, 1997a.

J.D. Tarpley and B.B. Balsley, Lunar variatiosn in the Peruvian electrojet, J Geophys Res 77, 1951-1958, 1972.

Vial, F., and J.M. Forbes, Monthly simulations of the lunar semi-diurnal tide, J. Atmos. Terr. Phys., 56, 1591-1607, 1994.

R.F. Woodman, Vertical drift velocities and east-west electric fields at the magnetic equator, J Geophys Res 75, 6249, 1970.

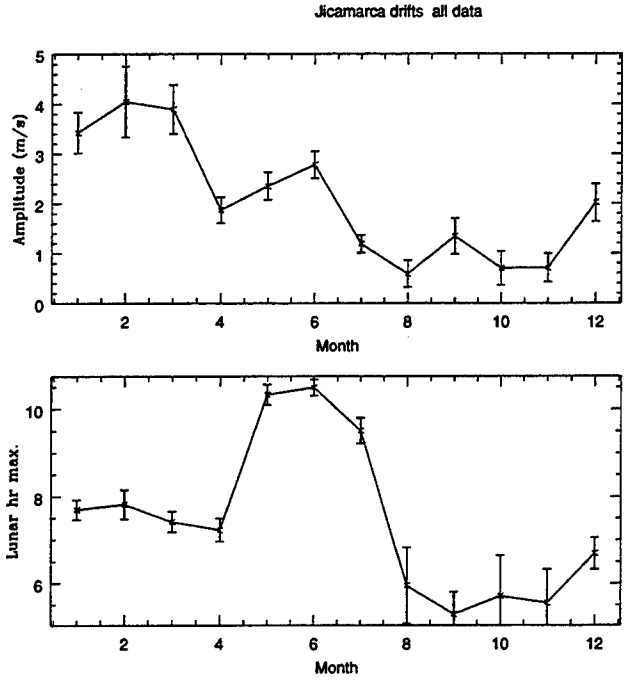


Figure 1: Variation with season of the phase and amplitude of the lunar tide in the vertical drifts

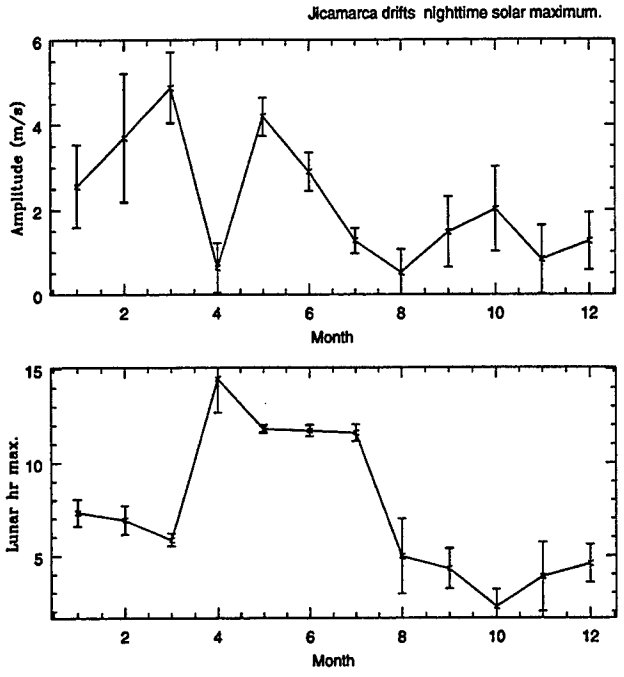


Figure 2: Lunar tides for nighttime and solar maximum.

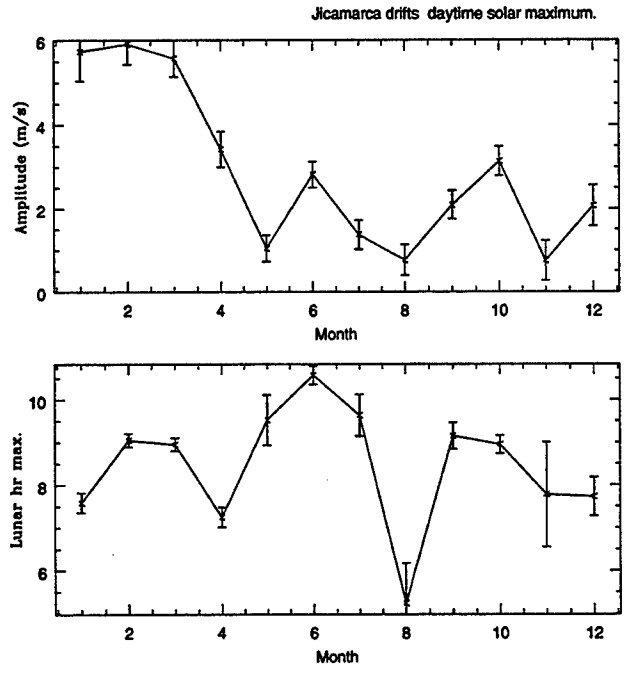


Figure 3: Lunar tides for daytime and solar maximum.

Assertion and Prediction of Magnetic storms and Disturbances through IEC Parameters over Anomaly Crest Region

M.DEVI, M.K.Barman and A.K.Barbara
Department of Physics, Gauhati University, Guwahati 781 014

The extension and movement of the equatorial anomaly generates a large change in the IEC even on its day to day value in the anomaly crest zone, thereby making the prediction of density near such locations extremely difficult. The situation gets more complex in geomagnetically disturbed and storm days. In this paper utilising the changes in IEC values and the (IEC) profile features due to the anomaly effects, a few IEC parameters are extracted to associate their occurrences with geomagnetic disturbances of different magnitudes and types and then to assert and predict a quiet (Q) and a disturbed (D) day through the parameters so defined. The IEC values taken for the study cover basically two solar activity periods and are mostly based on VHF RB data collected over Guwahati (26.2 N, 20–.64 mag lat), though IEC from latitudes of –8 to + 28.6 have also been incorporated for use in relevant aspects. The paper describes methods for extraction of parameters like "profile (P) factor", Post Equatorial Anomaly (PEA) and growth rate from IEC profiles for three sectors of a day ie., prenoon, postnoon and night hours separately for three seasons (summer, winter and two equinoxes) covering both low and high solar activity periods. The definition of Q and D days are made through profile features and the threshold values for Kp (Ap) for each season are set separately and also taking soalr activity index as another parameter. The relations between Kp & P factor, Kp & PEA, Kp & decay rate are evaluated after proper correction for solar activity. The prediction and assertion of Q/D days are then made by examining IEC profiles for each case where IEC data were not used for parameter extraction , reliability on the prediction is then assessed.

For geomagnetic storms, Sd is talen as an index and single isolated storms are analysed independently from the complex types such as successive or multiple storms. The basic four features that are extracted as storm prediction indices from the IEC profiles are (i) noon time depresseion /enhancement (ii) growth/decay rate (iii) night (pre dawn) enhancements and (iv) development (type) of scintillations. Prediction features so defined for each season are then examined for their reliability in assessing such conditions for latitudes situated +5 and –5 from Guwahati. The extracted prediction feartures for moderate & moderately severe conditions are found to be well applicable for stations –5 of Guwahati but the features fail to represent for stations 4 north of Guwahati.Severe storm features (for a few cases) are found to be applicable to stations even to 8 north of Guwahati. Finally the paper discusses the complex coupling processess between equator, low and mid latitudes. Electrojets, neutral winds are a few parameters taken into considerations for the process evaluation.

A review of equatorial E region irregularities from a broader perspective: anything new to discover?

J.-P. ST.-MAURICE (Department of Physics and Astronomy, University of Western Ontario, London, Ontario N6A 3K7, Canada)

It has always been assumed that an important reason for the presence of irregularities in the E region was related to the generation of electric fields on some much larger scale than the structures themselves. The electric fields necessarily generate currents in the E region. As a result irregularities will grow in response to a modified two-stream instability or gradient-drift mechanism. In other words, the consensus, with some evidence to back it up, has been that generating mechanisms invariably use a combination of electron Hall currents and of density gradients. Either the gradients are very steep and the currents are modest or it's the other way around. More sophisticated theories have been built around that basic theme. Some have considered so-called non-local effects, which mean different things to different people. Some view the nonlocal effects as a variation of the wavenumber with altitude, while others prefer to describe the phenomenon as a form of mode-coupling with the inhomogeneous medium and others still will say that the frequency changes with space and, as a result, they seek ways to avoid a Fourier decomposition. The best approach may well depend on the particulars of the problem being studied. Linear theories of a more local nature have also greatly gained in complexity through the inclusion of temperature perturbations to the system. The majority of these theories has focused on electron temperature fluctuations, although some of the recent work has also added ion thermal perturbations instead.

While linear theories (both fluid and kinetic) may be useful for an understanding of the conditions that are needed to trigger an instability, nonlinear work is needed if one is to understand observables such as ground-based radar or rocket in-situ spectra. The power and Doppler width are obvious properties that require nonlinear theories, but unfortunately, even the mean Doppler shift of linearly unstable modes is often different from linear expectations indicating that its behavior often requires a nonlinear explanation. Some of the theories that have been advanced have emphasized mode-coupling, followed by the production of linearly decaying modes and the necessary energy transfer to particles. Others have emphasized anomalous diffusion, usually via a resonance broadening mechanism. Either way, the nonlinear wave properties may well be affecting the transport properties of the plasma: at high latitudes the most obvious effect is a dramatic electron temperature increase when the linear growth rates become very large. In the equatorial regions, there may be a more subtle but equally important change taking place in the electron collision frequency.

The complexity of the theory rapidly gets out of hand when one tries to combine too many features in one single theory. For instance, a nonlocal nonlinear theory that includes thermal fluctuations in both ions and electrons is unlikely to be tackled any time soon. The hope is that (1) either such a complicated theory is not needed, namely, only one or two effects matter at any given time or (2) that numerical computations will offer a better way to make further inroads in our understanding if the complexity is that bad. However, numerical studies have their limitations too, though it is not up to this author to explore them.

Going back to theory: the fact that we are still arguing about mechanisms may either mean that we have not found the magic bullet or that there is no magic bullet. The likelihood that some important mechanism has been overlooked gets smaller as time goes on. In that sense, there is probably no magic bullet, that is, no easy answer to our questions about the various properties of the irregularities. But even if there is no magic bullet, there may well be some new approaches to old problems that may make our studies easier to handle. For instance, the nonlinear mode-coupling approach is particularly complicated because we insist on making a Fourier decomposition to a problem that refuses to have sines and cosines as a solution to the problem. Sophisticated closure schemes must therefore be sought. At the same time, once mode-coupling is introduced, one needs to handle a very large, if not infinite, number of modes. Perhaps the same physics could be described more simply without any Fourier analysis? A bit of the same problem surfaces with nonlocal theories in that a large number of modes suddenly needs to be invoked. This is not so surprising since one way to look at nonlocal effects is to imagine that the waves are coupling with the inhomogeneity of the medium. Once again, a simpler approach might be feasible if we move away from a strict Fourier decomposition. My presentation will highlight some of the points raised here, using specific examples mostly (but perhaps not entirely) from the published litterature.

East-West Asymmetry in Type 1 Electrojet Echoes at Jicamarca

J. L. Chau[1], D. T. Farley[2], and Ben B. Balsley[3]
[1] Radio Observatorio de Jicamarca, Instituto Geofísico del Perú, Lima
[2] School of Electrical Engineering, Cornell University, Ithaca, New York, USA
[3] CIRES, University of Colorado, Boulder, USA

1. Introduction

Evidence for asymmetries in the equatorial electrojet (EEJ) flow over Jicamarca were reported in the late 1960s and early 70s [*Balsley*, 1970; *Fejer et al.,* 1975; *Balsley et al.,* 1976] from ob servations made at Jicamarca (JRO) using small steerable 50 MHz antenna arrays. Similar observations were also performed in Africa [see references in *Hanuise and Crochet*, 1978]. Asymmetric structure was seen in both type 1 (two -stream) and type 2 irregul arities. More details on the characteristics of both types of echoes are given in the text by *Kelley* [1989]. When type 1 spectra are observed it is possible to deduce the E region neutral wind velocity if we assume that the observed Doppler velocity is $V_{ion\text{-}acoustic} + V_{wind} \sin\theta$, where θ is the zenith angle. If we plot the observations over a reasonable range of angles, we can deduce the neutral wind and the ion -acoustic speed, with a couple of caveats.

First of all, the plot of Doppler velocity vs $\sin\theta$ over a substantial range of θ must be a straight line, implying that our assumption above is correct, at least over this range of θ. We often get a straight line when the radar points west (over the Pacific Ocean), but we frequently do not when pointing e ast (over the Andes). Furthermore, even if we get straight lines in both plots, the slopes (which give the wind velocity) are often not the same, or the intercepts, which give us the ion -acoustic velocity, may be different. (When only type 2 irregulariti es are present there is also often an asymmetry, with the drift velocities to the east of Jicamarca less than those to the west, but this asymmetry will not be discussed here.)

The early studies were not very systematic. Only a few examples were publish ed with the intent of illustrating the effect and speculating on its cause. The thought at the time was that this would be followed up with more substantial studies of the morphology and statistics of the asymmetries and theoretical work on the cause or c auses. But this follow-up never happened – until now. An obvious possible source of asymmetry is orographic: The Andes are east of Jicamarca. Is there a significant coupling of gravity wave energy and momentum to the neutral wind in the E region? The n ecessary observations are straightforward to make at Jicamarca, and a lot more is known about gravity waves and their propagation than was known in 1970. This gravity wave coupling, if it exists, also might have a modest influence on the electrojet itself and the associated electric field, which couples to the F region.

East-West comparisons similar to those conducted more than twenty years ago resumed in April 1999, using the Jicamarca unattended system (JULIA). In this paper we report on the preliminar y results from these new observations.

2. Experiment Description

To study the East-West asymmetries, we have used wide beam antennas pointing obliquely to the East and West of JRO. A new coaxial collinear (CoCo) antenna array [see *Hysell and Burcham*, 2000, for the antenna details] was pointed 45 ° to the West, and one or two of the old steerable "mattress" antennas was pointed 60 ° to the East. We used small 20 kW transmitters for both beams. Occasionally we increased the strength of the East echoes by usi ng two mattresses and two small transmitters.

3. Preliminary Results

One of the first problems we had to face was discriminating between type 1 and type 2 echoes. We did this by fitting two Gaussian functions to the spectrum, as illustrated in Figure 1. The smooth black curve is the sum of the Gaussians, and the narrow Gaussian represents the type 1 echo. *Cohen* [1973] used a similar procedure. The light and dark solid lines mark the mean Doppler shifts, and the dashed lines measure the widths. Note t hat any small errors in the fit will affect the type 2 echo parameters more than the type 1, the subject of this paper.

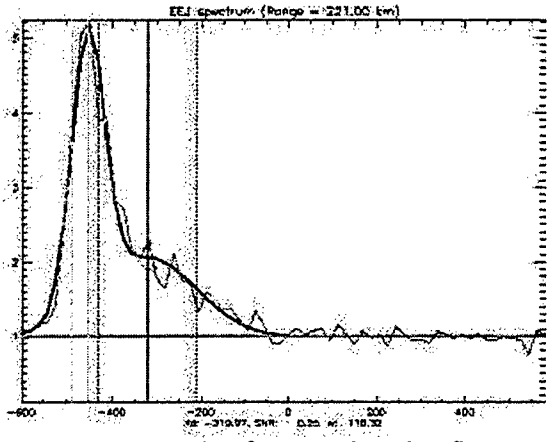


Figure 1. An Example of a two -Gaussian fit to an oblique EEJ spectrum.

In Figure 2 we show a normalized spectrogram (respect to the maximum of each channel) from the East (top) and the West (bottom) beams, along with the Doppler shifts of type 1 (white) and type 2 (black) echoes. On the right the power profiles as a function of height are shown. Note that the Doppler shifts of both echoes are positive for the East antenna and negative for the West antenna, a s expected for normal EEJ conditions during the day (i.e., westward direction). There is a small "ghost" signal due to small gain differences between the in -phase and quadrature channels.

A scatter plot of absolute values of type 1 Doppler velocities is p lotted as a function of time. For each time, the velocity of each range (> 120 km) is plotted in the vertical axis. Notice that there are regions of pretty good agreement in vertical dispersion (i.e., variances) and magnitude (e.g., between 1300 and 1400 L T), and also of disagreement (e.g., between 1200 and 1230 LT). An increase of Doppler is apparent starting at 1400 from 300 m/s up to 450 m/s around 1600 LT, and then a decrease follows. In addition, around 1300 LT there is crossover of velocities (i.e., a change in the West velocities from smaller to larger than those from the East).

Since the electrojet is a thin layer, we can convert range to zenith angle θ. We determine the height of the layer from the centroid of the echoes coming from overhead, through the antenna sidelobe of the West antenna (see the bottom panel of Figure 2). If we then plot the type 1 Doppler velocities as a function of $\sin\theta$ and fit a straight line to the points, the slope and intercept give the zonal wind and ion -acoustic speed, with errors proportional to the variances of the estimates and the fitting errors.

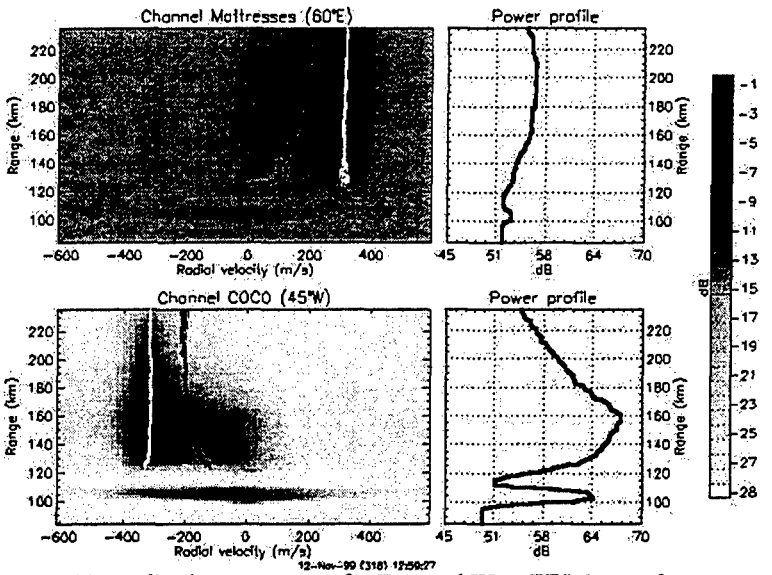


Figure 2. Normalized spectrograms for East and West EEJ data and power profiles as a function of range. Type 1 (in white) and type 2 (in black) Doppler velocities are plotted over the spectrograms. The gray scale on the far right shows the relative power in dB.

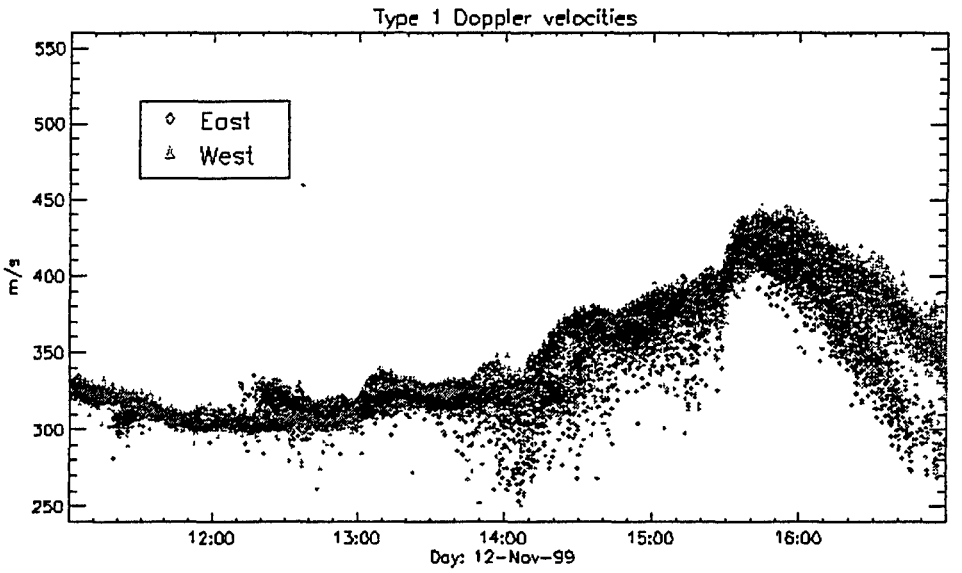


Figure 3. Scatter plot of type 1 Doppler velocities as a fun ction of time. Black symbols represent the East measurements and gray symbols the West measurements.

In Figure 4 we show a time series of the zonal winds and ion -acoustic speeds calculated in this manner. Winds obtained from the East data are represent ed in black while the winds from the West data are in gray. Again notice that there are regions of good agreement and small variances, but also there are regions of disagreement. For example, there is an unrealistic difference of acoustic speeds of more t han a factor of 2 (i.e., more than a factor of 4 in temperature) around 1515 LT. However, there are oscillations that are clearly geophysical.

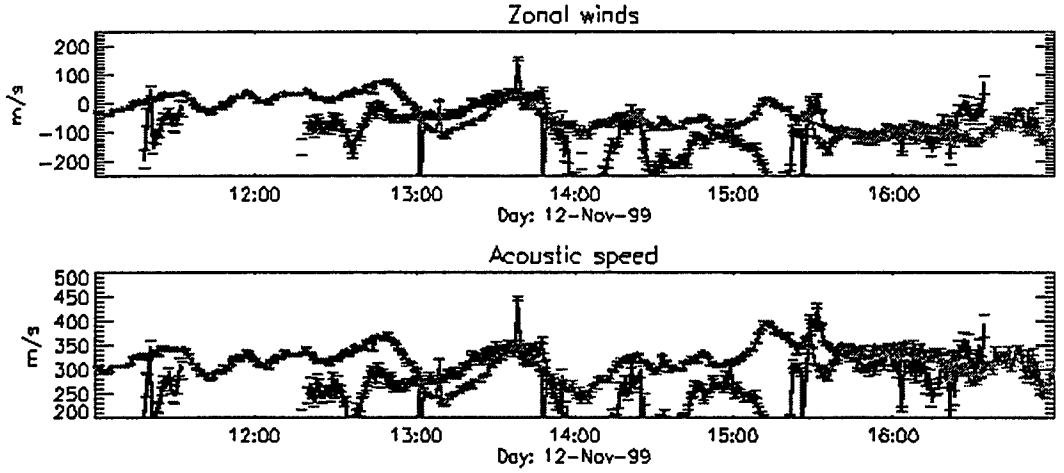


Figure 4. Time series of zonal winds and "ion -acoustic" speeds obtained with East (black) and West (gray) data.

From these preliminary results, we can see that the E -W asymmetry of the EEJ seen in the past is also present in our studies. We are continuing to make observations in this mode, and deeper analyses are currently underway in order to understand the or igin and variability of these asymmetries and to decide whether or not this approach is appropriate to measure the zonal winds and ion acoustic speeds in the equatorial *E* region.

References

Balsley, B. B., A longitudinal variation of electron drift velo city in the equatorial electrojet, *J. Geophys. Res., 75* , 4291-4297, 1970.

Balsley, B. B., B. G. Fejer, and D. T. Farley, Radar measurements of neutral winds and temperatures in the equatorial *E* region, *J. Geophys. Res., 81* , 1457-1459, 1976.

Cohen, R., Ph ase velocities of irregularities in the equatorial electrojet, *J. Geophys. Res., 78* , 2222-2231, 1973.

Fejer, B. G., D. T. Farley, B. B. Balsley, and R. F. Woodman, Oblique VHF radar spectral studies of the equatorial electrojet, *J. Geophys. Res., 80* , 1307-1312, 1975.

Hanuise, C., and M. Crochet, Oblique HF radar studies of plasma instabilities in the equatorial electrojet in Africa, *J. Atmos. Terr. Phys., 40* , 49-59, 1978.

Hysell, D. L., and J. Burcham, Ionospheric electric field estimates from radar observations of the equatorial electrojet, *J. Geophys. Res., in press* , 2000.

Kelley, M. C., *The Earth's Ionosphere,* Academic Press, 1989.

Electrodynamics of meteor trail evolution in the equatorial E–region ionosphere

Meers M. Oppenheim and Axel F. vom Endt

Center for Space Physics, Boston University

Introduction

Radar echoes from plasma trails created by micrometeors are routinely used to measure Mesospheric wind velocities. The accuracy of these measurements depend upon the assumption that meteor trail plasmas closely track neutral wind velocities. However, the highly magnetized electrons found in the E-region ionosphere cannot readily cross geomagnetic field lines and, therefore, the ions and meteor trail cannot easily track the neutral wind velocity. This talk will show that meteor trails travel primarily at velocities dominated by the $\boldsymbol{E}\times\boldsymbol{B}$–drift velocity of the trail electrons perpendicular to the geomagnetic field. In addition, the polarization electric field, common in the E–region near the geomagnetic equator, causes rapid growth of the gradient–drift/Farley–Buneman (GDFB) instability. This, in turn, rapidly develops into plasma turbulence. These effects will substantially modify the spectra and Doppler shifts of radar echoes from meteor trails

Micro-meteor trails near the geomagnetic equator evolve through three distinct stages. First, a large ambipolar electric field perpendicular to both the geomagnetic field and the trail develops as predicted by a simple analytical model. Second, plasma density waves grow asymmetrically on the edges of the trail as predicted by linear theory. Third, turbulence develops as shown by simulation results. Throughout this process, the electron $\vec{E}\times\vec{B}$–drift velocity governs the large-scale motion of the meteor trail rather than the neutral wind velocity. This plasma dynamics has important implications for the interpretation of meteor radar echoes.

Using theory and simulations, we show that an ionized O_2^+ / N_2^+ meteor trail, in the presence of a polarization electric field, $\boldsymbol{E}_0$, develops through a number of distinct stages. In the frame of reference moving with the neutral wind, the vertical $\boldsymbol{E}_0$ causes a horizontal $\boldsymbol{E}\times\boldsymbol{B}$–drift of the trail electrons. Since the ions are collisionally bound to the neutral gas, the electrons drift ahead of them creating a horizontal ambipolar electric field with the several effects. First, the trail ions accelerate to follow the electrons and maintain quasineutrality, causing the meteor trail to drift at the $\boldsymbol{E}\times\boldsymbol{B}$–drift velocity. Second, the electric field causes a secondary $\boldsymbol{E}\times\boldsymbol{B}$–drift of electrons parallel to the meteor trail. This secondary drift combined with the plasma density gradients makes the meteor trail plasma strongly unstable to the GDFB instability [*Fejer et al.*, 1975]. Simulations show this instability rapidly developing into turbulence.

Chapin and Kudeki [1994] presented a conduction current model to calculate the ambipolar electric field, E_x', across the meteor trail. Adding the effects of the plasma density gradient substantially modifies the ambipolar field. To do this, we consider a simplified 1-D, two-fluid model perpendicular to the meteor trail and the magnetic field. We assume quasineutrality, unmagnetized ions, collisionless electrons and a strictly vertical polarization field, E_z. This leads to the following equation of motion for the ions in the neutral frame of reference:

$$\partial_t v_i = -v_i\partial_x v_i + \frac{e}{m_i}E_x - v_{th,i}^2\frac{\partial_x n}{n} - \nu_i v_i \ . \quad (1)$$

The electron motion is given by the $\boldsymbol{E}\times\boldsymbol{B}$ drift velocity $v_e = -E_z/B_0$, which ignores electron diffusion and collisions. The quasineutrality condition, $\partial_x j = 0$, states that the current remains constant through the trail and the background plasma. Combining this condition with the assumed v_e gives $v_e\partial_x n = n\partial_x v_i + v_i\partial_x n$ with the general solution $v_i = v_e + \frac{C}{n}$. To determine the constant C, we assume a background plasma density of n_0, and an ion velocity far away from the trail of $v_i(x = \pm\infty) = 0$ in the frame of reference where the neutral gas is at rest. This yields

$$v_i = v_e\frac{\delta n}{n} \quad (2)$$

with $\delta n \equiv n - n_0$. This equation gives the velocity necessary to maintain a constant current density, j, given the changing plasma density in the meteor trail. At the peak of the trail $v_i \sim v_e$, while far away from the trail $v_i = 0$, as one expects in the neutral frame of reference.

We find the equilibrium electric field, E_x, by setting the partial time derivative on the left-hand-side of

Table 1. Physical parameters used in theory and simulations.

Parameter		Value
External magnetic field	B_0	2.5×10^{-5} T
External electric field	E_z	-5 mV/m
Neutral gas density	n_n	2.0×10^{18} m^{-3}
Temperature	T	250 K
e^--neutral coll. freq.	ν_{en}	1.7×10^4 Hz
Ion mass	m_b	5.0×10^{-26} kg
Peak/background ratio	n_e/n_0	6.95
Trail radius	r_t	0.5 m
Ion-neutral coll. freq.	ν_{in}	9.5×10^2 Hz
Grid size	$n_{x,z}$	128
Grid spacing	$\Delta_{x,z}$	8.0×10^{-2} m
Time step	Δ_t	1.0×10^{-5} s

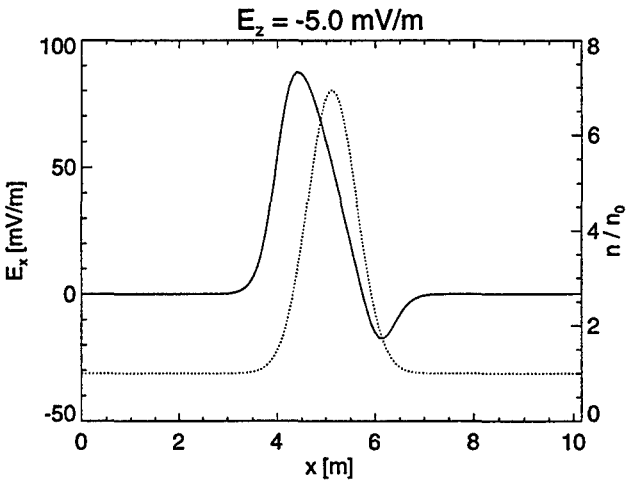


Figure 1. Plasma density enhancement of the meteor trail (dotted line) and electric field (solid line) from the 1-D model, parameters as in Table 1.

eqn. (1) to zero,

$$E_x = \frac{m_i}{e}\left[-\frac{\delta n}{n}\nu_i\frac{E_z}{B_0} + v_{th,i}^2\frac{\partial_x n}{n} + \frac{n_0\delta n}{n^2}\frac{\partial_x n}{n}\frac{E_z^2}{B_0^2}\right] \quad (3)$$

Steady-State and Linear analysis

This field is shown in Figure 1. The first term in eqn. (3) corresponds to the electric field predicted by *Chapin and Kudeki* [1994], symmetric to the trail. The second term, of similar magnitude and antisymmetric to the trail, describes the pressure influence. The third, convective, term is an insignificant quadratic correction. For the parameters in Table 1 this yields a peak ambipolar field perpendicular to the meteor trail of 87.4 mV/m. For stronger meteor trails, the density gradient increases with the peak trail density, maintaining the relative importance of the pressure term in calculating the ambipolar field.

The spatial asymmetry of the electric field, E_x, leads to an asymmetry in the growth rates of the GDFB instability, which are dominated by a term proportional to $\boldsymbol{E}\cdot\nabla n$ [*Fejer et al.*, 1975]. Note that the fluid theory neglects ion Landau damping, resulting in highest growth rates at high k.

Numerical Model

To study the evolution of meteor trails beyond the limits of linear theory we developed a numerical model for the 2-D, x–z plane perpendicular to the magnetic field, with x pointing east and z pointing up. We make the simplifying assumption of a strictly vertical meteor trail. Since the size of our simulation box is much smaller than the typical length of a meteor trail, we use periodic boundary conditions, making the trail essentially infinitely long.

Our 2-D simulation does not represent all details of the turbulent motion of a meteor trail. However, *Kaiser et al.* [1969] showed that parallel and cross-field diffusion rates of a meteor trail are similar. Since there is no instability parallel to the magnetic field, the physics of the linear instability should be well-represented in the plane perpendicular to the magnetic field. Additionally, the strongest nonlinear term, $\boldsymbol{\delta E}\times\boldsymbol{B}$, couples plasma perturbations in the perpendicular plane. While this does not capture all the physics, especially not the slow ambipolar diffusion parallel to the magnetic field nor the oblique modes, it does include the fast instability processes, the dominant nonlinearity and the slow cross-field diffusion.

We use a hybrid PIC / fluid model as in *Oppenheim et al.* [1995] to include all ion kinetic effects, but only fluid electron behavior. The collisions between ions and the neutral gas are modeled as hard-sphere collisions with an energy-dependent cross section [*Birdsall*, 1991]. The electrons are modeled as a fluid, without assuming quasineutrality.

At start-up, the simulation contains two ion populations, one for the background density and one for the meteor trail. We model the meteor trail as a column of

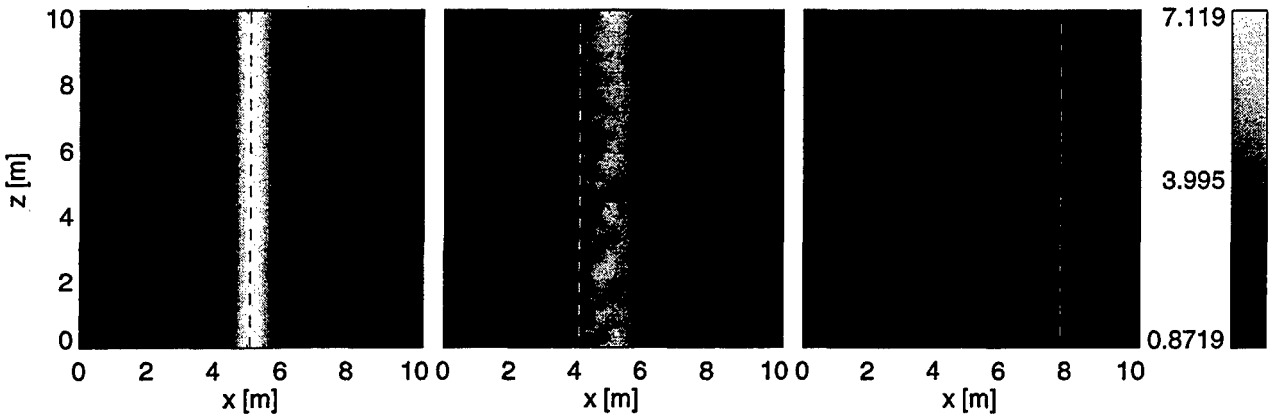


Figure 2. Plasma density enhancements n/n_0 (lower panels) at different times. All panels are in the $E \times B$ frame of reference, i.e. the frame in which the external vertical polarization field vanishes. The dashed vertical line, starting at the peak of the trail, tracks the motion of the neutral gas to the left. In the far right image, the line has crossed the left simulation edge and reemerged on the right due to the periodic conditions.

enhanced plasma density with Gaussian cross–section of radius r_t. The electron velocity is set to the Pedersen and Hall drift velocities, while the bulk ion velocity is given by eqn. (2). Setting electron density exactly equal to ion density starts the system with $\boldsymbol{E} = \boldsymbol{E}_{0,z}$. It takes only a few time steps, however, to reach the electric field shown in Figure 1.

Results

Our simulations progress through three distinct stages of meteor trail evolution shown in Figure 2: (a) the rise of an ambipolar field immediately after the formation of the trail, (b) the formation of a GDFB instability at the edges of the trail and (c) the development of turbulence. MPEG animations of these simulations as well as the color figure can be found at `http://astro.bu.edu/~meerso/meteor`.

The full ambipolar field develops after 20 time steps or 0.2 ms as shown in Figure 2(a). Averaging along the meteor trail yields a peak ambipolar field of 88.1 mV/m, agreeing closely with the value of 87.4 mV/m predicted by the 1-D model described earlier. The maximum value of the field seen in Figure 2(a) is actually somewhat higher due to the already growing instability in the electron density.

Further evolution of the meteor trail shows growth of an instability at the trailing westward edge, most prominent in the electric field as seen in Figure 2(b). The weaker electric field on the leading edge also points into the trail, as predicted by the 1-D model. However, we observe slower wave growth, as expected from the smaller $\boldsymbol{E} \cdot \nabla n$. The linear theory of the GDFB instability describes this stage of the meteor trail evolution.

The strong ambipolar field and steep gradients cause the GDFB instability to develop growing modes down to wavelengths of approximately a centimeter, before ion Landau damping suppresses the short wavelengths. To resolve these small wavelengths, we performed a set of simulation runs with a reduced grid spacing, Δ_z, and found the nature of the instability and turbulence remains substantially similar over a range of spatial scales. Since these small-scale runs do not cover the 3 m turbulence studied by 50 MHz radars, we present the results of the large-scale run. In this case, the hyper-diffusion terms provide the majority of damping at short wavelengths.

Plasma turbulence follows the linear stage, breaking the meteor trail into multiple segments as seen in Figure 2(c). During this stage, the plasma develops density irregularities at a broad range of wavelengths, including the 3 meter irregularities detected by 50 MHz radars. While the trail plasma still predominantly tracks the $\boldsymbol{E} \times \boldsymbol{B}$–drift and not the neutral wind speed, it does spread out in the direction of the neutral wind.

At later times, the periodic boundary conditions cause the meteor trail to begin interacting with itself. To study the evolution of these meteor trails further in time, one must increase the simulation size significantly. This would also allow for a more detailed study of the east–west asymmetry. For the current version of the simulation code, this exceeds today's computer capabilities.

Discussion and Conclusion

We began our analysis of meteor trail dynamics in the E–region by deriving a 1-D steady-state model of the densities and fields perpendicular to $\boldsymbol{B}_0$. This model includes the effects of the steep plasma density gradient and predicts a substantially larger ambipolar electric field than did earlier models. Additionally, our model predicts an asymmetric electric field driving a strong GDFB instability. A set of 2-D numerical simulations confirms the analytical model and also shows the development of plasma turbulence at a broad range of wavelengths. The later state of the instability shows the meteor trail breaking up into several strongly structured segments. These structures inside the meteor trail allow for non-specular reflection of radar beams with an east–west asymmetry.

These findings have significant consequences for interpreting meteor radar echoes. Near the geomagnetic equator, where one finds horizontal, northward $\boldsymbol{B}$ fields and large vertical polarization electric fields, the electron $\boldsymbol{E} \times \boldsymbol{B}$–drift velocity will dominate the east-west component of trail velocities. Hence, perpendicular to the geomagnetic field, meteor trail motions do not accurately reflect Mesospheric wind velocities and directions. In fact, Doppler radars may prove useful in estimating the polarization electric field in this region.

Acknowledgments. This work was supported by NASA through grant NAGS-7452 and the CCS at Boston University. We would like to thank S. Avery, A. Richmond, E. Kudeki, V. Dimant and G. Vetoulis for helpful discussions.

References

Birdsall, C. K., Particle-in-cell charged particle simulations, plus Monte Carlo collisions with neutral atoms, PIC–MCC, *IEEE Trans. Plasma Sci.*, *19*, 65–85, 1991.

Chapin, E., and E. Kudeki, Plasma-wave excitation on meteor trails in the equatorial electrojet, *Geophys. Res. Lett.*, *21*, 2433–2436, 1994.

Fejer, B. G., D. T. Farley, B. B. Balsley, and R. F. Woodman, Vertical structure of the VHF backscattering region in the equatorial electrojet and the gradient drift instability, *J. Geophys. Res.*, *80*, 1313, 1975.

Kaiser, T. R., W. M. Pickering, and C. D. Watkins, Ambipolar diffusion and motion of ion clouds in the earth's magnetic field, *Planet. Space Sci.*, *17*, 519–522, 1969.

Oppenheim, M. M., N. F. Otani, and C. Ronchi, Hybrid simulations of the saturated Farley-Buneman instability in the ionosphere, *Geophys. Res. Lett.*, *22*, 353, 1995.

M. M. Oppenheim and A. F. vom Endt, Center for Space Physics, Boston University, 725 Commonwealth Ave, Boston, MA 02215. (e-mail: meerso@bu.edu)

This preprint was prepared with AGU's LaTeX macros v5.01, with the extension package 'AGU++' by P. W. Daly, version 1.5d from 1997/04/28.

In-situ Observations in the Equatorial Electrojet: Outstanding Critical Problems

R. PFAFF, Jr., Electrodynamics Branch, Code 696, NASA, Goddard Space Flight Center, Greenbelt, MD 20771, USA

The current status of *in-situ* investigations in the equatorial electrojet is reviewed, including observations of zero-order, "DC" electrodynamic and plasma parameters as well as measurements of plasma instabilities and irregularities. The combined rocket/radar measurements gathered during the joint NASA/INPE Guará (Brazil) Campaign in 1994 helped resolve several key outstanding questions in electrojet physics including: (1) the relation of the vertical (polarization) DC electric field to the electrojet current and the electron number density and (2) the wavenumber spectrum, phase velocity, and angular distribution of primary two-stream waves associated with the peak electrojet current. Other results from rocket measurements from India and Brazil have also contributed to our expanding knowledge of the electrojet.

Notwithstanding the success of past programs, several unanswered problems remain for which combined *in-situ* and ground-based measurements would significantly advance our understanding of the equatorial electrojet. These include experiments that would reveal: (1) the role of neutral winds in characterizing the electrojet and, in particular, the relation of DC electric fields and neutral winds, currents, and plasma density in the nighttime case; (2) the role of winds, currents, DC electric fields, and plasma density during counter-electrojet conditions; (3) an explanation for the intense vertical, meter-scale waves observed on the topside of the electrojet associated with horizontal, laminar-like primary two-stream waves; and (4) the cause of steepened "square-wave" km scale waves and their interaction with the driving DC electric field and current. These outstanding critical problems will be discussed.

Coordinated study of ionospherie E region irregularities by rocket borne,ground based geomagnatic ,ionosonde,ionspherie drift and Dopplar radar data at Indian electrojet region.

R G RASTOGI,Physical Reasearch Laboratry,Ahmedabad–380009,India

The ionospheric soundings at the equatorial electrojet station,Kodaikanal in India had shown two main kinds of sporadic E echoes on the ionograms.One pattern consisting of assemblage of diffuse echoes near the E reigion ciritical frequeneies and later extending to high frequenies at virtual height of 100 km and transparent to reflections from higher heights,called equatorial sporadic E or Esq.Another pattern consisted of a diffuse layer at 100 km blanketing F1 and part of F2 trace and showup number of multiple reflections called blanketing Es or Esb.The Esq occurs only during the daytime house and is confined within a narrow belt around the dip equator and is associated with the equatorial electrojet.The Esb occrs mostly in late afternoon hours and its spatial morphology is not known at present.There are a less frequent occurrences of ledge or cusp type of sporadic layer starting from F1 layer and descending to the E region with the progress of time called Esc.This layer has very well defined ordinary and extrordinary traces and upper reflections start only after these frequencies.Rocket borne instruments have identified Esc as a thin ledge of ionisation protruding out of the general altitude profile of the ionisation density.The Esq irregularities are generated by the action of vertical Hall polarisation field with vertical gradient the cross field irregularities of wavelength from few metres to some 100 meters.The Esb is supposed to be the accumulation of ionisation from heigher latitudes towards the equator during the periods of weak electrojet.

The ionospherie drift experiment at Thumba in India had shown that the sudden disappearance of Esb is concurrent with the depression of H field below the nighttime base value and with the reversal of the dirft direction or the lectric field.The reversal of primary electric field causes a reversal of Hall polarisation field which now opposes the direction of plasma density gradient and the Esq irregularities disappear.

VHF back scatter radars over the equator have detected two types of irregularities.The first now called as type 1 occurs at an altitude of 106–108 Km and is due to the two stream irregularity mechanism when the streaming velocity in the electrojet exceeds the ion–acoustic velocity.The other called type 2 occurs at altitude of 100 Km is associated with gradient drift irregularity mechanism and is analogous to Esq on the ionograms.These different types of irregularities are identified on the bases of the Dopplar spectra of the back scatter echoes.During a counter electrojet period the type 2 (Esq) irregularities where found to disappear.

The VHF back scatter radar in east Africa reported that during a very strong counter electrojet event,the type 2 irregularities had first disappeared later type 1 irregularities where recorded during peak intensity period of counter electrojet.This was interpreted as due to revers streaming of electrons towards eastward direction when the eastward velocity of electrons exceeded the ion–acoustic velocity.Later the VHF back scatter radar at Thumba reported type 2 irregularities during counter electrojet period.

This paper describe the coordinated data analysis of the ionosonol and VHF back scatter radar data with the geomagnetic field records at Trivandrum and Alibag in India.

The Esq at the equatorial station develops about half an hour after the normal E layers are clearly seem.H at equator has to exceed H at non–electrojet station by reasonable amount before electrojet irregularities are seen.Strong Esq echoes and large electomagnetic uplifting of F layer are intimately associated phenomena.With the start of (CEJ),the Esq contitues to descent downward in the E region.Esq type of irregularities are developed at the top side of the Esc ladge where the plasma density gredient and Hall polorisation field are both downward.

Further descent of the layer produced blanketing,Esb,layer,on cases of abnormaly large (CEJ),the large negetive value of H,representing strong westward electrojet current.The streaming velocity exceeds ion–asoustic velocity and type 1 irregularities are observed by the Dopplar radars.

H field below the base value and with the reversed of the drift direction or the electric fieds.The reversal of primary electric field causes a reversed of Hall polorisation field which now opposes the direction of placms density gradient and the Esq irregularities disappear.

VHF baek seatles radars over the equitor have deteeted two types of irregularities.The first,now ealled as type occur at an altitude of 106–108 km and has due to the two strem irregularity mechanism when the streaming velocity in the electrojet exceeds the non–acoustie velocity.The other,called type 2 occurs at altitude of 100 km is associated with gradiant drift erregularity mechanism and is analagous to Esq on the ionograms.These different types of irreguarities are identified on the basis of the Dopplar spectra of the backscatter echoes.During a counter electrojet period the type 2(Esq) irregularities where found to disapper.

The VHF back scatter radar in East Africa reported that during a very strong counter electrojet event,the type 2 irregularities had first disappeared later type 1 irregularities where recorded during peak intensity period of counter electrojet.This was interpreted as due to reversed streaming of electrons towards easteard direction when the eastward velocity of the electrons exceeded the ion–acoustie velocity.Later the VHF backscatter radar at Thumba reported type 2 irregularities during counter electrojet peroid.

This paper describes the coordinated data analysis of the ionosonle and VHF backscatter radar data with the geomagnetic field records at Trivendrum and Alibag in India.

The Esq at the equitorial station develpos about hag an hour after the normal E layers are earlier seen. $\underline{\Delta}$H at equator has to exceed ΔH at non electrojet station by reasonable amount before electrojet irregularities are seen.Strong Esq echoes and large electromagnetic uplifting of the layer F layer are intemately associated phenomena with the start of (E),

the Esq disappears and remains so till ΔH again becomes positive.On certain occasions when Esc is present,the ledge continues to descent downward in the E rigion.Esq type of irregularities are developed at the topside of the Esc ledge where the plasma density grediant and hall polorisation field are both downwrd.Further descent of the layer may produced blanketing,Esb,layer,on cases of abnormly large (E), the large negative value of ΔH,representing strong westward electrojet current,the streaming velocity exceeds ion–acoustie velocity and type1 irregularities are observed by the Doppler radars.

Gradient Drift Instabilities and Turbulence in the Daytime and Nighttime Equatorial Electrojet

A. Bhattacharjee and S. Hu
Department of Physics and Astronomy, The University of Iowa, Iowa City

Type-II irregularities in the equatorial electrojet are generally attributed to gradient drift instabilities. Two key features of the daytime and nighttime equatorial electrojet, observed in situ and by ground-based radar, are the preponderance of large-scale irregularities with horizontal wavelengths of the order of a kilometer and power-law density fluctuation spectra. We discuss some recent developments in the theory of gradient-drift instabilities and turbulence that provide a unified perspective on these observations.

The theoretical studies discussed in this paper begin with ambient density and electric field profiles reconstructed from observations. Whereas the typical daytime electric field and density profiles are well known, data on the nighttime profiles are relatively sparse. There are no direct observations of nighttime electric field profiles, but nighttime density profiles have been measured (for instance, during the 1994 Guara campaign). In contrast with the daytime, the nighttime density profile is quite jagged. Assuming that the electric field profiles in the daytime and nighttime are similar (except for a sign reversal), we carry out a detailed nonlocal linear stability analysis of the observed background profiles by initial-value and eigenmode methods. The linear stability analysis prepares the way for nonlinear simulations which begin with a spectrum of linearly unstable modes that couple to each other and evolve eventually to a turbulent saturated state.

In the daytime, we find that gradient-drift instabilities with the largest linear growth rates occur with horizontal wavelengths of the order of 1 km [*J. Geophys. Res.*, *102*, 337, 1997]. These results provide an explanation, even at the level of linear theory, for the observed dominance of kilometer-scale irregularities in the daytime electrojet. The nonlinear evolution of these instabilities is shown to lead to saturated turbulent structures containing 1-2 km horizontal waves, with the linear instability drive at kilometer-scale wavelengths quenched by a direct energy cascade to short wavelengths that are damped by velocity shear and diffusion [*J. Geophys. Res.*, *103*, 20,749, 1998]. The electron density fluctuation spectrum as a function of wave number is nearly isotropic in the plane perpendicular to the background magnetic field, with a power law exponent between -3 and -2. The electron vertical velocity spectra, constructed from the simulation output, show 1-2 km vertical structures, qualitatively in accord with recent high-resolution radar observations at the Jicamarca Observatory in Peru.

In the nighttime equatorial electrojet, the observed jagged density profiles produce a linear instability spectrum quite different from that in the daytime. The spatial jaggedness of the background density profile provides density gradients pointing in both directions parallel and anti-parallel to the vertical electric field. This sets up locally unstable regions which are separated vertically from each other by locally stable regions. In the locally unstable regions, the sharp density gradient produces a much stronger linear instability drive than in the daytime case and provides much higher growth rates for the instabilities which have a maximum growth rate in the horizontal wavelength range 10-20m. Kilometer-scale waves are also excited at large growth rates relative to the daytime. The typical spatial scale of the alternating locally stable and unstable regions plays a key role in determining the spatial structures of the linearly unstable waves. The linearly unstable

waves with wavelengths less than the typical scale of jaggedness are only excited in the locally unstable regions, whereas the linearly unstable waves with their wavelengths larger than the typical scale of the jaggedness can tunnel into the locally stable regions and thus have global support.

The larger linear growth rates of short-wavelength (10-20m) gradient-drift modes shows that linear stability theory, by itself, cannot account for the observed dominance of kilometer-scale structures in the nighttime electrojet. In a way, this places a greater burden on a nonlinear theory for nighttime than for daytime. Our nonlinear simulations for nighttime show that in the linear growth phase, the short waves with the largest growth rates prevail over other modes so that the spatial structure of the fluctuations is initially dominated by short scales. These short-scale modes are detected first in the vertical local regions most favorable for instability. As these fastest growing modes grow in amplitude and enter the nonlinear growth phase, energy is transferred from them to other more slowly growing modes which include modes that have longer as well as shorter wavelengths. This energy transfer process removes energy from the fastest growing modes and tends to slow down their growth. In the meantime, large-scale modes with lower linear growth rates continue to grow, and take over as the new generation of the fastest growing modes. The fluctuations then begin to exhibit relatively large spatial scales. Furthermore, since the modes with larger wavelengths tunnel into vertical regions that are not only locally favorable but also unfavorable for instability, more of the vertical layer fills out. In the nonlinearly saturated state, a balance is realized between the linear instability drive of the unstable kilometer-scale modes and diffusion damping on the small-scale modes. The power spectra in the saturation phase have their power indices lie in the range between -3 and -2, similar to those in the daytime, with the largest power is contained in the wavelength range between 2 km and 4 km. It is the ability of the long waves to fill out the vertical layer, spanning regions in which the density gradients are favorable as well as unfavorable for stability, that makes them survive the mode competition in the nonlinear regime. Thus the saturated fluctuations in the nighttime show a preponderance of 2-4 km structures, qualitatively consistent with observations.

This research is supported by the NSF.

Radar interferometric observations of the E region irregularities over Gadanki

P B Rao, A K PATRA, T V Chandrasekhar Sarma, V K Anandan
National MST Radar Facility, P O Box 123, Tirupati 517502, AP, India.

R J Doviak and D S Zrnic
National Severe Storm Laboratory, 1313 Haley Circle, Norman, OK 73069, USA.

It is believed, in general, that the plasma density irregularities in the ionosphere are highly elongated along the magnetic field. The aspect angle of the small scale irregularities in the equatorial E region are found to be less than 0.4o (Kudeki and Farley, 1989) whereas it is found to be as high as 8o for the irregularities in the auroral E region (e.g., Hall et al., 1990; Hall and Moorcroft, 1992). In case of the mid latitude and anomaly region the aspect angle is found to be as high as 3o (Yamamoto et al., 1994; Chu and Wang, 1997). Detail measurements of the dependence of the radar scattering cross section on magnetic aspect angle is important to better understand the instability processes. Hence it is desirable to see what is the magnitude of the aspect angle and how it varies with height and time for the small scale irregularities at the low latitude just outside the electrojet region.

For this purpose we operated the Gadanki MST radar in space domain interferometer mode. The north–south antenna array was used and we used a baseline of 63 m. We have followed the interferometer technique introduced by Farley et al (1981). The cross–spectral magnitude and phase were obtained from which we derived the aspect angle. Using a special type of echo we could also measure the meridional drift of the irregularities at the lower part of the E region. In this paper we present observations of the aspect angle made on two days as diurnal cycles. We believe that these are the first results on the aspect sensitivity from the low latitude E region small–scale irregularities.

Our observation show that the aspect angles of these irregularities are in the range of 0.1o–0.9o with most of the values are close to 0.5o. These observations, however, do not show any systematic height dependence similar to that reported by Kudeki and Farley (1989) for the electrojet irregularities. The meridional drifts of the irregularities are found to be within 180 ms–1. After close inspection of the data we found that the drift observed using the interferometric technique does not agree with the drift derived from the line of sight phase velocities of the irregularities. It may me mentioned that Krishna Murthy et al (1998) have interpreted the line of sight phase velocity of the irregularities in the lower E region in terms of neutral wind.

Our results, although limited, are at variance with this viewpoint. These results are presented and discussed in detail in this paper.

References

Chu and Wang, Radio sci., 32, 817, 1997.
Hall et al., J. Geophys. Res., 95, 15281, 1990.
Hall and Moorcroft, J. Geophys. Res., 97, 19471, 1992.
Kudeki and Farley, J. Geophys. Res., 94, 426, 1989.
Krishna Murthy et al., J. Geophys. Res., 103, 20761, 1998.
Yamamoto et al., J. Geophys. Res., 29, 337, 1994.

A new 50 MHz coherent back–scatter radar at the equatorial electrojet site, São Luiz, Brazil: some initial results

M. A. ABDU (Instituto Nacional de Pesquisas Espaciais– INPE, 12201 970 Sao Jose dos Campos, Brazil),
C. M. Denardini, J. H. A. Sobral, I. S. Batista, P. Muralikrishna, and R. R. de Paula.

A VHF (50 MHz) pulsed doppler coherent back–scatter radar system developed at the Instituto Nacional de Pesquisas Espaciais –INPE has recently been put into operation at São Luis (2.33° S, 44.2° W, dip: –0.5°), a magnetic equatorial site, in Brazil. The modualr transmitting system consisting of 8 transmitters, each projected for 15 kW peak power, uses a coaxial –colinear array of 16 antennas each consisting of 48 dipoles aligned north–south that produces a beam of 3° north–south and 5° east–west. Progressive phase shift applied to the 8 transmitters allow operation with oblique beam tilted in east–west plane. A T–R switch system allows the echoes backscattered by ionospheric irregularities to be received by the same antenna array. The data acquisition system allows high time resolution (one measurement in 3 seconds) data collection, but the height resolution in the measurements carried out so far was limited to ~2.6 km only. The received echoes forming sets of 1024 or 512 pulses, are sampled in 16 or 32 height bins, and stored as one–file binary code which contains the in–phase and quadrature components. A fast Fourier Transform (FFT) algorith by Numerical Recipe in C is used to anlyse each data set. Doppler velocity spectra of the 3–m irregularities of the electrojet were recorded at 2.6 km height resolution between 90 and 132 kms. For better confidence, when necessary a few data files are used to integrate the total received power at each height, and the data processing system allows plotting of range–time–intensity maps for oblique as well as zenith beams by joining appropriate files. Improvements are being made to the system.

Although the radar is projected for a nominal transmitting peak pulse power of 120 kW, only a partial capability of ~40 kW has so far been used in the two campaign measurements of the electrojet irregularity dynamics carried out so far, the first one in August 1998 and the second one in December 1999. We have carried out some preliminary analysis of the data taken during these campaigns. The few days of data collected during the August 1998 campaign covered the period of the strong magnetic storm of August 26 (Dst < –140). The equatorial electrojet intensity was generally very weak and showed large fluctuations in response to prompt penetration of magnetospheric electric field, as could be confirmed also from magnetometer data from São Luis and high and middle latitude stations, and by auroral activity index (AE). Also, inhibition of the electrojet irregularity process were observed during long periods of time, which suggested the role of disturbance dynamo electric field associated with the storm. The height of the maximum intensity of the EEJ irregularities showed lowering (rising) before (after) midday. This feature is in similar to the observations of day time 150 km echoes observed over Jicamarca observatory. The December 1999 campaign covered an extensive interval of quiet electrojet conditions during which it is possible to analyze the salient features of the type I and type II electrojet irregularity dynamics. This paper will

present some results of a preliminary analysis of the electrojet irregularty dynamic features under quiet as well disturbed conditions over São Luiz.

Plasma instabilities in the Equatorial Electrojet region

R. Raghavarao

Nitya Laboratories Ltd.

202 Harita, Bhavanam Estate, Plot no. 15,

Somajiguda, Hyderabad - 500 082 [A.P.]

India

I. ABSTRACT

The recent results on the irregularities in the equatorial E-region plasma are reviewed. The plasma plumes occurring on certain nights in the E-region of the electrojet belt (Patra and Rao, 2000) are discussed and some new aspects for further investigation are suggested to elucidate on the causative mechanism(s) for the plume structure developments. It is necessary to establish experimentally whether the E-region plumes are caused by the long wavelength structures of the F-region plasma instability i.e. like the 'Fringe field effect' (Sekar et al. 1997) or such long wavelength structures are developed in situ under some special dynamical conditions.

The special features of 150 km irregularities are reviewed. In contrast to the type II in the electrojet region, they are weaker, confine to narrower(?) latitudinal belt around the dip equator and occur less frequently.

The mechanism already suggested for their generation by Kudeki and Fawcett (1993) and Tsunoda (1994) are critically discussed.

REFERENCES

Kudeki E. and C. D. Fawcett, High resolution observations of 150 km echoes at Jicamarca, Geophys. Res. Lett., 20, 1987-1990, 1993.

Patra A. K. and P. B. Rao, High resolution radar measurements of turbulence structures, to appear in J. Geophys. Res.,

Sekar R., R. Sridharan and R. Raghavarao, Equatorial plasma bubble evolution and its role in the generation of the irregularities in the lower F-region, J. Geophys. Res., 102, 20063-20067, 1997

Tsunoda R. T., Enhanced velocities and a shear in daytime E_{sq} over Kwajalein and their relationship to 150 km echoes over the dip equator, Geophys. Res. Lett., 21, 2741-2744, 1994.

Lower E-region drifts as measured by partial reflection radar over magnetic equator

T. K. RAMKUMAR[1], S. Gurubaran[1], and R. Rajaram[1,2]

1. Equatorial Geophysical Research Laboratory, Indian Institute of Geomagnetism, Krishnapuram, Tirunelveli 627 011, India.
2. Indian Institute of Geomagnetism, Colaba, Mumbai 400 005, India.

e-mail: egrl@vsnl.com

Introduction

The ambiguities present in the determination of the neutral winds at 98 km at Tirunelveli, situated close to the magnetic equator, India, by using partial reflection radar (PRR), which is operating at the medium frequency (MF) of 1.98 MHz, are investigated extensively. The partial reflection drifts measured in this region by the spaced antenna (SA) technique suffers sometime from the intense electric field provided by the Equatorial Electrojet (EEJ) which is situated at about 105 km. As a result, the observed drifts are a combination of both the neutral winds and the electron drift velocities. Some times it seems that the radar determines almost the electron drift velocities at this height as it is evident from the simultaneous measurement of the magnetic field variations observed at the ground by standard magnetometers which are located near the adjacent location, Trivandrum, India. The simultaneous day time measurements (6-20 Hr IST) of both the zonal and meridional components of the winds and the magnetic field variations show a high correlation coefficient of –0.88 and –0.70 respectively during December, 21, 1995. However, this is not the case for always. So one has to be very care in interpretating the results obtained by the partial reflection radar at this height near the dip equator region.

As the detailed investigation of the lower E-region drifts measured by the partial reflection radar (PRR) is under progress, one of the examples, which will be explained in the results and discussion section, is provided for this extended abstract. The study of mean winds, tides, planetary waves, and gravity waves, in the mesosphere and lower thermosphere (MLT) region which spans the altitude regime of 60-100 km, by using the partial reflection radar has been continuing for the last few decades [Vincent, 1984, for a review on the technique and its atmospheric applications]. The spaced antenna (SA) technique is being applied to study the horizontal wind motions and by using full correlation analysis PR radar gives valuable information on the spaced antenna parameters, namely, the fading time, the lifetime of the ground pattern, the pattern scale, and the pattern axial ratio [Lesicar, 1993, for a detailed discussion on these parameters]. However, near the dip equator, the interpretation of the spaced antenna drifts in terms of neutral winds is complicated by the presence of equatorial electrojet, an enhanced east-west current system flowing in a narrow latitudinal belt of $\pm$ 3° at an altitude of about 105 km centered about the magnetic equator. The type II irregularities produced by the

gradient drift or the **E×B** drift or the cross field instability in this region will sometimes produce strong echoes when compared to the normal echoes [Fejer and Kelley, 1980, for a review]. There are also occasions, the partial reflect drift technique employing the spaced antenna method will simply give the electron drift velocities [Chandra et al., 1971; Tabbagh et al., 1977; Gurubaran and Rajaram, 2000). So, one has to be very cautious in interpreting the results obtained in this region.

Observations

The partial reflection radar (PRR) which is operating at the medium frequency of 1.98 MHz located near the dip equator region Tirunelveli (8.7°N, 77.8°E, geographic; 0.18°N magnetic latitude, 0.35°N dip) has been yielding data on winds in the mesosphere and lower thermosphere in the altitude region (68-98 km) since the middle of 1992. The full correlation analysis of Briggs [1984] is being used to determine several dynamical and spaced antenna parameters. Valuable results on mean wind and tidal climatologies were reported earlier [Rajaram and Gurubaran, 1998; Gurubaran and Rajaram, 1999].

Simultaneous measurements of the H-component of the geomagnetic field variations observed near the another dip latitude station Trivandrum (8.5°N, 77.0°E, geographic; 0.33°N magnetic latitude) are utilized as a complementary to the drift measurements so that we can study the direct relations between them as whether the drift is due to neutal wind or electron drift velocities. This is based on the assumption that the short term magnetic field variations measured on the ground is mainly contributed by the electrojet current which is mostly due to the flow of electrons.

Results and Discussion

Though much of the work related to the present topic is under progress, we have limited ourselves to the December 21, 1995 event, which is illustrated in the Fig. 1, for the present extended abstract. The figure illustrates the hourly averaged values of the zonal and meridional components of the wind speeds and magnetic field variations ΔH observed during December 21, 1995 in the day time period of 6-20 hr IST. The negative sign applies for the westward and southward motions of the zonal and meridional wind components respectively. Winds (m/s) along with ΔH (nT) are plotted for the heights of 86 km, 90 km, 94 km, and 98 km with each height contains 15 points for the further calculation of the correlation coefficients between the components of the winds and the magnetic field variations. The positive sign in ΔH corresponds to the eastward current in the equatorial electrojet which is situated at about 105 km.

For the zonal wind and ΔH, the correlation coefficient varies from +0.15 to –0.88 (changes from low +ve to high –ve) for the heights of 86 km and 98 km respectively, with the values of –0.01 and –0.56 for the heights of 90 km and 94 km respectively. This high negative correlation coefficient which appears at 98 km shows that the drifts measured by the PR radar at this height seems to be due to electron drift velocities which flows in the westward direction as evidenced by the +ve value of magnetic field variations. The simultaneous occurrence of both the peak negative value of about –50 m/s

in the zonal wind at 98 km and the peak positive value of about +40 nT in ΔH at 12 Hr IST confirms further that the measured drift is corresponding to the electron drift velocities. Similarly, the correlation coefficient between the meridional wind and ΔH varies from +0.48 to –0.70 for the heights of 86 km and 98 km respectively, with the values of –0.18 to –0.59 for the heights of 90 km and 94 km respectively. However, the peak negative value of about –50 m/s in the meridional wind at 98 km occurs two hours earlier when compared to the zonal wind which has to be investigated further in the near future. However, it is observed that these were not repeated more often. For example, we have observed (not shown in the present extended abstract) correlation coefficient value of –0.75 and no correlation at 98 km during the days 11 and 01, December, 1995 respectively for the zonal wind component. The direction of the zonal wind and ΔH are as similar as in the case of December 21, 1995. For the meridional wind component, the values are –0.34 and 0.53. Here, we see that a high +ve correlation coefficient is observed during 01, December, 1995. For that we have observed that the meridional wind flows due northward. And, during June 01, 1995 (not shown here), the correlation coefficient shows high +ve value of 0.7 at 98 km. The drifts observed here is flowing eastward and also the magnetic field variations shows positive excursions as observed in the previous cases. This shows that the drifts observed during this period is not associated with the electron drift velocities and it is expected to be associated with pure neutral winds. So, while interpretating the results obtained at 98 km by using PR radar in the equatorial electrojet region one has to be very careful in ascertaining whether it measures neutral wind velocity or electron drift velocity.

Acknowledgments. This work is supported by the Department of Science and Technology, Government of India.

References

Briggs, B.H., The analysis of spaced sensor records by correlation techniques, Handbook for MAP, 13, 166-186, 1984.

Fejer, B. J., and M. C. Kelley, Ionospheric irregularities, Rev. Geophys. Space Phys., 18, 401-454, 1980.

Gurubaran, S., and R. Rajaram, Long-term variability in the mesospheric tidal winds observed by MF radar over Tirunelveli (8.7°N, 77.8°E), Geophys. Res. Lett., 26, 1113-1116, 1999.

Gurubaran, S., and R. Rajaram, Signatures of equatorial electrojet in the mesospheric partial reflection drifts over magnetic equator, Geophys. Res. Lett., To appear in Geophys. Res. Lett., 2000.

Lesicar, D., Study of the structure of partial reflection radar scatterers and their application in atmospheric measurements, Ph. D. Thesis, The University of Adelaide, 1993.

Rajaram, R., and S. Gurubaran, Seasonal variabilities of low latitude mesospheric winds, Ann. Geophys., 16, 197-204, 1998.

Tabbagh, J., D. A. Carter, B. B. Balsley, P. Broche, and M. Crochet, Irregularity drift velocities in the equatorial electrojet observed by both the close-spaced antenna technique and the Doppler radar method, J. Atmos. Terr. Phys., 39, 1035-1039, 1977.

Vincent, R. A., MF/HF radar measurements of the dynamics of the mesosphere region – A review, J. Atmos. Terr. Phys., 46, 961-974, 1984.

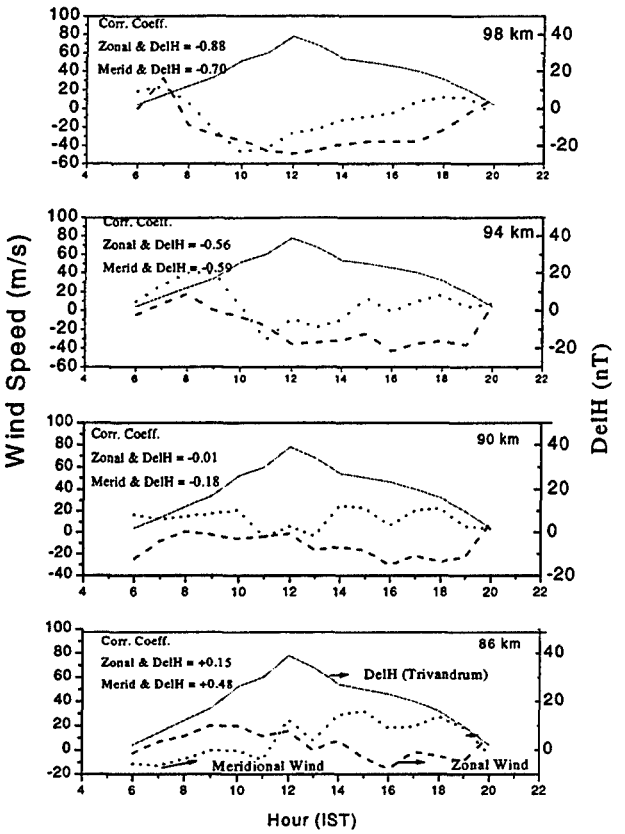


Fig. 1. Illustrates the averaged hourly values of zonal (dashed curve) and meridional (dotted curves) winds in m/s and the H-component of the magnetic field variations (solid curve) (ΔH) in nT during the time intervel of 6-20 hr IST for the heights of 86 km, 90 km, 94 km and 98 km. Correlation Coefficient values between the wind components and ΔH are also included for all heights. The high –ve correlation coefficient and the +ve and –ve peaks at 12 hr IST at 98 km confirms that the PR radar measures electron drift velocity during December 21, 1995.

Structural changes in tidal components in mesospheric winds as observed by the MF radar during counter electrojet events

S. SRIDHARAN[1], S. Gurubaran[1], K. U. Nair[1], R. Rajaram[1,2]

[1]Equatorial Geophysical Research Laboratory, Indian Institute of Geomagnetism, Krishnapuram, Tirunelveli 627 011, India
[2]Indian Institute of Geomagnetism, Colaba, Mumbai 400 005, India
Tel.: 91 462 579465; fax: 91 462 573306
e-mail: egrl@md3.vsnl.net.in, ssri_dhar@hotmail.com

Introduction

The equatorial electrojet (EEJ) is an intense band of east-west electrical current flowing in a narrow latitudinal belt around the dip equator in the E-region (90-120 km) during day time. This reflects in the daily variation of the horizontal component of earth magnetic field (H) at stations around dip equator showing a positive deviation in the day time with maximum value at about 10 to 12 hour local time. Sometimes, a negative deviation in H occurs in the after noon hours. This post-noon decrease of the horizontal component of geomagnetic field below the night time level indicating the reversal in the direction of the current system from the normal eastward flow to westward is often called as 'Counter Electrojet' (CEJ) [Gouin (1962), Gouin and Mayaud (1967)]. Though the morphological behaviour of CEJ have been studied in detail by several authors in the last three decades [Bartels and Johnston (1940), Hutton and Oyinloye (1970), Sastri and Jayakar (1972), Rastogi (1974, 1975), Mayaud (1977), Bhargava and Sastri (1977), Marriot et al. (1979), Reddy (1989), Somayajulu et al. (1993), Stening et al. (1996) and the references therein], the causative mechanism for its occurrence still remains an unsolved problem. One of the proposed mechanisms for its occurrence, namely, the possible reversal of the east-west electric field due to an abnormal combination of tidal winds of global scale [Forbes and Lindzen (1976), Marriott et al. (1979)] is generally accepted, though the relationship is yet to be confirmed. Theoretical studies based on the suggestion that the occurrence of CEJ is due to height varying local winds could not explain its occurrence fully [Richmond (1973), Reddy and Devasia (1981), Raghavarao and Ananda Rao (1987)]. The experimental evidence for the role played by the dynamical features in causing CEJ as predicted by theoretical studies has not been available for want of continuous wind measurements in equatorial mesosphere and lower thermosphere. With the installation of a partial reflection radar at Tirunelveli (8.7° N, 77.8° E, geographic; 0.3° N dip), continuous data on neutral winds are available since 1992. In this paper, we present the experimental evidence on the behaviour of zonal winds and the amplitude and phase variations of tidal wind components as observed by PR radar during CEJ events.

Observations

The wind data utilized in the present study were acquired by the MF radar operated at Tirunelveli in the spaced antenna mode. The system details, mode of operation and the method of wind determination are the same as described by Vincent and Lesicar (1991). Important results on mean winds and tidal climatologies observed over Tirunelveli were reported earlier [Rajaram and Gurubaran (1998), Gurubaran and Rajaram (1999)]. Hourly values of wind measurements in the altitude region 84-98 km were first subjected to meaningful statistics [Rajaram and Gurubaran (1998)] before subjecting the data into further analysis. Since all hourly slots may not be filled for altitudes below 84 km, this region is not included for the present analysis. The electrojet strength is derived from the differences between the horizontal component of magnetic field variations obtained from Trivandrum (8°29' N, 76°57' E, geographic; (0.5°N dip) and Alibag (18°39'N geographic; 12° N dip). It may be noted that Trivandrum is under the influence of both Sq and EEJ current systems whereas Alibag is under the influence of Sq current system only. In this way, the effects of magnetospheric currents may be eliminated

Data analysis

In order to see whether there is any relation between changes in the tidal components and the geomagnetic field variations, successive groups of quiet CEJ and EEJ events (Ap < 12) are identified for the years 1993-96. The groups of EEJ and CEJ are following: 09-11 Dec 95 with Ap values 9,5,4; 06-08 Dec 95 with Ap values 4,4,2; 08-10 Mar 96 with Ap values 6,4,2; 05-07 Mar 96 with Ap values 8,7,11. The hourly values for the CEJ and EEJ days are subjected to harmonic analysis to obtain the amplitude and phase of the tidal components for these groups of days.

Results

Figures 1a, b show the height variation of the amplitude of the diurnal, semi-diurnal and ter-diurnal tide components in zonal wind on EEJ days shown by line with open squares and on CEJ days by line with solid squares. In general, the amplitude and phase of the all the tidal components during CEJ days are substantially different from those on EEJ days. An important feature to be noted is that the semi-diurnal tidal component is larger during CEJ days and this is more clear in March 96 event. The amplitude of the ter-diurnal tide is also larger in CEJ days. But there is no distinct variation seen in the phase profile (not shown).

Figure 2 shows the afternoon (14-18 hour mean) EEJ strength (bottom panel) is compared with the 5-day mean semi-diurnal tide amplitude (Top panel) for a solstice month, July 1995, when the number of CEJ events are more. An interesting feature to be noted is that whenever the after noon EEJ strength is less, the amplitude of semi-diurnal tide was larger and vice-versa. It clearly reveals that the ΔH value decreases well below the night time level, whenever the semi-diurnal tide amplitude enhances.

Discussion and conclusion

The semi-diurnal tide in the mesospheric winds showing greater amplitude during counter electrojet days is the main result of our present study. Somayajulu et al. (1993) observed that the background wind and tidal components show different behaviour on CEJ days. The expected suppression of diurnal tide on CEJ days observed by Somayajulu et al. (1993) is not clearly seen in our present work. A notable feature they observed is that there is an increase in amplitude of the ter-diurnal tide on CEJ days which we also observed herein. The enhancement of semi-diurnal tide on CEJ days was not observed by them. Stening et al. (1996) hypothesize that the CEJ's are driven by semidiurnal tide of global nature. When the semi-diurnal tide having large amplitude on CEJ days reaches the dynamo region, it will tend to weaken the vertical polarization field resulting in the decrease of electrojet current density, if the background wind is also favourably westward [Somayajulu (1993)]. Marriot (1979) using Richmond's (1973) steady-state and 'infinite counductivity model' of the electrojet, found that the diurnal tide is the predominant generator of equatorial electric fields during the equinoxes producing an eastward electric field in the day time and a westward electric field during night. Because of its dominance, the CEJ events are rarely observed during equinoxes. But during solstices, the semi-diurnal tide, especially the (2,2) mode, becomes dominant and produces a westward electric field in the afternoon hours thereby causing CEJ, unless this effect is prevented by diurnal tide. In our present study, we have also found that a clear anti-correlation exists between the semi-diurnal tide amplitude and EEJ strength in the after-noon hours during a solstice month June 1995, indicating the influence of semi-diurnal tide in producing after noon CEJ events.

References

Bartels, J. and H. F. Johnston, J. Geophys. Res., 45, 260-308, 1940a.
Bartels, J. and H. F. Johnston, J. Geophys. Res., 45, 485-592, 1940b.
Bhargava, B. N. and N. S. Sastri, Ann. Geophys., 33, 329-332, 1977.
Forbes, J. M. and R. S. Lindzen, J. Atmos. Terr. Phys., 38, 911-920, 1976.
Gurubaran. S. and Rajaram. R., Journal of Geophys. Res., 26, 1113-1116, 1999.

Gouin, P., Nature, 193, 1145-1146, 1962
Gouin, P. and P. N. Mayaud, Ann. Geophys., 23, 41-47, 1967.
Hutton, R. and J. O. Oyinloye, Ann. Geophys., 26, 921-926, 1970.
Marriott, R. T. et a., J. Geomagn. Geoelectr., 31, 311-340, 1979.
Mayaud, P. N., J. Atmos. Terr. Phys., 39, 1055-1070, 1977.
Raghavarao. R. and B. G. Anandarao, Indian J. Radio and Space Phy., 16, 54-75, 1987.
Rajaram. R. and S. Gurubaran, Ann. Geophys., 16, 197-204, 1998.
Rastogi, R. G., J. Geophys. Res., 79, 1503-1512, 1974.
Rastogi, R. G., Indian Acad. Sci. 80A, 80-92, 1975.
Reddy, C.A. and C. V. Devasia, J. Geophys. Res., 86, 5751-5767, 1981.
Richmond, A. D., J. Atmos. Terr. Phys., 35, 1083-1103, 1973.
Sastri, N. S. and R. W. Jayakar, Ann. Geoelectr., 28, 581-591, 1972.
Somayajulu, et al., Geophys. Res. Lett., 20, 1443-1446, 1993.
Vincent, R. A., and D. Lesicar, Geophys. Res. Lett., 18, 825-828, 1991.

Figures

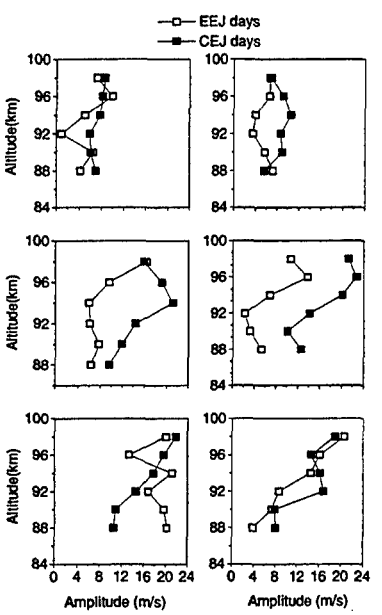


Fig.(1a) Fig.(1b)

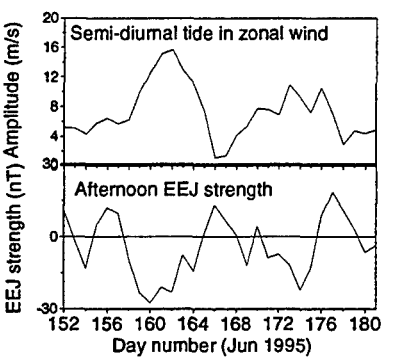


Fig.(2)

Figure captions

Fig(1a). Altitude profile of diurnal(bottom), semi-diurnal(middle) and ter-diurnal(top) tides in zonal wind on EEJ (09-11 Dec 95) and CEJ (06-08 Dec 95) days.
Fig(1b). Same as fig.1 except on EEJ (08-11 Mar 96) and CEJ (05-07 Mar 96) days.
Fig(2). Comparison of EEJ strength (14-18 hour mean) and semi-diurnal tide amplitude (5-day mean) in Zonal wind at 86 km

Short period oscillations of 2.8 m size irregularities in the E region over Gadanki

K.S.V. SUBBARAO, Sudha Ravindran and K.S. Viswanathan
Space Physics Laboratory
Vikram Sarabhai Space Centre
Trivandrum, 695 022, India
Email: spl_vssc@vssc.org

Abstract

Nighttime measurements of E region FAI of 2.8 m size are made on many days in summer and equinoctial months, using Indian MST radar at Gadanki (dip 12.5 deg. N), an equatorial location away from the magnetic equator and off the equatorial electrojet region. The observed Range–Time–Intensity and velocity maps are oscillatory, showing quasi–periodic behaviour with periods of 25–35 min. The amplitude and phase deduced corresponding to these periods at different altitudes indicate strong gravity wave modulation of the echoes. The observations are discussed in the light of local treatment of the instability mechanism.

Introduction

In the past, observations of E region irregularities were made and the nature of small scale irregularities was studied in detail, using VHF coherent backscatter radars, both at the equator and midlatitudes (e.g., Kelley, 1989; Yamamoto et al., 1994; Ogawa et al., 1995). At the equator, the echoes are continuous, seen during both day and night and are of both type I and type II irregularities. At midlatitudes, mostly type II irregularities occur at night, of intermittent nature and the echoes display wave–like features of 5–10 min period; while during post–sunrise period, they are continuous and observed in the region of 90 to 100 km (Yamamoto et al., 1997). However, limited cases of type I echoes in midlatitudes have been reported (e.g., Haldoupis et al., 1997; Huang and Chu, 1998). These features are attributed to the gradient instability process with some degree of altitude modulation of sporadic E by gravity waves. Also the nature of QP echoes in the nighttime midlatitude ionosphere has been investigated in some detail (e.g., Tsunoda et al., 1994). The spectra at midlatitudes are not as distinct as at the equator. The tropical latitudes are the least probed region for this aspect of study and so observations at low latitudes are valuable. Earlier, Krishna Murthy et al. (1998) have reported radar observations of E region irregularities at and off the magnetic equator in the Indian zone. We present here the results of the study carried out on 2.8 m size E region irregularities during nighttime, using observations by 53 MHz radar at Gadanki (13.5 deg. N, 79.2 deg. E).

Experimental Set–up

The detailed MST radar system characteristics are given by Rao et al. (1997). The spectral moment estimates, giving signal strength, mean Doppler velocity and velocity variance are obtained. The radar signal is received in the ionospheric coherent backscatter made of operation with the antenna beam oriented at 13.2 deg. off zenith due north in the meridian plane, transverse to the magnetic field. It is

positioned so as to satisfy the aspect sensitive condition for the field-aligned E region irregularities at the height of scattering. Usually at altitudes >100 km, the observed Doppler shift is positive (toward the radar) at night, which correspond to the downward drift of irregularities under the action of the westward electric field.

Observations and Results

The nighttime E region plasma at Gadanki is characterised by more turbulent structures and extends over a greater height range than during daytime. The Doppler spectra are generally quasi-Gaussian, type II and are quite variable both in range and time, from a narrow single peak to wide multiple peak. The nighttime spectra show significant fluctuations in contrast to that of daytime. The drift velocity of the irregularities does not generally exceed 40 m/s. The drifts in the altitude region of 100–115 km are mostly downward at night and upward occasionally.

The results are presented for two nights on September 5 and 7, 1994. Observations made at 1.2 km (corresponding to 8 microseconds pulse width) interval and time interval of mostly five min in the altitude region of 90–120 km are used for the present study. On occasions, close to midnight hours, in the altitude range of 105–110 km, the superposed fluctuations are strong enough even to reverse the normally expected positive Doppler (downward drift) to negative values, indicative of gravity wave modulation. This feature has been observed on these two nights in this altitude region with varying magnitudes, apart from the oscillatory nature of the drifts observed. For the purpose of analysis, the spectral moments obtained at several range bins are segmented for every one hour during 1900–0400 hr. By regression analysis, the periods are determined along with phase and amplitude at each range bin. It is found that periods in the range of 25–35 min are dominant. The amplitude of the wave is found to increase from lower to higher altitudes with phase propagation downwards. Further details will be presented later.

In view of the fact that the scattered signal is observed in the meridional plane, this feature is attributed to the formation of irregularities due to gradient drift instability mechanism in the presence of sporadic E layers with very sharp density gradients. This aspect has been discussed by Woodman et al. (1991) for midlatitude observations. Rocket-borne electron density measurements in the nighttime at SHAR (dip 10 deg. N) by Prakash et al. (1991) revealed small scale structures in the altitude profiles of electron density, lending credence to the observations at Gadanki. Further results are discussed in the full paper.

References

Haldoupis, C., D.T. Farley, and K. Schlegel, Ann. Geophys., 15, 908, 1997.
Huang C.M., and Y.H. Chu, Geophys. Res. Lett. 25, 3779, 1998.
Kelley, M.C., The earth's ionosphere: Plasma Physics and electrodynamics, 487 pp., Academic, calif., 1989.
Krishna Murthy, B.V., Sudha Ravindran, K.S. Viswanathan, K.S.V. Subbaro, A.K. Patra and P.B. Rao, J. Geophys. Res., 103, 20,761, 1998.
Ogawa, T., M. Yamamoto, and S. Fukao, J. Geophys. Res., 100, 12,173, 1995.
Prakash, S., S. Pal , and H. Chandra, J. Atmos. Terr. Phys., 53, 977, 1991.

Rao, P.B., A.K. Patra, T.V. Chandrasekhar Sarma, B.V. Krishna Murthy, K.S.V. Subbaro and S.S. Hari, Radio Sci., 32, 1215, 1997.
Tsunoda, R.T. , S. Fukao, and M. Yamamoto, Radio Sci., 29, 349, 1994.
Yamamoto, M., N. Komoda, S. Fukao, R.T. Tsunoda, T. Ogawa and T. Tsuda, Radio Sci., 29, 337, 1994.
Yamamoto, M., S. Fukao, R.T. Tsunoda, K. Igarashi and T. Ogawa, J. Atmos. Terr. Phys., 59, 1665, 1997.
Woodman, R.F., M. Yamamoto, and S. Fukao, Geophys. Res. Lett., 18, 1197, 1991.

VHF radar observations of field aligned irregularities at 85–95 km altitude over Gadanki

A K PATRA, S Sripathi, V Sivakumar, and P B Rao
National MST Radar Facility, P O Box 123, Tirupati 517502, AP, India.

It is well known that plasma turbulence could occur from height as low as ~80 km (Kelley, 1989 and the references therein). The source of ionospheric turbulence is usually considered to be plasma instability mainly due to Farley Buneman (two stream) and gradient drift instability. The two stream instability is normally observed at the equatorial and auroral E region. Gradint drift instability mechanism could operate at latitude but require a special relation between the density gradient and the drift velocity to make the plasma unstable. This requirement is often not fulfilled in the lower part of the E region. On the other hand the observational data show a significant level of turbulence at the lower part of the E region. Dimant and Sudan (1995, 1997) have recently developed a new plasma instability that is excited in the height region when a large electric field is applied. The validity of this theory so far has come through only one rocket observation made by Blix at al. (1996). Later Tsunada et al (1997) have interpreted their HF radar observations in terms of this new instability. On the other hand, Gurevich et al. (1996) developed a new theory which describes quantitatively the transfer of neutral turbulence to a plasma resulting in low–frequency plasma irregularities in the upper D and lower E regions. This theory does not require any threshold condition of the electron density gradient or electron drift velocity for the instability to set in.
In a separate work Schlegel and Gurevich (1997) have predicted that these irregularities could be detected by high power VHF radar. They have shown the scattering cross section to decrease with increasing radar frequency. In such a scenario, it is desired to have more radar measurements to validate the theory and understand the instability mechanism operating at this altitude region.
In this paper we report the Gadanki radar observations on the 85–95 km echo characteristics in terms of signal intensity, spectral characteristics and aspect sensitivity characteristics of these echoes. The Gadanki radar is a 53 MHz MST class radar located at a low latitude station (geomagnetic latitude 6.3oN).
It is noted that the irregularities occur in a narrow altitude region with typical thickness of 1–2 km. Signal strength could be as high as 30 dB. Further the spectral characteristics are remarkably different than that of the normal E region

irregularities (above 100 km). The Doppler velocities are often found to be in opposite direction to that of the normal E region irregularities. The spectra are very narrow and less variable with height and time. Typical mean Doppler velocity and velocity spectral width are ~10 ms−1 and ~30 ms−1 respectively. Using a long data set available with us we have performed a statistical study on these two parameters. It is found that the standard deviation of the mean Doppler velocity and spectral width are 10 ms−1 and 20 ms−1 respectively. The irregularities are found to be less aspect sensitive compared to that of the normal E region. They, however, are found to be discrete in terms of their position in the radar pulse volume. These results do not seem to be explained by the existing theories. The radar observations on the irregularities made using the Gadanki radar are presented and discussed in reference to these two theories. We believe that these observations will shed more light to understand the physical processes associated with the upper D and lower E region.

References

Dimant and Sudan, J. Geophys. Res., 100, 14605, 1995.
Dimant and Sudan, J. Geophys. Res., 102, 2551, 1997.
Gurevich et al., J. Geophys. Res., 102, 379, 1997.
Kelley, The Earths Ionosphere, Academy Press, 1989.
Schelegel and Gurevich, Ann. Geophys., 15, 870, 1997.
Tsunoda et al., Geophys. Res. Lett., 24, 1215, 1997.

Studies on the low latitude off–electrojet field aligned E region irregularities as observed by the Gadanki MST radar

A K PATRA, S Sripathi, V. Sivakumar and P B Rao
National MST Radar Facility, P O Box 123, Tirupati 517502, AP, India.

K S Viswanathan
Space Physics Laboratory, VSSC, Trivandrum 695022, India.

It is known from radar and rocket observations that meter scale density irregularities do exist in the E region of the ionosphere at all latitudes and longitudes. The small scale irregularities in the E region have been extensively studied by the radars in the equatorial and auroral regions (see reviews by Fejer and Kelley, 1980: Haldoupis, 1989). These irregularities have also been studied quite extensively at midlatitudes using radars in last two decades (e.g., Ecklund et al., 1981; Tanaka and Venkateswaran, 1982; Riggin et al., 1986; Yamamoto et al., 1991). While significant progress has been made in understanding the midlatitude sporadic E irregularities a very little is known about the irregularities that occur in between the equator and midlatitude. In the recent years some studies have been made of these irregularities in the anomaly region using the Chung–Li VHF radar (e.g., Pan et al., 1994; Chu and Wang, 1997) and in the low latitude region just outside the electrojet using the Gadanki MST radar and the Piura VHF wind profiler (e.g., Krishna Murthy et al., 1998; Choudhary and Mahajan, 1999; Patra and Rao, 1999: Woodman, et al., 1999). From these limited studies it is found that the gross feature of the irregularities occurring in the anomaly region is remarkably different in their occurrence and spectral characteristics to that of the low latitude. The low latitude irregularities are also very much different in their occurrence to that of the electrojet.
In this paper, we present the E region field aligned irregularity observations gathered with the Gadanki MST radar (13.5o N, 79.2o E, 6.3o geomagnetic latitude) during 1994–1997. These observations were made on many days as diurnal runs. Such a long data set allows us to characterize the low latitude FAI in the E region.
The Gadanki radar is a high power MST radar operating at 53 MHz. The radar beam can be oriented towards north in order to make it transverse to the geomagnetic field at the E and F region. We used the 13.2o off–zenith beam due north to study the E region FAI. The system description in detail can be found in Rao et al. (1995).

Gadanki observations on the E region FAI are found to be present both during daytime and nighttime, nighttime being more intense and dynamic. During daytime two distinct altitude regions viz., 85–95 km and 100–115 km are found to be unstable, the lower region being more common. The

signals are found to drop out especially for the upper region in general for about 3–4 hours around noontime. This behavior indicates that the instability criteria of the low latitude off electrojet instability are unlike that of the equatorial electrojet. During nighttime, signal is found to extend as high as 160 km unlike the equator. The upper E region echoes being a phenomenon confined typically to 2000–2400 hours. It may be noted that the equatorial E region instability is found to extend only upto 135 km (Woodman, 1994). On many occasions, the signal intensity undergoes quasi periodic variations similar to that of the midlatitude with periods 10–20 minutes. This seems to be due to the presence of medium scale gravity waves. During nighttime the echoing region can broadly be separated into 3 regions. The most important characteristics of these layers is that they show descending structures in the RTI display irrespective of time. The descend rate, however, changes from day to night with values of ~0.5 km/hour during daytime to ~2 km/hour during nighttime.
The Doppler velocities corresponding to the echoing layers observed below ~97 km are downward during daytime and upward during nighttime, while that corresponding to the upper layers are upward during daytime and downward during nighttime. The Doppler velocities corresponding to the upper layers seem to correspond to the zonal electric field. Although this is the general trend, there is deviation too at times. The opposite signature in the Doppler velocity is one of the most remarkable feature in our data.
The Gadanki observations seem to resemble to equatorial one in the sense that the echoing layers occur in the form of thin layered structure in the lower altitude and resemble to the midlatitude in the sense that they occur as periodic structures with period close to the medium scale gravity wave.
Using such a long database we have performed a statistical study of the radial velocity and spectral width transverse to magnetic field. It is found that at lower altitude the magnitude of the mean drift and standard deviation of the mean drift are ~5 ms−1 and 10–20 ms−1 respectively. At the higher altitudes these are found to be 20–30 ms−1 and 10–30 ms−1 respectively. At the lower altitudes the mean of the spectral width (half power full width) and the standard deviation of the spectral width are 35–40 ms−1 and ~20 ms−1 respectively, whereas they are ~70 ms−1 and 50–60 ms−1 respectively. These values are similar to that reported recently by Woodman et al. (1999). We have also made statistical study on the relationship of the signal strength and the spectral with. It is found that at the lower altitudes, the spectral width is found to saturate with increasing signal strength. For the upper region echoes the case is just reverse. Spectral width is found to exponentially increase with increasing intensity. This is found to be due to the domination of the large scale waves at this height region. Our high resolution measurements support this view points. These observations show that the lower and the upper E region exhibit quite different characteristics in their occurrence and spectral

signature. However, the downward motion of the layers is found to be a common feature. Simultaneous ionosonde observations made at Sriharikota at about 80 km east of the radar site has been taken to monitor the ionospheric conditions. These results in terms of the instability mechanism and their potential to derive electric field and neutral wind and study the gravity wave dynamics is presented and discussed in the light of current understanding.

References

Choudhary and Mahajan, J. Geophys. Res., 104, 2613, 1999.
Chu and Wang, Radio Sci., 32, 817, 1997.
Ecklund et al., J. Geophys. Res, 86, 858, 1981.
Fejer and Kelley, Rev. Geophys., 18, 401, 1980.
Haldoupis, Ann. Geophys., 7, 239, 1989.
Krishna Murthy et al., J. Geophys. Res., 103, 20761, 1998.
Pan et al., Geophys. Res. Lett., 21, 1763, 1994.
Patra and Rao., J. Geophys. Res., 104, 24667, 1999.
Rao et al., Radio Sci., 30, 1125, 1995.
Riggin et al., J. Geophys. Res., 91, 8011, 1986.
Tanaka and Venkateswaran, J. Atmos. Terr. Phys., 44, 381, 1982.
Yamamoto et al., J. Geophys. Res., 96, 15943, 1991.
Woodman, Proc. COSPAR colloquium on low latitude ionospheric physics, 83, 1994.
Woodman et al., Radio. Sci., 34, 983, 1999.

Nonlocal Effects on Gradient Drift Instabilities in the Equatorial Electrojet

S. Hu and A. Bhattacharjee
Department of Physics and Astronomy, The University of Iowa, Iowa City

Both ground-based radar observations and *in situ* rocket measurements show that type II irregularities are attributed to gradient-drift instabilities. It is widely believed that velocity shear, produced by the spatial dependence of the background electric field, has a subtle effect on the linear eigenmode problem and makes it intrinsically nonlocal even for short wavelengths. In this paper, we present analytical as well as numerical results elucidating the effects of density gradients and velocity shear, applicable to realistic daytime and nighttime equilibrium profiles.

In a local analysis, it is implicitly assumed that if a wave, with wave number k_x in the east-west direction and a phase velocity V_{ph}, satisfies the resonance condition $\omega = k_x V_{ph}$ at a given altitude z, it does so for all values of z. However, the phase velocity $V_{ph}(z)$ is produced by a spatially-varying electric field $E_z(z)$ and is altitude-dependent. Consequently, a wave in resonance at a given altitude need not be so at another altitude. This mistuning of the wave resonance leads to phase decoherence and a suppression of the wave amplitude as the wave propagates from a resonant region to a non-resonant one. This modification of the phase velocity is essentially a nonlocal effect and produces a spatially structured wave envelope in the vertical direction.

The crucial local parameter that determines the growth rate of the gradient-drift instability is $E_z(z)/L_n$, where $L_n = (d \ln N_0/dz)^{-1}$ is the spatial scale of the equilibrium density profile $N_0(z)$. Since this parameter varies continuously with z, an important question is how a nonlocal mode envelope emerges from the superposition of localized modes in the vicinity of the location where the parameter $E_z(z)/L_n$ is maximal.

In order to elucidate these nonlocal features of the gradient-drift instability, we have derived a reduced model from the governing equations of the gradient-drift waves. For realistic daytime and nighttime equilibria, we solve the reduced model equation, which corresponds to that of a quantum harmonic oscillator with a complex potential, and obtain analytical nonlocal solutions. These analytical solutions are also tested by means of numerical solutions. Analytical expressions are obtained in closed form for the growth rates of unstable eigenmodes. These expressions depend manifestly on local as well as nonlocal parameters. The limits of validity of local theory, especially at nighttime when density gradients are large, will be discussed.

This research is supported by the NSF.

A Possible Spectrum of Plasma Fluctuations Caused by Neutral Turbulence in the Equatorial Ionosphere

Yu. Kyzyurov (*Main Astronomical Observatory NASU, 03680, Kiev-127, Ukraine*)

Introduction

Turbulence of the neutral atmosphere is very important to dynamics of the lower ionosphere. In particular, this turbulence plays a major role in creating ionospheric irregularities below the turbopause at middle latitudes and in creating the irregularities below the auroral and equatorial electrojets [Ref. 1-3]. Recently, the process of generation of ionospheric plasma irregularities by turbulent neutral wind and the spectrum of such irregularities were discussed in [Ref. 4, 5]. A new theory which describes quantitavely the transfer of neutral turbulence to ionospheric plasma turbulence was developed in the first work [Ref. 4]. In this theory the ionospheric turbulence was presented as the superposition of linear plasma waves (the drift mode). One of the results of [Ref.4] is an analytical expression for the spectrum of electron density fluctuations. Unfortunately, the developed theory concerns only the excitation of turbulence in homogeneous plasma and entirely ignores a gradient of background ionization, though such a gradient plays an important role in generation of irregularities by neutral turbulence in the ionosphere [Ref. 1]. A situation of conventional fluid turbulence creating plasma irregularities through mixing in a weakly ionized gas was considered in [Ref. 5]. In this consideration, plasma component was regarded as a passive contaminant and the presence of a background ionization gradient (which was not too strong) was taken into account. An attempt to apply the approach of [Ref. 5] (with some modifications) to the case of plasma irregularities in the equatorial ionosphere below the electrojet region [Ref. 3] is made in the present report.

Simplifying approximations and the governing equation

Suppose that the plasma consists of neutrals, singly charged ions and electrons, and the motion of neutrals is given (the neutral gas is assumed to be unaffected by collisions with the ionized component). Sufficiently slow processes in such plasma may be described by the quasi-hydrodynamic equations in the following form [Ref. 1]:

$$\partial \mathbf{V}_j/\partial t+(\mathbf{V}_j\nabla)\mathbf{V}_j+\nu_j(\mathbf{V}_j-\mathbf{U})=q_j\mathbf{E}/m_j+\omega_{Bj}(\mathbf{V}_j\times\mathbf{b})-v_{Tj}^2\nabla N_j/N_j, \quad (1)$$

$$\partial N_j/\partial t+\nabla(N_j\mathbf{V}_j)=J-\alpha_r N_j^2, \quad (2)$$

where $\mathbf{V}_j(\mathbf{r}, t)$, v_{Tj}, $N_j(\mathbf{r}, t)$, m_j, and ω_{Bj} are respectively, the velocity, thermal velocity, number density, mass and cyclotron frequency of the particle specie j, j=e for electrons and j=i for ions, ν_j is the charged particle neutral collision frequency, q_j is the particle charge ($q_i=-q_e=e$), $\mathbf{U}(\mathbf{r}, t)$ is the neutral gas velocity, $\mathbf{E}$ is the electric field, $\mathbf{b}=\mathbf{B}/B$ is the unit vector along the magnetic field $\mathbf{B}$, J is the rate of ionization per unit volume, and α_r is the recombination coefficient. The effects of collisions between chared particles are neglected.

Without giving the details (see [Ref. 5]) we outline the steps necessary for obtaining the equation govening evolution of plasma density fluctuations caused by variations in velocity field of neutrals: 1) the 'inertia' terms on the LHS of Eq.(1) are neglected, since we consider the processes with length-scales larger than the ion mean free path, $l>>\Lambda_i$, and with time-scales larger the inverse value of ion-neutral collision frequency, $t>>\nu_i^{-1}$; 2) quasi-neutrality ($N_e=N_i=N$) and isothermality are assumed; 3) in the situation $\nu_i>>\omega_{Bi}$, $m_i\nu_i>>m_e\nu_e$, the only electric field considered is that requiered to prevent charge separation (due to the field $\mathbf{E}$, electrons tend to follow ions), i.e. the ambipolar diffusion approximation is accepted; 4) in the presence of neutral

turbulence, the velocity of neutrals and the plasma density are divided into regular (mean) and fluctuating (random) parts: $\mathbf{U}=\mathbf{U}_0(\mathbf{r})+\mathbf{u}(\mathbf{r}, t)$, $\mathbf{U}_0>\mathbf{u}$, and $N=N_0(\mathbf{r})+n(\mathbf{r}, t)$, $N_0>n$; 5) it is supposed, that the length-scale of the random ingradients, $\mathbf{u}$ and n, is small compared with the spatial scale of variation of mean quantities, $l<L_N\leq L_U$; 6) the neutral turbulence and generated irregularities are regarded as nearly isotropic (it is consistent with data of [Ref. 3]); 7) our attention is restricted to incompressible motions of neutrals for which $\nabla\mathbf{U}=0$. Taking into account an effect of recombination in a linear approximation on the perturbed plasma density, the governing equation for the fluctuations with length-scales smaller than the length-scale of a regular gradient in background ionization, $L_N=N_0/|\nabla N_0|$, is

$$\{\partial/\partial t-D_A\nabla^2+\tau_r^{-1}\}\delta n+\nabla(\delta n\cdot\mathbf{u})=-L_N^{-1}(\mathbf{u}\cdot\mathbf{h})-\beta_i\nabla(\mathbf{u}\times\mathbf{b}). \quad (3)$$

Here $\delta n(\mathbf{r}, t)=N_0^{-1}n(\mathbf{r}, t)$, $D_A\approx v_s^2/\nu_i$ is the ambipolar diffusion coefficient ($v_s^2=v_{Ti}^2+m_e v_{Te}^2/m_i$), $\tau_r=(2\alpha_r N_0)^{-1}$ is the recombination time, $\mathbf{h}=L_N N_0^{-1}\nabla N_0$ is the unit vector along the gradient of N_0, and $\beta_i=\omega_{Bi}/\nu_i$.

After rewriting Eq.(3) for Fourier components of the plasma fluctuation and neutral velocity fields, we obtain

$$(D_Ak^2+\tau_r^{-1}-i\omega)\delta n(\mathbf{k},\omega)+ik_j\int d\mathbf{k}'d\omega'\delta n(\mathbf{k}',\omega')\cdot u_j(\mathbf{k}-\mathbf{k}',\omega-\omega')=$$
$$=-L_N^{-1}(\mathbf{h}\cdot\mathbf{u}(\mathbf{k},\omega))-i\beta_i\mathbf{k}(\mathbf{u}(\mathbf{k},\omega)\times\mathbf{b}). \quad (4)$$

The convolution term on the LHS of Eq.(4) represents the contribution of mode interactions in the process of plasma fluctuation generation. If we take it into account phenomenologically through the coefficient of turbulent diffusion D_T, then

$$((D_A+D_T)k^2+\tau_r^{-1}-i\omega)\delta n(\mathbf{k},\omega)=-L_N^{-1}(\mathbf{h}\cdot\mathbf{u}(\mathbf{k},\omega))-i\beta_i\mathbf{k}(\mathbf{u}(\mathbf{k},\omega)\times\mathbf{b}). \quad (5)$$

If in the lower ionosphere the Schmidt number is near unity, i.e. $D_A\approx\mu_n$ (μ_n is the kinematic viscosity of neutral gas), as in the case of most fluids and gases, then we may regard that $D_T\approx\varepsilon^{1/3}k^{-4/3}$ (ε is the turbulence energy dissipation rate).

Spectrum of plasma fluctuations

We consider the situation when statistical properties of the velocity field $\mathbf{u}$ are assumed known. Since experimental data (see, e.g., [Ref. 6]) show that the assumption of exponential relaxation of the $\mathbf{u}$-field correlations in time is often valid and the rlaxation time of turbulent eddy with scale k^{-1} is $\tau_k^{-1}=\mu_n k^2+\varepsilon^{1/3}k^{2/3}$ then the space-time spectrum tensor of the $\mathbf{u}$-field may be written as

$$\Phi_{ij}(\mathbf{k},\omega)=(k^2\delta_{ij}-k_ik_j)\cdot E(k)/\Omega_\Phi(\mathbf{k},\omega), \quad (6)$$

where $\Omega_\Phi(\mathbf{k},\omega)=4\pi^2k^4\tau_k(\omega^2+\tau_k^{-2})$, $E(k)=C_1\varepsilon^{2/3}k^{-5/3}$ is the energy spectrum function in the inertial range of wavenumbers, $k_0<k<k_\mu$ ($k_0^{-1}\approx L_U$ is a length-scale in which the kinetic energy of turbulence is generated, $k_\mu^{-1}\approx(\mu_n^3/\varepsilon)^{1/4}$ is a viscous length-scale at which say viscous dissipation is adequate to dissipate the energy at the rate ε), C_1 is a dimensionless constant of order unity ($C_1\approx1.4$).

Using known relations for the statistically homogeneous and stationary random fields

$\langle u_i(\mathbf{k},\omega)\cdot u_j^*(\mathbf{k}',\omega')\rangle=\Phi_{ij}(\mathbf{k},\omega)\delta(\mathbf{k}-\mathbf{k}')\delta(\omega-\omega')$, $\langle\delta n(\mathbf{k},\omega)\cdot\delta n^*(\mathbf{k}',\omega')\rangle=\Psi(\mathbf{k},\omega)\delta(\mathbf{k}-\mathbf{k}')\delta(\omega-\omega')$,

where the star denotes a complex conjugate, and taking Eqs.(5) and (6) into account we then obtain an expression for the wavenumber-frequency spectrum of relative variations in plasma desity

$$\Psi(\mathbf{k},\omega)=(L_N^{-2}(\mathbf{h}\times\mathbf{k})^2+\beta_i^2k^2(\mathbf{b}\times\mathbf{k})^2)\cdot k^2E(k)/\Omega_\psi(\mathbf{k},\omega), \quad (7)$$

here $\Omega_\psi(\mathbf{k},\omega)=(\omega^2+(D_Ak^2+\varepsilon^{1/3}k^{2/3}+\tau_r^{-1})^2)\cdot\Omega_\Phi(\mathbf{k},\omega)$.

The spatial spectrum of plasma density fluctuations $P(\mathbf{k})$ is defined by the zero-time-delay correlation function, $\langle\delta n(\mathbf{r}, t)\cdot\delta n(\mathbf{r}', t)\rangle=\int d\mathbf{k}P(\mathbf{k})\exp(i\mathbf{k}(\mathbf{r}-\mathbf{r}'))$, and $P(\mathbf{k})$ is related with $\Psi(\mathbf{k},\omega)$ as

$$P(\mathbf{k})=\int d\omega \Psi(\mathbf{k},\omega).$$

After integration, we have

$$P(\mathbf{k})=(L_N^{-2}k^{-2}(\mathbf{h}\times\mathbf{k})^2+\beta_i^2(\mathbf{b}\times\mathbf{k})^2)\cdot E(k)/\Omega(k), \quad (8)$$
$$\Omega(k)=4\pi k^2(D_A k^2+\varepsilon^{1/3}k^{2/3}+\tau_r^{-1})\,((D_A+\mu_n)k^2+2\varepsilon^{1/3}k^{2/3}+\tau_r^{-1}).$$

$P(\mathbf{k})$ is often called the three-dimensional power spectral density (PSD) of the fluctuations. Using Eq.(8) we may obtain the root-mean-square level of relative plasma density fluctuations: $<(n/N_0)^2>^{1/2}=<(\delta n)^2>^{1/2}=(\int d\mathbf{k}\, P(\mathbf{k}))^{1/2}$, the integration over the surface of the sphere of radius k in $\mathbf{k}$-space then gives

$$<(\delta n)^2>=\int dk\, P_1(k) \quad (9)$$

with

$$P_1(k)=8\pi k^2(3\Omega(k))^{-1}(L_N^{-2}+\beta_i^2k^2)\cdot E(k), \quad L_N^{-1}<k<k_d \quad (10)$$

($k_d\approx(\varepsilon/D_A^3)^{1/4}$, the diffusive length-scale k_d^{-1} is analogous to the viscous length-scale k_μ^{-1} for the neutral atmosphere turbulence, in our case $k_d=k_\mu$).

It is seen from Eq.(9) that $P_1(k)dk$ is the contribution to the power level of relative plasma density fluctuations from the wavenumber range (k, $k+dk$) ($P_1(k)$ is the one-dimensional PSD of the fluctuations). To estimate the rms fluctuation level we take the following values of parameters which are quite realistic for the equatorial ionosphere below the electrojet region [Ref. 3, 7]: $L_N\sim10^4$ m, $N_0\sim2\cdot10^9$ m^{-3}, $\beta_i=\omega_{Bi}/\nu_i\sim0.01$, $D_A\approx\mu_n\sim1.7$ m^{2}s^{-1}, $\varepsilon\sim0.05$ m^{2}s^{-3}, $\alpha_r\sim3\cdot10^{-13}$ m^{3}s^{-1}. Then in the length-scale range 3.15 m – 700 m ($k_d^{-1}=3.15$ m is a lower value of irregularity size, and an upper one, $l_m=700$ m, is chosen as a semithickness of the layer of irregularities seen by the rocket probe [Ref. 3]) the rms level is about 2.8%. Figure 1a (solid line 1) represents the self-normalized 1D spectrum ($P_1(k)/P_1(k_m)$, $k_m=l_m^{-1}$) in this case. For comparison with the previous case, the self-normalized PSD under another value of the mean plasma density gradient, $L_N\sim5\cdot10^3$ m, is also illustrated in Fig.1a (solid line 2), the rms fluctuation level is about 5%. So an analytic expression Eq.(10) for the 1D spectrum of the plasma fluctuations can explain both a power-law shape for the spectrum of ionospheric irregularities in general and some possible departures of the spectral shape from a simple power-law form with a constant index. In particular, these departures can be due to changes in the relative importance of the interaction of plasma imbedded in the turbulent motions of neutral gas with the geomagnetic field and breakdown of the background plasma density gradient by neutral turbulence in the generation of irregularities of different scales [Ref. 8]. However for comparison with the spectra measured during say rocket experiments a somewhat another 1D spectrum obtained from $P(\mathbf{k})=P(k_\perp\cos\varphi,\ k_\perp\sin\varphi,\ k_z)$ is more suitable, namely $P_1(k_z)$ (when $\mathbf{z}$ is along a sounding rocket trajectory),

$$P_1(k_z)=\int_0^{\sqrt{k_d^2-k_z^2}} k_\perp dk_\perp \int_0^{2\pi} P(\mathbf{k})d\varphi=\int_0^{\sqrt{k_d^2-k_z^2}} Q(k_\perp,k_z)k_\perp dk_\perp, \quad (11)$$

$$Q(k_\perp,k_z)=\pi(k^2\Omega(k))^{-1}(2k_\perp^2L_N^{-2}+\beta_i^2k^2(k_\perp^2+k_\perp^2\cos^2\theta+2k_z^2\sin^2\theta))\cdot E(k),$$

where $k^2=k_\perp^2+k_z^2$, θ is an angle between $\mathbf{b}$ and $\mathbf{h}=(0, 0, 1)$, $\theta=90^\circ-I$ (I is the magnetic dip angle, $I\approx0.5^\circ$ is chosen in the present case).

Two examples of the spectral form ($P_1(k_z)/P_1(k_m)$, $k_m=l_m^{-1}$) predicted by Eq. (11) for above-mentioned values of parameters are shown in Fig. 1b.

Conclusion

In the equatorial ionosphere below the electrojet region, the neutral atmosphere turbulence can produce plasma irregularities and their spectrum can be described by Eq. (8). There is quite good

agreement between the forms of irregularity spectra obtained theoretically and the spectra measured during a rocket experiment [Ref. 3]. The estimations of fluctuation level are consistent with data of ionospheric observations too. As regards further investigations, an elimination of some simplifications can improve the present results. In particular, among such simplifications there is ignoring the presence of charged dust and aerosols in the lower ionosphere. To test more rigorously results of this report a combined rocket/radar experiment in which the irregularity spectrum and pertinent ionospheric parameters are simultaneously measured seems to be very important.

References

1. Gershman, B.N., *Dynamics of ionospheric plasma* (in Russian), Nauka, Moscow, 1974.
2. Cho, J.Y.N., W.E. Swartz, M.C. Kelley, and C.A. Miller, *Geophys. Res. Lett.*, **20**, 2291, 1993.
3. Røyrvic, O., and L.G. Smith, *J. Geophys. Res.*, **89**, 9014, 1984.
4. Gurevich, A.V., N. D. Borisov, and K.P. Zybin, *J. Geophys. Res.*, **102**, 379, 1997.
5. Kyzyurov Yu.V., P.P. Malovichko, and S.F. Nosov, *Kinematika Fiz. Nebesn. Tel*, **15**, 455, 1999.
6. Belikovich, V.V., and E.A. Benediktov, *Geomagn. Aeron.*, **35**, 91, 1995.
7. Kudeki, E., D.T. Farley, and B. Fejer, *Geophys. Res. Lett.*, **9**, 684, 1982.
8. Kyzyurov Yu.V., P.P. Malovichko, and S.F. Nosov, *Kinematika Fiz. Nebesn. Tel*, **15**, 467, 1999.

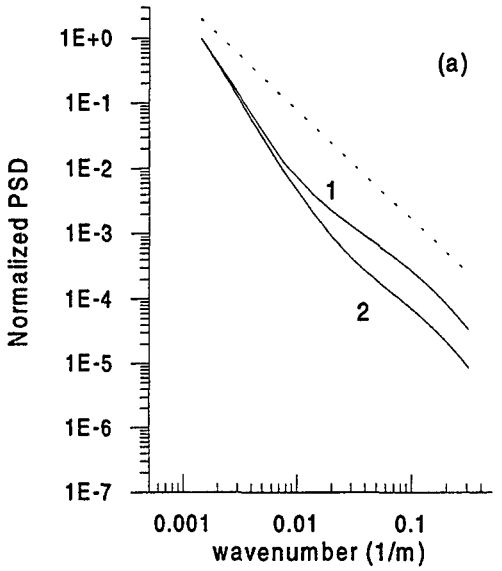


Fig.1a. Self-normalized spectra of plasma density fluctuations, $P_1(k)/P_1(k_m)$, predicted by Eq.(10) when L_N~10^4 m (solid line 1) and L_N~$5 \cdot 10^3$ m (solid line 2). The dashed line represents the slope of the Kolmogorov spectrum $k^{-5/3}$.

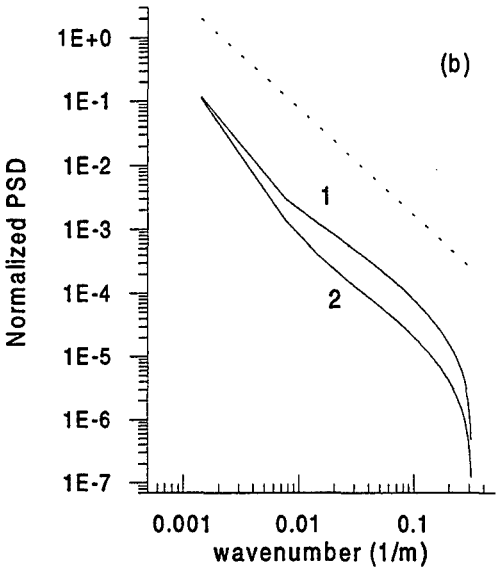


Fig.1b. Normalized PSD of plasma density fluctuations, $P_1(k_z)/P_1(k_m)$, predicted by Eq.(11) when L_N~10^4 m (solid line 1) and L_N~$5 \cdot 10^3$ m (solid line 2).

The Pohnpei Radar Observatory

Warner L. Ecklund
Boulder, Colorado, USA
Roland T. Tsunoda
SRI International
Menlo Park, California, USA

Introduction. The 50 MHz wind profiler site, located on the island of Pohnpei in the Federated States of Micronesia (6.96°N, 158.19°E), was established in 1984 by NOAA's Aeronomy Laboratory with support from the National Science Foundation. The profiler was operated with a single vertical beam until 1990, when a 5–beam antenna was installed. Pohnpei is located within 0.5° of the magnetic dip equator and strong "clutter" from magnetic–field–aligned irregularities in the ionosphere has always been present in the profiler returns. The profiler was used for the first time in 1993 to demonstrate that the so–called 150 km echo in the ionosphere could be detected with radars less sensitive than the Jicamarca incoherent–scatter radar (Kudeki et al., 1998). In early 1997, ionospheric measurements were made with the profiler and used to illustrate anomalous electrodynamics at the base of the equatorial electrojet (Tsunoda and Ecklund, 1999). The same data set was used to extract a more comprehensive description of the 150 km echoes (Tsunoda and Ecklund, 2000). In 1998, a frequency–agile radar (FAR) system (Tsunoda et al., 1995) and a magnetometer were installed at the field site and operation of the site was assumed by SRI International. The field site with this cluster of sensors is now called the Pohnpei Radar Observatory (PRO). In this presentation, we describe the PRO facility and discuss ongoing and planned research topics.

The PRO Facility. The 50 MHz system at the PRO today (the PRO–50) utilizes most of the original wind–profiler system, but with a few modifications. The antenna array is 100 m ×100 m in size and consists of 32 strings of 100–m long COCO antennas; adjacent strings are separated by a half wavelength. The array is currently configured so that the antenna beam can be steered electronically between the vertical and two oblique directions (±14.3° zenith angle) in the magnetic east–west plane. The two–way 3–dB antenna beamwidth is about 2°. The wind–profiler electronics have been modified to allow the use of longer pulse widths: matched–receiver radial resolutions of 0.5, 1, 2, 5 and 10 km can now be selected. The wind–profiler amplifier has been replaced with a broadband FAR amplifier, which is capable of 4 kW peak power and a 10 percent maximum duty cycle. The PRO–50 has been shown capable of detecting not only electrojet and 150–km echoes, but also backscatter plumes from the F layer that have been observed to extend up to 1400 km in altitude.

The FAR system is currently configured at the PRO to operate in three modes, as a 24.5 MHz radar, an ionosonde, and a frequency–agile high–frequency (HF) radar. Broadband amplifiers capable of 8 kW peak power are used for all three modes. In the 24.5 MHz radar (PRO–24) mode, the FAR uses a set of 16 4–element Yagi antennas that are collocated with the COCO array. The Yagi array is configured to allow mechanical steering of the antenna beam. The PRO–24 is capable of providing measurements similar to that of the PRO–50, but at a lower operating frequency. For the ionosonde and

HF–radar modes, the FAR switches to two broadband dipole antennas that are also collocated with the COCO array. In the HF radar mode, the FAR can dwell at any operating frequency between 2 and 30 MHz.

The PRO electronics is located at the edge of the 100 m ×100 m antenna field in two air–conditioned buildings. The equipment operates continuously and unattended except for weekly visits to the site by support personnel to change recording media. The PRO–50 records 256 point average Doppler spectra at up to 180 heights with typical time resolution of less than one minute. The system runs two different sets of parameters depending on time of day. The daytime parameters are set to give good radial resolution on the strong electrojet echoes and data samples extend up to about 180 km to study the 150 km echoes. The nighttime parameters are set to give a radial resolution of 10 km and data samples extend up to about 1200 km for spread–F studies. The PRO–50 has been operating continuously since June 1999. The FAR system is currently being tested to operate sequentially in all three of the mentioned modes with different sets of operating parameters depending on the time of day.

Unique Capabilities. The cluster of sensors at the PRO provides some unique capabilities that should prove to be extremely useful for investigations of the equatorial ionosphere and associated electrodynamics. In particular, the PRO–50 is one of only two radars that have detected the 150–km echoes. Because 150 km echoes have been shown to provide accurate estimates of the equatorial electric field (Woodman and Villanueva, 1995), the PRO–50 is the only ground–based sensor outside of the American sector that is capable of doing so. Moreover, the PRO–50 is the only tri–beam radar with high–resolution measurement capabilities located on the magnetic dip equator. With three beams, we can determine the drift velocity vector in the plane transverse to the geomagnetic field and cross check for measurement consistency. With three beams, we can observe the time evolution of features as they drift zonally from one beam to the next. High–resolution measurements are particularly important for investigations of the equatorial electrojet where the polarization electric field can vary rapidly with altitude. The FAR provides measurements that are complementary to those by the PRO–50. The PRO, in fact, is the only equatorial observatory where measurements by a cluster of sensors are made continuously throughout the year.

Research Topics. A number of interesting research topics can be pursued with the PRO. The rapidly growing database in a longitude sector that has not had routine coverage in the past has some obvious but important applications. For example, it can be used to determine the seasonal occurrence patterns for 150–km echoes and F–region backscatter plumes in the central Pacific region. The database can also be used to investigate the day–to–day variability of equatorial spread F as it appears in ionograms and in the form of F–region backscatter plumes, a topic of considerable interest to the National Space Weather Program. The electric field estimates provided by the 150–km echoes can be used to investigate various aspects of electrojet physics, e.g., the nature of the polarization electric field that develops. Moreover, with the ability to measure accurately the equatorial electric field with 150–km echoes, it is possible to evaluate the feasibility of using the mean Doppler velocities associated with electrojet echoes as a means for estimating the equatorial electric field. This kind of evaluation is crucial if we hope to monitor the electric field continuously as a function of time of day because the 150 km

echoes are usually detectable with the PRO–50 only from about 1000 to 1500 local time on some days. We also plan to compare the strength of the 150 km echoes at 50 and 24.5 MHz, if possible, in our continuing efforts to better understand the 150 km echoes.

Research Results and Future Plans. Observations of field–aligned irregularities with the PRO–50 using the three antenna beams have revealed some interesting results. For example, the strength of the 150 km echoes is usually 10 to 15 dB stronger on the 14.3° east and west beams than on the vertical beam; in addition, the 150 km echoes occur most frequently on the west beam. This asymmetry has led us to consider new hypotheses regarding the source of these echoes (Tsunoda and Ecklund, 2000). We are considering options to expand the beam steering capability of the PRO–50 array and to increase the number of off–zenith beams to study the occurrence of the 150 km echoes as a function of zenith angle. Improved steering will also allow us to observe changes in the Doppler spectra as the beam is pointed more along the direction of the irregularity drift. The availability of beams at larger zenith angles would facilitate detection of type 1 echoes, which will allow us to study the effects of the neutral wind at altitudes where type 1 peaks are present. Unwanted sidelobe echoes from the strong electrojet at times make it difficult to cleanly observe the altitude range where weaker 150 km echoes occur. Improved beam steering will include amplitude tapering of the array to significantly reduce unwanted sidelobes.

Kudeki, E., C.D. Fawcett, W.L. Ecklund, P.E. Johnston and S.J. Franke, Equatorial 150–km irregularities observed at Pohnpei, Geophys. Res. Lett., **25**, 4079, 1998.

Tsunoda, R.T. and W.L. Ecklund, On the nature of radar echoes below 95 km during counter streaming in the equatorial electrojet, Geophys. Res. Lett., **26**, 2717, 1999.

Tsunoda, R.T. and W.L. Ecklund, On the nature of 150–km radar echoes over the magnetic dip equator, Geophys. Res. Lett., in press, 2000.

Tsunoda, R.T., R.C. Livingston, J.J. Buonocore, and A.V. McKinley, The frequency–agile radar: A multifunctional approach to remote sensing of the ionosphere, Radio Sci., **30**, 1623, 1995.

Woodman, R.F. and F. Villanueva, Comparison of electric fields measured at F–region heights with 150–km irregularity drift measurements, 9th ISEA Symposium, Bali, Indonesia, 20–24 March, 1995.

Large Scale Structure in the Equatorial Electrojet

FEI LU, D. T. Farley, and W. E. Swartz (all at School of Electrical and Computer Engineering, Cornell University, Ithaca, NY)

We have been studying observations of the equatorial electrojet made using the large Jicamarca VHF radar with very high resolution in altitude (~150 or 300 m) and time (~2 s) over two full days. Doppler spectra, power, and interferometer (single E–W baseline) data are available with this resolution. Most past studies of the electrojet plasma instabilities have focussed on the spectral properties of the echoes, the plasma instabilities responsible for the 3–meter waves, and the behavior of "hot spots" via radar imaging. Here, however, we focus on the larger scale structure shown in simple range–time–intensity plots of the data. In these plots the small–scale structure responsible for the VHF echoes acts as a tracer of the large scale structure, much as does the froth on an ocean wave. The RTI plots show an enormous variety in the structure of the echoing region. One example of such a plot is shown in Figure 1. This are nighttime observations, which always shows much more structure than daytime data because the recombination times are long at night and so dynamical processes dominate chemical ones. In this figure we see kilometer–scale layers that persist in time (slightly below 120 km), layered, periodic structures that move downward with time (between 100 and 105 km), and much thinner layers (95–100 km and mostly between 4.3 and 4.7 hours LT). But in addition to this layering there are obvious rapid variations that are fairly coherent (i.e., nearly coincident in time) throughout the entire echoing altitude range. The periods of these variations range from the order of one minute (see the top edge of the echoing region, for example) down to values of the order of 10 s or so.

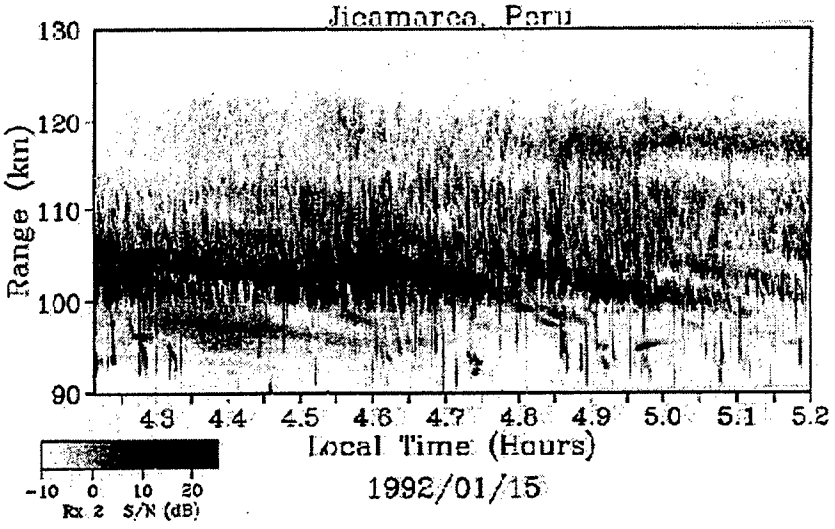


Figure 1. Range–time–intensity plot of nighttime echoes from the equatorial electrojet. Note the fixed layer at the top, the large scale periodic descending structures in the 100–105 km height range, and the very rapid variations that extend in a coherent way throughout the layer.

It seems a bit surprising that it is the short period, not the long period, waves that extend throughout the echoing region, sometimes crossing the more or less stable region at about 115 km.

Plots of power vs. time at a particular altitude (slices through the RTI plot) are very spiky, and so Fourier analysis of these time series does not seem to tell us much about the physics, and certainly leads to no insights regarding the rapid, but coherent, features. At the time of writing we are exploring the use of wavelets in an effort to better quantify what we see, but it is not yet clear how useful these will be. By the time of the Symposium we hope to have studied several different time periods, with RTI plots that look quite different, in an effort to determine why these periods appear so different and what features, if any, they have in common.

Equatorial electrojet effects in the Sudden commencement, Disturbance daily and Storm time variations of geo–magnetic storms.

R.G.RASTOGI,Physical Research Laboratory, Ahmedabad–380009,India.

A magnatic storm is characteristed by a sudden comencement(ssc) with an increase of horizontal field H at all stations in low middle letitude, main phase by a large and repid decrease of the H field finally by recovery phase. The whole history of this storm time. (Dst) variations last about 3–4 days. There is an additional Disturbance daily(SD) variations derived by subtracting the mean daily variations on International Quite days (Sq) from the mean daily variations on the International Disturbed days (Sd). The present paper would describe the results of the observations of H,Y and Z fields at Trivendrum, Kodai kanal,Annamalainagar and Alibag in India, covering a period of 1958 to 1992. Further data from 13 Indian stations togather with the correspondin data from former U.S.S.R. stations provide data form 19 stations situated within of narrow belt of longituteds extending form the magnatic equator to the auroral region.

It is shown that the daily enhancement of the emplitude SSC impluse in H is strong at equatorial station Trivendrum but is distinct even at non equatorial station Alibag. Significant effact of SSC are observed in Y as well as Z fields.The daily varitions of SSC (Z) at Trivendrum is even larger than the corresponding of SSC (H). The letitudinal variations of SSC (H) during the day time shows the well known electrojet effects over the magnatic equator, but during the night time a mild minimum of SSC (H) is seen over the magnatic equator.The SSC impluses in aY field show systemeti variations with time of the dayy and with season emphesizing the effact of the solar disturbance front with the geomegnetic meridian at the station.

The day to day deviation of ΔH decreses with increasing magnatic activity Kp while corresponding ΔY increases with increasing Kp. The factor $\Delta Y / \Delta H$ is very well correlated with the sign of difference between the ground and dipole declaination at the place the disturbance daily variations of Y at low letetudes depends in sign and megnitude on the geo magnetic longitudes of the place.

The disturbance daily variation of H shows a prominant depression at electrojet stations in India around mid day hours besides the down maximum and dusk minimum. No such mid day decrease is seem at Kodai kanal. Further the mid day minimum in ΔH in Indian longitudes shows charectrestics equiratorial elecrojet effects and decreases with increasing distance of the station from the magnatic equator. There is a corresponding mid day intensification of the Disturbance daily variations of vertical field at equatorial stations this elearle indicates that along the Indian longitudes there is a systemetic decrease of the solar daily variations of the equatorial elecrojet current on geomegnetic disturbed days.

The maximum decrease of the H field at the peak of the main phase of the storm

was shown to have a pronounced effect over the megnatic equator.It was suggested that besides the usual equatorial ring current effects during a megnatic storm,a westward electric field is superposed on the ionosphere at low latitudes in Indian sector.

On certain occasion a large decrease of H occures around noon hours at an electrojet stations successively on a number of days.This minimum ΛH moves westward with the Sun and goes round the world for few days,suggesting an anti–Sq current at low latitudes tied to the position of the Sun.

During the storm period when the megnatic sphere is compressed by the solar wind and scalar value B of the interplanetary megnatic field(IMF) is large the fluctuations in the component of IMF perpendicular to the ecliptic (Bz) has an instenteneous large temporary effect in the equatorial electrojet current affecting the H and Z fields al low latitudes and cosing a sudden disappearence

of Esq on the ionograms or with the absense of echoes on the VHF radars.

The high time resolutions observations of Doppler shifts on the back scatter echoes by VHF radars at Thumba,India have shown a close correspondence between SSC (H) with the amplitude and Doppler shifts of the echoed confirming the super positions of an eastward electic field over the equatorial ionosphere during sudden storm commencement.

Latitudinal Study of the Equatorial Electrojet Using a Ship-borne VHF radar: Preliminary results

R. F. Woodman, J. Briceño, J. L. Chau, and M. F. Sarango
Radio Observatorio de Jicamarca, Instituto Geofísico del Perú, Lima

In this work we present the preliminary results of a latitudinal study of the equatorial electrojet (EEJ). The study is based on observations made with a VHF radar on board the Peruvian scientific vessel "Humboldt". The radar has a COCO (Coaxial - Collinear) array of 21m x 24 m (see F igure 1 for a side view of the antenna array and the vessel).

The radar observations have been made south of Lima when the vessel was going to, or coming back from, Antarctica. In addition, a campaign was run when the vessel was performing an oceanic rese arch south of Lima (see Figure 2 for the route followed during this campaign). The Humboldt measurements, when possible, have been complemented with concurrent measurements of the EEJ at the Jicamarca Radio Observatory (JRO) as a control, in order to disc riminate between temporal and spatial characteristics. Two types of EEJ observations were made at JRO: "vertical" and oblique (west of the observatory). In Figure 3, we show an example of the concurrent EEJ measurements made with the Humboldt (top), and Ji camarca (middle and bottom) systems.

In summary, EEJ observations have been made between ~0.65 °N (over Jicamarca) and ~5 °S dip latitude. The data sets taken in this mode are currently being analyzed.

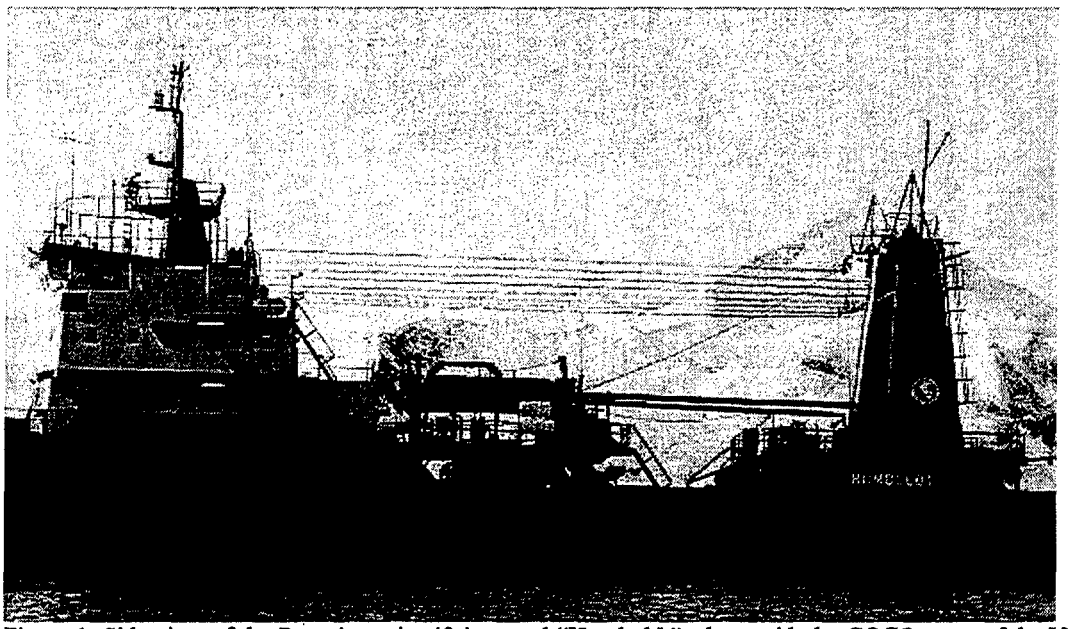


Figure 1. Side view of the Peruvian scientif ic vessel "Humboldt", along with the COCO array of the VHF radar.

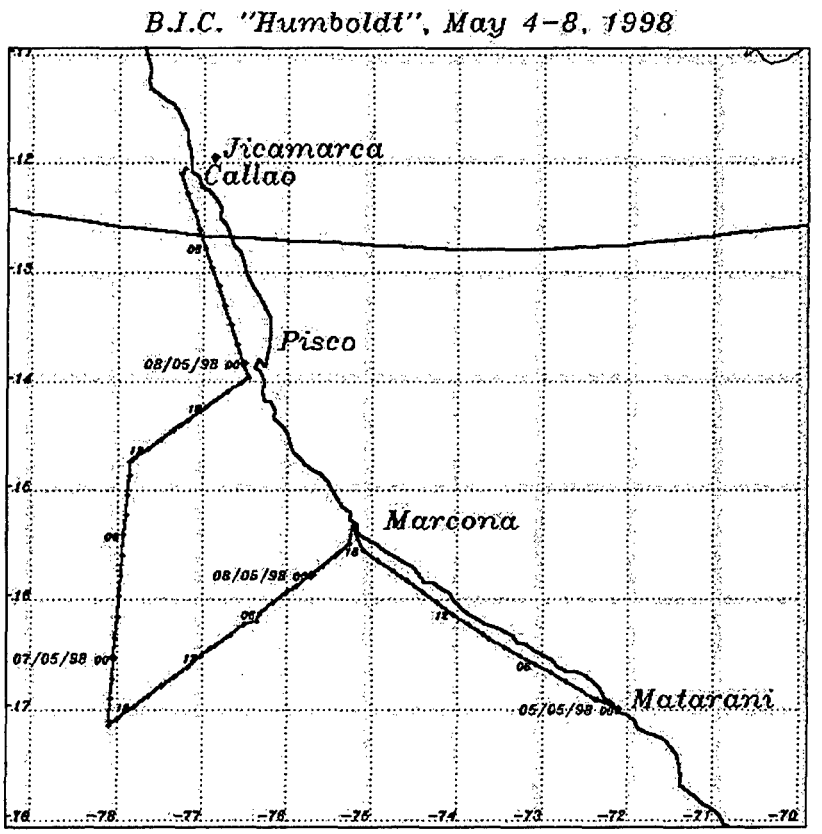


Figure 2. Humboldt route for May 1998 observations. The magnetic equator is denoted with a transverse curve.

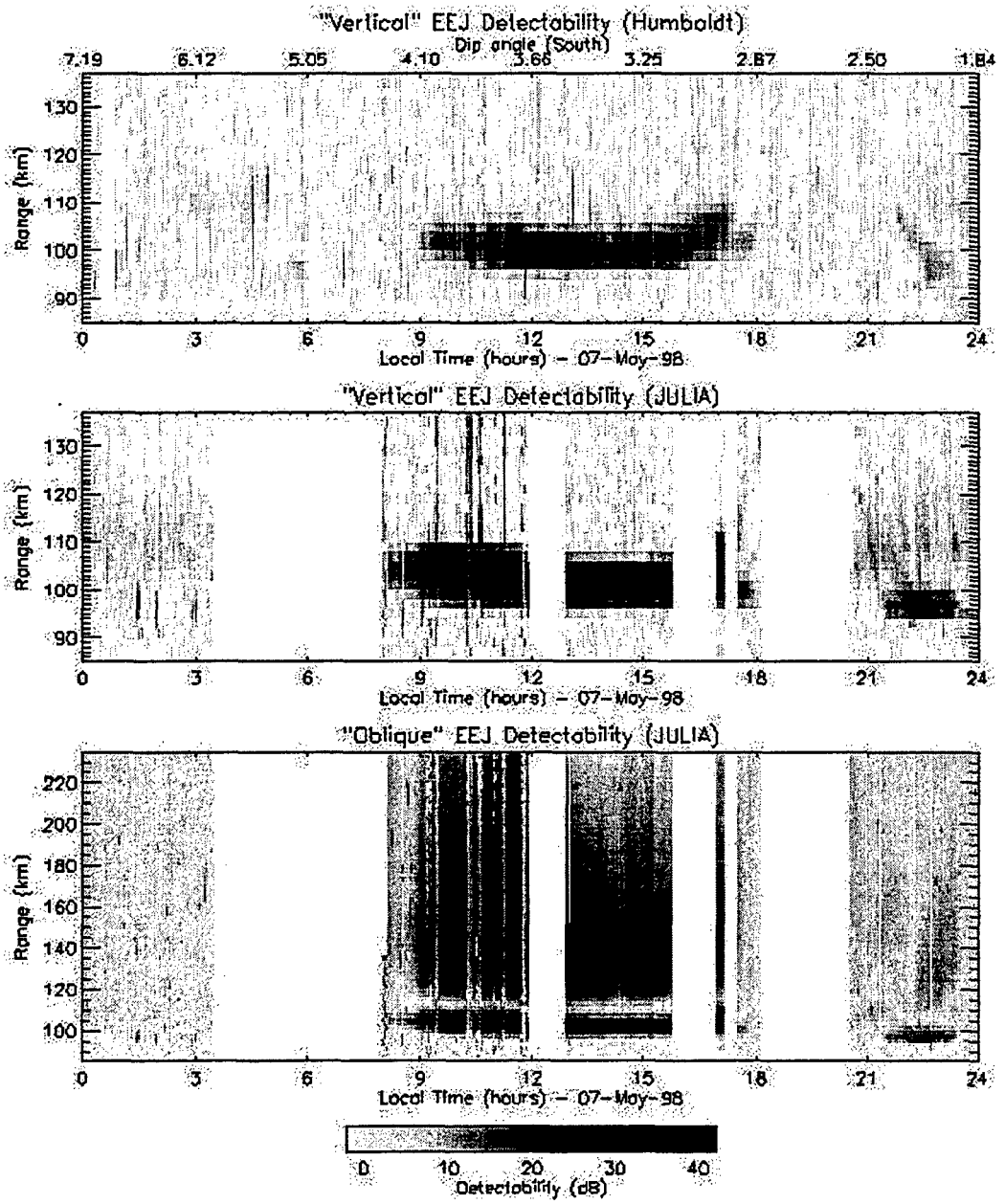


Figure 3. Concurrent observations of the EEJ south of Lima (with the Humbol dt radar) and over Jicamarca (~0.65 °N dip latitude), along with oblique EEJ observations West of Jicamarca (bottom plot).

Field-Aligned Irregularities in the Midlatitude *E* Region: A Review

R. TSUNODA (SRI International, Menlo Park, California, USA)

Chronology

The existence of small-scale field-aligned irregularities (FAI) in the midlatitude *E* region has been known for more than 45 years [*Peterson et al.*, 1955]. Radars operating at frequencies between 9 and 144 MHz have been used to detect backscatter from these FAI, indicating the presence of spatial scales between 1 and 17 m [*Bourdillon et al.*, 1995; *Koehler et al.*, 1997]. These FAI have been shown to occur primarily at night and to be associated with sporadic *E* (E_s), both favoring appearances during local summer months. They have been shown to correlate statistically and on a one-to-one basis.

Interest in FAI in the midlatitude *E* region was ignited by the discovery of quasi-periodic (QP) striations in range-time-intensity plots [*Yamamoto et al.*, 1991]. This behavior resembles the QP variations in mean Doppler velocity associated with radar echoes, which were reported earlier [*Ecklund et al.*, 1981; *Riggin et al.*, 1986]. The growth in interest, however, has grown largely from the realization that the underlying process is anomalously energetic. The presence of anomalous energetics was inferred from the occurrence of the so-called type-1 echoes [*Schlegel and Haldoupis*, 1994] and broad Doppler spectra associated with the so-called type-2 echoes [*Tsunoda et al.*, 1994]. Later, these inferences were validated by rocket measurements of large electric fields [*Nakamura et al.*, 1998; *Pfaff et al.*, 1998; *Yamamoto et al.*, 1998]. With the deployment of radars and their operation from different locations, an interesting variety of features associated with QP echoes was uncovered, all adding fuel to the growing interest in this research topic.

Interpretation of QP echoes has followed observational evidence with general acceptance of the gradient-drift instability as the basic source mechanism. To explain the QP nature of the FAI, *Woodman et al.* [1991] suggested that E_s layers could be modulated in altitude by an atmospheric gravity wave (AGW). *Tsunoda et al.* [1994] suggested that a polarization electric field could develop if the altitude modulation becomes sufficiently extended in altitude. To explain the occurrence of type-1 echoes, *Haldoupis et al.* [1996] suggested that a strip-like E_s region could have a geometry similar to the equatorial electrojet, which would produce a strong polarization electric field. The finding by rocket of an intense velocity shear in the neutral wind has led others to consider seeding and growth in QP properties from the velocity shear in the neutral gas [*Larsen et al.*, 1998].

Status of Understanding

In this review, we will discuss the following topics that arise from our current understanding of FAI in the midlatitude *E* region:

- Size, shape, orientation, and movement of QP striations
- Relationship of FAI to E_s
- Evidence and sources of large electric fields
- Velocity shear
- Continuous and non-QP echoes

References

Bourdillon, A., C. Haldoupis, and J. Delloue, High frequency Doppler radar observations of magnetic aspect sensitive irregularities in the midlatitude *E* region ionosphere, *J. Geophys. Res., 100*, 21,503, 1995.

Ecklund, W.L., D.A. Carter, and B.B. Balsley, Gradient drift irregularities in midlatitude sporadic *E*, *J. Geophys. Res.*, *86*, 858, 1981.

Haldoupis, C., K. Schlegel, and D.T. Farley, An explanation for type 1 radar echoes from the midlatitude *E* region ionosphere, *Geophys. Res. Lett., 23*, 97, 1996.

Koehler, J.A., C. Haldoupis, K. Schlegel, and V. Virvilis, Simultaneous observatiions of *E* region coherent radar echoes at 2–m and 6–m radio wavelengths at midlatitude, *J. Geophys. Res., 102*, 17,255, 1997.

Larsen, M.F., S. Fukao, M. Yamamoto, R. Tsunoda, K. Igarashi, and T. Ono, The SEEK chemical release experiment: Observed neutral wind profile in a region of sporadic *E*, *Geophys. Res. Lett., 25,* 1789, 1998.

Nakamura, M., H. Noda, I. Yoshikawa, and N. Iwagami, DC electric field measurement in the SEEK campaign, *Geophys. Res. Lett., 25*, 1777, 1998.

Peterson, A.M., O.G. Villard, R.L. Leadabrand, and P.B. Gallagher, Regularly observable aspect–sensitive radio reflections from ionization aligned with the earth's magnetic field and located within the ionospheric layers in middle latititudes, *J. Geophys. Res., 60*, 492, 1955.

Pfaff, R., M. Yamamoto, P. Marionni, H. Mori, and S. Fukao, Electric field measurements above and within a sporadic–*E* layer, *Geophys. Res. Lett., 25*, 1769, 1998.

Riggin, D., W.E. Swartz, J. Providakes, and D.T. Farley, Radar studies of long–wavelength waves associated with midlatitude sporadic *E* layers, *J. Geophys. Res., 91*, 8011, 1986.

Schlegel, K., and C. Haldoupis, Observations of the modified two–stream plasma instability in the midlatitude *E* region ionosphere, *J. Geophys. Res., 99*, 6219, 1994.

Tsunoda, R.T., S. Fukao, and M. Yamamoto, On the origin of quasi–periodic radar backscatter from midlatitude sporadic *E*, *Radio Sci., 29*, 349, 1994a.

Woodman, R.F., M. Yamamoto, and S. Fukao, Gravity wave modulation of gradient drift instabilities in midlatitude sporadic *E* irregularities, *Geophys. Res. Lett., 18*, 1197, 1991.

Yamamoto, M., S. Fukao, R.F. Woodman, T. Ogawa, T. Tsuda, and S. Kato, Midlatitude *E* region field aligned irregularities observed with the MU radar, *J. Geophys. Res., 96*, 15,943, 1991.

Yamamoto, M., T. Itsuki, T. Kishimoto, R.T. Tsunoda, R.F. Pfaff, and S. Fukao, Comparison of *E* region electric fields observed with a sounding rocket and a Doppler radar in the SEEK campaign, *Geophys. Res. Lett., 25,* 1773, 1998.

SPORADIC-E LAYERS AND PLASMA INSTABILITIES AT MID-LATITUDES. Some experimental evidence

J.DELLOUE Universite Pierre et Marie Curie, Paris
M. Nicollet de la Grilliere and N. Cavaciuti
Service d'Aeronomie Universite Pierre et Marie Curie, Paris
M.Six Institut de Physique du Globe de Paris
A. Bourdillon Universite de Rennes, Rennes, France

A description based on data collected by a HF radar and two vertical ionosondes is attempted of dynamical events in the E-region at mid latitudes at times of occurrence of field-aligned irregularities.

During SPOREX 98, an experiment conducted around the summer solstice of 1998, a HF radar located near Valensole (43,8 deg N;6,1 deg E) in South Eastern France operated on four frequencies (9.0, 12.5, 14.9, 17.1 MHz) and five adjacent beams 2 degrees in width at 15 MHz in the general direction of magnetic North in order to detect field-aligned irregularities in the E-region at night over the Grenoble area (45.5 deg N; 5.95 deg E) 170 km north of Valensole

At the same time two vertical ionosondes were operated near Grenoble under the ionospheric volume scanned by the radar. A common transmitting antenna omnidirectional in azimuth and radiating in a fairly broad cone centered around the vertical,thus allowing for the observation of oblique echoes was used for both ionosondes. Signals reflected or scattered by the ionospheric layers were received on two pairs of loops spaced by 50 m and oriented respectively in N.S and E.W directions thus providing direction of arrival measurements capabilities.

One of the ionosondes was a Canadian Advanced Digital Ionosonde (CADI) with great flexibility of operation and near real-time capabilities of data monitoring. Built-in pre-processing of data prior to recording which saves storage place but precludes further access to raw data and a rather poor resolution in range (6 km) are limitations that cannot be overcome. Ionograms were run each minute between 1 and 8 MHz and 6 fixed frequencies (2.1 2.4, 2.7, 3.0, 3.3, 3.6 MHz) were sampled successively in the intervals between ionograms.

Processing of data provided by CADI is detailed in a companion poster. Among other results sporadic E layers most likely distorted by gravity Waves were observed to move over the site from various directions

The second ionosonde was a laboratory model, named R4F, with a resolution in range of 2-3 km and digital recording of raw data without any pre processing. R4F thus provides much more detailed informations than CADI but at the price of much heavier processing. Ionograms from 1 to 8 MHz were run each minute and 4 fixed frequencies (1.2, 2.4, 3.1 and 5.5 MHz) were sampled successively in the intervals between ionograms.

Experimental evidence is shown that two Sporadic E-layers incoming from different directions at different heigths cross over the ionosonde site at times when the HF radar detects field-aligned irregularities over the same area. Complex short-lived stratifications and rapid transient plasma flows can be seen on the ionograms as well as on fixed frequency profiles.

Non-local Theory of Mid-latitude E-region Plasma Instabilities

J. M. Rosado-Román (now at University of Puerto Rico, Mayaguez), W. E. Swartz, D. T. FARLEY, and C. E. Seyler (all at School of Electrical Engineering, Cornell University, Ithaca, NY)

Echoes from mid-latitude E-region plasma instabilities have been observed from Puerto Rico at times when the Arecibo incoherent scatter radar shows no evidence of tilted structure due to gravity waves in the E region. We have developed a non-local model of the instability that accounts for the crucial role played by shorting effects along inclined (the dip angle at Arecibo is about 50°) magnetic field lines. A sample calculation for a thin Gaussian shaped layer with a gradient length of 500 m and an electric field of 3 mV/m (pretty strongly driven conditions) shows that waves will in fact grow on the expected side (the side that would be unstable with equatorial geometry) of the layer, *in spite of the shorting effects*. For these conditions the fastest growing mode has a wave-length of about 20 m. At substantially longer wavelengths, the waves couple to the stable side of the layer and are damped. Waves with much shorter lengths are damped by diffusion.

The growing mode is confined mainly to the top or bottom of the layer, which means that it can be thought of as consisting of a spectrum of plane waves with **k**-vectors pointing nearly, but not exactly, perpendicular to the magnetic field. The mean angle and the angle of the largest amplitude component are slightly off perpendicular.

An interesting aspect of the theory is that it predicts that the density and electric field perturbations should maximize at slightly different altitudes, with the field perturbations being farther from the layer peak, where the electron densities are lower. This prediction could be tested by rocket measurements, but so far there seems to be no convincing evidence one way or the other.

For numerical reasons, the calculation ignores the always destabilizing effect of ion inertia, and so we have underestimated the growth rates somewhat, especially in the strongly driven case. Therefore we cannot study type 1 irregularities without modifying the theory, but it seems clear that they would be confined to one side of the layer for the same reasons that the type 2 waves are.

50 MHz CONTINUOUS WAVE INTERFEROMETRY OBSERVATIONS FROM THE UNSTABLE MIDLATITUDE E-REGION IONOSPHERE

Christos Haldoupis and Anastasios Kamburelis (Physics Department, University of Crete, Iraklion, Crete, Greece, email: chald@physics.uoc.gr, tlf:+30-81-394222, Fax: +30-81-394201), Kristian Schlegel (Max-Planck-Institut für Aeronomie, Lindau, Germany), and Alain Bourdillon (Laboratoire Radiocommunications, Univerité de Rennes 1, Rennes, France)

The radar interferometer technique, which has been applied in the past years to studies of short wavelength plasma turbulence in the earth's ionosphere, can provide, in addition to the Doppler spectrum, estimates of the mean size, mean angular position, and transverse velocity of localized unstable regions in the plasma. Here we describe the conversion of SESCAT (Sporadic E SCATter experiment, a bistatic 50 MHz continuous wave (CW) Doppler radar located in the island of Crete, Greece) to an interferometer that is capable to investigate short term dynamics of backscatter regions in the midlatitude E region ionosphere with mean transverse sizes as small as a couple of kilometers. The first results show that SESCAT, which provides high quality spectra and excellent temporal resolution, has its measurement capabilities enhanced significantly when operated as interferometer. In this paper we will present and discuss results of azimuthal SESCAT interferometry for typical midlatitude echoes, that is, type II echoes having broad spectra at small mean Doppler velocities, and for another spectral signature characterized by very narrow spectra at small Doppler shifts. In addition we will present examples of uncommon type I echoes characterized by large line-of-sight velocities due to elevated electric fields. In the latter case, the cross-phase changes with time indicate rapid zonal movements of backscatter, presumably due to neutral winds, having at times velocities as high as 150 to 180 m/s, that is, well above typical neutral wind velocities at midlatitude. Finally, an effort is made to interperet the interferometry findings within the framework of our present theoretical understanding.

Paper for oral presentation at:
10th International Symposium on Equatorial Aeronomy (ISEA)
Antalya, Turkey, May 16-24, 2000.
Session 6: Midlatitude E-Region Irregularities and Related Phenomena

Recent results of MU radar observations of mid-latitude E region field-aligned irregularities

T. OGAWA (Solar-Terrestrial Environment Lab., Nagoya Univ., Toyokawa, Japan)
K. Nozaki (Communications Research Lab., Tokyo, Japan)
M. Yamamoto and S. Fukao (Radio Atmospheric Science Center, Kyoto Univ., Uji, Japan)

The 46.5-MHz middle and upper atmosphere (MU) radar at Shigaraki, Japan has been a very powerful tool to study the 3.2-m scale mid-latitude E region field-aligned irregularities (FAI) associated with sporadic E layers (Es). Since detailed characteristics of quasi-periodic (QP) and continuous radar echoes observed in summer with the MU radar were first reported by Yamamoto et al. (J. Geophys. Res., 1991), similar echoes (in particular, QP echoes) have also been found at low- and mid-latitude regions other than Japan. This paper briefly introduces previous MU radar observations of FAI, and then presents recent results including some new findings. We also give a working model to explain the FAI generation causing QP echoes.

We conducted MU radar observations of FAI associated with Es in the summer of 1999. Simultaneous observations of the E region were made by using the following instruments; (1) an FM-CW sounder (FCS), located at 130 km north of the MU radar site, to observe reflection heights of HF radio waves of 3 and 4.5 MHz with a time resolution of 2 min and a height resolution of 1 km and (2) a routine ionosonde at the MU radar site to scale Es parameters such as foEs and fbEs. The MU radar beam was perpendicular to the geomagnetic field at the 100 km height just over the FCS location. The Es activity was very strong from 1900 LT on August 16 to 0800 LT on August 17, 1999. The results and implications from this multi-instrument study are as follows:

1. FAI occurrence and strength are strongly dependent on the difference between foEs and fbEs (i.e., foEs-fbEs) while they are poorly correlated with foEs. It is known that electron density distribution in an Es is not always uniform but structured. When structured, fbEs represents electron density of background Es while foEs does that of locally enhanced density region. Then foEs-fbEs can be a measure indicative of the strength of electron density gradients within Es. Our results clearly indicate that FAI is enhanced with increasing foEs-fbEs, suggesting that FAI generation is closely related to the localized density-gradients in Es.

2. Quasi-periodic (QP) radar echoes were very active before midnight. The heights where QP echo intensities are maximal correspond well to the Es heights determined from the FCS soundings. This suggests that the strongest irregularities coexist with Es, being a very reasonable result. However, the height variation of the QP echoes (100-130 km) is different from that of the Es height variation (103-113 km) observed by the FCS. This fact means that existing models for QP echo occurrence, which require a deep modulation of Es height comparable to height extent of QP echoes (30 km in our case), are not applicable to our case. We propose a new working model to explain our results in which polarized electric fields originated from the gradient-drift instability occurring around localized regions within an Es are mapped upward to some extent along the geomagnetic field to produce relatively weak irregularities above the Es through the combined action of these fields and in-situ density gradients.

3. Typical "continuous" echoes appeared below 100 km after sunrise. New finding from the current observations is "morning QP echoes" (MQE) that occurred below 100 km just after the subsidence of the continuous echoes; until now MU radar QP echoes have been believed to occur above 100 km for the period from sunset to midnight. At present we don not know the generation mechanism(s) of these continuous and MQE echoes. There seems no physical relation between Es and the irregularities responsible for these echoes since Es heights after sunrise are always higher than 100 km.

Detailed electrodynamics to produce the mid-latitude Es irregularities as observed by the MU radar is very complicated and still unknown. In the future we need more sophisticated simultaneous observations of Es plasma and Es irregularities in addition to neutral wind motions and atmospheric gravity waves. Simulation works are also highly necessary.

Large scale E-region electric field structure due to gravity wave winds

L. J. GELINAS, M. C. Kelley (Dept. of Electrical Engineering, Cornell University, Ithaca, NY)

M. F. Larsen, D. Hysell (Dept. of Physics, Clemson University, Clemson, SC)

An in-situ measurement of mid-latitude E-region electric fields and neutral winds by two consecutively flown sounding rockets has provided an excellent data set to study electric field perturbations due to neutral winds. The two rockets were launched on the night of February 19, 1998 from Puerto Rico as part of the Coqui II campaign. The Sporadic Atom Layers sounding rocket (SAL), launched at 8:09 LT with the mission of characterizing the electrodynamics and chemistry of sporadic sodium layers (Na_s), was instrumented with a set of orthogonal electric field probes, Langmuir, impedance and DC plasma probes. Altitude profiles of zonal and meridional mesospheric neutral winds were determined from a TMA release rocket launched 30 minutes later. Horizontal structure of localized short wavelength gravity waves was revealed by ground-based airglow images.

The DC electric field measured by the SAL rocket shows a strong correlation with the neutral wind profile, indicating that the local ionospheric parameters are influenced by neutral atmospheric motions. The eastward and north-up components (perpendicular to **B**, assuming zero parallel electric field) of the SAL electric field data on the rocket upleg and downleg trajectory are plotted vs. altitude in Figs. 1 and 2. There is a pronounced large-scale vertical fluctuation in the electric field corresponding to a vertical wavelength of 21 km. Considering the horizontal motion of the rocket across the region, the electric field profiles agree with a horizontal structure with wavelengths of approximately 15 km eastward and 40 km northward.

The neutral wind profile derived from the TMA release trail is shown in Fig. 3. The vertical wavelength of the meridional wind structure is 21 km, identical to the vertical wavelength of the electric fields in Figs. 1 and 2. A localized gravity wave with horizontal wavelengths (15 km eastward, 40 km northward) similar to the measured electric field structure was recorded by the ground-based airglow imager. We attribute the meridional winds of

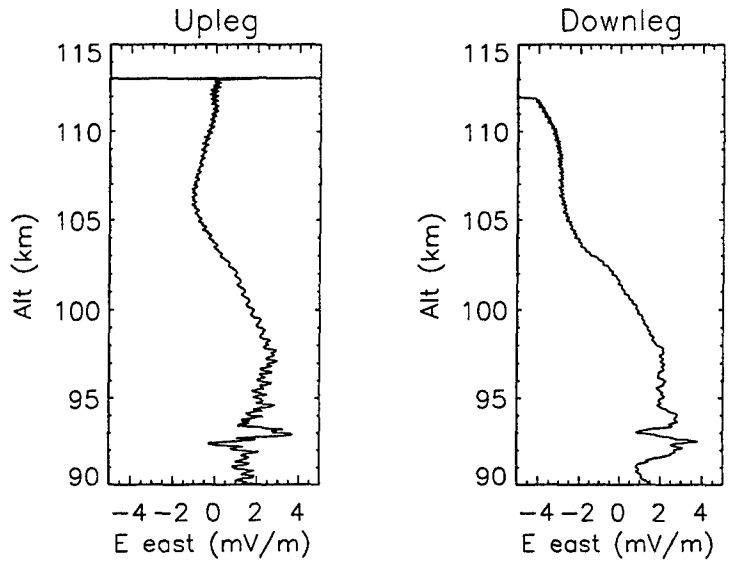


Figure 1: Eastward component of SAL electric field.

Fig. 3 to this short horizontal wavelength gravity wave. We believe that the zonal winds of Fig. 3 are large horizontal scale neutral winds unrelated to the observed electric field structure; a long-lived plasma layer located at the convergent node of the zonal winds supports this assumption.

Electric field structures similar to those measured on SAL were were also observed during the SEEK campaign at higher altitudes, presumably mapped from below along the magnetic field lines (Pfaff, GRL *25*, 1998). Farley (JGR *64*, 1959) described electric field mapping, and found that large scale waves should map for long distances along the field lines. Following the method proposed by Farley, we assume a spatial form for the perpendicular (to **B**) electric field induced by the gravity wave winds, and solve for the amplitude and parallel component of the electric field satisfying $\nabla \cdot \mathbf{J} = 0$. In this case we consider electric fields inside the "source region", where the current varies with altitude according to the neutral wind profile, including a "source term" describing the motion of ions in the neutral wind. The solution to this simplified analytical equation adequately describes the amplitude of the observed perpendicular electric field, and also predicts a small

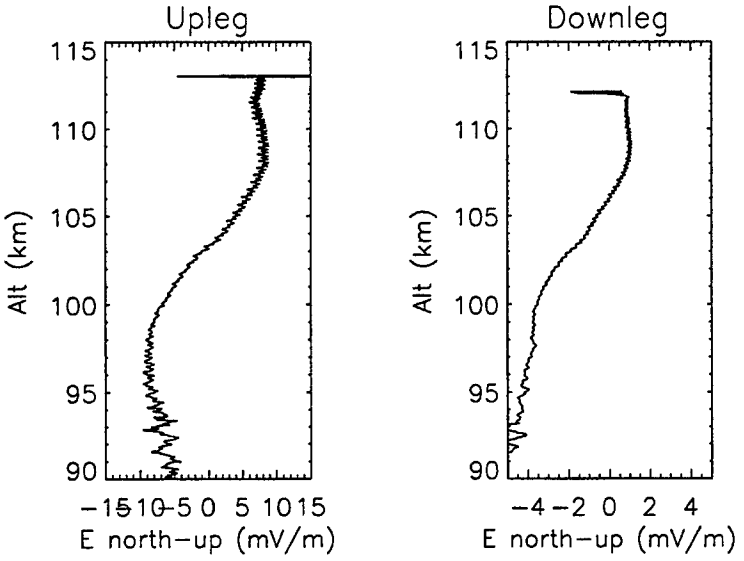


Figure 2: North-up (perp B) component of SAL electric field.

(0.5 mV/m) parallel electric field with the same wavelength characteristics as the gravity wave wind field. In addition, we compare this analytical result with 3-D simulations of the ionospheric potential due to a localized gravity wave packet.

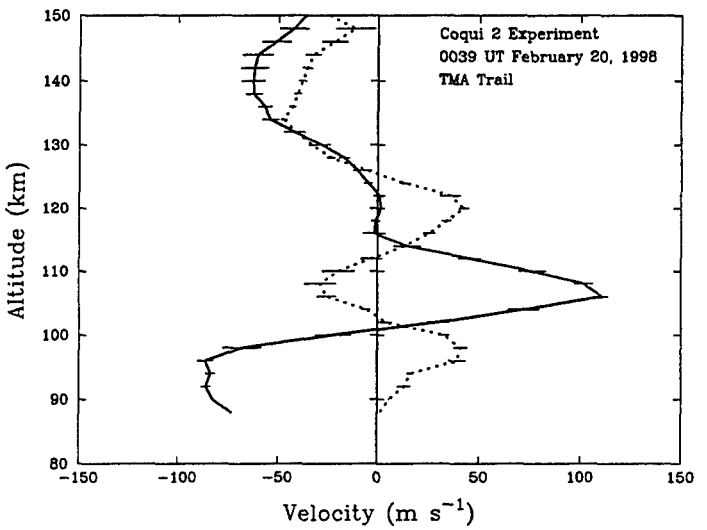


Figure 3: Zonal (solid line) and meridional (dotted line) neutral wind profile from TMA release rocket.

Long period variations in midlatitude E region coherent radar backscatter and sporadic E layers. Evidence for a relation with planetary waves

C. HALDOUPIS, Physics Department, University of Crete, Iraklion, Greece
M. Voiculescu, Physics Department, University of Galati, Galati, Romania
D. Pancheva, The Department of Physics, University of Wales, Aberystwyth, UK
S. Shalimov, Institute of Physics of the Earth, Moscow, Russia

The interest in the study of midlatitude *E* region coherent backscatter phenomena, which exist in close connection with E_s layers, has grown remarkably in recent years. The research has focused so far on a variety of topics that include the investigation of morphological features, the relation to E_s layers, the Doppler spectrum properties, the instability mechanisms, the electrodynamics of the plasma, the generation of large polarisation electric fields, the characteristics of pronounced periodicities in backscatter and the effects of neutral atmospheric motions, particularly the role played by gravity waves. The possible relationship with planetary waves (PW) is the latest topic added to the list.

The latter was hinted by recent studies of long term variations in the unstable midlatitude E region ionosphere which suggested that PW may play a role in coherent backscatter occurrence (Tsunoda et al., 1998; Voiculescu et al, 1999) and the formation of strong sporadic E layers, E_s (Voiculescu et al, 1999; Shalimov et al., 1999). These studies are the latest to report large-period wavelike effects on midlatitude ionospheric plasma processes most likely caused by neutral atmospheric oscillations of global scale, that is, planetary waves, which are known to exist in the mesosphere and lower thermosphere (MLT). Planetary waves are large scale quasi-periodic oscillations in temperature, wind, density and pressure with periods near 2, 5, 10 and 16 days, which affect atmospheric dynamics and ionospheric processes in the region between 80 and 150 km (*Forbes,* 1996).

The recent evidence presented by *Tsunoda et al.* [1998] and *Voiculescu et al.* [1999], about a possible link of backscatter occurrence with travelling planetary waves, is quite intriguing and opens a new dimension in the research of the unstable midlatitude *E* region ionosphere and its interaction with the neutral atmosphere. In

particular, the results reported by *Voiculescu et al.* [1999], which suggested that PW may contribute in the formation of strong sporadic *E layers*, introduced a new option into the long-going research of sporadic *E* layer phenomena. Given the close dependence of midlatitude backscatter to strong E_s, a physical understanding of the relation between E_s and PW could also help explain the long term periodicities seen in backscatter occurrence. A first step in this direction was made by *Shalimov et al.* [1999], who tried to formulate the PW role on strong E_s production. They presented a simplified model based on the notion of ion-converging properties of horizontal wind sears associated with regions of positive vorticity within a zonally propagating planetary wave (for details see presentation by Shalimov et al., session 6 of ISEA-10).

Obviously, the postulation of PW effects on the midlatitude *E* region ionosphere is an attractive new element into the physics of the relevant phenomena, which demands for additional research, both experimental and theoretical. In particular, it is important that the existence of this PW relationship is substantiated further by means of additional experimental evidence. The present paper aims in serving this purpose.

In this work, measurements of midlatitude *E* region coherent backscatter obtained during four summers with Sporadic E Scatter experiment (SESCAT), a 50 MHz Doppler system operating in Crete, Greece, and concurrent ionograms from the same ionospheric volume obtained with a CADI (Canadian Advanced Digital Ionosonde) for one of these summers, were used to analyse the long-term variability in echo and E_s occurrence. Power spectrum analysis showed dominant spectral peaks in the range of 2-9 days, the most commonly observed periods appearing in two preferential bands, 2-3 days and 4-7 days. No connection with geomagnetic activity was found. The characteristics of these periodicities compared well with similar properties of planetary waves, which suggested the possibility that planetary waves were responsible for the observed long-period quasi periodic variations. In addition, these findings indicated a likely close relation between planetary wave activity and the well known but not well understood seasonal E_s dependence.

To test the PW postulation, we used simultaneous neutral wind data from the mesopause region around 95 km, measured from Collm, Germany. Direct comparison of the long-term periodicities in echo and and strong E_s layer occurrence with those in the neutral wind show some reasonable agreement. An example of this comparison is illustrated in Figure 1.

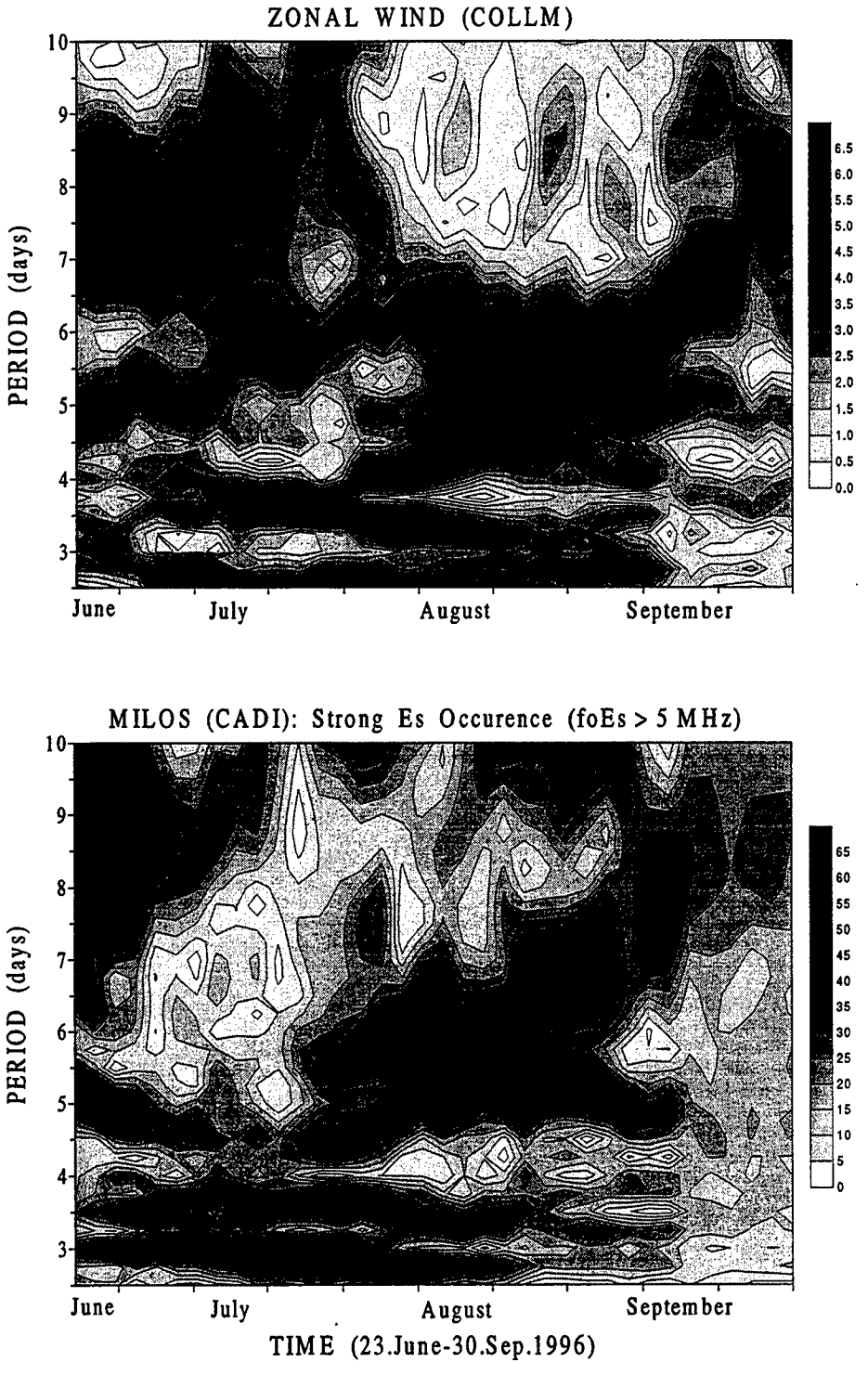


Figure 1. Simultaneous PTI (Period-Time-Intensity) spectrograms of strong sporadic E layer occurrence (bottom panel) observed with a CADI in central Aegean, Greece, and the zonal neutral wind component (top panel) at about 95 km height measured from Collm, Germany.

Figure 1 shows the concurrent spectrograms of strong sporadic E layer occurrence measured in Milos, Greece and the zonal neutral wind near 95 km measured in Collm, Germany from June 19 to September 30, 1996. The CADI specrtogram shows a 5-day wave band at the beginning of the interval, which also exists in the zonal wind, whereas a 7-8 day periodicity is also present in both PTI plots up to middle of July. This activity is followed by periodicities in the 2- to 4-day period band existing in both spectrograms throughout July and first part of August. The second half of this summer interval is characterised in both time sequences by longer period variations, mostly in the 5- to 7-day band which become rather dominant after about middle of August. In addition, a clear tendency is evident in both PTI plates for the periods to increase as time progresses from mid July to the end of September, when finally a 7- to 8-day periodicity dominates both phenomena. Overall, we can state that there is a good deal of similarity between the prevailing periodicities in both phenomena. This comparison is supportive of a PW role in E_s formation.

The new evidence presented in this paper, although not fully conclusive, is the first direct indication in favour of a planetary wave role on the unstable midlatitude E region ionosphere. This suggests that planetary waves is a viable option and a new element into the physics of midlatitude E_s layers that needs to be considered and thoroughly investigated.

References.

Forbes, J. M., Planetary waves in the thermosphere-ionosphere system, *J. Geomag. Geoelectr., 48,* 91, 1996.

Shalimov, S., C. Haldoupis, M. Voiculescu, and K. Schlegel, Midlatitude E region plasma accumulation driven by planetary wave horizontal wind shears, *J. Geophys. Res., 104,* 28207, 1999.

Tsunoda, R. T., M. Yamamoto, K. Igarashi, K. Hocke, and S. Fukao, Quasi-periodic radar echoes from midlatitude sporadic E and role of the 5-day planetary wave, *Geophys. Res. Lett., 25,* 951,1998.

Voiculescu, M. C. Haldoupis, and K. Schlegel, Evidence for planetary wave effects on midlatitude backscatter and sporadic E layer occurrence, *Geophys. Res. Lett., 26,* 1105, 1999.

A new mechanism for midlatitude E region plasma accumulation driven by planetary wave horizontal wind shears

S.SHALIMOV (Institute of Physics of the Earth, Moscow, Russia), C.Haldoupis (Physics Department, University of Crete, Iraklion, Greece), M.Voiculescu (Physics Department, University of Galati, Galati, Romania), and K.Schlegel (Max-Planck-Institut fuer Aoronomie, Katlenburg-Lindau, Germany)

Recent experimental studies of the unstable midlatitude E region ionosphere suggested that planetary waves (PW) could play a role in coherent radar backscatter occurrence (*Tsunoda et al.,* 1998; *Voiculescu et al.,* 1999) and the formation of strong sporadic E layers (*Voiculescu et al.,* 1999). Here we present a new idea and a simple formalism on the role played by planetary waves in midlatitude E_s production. A new mechanism is proposed for large-scale plasma accumulation of metallic ions in the midlatitude E region ionosphere driven by PWs in the lower thermosphere. The main idea relies on the ion-converging properties of large-scale horizontal wind shears which accompany regions of positive vorticity, or cyclonic motion, within a zonally propagating planetary wave. Conceptually, the proposed model is similar to the well-nown wind shear mechanism of E_s formation, but with the geometry "turned on its side".

It is widely accepted that the mechanism responsible for midlatitude E_s is the wind shear theory introduced first by *Whitehead,* [1961]. In this model, a mainly east-west neutral wind that changes with height can provide a vertical wind shear which, having the correct sense and under the action of the Lorentz force, can redistribute and accumulate long-lived metallic ions into a thin layer. For a given vertical wind shear, this mechanism is expected to be more effective in an area where the plasma density is enhanced than in an area of low plasma concentration. Taking this into consideration we introduce the idea of plasma accumulation in areas of positive vorticity of a PW under the action of the vertical component of the magnetic field, therefore, conditions for E_s production in these areas would optimize.

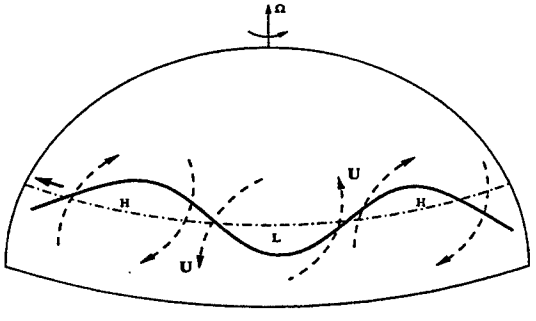


Figure 1. Visualization of a westward travelling planetary wave

A travelling planetary wave, depicted in Figure 1 in agreement with the visualization given by *Holton* [1982], is characterized by air rarefactions (lows) and compressions

(highs) accompanied, under conditions of geostrophic balance, by a cyclonic and anticyclonic vortex in the wind field and thus regions of positive and negative vorticity, respectively. This means that PW are associated with large-scale wind shears in the horizontal plane because of the cyclonic and anticyclonic vortices.

Figure2 shows a horizontal shear in the wind associated with the cyclonic vortex of an elliptically polarized PW. Since ion-neutral collision frequency exceeds the gyrofrequency, $\nu_{in} > \Omega_i$ at lower E region heights, the ions drift along with the neutral velocity $\mathbf{U}$ but in this way also experience a Lorentz force, $\frac{\Omega_i}{\nu_i}(\mathbf{U} \times \mathbf{B}$, which deflect them at an angle to the wind velocity. Given the vertical magnetic field component $B_z = -B \sin I$ at a midlatitude location of a dip angle I, ions are forced to move horizontally and converge inward in areas of cyclonic motion where the vortivity is positive, whereas they diverge outward in anticyclonic areas of negative vorticity. As for the electrons, they are strongly magnetized ($\Omega_e >> \nu_{en}$), therefore they are unaffected by the neutral wind and move along the field lines to neutralize the space charge set up by the ion motion. Under these conditions, the horizontal motion of the ions in the PW configuration of Figure1 leads to plasma accumulation inside the cyclonic vortices and plasma depletion inside the anticyclonic vortices.

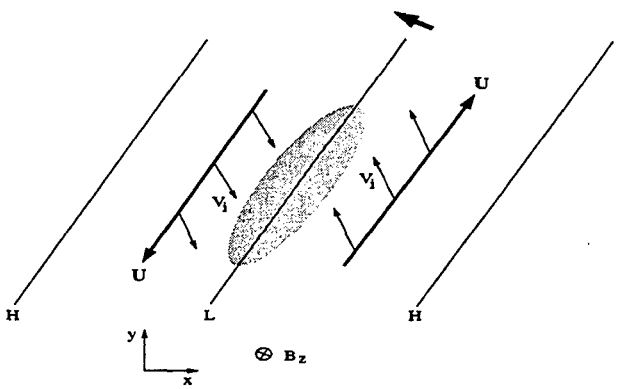


Figure 2. Plasma convergence produced by cyclonic winds within a planetary wave

As said, the situation described above and illustrated schematically in Figure 2 is similar to the well-known vertical wind shear mechanism of sporadic E layer formation, but with the geometry being now in the horizontal rather than the vertical plane. There are, however, important differences between the two cases which relate to the characteristic scales involved, in both space and time. For example, the vertical wind shears, which are often associated with gravity waves, have characteristic scales much smaller than the horizontal wind shears associated with planetary waves. As shown quantitatively by Shalimov et al. [1999] and will be explained in this presentation, the large scales associated with planetary waves play the key role in the overall effect of the PW plasma accumulation process because they help reduce plasma diffusion. In particular, because of the long times required for ambipolar diffusion, the new mechanism can lead to significant plasma accumulation inside large horizonatl areas in the midlatitude E region, thus acting as complementary to the vertical wind shear process so that strong sporadic E layers

can form more efficiently and frequently.

The present model provides a physical base for understanding the long-term periodicities in occurrence but also the seasonal dependence of strong sporadic E layers at midlatitude. Although this dependence is well established experimentally, is not yet understood since it is completely inexplicable from the wind shear theory of E_s formation and remains one of its weakest points (e.g., see *Whitehead*, 1989). Our mechanism provides a basis for explaining the E_S morphology without discrediting the vertical wind shear process. This is supported by the PW climatology published in the literature, which shows clearly that the overall PW activity maximizes during summer e.g., see *Jacobi et al.*, 1998; *Müller and Nelson*, 1978). This is particularly true for PW with periods in the range from 2 to 3 days, known as quasi two-day waves (QTDW), which represent the strongest component in the PW spectrum. Also, the quasi 5-day waves with period in the range from 4 to 7 days, have week maxima in early summer and in August, although there are years when they prevail during the entire summer as well.

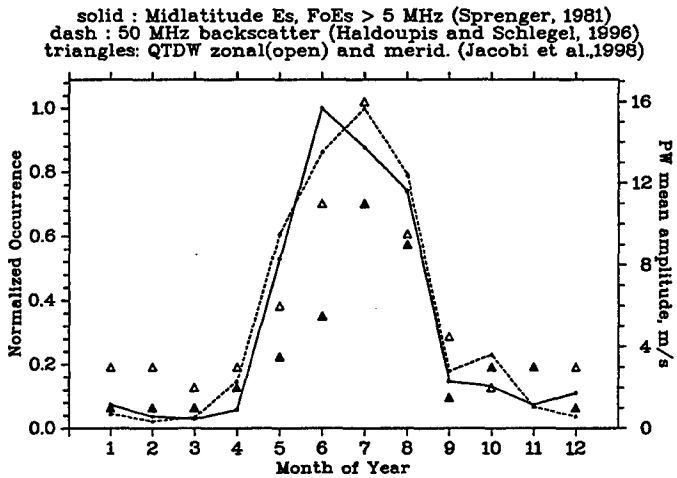


Figure 3. Seasonal dependences superimposed for comparison. See text for details

Figure 3, which is based on published results, emphasizes the apparent proximity in the seasonal dependences between strong E_s layer occurrence (from *Sprenger*, 1981), midlatitude coherent backscatter at 50 MHz (from *Haldoupis and Schlegel,* 1996), each normalized to its maximum and identified by the solid and dash lines, respectively, and the seasonal variation of the QTDW mean amplitude marked in Figure 3 by open (zonal wind component) and solid (meridional wind component) triangles (from *Jacobi et al.,* 1998). Based on the predictions of our mechanism, the good agreement betweent all seasonal dependences shown in Figure 3 is maybe a reasonable indication in support of the postulation on the role played by planetary waves in the occurrence of strong sporadic E layers at midlatitude. We need to stress, however, this model is the simplest possible and there is need for further

theoretical development to study time varying effects, as well as the effects of the ambient electric field for the more general case of an elliptically polarized cyclonic vortex acting on both the vertical and horizontal magnetic field components.

List of References

Haldoupis, C., and K. Schlegel, Characteristics of midlatitude coherent backscatter from the ionospheric E region obtained with Sporadic E Scatter Experiment, *J. Geophy. Res., 101*, 13,387, 1996.

Holton, J.R., *An Introduction to Dynamic Meteorology*, Academic, San Diego, Calif., 1982.

Jacobi, Ch., R. Schminder, and D. Kurschhner, Planetary wave activity obtained from long-period (2-18 days) variations of mesopause region winds over cenrtral Europe (52° N; 15° E), *J. Atmos. Sol. Terr. Phys., 60*, 81, 1998.

Muller, H. G., and L. Nelson, A travelling quasi 2-day wave in the meteor region, *J. Atmos. Terr. Phys., 40*, 761, 1978.

Shalimov, S., C. Haldoupis, M. Voiculescu, and K. Schlegel, Midlatitude E region plasma accumulation driven by planetary wave horizontal wind shear, *J. Geophys.Res., 104*, 28,207, 1999.

Sprenger, K., Diurnal and seasonal variations of occurrence of sporadic E-layers over central Europe, *Gerlands Beitr. Geophys., 25*, 305, 1981.

Tsunoda, R.T., M. Yamamoto, K. Igarashi, K. Hocke, and S Fukao, Quasiperiodic radar echoes from midlatitude sporadic E and role of the 5-day planetary wave, *Geophys. Res. Lett., 25*, 951, 1998.

Voiculescu, M., C. Haldoupis, and K. Schlegel, Evidence for planetary wave effects on midlatitude backscatter and sporadic E occurrence, *Geophys. Res. Lett., 26*, 1105, 1999.

Whitehead, J.D., The formation of the sporadic E layer in the temperate zones, *J. Atm. Terr. Phys., 20,* 49, 1961.

Inferred Vertical Ion Drifts Associated with Intermediate Layers Observed by Arecibo Observatory

G. D. Earle (University of Texas at Dallas), R. L. BISHOP (University of Texas at Dallas), and S. Collins (Cornell University)

The El Coqui II sounding rocket campaign took place in Puerto Rico during February and March of 1998. During the campaign the Arecibo ISR provided daily ground–based support for the launches. The data obtained during this period provide an excellent resource for studying intermediate/descending layers over Arecibo, because the focus of the rocket campaign was the E region and upper mesosphere. During late February to early April the radar was operational and supporting the campaign for about 35 nights, and descending layers in the E–region were observed on 33 of these, or roughly 94% of the time.

Figure 1 shows a gray–scale plot of ISR data taken shortly after sunset on March 22, 1998. The figure shows layer altitude and plasma density versus time, with the gray–scale level indicating the density. A single intermediate layer begins to form and descend shortly after sunset, and the descent continues over a period of several hours. The relatively smooth descent is occasionally punctuated by intervals when slight upwelling occurs. The descending layer gradually approaches the altitude of sporadic–E layers, with which they sometimes merge in the early morning hours (Shen *et al.*, 1976). The rate of descent for layers above Arecibo is initially quite fast, about 35–50 km/hour. This rapid descent slows rather abruptly to approximately 5 km/hour once the layer drops below 135 km. The descent is continuous; there are no intervals

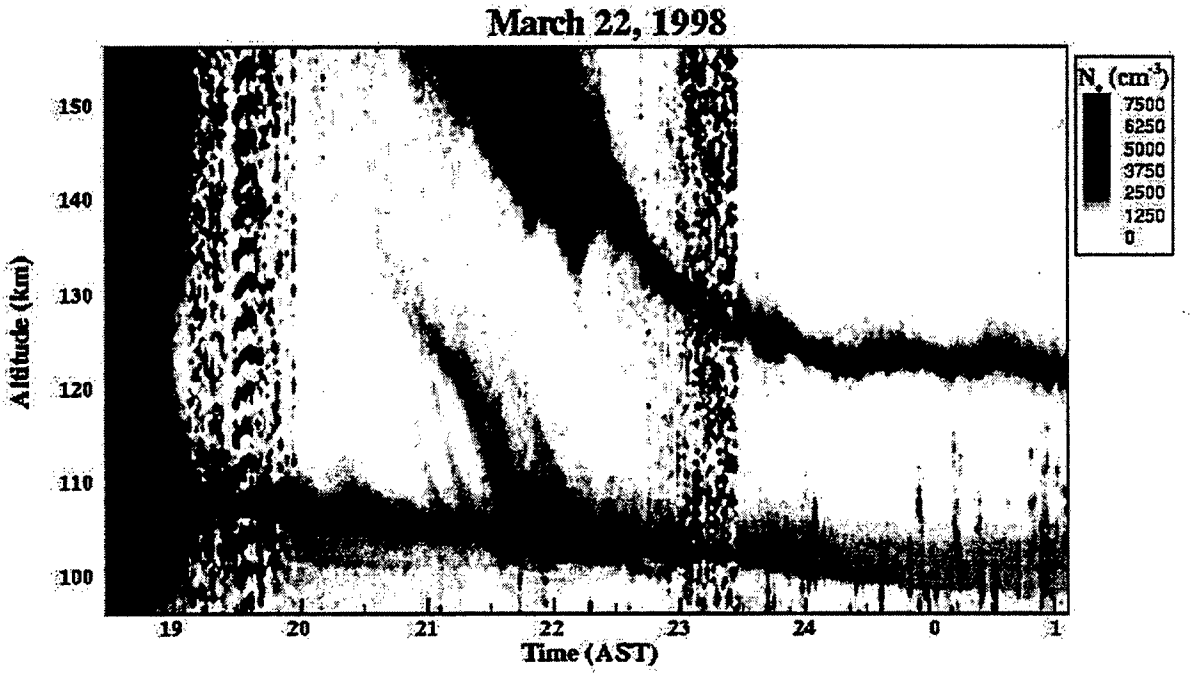


Figure 1.

in which the layer disappears from view. These trends are generally considered the norm for intermediate layers over Arecibo, largely because of their similarity to the earlier observations by Shen *et al.* (1976) and Mathews *et al.* (1993). It is shown here to establish a baseline against

which to compare data from other nights, when a wide range of variability is observed in the behavior of the descending layers.

Figure 2 shows an example of a very different layer event over Arecibo in March 1998. The local time interval plotted in Figure 2 is the same as Figure 1. Despite the similar times and dates of the observations the behavior of the descending layer is quite different in Figure 2. The most obvious difference is that the night shown contains a sequence of two layers appearing in rapid succession, rather than a single event. This succession of layers form at about the same initial altitude over a period of a few hours, and initially they behave much like the layer in Figure 1. The first layer in Figure 2 fades away just before local midnight, at about the same time as the second layer approaches its altitude. Fifteen minutes later this second layer experiences a strong upwelling that lasts for over thirty minutes. The layer disperses somewhat during this excursion, but later converges again and continues to descend.

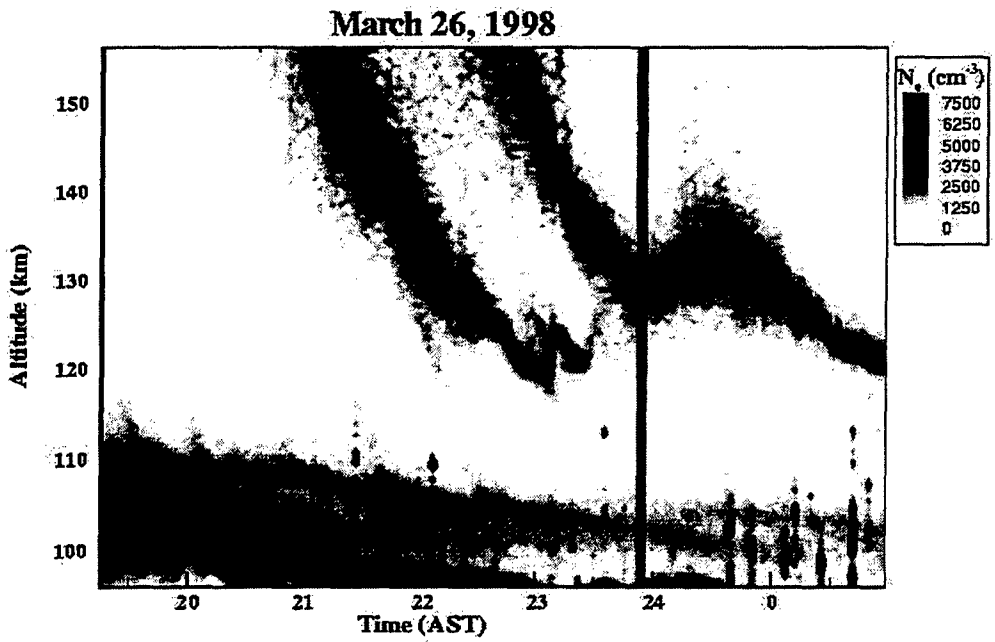


Figure 2.

Another fairly common event over Arecibo during March 1998 was the abrupt disappearance of descending layers. Over our two–month database spanning late February to early April it actually occurs much more frequently than the "typical" behavior shown in Figure 1. The number of layers observed on any one night, the interval between successive layers, the altitude at which they fade out, and the concurrent behavior of higher and lower altitude layers during the fade out are all variable during these events. However, the overall morphology of the layers themselves is similar in all cases.

Previous studies focussed on the normal behavior of the layers, including their composition, the periodicity of their appearance, or the wind fields associated with their gradual descent from the bottomside F–region to altitudes of about 110 km. We contrast these characteristics with ISR evidence of anomalous layer behavior, including short–lived intermediate layers that abruptly disappear midway through their descent. The causes of this behavior are investigated, including the effects of diffusion and recombination. We evaluate the relative importance of several mechanisms to explain the abrupt disappearance, and we calculate

the vertical ion drifts and meridional wind profiles that are consistent with the observed behavior.

Acknowledgments. The authors thank the staff of the Arecibo Observatory for their assistance in obtaining and archiving the data used in this study. This work was partially supported by NASA grant NAG5–5086.

References

Mathews, J.D., Y.T. Morton, and Q. Zhou, Observations of ion layer motions during the AIDA campaign. *J. Atmos. Solar Terr. Phys.*, 55, 447, 1993.

Shen, J.S., W.E. Swartz, D.T. Farley, and R.M. Harper, Ionization Layers in the Nighttime E–region Valley Over Arecibo, *J. Geophys. Res.*, 81, 5517, 1976.

Explaining Mid–latitude E–region Plasma Instabilities

D. T. FARLEY (School of Electrical Engineering, Cornell University, Ithaca, NY)

Since the 1960s much effort has been devoted to understanding the plasma instabilities in the equatorial and auroral E regions. The basic physics of the instabilities for these regions is now pretty well understood, although there is much still to be learned about the nonlinear saturated state. It was not until the early 1980s, however, that we learned that similar instabilities occur in the mid–latitude E region, albeit less frequently. After the discovery, however, little or nothing was written about the theory and interest in the phenomenon seemed to wane. Only in the 1990s have we seen a surge of interest in these instabilities, and several efforts have been made to try to explain them.

Questions. There are two major questions to deal with: (1) What causes the basic instability, in spite of the shorting (damping) effect of the inclined magnetic field, and (2) what causes the quasi–periodic (QP) structure that is often (but not always) seen? This talk will deal mainly with the first question.

There is a lot of evidence that suggests that the mid–latitude instabilities are closely related to the equatorial and auroral instabilities, i.e., that the gradient–drift and (occasionally) two–stream mechanisms play an important role. We know that the instabilities are closely associated with thin nighttime layers of metallic ions (sporadic–E layers). These layers have very sharp vertical gradients and are often "patchy" in the horizontal dimensions. The long standing theoretical problem has been how to deal with the fact that the inclined **B** field couples the unstable side (top or bottom, depending on the wind and/or electric field) with the opposite, stable side. Experiments show that the irregularities are highly aligned with the magnetic field, so that perturbation electric fields that try to grow on one side of the layer should be shorted out on the other.

Special geometry? In recent years there have been several attempts to get around this problem by invoking very special layer geometry, caused perhaps by gravity waves, whereby the electron density gradients become perpendicular to the magnetic field, or nearly so. This idea has gained some acceptance, especially since no other explanation has been put forward, but this explanation seems to me to have two serious arguments against it. First of all it is quite contrived, since the layer perturbations have to be quite large (several kilometers vertically) and the geometry has to be just right. Secondly, and more importantly, there seems to be no direct evidence that these perturbations actually occur, and in fact recent observations at Arecibo show that the plasma instabilities can occur when incoherent scatter radar (ISR) observations of the sporadic–E layer itself show no sign whatsoever of undulations. So if we can't expect the layers to line up properly with the magnetic field, what *is* the explanation? How does nature avoid the shorting effects?

Non–local theory. The explanation, I believe, is described in the 1999 Cornell PhD thesis of J. Rosado–Román (unpublished elsewhere as yet, but discussed in another talk at this Symposium). If one does a full non–local calculation that searches for unstable modes that are not exactly plane waves, one finds that there are indeed such modes that are linearly unstable. These modes are nearly plane waves and have phase fronts that are

nearly–but not quite–aligned with **B**. Not surprisingly, the unstable modes are confined mostly to the unstable (for equatorial geometry) side of the layer, with only a small amplitude extending into the stable side. Such waves have relatively short wavelengths (a few tens of meters or less), thereby reducing the top–to–bottom coupling, and so the waves have to be pretty strongly driven to overcome diffusive damping. But the key point is that *no special layer geometry with respect to the magnetic field is required.* The theory assumes a thin, uniform horizontal layer.

Strong driving forces? The fact that the instability occurs only when it is strongly driven raises another major question: The mid–latitude E region normally has moderate electric fields and moderate wind velocities, and so where do these strong driving forces come from? Often the strong drivers simply are not there; sporadic–E layers are very common at night (they are almost always seen on Arecibo ISR profiles), but the VHF radar echoes from the plasma instabilities are much less frequent. But sometimes the drivers are able to generate even type 1 waves, which need electric fields of the order of 10 mV/m or more, a field much larger than mid–latitude dynamo electric fields.

I believe the answer to the puzzle of the drivers is related to the patchy nature, for which there is lots of evidence, of most sporadic–E layers. If we have a highly conducting patch surrounded by a region of lower conductivity, an applied electric field and/or horizontal wind can induce a much larger (by a factor approaching the ratio of the Hall to Pedersen conductivity) horizontal electric field, via exactly the same mechanism that produces a large vertical polarization field at the magnetic equator. Since this amplification factor can be of the order of ten or so, there is no fundamental problem in generating the large drivers.

Current closure. But there is still one last hurdle. If we have a completely isolated patch, no horizontal currents can flow, which means that additional polarization fields build up, canceling out the induced Cowling field. Put another way, it is the electron drift velocity that drives the instability, not an electric field or wind, and so if there is no current because the patch is surrounded by an insulating medium, there will be no instability. There has to be some way to close the currents induced in our patch if it is to be unstable. The current can close either in the F region or elsewhere in the E region. All that is required is that $\mathbf{E} + \mathbf{U}\times\mathbf{B}$, where **U** is the neutral wind velocity, be significantly different in the two regions. The E– and F–region winds will almost always be different, but we might have to worry about the conductivity in the intervening valley region for this type of closure. In any case, we know that there are sometimes strong wind shears (horizontal and/or vertical) in the E–region wind, and that is all we need.

QP echoes. Finally, just a few thought on QP echoes. The observed period of oscillation of these is sometimes long enough to suggest that gravity waves might be involved, but there is now considerable radar data showing QP signatures with periods much too short for gravity waves. Is it possible that these short periods are electromagnetic in origin, something like the large–scale structure seen at the equator? This is just a speculation at this point, but it seems worth thinking about.

Effects of Neutral Gas Motions on Midlatitude E Region Irregular Structure

Ludmila Kagan
(Radiophysical Research Institute (NIRFI),
25 B.Pecherskaya St., Nizhny Novgorod 603600, Russia, e–mail:
kagmil@nirfi.sci–nnov.ru)

Recently developed intensive experimental and theoretical studies on midlatitude backscatter have shown an extremely important role of neutral gas dynamics (including both relatively short and long–term variations) in E–region plasma structuring. Neutral wind activity affecting midlatitude backscatter includes a regular wind, gravity waves and even tidal modes and planetary waves. The neutral wind approach allows to create a consistent physical model without invoking any other instability source like traditionally considered imposed electric fields and to explain both sporadic–E associated and Es–independent backscatter. Despite a lots of work has been done in this direction during last three years, there are still some open issues as, for example, affection of the neutral turbulence on the sporadic–E structure and possible influence of the Es structure on the backscatter type.

High Resolution MU Radar Observations of Large–Scale Waves in the Lower E–Region

S. Fukao, P. B. Rao, M. Yamamoto, A. Uchida, and I. Hassenpflug

Radio Science Center for Space and Atmosphere
Kyoto University, Uji, Kyoto 611–0011, Japan

Abstract

The MU radar was operated with high range and time resolutions of 150 m and 10 s for a few days in February 2000 to investigate specifically the large–scale (kilometer–scale) waves in the midlatitude E–region over Shigaraki (34.9N, 136.1E). The observations show evidence for the excitation of the large–scale waves, which are seen for the first time in the lower E–region over an altitude range of about 92 to 97 km. The height–time–intensity (HTI) maps show that the large scale structures have vertical wavelengths of the order of about 1 to 2 km and quasi–periods of few tens of seconds. The range rates are found to vary over +/– 20 m/s. The Doppler velocities are found to be in the range of about –50 m/s to 20 m/s and show significant height–time variations. The velocity spectral widths are found to be of the order of 100 to 150 m/s. These characteristics seem to resemble closely to that observed over the equatorial and low latitudes, although differ quantitatively in some respects. Finally, the observations are discussed in the light of the current understanding of the large scale plasma turbulence in the lower E–region.

———

Shoichiro Fukao fukao@kurasc.kyoto–u.ac.jp

30 MHz radar interferometer observations of midlatitude *E* region irregularities

D. L. HYSELL and J. D. Burcham

Dept. of Physics and Astronomy, Clemson University, Clemson, South Carolina, 29634, USA

1. Introduction

The Clemson University 30 MHz radar was used to observe coherent scatter from the midlatitude *E* region ionosphere throughout the summer of 1999. The radar is a Doppler interferometer designed mainly to study plasma instabilities and irregularities associated with sporadic *E* layers. Of particular interest are the irregularities which produce the so-called quasi-periodic (QP) echoes first observed over Japan almost a decade ago. However, since it began operation in the summer of 1998, the radar has observed a variety of other remarkable phenomena, including type I radar echoes. Here, we present our latest experimental results and discuss their theoretical implications.

In this paper, we examine interferometric observations of QP echoes made during a NASA sounding rocket experiment. We implement an in-beam imaging technique that permits us to visualize the scattering structures underlying the echoes. Three principle findings are presented. 1) The striations can be interpreted as the signatures of spatially-localized targets drifting horizontally. The slant ranges of the echoes and the intensity of the echoes versus range are precisely what would be expected for quasi-point targets with finite aspect angle sensitivity. 2) The spatially-localized targets are distributed essentially randomly in range and azimuth and do not appear to be organized along wavefronts, as might be expected if the phenomenon were gravity wave induced. The drifts of the targets undergo semidiurnal variation. 3) The large electric fields (~10-20 mV/m) measured *in situ* and implied by the existence of type I echoes can be produced without gravity wave deformation of the underlying sporadic *E* layer. Polarization electric fields naturally arise in patchy sporadic *E* ionization layers so long as the layer is elongated and the electrostatic coupling between the *E* and *F* region is strong.

2. Experiment Description

Our radar is located near Clemson University (34.7°N, 82.8°W, 46.7°N geomagnetic) and operates at 29.795 MHz. It nominally uses two solid-state transmitters which deliver 4 kW of peak power each at a duty cycle of up to 15%. Each transmitter is connected to an array of four five-element Yagi antennas which together form an interferometer with a magnetic east-west baseline. A third array composed of a single Yagi antenna is situated so as to form an isosceles triangle with the other two. This antenna affords two additional interferometry baselines with components parallel to the magnetic meridian. A diagram of the antenna, which indicates the sub-array separations in wavelengths, is show in Figure 1. During the experiments in question, we usually transmitted a 28-bit Barker coded pulse with a baud length of 1.9 km. The pulse repetition frequency was 250 Hz, which for a 30 MHz radar implies a maximum Nyquist Doppler velocity of ±625 m/s.

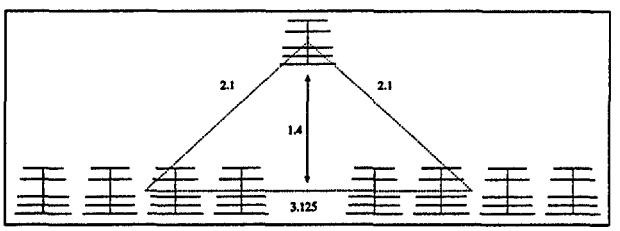


Figure 1. Layout of the interferometer antenna array. The array's main beam is directed toward magnetic north.

3. Quasi-Periodic Echoes

Radar observations were typically made between 0100-0800 UT (UT=LT+4 hrs). Echoes were most prevalent between 0130 and 0530 UT, when the likelihood of occurrence at any given time was essentially uniform at just over 50%, but were observed as early as 0100 UT and as late as 1030 UT. Virtually all of the echoes seen were of the quasi-periodic variety. Some of these were also accompanied by layers of diffuse backscatter.

A dramatic example of QP echoes is presented in range-time-intensity (RTI) format in Figure 2. In this example, quasi-periodic echoes were visible over a period of more than three and a half hours without interruption. The thin striations have range rates from 25–130 m/s, periods of a few minutes, and range separations from 5–15 km. The lifetimes of individual striations vary from 1–15 minutes. QP echoes like these tend to occur in slowly descending layers. This figure is considerably busier than many of the early QP echo observations, and we can find instances when 8 or 9

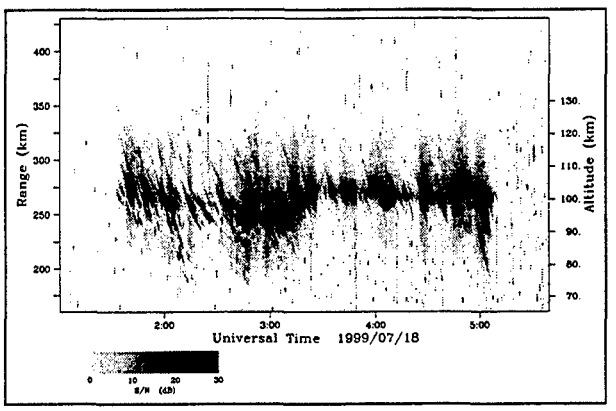


Figure 2. Range time intensity plot depicting a QP echo event.

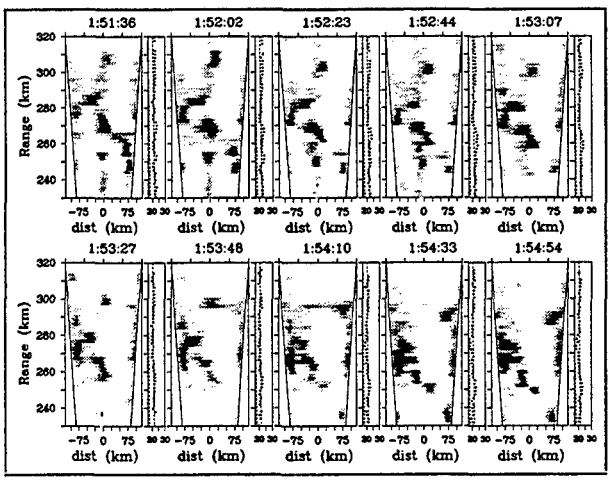


Figure 3. In-beam radar images of irregularities underlying the QP echoes. The axes of the figures represent range and azimuth.

striations are present simultaneously. This event is similar to the one presented by *Tsunoda et al.* [1999] which also exhibited a high multiplicity of simultaneous striations. Such events may cast doubt on the correspondence between striations and individual, thin, tilted sporadic *E* ionization layers.

3.1. In-beam Radar Images

We have used Capon's method to compute three- dimensional images of the QP echoes in range, azimuth, and zenith from our interferometry data [*Capon*, 1969]. There being no simple way to present three- dimensional datasets in a journal, we then integrated out the zenith angle dependence and plotted the reduced brightness distribution as a function of azimuth angle and range. Examples images are presented in

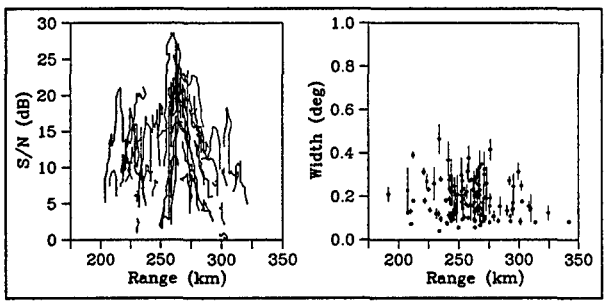


Figure 4. Aspect angle sensitivity analysis of the QP echoes. The panel on the left shows the range-intensity histories of a subset of the QP echoes. From these can be inferred the aspect angle half widths of the underlying scatterers, which are plotted in the panel on the right.

Figure 3. Each image covers azimuth angles between ± 20°, converted here to a transverse distance scale. The plots depict the signal-to-noise ratio in dB in grayscale format. The incoherent integration time for the analysis is 10 s. Beside each image is a narrow plot showing the first moment average elevation angle of the backscatter in degrees as a function of range. The dashed line at larger (smaller) angles represents the elevation angle we would expect assuming perfectly field-aligned backscatter from the main beam (from the secondary sidelobes) propagating along straight lines.

What Figure 3 and numerous other images like it demonstrate is that underlying each QP echo on the RTI map is a spatially localized, drifting scattering patch. In this particular example, there are times when 8 or 9 discrete patches are visible at once. Over time, the patches can be seen to drift toward the radar, exhibiting the negative range rates that give QP echoes their tilts. Patches form, drift for a time, and then vanish, sometimes in as little time as a minute. Longer-lived patches can linger for up to a quarter hour. As is typically the case, these patches drift westward at speeds comparable to their range rates. Viewing animated sequences of such images reveals that neighboring patches drift at somewhat different velocities from one another.

3.2. Aspect Angle Sensitivity

Along with the effects of azimuth angle and refraction, the finite aspect sensitivity of field aligned echoes also decouples their range and altitude. We moreover argue that the aspect sensitivity of the echoes is the key to interpreting the striations in RTI diagrams like Figure 2. Seeking to demonstrate this, we implemented a computer algorithm that identifies and analyzes individual striations and keeps track of their coordinates and intensities. The algorithm detected 280 striations in the RTI plot for July 18. Figure 4 shows

the results of a particularly revealing analysis. In the left panel are plotted the signal-to-noise ratios of individual striations versus range. (Curves for only one quarter of all the striations are plotted here to keep down clutter.) As the QP echoes appear, move toward the radar, and ultimately disappear, their signal strengths pass through maxima. Different striations maximize at different ranges and give rise to approximately parabolic curves in this figure.

Now suppose the echo intensity varies with aspect angle according to

$$I = I_o \exp\left(-\theta^2/2\sigma^2\right) \quad (1)$$

where θ is the angle the radar wavevector makes with the geomagnetic field and σ is the RMS half width of the wavevector distribution. In that case, we can determine σ by fitting parabolas to the curves in Figure 4 and then converting from range width to aspect angle width using the appropriate geometric transformations. We have performed such an analysis to produce the plot on the right side of Figure 4, which depicts the RMS aspect angle half width inferred from the time histories of the striations. Only data points with error bars less than 0.2° are shown. Values range mainly between 0.1 and 0.4° with the largest value being 0.5°. For comparison, a target with an aspect angle half width of 0.5° is attenuated by 30 dB when probed at an angle of ±1.85° off perpendicular. For a target drifting meridionally at a constant 100 km altitude, this excursion of angles corresponds to a 50 km excursion in range.

Kudeki and Farley [1989] measured the aspect sensitivity of plasma irregularities in the equatorial electrojet using long-baseline radar interferometry. They found RMS aspect angle half widths in the range between 0.1 and 0.4°. The agreement between the low-latitude measurements and our estimates supports our conjecture that QP echoes reflect the presence of horizontally drifting, spatially localized scatterers with finite aspect sensitivity. If so, then the range rates of the QP echoes are mainly indicative of the meridional drift of the scatterers.

4. Type I Echoes

Figure 5 shows Doppler spectra computed from echoes associated with a very dense sporadic E layer. In the range gates between 190 and 194 km, the spectra shift out to large negative frequencies and take on first moment Doppler shifts between -250 and -320 m/s (denoting propagation away from the radar). The event lasted for approximately two minutes, during which time the patch of echoes in question approached the radar with a range rate of approximately 40 m/s. In these respects, the event is quite similar to the one reported on by *Huang and Chu* [1998] and observed with the

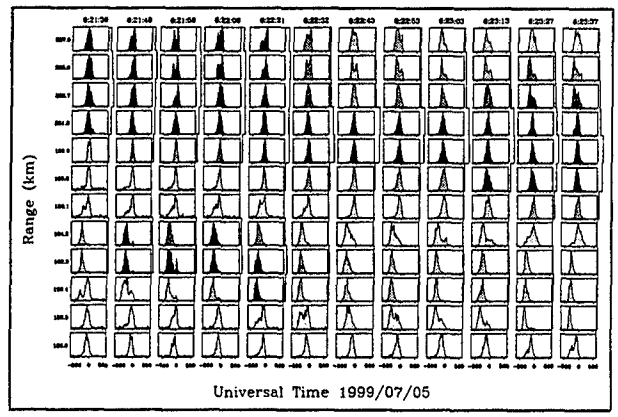


Figure 5. Doppler spectra indicating the presence of type I irregularities.

Chung-Li VHF radar. The range of Doppler shifts seen here is also similar to that described by *Schlegel and Haldoupis* [1994].

Haldoupis et al. [1997] explain the anomalously large electric fields required to excite type I echoes at midlatitudes by appealing to the same mechanism that generates large polarization fields and Hall currents in the equatorial E region. The situation at midlatitudes is somewhat different, however. Suppose a localized electron density enhancement associated with a patchy sporadic E layer is exposed to a meridional electric field imposed from above by the F region dynamo. Where zonal conductivity gradients exist, zonal polarization electric fields will arise to maintain a solenoidal current. The magnitude of the polarization electric field will be greater than he background meridional field by as much as the ratio of the Hall to the Pedersen conductivity, depending on the efficiency. Consequently, a strong Hall or Cowling current will begin to flow. However, because the layer has a finite extent in the meridional direction, and because the Cowling current necessarily has a vertical flow component at mid latitudes, the Cowling current cannot close in the E region. It may however close in the F region if the electrostatic coupling is good enough. Another way of saying this is that the conductivity in the F region can short out charges that would otherwise accumulate and impede the flow of the Cowling current in the E region.

Why should the Cowling current close in the F region if the original Hall current set up by the background meridional field did not? It is well known that the electrostatic coupling between the E and F regions is a strong function of the transverse scale size of the potential structures that map along **B** [*Farley*, 1959]. If the sporadic E layer is elongated in the meridional direction, then it is possible for meridional polarization electric fields in the E region to be shorted out

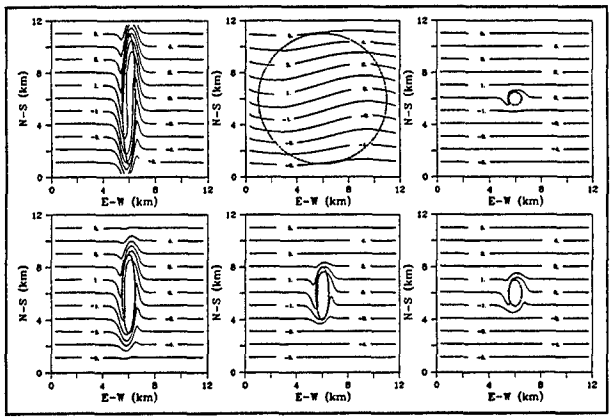


Figure 6. Cuts through the 3D simulation volume showing equipotentials associated with polarized, elongated *E* region ionization irregularities.

by the *F* region while the zonal polarization electric field is not. The critical size that must (must not) be exceeded in the meridional (zonal) direction is approximately 1 km. An analysis of the polarizing of elongated *E* region ionization patches was performed by *Shalimov et al.* [1998].

We can illustrate the process by numerically evaluating the quasineutrality condition $\nabla \cdot \mathbf{J} = 0$, where

$$\mathbf{J} = (\sigma_P \hat{b} \times -\sigma_H)(\mathbf{E} \times \hat{b}) + \sigma_o(\mathbf{E} \cdot \hat{b})\hat{b}$$

where $\hat{b}$ is a unit vector in the direction of the geomagnetic field and σ_P, σ_H, and σ_o are the Pedersen, Hall, and parallel conductivities. The model (2) has been written in discrete form and solved computationally with a multigrid method. Iteration takes place on an 80x80x360 grid with grid spacing of 150 m and with dimensions of 12x12x54 km on a side. The simulation volume includes altitudes between 80 and 134 km. A southward electric field of 1 mV/m is imposed from the top of the model. Model conditions were set appropriately for a time of local midnight in midsummer during moderate solar flux conditions. For a sporadic *E* layer, we consider a Gaussian ellipsoid with a centroid altitude of 97 km and a half-width of 1 km in the vertical direction. The peak density in the layer is $2 \times 10^{11}\text{cm}^{-3}$. The transverse dimensions of the ellipsoid can be varied to gauge the effect on the resulting polarization field.

The results of six model runs are shown in different panels in Figure 6. In the first panel on the top row, the sporadic *E* layer is given Gaussian half-widths of 250 m and 2.5 km in the zonal and meridional directions, respectively. The panel on the top left of Figure 6 shows equipotential curves in a horizontal plane representing a cut through the model at 97 km altitude. We can see that the layer has become strongly polarized in the zonal direction and that the background electric field has been rotated within and amplified by a factor of approximately 10 over background. The equipotentials can be interpreted as streamlines along which the magnetized electrons flow. A strong meridional Hall current is indicated by the bunched equipotentials at the center of the layer. Given an equatorward background electric field, the electrons carrying the Cowling current will drift poleward. This explains why the Doppler shifts of QP echoes are mainly consistent with waves propagating away from the radar.

More elongated sporadic *E* layers are conducive to the generation of stronger polarization electric fields, as are higher peak plasma densities. So is a stronger background dynamo field. Seasonal average St. Santin radar data show that a 2 mV/m equatorward dynamo field is typical for postmidnight hours in June solstice *Richmond et al.* [1980]. Extreme values can of course be much larger. This model therefore has no trouble accounting for occasional 20 mV/m polarization electric fields in sporadic *E* layers.

References

Capon, J., High-resolution frequency-wavenumber spectrum analysis, *Proc. IEEE, 57*, 1408, 1969.

Farley, D. T., A theory of electrostatic fields in a horizontally stratified ionosphere subject to a vertical magnetic field, *J. Geophys. Res., 64*, 1225, 1959.

Haldoupis, C., D. T. Farley, and K. Schlegel, Type-1 echoes from the midlatitude *E*-region ionosphere, *Ann. Geophys., 15*, 908, 1997.

Huang, C. M., and Y. H. Chu, First observations of type-1 sporadic *E* irregularities in the equatorial anomaly region using the Chung-Li VHF radar, *Geophys. Res. Lett., 25*, 3779, 1998.

Kudeki, E., and D. T. Farley, Aspect sensitivity of equatorial electrojet irregularities and theoretical implications, *J. Geophys. Res., 94*, 426, 1989.

Richmond, A. D., et al., An empirical model of quiet-day ionospheric electric fields at middle and low latitudes, *J. Geophys. Res.*, p. 4658, 1980.

Schlegel, K., and C. Haldoupis, Observation of the modified two-stream instability in the mid latitude *E* region, *J. Geophys. Res., 99*, 6219, 1994.

Shalimov, S., C. Haldoupis, and K. Schlegel, Large polarization electric fields associated with midlatitude sporadic *E*, *J. Geophys. Res., 103*, 11,617, 1998.

Tsunoda, R. T., J. J. Buonocore, A. Saito, T. Kishimoto, S. Fukao, and M. Yamamoto, First observations of quasi-periodic radar echoes from Stanford, California, *Geophys. Res. Lett., 26*, 995, 1999.

On the role of neutral wind shear instabilities in seeding quasi-periodic structures in sporadic E

M. F. Larsen
Department of Physics, Clemson University, Clemson, South Carolina

Quasi-periodic echoes with periods in the range of a few minutes to approximately 10 minutes have been found to be a common feature of midlatitude sporadic E since their discovery at the MU radar in Japan in the early 1990's. There are only a handful of direct measurements of the neutral winds in connection with the occurrence of sporadic E layers, but a consistent feature of all the observed profiles is that the ionization layers were found to be embedded in large shears that were either unstable or marginally unstable in the Richardson number sense. Estimates of the neutral wind shears based on rocket measurements of electron density profiles or incoherent scatter radar measurements have also suggested that unstable shears are common characteristic of sporadic E layers. The possible role of shear instabilities and the associated Kelvin-Helmholtz structure in seeding the plasma instabilities that produce the quasi-periodic radar echoes is discussed in this talk. The proposed mechanism has the advantage that the seed structure is generated in situ as part of the same neutral wind structure that serves to initiate the generation of the sporadic E layer. In addition, the range of observed periods can easily be explained. Since the Kelvin-Helmholtz structure is embedded in the shear flow and moves with the mean flow in the shear layer, the period observed in the ground-based frame is simply a product of the horizontal wavelength and the mean flow velocity at the center of the unstable region. Finally, a typical feature of the radar observations has been that the quasi-periodic structure often ebbs and wanes in intensity over a period of 30 to perhaps 60 min. Recent simulations of unstable neutral shears show that the time scale for the build up and eventual restabilization of the shear flow is 30 to 40 minutes, comparable to the time scale found in the observations. The relationship of the shear instability seeding mechanism to other proposed mechanisms for explaining the quasi-periodic structure will also be discussed.

Observations of *E* Region Field-aligned Irregularities just Outside the Equatorial Electrojet Region

J. L. Chau[1,2], R. F. Woodman[1], and L. A. Flores[2]
[1] Radio Observatorio de Jicamarca, Instituto Geofísico del Perú, Lima
[2] Laboratorio de Física, Universidad de Piura, Piura, Perú

1. Introduction

We have used the Piura VHF radar (5 °12'S, 80 °38'W, ~7.5 °N dip latitude), just outside the equatorial electrojet region, in northern Perú (see Figure 1) to gather echoes from 3-m *E* region field-aligned irregularit ies (FAI). Our observations are based on short campaigns of few consecutive days taken since 1995 at different times of the year. *E* region FAIs over Piura are confined to the 95 -120 km altitude and present spectral characteristics similar to type 2 equator ial electrojet (EEJ) echoes. However, despite of being at only 7 °N dip latitude, they appear mainly at nighttime and early morning, and thus do not present a temporal similarity to the EEJ. We observe the existence of two well-defined types of echoes: 1) l ower *E* region echoes (95 -105 km), and upper *E* region echoes (105-120 km). The lower echoes present a layering characteristic while the upper layer is more structured. In this latter region, the so -called quasiperiodic (QP) echoes have been observed with po sitive, vertical, and negative slopes and their characteristics are compared to those observed at mid latitudes. In addition, a relationship between concurrent *E* region irregularities over Piura and *F* region irregularities over Piura and Jicamarca is prese nted.

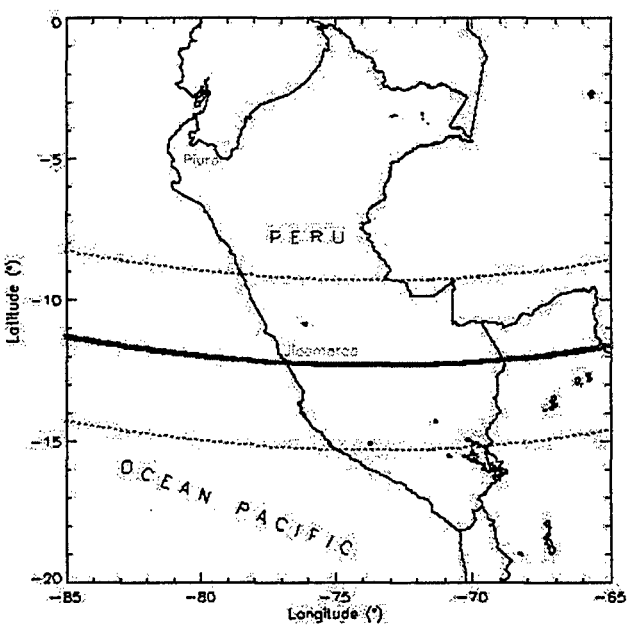


Figure 1. Geographic map of Peru. The thick solid line represents the magnetic equator at 100 km. The dashed lines represent the typical latitudinal extension of the equatorial electrojet.

2. Results

2.1 Preliminary observations

Observations of *E* region irregularities over Piura have been carried out since 1991, sporadically, few times a year. Woodman et al. [1999] have presented the characteristics of these irregularities, based on the observations between 1991 and 1996. In Figure 2, we present th e diurnal characteristics of these echoes, but this time including data until 1999 [i.e., 1995 (25-Jul to 3-Aug, 15-18 Dec); 1996 (20-Oct to 4-Nov); 1998 (27-30 Jul, 10-21 Oct, 27-Oct to 5-Nov); 1999 (5-15 Feb, 8-14 Apr, 26-Jul to 2-Aug, 25-Oct to 1-Nov)]. The main diurnal characteristics reported by Woodman et al., [1999] are again observed, i.e., (1) echoes are almost absent during the day, (2) there are mainly two echoing regions (lower and upper), and (3) the upper E region appears around 2300 LT and di sappears around 0600 LT.

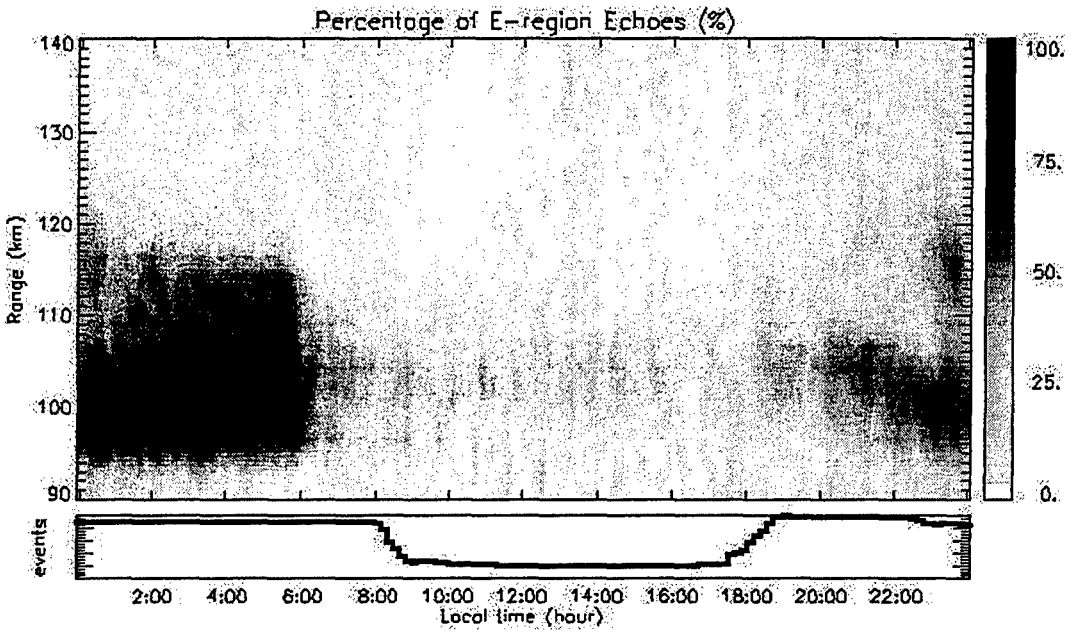


Figure 2. Percentage of *E* region echoes. The time -altitude bin is 30 min x 2 km altitude. We have averaged data between 1995 and 1999.

2.2 Quasiperiodic echoes

As recently observed at midlatitudes, we have also observed QP echo es over the Piura radar, which is located in the equatorial region (geographic and magnetic), but just outside the electrojet region. The first clear observations over Piura of QP were obtained in 1998 and they have been reported by Chau and Woodman, [1999]. At that time, the QP echoes presented, mainly, striations with positive slopes. New systematic observations (taken over different seasons during 1999) have revealed a pronounced existence of striations with negative, vertical, and positive slopes. In Fi gure 2, we present a somehow complicated example of "QP" ("M" shape?) echoes taken in October 1999. Note the negatives slopes before 0130 LT and the positives slopes after that.

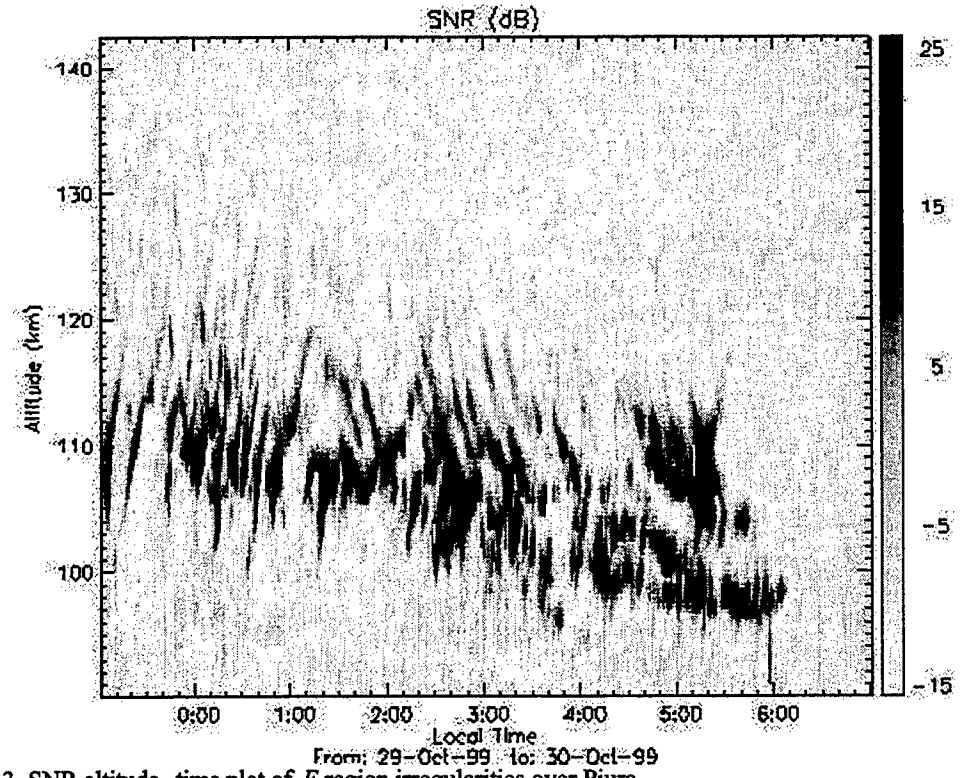


Figure 3. SNR altitude -time plot of *E* region irregularities over Piura.

2.3 *E* vs *F* region irregularities

In addition to the observations of *E* region irregularities over Piura, we have also made few observations of the *F* region irregularities. Moreover, most of these observations have been complemented with concurrent observati ons of *F* region irregularities over Jicamarca. In Figure 4, we show the total power of a concurrent observation of spread F over both sites. Note that the height coverage of spread *F* over Piura is smaller than over Jicamarca, and this is mainly due to less sensitivity (antenna size difference ~ -10 dB, pulse width difference ~ -3dB). Preliminary statistics from these concurrent observations have shown that when *F* region irregularities are observed over Piura, the *F* region irregularities over Jicamarca are ei ther bottomside of topside.

3. Future work

We are planning to continue observing these irregularities almost continuously by "stealing" *E* region signals when the Piura wind profiler is working in its normal mode. These new observations will allow us to get the day-to-day and seasonal characteristics of these echoes. In addition, we will install new receiving antennas close to the radar to apply interferometry/imaging techniques and therefore try to better understand the scattering processes of these irre gularities.

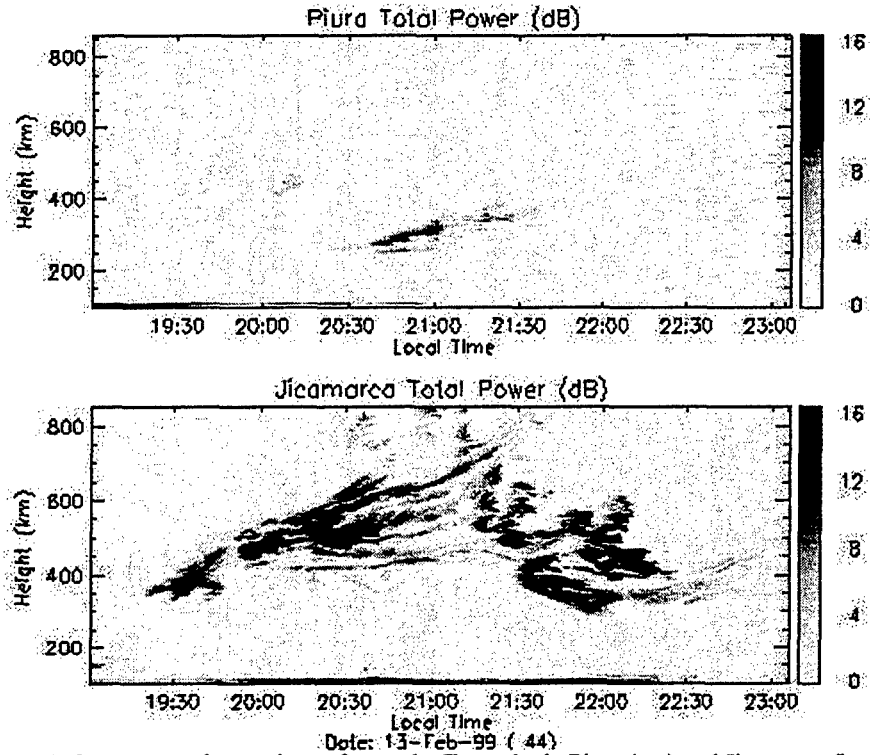


Figure 4. Concurrent observations of spread F over both, Piura (top) and Jicamarca (bottom).

References

Chau, J. L. and R. F Woodman, Low -latitude quasiperiodic echoes observed with the Piura VHF radar in the E region, *Geophys. Res. Lett, 26*, 2167-2170, 1999.

Woodman, R. F., J. L. Chau, F. Aquino, R. R. Rodriguez, and L. A. Flores, Low - latitude field-aligned irregularities observed in the E region with the Piura VHF radar: First results, *Radio Sci., 34*, 983-990, 1999.

Coherent radar echoes from tidal ion layers in mid-latitude E-region

Julio Urbina, Erhan Kudeki, and Steven J. Franke

University of Illinois at Urbana-Champaign, Department of Electrical and Computer Engineering, Urbana, IL 61801

Sixto Gonzalez, and Qihou Zhou

Arecibo Observatory, Arecibo PR 00612

Stephen C. Collins

School of Electrical Engineering, Cornell University, Ithaca, NY 14853

Abstract. A 50 MHz radar interferometer was used near Salinas, Puerto Rico, to probe the meter-scale E-region plasma density irregularities during two campaigns conducted in 1998. During the February-April period E-region echoing layers were primarily observed between 90 and 100 km heights. The layers were typically thin ($\sim$1 km) and unstructured, although in several cases short period ($\sim$90 s) layer oscillations were observed. During the June-July period E-region echoes showed more varied characteristics. In addition to low altitude layers, quasi-periodic structures with descending echoing layers were observed at altitudes above 100 km. Zonal motions detected during descending layer events were at times variable and oscillated between westward and eastward directions while the layer descent rates remained fixed.

1. Introduction

During 1998, a 50 MHz radar interferometer was deployed in Camp Santiago (17.998°N, 66.285°W) at Salinas, Puerto Rico, to make observations of meter-scale E-region plasma density irregularities in support of the NASA Coqui 2 rocket campaign. The radar operated during February 16-April 4 and June 22-July 5. This paper reports the general characteristics of the E-region radar echoes detected during these periods and compare the observed events with the E-region electron density data obtained with the Arecibo incoherent scatter radar. In section 2 we describe the experiment geometry and the characteristics of the Camp Santiago radar system. In section 3 we present examples of the Camp Santiago backscatter radar data and simultaneously measured Arecibo electron density maps. The results are discussed in section 4.

2. Experiment geometry and radar parameters

A 50 MHz radar interferometer system was set up in Camp Santiago, Salinas, Puerto Rico to probe the meter-scale plasma density irregularities at E-region heights approximately 65 km to the N-NE of Arecibo (see Figure 1).

Figure 1. A map showing the Coqui 2 experiment geometry at E-region heights: Line segments indicate the geographical coordinates (longitude and latitude) where the viewing directions from Camp Santiago (S) system crosses the Earth's magnetic field at an angle of 90° at different radar ranges and between the first nulls of the gain patterns of the transmitting antenna. The solid lines corresponds to radar ranges of 120, 130, 140, ..., 200 km and approximate heights of perpendicularity at 90, 95, 100, ..., 140 km are shown by the dotted lines.

The radar antenna was composed of two phased sub-arrays of eight 24-element coaxial-coaxial (COCO) strings, separated by 50 m distance in the geomagnetic east-west direction. The antenna beam was pointed to the north in the magnetic meridian plane. In azimuth the half-power beamwidth was $\sim 3.4°$ (corresponding to $\sim$ 18 km east-west extent between the half-power points for the radar scattering volume at 150 km range), while in elevation the gain pattern peaked in the direction perpendicular to the geomagnetic field at E-

region heights at $\sim 41^{\circ}$ elevation angle. In reception the two sub-arrays of the antenna were sampled independently for interferometric analysis of the echo signals.

Backscatter radar observations were conducted using 11-baud Barker coded pulses with 1.05 km baud length. The interpulse period (IPP) was 4 ms and 96 ranges were sampled at 1.05 km intervals starting at 120 km range. The solid and dashed contours in Figure 1 indicate the range and altitudes, respectively, where the radar viewing direction was perpendicular to the geomagnetic field between the first nulls of the antenna gain pattern (indicated by the extent of the solid line contours). Since the two sets of contours are nearly parallel and E-region irregularities are highly aspect sensitive (i.e., field-aligned) the echo altitudes can be determined unambiguously from the observed echo range using the range-to-height mapping apparent in Figure 1. According to interferometric aspect sensitivity measurements of *Huang et al.* [1995] the magnetic aspect width of meter-scale mid-latitude E-region irregularities at ~100-102 km altitude is $\sim 0.2^{o}$. Thus, for example, the altitude of an echo observed at 150 km range can be determined as ~100 km from Figure 1 with an uncertainty of less than ±400 m. The radar power maps presented in the next section will be labeled in terms of derived echo altitudes on the vertical axes, but the reader should keep in mind the one-to-one correspondence between range and height discussed in this section and depicted in Figure 1.

3. Observations

During the February 16-April 4 period, the 50 MHz backscatter radar at Camp Santiago detected a total of 38 distinct echoing events from E-region heights. Twenty-eight of these events correspond to thin, mostly unstructured and semi-continuous backscatter layers observed below 100 km altitude. Ten events were associated with shorter duration, structured, and quasi-periodic layers observed above 100 km altitude.

Figure 2(a) depicts a typical example of the unstructured (horizontally) backscatter layers observed below 100 km. The Arecibo electron density map covering the same altitude range and observation times is presented in Figure 2(b). Notice that the altitude of the backscatter layer coincides very closely with the altitude of the electron density layer shown in Figure 2(a). Not all the electron density layers detected by Arecibo were accompanied by backscatter layers, but nearly all backscatter layers detected at Camp Santiago in the 90 to 100 km altitude range were associated with Arecibo electron density layers either at the same or nearby heights (see further examples of coincident Arecibo and Camp Santiago data in [*Kane et al.* 2000]).

Figure 2. a) A typical tidal ion layer observed during February-April period. b) Arecibo electron density map (vertical lines between ~20.20-20.40 hr are due to external interference).

The relatively long duration and slowly descending electron density layers observed at Arecibo in the 90-100 km altitude range are known as tidal ion layers [e.g., *Mathews* 1998]. The comparisons of Camp Santiago and Arecibo data therefore suggest that the predominant E-region backscatter observed during the February-April time period was due to the destabilization of tidal ion layers. Radar backscatter from tidal ion layers during this period was predominantly red-shifted (motions away from the radar in northward direction). Time variation of the echo layers was gradual and in many occasions the layer strength oscillated with a period of about 1-2 hrs. The layers showed no detectable altitude modulations except for three occasions (see below). Finally interferometric analysis of the echoes from tidal ion layers did not reveal significant localization of the Bragg scale structure within the radar scattering volume (again with three exceptions). By and large, backscatter from tidal ion layers was due to a "volume filling" distribution of the Bragg scale structures (either a homogeneous distribution or more likely short scale structuring in zonal direction compared to $\sim$ 18 km extent of the radar scattering volume). In Figures 3(a) and (b), we present Camp Santiago and Arecibo radar data of a low-altitude event showing different characteristics than those discussed above. The backscatter map in Figure 3(a) shows a quasi-periodic layer with $\sim$ 90 s period, while the electron density map in Figure 3(b) shows similar period structures on the topside of a layer at approximately the center height of the backscattering region. Finally, the interferometric phase plot shown in Figure 3(c) indicates that on this occasion the 3-m scale irregularities were localized in the scattering volume, and were drifting in the westward direction with approximately 100 m/s speed. The backscattered signals were blue-shifted in this event suggesting southward irregularity motions at $\sim$ 50 m/s.

Figure 3. a) A backscatter from a quasi-periodic tidal ion layer observed at Camp Santiago, b) Arecibo electron density, c) Data showing a relative high westward drift (~100 m/s).

Ten additional backscattering events observed during the February-April period were quasi-periodic and occurred between 100 and 110 km altitudes (majority close to 102 km). An example is shown in Figure 4(a) . The duration of these events were in 10 to 30 m range and the observed periods were ~45 s to ~2 min. Doppler shifts of either sign were observed during these events and interferometric zonal mo-

Figure 4. a) Data showing a high altitude quasi-periodic event. b) A quasi-periodic event observed during the summer campaign.

tions were also variable. The descending layers were typically about 2- 3 km deep in altitude, and in no occasion exceeded 5 km. Occasionally quasi-periodic events with ascending layers were observed.

During the June 22-July 5 summer observation campaign a total of 14 backscattering events were observed. The echoes were more intense and variable in this period than during February-April. The scattering layers were observed at higher altitudes (only two layers were observed below 95 km) and several quasi-periodic scattering events similar to those reported elsewhere [e.g., *Yamamoto et al.* 1991] were seen. One such event is shown in Figure 4(b). The period between the descending layers was about 4-5 min., several of the layers descended by as much as 10 km in height, and observed Doppler velocities fluctuated between ±50 m/s during the event. Furthermore, interferometric phase angle measurements indicated predominantly eastward motions with occasional direction reversals while the descent rate remained constant.

4. Discussion

4.1. February-April observations:

During this period the most frequently observed backscattering events were associated with tidal ion layers. Tidal ion layers observed at Arecibo evolve slower than the higher altitude sporadic-E layers (controlled by tidal and gravity-wave dynamics, respectively) and it is reasonable to assume that their spatial scales in the horizontal direction would be larger than typical horizontal scales of gravity wave events responsible for the higher altitude sporadic-E layer formations. The high degree of coincident layer measurements at Arecibo and Camp Santiago in the 90 to 100 km altitude region suggests that horizontal scales of tidal ion layers may be much larger than the ~65 km separation between Arecibo and the E-region volume probed by the Camp Santiago radar. Large horizontal scales would also be consistent with the virtual absence of height fluctuations in the backscatter detected from tidal ion layers as well as the relatively long duration of the echoing events from these layers. In addition, this conjecture is supported by the fact a 50 MHz backscatter radar operated by Cornell University ~100 km to the N-NW of the Camp Santiago also observed backscatter from tidal ion layers during the same periods as at Camp Santiago [*Private Communication, W. Swartz*, 2000].

The general characteristics of the echoes from tidal ion layer described in the previous section are remarkably different from quasi-periodic E-region backscatter much discussed in the recent literature [e.g., *Chau and Woodman* 1999; *Hysell and Burcham* 1999; *Tsunoda et al.* 1998]. Most importantly, the absence of short period gravity-wave scale modulations of these echoing layers seem to suggest that the destabilizing mechanism of the layers must be immune to field-aligned shorting of the perturbation electric fields [e.g., *Woodman et al.* 1991] which drive the instabilities causing the growth of small scale density structures. We think that increased collision frequencies at the relatively low altitudes of these layers (<100 km) is the main reason why field-aligned shorting is not a major factor. At higher altitudes, where parallel conductivities are higher, the echoing layers are observed to be invariably modulated (the 10 events described in the previous section) and non-continuous, presumably due to the shorting effect described in *Woodman et al.* [1991].

It is therefore reasonable to conjecture that destabilization of tidal ion layers and radar backscatter observed from these low-altitude layers may be a simple consequence of gradient-drift instability acting on the sharp density gradients of the layers [e.g., *Kagan and Kelley* 1998]. In the absence of field-aligned shorting the gradient-drift action on the layer can be explained in terms of the local-linear theory outlined for the equatorial E-region geometry [e.g., *Fejer and Farley* 1975]. The downward density gradients of the topside of the layers would be destabilized, for instance, by a combined effect of eastward electron drifts (the normal $\vec{E} \times \vec{B}$ drift direction after sunset) and westward neutral winds. Secondary instabilities growing on zonal density gradients of the primary irregularities (growing either on the bottomside or the topside of the layers, it doesn't matter) would be most favored in case of northward neutral winds since the normal meridional electron $\vec{E} \times \vec{B}$ drift during the same time period is southward (and downward) [e.g.,*Kelley* 1989]. This picture of secondary wave generation is consistent with a large fraction of the February-April data indicating northward drifts (red-shift) of the secondary irregularities observed by the radar. At altitudes lower than 100 km where the ratio $\psi_o \equiv \nu_e \nu_i / \Omega_e \Omega_i \geq 1$ [e.g., *Fejer and Farley* 1975] the phase velocity of secondary waves detected as radar Doppler velocity is primarily the velocity of the neutrals (and collision dominated ions in the region.) Finally, it is not surprising that an overwhelming majority of the observations suggested a "volume filling" irregularity distribution. The horizontal scale size of primary gradient-drift waves growing on layer boundaries with characteristic depths of a km or less cannot be expected to be larger than the layer depths. Thus given a scattering volume size approaching 20 km in the east-west direction, even interferometric techniques (using only two antennas) prove insufficient to isolate distinct spots of enhanced backscatter. The exceptions in the low-altitude layer observations during the February-April period were three events (out of 28) associated with quasi-periodic modulations, echo localizations, and southward Doppler velocities. Since the southward Doppler velocity suggests southward ion and neutral motion, which is in the same direction as the normal electron $\vec{E} \times \vec{B}$ motion after sunset, the secondary irregularities observed during these events must have been weakly driven (i.e., small electron drift velocity with respect to ions). Perhaps that is the reason why radar backscatter is not continuous, and is localized to small regions (identified and tracked by interferometry) where intermediate scale perturbations must have the

right combination of density gradients and polarization electric fields to destabilize the secondary waves observed by the radar. In case of the February 25 event shown in Figure 3(a), the intermediate scale perturbations causing secondary wave growth must have been associated with the topside structure in the Arecibo electron density map shown in Figure 3(b).

4.2. June-July observations:

During the summer campaign we observed several quasi-periodic events with ~5 min periodicity similar to events reported elsewhere [e.g., *Yamamoto et al.* 1991; *Hysell and Burcham* 1999]. The altitude extent of the quasi-periodic descending layers observed during these events (see Figure 4(b)) reached and exceeded ~10 km in some cases. Since the zonal motions of the irregularities within the descending layers (probed by interferometry) did not correlate with the descent rates we can rule out zonal motions as a possible cause of the descending signatures observed in power maps. Meridional motion of a localized unstable region at a fixed height can also be ruled out as a possible explanation because of the aspect sensitivity constraints discussed in section 2. We therefore have to conclude that the descent signatures observed in power maps must be due to true altitudinal descent of unstable regions, most likely thin sporadic-E layers extended in the meriodional direction. Descent of localized regions (unlayered, and blob-like) cannot explain the extended layer structures since in that case aspect sensitivity constraint would be satisfied only at a single altitude.

Thus we are suggesting that the quasi-periodic backscattered power signatures observed in Camp Santiago and possibly elsewhere (with periods on the order of the Brunt-Vaisala period and observed above 100 km altitude) may be a simple consequence of the descent of enhanced density layers concentrated in the maximum shear zones of downward phase propagating (upward energy propagating) gravity waves. This scenario is in principle different from the scenario outlined in *Woodman et. al.* [1991] where gravity waves are envisioned to distort the layers which have already been formed and dumped to E-region altitudes presumably by some prior wave activity. We are suggesting instead that we get backscatter from layers while they are being formed and simultaneously dragged down in altitude as explained in classical cork-screw sporadic-E layer formation theory [*Whitehead* 1961]. Since the trajectories of the layers being formed by the cork-screw mechanism can directly account for the observed radar signatures there may not be any need to seek additional factors to explain quasi-periodic events. We note that depending on the propagation vector of the gravity wave causing the cork-screw action, descending layers trapped to shear zones can even account for occasional ascending layer signatures reported in the literature.

Acknowledgments. This research was supported by NASA under grant NAG5-5087 to the University of Illinois. We thank Colonel F. Sanchez and staff of the Puerto Rican National Guard at Campamento Santiago near Salinas, Puerto Rico, for their logistical support for radar operations at Campamento Santiago during the 1998 Coqui 2 NASA Sounding Rocket Campaign. We also thank Craig Tepley, and the staff and technicians of the Arecibo Observatory for their help during the project. We thank Angel Alejandro for processing a substantial amount of the Arecibo ISR data. We are very grateful to John Brosnahan in helping us to setup the radar for our experiment.

References

Chau, J., and R. F. Woodman, Low-latitude quasiperiodic echoes observed with the piura vhf radar in the e region, *Geophys. Res. Lett.*, *26*, 2167–2170, 1999.

Fejer, B. G., and D. T. Farley, Vertical structure of the vhf backscattering region in the equatorial electrojet and the gradient drift instability, *J. Geophys. Res.*, *80*, 1313–1324, 1975.

Huang, C. M., E. Kudeki, S. J. Franke, C. H. Liu, and J. Rottger, Brightness distribution of mid-latitude e-region echoes detected at the chung-li vhf radar, *J. Geophys. Res.*, *100*, 14,703, 1995.

Hysell, D. L., and J. D. Burcham, Hf radar observations of quasi periodic e layer echoes over north america, *J. Geophys. Res.*, *104*, 4361–4371, 1999.

Kagan, L. M., and M. C. Kelley, A wind-driven gradient drift mechanism for mid-latitude e-region ionospheric irregularities, *Geophys. Res. Lett.*, *25*, 4141–4144, 1998.

Kane, T. J., B. W. Grime, S. J. F. Steven, E. Kudeki, J. Urbina, M. C. Kelley, and S. C. Collins, Joint observations of sodium enhancements and field-aligned ionospheric irregularities, *Geophys. Res. Lett.*, *this issue*, 2000.

Kelley, M. C., *The Earth's Ionosphere*, vol. 43, Academic, 1989.

Mathews, J. D., Sporadic e: current views and recent progress, *J. Atmos. Terr. Phys.*, *60*, 413–435, 1998.

Tsunoda, R. T., S. Fukao, M. Yamamoto, and T. Hamasaki, First 24.5 mhz radar measurements of quasi-periodic backscatter from field-aligned irregularities in midlatitude sporadic e, *Geophys. Res. Lett.*, *25*, 1765–1768, 1998.

Whitehead, J. D., The formation of sporadic-e layer in the temperate zones, *J. Atmos. Terr. Phys.*, *20*, 40–58, 1961.

Woodman, R. F., M. Yamamoto, and S. Fukao, Gravity wave modulation of gradient drift instabilities in mid-latitude sporadic e irregularities, *Geophys. Res. Lett.*, *18*, 1197–1200, 1991.

Yamamoto, M., S. Fukao, R. F. Woodman, T. Ogawa, T. Tsuda, and S. Kato, Mid-latitude e region field-aligned irregularities observed with the mu radar, *J. Geophys. Res.*, *96*, 15,943–15,949, 1991.

S. J. Franke, E. Kudeki, J. Urbina, Department of Electrical and Computer Engineering, University of Illinois, 1308 W. Main St., Urbana, IL 61801.

S. Gonzalez and Q. Zhou, Arecibo Observatory, Arecibo, PR 00612

S. C. Collins, School of Electrical Engineering, Cornell Univerisity, Ithaca, NY 14853

Received January 21, 2000; accepted March 16, 2000.

Comprehensive *In-situ,* TMA Trail, and Ground-based Observations in the Lower Ionosphere in the Presence of Quasi-Periodic VHF Radar Echoes

R. PFAFF, H. Freudenreich, M. Acuña NASA/Goddard Space Flight Center, Greenbelt, MD
E. Kudeki, S. Franke, J. Urbina, Univ. of Illinois, Urbana-Champaign, IL
M. Larsen, D.Hysell, Clemson University, Clemson, SC
J. Clemmons, Aerospace Corporation, El Segundo, CA
G. Earle, R. Heelis, R. Bishop, Univ. of Texas at Dallas, Richardson, TX
S. Bounds, University of Iowa, Iowa City, IA

A combined rocket/radar investigation of the electrodynamics and neutral-plasma coupling associated with sporadic-E layers and quasi-periodic backscatter radar echoes was carried out from Wallops Flight Facility, Virginia (USA) during summer, 1999. On July 4, 1999 (23:58 LT), a rocket consisting of a main and sub-payload was launched into the lower ionosphere while strong quasi-periodic VHF echoes were observed simultaneously with the Univ. of Illinois 50 MHz backscatter radar. The radar was situated at Ft. Macon, N. Carolina so that its beam would be both perpendicular to the magnetic field and also intersect the rocket location near 105 km. The rocket apogee was purposely limited so that the payloads would dwell in the sporadic-E region (90-115 km). The main payload included vector DC and AC electric field detectors gathered with 6.0m tip-to-tip, orthogonal booms, a DC magnetometer, an ion mass spectrometer, an ionization gauge, and spaced-electric field receivers to measure the wavelength and phase velocity of the unstable plasma waves. The sub-payload was instrumented to measure DC and wave electric fields and plasma density. A separate rocket was launched 4 minutes later which released luminous TMA trails to measure the neutral wind, its velocity shear, and embedded neutral structures. The payloads successfully pierced a well-defined, 2-3 km thick metallic sporadic-E layer of approximately 10^5 cm^{-3} centered near 103 km altitude observed by the *in-situ* density and ion mass spectrometer probes, as well as by a ground-based ionosonde at the launch site. *In-situ* DC electric field measurements revealed steady ~5mV/m ambient meridional fields throughout the lower ionosphere (above and below the layer) with 1-2 mV/m amplitude, large scale structures that were most intense in the region of 90-110 km during the downleg trajectory of the payload. The wavelengths of these structures were approximately 2-4 km and may be related to the seat of the quasi-periodic echoes. Intense (~5 mV/m), higher frequency (shorter scale) broadband waves were also observed *in-situ,* both above and below the layer, consistent with the VHF backscatter observations during the time of the launch. Neither the large scale nor short scale plasma waves appeared to be distinctly organized by the sporadic-E density layer. The TMA release showed large amplitude (~ 100 m/s) meridional winds near 102-105 km, with the most intense shears directly below these altitudes, where the short scale electric field fluctuations were most intense. The observations will be presented and discussed in the context of current theories regarding quasi-periodic echoes.

Effect of Ion Composition on the Shape of 1D Spectrum of Sporadic-*E* Plasma Irregularities Generated by Neutral Air Turbulence

Yu. Kyzyurov (*Main Astronomical Observatory NASU, 03680, Kiev-127, Ukraine*)

Introduction

It is known that the most widely accepted mechanism for the production of mid-latitude sporadic-*E* layer is contained in the windshear theory (Whitehead, 1989). According to this theory, a mainly east-west neutral wind due to tides or gravity waves moves the ions vertically in the *E*-region of the ionosphere, and a vertical shear in this wind compresses the ions into a thin layer. The mechanism is not very effective for the molecular ions which make up the greater part of the total ion content, since these have a lifetime less than the formation time of the layer; rather, the process acts on atomic metal ions (produced as a by-product of meteor entry). These are thought to have very long lifetimes in the *E*-region since the recombination reaction for monatomic ions is very slow compared to the dissociative recombination of molecular ions. Recent data from the coordinated multi-instrument campaign support the windshear theory (Fukao *et al.*, 1998). A sporadic-*E* layer can be caused by the windshear mechanism in the auroral ionosphere too (e.g., Steinweg *et al.*, 1992). It is clear that the detectability of the layer follows closely any changes in the dynamic state of the local atmosphere; in particular it is a sensitive function of the convergent shear region of neutral wind, and also the degree of turbulent mixing in that location. Chimonas (1974) has investigated the effect of neutral turbulence on a sporadic-*E* layer and has shown particularly that the turbulence can reduce the peak amplitude of a typical layer by one order of magnitude from its non-turbulent state amplitude, and that the relation between intensification of the shear and turbulent breakdown can be reflected in intensification of the layer up to a condition when it decays into background ionization. The present report is devoted to study of plasma irregularities generated by neutral air turbulence in the mid-latitude sporadic-*E* layer. An analytic expression describing the spectrum of such plasma fluctuations is discussed for the cases of different ion compositions of the layer.

1D spectrum of sporadic-*E* plasma irregularities

Since usually atmospheric turbulence in the lower ionosphere can be regarded as a Kolmogorov-type one in an incompressible fluid, then the wavenumber-frequency tensor of its velocity field **u** in an inertial range of wavenumbers may be expressed as

$$\Phi_{ij}(\mathbf{k},\omega)=\langle u_i(\mathbf{k},\omega)u_j^*(\mathbf{k},\omega)\rangle=\frac{(\delta_{ij}-k_ik_j/k^2)(\mu_n k^2+\varepsilon^{1/3}k^{2/3})\cdot C_1\varepsilon^{2/3}k^{-5/3}}{4\pi^2k^2(\omega^2+(\mu_n k^2+\varepsilon^{1/3}k^{2/3})^2)}, \qquad (1)$$

$$k_e<k<k_K,$$

where μ_n is the kinematic viscosity of neutral gas, ε is the rate of dissipation of turbulent energy, k_e is the wavenumber for energy containing eddies, $k_K=(\varepsilon/\mu_n^3)^{1/4}$ is the Kolmogorov dissipation wavenumber, C_1 is a dimensionless constant of order unity, δ_{ij} is the Kronecker delta.

To obtain an expression for the spectrum of plasma fluctuations generated by neutral air turbulence in the E_s-layer a system of 3-fluid equations was used, the processes of ambipolar diffusion and recombination were taken into account, and the density of quasi-neutral plasma, N, was considered as a passive scalar field. If the spectral tensor of random velocity field of neutral gas takes the form Eq. (1) then the 3D spectrum for the plasma fluctuations with length-scales smaller than the thickness of the layer, L_s, may be written as (Kyzyurov, 1999)

$$P(\mathbf{k}) = \frac{(L_N^{-2}k^{-2}(\mathbf{n}\times\mathbf{k})^2 + \frac{\Omega^2}{\nu^2}(\mathbf{b}\times\mathbf{k})^2)\cdot C_1\varepsilon^{2/3}k^{-5/3}}{4\pi k^2(2\alpha_r N_0 + (D_a+\mu_n)k^2 + 2\varepsilon^{1/3}k^{2/3})(2\alpha_r N_0 + D_a k^2 + \varepsilon^{1/3}k^{2/3})}, \quad (2)$$

$$L_s^{-1} < k < k_K,$$

where $\mathbf{n}=L_N N_0^{-1}\nabla N_0$ is the unit vector along the gradient of mean plasma density N_0 with a length scale L_N, $\mathbf{b}=\mathbf{B}/B$ is the unit vector along the geomagnetic field $\mathbf{B}$, $\Omega=eB/m_i c$ is the ion gyrofrequency, m_i is the mean ion mass, ν is the ion-neutral collision frequency, α_r is the recombination coefficient, $D_A \approx v_s^2/\nu$ is the ambipolar diffusion coefficient, $v_s^2=K_B(T_i+T_e)/m_i$ is the ion-acoustic velocity, K_B is Boltzmann's constant, $T_{i(e)}$ is the ion (electron) temperature. This expression permits a rms level of the relative plasma-density fluctuations to be made:

$$\langle\frac{\delta N^2}{N_0^2}\rangle = \int d\mathbf{k}P(\mathbf{k}) = \int_{k_1}^{k_2} dk P_1(k), \quad (3)$$

where

$$P_1(k) = \frac{2(L_N^{-2} + \frac{\Omega^2}{\nu^2}k^2)\cdot C_1\varepsilon^{2/3}k^{-5/3}}{3(2\alpha_r N_0 + (D_a+\mu_n)k^2 + 2\varepsilon^{1/3}k^{2/3})(2\alpha_r N_0 + D_a k^2 + \varepsilon^{1/3}k^{2/3})}. \quad (4)$$

The spectrum $P_1(k)$ is the one-dimensional power spectral density (1D PSD) of the plasma fluctuations and can be convenient for explaining possible changes in the spectral form, which result from changes in a relative role of different processes in the creation of the irregularities in different wavenumber ranges (Kyzyurov, 1999).

In order to predict the spectrum expected from an experiment a 1D spectrum in other form can be derived by use of $P(\mathbf{k})$, Eq. (2), namely,

$$S_1(k_\parallel) = \int_0^{\sqrt{k_K^2-k_\parallel^2}} k_\perp dk_\perp \int_0^{2\pi} P(k_\perp\cos\varphi, k_\perp\sin\varphi, k_\parallel)d\varphi = \int_0^{\sqrt{k_K^2-k_\parallel^2}} S(k_\perp, k_\parallel)k_\perp dk_\perp \quad (5)$$

with

$$S(k_\perp, k_\parallel) = \frac{(2L_N^{-2}k_\perp^2 + \frac{\Omega^2}{\nu^2}k^2(k_\perp^2 + k_\perp^2\cos^2\theta + 2k_\parallel^2\sin^2\theta))\cdot C_1\varepsilon^{2/3}k^{-5/3}}{4k^4(2\alpha_r N_0 + (D_a+\mu_n)k^2 + 2\varepsilon^{1/3}k^{2/3})(2\alpha_r N_0 + D_a k^2 + \varepsilon^{1/3}k^{2/3})},$$

if the sounding rocket trajectory is along the direction of the mean plasma-density gradient, $\mathbf{n}=(0,0,1)$. Here $k^2=k_\perp^2+k_\parallel^2$, $\theta=90^\circ-I$ is an angle between $\mathbf{b}$ and $\mathbf{n}$, I is the magnetic dip angle.

Ion composition dependence of the irregularity spectrum

To analyze the influence of the sporadic-E ion composition on the irregularity spectrum, Eq. (5), the parameters which must be changed with a change in the ion composition should be determined. It is obvious that an increase in the concentration of heavy metallic ions such as Fe^+ results in both a reduction in the rate of recombination and an increase in the mean ion mass (hence, D_A and Ω/ν decrease). The other relevant parameters are considered to be unchanged and have the following typical values for the mid-latitude E_s-layer near 95 km height: $L_N \approx L_s \sim 2\cdot10^3$ m, $N_0 \sim 7.6\cdot10^{10}$ m^{-3}, $\mu_n \sim 4$ m^{2}s^{-1}, $\varepsilon \sim 0.1$ m^{2}s^{-3}, $I=45^\circ$ (e.g., Yamamoto *et al.*, 1998; Schlegel and Gurevich, 1997). We estimated the rms level of the plasma density fluctuations (Eq. (3)) and the spectral shape (Eq. (5)) for three different cases: 1) the ion composition is close to the usual one in the ionosphere (the mean ion mass, m_i, corresponds to 31 a.m.u., and the value of the

recombination coefficient, α_r, is about $4 \cdot 10^{-13}$ $m^3 s^{-1}$); 2) the concentration of Fe^+ ions of 40% in the layer (m_i corresponds to 41 a.m.u., $\alpha_r \sim 2.5 \cdot 10^{-13}$ $m^3 s^{-1}$); 3) the concentration of Fe^+ ions of 70% in the layer ($m_i \sim 50$ a.m.u., $\alpha_r \sim 1.5 \cdot 10^{-13}$ $m^3 s^{-1}$) (Bakhmetyeva *et al.*, 1996). If in the first case the parameters D_A, Ω, ν, and m_i are denoted by a subscript 0 ($D_{A0} \approx \mu_n \sim 4$ $m^2 s^{-1}$, and $\Omega_0/\nu_0 \sim 0.01$), then for the other cases one can write $D_A = (m_{i0}/m_i)^{1/2} D_{A0}$, and $\Omega/\nu = (m_{i0}/m_i)^{1/2} \Omega_0/\nu_0$. Under the chosen values of the parameters and for the range of irregularity sizes, $l_K < l < 0.5 L_s$ ($l_K = k_K^{-1} \approx 5$ m). Eq.(3) gives the next values for the rms level of the plasma density fluctuations generated by neutral air turbulence in the sporadic-*E*: the first case – about 3%, the second – 4.2%, and the third – 6%, i.e. the rms level of the plasma fluctuations increases with a rise in the concentration of Fe^+ ions. Figure 1 shows the self-normalized spectra, $S_1(k_\parallel)/S_1(k_0)$ ($k_0^{-1} = 0.5 L_s$), predicted by Eq. (5) in the present cases: lines 1, 2, and 3 represent the first, the second, and the third, respectively. It seen that a rise in the concentration of slowly recombining ions in the sporadic-*E* increases the slope of the irregularity spectrum. In order to analyze the fine structure of the irregularity spectrum (say its departure from a simple power-law form with a constant spectral index) the expression for $P_1(k)$, Eq. (4), is more convenient (Kyzyurov, 1999) and it is quite acceptable to this aim in the wide range of wavenumbers, $L_s^{-1} < k < k_K$, excepting the wavenumber region near the Kolmogorov dissipation wavenumber, k_K (see Figures 2 and 3). In particular, Eq. (4) allows us to conclude that an increase in the concentration of Fe^+ ions widens the wavenumber range for the plasma irregularities created through destruction of mean plasma density gradient by neutral turbulence (since Ω/ν decreases).

Conclusion

Thus, the ion composition of sporadic-*E* exerts apparent influence on the shape of the spectrum of plasma density fluctuations created by the neutral atmosphere turbulence. The analysis of the irregularity spectrum under different concentrations of Fe^+ ions in the layer shows that the presence of slowly recombining ions increases the slope of spectrum and the rms level of the plasma fluctuations.

References

Bakhmetyeva, N.V., V.V. Belikovich, Yu.A. Ignatyev, and A.A. Ponyatov, Determination of the effective recombination coefficient and the meteoric ion concentration in the mid-latitude sporadic-*E* layer, *Geomagn. Aeron.*, **36**, 36, 1996

Chimonas, G., Turbulent diffusion as a controlling factor in sporadic-*E*, *J. Atmos. Terr. Phys.*, **36**, 235, 1974.

Fukao, S., M. Yamamoto, R.T. Tsunoda, H. Hayakawa, and T. Mukai, The SEEK (Sporadic-*E* experiment over Kyushu) campaign, *Geophys. Res. Lett.*, **25**, 1761, 1998.

Kyzyurov, Yu., On the spectrum of mid-latitude sporadic-*E* irregularities, *Ann. Geophysicae*, in press, 1999.

Schlegel, K., and A.V. Gurevich, Radar backscatter from plasma irregularities of the lower *E* region induced by neutral turbulence, *Ann. Geophysicae*, **15**, 870, 1997.

Steinweg, A, D. Krankowsky, P. Lämmerzahl, and B. Anweiler, Metal ion layers in the auroral lower *E*-region measured by mass spectrometers, *J. Atmos. Terr. Phys.*, **54**, 703, 1992.

Whitehead, J.D., Recent work on mid-latitude and equatorial sporadic-*E*, *J. Atmos. Terr. Phys.*, **51**, 401, 1989.

Yamamoto, M., T. Ono, H. Oya, R.T. Tsunoda, M.F. Larsen, S. Fukao, and M. Yamamoto, Structures in sporadic-*E* observed with an impedance probe during the SEEK campaign: Comparisons with neutral-wind and radar-echo observations, *Geophys. Res. Lett.*, **25**, 1781, 1998.

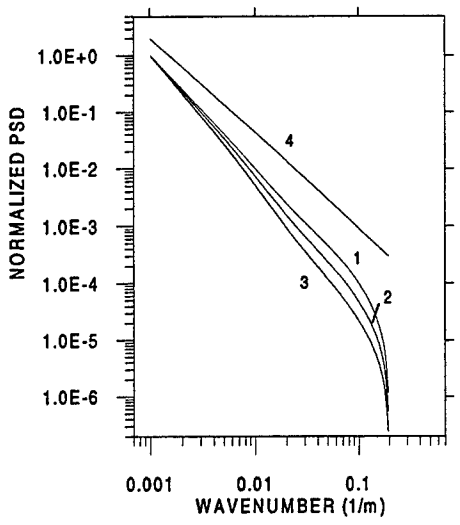


Fig. 1. Self-normalized PSD of plasma density fluctuations, $S_1(k_\parallel)/S_1(k_0)$, predicted by Eq.(5) for different concentrations of Fe^+ ions in the E_s-layer: <10% – line 1, about 40% – line 2, 70% – line 3. The line 4 represents the slope of the Kolmogorov spectrum $k^{-5/3}$.

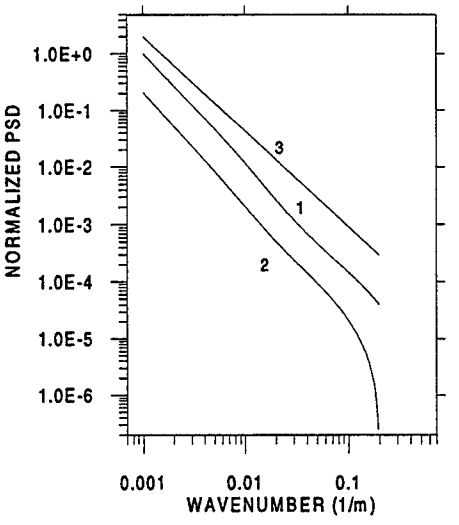


Fig. 2. Normalized PSD of the fluctuations, $P_1(k)/P_1(k_0)$ (line 1), and $S_1(k_\parallel)/P_1(k_0)$ (line 2), when the sporadic-E ion composition is close to the usual one in the ionosphere; the line 3 represents the slope $k^{-5/3}$.

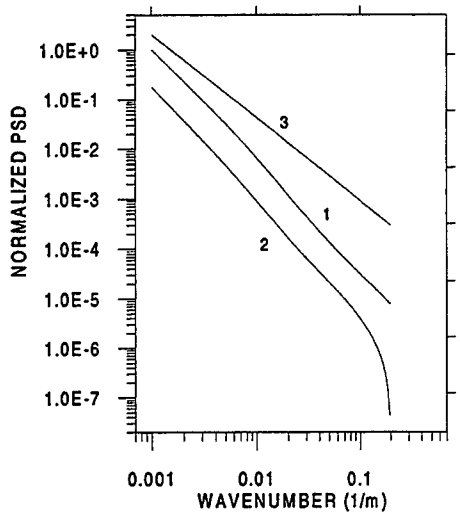


Fig. 3. Normalized PSD of the fluctuations, $P_1(k)/P_1(k_0)$ (line 1), and $S_1(k_\parallel)/P_1(k_0)$ (line 2), when the concentration of Fe^+ ions in the E_s-layer is about 70%; the line 3 represents the slope $k^{-5/3}$.

MODULATION OF SPORADIC E LAYERS BY GRAVITY WAVES AT MID-LATITUDES: An experimental approach

M. Nicollet de la Grilliere ; N. Cavaciuti
Service d'Aeronomie. Universite Pierre et Marie Curie. Paris. France

Woodman et al. (1991) suggested that the gradient drift instability Mechanism, invoked to account for the generation of field -aligned irregu larities at E-layer level at mid-latitudes, would be much more efficient if sporadic E layers distorted by gravity waves were involved. Later, Huang and Kelley (1996) produced results of theoretical computations indicating that gravity waves might induce such distortions.

As part of SPOREX 98 experiment two vertical ionosondes were operated around the summer solstice of 1998 near Grenoble (45,5 deg N; 5.95 deg E) while Valensole HF radar (43,8 deg N; 6,1 deg E), 170 km South, was activated to detect field-aligned irregularities at E-layer level over the Grenoble area. Data collected by one of the ionosondes (Canadian Advanced Digital Ionosonde) are presented and interpreted in the poster. Ionograms (1-8 MHz) were run each minute and 6 fixed frequencies (2.1, 2.4, 2.7, 3.0, 3.3, 3.6 MHz) were sampled successively in the intervals of the ionograms.The transmitting antenna was omnidirectional in azimuth and radiated in a fairly broad cone centered on the vertical, thus allowing for the observation of oblique echoes. Signals reflected or scattered by the ionospheric layers were received on two pairs of loops spaced by 50 m and oriented respectively in N.S and E.W directions. Built-in pre-processing before recording of data is a characteristic feature of CADI which precludes access to raw data - a limitation that should be kept in mind -.

Post-processing of data thus provided by CADI included computation of pha se differences for each pair of loops and their conversion into angles of arrival The position of each reflecting or scattering source was then res tored in three dimensions as a function of time. Radial speed of the source was also computed.

Drifting patterns of reflecting or scattering points could be observed on the time plots of the various parameters involved: horizontal direction of propagation, phase speed and period were measured for each of these patterns.

An interpretation in terms of specular reflection or scattering of the transmitted pulses by distorted isoelectronic surfaces at E-layer level, based on model computations for several types of distortions, is proposed which accounts for most of the observed features and suggests the passing over the ionosonde, or nearby, of Sporadic-E layers modulated by gravity waves.

An attempt to correlate the occurrence of such events with the observa tion of backscatter from field-aligned irregularities at E-layer level by Valensole HF radar is given in a separate oral presentation.

Effects of molecular ions in the night-time equatorial F region irregularities.

E.A. Kherani and R. SEKAR (Physical Research Laboratory, Ahmedabad - 380 009, India.)

The large scale plasma irregularities in equatorial F region associated with nighttime equatorial spread F (ESF) phenomenon are generally believed to be generated by collisional Rayleigh-Taylor instability mechanism driven by gravity (Haerendel, 1974). Earlier linear theories (Haerendel, 1974; Hanson et al, 1986, Sekar and Raghavarao, 1987) and also the nonlinear theories (Ossakow, 1981 and Sekar et al, 1994) did not explicitly show any dependence on mass of the ions. These theories are applicable for single ionic constituent namely, O^+. The ion composition measurements during daytime reveal a cross -over from molecular ions to atomic ion which usually takes place in the lower F region around 200 km. However this cross-over altitude considerably varies in the equatorial region due to electrodynamical effects. A detailed numerical calculation (Anderson and Rusch, 1980) of the background ion densities revealed that the cross-over from NO^+ to O^+ takes place even at the base altitude of the F region depending upon the magnitude of the vertical drift during evening hours.

Ionization hole experiment conducted from India during evening hours (Sridharan et al, 1997) revealed that the molecular ions were dominant till the apogee of the rocket (292 km). Earlier experiments during nighttime (Plumex) also revealed that NO^+ was dominant ion up to the base of the F region and its concentration progressively reduced with altitude (Narcisi and Szuszczewicz, 1981). The satellite measurements (Brinton et al, 1977) supports these results. In view of these composition measurements, the role of molecular ions on the collisional Rayleigh-Taylor instability was examined (Sekar and Kherani, 1999) using linear perturbation analysis. This analysis revealed that the growth rate of the instability depends on the number densities and masses of both the ion species and the introduction of molecular ion reduces the growth rate. This is in contrast to the earlier results based on single ionic constituent wherein the growth rate is independent of number density and mass. However, the linear analysis is limited to zero order conditions during the initial phase of the instability while nonlinear analysis is needed to provide the evolutionary phase. The results obtained by nonlinear analysis in the presence of molecular ions are discussed in this paper.

Numerical model:

The basic plasma fluid equations applicable to the equatorial nighttime F re-

gion were reduced to following coupled differential equations in the presence of two dominant ion,

$$\nabla.[\sum_{i=1}^{2}(\nu_{in}.N_i.m_i)\nabla\phi] = B.[-g + W_y.\nu_{in} + (E_{xo}/B)\nu_{in}].\frac{\partial\sum_{i=1}^{2}(N_i.m_i)}{\partial x} \quad (1)$$

$$\frac{\partial N_1.}{\partial t} - \frac{\partial}{\partial x}[(N_1/B).(E_{yo} + \frac{\partial\phi}{\partial y}] + \frac{\partial}{\partial y}[(N_1/B).(-E_{xo} + \frac{\partial\phi}{\partial x})] = -\nu_R.N_1 \quad (2)$$

$$\frac{\partial N_2.}{\partial t} - \frac{\partial}{\partial x}[(N_2/B).(E_{yo} + \frac{\partial\phi}{\partial y}] + \frac{\partial}{\partial y}[(N_2/B).(-E_{xo} + \frac{\partial\phi}{\partial x})] = \nu_R.N_1 - \alpha.(N_1+N_2).N_2 \quad (3)$$

where $N_{1,2}$, ϕ, ν_R and α represent ion number densities of O^+ and NO^+, the perturbation potential, the loss rate of atomic oxygen ion controlled by charge exchange process and the reaction rate constant for dissociative recombination respectively. The symbols g, ν_{in},E_{xo}, E_{yo} , W_y and B correspond to acceleration due to gravity, ion-neutral collision frequency, the ambient electric field in zonal and vertical directions, the vertical wind velocity and the strength of earth's magnetic field respectively. These equations are solved numerically in a two dimensional plane perpendicular to Earth's magnetic field line.

Results:

This investigation revealed that:

(1) NO^+ is transported along with O^+ to the higher altitude region where plasma density depletion is formed.

(2) NO^+ number densities inside the depletion is larger than the ambient density while O^+ number density inside the depletion is less than the outside similar to the satellite observations (McClure et al, 1979).

Further, the variations in occurrence of NO^+ inside the depletion are being investigated by varying the relative concentrations of NO^+ and O^+ at the base of the F region.

References:

Anderson, D.N. and Rusch,D.W. (1980), Composition of the night-time ionospheric F_1 region near the magnetic equator, *Journal of Geophysical Research,* **85**, *569.*

Brinton, H.C. (1977), Variations in thermospheric hydrogen and oxygen inferred from ion chemistry, in *Proceedings of Atmosphere Explorer, Bryce Re-*

port, National Aeronautics and Space Administration, Washington, D.C..

Haerendel G. (1974), *Theory of equatorial spread-F, unpublished report, Max-Planck-Institut fur Physik and Astrophysik, Garching, F.R.G.*

Hanson, W.B., Cragin, B.L. and Dennis, A. (1986), The effect of vertical drift on the equatorial *F* region stability, *Journal of Atmospheric and Terrestrial Physics* **48**, *205.*

McClure, J.P., Hanson, W.B. and Hoffman, J.H. (1977), Plasma bubbles and irregularities in the equatorial ionosphere, *Journal of Geophysical Research*, **82**, 2650.

Narcisi, R.S. and Szuszczewicz, E.P. (1981), Direct measurements of electron density, temperature and ion composition in an equatorial spread *F* ionosphere, *Journal of Atmospheric and Terrestrial Physics,* **43**,*463.*

Ossakow, S.L. (1981), Spread *F* theories-a review, *Journal of Atmospheric and Terrestrial Physics,* **43**, *437.*

Sekar R., and Raghavarao R. (1987), Role of vertical winds on the Rayleigh-Taylor mode instabilities of the night-time equatorial ionosphere, *Journal of Atmospheric and Terrestrial Physics* **49**, *981.*

Sekar R., Suhasini R. and Raghavarao R. (1994), Effects of vertical winds and electric fields in the nonlinear evolution of equatorial spread *F*, *Journal of Geophysical Research,* **99**, *2205.*

Sekar R. and E.A. Kherani, (1999), Effects of molecular ions on the Rayleigh-Taylor instability in the night-time equatorial ionosphere, *Journal of Atmospheric and Solar Terrestrial Physics,* **61**, *399-405.*

Sridharan R., Chandra H., Das S.R., Sekar R., Sinha H.S.S., Pallam Raju D., Naraynan R., Shikha Raizada, Misra R.N., Raghavarao R., Vyas G.D., Rao P.B., Ramarao P.V.S., Somayajulu V.V., Babu V.V. and Danilov A.D. (1997), Ionization hole campaign - a coordinated rocket and ground-based study at the onset of equatorial spread *F*: first results, *Journal of Atmospheric and Solar Terrestrial Physics,* **59**, *2051.*

First observations of an F-region turbulent upwelling coincident with severe E-region plasma and neutral perturbations

Wesley E. Swartz, Steve Collins, Michael C. Kelley
School of Electrical Engineering, Cornell University, Ithaca, NY 14853

Erhan Kudeki, Steve Franke, Julio Urbina
Electrical and Computing Engineering, University of Illinois, Urbana, IL

Michael P. Sulzer, Sixto González, Nestor Aponte
Arecibo Observatory, Arecibo, PR 00612

A cyclic upwelling of the mid-latitude F-region over Puerto Rico during the night of February 20, 1999 accompanied intense coherent VHF radar backscatter from the E-region and purturbations in neutral sodium in the mesosphere. Simultaneous observations of the event were made with the sodium lidar located at the Arecibo Observatory, the Cornell University Portable Radar Interferometer (CUPRI) located near Isabela, PR, the University of Illinois VHF radar located at Salinas, PR, and the Arecibo incoherent scatter radar. On this geomagnetically quiet night a steep wall of F-region ionization suddenly appeared over Puerto Rico separating low densities to the north from high densities to the south. This is shown in Figure 1 where the cycling of the Arecibo azimuth positions causes the beam to move in and out of the high and low density regions. This figure also shows that the height of the F-region maxima differed by about 100 km between these two regions. The E region exhibited differences in height of 1 to 3 km. This is shown in Figure 2. The RTI from the CUPRI radar in Figure 3 shows the intense echoes that began around 2327 LT. The echoing regions seen by both VHF radars were highly structured with multiple filaments. Over the next half-hour the Doppler shifts of most of the VHF echoes exceeded 300 m/s directed north and upward. Samples of the narrow spectra seen with CUPRI are shown in Figures 4 and 5. Also one time was selected where the spectra were more spread and had significant returns at positive Doppler shifts. The Arecibo lidar showed an intense sodium layer (Figure 6) starting at 101-km altitude and staying at this same altitude until the time VHF echoes began and thence it fell 2 km over a time span of about half an hour. It appears that there was strong coupling between the E and F regions during this event. Further aspects of this event will be discussed along with several precussor events.

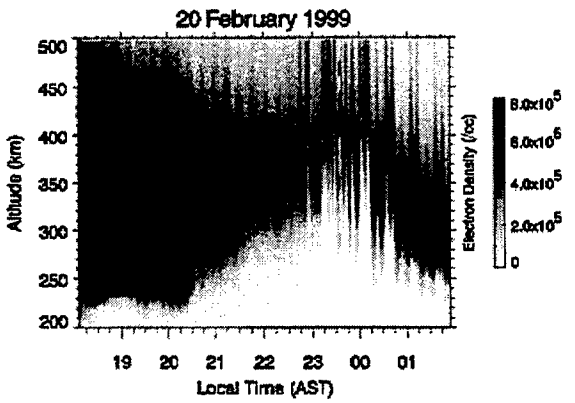


Figure 1: F-region electron densities measured by the Arecibo ISR.

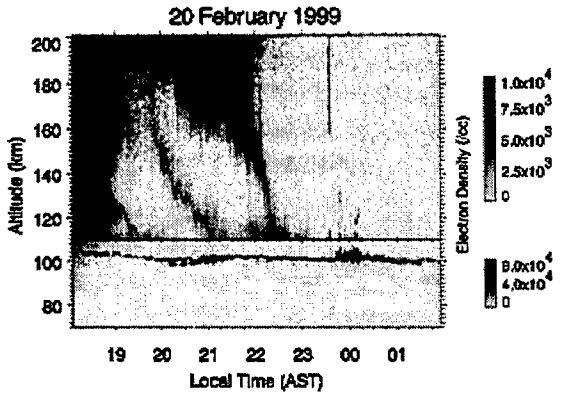


Figure 2: Lower F-region and E-region densites. Note the height of the E-layervaried horizontally.

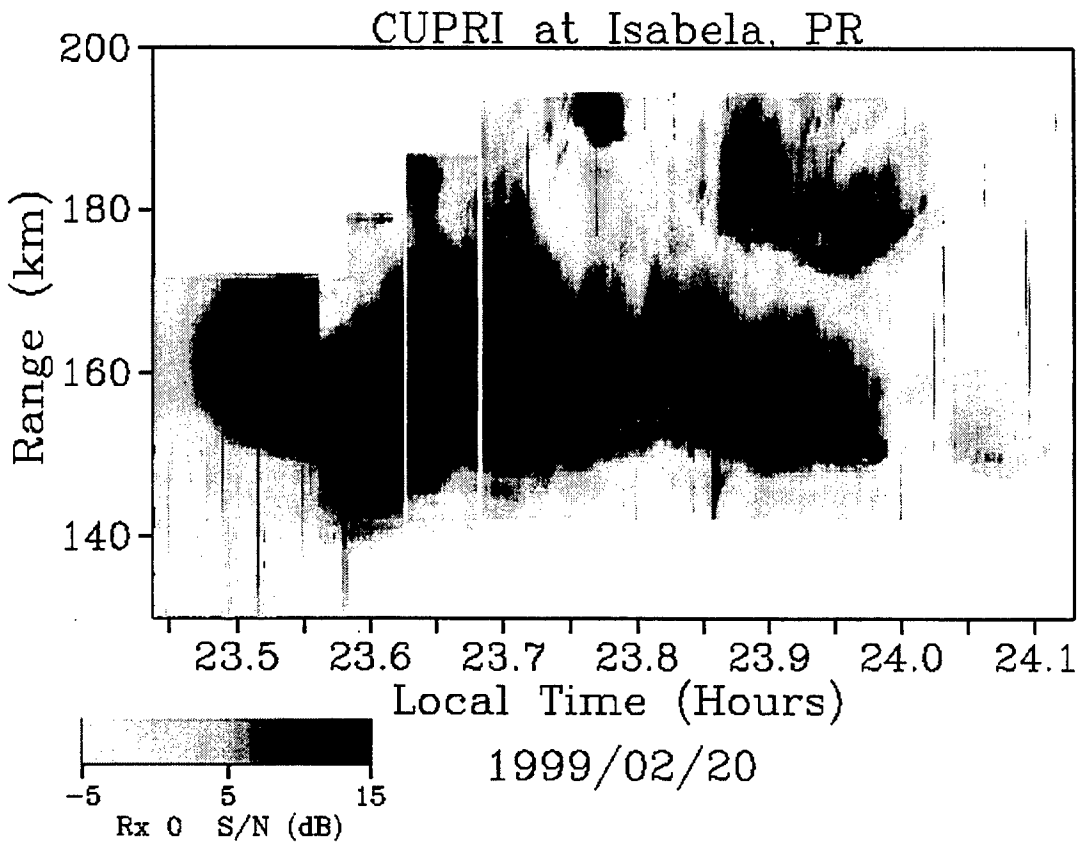


Figure 3: Range-time-intensity plot of turbulent Es as observed with the CUPRI radar.

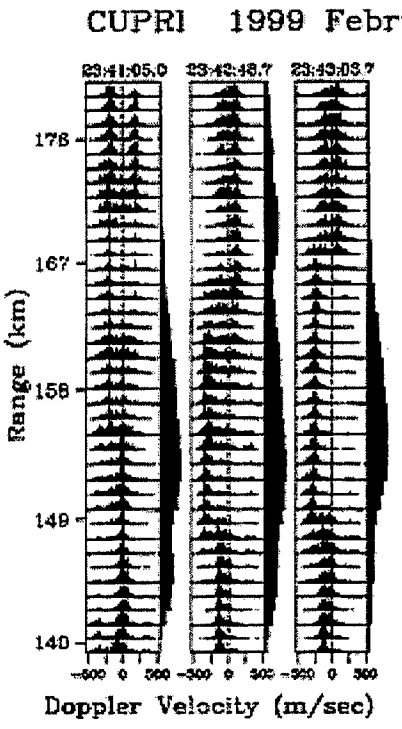


Figure 4: Selected CUPRI spectra of sporadic-E echoes during the time of turbulent activity.

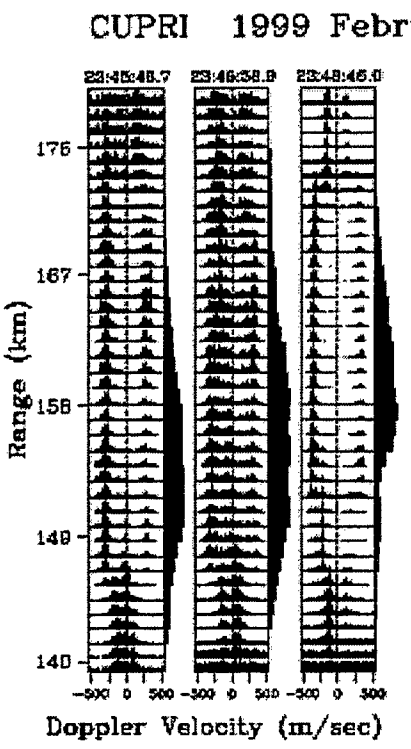


Figure 5: Additional spectra of sporadic-E echoes.

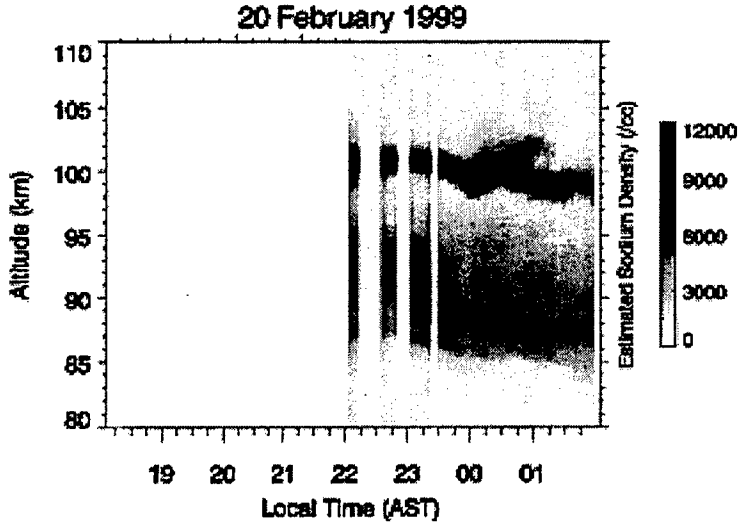


Figure 6: Lidar returns from the sodium layer.

Mesoscale Structure in the Mid-Latitude Ionosphere: A Review of Caribbean Observations

M. C. KELLEY (School of Electrical Engineering, 318 Rhodes Hall, Cornell University, Ithaca, NY 14853, USA)

Over the last decade or so, interest has increased in the structure of the mid-latitude ionosphere. The first breakthrough involved observations by the MU radar in the middle to late 1980's. Coherent echoes indicating turbulent plasma at scales as small as 3 m were reported, with line-of-sight Doppler shifts of several hundred m/s. These unusual scattering events were limited to summer and solar minimum conditions over the Japanese site. Nonetheless, based on some early results by Behnke at Arecibo, which showed no obvious relationship to seasonal effects, a campaign was organized at Arecibo just before the facility was reduced in capability during the Gregorian upgrade. This 10-Day Run in 1993 featured several all-sky imagers and a coherent scatter radar (CSR), in addition to the incoherent scatter radar (ISR) system. No *F*-region CSR echoes were obtained.

Early in 1997 we returned for over a year of observations that included the spectacular night of November 22/23, 1997, shown in Figure 1.

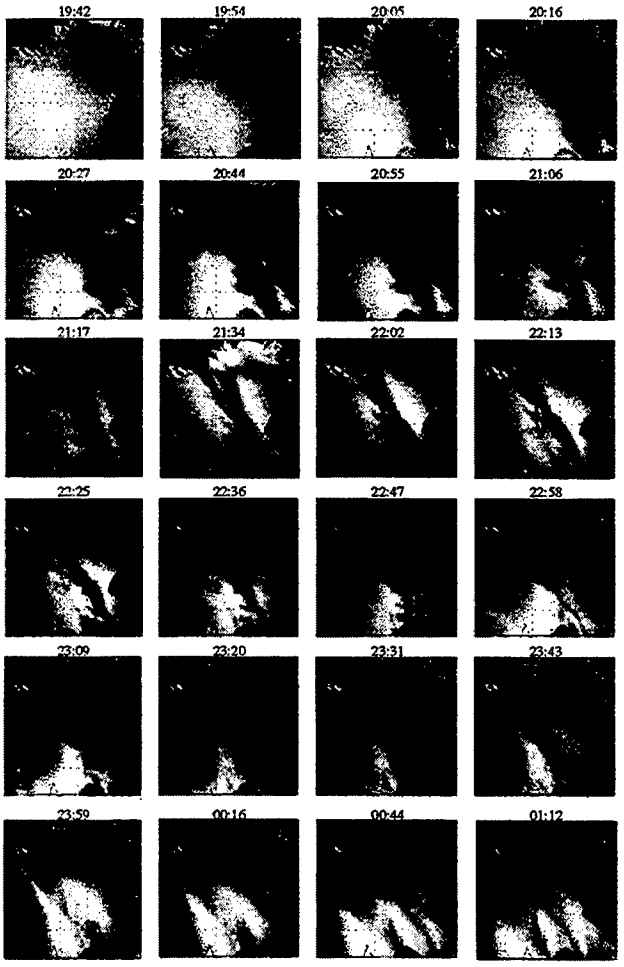


Figure 1.

Here we report on these and other results coming from efforts first planned in the January 1997 Workshop (held in Puerto Rico), which dealt with the post upgrade science thrusts in the Arecibo sector. That same month, our new bare CCD imager was fielded at Arecibo, which has provided many new insights into the mesoscale structure of the region. Most surprising was the intensity of the structuring that accompanied high magnetic activity. We have seen similar behavior during four different magnetic storms.

On this night just after sunset, we see a dark airglow region surge poleward at high velocity (~500 m/s), bifurcating several times. Later in the evening, it was joined by another feature and, eventually, four parallel and virtually identical structures. The airglow bands are at an angle to the magnetic meridian and move slowly (≅50 m/s) toward the southwest. Kp was as high as 6^{+}. The same tilt and apparent velocity is exhibited by weaker features that form during any level of Kp, as illustrated in Figure 2.

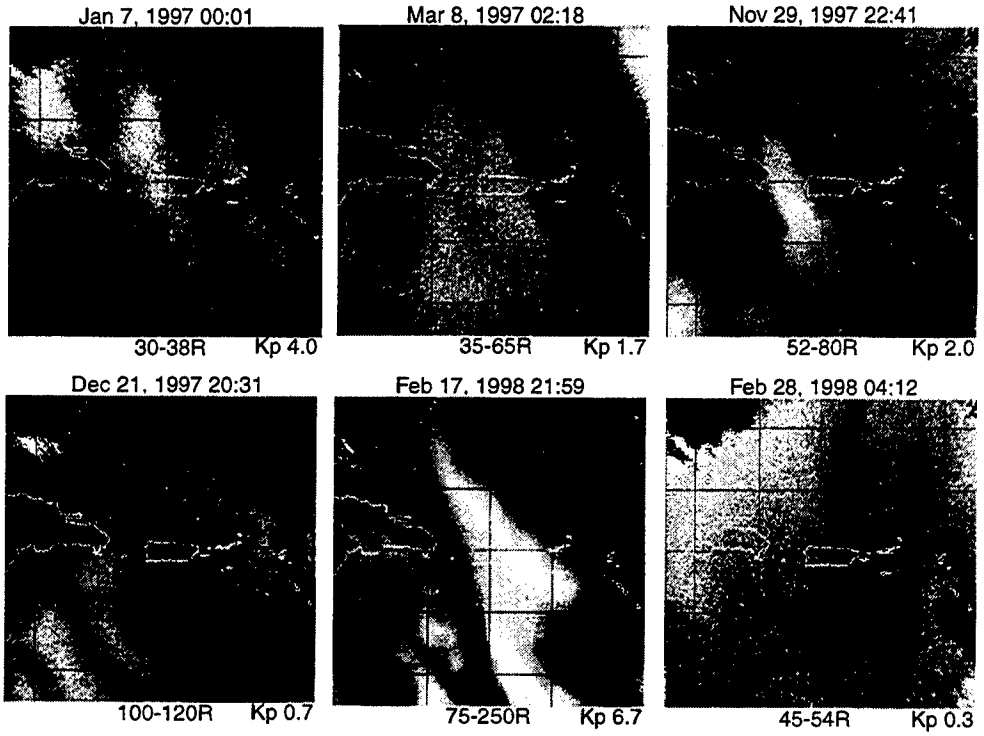


Figure 2.

With the renewed beam-steering capability at Arecibo, we have recently been able to characterize the electric fields inside the low airglow regions. A reproducible pattern emerges in which the dominant electric field is poleward, which corresponds to the westward velocity component usually measured for these features. This pattern is shown for four events in Figure 3. This observation is in agreement with the radially outward electric field found in conjugate examples of mid-latitude electric fields reported on the DE satellite. CSR echoes have also been obtained on a few nights in 1998. It has been popular to invoke the Perkins instability to explain these phenomena, but there are serious difficulties with this explanation, not the least of which is the incorrect prediction of the disturbance propagation velocity.

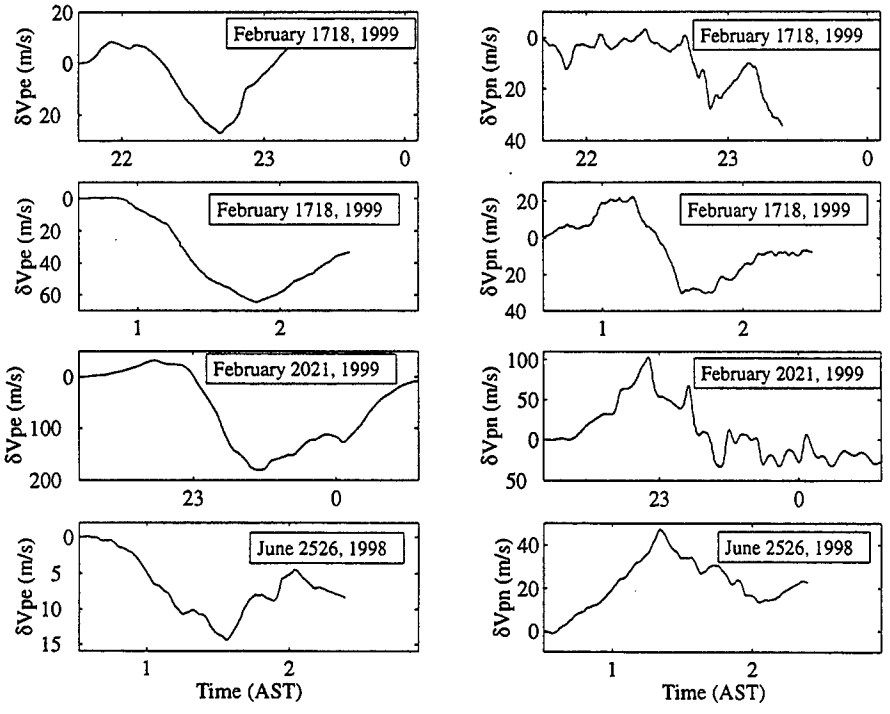

February 1718, 1999
February 1718, 1999
February 1718, 1999
February 1718, 1999
February 2021, 1999
February 2021, 1999
June 2526, 1998
June 2526, 1998
δVpe (m/s)
δVpn (m/s)
Time (AST)
Time (AST)

Figure 3.

Band-like structures of mid-latitude F-region field-aligned irregularities (FAIs) observed with the MU radar

S. FUKAO, and M. Yamamoto (Radio Science Center for Space and Atmosphere, Kyoto University, Uji, Kyoto 611-0011, Japan), A. Saito (Department of Geophysics, Kyoto University, Kyoto 606-8502, Japan)

The mid-latitude F-region field-aligned irregularities (FAIs) observed with the MU radar at Shigaraki (34.85°N, 136.10°E) in Japan show marked upwelling structures with large Doppler velocities up to 200 m/s.

Band-like structures of the FAIs are studied based on the data from multibeam observations of the MU radar. They appear, almost always, in the bottom side of the ionospheric F-region which is simultaneously observed by the same radar. The structure is well correlated with passage of the traveling ionospheric disturbances which are simultaneously observed with GPS.

Precise investigation of the echoes on June 12, 1995 show that the band-like structure spatially elongates from northeast toward southwest, and propagates southwestward with the phase velocity of 145 m/sec. Averaged Doppler velocity of the echoes is northwestward with the speed of 77 m/sec, which corresponds to the northeastward electric field of 3.2 mV/m. The relationship between the propagation direction and the electric field is favorable for the generation of Perkins instability.

From all multibeam observations in 1995–1997, band-like structures are found in ten cases. They show west-southwestward phase propagation, 10–30 minutes of periodicity, and 100–200 km wavelength. Electric fields estimated from the Doppler velocities are all directed northeastward with the range of 2.4–6.4 mV/m. The study reveals that the Perkins instability is the probable candidate to generate the band-like structure of the F-region FAIs.

Traveling Disturbances in the Nighttime Mid-latitude F-region Ionosphere

A. SAITO[1] and S. Fukao[2]

1. Department of Geophysics, Graduate School of Science, Kyoto University
2. Radio Atmospheric Science Center, Kyoto University

1. Introduction

Traveling disturbances in the mid-latitude ionosphere have been observed for several decades with several observational methods such as ionosondes, HF Doppler radar, and satellite beacon. Recent improvement of techniques are revealing many new features of traveling disturbances in the nighttime mid-latitude ionosphere.

The 3-m scale field-aligned irregularities (FAI) in the mid-latitude F-region ionosphere were found with the MU radar to appear from 22:00 to 05:00 in local time and have intense Doppler velocity up to 100 m/s [Fukao et al., 1991]. All-sky CCD camera observed band-like structures of 630nm air-glow band in the bottomside of the nighttime mid-latitude F-region [Mendilo et al., 1997; Taylor et al., 1998]. Similar band-like structures have been observed in the total electron content(TEC) observation with a GPS receiver array in Japan [Saito et al., 1998].

Several characteristics of the traveling disturbances revealed by these observations indicate that traveling disturbances in the mid-latitude ionosphere cannot be attributed to the perturbations of plasma by acoustic gravity waves as classical theory [Miller et al., 1998].

2. F-region field-aligned irregularities

Coherent echo of the F-region field-aligned irregularities have been observed by the MU radar since 1987. Figure 1 shows the spatial structure of the F-region FAI detected by the 15-beam observation on June 27, 1997.

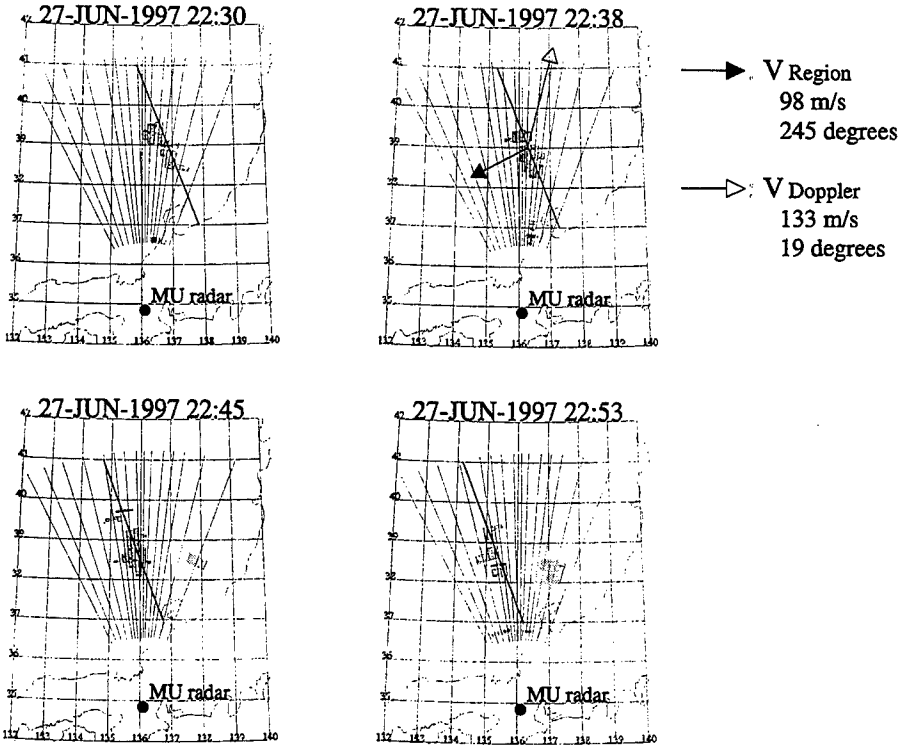


Figure 1. F-region FAI observation by the MU radar

Hatched area represents the regions where the echo from FAI were detected. The FAI region can be seen to form band-like structure which elongates from northwest to southeast, and travel to the southwest. The wavefront and the traveling velocity of this structure is represented by the movement of the thick line in Figure 1, whose velocity is 98 m/s and directs 25 degrees south from west. Assuming the Doppler velocity of FAI is uniform within the field of view, the velocity vector of the Doppler velocity can be estimated with the multi-beam observation. The estimated Doppler velocity vector is 133 m/s and directs 19 degrees east from north. The relative velocity between the Doppler velocity and the traveling velocity is 190 m/s. The second band can be seen in the east-side beams at 22:45 and 22:53.

3. Total electron content observation in Japan

GEONET is a GPS receiver array operated by Geographical Survey Institute to monitor the crustal movement of Japan. The number of receiver is more than one thousand and its average spacing is about 25 km. Using this high density network, total electron content over Japan can be detected with high temporal (30 second) and spatial (0.15 degrees) resolution [Saito et al, 1998]. The TEC distribution on August 4, 1999 is shown in Figure 2.

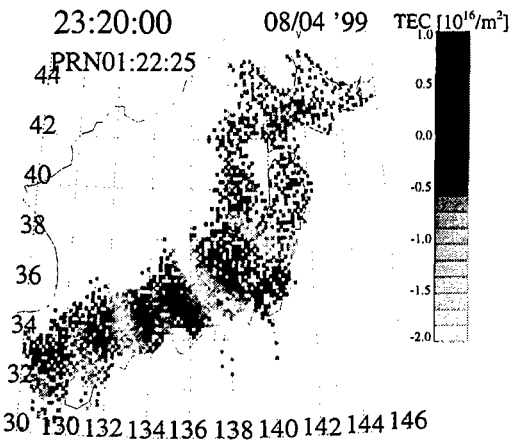


Figure 2. TEC observation by GEONET

These TEC data is high-pass filtered with 1 hour cut-off period. In the western part of Japan, several wavefront elongating from northwest to southeast can be seen. These structures traveled to southwest in about 100 m/s. These type of traveling structures are observed mainly in 20:00 to 02:00. Their amplitude is up to several percent of the background value of TEC.

4. FRONT campaign

All-sky CCD camera also observed the traveling disturbances in the nighttime mid-latitude F-region as the MU radar and the GPS network. F-region Radio and Optical measurement of Nighttime TID (FRONT) campaign has been conducted in May 1998 and August 1999 to clarify the relationship among these disturbances detected by different observation techniques. Five of all-sky CCD cameras were scattered in Japan to observe the 630nm band airglow in the wide area. The band-like structure of airglow and TEC shows good correspondence, which indicates the TEC variations are mainly contributed by the electron density variations in the bottomside of F-region ionosphere. The F-region FAI were observed to have lower occurrence rate than those of TEC and airglow structures, and not to have one-to-one correspondence to them. Band-like type of the F-region FAI, however, travels in the similar phase velocity to that of traveling disturbances of TEC and airglow, when they coexists. Furthermore, the FAI tend to appear at the night when the amplitude of the traveling disturbance of TEC are intense. Fabry-Perot interferometer were installed at two sites to detect the neutral wind in the bottomside of the F-region.

References

Fukao, S., et al., Turbulent upwelling of the mid-latitude ionosphere, 1. Observational results by the MU radar, *J. Geophys. Res., 96,* 3725-3746, 1991.

Mendilo, M. M., J. Bauumgardner, D. Nottingham, J. Aarons, B. Reinisch, J. Scali, M. C. Kelley, Investigations of thermospheric-ionospheric dynamics with 6300-Åimages from the Arecibo observatory, *J. Geophys. Res., 102,* 7331-7343, 1997.

Miller, C. A., W. E. Swartz, M. C. Kelley, M. Mendilo, D. Nottingham, J. Scali, and B. Reinisch, Electrodynamics of midlatitude spread *F* 1. Observations of unstable, gravity wave-induced ionospheric electric fields at tropical latitudes, *J. Geophys. Res., 102,* 11,521-11,532, 1997.

Saito, A., et al., High resolution mapping of TEC perturbations with the GSI GPS network over Japan, *Geophys. Res. Let., 25,* 3079-3082, 1998.

Taylor, M. J., Jahn, J.-M., Fukao, S, Saito, A., Possible evidence of gravity wave coupling into the midlatitude F region ionsphere during the SEEK campaign, *Geophys. Res. Lett., 25,* 1801-1804, 1998.

Kelley, M.C., and S. Fukao, Turbulent upwelling of the mid-latitude ionosphere, 2, Theoretical framework, *J. Geophys. Res., 96,* 3747-3753, 1991.

Equatorial and tropical latitude spread F study based on ionosonde,VHF backscatter radar and radio scintillation observations.

R G RASTOGI,Physical Research Laboratory,Ahmedabad,380009,India

The occurrence of spread echoes in the F region of the ionosphere at an equatorial station has assumed great importance due to its association with various plasma processes.The effect of these irregularities is felt in almost any ionospheric experiments at equatorial latitudes viz inospheric drift observations, VHF backscatter and forward scatter radar observations, HF VHF, and UHF radio propagation etc.However inspite of a large number of inosondes at equatorial latitudes not much attention has been paid to the spatial and temporal features of these irregularities and some conflecting conclusions have been drawn.

The occurrence of spread F at stations within the equatorial electrojet are seen at post sunset hours following a rapid rise of the F layer. At initial stages, the spread echoes are observed at a height close to the base of the F layer extending to large range of exploring frequency. Later number of scatter layers with constant height occur in the ionograms, sometimes covering the entire height regions of the record.These are called RANGE TYPE of equatorial spread F. With tune this transforms into FREQUENCY TYPE EQUATORIAL SPREAD, when an assemblage of individual disconnected scatters echoes are observed the height range of which increases as one approaches the crictial frequency of the layer. The spread F at Huancayo shows a remarkable seasonal variations with almost 100% occurrence during December solstices and almost no spread F during June solstices. It was shown that during December solstices the E region horizontal drift (VxE) changes to eastward direction normally after the inosphereic sunset while during June solstices dirft reversed even before sunset No such systematic behaviour is seen in the time of the reserval of Sq electric field or in the occurrence of spread F in Indian longitude sector.It was suggested that equatorial spread F is generated as the cross–field plasma instability by the action of vertical F region elecric field with the sharp plasma density gradiant at the base of the F layer. Longitudinal varitions in the occurance of spread F is due to the correspondent varition in the time of post–sunset reversal of Sq field.

The character of spread F on the ionograms at a tropical latitudes consists of the apearence of small additional traces parallel to the original p'–f traces suggesting off–vertical reflection from undulations in iso–ionization contour surfaces.These additorial traces increase in number and extend to lower frequencies.At the earlier stages these can be desiegnated as FREQUENCY TYPE tropical spread F with the intensification of these traces the whole ionogram turns into RANGE TYPE tropical spread F.Comparing simultaneous ionograms at the chain of low and tropical latitude stations it is shown that the first occurrence of spread F is systematically delayed at a station farther from the magnatic equator.Using special digital recording of the Faraday rotation of VHF signals from the ATS satellite at a chain of stations in India,it has been shown clearly that the occurrence of spread F is associated with the intensification of the equatorial F region ionization anomaly.The whole phenomenon of equatorial spread F is anologous to the daytime.F region plasma fountain.The irregularities develop at the base of the F region over the equator after sunset if the daytime Sq electric field direction remains eastward.These irregularities are lifted upward by the ExB force or by the buoyancy effects.Later these drift away from the equator guided by the magnatic lines of force to higher latitudes.

VHF back scatter radar indicate strong duffuse echoes at multiple heights during the Range Type of spread F stage but the frequency type of spread F do not scatter 50 MHz radio waves.The vertical F region drift (VzF) observations of Jicamarca Doppler radar has shown that the reversal of VzF to upward direction after its usual post evening reversal at any time of the night is followed by the appearrence of the range type of spread F.Some of these events are shown to the associated with the electric field –V x Bz from the magnatosphere due to sudden reversal of interplanetory magnetic field latitude from southward to northward direction.

VHF radio beacons from artificial satellites passing through region of spread F undergo rapid changes of amplitude and and phase.Multifrequency scintillation observations of ATS–6 HF and VHF radio beacoms at a number of stations provide additional features of the irregularities associated with spread F.The results of radio scintillation of 240 MHz radio beacom at a chain of some 20 station in India are also discussed.Finally the results of rocket soundings of equatorial ionospere during spread F will be described.

The phenomenon of equatorial spread F is one of the menifistation of the horizontal electric field over the magnetic equtor where the magnetic field and plasma density gradients are normal to it in a similar fashion as the daytime equatorial dlectrojet and F region ionization anomaly belt.

Electric Field Effects on Equatorial *F* Region Plasma Irregularities

B. G. FEJER (Center for Atmospheric and Space Sciences, Utah State University, Logan, UT 84222–4405, USA)

Ionospheric plasma irregularities with a large range of scale sizes are generated in the nighttime equatorial ionosphere in one of most dynamic processes in the earth's upper atmosphere. These highly anisotropic irregularities, collectively known as equatorial spread *F*, produce spreading of nighttime equatorial ionogram traces and, more importantly, represent a diffraction screen which causes interference to satellite communication and navigation signals crossing the unstable regions.

The vertical drift velocity (eastward electric field), which controls the height of the nighttime *F* layer and, therefore, reduces the collisionality of the *F* region, is the single most important parameter for the generation of these irregularities. The equatorial zonal electric field also affects directly the growth rate of the Rayleigh–Taylor instability through the electrodynamic drift term and indirectly by controlling both the steepeness of the bottomside plasma density gradient and the ratio between the *F* and the *E* region magnetic field line integrated conductivities at night. On the other hand, the zonal electric field is generated mostly by the combined effects of the low latitude thermospheric neutral wind and conductivity distribution.

The importance of the vertical plasma drift velocity on the generation and evolution of *F* region irregularities has been known from several studies using data from different longitudinal sectors. The threshold layer height and plasma drift velocity for the generation of strong irregularities changes with solar flux and should also have a strong longitudinal dependence, as a result of the noticeable latitudinal changes of the magnetic field line integrated conductivities. Therefore, the specification of this longitudinal dependence is the first fundamental step for the development of realistic global spread *F* predictive models. The forecast of these irregularities also requires a much better understanding of not only the correlation time and lengths of the equatorial vertical plasma drift velocities and thermospheric neutral winds, but also of the short term variability of the instability driving and damping terms due, for example, to gravity waves driven by lower atmospheric processes.

Several different approaches have been recently proposed for improving our understanding of the conditions for the occurrence of spread *F* irregularities and to forecast their evolution from weak bottomside layers to strong scattering regions, large plasma depletions, and radar plumes. These include the use of longitudinal and latitudinal chain experiments involving ground–based radio, radar and optical observations complemented by in situ measurements, and the also use of extensive in situ data from satellite constellations together with global ionospheric models and data assimilation techniques.

In this talk, we will initially review some recent results which highlight the dominant role of the vertical plasma drift velocity in the generation of these irregularities. Then, we will discuss the main challenges we face in improving their understanding and forecasting.

Radar observations of the nighttime equatorial ionosphere at two locations in the Indian region

K.S.V. SUBBARAO[1], K.S.Viswanathan[1], A.K. Patra[2] and N. Ramachandran[1]

[1]Space Physics Laboratory, Vikram Sarabhai Space Centre, Trivandrum – 695022, India
[2]National MST Radar Facility, Gadanki – 515502, India

Introduction

The equatorial ionosphere becomes highly disturbed on some nights due to the presence of plasma irregularities in the F region, which have a wide range of scale sizes ranging from a few hundreds of kilometres to a few centimetres. The generation of large scale irregularities is widely accepted to be due to the Rayleigh – Taylor instability (Haerendel, 1974). Small scale irregularities (1–10 m) have been extensively studied by means of radar observations (e.g. Farley et al., 1970; Woodman and LaHoz, 1976; Tsunoda, 1980; Hysell et al., 1994; Patra et al., 1997). The generation mechanism of small–scale irregularities (Huba and Ossakow, 1979; Hysell et al., 1976) is not well understood. Simultaneous radar observations in the small–scale regime will help to understand the characteristics of these irregularities. Radar observations of equatorial spread F (ESF) on the same night are very few (Rao et al., 1997; Swartz and Woodman, 1998). Radar observations of nighttime ionospheric irregularities were taken simultaneously at Trivandrum (8.5 deg.N, 77 deg.E, dip 0.5 deg.N) and Gadanki (12.5 deg.N, 79.2 deg.E, dip 12.5 deg.N), two locations in the Indian equatorial region. At Trivandrum observations of 8.3 m size irregularities were conducted by using a HF radar. Observations of 2.8 m size irregularities were carried out at Gadanki by operating the Indian MST radar in the ionospheric mode. Results of observations taken on two nights February 29 and March 1, 1996 are presented .

Experiments

The HF radar at Trivandrum is a coherent pulsed Doppler system operating at 18 MHz having a peak power aperture of 5×10^8 Wm^2, a phase coherent receiving system with a quadrature channel and a PC based data acquisition system. The radar employs Doppler Beam Swinging (DBS) technique with beam orientations of vertical and ± 30 deg. off zenith in the E–W plane. For the present study the radar was operated in the vertical position and west position with a pulse repetition frequency of 100 Hz, pulse width of 100 microseconds giving an altitude resolution of 15 km. The radar data at Trivandrum is supplemented with ionosonde data. The MST radar at Gadanki is a coherent pulsed Doppler radar operating at 53 MHz with a peak power aperture of 3×10^{10} Wm^2. A detailed system description of the radar is given in Patra et al., (1995, 1997). As Gadanki is a location away from the magnetic equator, for F region observations the radar beam is oriented 14.8° due magnetic north for achieving perpendicularity to the magnetic field at a height of 330 km. For the radar beam width of 3° the condition of perpendicularity to the magnetic field is satisfied over the height range of 150–550 km. For this study the radar was operated with a pulse repetition frequency of 250 Hz, a pulse width of 32 microseconds giving an altitude resolution of 4.8 km.

The signal power and Doppler velocity of irregularities are estimated from the Doppler spectra recorded at Trivandrum and Gadanki. Height–time–intensity (HTI) and height–time–velocity (HTV) plots are generated and form the basis for the results. The HTI and

HTV plots for February 29, 1996 for Trivandrum and Gadanki are shown in Figs. 1 and 2 respectively.

Results

The HTI plots at Trivandrum and Gadanki look similar on February 29, 1996 (Fig1) and also on March 1, 1996 (not shown). Spread F activity in terms of height extent and signal power of irregularities is greater on March 1 than on February 29. Signals, from E region altitudes are present throughout the night of Feb. 29. At both the locations and on both the days the radar plumes are vertically erect implying that shears in the background zonal plasma drift in the altitude range of the plumes is not significant (Zalesak et al., 1982, Sekar and Kelley et al., 1998)

Doppler velocities of signals from bottomside spread F at the time of onset of spread F and later from higher heights also are found to be downward at Trivandrum on February 29 (bottom panel). The downward velocities are about 25 m/s. At Gadanki the Doppler velocity (bottom panel) of weak bottomside spread F signals are mostly upward till 2020 hr. After 2230 hr the velocities are downward in the region of the plumes. The downward velocities are in the range 25–30 m/s. On March 1, both upward and downward velocities are observed at the time of onset of spread F at both the stations. During the later phase of spread F the velocities are mostly downward at both the places. The downward velocities are about 50–60 m/s at both the places. The Doppler velocities on March 1 and February 29, 1996 observed by the HF radar at Trivandrum and by the VHF radar at Gadanki are of the same magnitude. The Doppler velocities observed on March 1 are greater in magnitude than on Feb.29 at both the locations.

References

Farley, D.T, B.B. Balsley, R.F. Woodman and J.P. McCure, J.Geophys.Res., 75, 7199–7216, 1970
Haerendel, G, Pre–print, Max–Planck Institut fur Physik and Astrophysik, Garching, FRG, 1974
Huba, J.D and S.L. Ossakow, J. Geophys. Res., 84, 6697–6700, 1979
Hysell D.L., M.C. Kelley, W.E. Swartz and D.T.Farley, J.Geophys.Res., 99,15085, 1994
Ossakow, S.L., J.Atmos. Terr.Phys., 43, 437–452 1981
Patra A.K., P.B.Rao, V.K. Anandan and A.R. Jain, J.Atmos. Terr.Phys., 59, 1633–1641, 1997
Patra A.K., P.B. Rao and A.R. Jain Radio Sci 30, 1159–1165, 1995
Rao, P.B., A.K. Patra, T.V.C Sharma, B.V. Krishna Murthy, K.S.V.Subbarao and S.S.Hari, Radio Sci., 32, 1215–1237, 1997
Sekar R and M.C. Kelley, J.Geophys. Res., 107, 20735–20747, 1998
Swartz, W.E and R.F.Woodman, Geophys. Res. Lett., 25, 17–20, 1998
Tsunoda, R.T., Geophys. Res. Lett., 3, 848–850,1980
Woodman R.F and LaHoz, Geophys. Res., 81, 5447–5466, 1976
Zalesak S.T., S.L. Ossakow and P.K. Chaturvedi, J.Geophys. Res., 151–166, 1982

Quasiperiodic Echoes from Equatorial Field-aligned Irregularities Observed over Jicamarca

R. F. Woodman and J. L. Chau
Radio Observatorio de Jicamarca, Instituto Geofísico del Perú, Lima

1. Introduction

Quasiperiodic (QP) echoes from *E* region field-aligned irregularities (FAI) were first observed at midlatitudes by *Yamamoto et al*. [1991] using the middle and upper (MU) atmosphere radar in Japan. Since then different campaigns, including radars with different wavelenghts and in situ measurements [e.g., the SEEK campaign in Japan, see *Fukao et al.*,1998 for details], have been taken placed at midlatitudes in order to unde r-stand this phenomenon.

Until recently, this type of echoes was thought to be only a midlatitude phenom e-non. However, lately they have also been observed at low latitudes, but outside the equatorial electrojet (EEJ) region [*Choudhary and Mahajan* ,1999, *Chau and Woodman* , 1999]. Radar observations of QP echoes have been made at VHF and HF frequencies, from 5°S up to 37.4°N and dip angles (in the northern magnetic hemisphere) ranging from 12.5° up to 65°, mainly in the Asian and American sector. *Chau and Woodman* [1999] has given a summary of the characteristics of most of these observations.

Existing theories have explained the existence of Q P echoes in terms of atmo s-pheric gravity waves (AGW) modulating the sporadic *E* (E_s) layers in such a way to make them nonlocally unstable to gradient drift processes [*Woodman et al.*, 1991, *Tsunoda et al.*, 1994]. However, from the recent results obtained a t different sites (e.g., positive slopes of the striations, very short time periods) these theories need to be revisited.

Is the occurrence of QP echoes in the *E* region a global phenomenon? As far as we know, QP echoes have not been reported in either th e EEJ region or in the southern magnetic hemisphere. In this letter, we report what appears to be the first observation of QP echoes in the EEJ region. These echoes have been recorded at the Jicamarca Radio Observatory (JRO) (1.35 °N dip angle) in October 20, 1993, while a strong spread *F* event occurred. These equatorial QP echoes are somehow similar to those reported at midlat i-tudes, and they could have been observed as early as 1984 (see next section for d etails).

2. QP Observations

In Figure 1, we pre sent an altitude-time distribution of signal-to-noise ratio (SNR) of a spectacular spread *F* event. Such event was recorded at JRO on October 20, 1993 in a vertical-drift observational mode. An approximate horizontal scale, parallel to the time axis, has be en added to the figure by assuming that the zonal plasma drift is eastward with a constant value of 110 m/s. Characteristics of similar types of spread *F* events have been reported and discussed extensively in the literature [e.g., *Woodman and La Hoz* , 1976; *Kelley et al.*, 1981; *Hysell et al.*, 1990] and we will not discussed them fu rther.

In this letter, we concentrate our efforts in describing the QP echoes observed below 200~km. Before we continue fu rther, it is important to note that similar QP echoes have been observed, but not discussed, in previous spread *F* events (e.g., *Hysell et al.*

[1990, Figure 1], after 2130 LT; and *Kelley et al.* [1981, Figure 3]) and they have been associated to the so -called valley -type echoes [*Woodman and La Hoz* , 1976].

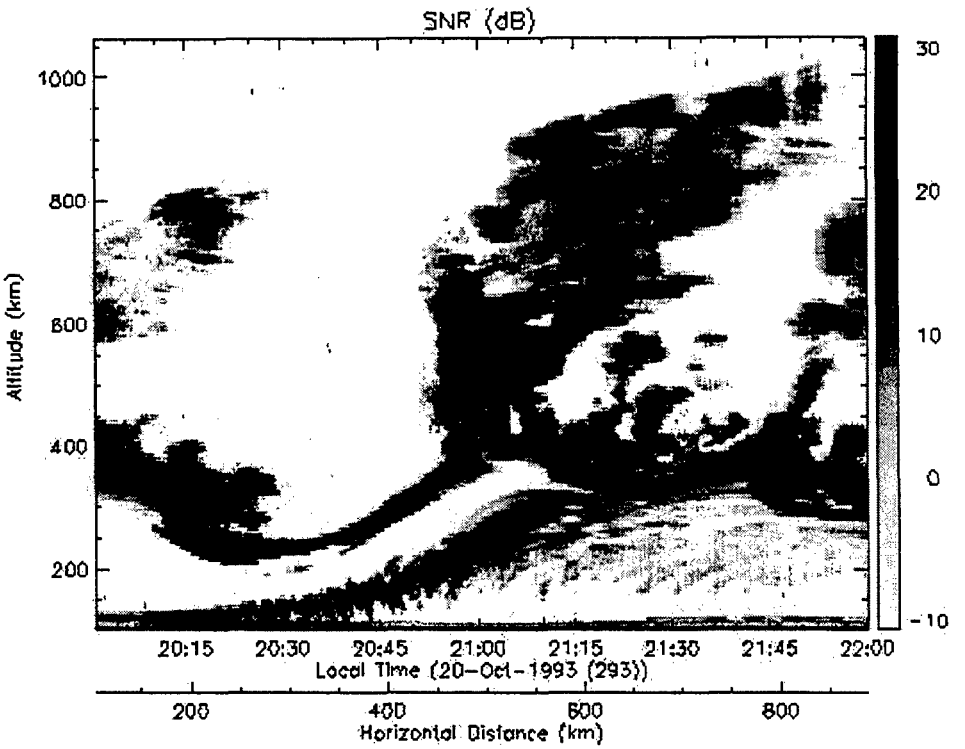


Figure 1. Altitude -time distribution of signal -to-noise ratios during a spread *F* event. An approximate horizontal scale has been added to the time axis, assuming a consta nt drift speed of 110 m/s. Note the well-defined quasiperiodic striations below 200 km.

In Figure 1, QP striations with negative slopes are observed before 2100 LT and below 200 km, while QP striations with positive slopes are observed after 2110 LT and centered around 185 km. The latter show an alt itude-rate of ~80 m/s, are weaker and are characterized by larger time per iods (~4 min) and larger striation spacings (~40 -50 km) than the former. Moreover, the mean Do ppler velocities (positive towards the radar) of the latter echoes are negative (~ -10 to –20 m/s), and the spectral widths are betwe en 50 and 100 m/s, r esults not shown here.

In order to better describe the other QP striations (i.e., before 2100 LT), in Figure 2 are shown the SNR, Doppler velocity and spectral widths of such striations. From Figure 2a, these striations present a perio d of ~1.5 min, and striation spacings of ~20 km. The center of these striations increases with increasing time at a rate of ~47 m/s starting at 120 km. The slope of the striations is negative with an altitude rate of –417 m/s.

In Figure 2b, the region be tween 120 and 140 km present à positive mean Doppler velocity (~50 m/s), while above 140 km, the mean Doppler velocity is negative. Note some aliasing problems (dark spots above 140 km) that are due to the sampling fr equency used. The mean spectral widths are between 30 and 60 m/s (Figure 2c).

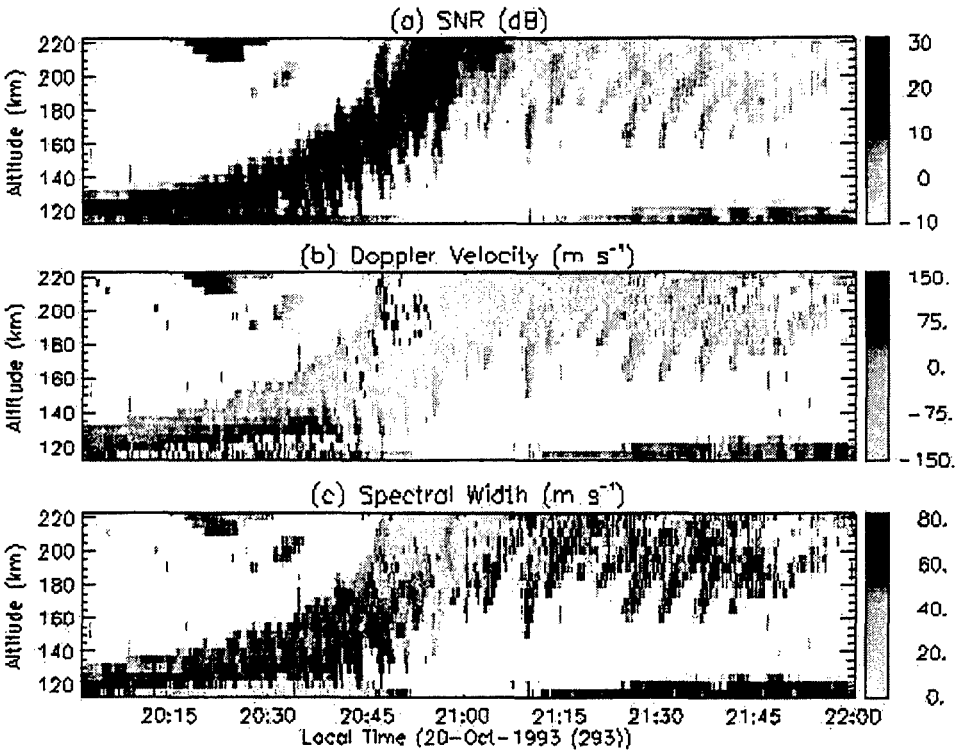


Figure 2. Altitude -time distributions of a) SNR, b) Do ppler velocity, and c) Spectral width, from 2030 LT to 2100 LT, when quasiperiodic echoes are clearly observed in the equatorial *E* region.

3. Summary

We have reported the first observations of QP echoes from field -aligned irregularities in the equatorial electrojet region (1.35 °N dip angle). For the data we have presented, we have identified basically two regions of QP echoes. The first QP region ap - pears below 200 km and before 2100 LT and with time periods of 1.5 min. The main characteristics of the striations in this first region are: negative slopes with high altitude rates (-417 m/s), spacings of 20 km, and their centers increase with increasing time.

The second QP region appears after 2110 LT and is centered around 180 km with periods of about 4 min. The main characteristics of these striations are: positive slopes with an 80 m/s altitude rate, and spacing of 40 to 50 km.

Apparently, the characteristics of these equatorial QP echoes are, in general, sim i- lar to those observed at midlatitudes. Although our observations are based only on few hours of data, we think th at they are a common event that occurs over Jicamarca under special circumstances. Nevertheless, a question remains, are they produced by similar physical processes as the ones responsible for the midlatitude QP echoes? Whatever the answer, it would help u s understand the physical mechanisms responsible for what appears to be a ubiquitous manifestation of *E*-region echoes.

References

Chau, J. L. and R. F Woodman, Low -latitude quasiperiodic echoes observed with the Piura VHF radar in the *E* region, *Geophys. Res. Lett, 26*, 2167-2170, 1999.

Choudhary, R. K.. and K. K. Mahajan, Tropical E region field aligned irregular i-ties: Simultaneous observations of continuous and quasiperiodic echoes, *J. Geophys. Res., 104,* 2613-2619, 1999.

Fukao, S., M. Yamamoto, R. T. T sunoda, H. Hayakawa, and T. Mukai, The SEEK (Sporadic -*E* experiment over Kyushu) campaign, *Geophys. Res. Lett, 25* , 1761-1764, 1998.

Hysell, D. L., M. C. Kelley, W. E. Swartz, and R. F. Woodman, Seeding and layering of equatorial spread F by gravity waves, *J. Geophys. Res., 95,* 4361-4371, 1990.

Kelley, M. C., M. F. Larsen, C. La Hoz, and J. P. McClure, Gravity wave initi a-tion of equatorial spread *F*: A case study, *J. Geophys. Res., 86,* 9087-9100, 1981.

Tsunoda, R. T., S. Fukao, and M. Yamamoto, On the ori gin of quasi-periodic r a-dar backscatter from midlatitude sporadic *E*, *Radio Sci., 29,* 349-365, 1994.

Woodman, R. F. and C. La Hoz, Radar observations of *F* region irregularities, *J. Geophys. Res., 81,* 5447-5466, 1976.

Woodman, R. F., M. Yamamoto, and S. F ukao, Gravity wave modulation of gradient drift instabilities in midlatitude sporadic *E* irregularities, *Geophys. Res. Lett., 18,* 1197-1200, 1991.

Yamamoto, M., S. Fukao, R. F. Woodman, T. Ogawa, T. Tsuda, and S. Kato, Midlatitude *E* region field-aligned irregularities observed with the MU radar, *J. Geophys. Res., 96,* 15943-15949, 1991.

Two-Dimensional Non-linear Modeling of Equatorial Spread F

V. ECCLES (Space Environment Corporation, 399 North Main Str., Ste 325, Logan, UT)

1. Brief Review of Ancient History of ESF Theory

Non-linear modeling of Equatorial Spread F (ESF) is over twenty year old. A number of numerical simulations of various levels of reality have been used to help understand plasma plume structure and initiation. New directions in non-linear modeling may add new insights.

It was 50 years ago that the seminal ideas of ESF understanding were published. *Johnson and Hulburt* [1950] first recognized the unstable condition of the nighttime equatorial F region. The equatorial F region is supported by the magnetic field and the lack of cross-field diffusion. The conditions of a lifted evening ionosphere at the equator creates an unstable positive gradient of plasma density against the desire of downward gravity, classic Rayleigh-Taylor conditions. Zonal perturbations on the bottomside gradient will build up space charge and electric fields to maintain a continuous zonal current across the perturbations. The resulting electric fields cause downward drifting of the dense regions and lifting of the rarified regions enhancing any irregularities in the F region plasma. Meanwhile, *Baker and Martyn [1953]* developed an ionosphere dynamo model based on the assumption that lower ionosphere electric fields were electrostatic, which is equivalent to assuming equipotential magnetic field lines. *Dungey* [1956] moved the F region instability concepts discussed in *Johnson and Hulburt* [1950] to a equipotential field line concept. *Farley* [1959] provided a thorough look at the validity of the equipotential field-line assumption and determined that for the low-latitude ionosphere it is valid down to approximately 1-km scale size structure.

Later, *G. Haerendel* [unpublished manuscript, 1972] expanded the concept of vertically extended Rayleigh-Taylor irregularities to include a 'hierarchy of instabilities', where instabilities of smaller and smaller scale size occur on the sharp gradients of larger instabilities. Each scale driven by other instability mechanisms such as the gradient-drift instability. He as well stressed the importance of examining the instability in terms of flux-tube integrated quantities. This is discussed in again in a published paper [*Balsley, Haerendel, and Greenwald*, 1972] in a defense of Rayleigh-Taylor as the primary mechanism of Spread F. In that paper the post-sunset lifting of the ionosphere was shown to be an important precursor to the appearance of Spread F due to the increase of Ohmic resistance on the bottomside. This leads to larger polarization electric fields in the maintenance of gravity-driven current across the irregularities.

There was recognized problem that the F region ionosphere should be very smooth at sunset and may not have sufficient perturbations to initiate the Rayleigh-Taylor driven spread F. *Whitehead* [1971] proposed that gravity waves could produce initial F region perturbation. *Röttger* [1973] used HF radio propagation to determine that the Spread F appears within quasi-periodic structures in E-W extension of approximately 380-km wavelength. He suggested that the wave structure was caused by atmospheric gravity waves. Later Röttger [1976] tried to relate spread F occurrence to tropospheric weather disturbances, which could generate upper atmosphere gravity waves. *Woodman and La Hoz* [1976] presented excellent experimental results of the Jicamarca radar to examine rising, tilted 'plumes' associated with spread F phenomenon and drew a picture of a rising plasma bubble rising through the F region plasma. The same year the first two-dimensional simulation of the Rayleigh-Taylor generated spread F plume was presented by *Scannapieco and Ossakow* [1976]. Their non-linear treatment demonstrated that the ESF plasma plume could pierce the F region and continue in the otherwise stable topside.

Much has been done in the remaining 25 years, such as, including off-equator E region perturbations to seed spread F and other seeding concepts [*Huang and Kelley*, 1996abc]. However, we have been mostly been confirming and expanding on the details of the above seminal concepts. The physics of low-latitude electrodynamics was worked

out in the 1950's. Rayleigh-Taylor, drift mode and other instabilities were beat to death in the 1970s with linear theory. Gravity wave seeding was studied in the 70's through 90's. However, we still are baffled by the sporadic nature and the seeding details of ESF. Part of the reason for the incomplete picture may be the incomplete non-linear modeling done. The ESF phenomenon is, by nature, a non-linear phenomenon. There has been remarkably little non-linear modeling given the computer power available today.

2. Brief Review of Non-Linear Modeling

Modeling skills for ESF were honed on mid-latitude Barium releases, which presented many of the same instability features? The electrodynamics and plasmadynamics were generally field-line-integrated models that squashed the three-dimensional ionosphere to two-dimensions. *Scannapieco and Ossakow* [1976] turn their two-dimensional non-linear code on end to model ESF plumes. They used periodic boundary conditions and local values of plasma and conductivity. *Zalesak and Ossakow* [1980] examine the development of plasma bubbles from large-scale ionosphere perturbations with much improved numerical techniques. *Zalesak et al.* [1982] were able to demonstrate plasma plume bifurcation as they included more accurate field-line-integrated values of the ionosphere. *Sekar et al.* [1994] examined the effects of vertical winds and electric fields on ESF development with codes similar to those used earlier. *Huang and Kelley* [1996] expanded the number of papers based the field-line-integrated non-linear ESF model. They examined seeding of plasma plumes by gravity waves and structured electric fields. *Hysell and Burcham* [1998] examined the conditions of bottom to topside penetration of plasma depletions.

The non-linear modeling of the medium-scale structure of ESF has gotten progressively more refined with greater resolution and realism in the field-line-integrated quantities. However, some model simplifications limit our ability to understand the non-linear development of ESF. The current efforts of simulation of ESF plasma plumes are using two-dimensional electrodynamics, two-dimensional plasma dynamics, and two-dimensional seeding (with some exception, e.g., Huang and Kelley [1996]). For many reasons this is still adequate for continued investigation, but some approximations need to be removed for progress. For example, the lack of dayside/nightside chemistry removes the development of ESF from the pre-sunset ionosphere where seeding might begin. The use of periodic boundary conditions removes realistic ionosphere tilts. Recent modeling efforts of *Eccles* [1999] and *Retterer* [1999] have tried to remove simplifications of previous field-line-integrated models. How far can the two-dimensional model take our understanding of ESF development?

3. Field-Line-Integrated Electrodynamics

From the earliest papers of the 1950s it was acknowledged that medium- and large-scale electrodynamics in the low-latitudes is electrostatic in nature and can be reduced to a two-dimensional numerical problem. Field-line-integrated quantities must be calculated along dipole field lines from hemisphere to hemisphere. This is adequate down to 1-km scale lengths. While the earliest non-linear simulations used local values of conductivity and plasma density, most recent simulations have used field-line-integrated quantities or close approximations. The quantities include conductivity, mass density, neutral wind drivers. The values are represented in the plane of the dip equator where the currents, potential, and plasma drift velocities are determined. This is confusing to those not accustom to the collapsed electrodynamics model. Vertical currents and vertical neutral winds in the model are really integrations of the meridional local values perpendicular to the field line and may not be vertical at all. Field-line integrated electrodynamics is not a compromise for ESF model of scale sizes to 1 km.

There are still improvements to be made in the electrodynamics models through better boundary conditions. Removing the periodic boundary constraint and expanding the modeled region to include the pre-sunset ionosphere is a necessary step to examine the

early seeding of the post-sunset irregularities. A very suitable way to obtain the proper non-periodic boundary conditions is to embed the high-resolution grid of electrodynamics in a lower resolution grid of global electrodynamics. Much of the geometry of the sunset ionosphere can be properly modeled in this context.

4. Field-Line-Integrated Plasmadynamics

To accommodate slow and small computers the plasma dynamics of the plasma plume models have used two-dimensional plasma transport in a field-line-integrated context, i.e., two-dimensional densities, two-dimensional chemistry, two-dimensional motion. Because diffusive cross-field motion is very small in the F and upper E regions, one can assume that the plasma on a field line drifts as a unit. Thus, the field-line-integrated density is a realistic quantity through time. The main assumption of the two-dimensional plasma model is that the plasma distribution along a field line in the perturbed situation will be proportional to the unperturbed background distribution:

$$N_e(\varphi, L) = aN_{eo}(\varphi, L) \tag{1}$$

$$n_e(\varphi, L, l) = an_{eo}(\varphi, L, l) \tag{2}$$

l is the dimension along the field line. L is radius. j is longitude. N_e is integrated electron density. n_e is the local electron density. This approximation undoubtedly fails to some extent within a rapidly rising plume, though this is not the most grievous problem of the two-dimensional plasma dynamics. If the two-dimensional region to be modeled begins in the pre-sunset ionosphere, then chemical decay of the bottomside must be attempted with two-dimensional plasma chemistry. The two-dimensional mass equation for O^+ is:

$$\frac{\partial N_{O+}}{\partial t} + \frac{1}{R_E}\frac{\partial N_{O+}V_L}{\partial L} + \frac{1}{R_E L}\frac{\partial N_{O+}V\varphi}{\partial \varphi} = P_{O+} - BN_{O+} \tag{3}$$

Where the production is the integrated photoionization source term for O^+ and B is the O^+ density-weighted reaction rate of O^+ reacting with N_2 and O_2:

$O^+ + N_2 \longrightarrow NO^+ + N$ k1

$O^+ + O_2 \longrightarrow O_2^+ + O$ k2

Combining the two loss reactions a single loss rate gives:

$$\beta = k_1[N_2] + k_2[O_2] \tag{4}$$

In the field-line-integrated weighting for B, the two-dimensional equivalent of β, we have

$$B = \frac{1}{N_{O+}}\int \beta n_{O+} dl \tag{5}$$

How well does the combination of production and loss work? The problem is that there is no account of transport along the field line. The best that can be done with equation (3) is to adjust the chemistry to drive the two-dimensional plasma solution to the field-line-integrated background value, but the solution will always be flawed. The better solution is to drive a high resolution, three-dimensional model of plasma dynamics with two-dimensional electrodynamics. However, the approximate chemistry of equation (3) still works to a degree and can be used to examine the effects of pre-sunset seeding.

4. Possibilities of the Two-Dimensional ESF Model

The two-dimensional electrodynamics is not a limiting approximation to our understanding. With improved boundary conditions and expanded grids we can examine new details of seeding and early plume development. Though two-dimensional plasmadynamics is flawed, it does allow for studies of pre-sunset seeding. In simulations using a 3 m/s velocity gravity wave disturbance in the afternoon ionosphere, one can obtain a 10% perturbation in the integrated F-region density at the solar terminator.

Even with the improved modeling capabilities in the field-line-integrated context, the next real advance will come with the addition of three-dimensional modeling of the plasma and the seeds. How the plasma perturbations and the seeding structures in the

thermosphere interact is fundamentally a three-dimensional problem, even though the electrodynamics can remain field-line-integrated electrodynamics.

References

Balsley, B.B., G. Haerendel, and R.A. Greenwald, *J. Geophys. Res. 77*, 5625, 1972.
Baker, W.G., and D.F. Martyn, *Phil. Trans. Royal Soc. London, A, 246*, 281, 1953.
Dungey, J. W., *J. Atmos. Terr. Phys. 9*, 304, 1956.
Eccles, J.V., *IES-99*, Ed. J. Goodman, 545, 1999.
Farley, D.T. Jr., J. Geophys. Res. 65, 869, 1959.
Huang, C., and M.C. Kelley, *J. Geophys. Res. 101*, 283, 1996a.
Huang, C., and M.C. Kelley, *J. Geophys. Res. 101*, 293, 1996b.
Huang, C., and M.C. Kelley, *J. Geophys. Res. 101*, 303, 1996c.
Hysell, D.L., and J.D. Burcham, *J. Geophys. Res. 103*, 29,155, 1998.
Johnson, M.H., and E.O. Hulburt, *Phys. Rev. 79*, 802, 1950.
Retterer, J.M., *IES-99*, Ed. J. Goodman, 688, 1999.
Röttger, J., *J. Atmos. Terr. Phys. 35,* 1195, 1973.
Röttger, J., *J. Atmos. Terr. Phys. 38*, 97, 1976.
Scannapieco, A.J., and S.L. Ossakow, *J. Geophys. Res. 83*, 2066, 1976.
Sekar, R., R. Suhasini, and R. Raghavarao, *J. Geophys. Res. 99*, 2205, 1994.
Whitehead, J.D., *J. Geophys. Res. 76*, 238, 1971.
Woodman, R.F., and C. La Hoz, *J. Geophys. Res. 81*, 5447, 1976.
Zalesak, S.T., and S.L. Ossakow, *J. Geophys. Res. 85*, 2131, 1980.

Production of electric field perturbations by gravity wave winds in the E region through Hall conductivity suitable for initiating equatorial spread F.

SATYA PRAKASH
Physical Research Laboratory, Ahmedabad, 38009, India

It is now well accepted that the appropriate seed irregularities should be present in the F region base to initiate the growth of equatorial spread F (ESF) through the Rayleigh Taylor instability (RTI). The required seed irregularities can only be produced in the base of the F region through zonal component of perturbation electric field with desired characteristics. The perturbation electric field (PEF) should have the following characteristics. (1) The amplitude of the PEF should be sufficiently large. (2) Horizontal wave length to cover the observed range of spacing between the plumes. (3) The inclination of the PEF vector from the zonal direction should be small. Under this condition the growth rate of RTI would be relatively larger. (4) The PEF should have a resonance with the seed irregularities.

From *Kelley et al.* [1981] and *Hysell et al.* [1994], VHF radar maps over Jicamarca show that on many strong equatorial spread *F* days the plumes are uniformly spaced with a separation of 50 to 150 km. Vertical scale sizes of striations associated with the plumes observed by *Hysell et al.* [1994] are even smaller. If the equatorial spread *F* plumes are initiated by gravity wave winds, this would require some of the gravity waves to have horizontal wavelengths as small as 50 km.

During night time the conductivity in the F region is much larger than that in the other regions therefore it is generally believed that these PEF are produced in the F region by the gravity wave winds. In the *F* region the existence of gravity waves with wavelengths in the range mentioned above has not been established. As the geomagnetic field line can be assumed to be fully conducting, these PEF can be produced any where on given geomagnetic field lines passing through the base of the F region. There is, therefore, a need to explore whether the electric field perturbations can be produced in the *E* region and mapped up to the *F* region via the geomagnetic field line.

Prakash and Pandey, [1980, 1985] showed that the efficiency for generation of the PEF is large when the region in with the wavefront of the gravity waves are parallel to the geomagnetic field line overlaps with the region of high Pedersen conductivity. In this mechanism the electric fields are produced through Pedersen conductivity. The efficiency of generation of PEF in the E region would be much smaller than that in the F region as the conductivity in E region is much smaller than that in the F region. In the E region the Hall conductivity is much larger than the Pedersen conductivity and therefore the possibility of PEF being produced through the Hall conductivity was explored [Prakash, 1996, 1999].

In earlier studies, it was found that the Hall conductivity term in the $\nabla.J$ equation cancels out and thus ruling out the generation of PEF through Hall conductivity. Recently using flux tube integrated parameters, Prakash [1996,99] found that under the following conditions the contribution of the Hall conductivity to $\nabla.J$ equation does not cancel out and the PEF can be produced efficiently. The conditions for the generation of PEF through Hall conductivity are: (1) The vertical wavelength of the gravity wave is similar or

larger than the thickness of the E layer. The thickness of the E layer is reduced by the radially inward fields transmitted from the F region which are generated there by the eastward zonal winds. These fields transport the plasma from 120 km region to the lower region (2) Unlike in the case of generation of PEF through Pedersen conductivity, the wave fronts of the gravity waves should not be parallel to the geomagnetic field line. This avoids the cancellation of the PEF produced through the horizontal wind component by the PEF produced through the radial wind component.

Horizontal wavelength of the seed irregularities: This spacing corresponds to the horizontal wave length of gravity wave . In the *F* region the existence of gravity waves with wavelengths in the range mentioned above has not been established. The studies by Kochanski [1964] show that in the *E* region, the gravity waves have a much wider range of scale sizes than the above mentioned range of wavelengths. There is, therefore, a need to explore whether the electric field perturbations can be produced in the *E* region and mapped up to the *F* region via the geomagnetic field line.

Angle of inclination of PEF: The angle of inclination from the zonal direction of the PEF produced through the Hall conductivity is much smaller than those produced through Pedersen conductivity. This would give a larger growth rate for the RTI.

Resonance between seed irregularities and PEF: In connection with the growth of the seed irregularities, an additional factor which is favorable to the PEF produced in the E region is as follows. The gravity wave in the E region with vertical wavelengths in the range of 12 to 24 km would have a phase velocity in the range of 40 to 80m/sec.From the proposed mechanism the PEF are produced most efficiently on the geomagnetic field line on which the flux tube integrated Pedersen conductivity in the F region is comparable to the flux tube integrated Pedersen conductivity below F region. On this geomagnetic field line the drift velocity of the plasma in the F region will be nearly half of the zonal wind velocity in the F region. Therefore the gravity wave in the E region propagating in the eastward direction can have good resonance with the seed irregularities during the period of their growth.

Amplitude of PEF: The efficiency of generation of PEF through Hall conductivity is much larger than that through the Pedersen conductivity due to the following reasons: (1) The internal conductance of the generator producing PEF through Hall conductivity is many times larger than that through Pedersen conductivity. The load conductance in the two cases remain the same. (2) While the PEF produced through Hall conductivity will be mainly parallel to the winds, the ones produced through Pedersen conductivity will be mainly perpendicular to it. For a given gravity wave wind amplitude, the zonal component of the gravity wave winds would be much larger than its radial component. (3) The thickness of the Hall conductivity layer is smaller than for the Pedersen conductivity layer. Thus the efficiency factor for the production of PEF through Hall conductivity would be larger than that through Pedersen conductivity. (4) The angle of inclination from the zonal direction of the PEF produced through the Hall conductivity is much smaller than those produced through Pedersen conductivity. This would give a larger efficiency for the production of the PEF through Hall conductivity.

Eight conditions favorable for generating sufficiently large amplitude electric field

perturbations and growth of seed irregularities are given below:

(1) The amplitude of gravity wave winds is large: The estimated amplitude of the gravity wave winds is 20 m/s. The amplitude of PEF is proportional to the amplitude of the gravity wave winds.

(2) The vertical wavelength of the gravity wave is large compared to the thickness of the E layer. Gravity waves with wavelength as large as 24 km have been observed in the *E* region [*Kochanski*, 1964; *Prakash et al., 1991; Prakash*, 1996] while half conductivity thickness of the E layer is about 15 km. The efficiency for the production of PEF increases with the increase of the ratio of the vertical wavelength of the gravity wave to the half conductivity thickness of the E layer.

(3)The wind in the F region is eastward and large. Eastward winds as large as 200m/s [*Sipler*, 1983; *Wharton*, 1984; *Meriweather*, 1986] have been observed in the *F* region during the growth period of equatorial spread *F*. The thickness of the E layer decreases with the increase in the eastward winds in the F region.

(4) The flux tube integrated Hall conductivity is large. Hall conductivity is proportional to the square root of the strength of the nighttime sources of ionization. The amplitude of PEF increase with the increase in the Hall conductivity.

(5) The flux tube integrated Pedersen conductivity (Σ_{PM}) is the middle region is small. The load on the generator decreases with the decrease in Σ_{PM}. From *Zalsek et al.* [1982], the growth rate γ for Rayleigh Taylor instability will also be large when the conductivity in the lower region is small.

(6) The angle of inclination φ of the PEF from the zonal direction is small. This is satisfied when gravity waves producing these electric field perturbations propagate in a near zonal direction. As discussed earlier, the growth rate of Raleigh Taylor instability is large when φ is small.

(7) The ratio of the flux tube integrated Pedersen conductivity in the F region and that in the lower region (middle region and the E region) lies in the range of 0.5 to 2.0. In this range the amplitude of PEF is maximized.

(8) The Doppler-shifted period of the electric field perturbations in the frame of reference of the plasma in the *F* region base is much larger than the period available for the growth of seed irregularities. This is satisfied when gravity waves with wavelength in the range of 8 to 24 km, propagate in a near eastward direction and winds in the *F* region are eastwards and in between 100 and 200m/s.

The block diagrams shows various steps in the generation of PEF and their transmission to the base of the F-region.

(i) Eastward winds [Block 1] operating on the F region plasma produce downward electric field E_ρ[Block 2] which is transmitted to E region via the geomagnetic field lines.

(ii) The night time Ionizing Radiation [Block 11] maintain the night time E-layer [Block 7]. The electric fields E_ρ gives rise to the downward transport of plasma in the 130 km region thereby reducing the half density thickness of the E-layer and thereby in the flux tube integerated Pedersen and Hall conductivity.

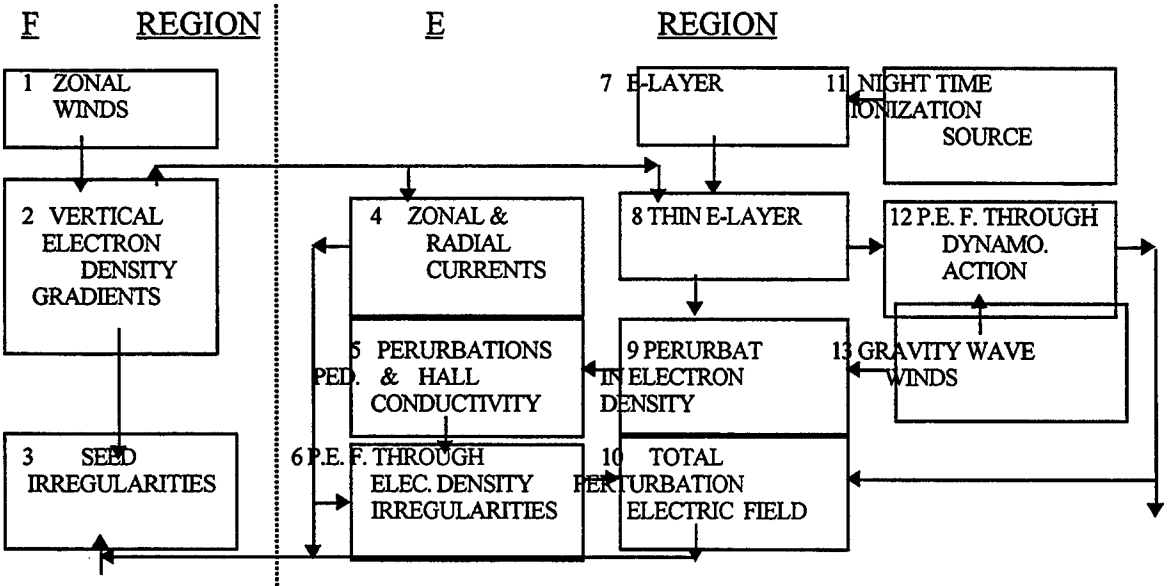
(iii) Gravity wave winds[Block 13], the electric fields E_ρ and zonal electric field E_y operate over the thin E-layer [Block 8] and give rise to perturbation in electron density [Block 9] and thus perturbations in the flux tube integerated Pedersen and Hall conductivity [Block 5].

(iv) The zonal currents and the vertical currents [Block 6] due to the electric fields E_y and E_p [Block 2] flowing through the non-uniformly conducting E-region [Block 5] give rise to the PEF due to perturbation in conductivity in the E-region[Block6].

(v) Gravity wave winds [Block 13] operating over thin E-layer [Block 8] generate PEF in the E-region through dynamo action both through Pedersen and Hall conductivities [Block 12].

(vi)The PEF produced through electron density irregularities [Block 6] and those through the dynamo action [Block 12] have nearly same phase and therefore reinforce each other [Block 12].

(vii) The total PEF [Block 10] when transmitted to the base of the F-region [Block 2] would give rise to the perturbations in the electron density in this region [Block 3].These perturbations act as the seed irregularities for the growth of RTI.



Hysell, D.L., M. C. Kelley, W. E. Swartz, and D. T. Farley, VHF radar and rocket observations of equatorial spread F on Kwajalein, *J. Geophys. Res., 99*, 15,065, 1994.

Kelley, M. C., M. F. Larsen, C. A. LaHoz, J. P. McClure, Gravity wave initiation of equatorial spread *F*: A case study, *J. Geophys. Res., 86*, 9087,1981.

Kochanski, A., Atmospheric motion from sodium cloud drifts, *J. Geophys. Res., 69*, 3651, 1964.

Meriwether, J. M., Jr., J. W. Moody, M. A. Biondi, and R.G. Roble, Optical interferometric measurements of nighttime equatorial thermospheric winds at Arequipa, Peru, *J. Geophys. Res., 91*, 5557, 1986.

Prakash, S., and R. Pandey, On the production of polarization fields in the thermosphere, *Proc. of the 6th International Conference on Equatorial Aeronomy, Arecibo, Puerto Rico*, Pap.1-5 ,1980

Prakash, S., and R. Pandey, Generation of electric fields due to the gravity wave winds and their transmission to other ionospheric regions, *J. Atmos. Phys., 47*, 363,1985.

Prakash, S., S. Pal, and H. Chandra, In situ studies of spread *F* over Shar -steep gradients in the bottomside *F* region and transition wavelength results, *J. Atmos. Terr. Phys., 53*, 977, 1991

Prakash, S., Generation of electric field perturbations suitable for triggering of equatorial spread *F* by gravity waves in the *E* region and zonal winds in the *F* region, *Indian J. Radio Space Phys., 25*, 211,1996.

Prakash, S., Production of electric field perturbations by gravity wave winds in the E region suitable for initiating equatorial spread F, *J. Geophys. Res., 104*, 10051, 1999.

Sipler, D.P., M. A. Biondi, and R. G. Roble, F region neutral winds and temperature in equatorial latitudes: Measured and predicted behaviour during geomagnetically quiet conditions. *Planet. Space. Sci., 31*, 53, 1983.

Wharton, L. E., N. W. Spencer, and H. G. Mayr, The Earth's thermospheric super rotation from Dynamic Explorer 2, *Geophys. Res. Lett., 11*, 531, 1984.

Zalesak, S. T., S. L. Ossakow, and P. K. Chaturvedi, Nonlinear equatorial spread *F*: The effect of neutral winds and background Pedersen conductivity, *J. Geophys. Res., 87*, 151, 1982.

Equatorial Spread–F Irregularities Under Disturbed Geomagnetic Conditions

J. H. SASTRI
Indian Institute of Astrophysics
Bangalore – 560 034, India

An overview will be presented of the current understanding of the behavior of equatorial spread–F (ESF) irregularities of various scale sizes during geomagnetically disturbed periods. Special attention will be paid to recent work on postmidnight generation of ESF and its origin. Some of the major unresolved issues concerning the geomagnetic disturbance–time patterns of ESF will be highlighted and suggestions to achieve an improved understanding of the physical processes at work will be advanced, keeping in view the current experimental and theoretical capabilities of the global research community.

Abstract of Invited Paper for Session 7 at ISEA10.

Results from the Guará Campaign High-Altitude Spread F Rocket Experiment

JAMES LABELLE

Department of Physics and Astronomy, Dartmouth College, Hanover, New Hampshire, USA

JOERG-MICHA JAHN

Southwest Research Institute, San Antonio, Texas, USA

The Guará campaign high-altitude equatorial spread F sounding rocket was launched from Alcântara, Brazil (2° 18.75' South, 44° 22.3' West, dip angle 1.5° at 300 km altitude), at 1955 LT (2255 UT) into an active topside spread F event monitored simultaneously with the Cornell University Portable Radar Interferometer (CUPRI) and with other ground-based instruments. Spread F plasma irregularities observed up to 822 km altitude correlate well with plumes observed simultaneously with a coherent backscatter radar. Matching 1–10 km features in the rocket and radar data over the altitude range 300–800 km implies an eastward drift speed of $\sim$ 110 m/s, versus 95 m/s at 400–500 km based on radar interferometry. Combining these two measurements implies an average upward drift of 30 m/s for the highest altitude structures. The amplitude difference between low- and high-altitude 10-km density structures, if attributed to temporal effects, implies an effective diffusion coefficient (decay time constant) of 500-1000 m^2/s ($2–4\times10^{-4}$ s^{-1}), which agrees with previous estimates from other techniques and supports the idea that the decay of spread F turbulence occurs in a scale-independent manner.

The Guará high-altitude spread F rocket also directly measured electric fields in the altitude range 450–950 km, both inside and outside of the plasma depletions. Outside of the depletions, the electric field was primarily vertical and in the range 3-4 mV/m, implying zonal flow the order of 200 m/s which exceeds average quiet time drifts determined from statistical studies of radar data. However, drifts of this magnitude have been reported, and their observation in this event supports the notion that active spread F conditions are associated with higher than usual eastward plasma drifts. Within the spread F plasma depletions, the vertical electric field became comparable to the zonal component, and individual plasma bubbles were rising with speeds of up to 100 m/s. No large (> 10 mV/m) electric fields were observed in these plasma depletions, however.

The Guará spread F rocket provided the first rocket measurements of the spectra of equatorial spread-F irregularities at altitudes significantly above 600 km, in what is believed to be the inertially dominated regime of spread-F. On upleg the payload remained continuously in these plumes up to an altitude of 822 km. Analysis by D. Hysell [personal communication, 1999] confirms that this altitude is well within the region where inertially dominated turbulence should be observed at the longitude, season, and local time of the launch. Power spectra of electron density fluctuations show characteristic dual-power law behavior with spectral indices of -1.7 at frequencies below 60 Hz and -5 at frequencies above 60 Hz. Shock-like coherent structures characterized the density waveforms. The electric field fluctuations had spectral indices ranging from -3 to -4. None of these spectral characteristics depended on altitude. In short, contrary to predictions based on two-dimensional simulations of spread-F, all data up to 822 km remained in agreement with previous measurements of collisional spread-F below 600 km. The high-altitude irregularities were relatively small-amplitude, however, so the the absence of inertial regime spectra may be consistent with Hysell's hypothesis of an amplitude threshold required for the irregularities to take on the characteristics of the inertially dominated turbulence.

Changes in ionospheric height near the magnetic equator and onset of equatorial spread *F*

TAKASHI MARUYAMA
Hiraiso Solar Terrestrial Research Center, Communications Research Laboratory, Ibaraki, Japan
Kenro Nozaki
Communications Research Laboratory, Tokyo, Japan
and Mamoru Yamamoto
Radio Atmospheric Science Center, Kyoto University, Uji, Kyoto, Japan

Abstract

Changes in the ionospheric height during post–sunset hours are analyzed for two locations near the magnetic equator, Cebu Island (124 deg. E, 10.3 deg N; 2.4 deg. N in diplatitude) and Manila (121 deg. E, 14.6 deg. N; 7.3 deg. N in diplatitude), both in Philippines. Ionograms were obtained every 5 minutes during the first WestPac (Western Pacific) ionospheric campaign conducted in March 1998. The ionospheric heights at two stations varied in the same way on some days and did a different way on the other days. Equatorial spread *F* during evening hours was observed on two days. The difference in the height changes at two stations is complicated on those days. The ionospheric height changes are interpreted by comparing with model calculations.

Introduction

Ionospheric *F* region height is determined by both chemical and dynamic processes, i.e., productions and losses of ions, **EXB** drifts, and momentum transfer from the thermospheric winds. After the sunset, the electron density rapidly decreases at lower altitudes by recombination. As a result, *F* region bottom height rises and dynamical processes play an important role in the ionospheric height changes if the height is maintained at high altitudes. At the same time, apparent heights (*h'F*) observed by an ionosonde become a good indicator of real layer heights. At low to equatorial latitudes, the eastward (westward) zonal electric field pushes up (down) the ionosphere in the direction of **EXB** and the equatorward (poleward) wind pushes up (down) the ionosphere along the magnetic field line by the ion–neutral collision. Therefore, *h'F* observations provide information on dynamic processes in the ionosphere.

On the other hand, spread *F* has been a big research theme of the equatorial ionosphere for a long time. The basic mechanism of the onset of equatorial spread *F* or plume is gravitational Rayleigh–Taylor instability in conjunction with **EXB** drift instability. Based on this idea, we anticipate that the ionosphere is destabilized when the layer is high where the ion–neutral collision frequency is low and localized polarization electric field due to the gravitational current flowing eastward can be easily set up at density fluctuations. High ionospheric heights are attained by the upward **EXB** drift due to the eastward electric field. At the same time, the eastward Pedersen current sets up perturbation electric field at density fluctuations. Thus, if this simple picture is the only physical mechanism to destabilize the ionosphere, we anticipate an onset of equatorial spread *F* when the layer is drifting upward. Actually, spread *F* onset is often when the ionosphere is rising. In some cases, however, spread *F* starts when the layer is descending [*Kelley et al.*, 1981]. In the latter cases, the eastward neutral wind is thought to destabilize the ionosphere in combination with a zonal gradient of electron density, which may be attained by a spatial resonance mechanism [*Kelley et al.*, 1981].

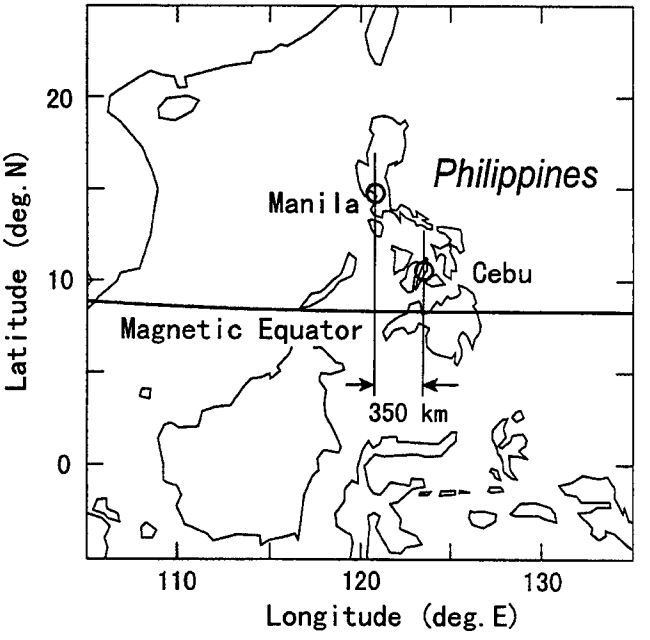
On a practical view point of Space Weather, the change in the ionospheric height can be a good

measure for predicting spread *F* or intense ionospheric scintillations. Eastward electric fields or upward drift velocities can be estimated from *h'F* during evening hours. Once the upward drift velocity is estimated, the growth rate of Rayleigh–Taylor instability is calculated. A case study shows that spread *F* appears when the integrated growth rate exceeds some threshold value [*Kelley and Maruyama*, 1992]. As pointed above, there is a problem in predicting spread *F* onset based on the ionospheric height changes only. That is, we know cases of destabilization of the ionosphere after turning the vertical drift direction from upward to downward. We need more investigation of the relationship between the height changes and spread F onset.

Observation

We have conducted ionospheric observation every 5 minutes at two closely separated stations near the magnetic equator as a part of first Western Pacific Ionosphere Campaign (WestPac). One is in Cebu Island (124 deg. E, 10.3 deg. N; 2.4 deg. N in diplatitude), using a portable FM/CW sounder, and the other is Manila station (121 deg. E, 14.6 deg. N; 7.3 deg. N in diplatitude), both in Philippines, from March 2 to 12, 1998. The locations are shown in Figure 1. As two stations are separated by about 350 km in the east–west direction, and by about 5 degrees in latitude, we must be careful of this geometry in interpreting the data from two stations.

Figure 1



The ionospheric height changes during evening hours at two stations showed a different feature from day to day. Comparing two stations, we note cases are summarized into three types. (*a*) The heights at two stations vary almost identical; (*b*) they vary in the same way but the height at Cebu is always higher than that at Manila by 20–30 km; and (*c*) they vary with a fairly different way. Typical examples are shown in Figures 2(*a*)–(*c*). This day–to–day difference is interpreted by comparing with model calculations using various **EXB** drift patterns, especially the strength of evening enhancement, and HWM90 thermospheric wind model.

Figure 2(*a*)

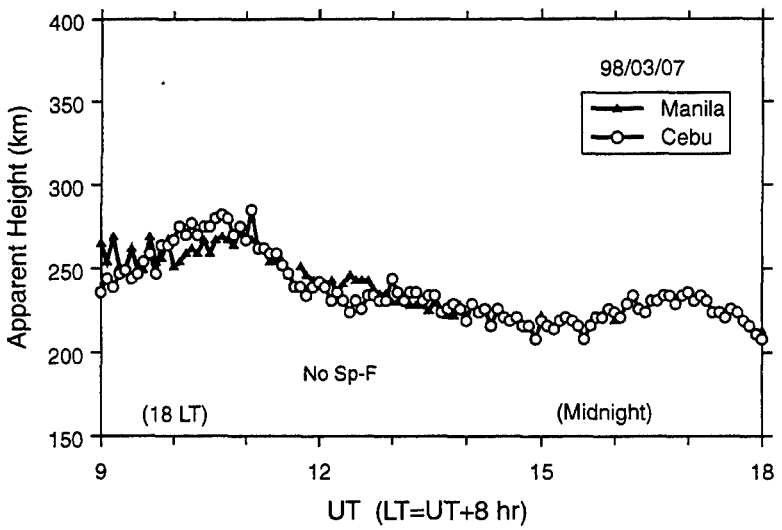
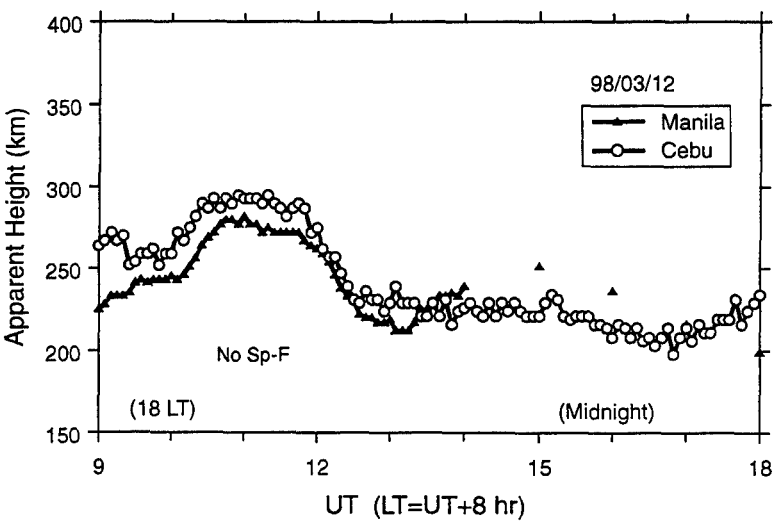


Figure 2(*b*)

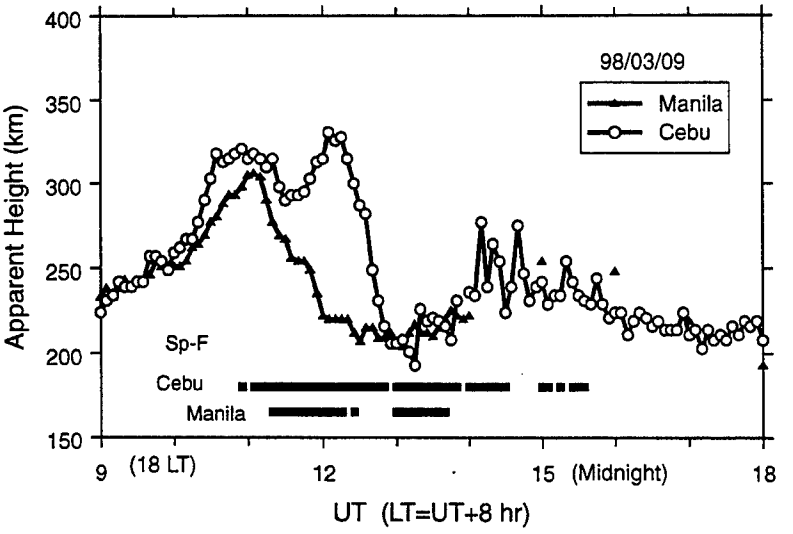


Results

Case *a* is interpreted as that both minimum ionospheric heights at two stations are primarily controlled by the chemical process, which doesn't very much depend on latitude we are considering, because of small evening enhancement of upward **EXB** drift.

While in case *b*, the constant height difference might be caused by declining of isoelectron contours toward latitude as a result of **EXB** drift. Including thermospheric wind model, further, we can reproduce the observations quite well.

Figure 2(*c*)



Case *c* is much complicated, and the plots for March 9, 1998 are shown in Figure 2(*c*). Before 10 UT (18 LT), the heights at two stations are the same and they may be governed by the chemical process. The layers started to rise at 10 UT and the difference between two stations increased with time. This period corresponds to the evening enhancement of the upward drift. The layer heights reached their maximum value at 11 UT and the drift direction turned to downward. At 11:30 UT, the layer at Cebu started to rise again, while that at Manila continued to descend. Eventually, the height difference between two stations reached up to 110 km at 12:05 UT. The last part of the height changes (11:30–13:00 UT) cannot be reproduced by a simple model, and it is natural to interpret that the difference should be spatial structure in the east–west direction.

Another important signature on this day is spread *F* occurrence. Similar height changes associated with spread *F* were observed on March 3, 1998. Although we have only two days during the campaign, the spread *F* occurrence and peculiar height changes seem to be connected to each other. One possibility is the zonal density gradient effect as pointed out by *Kelley et al.* [1981]. However, two cycles of undulation of layer height were observed at Cebu, but only one at Manila. Therefore, the connection with gravitational wave activities is not immediately concluded. Another possibility is that the observed height changes themselves are the manifestation of a long–wavelength of gravitational Rayleigh–Taylor instability. At any rate, we need more investigations. Further WestPac campaigns are planned.

References

Kelley, M.C., M.F. Larsen, C. LaHoz, and J.P. McClure, Gravity wave initiation of equatorial spread F: A case study, *J. Geophys. Res.*, *86*, 9087–9100, 1981.

Kelley, M.C. and T. Maruyama, A diagnostic model for equatorial spread *F*, 2. The effect of magnetic activity, *J. Geophys. Res.*, *97*, 1271–1277, 1992.

ROCSAT-1 satellite: Characterization of ion density and velocity structures in equatorial plasma bubbles

H. C. YEH , S. Y. Su, J. M. Wu, L. F. Lee, S. C. Yang, H. L. Chen and K. Y. Chen (all at Institute of Space Science, National Central University, Chung-Li, Taiwan; E-mail: yeh@jupiter.ss.ncu.edu.tw); R. A. Heelis (William B. Hanson Center for Space Sciences, The University of Texas at Dallas, Richardson, Texas, 75803, USA)

The ROCSAT-1 satellite was successfully launched on 27 January 1999 into a circular orbit with an altitude of 600 kilometers, and an orbital inclination of 35 degrees. The onboard Ionospheric Plasma and Electrodynamics Instrument (IPEI) consists of 4 sensors to take in-situ measurements of ion density, temperature, composition and drift velocity over a large dynamic range with high sensitivity. The two ion drift meters are configured to measure velocity components in both cross-track directions simultaneously. Over the passing year, equatorial plasma bubbles were observed by ROCSAT-1 under diversified geophysical conditions. In this report we present examples that typify these bubble observations. Their dependencies on local time, longitude as well as geomagnetic and solar activities are examined. Moreover, we analyze the high resolution (at 1024 Hz sampling rate) data of ion density and the two cross-track velocity components of the bubbles to study their correlation and spectral features at various spatial scales. The spectral index and the wavelength of the break in the spectrum at intermediate (0.1 - 1 km) and transitional (< 100 m) wavelengths are of particular interest.

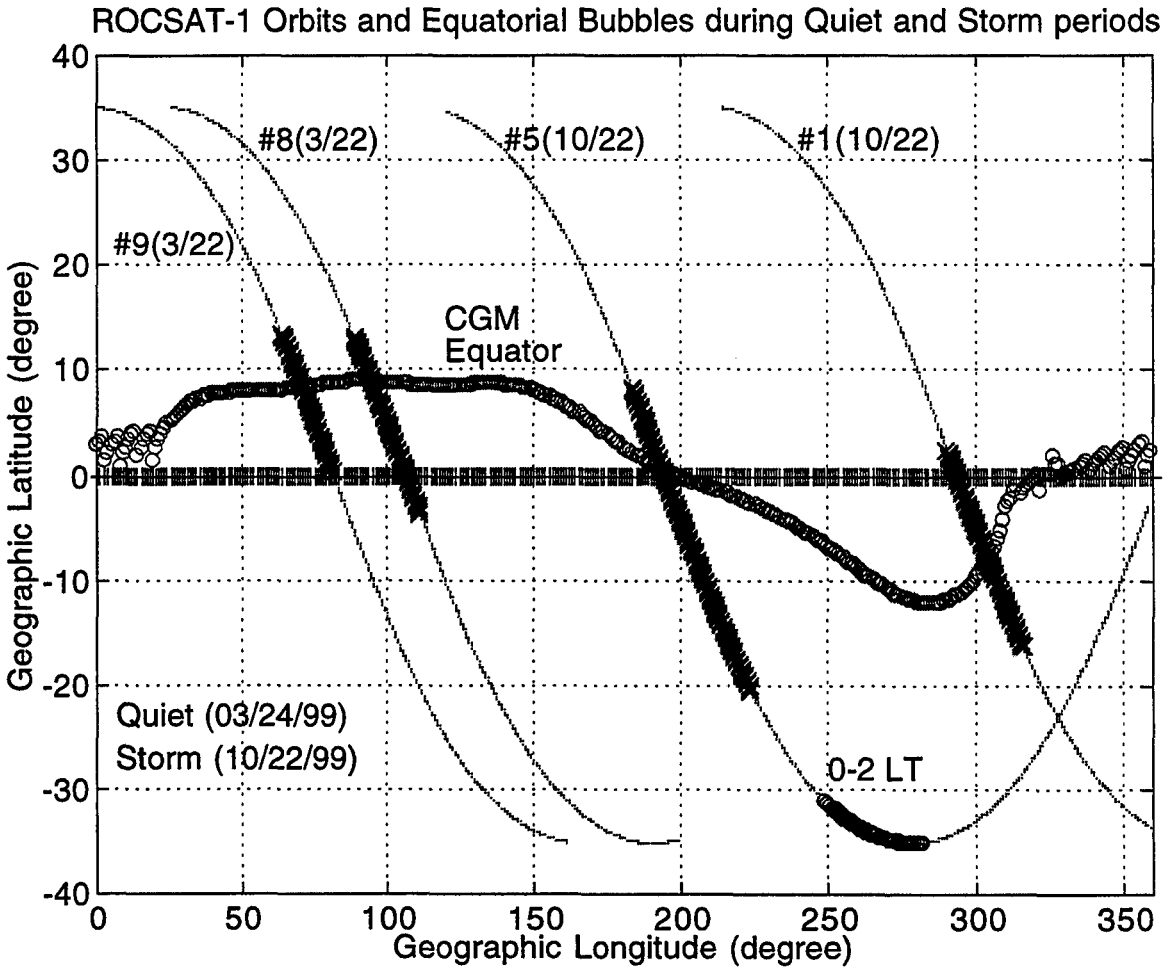


Figure 1. ROCSAT-1 orbits in geographic coordinates. Equatorial plasma bubbles were observed at locations marked by "x". Low latitude bubbles are marked by "o" along orbit #5.

Figure 1 shows the satellite trajectories in geographical coordinates for the four passes of interest in this report. March 24 is a geomagnetically quiet day with Kp =0+,1,1,2,1,1-,0+,0+ for each 3-hour slot and with F10.7-cm =106.7 for the solar flux condition. During the time interval of orbit #8 (orbit #9) on March 24, Kp was 1 (1-). In contrast, October 22 is a magnetic storm day with Kp =7, 8-,8,5+,5-,4+,6-,3+ and the solar flux F10.7-cm =158.8 for the day. The orbit #1 on October 22 was during the expansion phase (Kp=7), while the orbit #5 was during the main phase (Kp=8) of the October 22 storm. The crossed segments along the satellite trajectories identify the equatorial bubble structures. These bubble structures are located near, but on both sides of the Corrected Geomagnetic (CGM) equator. Most of the bubble structures were seen in the local time sector between 19 LT and 22 LT. During the main phase of the October 22 storm plasma bubbles were seen to span the wider latitude and local time ranges. The circled segment of orbit #5 on 22 October 1999 identifies a region of post-midnight plasma bubble at tropical latitudes (~ 15° MLAT) in the South America longitude.

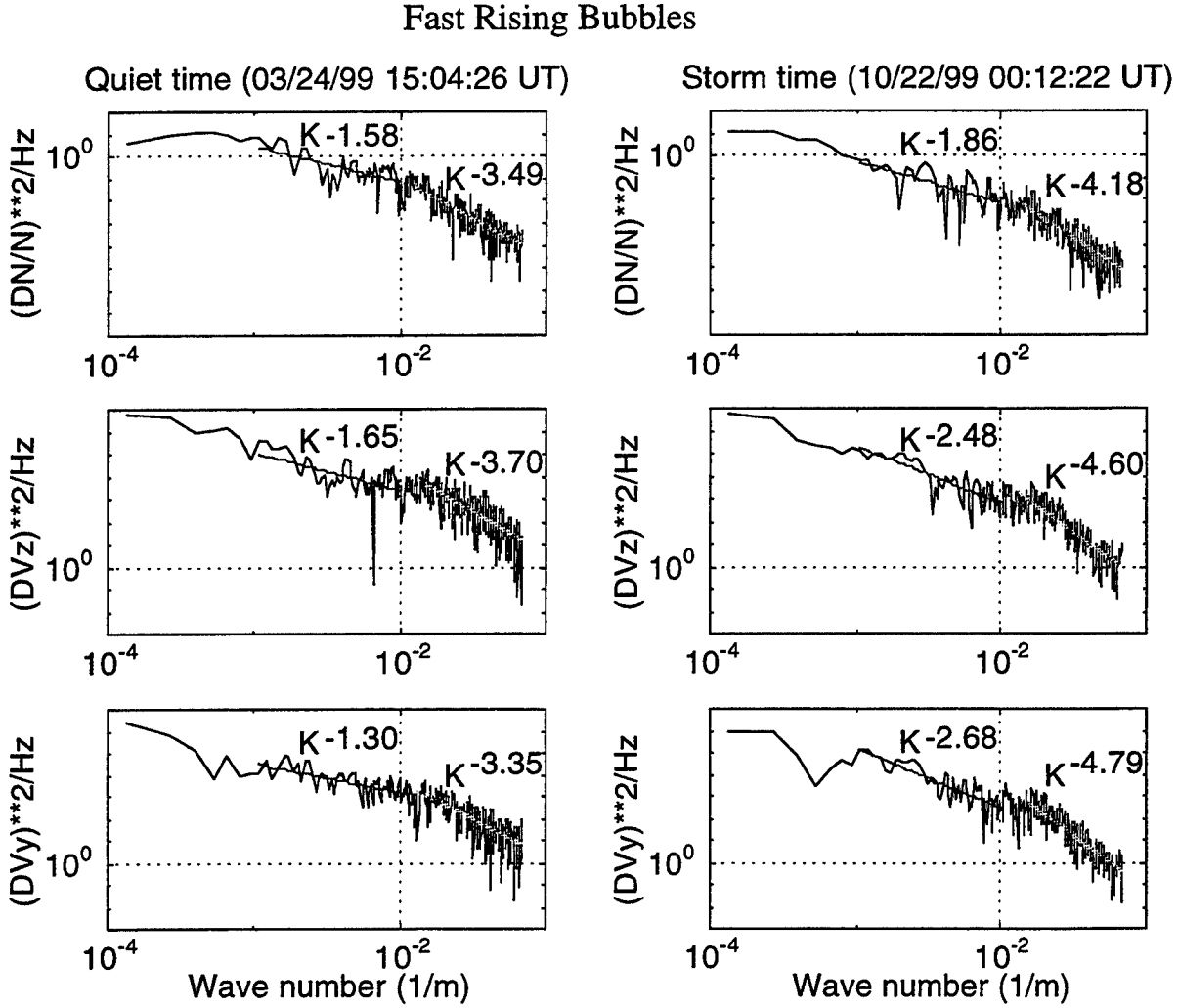


Figure 2. Power spectral density for two fast rising (>1500 m/s) bubbles. Storm time data from orbit #1 (Kp = 7) and quiet time data from orbit #9 (Kp = 1^-). The local time for these spectra is about 19.5 LT.

Large upward ion drift is frequently found to collocate with the density minimum inside a density depletion region. These fast rising bubbles seem to be seen only at early night hours (around 19.5 LT in our examples). The cause of these high speed upward drifting ions in the bubbles with respect to the surrounding plasma has been an interesting research subject. It is generally accepted that the occurrence of fast rising bubble is related to the evening prereversal enhancement of vertical drift, and thus also related to the geomagnetic conditions. Figure 2 presents the power density spectra of the high resolution density (DN/N) as well as the cross-track velocity components DV_z (vertical) and DV_y (horizontal) for two representative fast rising bubbles under the extreme geomagnetic conditions. Each spectrum is fitted with a dual power law representation K^{-n} for two wavelength ranges to derive the spectral index n. As shown, all spectra in Figure 2 have a spectral break at wavelength between 70 - 90 m. In both intermediate and transitional wavelength ranges, the three quiet time spectra have about the same spectral

index. However the quiet time spectral indices are smaller than those of the vertical spectra derived from the rocket experiments in the respective wavelength ranges. Comparing storm time spectra with quiet time spectra, the storm time spectra in general have the steeper slopes in both intermediate and transitional wavelength ranges. The storm time spectral indices are more closer to those values of the rocket observed spectra at lower altitudes. During the expansion phase of the storm, ion-neutral collision frequency at the 600 km altitude may be significantly increased. According to theory, the collision processes will damp short wavelengths. This may explain the steeper spectra observed during the storm time.

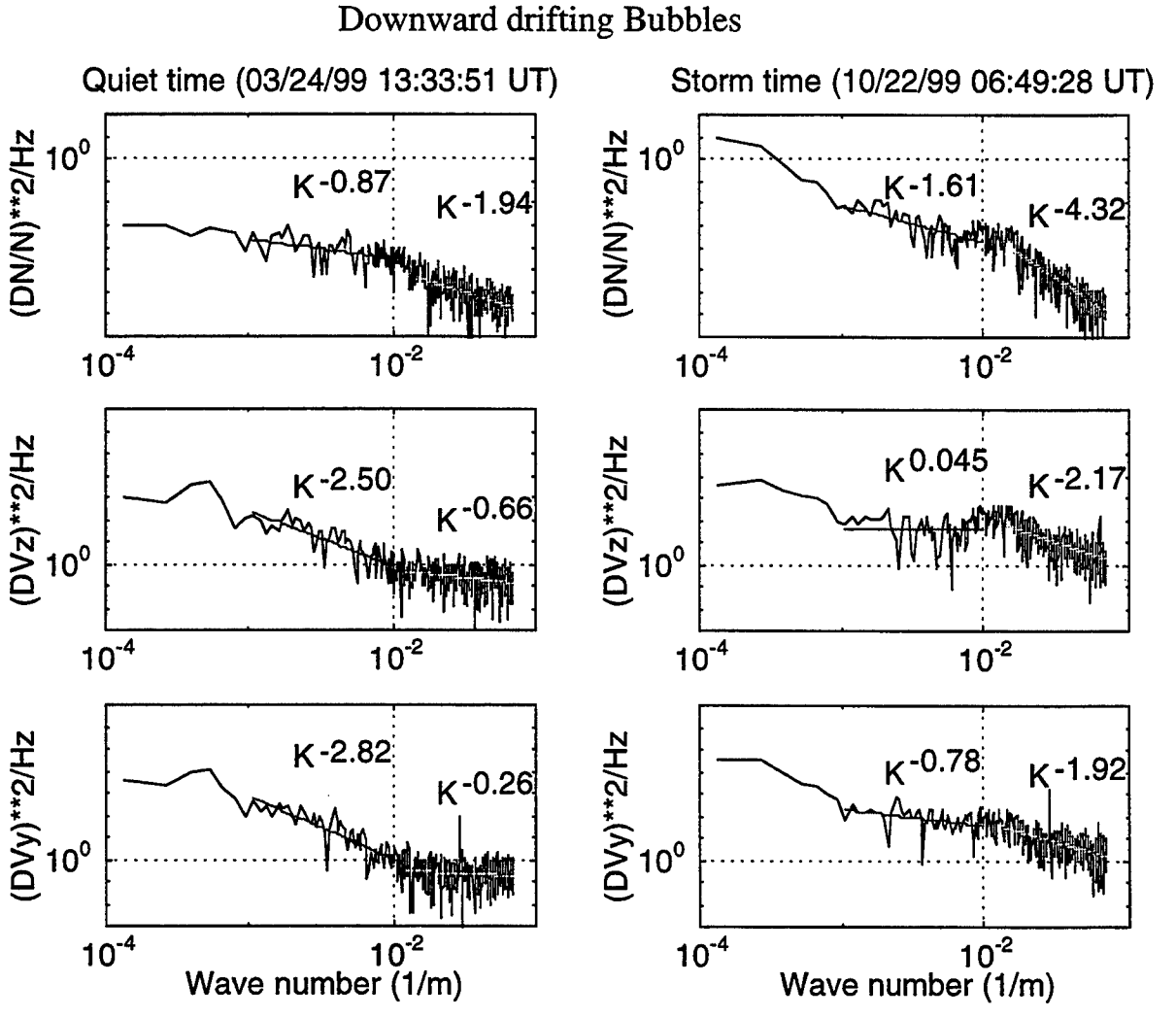


Figure 3. Power spectral density for downward drifting (>100 m/s) bubbles. Storm time data from orbit #5 (Kp=8) and quiet time data from orbit #8 (Kp=1). The local time of these spectra is around 21 LT.

Contrary to the fast rising bubble, large downward ion drift is sometime found to collocate with the density minimum inside a density depletion region. Such downward drifting bubbles are mostly found in the late evening hours. Figure 3 presents some spectral features of two selected down drifting bubbles. As shown in the figure, the spectral shapes vary greatly with geomagnetic conditions. During the storm time the density spectrum can still be described by a dual power law K^{-n}. The density spectral indices are comparable to those of vertical density spectra in the respective wavelength ranges. The two velocity spectra flatten at the intermediate wavelengths. However the Boltzmann relation exists between $(DN/N)^2$ and $(DV_z)^2$ at the transitional wavelengths. The power spectral density levels of the quiet time spectra are much weaker than those of the storm time spectra. Both components of ion drift no longer have the small scale fluctuation. The spectral slope of the density spectrum becomes shallower at both intermediate and transitional wavelengths.

Ionospheric irregularity zonal velocities over Cachoeira Paulista

E.R.DE PAULA, I.J.Kantor, J.H.A.Sobral, H.Takahashi, D. C. Santana, D.Gobbi, A.F. de Medeiros, L.A.T. Limiro (INPE, São José dos Campos, SP, Brazil), H.Kil, P.M.Kintner (Cornell University, Ithaca, NY, USA), M.Taylor (Utah State University, Logan, UT, USA)

We have studied the zonal drift velocity of nighttime ionospheric irregularities from Cachoeira Paulista (22.41°S, 45°W, dip angle –26°), a station under the Equatorial Anomaly, from December 1998 to February 1999 using L1 band GPS receivers and OI 630 nm all–sky images. The average decimetric solar flux index for this period of increasing solar activity was about 145. The GPS technique used receivers spaced 55 m in the magnetic east–west direction and probed small scale plasma structures (scale sizes about 400 m) at altitudes near 350 km. The zonal irregularity drift velocities measured by this technique were eastward with values of about 150 m/s at 20 LT, about 120 m/s around midnight, and decreased further in the post–midnight sector. The standard deviations of these drifts decreased significantly in the post–midnight sector. The spaced receiver GPS zonal drifts from Cachoeira Paulista are systematically larger than the Jicamarca incoherent scatter radar zonal drifts, which is consistent with results from previous studies. Analysis of magnetic activity effects showed smaller eastward drifts and earlier reversal times to westward drifts during disturbed conditions compared to geomagnetically quiet periods. The zonal drifts of large scale plasma structures were obtained using OI 630 nm photometer images from a nominal height of 250 km which were projected to 350 km over Cachoeira Paulista along magnetic field lines. These photometer derived zonal drifts are also eastward, but have magnitudes smaller than the GPS eastward drifts, particularly in the pre–midnight sector. We will discuss these two drift measurement techniques and the interpretation of our results.

M. PALMROTH (Geophysical Research, Finnish Meteorological Institute, P.O. Box 503, Helsinki, 00101, Finland), H. Laakso (Geophysical Research, Finnish Meteorological Institute, P.O. Box 503, Helsinki, 00101, Finland), B. G. Fejer (Center for Atmospheric and Space Sciences, Utah State University, UMC 4405 Logan, UT 84322–4405) and R. F. Pfaff Jr. (NASA/Goddard Space Flight Center, Mail Code 696, Greenbelt, MD 20771)

DE–2 observations of morningside and eveningside plasma density depletions in the equatorial ionosphere

The occurrence of equatorial density depletions in the nightside F–region ionosphere has been investigated using observations gathered by the polar–orbiting Dynamics Explorer–2 (DE–2) satellite from August 1981 to February 1983. A variety of electric field/ plasma drift patterns were observed within these depletions, including updrafting, downdrafting, bifurcating, converging, subsonic and supersonic flows. The depletions, 116 events in total, are distributed over two groups: Group I (eveningside depletions) consists of the events in the 19–23 MLT sector, and group II (morningside depletions) is the events in the 23–06 MLT sector. A statistical analysis reveals clear differences in the density depletion occurrence rates between the two groups. Magnetic activity appears to suppress the generation of eveningside depletions with a delay of 2–3 hours. In the morningside the probability of observing depletions increases instantly with increasing magnetic activity, yet the best correlation is found with a 2–hour delay. This indicates that in the premidnight sector the substorm–induced dynamo and prompt penetration electric fields induce westward electric fields in the equatorial ionosphere 2 hours after the onset in the auroral region. In the postmidnight sector high–latitude ionospheric disturbances induce instantly equatorial eastward electric fields that move the F layer to higher altitudes, where it can become unstable to the Rayleigh–Taylor (RT) instability. Eveningside depletions were observed at all longitudes except those over the Pacific Ocean, while the morningside depletions occurred mostly over the Pacific and Atlantic–African sectors.

Interaction of two long wavelength modes in the nonlinear numerical simulation model of equatorial spread *F*. P7-3

R. SEKAR, E.A. Kherani (Physical Research Laboratory, Ahmedabad - 380 009, India.)
and
P.B. Rao, A.K. Patra (National MST radar facility, Gadanki - 515 502, India.)

Plasma irregularities during nighttime in the equatorial F region manifest themselves in many different forms on VHF radar maps ranging from spectacular rising plumes and multi-plumes to modest bottomside spread-F events. The bottomside spread F events were shown (*Sekar and Kelley, 1998*) to be due to the combined action of vertical shear in the zonal plasma drift and the westward electric field associated with a certain zonal electric field temporal pattern. While the plumes which extend from bottomside to the topside of the ionosphere were identified by earlier experiments (*Szuszczewicz et al, 1980*) as the manifestation of large scale plasma bubbles generated by the action of generalized Rayleigh-Taylor instability which is believed to be the primary causative mechanism for the generation of long wavelength irregularities. Multi-plumes are thought to be generated by the action of the Rayleigh-Taylor instability seeded by the gravity waves (*Huang and Kelley, 1996*) in the neutral atmosphere. Further, a unique pattern observed by Indian MST radar in ionosphere mode, consisting of two plumes along with a prominent descending structure was reported (*Patra et al, 1997*) earlier. The Doppler velocities inside the descending structure were predominantly downward with a peak value of about 70 ms^{-1} which was significantly above that of the ambient plasma drift. As the plasma plume is generally expected to move upward, down drafting of the plasma structures is yet to be understood comprehensively.

Numerical model:
In order to understand these downward velocities and evolutionary plasma structures of ESF, nonlinear numerical simulation model of ESF (*Sekar et al, 1994, 1995*) is adopted for the present investigation.

$$\nabla.(\nu_{in}.N.\nabla\phi) = B.[-g + W_y.\nu_{in} + (E_{xo}/B)\nu_{in}].\frac{\partial N}{\partial x} \qquad (1)$$

$$\frac{\partial N}{\partial t} - \frac{\partial}{\partial x}[(N/B).(E_{yo} + \frac{\partial \phi}{\partial y}] + \frac{\partial}{\partial y}[(N/B).(-E_{xo} + \frac{\partial \phi}{\partial x})] = -\nu_R.N \qquad (2)$$

Here N, ϕ and ν_R represent the electron number density, the perturbation potential and the recombination rate respectively. The symbols g, ν_{in}, E_{xo}, E_{yo}, B and W_y correspond to acceleration due gravity, ion-neutral collision frequency, the ambient electric field in zonal(x) and vertical(y) directions, the strength of Earth's magnetic field and vertical wind respectively.

The model describes the spatial distribution of the perturbed potential generated by the generalized Rayleigh-Taylor instability in a slab geometry alongwith temporal evolution of total plasma density. These equations are solved numerically in a two dimensional plane perpendicular to Earth's magnetic field. For seeding the above instability, gravity waves in the neutral atmosphere is thought to be a potential source. As the spectra associated with the gravity waves are diverse, it becomes important to investigate the development of ESF with different modes simultaneously. As a first step, an investigation is made with two long wavelength modes as initial perturbation in the simulation model of ESF.

Results:

This investigation reveals that the longer wavelength mode developed into bottomside structure, while the second mode developed into multiple plumes. Further, the interaction between the modes has been shown to modify the electric field structures. This interaction is also found to vary considerably depending upon the amplitudes of two long wavelength modes and also the initial phase difference between these modes. With the introduction of two long wavelength modes as the initial plasma density perturbation with appropriate amplitudes and phase delay, it is possible to reproduce a descending ESF structure similar to the one that was observed by Indian MST radar.

References:

Huang C.S. and M.C. Kelley, 1996, Nonlinear evolution of equatorial spread F 2. Gravity wave seeding of Rayleigh-Taylor instability, *J. Geophys. Res.*, **101**, *293-303.*

Patra A.K., P.B. Rao, V.K. Anandan and A.R. Jain, 1997, Radar observations of 2.8 m equatorial spread-F irregularities, *Journal of Atmospheric and Solar Terrestrial Physics,* **59**, *1633-1641*

Sekar R. and M.C. Kelley, 1998, On the combined effects of vertical shear and zonal electric field patterns on nonlinear equatorial spread F evolution, *J. Geophys. Res.*, **103**, *20,735-20,747.*

Sekar R., Suhasini R. and Raghavarao R. 1994, Effects of vertical winds and electric fields in the nonlinear evolution of equatorial spread *F*, *J. Geophys. Res.*, **99**, *2205.*

Sekar R., R. Suhasini and R. Raghavarao, 1995, Evolution of plasma bubbles in the equatorial *F* region with different seeding conditions, *Geophys. R es. Lett.*, **22**, *885-888.*

Szuszczewicz, E.P., Tsunoda, R.T., Narcisi R. and Holmes, J.C., 1980, Coincident radar and rocket observations of equatorial spread-*F*, *Geophysical Research Letter*, **7**, *537-540.*

A STUDY OF THE IONOSPHERIC PLASMA BUBBLES CLIMATOLOGY OVER BRAZIL, FOR A PERIOD OF 22 YEARS (1977-1998)

J. H. A. SOBRAL[1], M. A. ABDU[1], H. TAKAHASHI[1], M. J. TAYLOR, E. R. DE PAULA[1], C. J. ZAMLUTTI[1], M. G. DE AQUINO[1]

[1]Instituto Nacional de Pesquisas Espaciais –INPE, Caixa Postal 515, 12201-970 São José dos Campos, Brazil
[2]Utah State University, Logan, Utah, United States of America

ABSTRACT

The nocturnal phenomenon of the large-scale ionospheric plasma depletions, or plasma bubbles, has been extensively surveyed over Brazil, for more than two decades through optical (Sobral et al. 1980a,b, 1981, 1985, 1991, 1999; Sobral and Abdu 1990; Taylor et al., 1997; Fagundes et al., 1997; Sahai et al., 1981, 1999) and radiofrequency (Abdu et al., 1982,1983,1985,1987, 1998) techniques and rocket soundings (Abdu et al. 1991; Sobral et al. 1997).

The occurrence characteristics of the large scale ionospheric plasma depletions, during the period of 1977-1998, with solar activity, season and geomagnetic activity, is studied here based on data from 934 days of experimental observations of the atomic oxygen 630 nm nocturnal airglow, by means of scanning photometers and imagers located at Cachoeira Paulista (44.5°W, 33°S, 28°S dip).

The groups of years representing the solar cycle maximum and minimum of this study were chosen based on the average of their yearly sunspot number. In this way, the solar maximum period was formed by the years 1978-1982, 1988-1992, included 442 days of experiments of the OI 630 nm nocturnal airglow and had sunspot number range/average 92.5-157.6/ 129,9. Analogously, the solar minimum period was 1977, 1983-1987 and 1993-1998, included 492 days, and had sunspot number range/average 8.7-66.6/33.1. The frequency of occurrence for the period of 1977-1998 was 42.1%.

The complete solar activity period presented maximum and minimum frequency of occurrence 86 %, in January, and 11.2%,in May, respectively. The solar maximum period presented maximum and minimum frequency of occurrence of 83.33 % in October and 10.5% in May, respectively. January closely followed October with 82.6%. The solar minimum period presented maximum and minimum frequency of occurrence 90% in January and 12.2 % in May, respectively.

The maximum/minimum frequency of occurrençe during the complete solar cycle occurred in the October-March/April-August time frames, respectively (Fig. 1a). Accordingly, for solar maximum and minimum periods such groups were, respectively, September-April/May-August (Fig. 1b) and October-March/April-September (Fig. 1c).

During the solar minimum period, the season of minimum frequency of occurence, April-September, is 2 months longer than that of the solar maximum (May-August. See also Fig. 1c).

Figs. 3 to 9 show the variation of the frequency of occurrence of the plasma as a function of different time intervals of Kp.

The frequency of occurrence of the plasma bubbles over Cachoeira Paulista is clearly seen to fall with the Kp amplitudes in Figs. 3 and 5. Figs. 7 and 9 also show that trend, but it does it to a less degree towards the extreme values of Kp due to less number of samples (see Figs. 8 and 10).

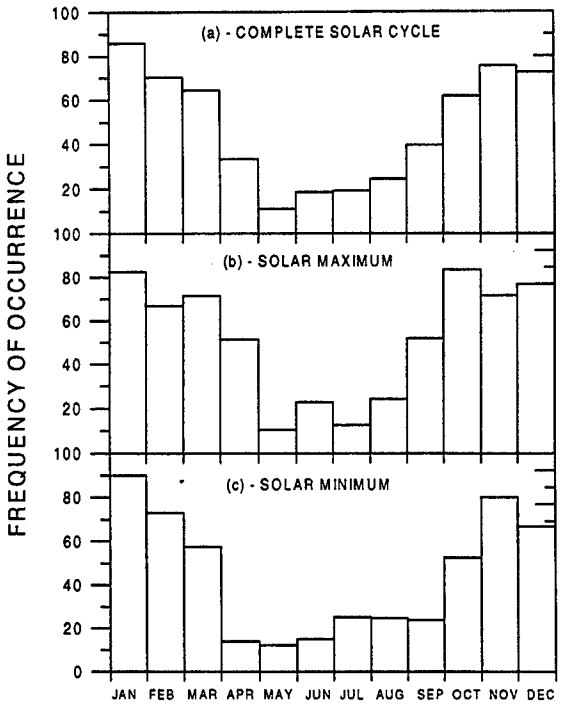


Fig. 1. Frequency of occurence of the plasma bubbles over Cachoeira Paulista for the following periods: (a) compete solar cycle (1977-1998, 934 days), (b) solar maximum (1978-1982, 1988-1992, 442 days), and (c) solar minimum (1977, 1983-1987 and 1993-1998, 492 days).

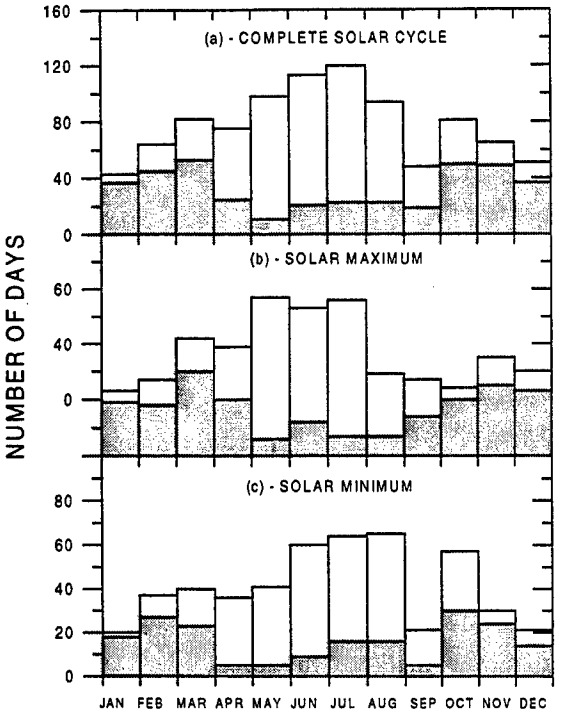


Fig. 2. Monthly statistics from which Fig. 1 was made. The vertical axis represents the number of days in which the bubbles were and were not observed, which are represented by dark and clear areas, respectively. The histogram amplitude has origin in the horizontal axis for both cases.

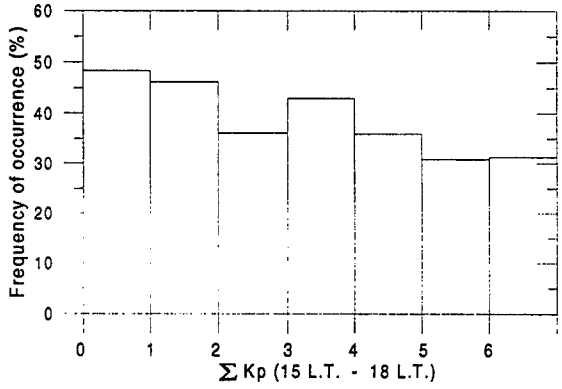


Fig. 3. Frequency of occurrence of the plasma bubbles over Cachoeira Paulista as a function of the three-hourly values of Kp in the local time interval of 15-18.

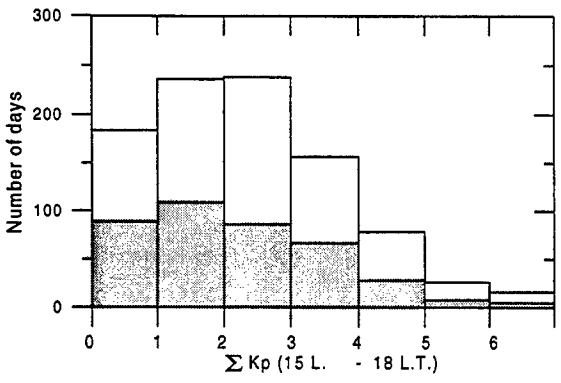


Fig. 4. Statistics from which Fig. 3 was made. The vertical axis represents the number of days in which the bubbles were and were not observed, which are represented by dark and clear areas, respectively. The histogram amplitude has origin in the horizontal axis for

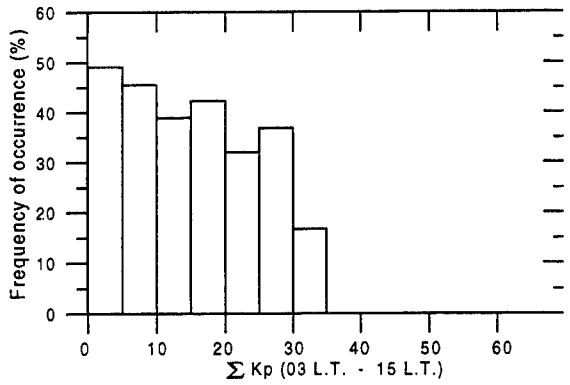


Fig. 5. Frequency of occurrence of the plasma bubbles over Cachoeira Paulista as a funtion of the three-hourly Kp values summed over the time interval of 03-15

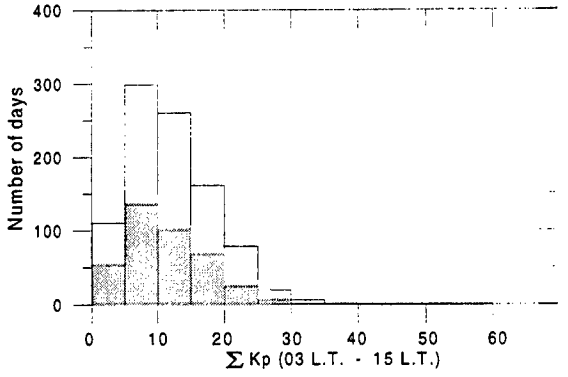


Fig. 6. Same as Fig. 4 except for the Kp time interval

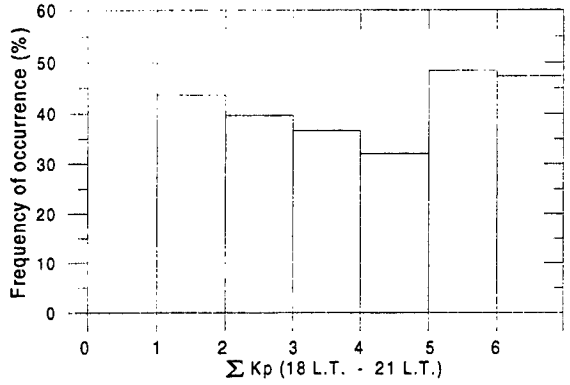


Fig. 6. Same as Fig. 4 except for the Kp time interval

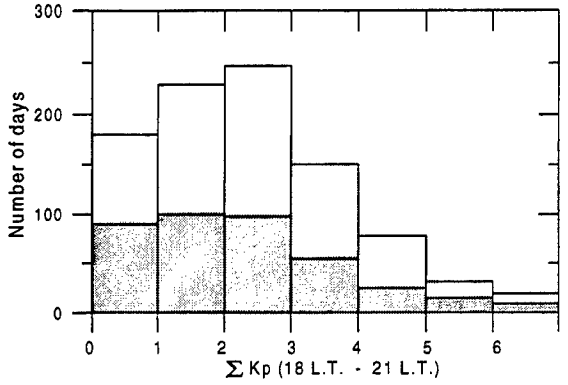


Fig. 8. Same as Fig. 4 except for the Kp time interval.

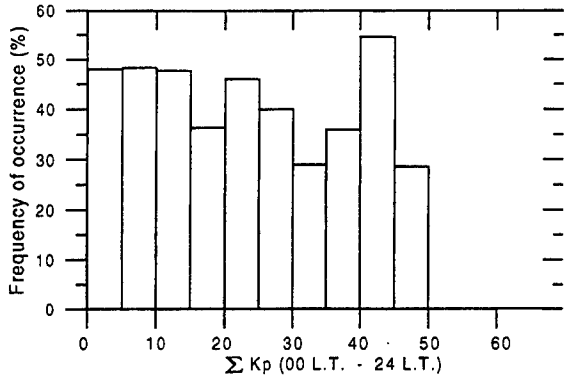


Fig. 9. Same a as Fig. 5 except for the Kp time interval.

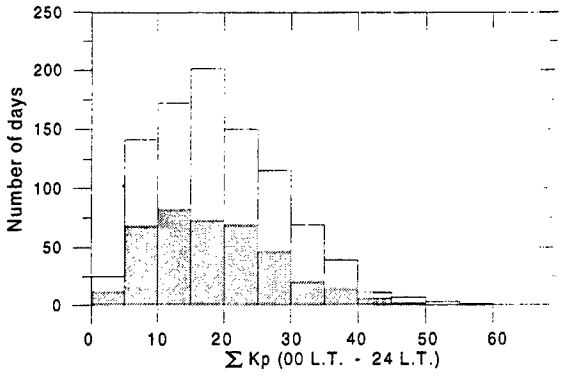


Fig. 10. Same as Fig. 4 except for the Kp time interval.

Acknowledgements: This work was partially supported by the Brazilian Funding institutions Fundação de Amparo à Pesquisa do Estado de São Paulo – FAPESP and Conselho Nacional de Desenvolvimento Científico e Tecnológico. In complement to the INPE photometer system data the present data set included some optical images of the OI 630 nm for the years of 1994 and 1995 obtained by the Dr. M. Mendillo's Boston University imager, located at Cachoeira Paulista.

References

Abdu, M. A., Medeiros, R. T., Sobral, J. H. A. , 1982. Equatorial Spread-F Instability Conditions as Determined from Ionograms. Geophys. Res. Lett., 9(6), 692.

Abdu, M. A., Medeiros, R. T., Sobral, J. H. A., Bittencourt, J. A. , 1983. Spread F Plasma Bubble Vertical Rise Velocities Determined from Spaced Ionosonde Observations. J. Geophys. Res., 88(All), 9197.

Abdu, M. A., Batista, I. S., Sobral, J. H. A., 1985. Equatorial Ionospheric Plasma Bubble Irregularity Occurrence and Zonal Velocities under Quiet and Disturbed Conditions form Polarimeter Observations, J. Geophys. Res., 90(A10), 9921.

Abdu, M. A., Sobral, J. H. A., Nakamura, Y., 1987. Equatorial Plasma Bubble Zonal Velocity Height Gradients from Spaced VHF Polarimeter and Scanning 630 nm Measurements. Geophys. Res. Lett., 14(19), 965.

Abdu, M. A., Muralikrishna, P., Batista, I. S., Sobral, J. H. A., 1991. Rocket Observations of Equatorial Plasma Bubbles over Natal, Brazil, using a High Frequency Capacitance Probe. J. Geophys. Res., 96(A5), 7689.

Abdu, M. A., Sobral, J. H. A., Batista, I. S., Rios, V. H., Medina, C., 1998. Equatorial Spread-F Occurrence Stastistics in the American Longitudes: Diurnal, Seasonal and Solar Cycle Variations. Adv. Space Res., 22(6), 851.

Fagundes, P. R., Sahai, Y., Batista, I. S., Bittencourt, J. A., Abdu, M. A., Takahashi, H., 1997. Vertical and zonal equatorial F-region plasma bubble velocities determined from OI 630 nm nightglow imaging. Adv. Space Res. 20 (6), 1297.

Sahai, Y., Bittencourt, Teixeira, N. R., Takahashi, H., 1981. Plasma irregularities in the tropical F-region detected by OI 7774 A and 6300 A nightglow measurements, J. Geophys. Res. 86(A5), 3496.

Sahai, Y., Fagundes, P. R., Bittencourt, J. A., 1999. Solar cycle effects on large scale equatorial F-region plasma depletions. Adv. Space Res. 24, 11, 1477.

Sobral, J. H. A., Abdu, M. A., Batista, I. S., 1980a. Airglow Studies on Ionosphere Dynamics over Low Latitude in Brazil. Ann. Geophys. 36(2), 199-204, 1980a.

Sobral, J. H. A., Abdu, M. A., Batista, I. S., Zamlutti, C. J., 1980b. Association Between Plasma Bubble Irregularities and Airglow Disturbances over Brazilian Low Latitudes. Geophys.Res.Lett., 11(7), 980.

Sobral, J. H. A., Abdu, M. A., Zamlutti, C. J., Batista, I. S., 1981. Wave Disturbances in the Low Latitude Ionosphere and Equatorial Ionospheric Plasma Depletions. J.Geophys.Res., 86(A3), 1374.

Sobral, J. H. A., Abdu, M. A., Sahai, Y., 1985. Equatorial Plasma Bubble Eastward Velocity Characteristics from Scanning Airglow Photometer Measurements over Cachoeira Paulista. J. Atmos. Terr. Phys., 47(8-10), 895.

Sobral, J. H. A. and Abdu, M. A., 1990. Latitudinal Gradient in the Plasma Bubble Zonal Velocities as Observed by Scanning 630mm Airglow Measurements. J. Geophys. Res., 95(A6), 8253.

Sobral, J. H. A., Abdu, M. A., 1991. Solar Activity Effects on Equatorial Plasma Bubble Zonal Velocity and its Latitude Gradient as Measured by Airglow Scanning Photometers. J. Atmos. Terr. Phys., 53(8), 729.

Sobral, J. H. A., Abdu, M. A., Muralikrishna, P., Takahashi, H., Sawant, H. S., Zamlutti, C. J., Aquino, M. G. S., 1997. Horizontal Gradients of the Nocturnal OI 557.7 nm and OI 630 nm Photoemission Rates in the Equatorial Ionosphere based on Rocket Electron Density Data. Adv. Space Res., 20(6), 1317-1320, 1997.

Sobral, J. H. A., Borba, G. L., Abdu, M. A., Batista, I. S., Sawant, H. S., Zamlutti, C. J., Takahashi, H., Nakamura, Y., 1997. Post-Sunset Wintertime 630.0 nm Airglow Perturbations Asssociated with Gravity waves at Low Latitudes in the South American Sector. J. Atmos. Terr. Phys., 59(13), 1611.

Sobral, J.H.A., Abdu, M.A., Takahashi, H., Sawant, H.S., Zamlutti, C.J., Borba, G.L., 1999. Solar and geomagnetic activity effects on nocturnal zonal velocities of ionospheric plasma depletions. Adv. Space Res., 24, 11, 1507.

Taylor, M. J., Eccles, J. V., Labelle, J. and Sobral, J. H. A., 1997. High-Resolution OI (630 nm) Image Measurements of F Region Depletion Drifts During the Guará Campaign. Geophys. Res. Lett., 24(13), 1699-1702, 1997.

The Space Weather Program – Recent Advances

Sunanda Basu, R. A. Behnke and R. M. Robinson
Atmospheric Sciences Division
National Science Foundation
Arlington, VA 22230

Abstract

The National Space Weather Program (NSWP) in the US, a multiagency partnership between government, academia, and industry was established in October 1994. The first Implementation Plan for the Program was published in January 1997 and widely circulated in the community. The overarching goal of the NSWP is to provide accurate and reliable space environment observations, specifications, and forecasts. The purpose of this presentation is to review the progress achieved in attaining this goal. In particular, attention will be focussed on the basic research in the low latitude Ionosphere/Thermosphere area that has been funded under the NSWP, the development of metrics for physical parameters involved in space weather to chart progress in a more quantitative manner, the effort made in establishing a Community Coordinated Modeling Center (CCMC), and international activities for establishing a global space weather initiative.

Introduction

The US National Space Weather Program (NSWP) was established in October, 1994, when the Committee for Space Environment Forecasting under the Federal Coordinator for Meteorological Services and Supporting Research (FCMSSR) established a working group to develop a strategic plan that would address the nation's needs for space environmental forecasting. At the same time, FCMSSR created the NSWP Program Council, which first met in March of 1995. During that meeting, the Program Council approved the Strategic Plan, which was developed by the Working Group, and recommended that the Group begin working on an implementation plan for the program. The Implementation Plan was completed in late 1996 and approved by the Program Council in January of 1997.

Recognizing that the Implementation Plan was to be a living document, the Program Council recommended periodic updates to the Plan. The first update to the Implementation Plan is under preparation. It covers Space Weather activities occurring between 1996–1998. It begins with a summary of progress to date in each of the activity areas outlined in the original plan. It concludes with an evaluation of how far the program has come in achieving the near–term goals of the NSWP and recommendations for updating the timelines based on progress made and changes in strategies.

In this brief overview, we will provide a synopsis of the equatorial ionospheric research that has been funded in the ionosphere/thermosphere area in the first two years of the NSWP competition (FY 96 and 97), describe the effort to develop a set of space weather metrics and the Community Coordinated Modeling Center (CCMC), as well as provide some information on international activities which may lead to a more global space weather initiative.

Basic Research in the Low Latitude Ionosphere/Thermosphere Area

The NSWP goals involve the ability to predict the space environment. Hence, basic scientific research must be conducted to improve our fundamental understanding of the physical processes involved in three broad areas: the sun and solar wind, the magnetosphere and the ionosphere/thermosphere system. In June 1995, a working group for each of these areas was assembled to formulate plans for addressing its space weather goals. Fifteen topics were identified in these three areas and they are laid out in Figure 3–1 of the NSWP Implementation Plan. The funding initiatives in 1996 and 1997 were targeted to address some of these priority

areas. The ultimate goal is to develop an operational model that incorporates basic physical understanding to enable specification and forecasting of the space environment. Given the low latitude emphasis of this meeting, we provide a brief description of the funded research relevant to this region of the atmosphere.

• A University of Southern California project aims to develop a data assimilation model based on a physics–based model of the ionosphere and measurements of total electron content determined from GPS satellite signals. Tomographic techniques based on GPS signals received at a single station work well only when the ionosphere is relatively unstructured. When combined with a physics–based model, these tomographic determinations can be made more accurately. The investigators will also study the benefits gained from using data from a satellite–borne GPS receiver in low Earth orbit. This approach has the potential to provide a means to specify the global state of the ionosphere on a continuous basis. This group, together with the Utah State University group, have been funded by the DoD to develop an ionospheric data assimilation model which will be very useful for space weather purposes.

• U. of Colorado scientists are conducting another study based on GPS signals. This study makes use of GPS signals received in low Earth orbit by the TOPEX/POSEIDON satellite. The research will concentrate in particular on the ionospheric effects produced by large magnetic storms.

• Because the topside ionization can contribute 70 to 80 percent of the total column density, it is important to understand how the electron density profile behaves above the F region peak. This is the topic of a study conducted by scientists at Hughes STX who will use data from topside sounders on satellites, incoherent scatter radars, and in situ measurements of electron density to develop a topside ionosphere model. The model will provide a global specification of the topside ionosphere as a function of UT, local time, season, solar cycle, and magnetic activity.

Although several models have been successful in reproducing the large–scale behavior of the ionosphere, the specification and prediction of ionospheric irregularities still poses a serious problem to modelers. The NSWP has supported several projects whose aim is to better understand these irregularities, particularly at the equator where their effects produce serious problems in communication and navigation systems.

• A project being undertaken at SRI International involves the deployment of a meridional chain in the Western Pacific (WestPac chain) of ionospheric sounders spanning the magnetic dip equator. The data will be used to study the development of equatorial spread F, including its spatial structure and dependence on ionospheric properties in the conjugate E regions.

• Scientists at the Space Environment Corporation are studying equatorial spread F in a similar manner. Using data from the WestPac chain of ionosphere stations, the investigators will examine the parameters that control the onset of the Raleigh–Taylor instability. The observations will be assimilated into models to identify the driving mechanisms and establish the existence of possible precursor events for equatorial spread F.

• Another study of equatorial spread F is being conducted at Utah State University using data from the Jicamarca radar in Peru, along with ionosonde and satellite measurements. The measurements will be used to determine the height–dependent ambient electrodynamic conditions immediately prior to the occurrence of spread F, the location of the initial unstable layer, and its temporal and spatial evolution for different seasons and flux conditions. The combined data set will also allow the investigators to study the role of meridional neutral winds and magnetic declination on spread F formation. When the initial conditions for spread F have been determined, the results will be merged with a global ionosphere model.

• A theoretical study being undertaken at Cornell University also strives to achieve a predictive capability for bottomside equatorial spread F. This study makes use of numerical simulation and modeling of the F layer along with observational data from the Jicamarca radar to formulate a theoretical basis for the observations.

• Scientists at the University of Texas at Dallas are taking a different approach to the prediction of equatorial spread F. This involves the development of a neural network using input data from the DMSP satellite and various ground–based observing systems. Historical data are used to determine the combination of circumstances likely to lead to equatorial spread F development. Once the technique has been validated, the model will be

examined in detail and contrasted with the output of models based on fundamental plasma physics in order to identify the most critical driving elements of such models.

In view of the progress made in the physical understanding, availability of new observations and improvements in our modeling capability, the various timelines provided in the NSWP Implementation Plan have been revised. These will be shortly available as part of the updated implementation plan.

Development of Metrics for the NSWP

A "space weather metric" is a quantitative measure of the ability of a scientific algorithm or model to predict or nowcast the value of a physical parameter involved in space weather. A specific metric has three elements:

- A parameter defined at some position and time (for example, the F–region peak electron density at mid–latitude every hour for the next day);
- An observable to which a prediction can be compared (e.g., density measurement by an incoherent–backscatter radar facility);
- A criterion by which the metric is quantified (e.g., RMS difference between prediction and observation).

The Space Environment Center (SEC) of the National Oceanic and Atmospheric Administration (NOAA) and the U. S. Air Force 55th Space Weather Squadron provide space forecasts and nowcasts for a wide variety of practical applications. Those agencies have developed "application metrics" for measuring the value and validity of the specific services they provide. However, for the purpose of measuring the overall progress of the NSWP, it is useful for the scientific community to define a separate and broader set of metrics, for the following reasons:

- Application metrics change as technologies change. Metrics for the NSWP must remain valid at least for the ten–year life span of the Program.
- Scientific metrics must be open to the scientific community, but application metrics often involve defense secrets (military) or trade secrets (commercial users). (However, it should be noted that application metrics developed by the NOAA Space Environment Center are public and involve no proprietary information.)
- Although there is remarkable overlap between parameters that are important to the application community and scientifically important parameters, the overlap is not 100%. For example, ring–current ions are an important element of magnetospheric physics but have little direct effect on present technological systems.
- To measure progress, scientific metrics should have a scale that encompasses both presently available scientific algorithms and the best that we could hope for, by the end of the NSWP. Present algorithms are not good enough to make useful predictions of all aspects of space weather and might thus score zero on some application metrics. There is also a chance that our ability to predict some parameters will, by the end of the NSWP, exceed what is needed for present technologies. A good scientific metric should encompass both extremes.

Though metrics play a major role in some fields of physical science (notably meteorology), their use is far from universal, and most space scientists are unused to dealing with them. Our study panels were designed to include representatives from NOAA/SEC and the Air Force who are familiar with the needs of the users of space–weather services, and to include some people with experience with metrics. A major goal of the present study has been to acquaint the space–physics research community with the idea of metrics and to initiate scientific discussion of the subject. To this end, a special session was held at the Fall 1997 meeting of the American Geophysical Union, and metrics presentations have been given at three other large meetings.

We recommend that the following types of metric evaluations be undertaken as soon as possible to establish a regular program of scientific metrics for space–weather capabilities:

Type 1. Measurements should be made at a regular cadence and compared systematically with algorithm or model predictions, to establish statistically valid baseline metrics. In addition to the overall averages, average errors should be recorded for different conditions (e.g., *Kp* levels in the case of magnetosphere–ionosphere metrics).

Type 2. When groups of scientists carry out event studies, comparing various models and other algorithms to observations, they should evaluate their models and algorithms in terms of the same standard metrics

used in the statistical analyses of item 1. This would help to tie event studies and campaigns, which are a regular feature of cooperative research programs (e.g. CEDAR, GEM, SHINE) as well as some NASA spacecraft programs, to progress of the NSWP.

Care must be taken to withhold, from the input suite, any data that will be used to test the model. In some cases, withholding those data may artificially degrade model performance. This is an advantage of testing of type 2 as part of scientific campaigns, which generally utilize more data than is routinely available at the forecast centers. Those additional data could be used for testing without degradation of the input stream.

This metrics study is divided into three disciplinary areas: Ionosphere–Thermosphere, Magnetosphere–Ionosphere, and Solar–Interplanetary. The following paragraphs list metrics appropriate only for the ionosphere–thermosphere area. The physical systems are, of course, closely coupled. A physical model of Earth's magnetosphere must be driven by information about the solar wind, and a physical model of the Earth's ionosphere and thermosphere must be driven by inputs from both the magnetosphere and the Sun. Therefore, some of the metrics listed in the M–I section were, in fact, forced by the needs of I–T models, and all of the metrics listed in the S–I section represent requirements of the M–I and I–T models. The complete metrics information is available on the Web (http://rigel.rice.edu/~wolf/swmetrics.html).

The principal ionosphere–thermosphere parameters that need to be predicted are shown in Table 1, grouped according to priority. Ability to forecast or nowcast ionosphere–thermosphere weather should be judged according to ability to deal with the parameters listed.

Table 1 — Priority List of Key Physical Parameters for the Ionosphere and Thermosphere

First Priority:
Electron density N_e, including intrinsic variability
Neutral mass density , including intrinsic variability
N_e/N_e, the amplitude of the electron density irregularities
Second Priority:
Neutral and ion composition
Thermospheric winds and temperatures
Low–latitude ion drifts
Third Priority:
Electron and ion temperature
Fourth Priority:
Minor species

For each physical parameter, metrics should be defined that measure ability to forecast and nowcast the climatological mean, the one–sigma limits in the daily values ("day to day variability"), a particular time interval (e.g., one–day forecast), and the departure from the climatological mean over a particular interval. An additional set of metrics is needed to specify and forecast macroscopic features that can dominate certain regions of the ionosphere–thermosphere domain, including the Appleton anomaly, high–latitude features (subauroral trough, tongues and holes in polar–cap ionization, neutral–density holes), equatorial pre–reversal enhancement in vertical ion drift, transient ionospheric disturbances (TID's), and the ratio of atomic oxygen to molecular nitrogen column abundance.

Table 2.
Priority Ionosphere–Thermosphere Metrics

Category	Parameter	Place	Time	Cadence	Data	Criterion
F–region ionosphere	*Minimum:* NmF2, hmF2 *Desired:* N_e(200–600), Δh ~ 20 km	Low, mid, and high latitudes	03–09LT 09–15 LT 15–21 LT 21–03 LT	Hourly	Ionosonde or Incoherent scatter radar (Jicamarca, Arecibo, Millstone Hill, and Sondre Stromfjord)	RMSE
High–latitude structure	N_e (~800 km)	Orbit plane of polar satellite Poleward of 45^0 mag. lat. x ~ 100 km	Every orbit	Every orbit	DMSP–SSIES	RMSE
Pre–reversal enhancement	Peak magnitude of vertical ion drift V_i(400 km)	Magnetic equator	16–20 LT	Daily	Incoherent scatter radar (Jicamarca)	Obs–model or RMSE
Scintillation/ Ionospheric irregularities	σ_ϕ, S_4 at 250 MHz and 1 GHz	Between + 20 and – 20 degrees dip latitude	18–04 LT Δt ~ 1 hr	Daily	Geostationary & GPS satellites	RMSE
Electron content	Peak TEC and N/S latitude location of Equatorial Ionization Anomaly	N/A	Every orbit of observation	Every orbit of observation	TOPEX	(obs–model)/obs or RMSE

No single metric adequately represents our overall ability to forecast and nowcast the state of the ionosphere and thermosphere. Table 2 presents a focused set of five. The best single metric is judged to be the first entry of Table 2: the RMS error in the electron density from 200 km to 600 km, for stations at low, mid, and high latitudes. The selection in Table 2 is based on two criteria – the importance of the parameter in describing the state and condition of the I–T system, and the availability of routine, accurate measurements of quantifying our forecast and nowcast capabilities. A more comprehensive framework, and a detailed reference to measurement and model accuracies can be found in the report of the Ionosphere–Thermosphere Panel on the Web. Using the electron density as the most important I–T parameter, we urge users to utilize the incoherent scatter radar measurements to determine the performance metric of different models as outlined below.

NSWP Ionosphere–Thermosphere Metric 1

The four incoherent scatter radars of the U. S. meridional chain represent a convenient means to routinely measure electron densities in the altitude range 200 km to 600 km with 20 km altitude

resolution. Because the radars are operated for at least 24 hours continuously approximately each month in support of the World Day experiments, metrics can be determined on nearly a monthly basis. This ensures adequate sampling as a function of season. The numerous observation periods per year will also ensure good sampling during quiet, moderate, and disturbed geomagnetic periods.

The NSWP ionosphere–thermosphere metric to be determined for each of the four incoherent scatter radars is given by the following formula:

$$\Delta = \frac{1}{24 \times 21} \sum_{t=0}^{23} \left\{ \sum_{h=200,20}^{600} \left[n_{o;t}(h) - n_{m;t}(h) \right]^2 \right\}^{1/2}$$

Where $n_{o;t}(h)$ is the observed density at altitude h and time t and $n_{m;t}(h)$ is the corresponding model value. This gives the RMS error in the density measured/computed hourly at 21 altitudes, averaged over 24 hours.

Allowed inputs for the models

Allowed inputs for the models include A_p, K_p, F10.7, and all normally available satellite data.

Community Coordinated Modeling Center (CCMC)

The USAF and NOAA have operational responsibility for providing space weather support to their respective customers. Improvements to operational capability have been slowed by lack of a comprehensive process to coordinate basic research, observations and model development, and transition value–added capabilities to operations. An AF/NASA partnership Models Working Group studied this problem and recommended the formation of a Community Coordinated Modeling Center. This effort, when coupled with the National Space Weather Program's Strategic & Implementation Plans, identified several deficiencies and outlined the components necessary for a research effort to accurately model the energy flow from the sun and its impact on the near–earth space within the next 10 years. Some of the deficiencies agreed upon by the various agencies include: lack of research coordination among labs, academia, and funding institutions; insufficient synergy between research and operational communities; no comprehensive validation process for research or operational models; no common software development standards and criteria for models, and no efficient process to transition research–grade models to an operational setting.

The CCMC concept was initiated in 1998 as a result of DoD efforts to provide a means of more effective transitioning of research models to operations. Subsequent multi–agency efforts have led to a conceptual design and management plan for the center. Participating agencies have all offered support for the CCMC including the purchase of computational assets, physical infrastructure for the center, scientific and technical support, and post–doctoral research support. Present plans call for 32 IBM SP2 processors at the Air Force Weather Agency (AFWA) in Omaha. The CCMC front–end computers and work stations will be at Goddard Space Flight Center with a high–speed data link between the two sites to ensure immediate and seamless operation of the center. Access to other high–speed DoD computers will also be enabled as needed. The Consortium Members are AF/XOW (Air Force Directorate of Weather), SMC (Space and Missiles Systems Center), AFOSR (Air Force Office of Scientific Research), AFRL (Air Force Research Lab), NASA (National Aeronautics and Space Administration), NOAA (National Oceanic and Atmospheric Administration), and NSF (National Science Foundation).

It is hoped that to a large extent, the deficiencies listed above can be addressed by establishing a center for research and development for space weather models, namely the CCMC. A well–coordinated partnership with Rapid Prototyping Centers (RPC) operated by the SMC/AFRL and NOAA will provide a

conduit to transition research models to operational models in an expedient manner.

International Space Weather Activities

The Scientific Committee for Solar–Terrestrial Physics (SCOSTEP), during its 9th Quadrennial Symposium at Uppsala in August 1997 helped organize a special evening session to: "Consider International Space Weather Issues." We gave a presentation on the US National Space Weather Program at that meeting. Similar reports were presented by representatives of a number of other countries which have space assets and desire to understand and forecast disturbances in near–Earth space that affect their operation. After the meeting, the group (of several hundred participants) voted to ask SCOSTEP to lead an oversight effort to provide a coordinated international space weather program. This will be done as part of S–RAMP, which stands for "STEP– Results, Applications and Modeling Phase", a new program adopted by SCOSTEP for the period 1998–2002. S–RAMP is to be the follow–on program to STEP (Solar Terrestrial Energy Program). Dan Baker is Chair of the Steering Committee of S–RAMP and one of the authors (SB) is one of nine members of the Committee. At the Uppsala meeting, a Space Weather Working Group of S–RAMP was set–up with H. Koskinen of Finland as Chair. A meeting of this Space Weather Working Group was convened at the COSPAR General Assembly in Nagoya, Japan in July 1998 to discuss future activities. J. Kozyra, a member of that Working Group reported on the new International Space Weather Clearninghouse web site established at the University of Michigan (URL: http://aoss.engin.umich.edu/intl_space_weather/sramp/).

The American Geophysical Union's fifth Western Pacific Geophysics Meeting was held in Taipei, Taiwan, in July 1998 after the COSPAR Meeting. One of the authors (RAB) gave a talk there on the US NSWP program. This was followed by similar talks on national space weather programs in Japan, Taiwan, Korea, Canada and Australia by scientists representing those countries. The S–RAMP Steering Committee met in Taipei and identified the especially active solar period of April–May 1998 as a "Special Study Interval". The Committee encourages scientists involved in all aspects of solar physics, interplanetary and magnetospheric physics, upper atmosphere and middle atmosphere physics, and Space Weather topics to concentrate on phenomena recorded by the extensive array of satellites and ground–based facilities operating at this time.

The Committee also approved the idea of organizing the First S–RAMP Space Weather Month for the fall of 1999 (actually became September 1999). The period 6–24 September 1999 was listed as an alert interval in the 1999 Incoherent Scatter Radar World Day Calendar (http://www.eiscat.no/URSI_ISWG/) with a three–day floating period to be chosen based on magnetic activity. The objective of this campaign was to study the effects of space weather disturbances on the coupled magnetosphere–ionosphere–thermosphere system on a global scale including the impacts on technological systems such as electric power grids, satellites, and ground or space based communication and navigation systems. The data acquisition phase of the S–RAMP Space Weather Month campaign was quite successful. A recurrent high speed coronal hole wind arrived at the Earth on September 12, triggering a long interval of elevated magnetic activity. The scheduled Incoherent Scatter Radar World Days coordinated observation period, September 15–17, occurred during this magnetically active interval. A major magnetic storm (near real–time Kyoto Dst reaching ~–177 nT), followed on September 22–23, triggered by the arrival of an interplanetary shock and solar ejecta with associated southward IMF Bz reaching –20 nT. The solar origin of the ejecta is not yet well established.

A number of important efforts in the forecast, research and user communities were undertaken during the campaign. A variety of archives containing data, predictions and model–outputs are already in existence for this period and more are coming on–line all the time. A master table of data sets, model outputs, temporal coverage and contact information for the September 1999 campaign period has been provided to the community on the Space Weather Month campaign web pages (URL given above). The purpose of the table is to support collaborative analysis efforts throughout the international community.

Coordinated analysis efforts are planned prior to the First S–RAMP Conference (in Sapporo, Japan on 2–6 October 2000). Details of these efforts will be circulated as they become available.

The European Space Agency (ESA) organized a Workshop on Space Weather during 11–13 November 1998 at ESTEC, Noordwijk, The Netherlands. One of the goals was to determine the current state of the field in different countries. The second goal was to put together a global picture concerning all scientific, technological, economical and environmental issues concerning space weather with the emphasis being placed on defining potential user requirements for European Space Weather Services.

Special Space Weather sessions were held at the AGU Meeting in Boston in May 1999, organized by H. Koskinen, and at the IUGG/IAGA Meeting in Birmingham in July 1999, organized by D. Boteler. A session on Space Weather Effects on Systems was organized at the URSI General Assembly in Toronto in August 1999 by one of us (SB). It is hoped that the ionospheric effects community represented at the present ISEA Meeting will participate in collaborative data analysis activities being organized under the auspices of the International Space Weather Working Group for the September 1999 S–RAMP Space Weather Month.

Acknowledgement

The National Space Weather Program in the US is an Interagency effort involving: National Science Foundation, National Aeronautics and Space Administration, and the Departments of Commerce, Defense, Energy and Interior, with the Coordination being provided by the Federal Coordinator for Meteorological Services and Supporting Research. We thank Michael Babcock for his efforts in updating the NSWP Implementation Plan and J. H. Allen for his help with the coordination of international space weather activities. We also thank R. A. Wolf and T. J. Fuller Rowell for their efforts in organizing the NSWP Metrics document.

References

The National Space Weather Program: The Strategic Plan, August 1995.

The National Space Weather Program: The Implementation Plan, January 1997.

GPS and Ionospheric Equatorial Scintillations: A Curse and A Blessing

P.M. KINTNER, H. Kil, B. Ledvina, and F. Mota (School of Electrical Engineering, Cornell University, Ithaca, NY 14853, USA)

E. de Paula (INPE–DAE, C.P. 515, 12.201–970 São Jose dos Campos, São Paulo, Brazil)

We describe an inexpensive GPS receiver design for observing ionospheric scintillations of the L1 signal. The design has the singular advantage of being open–architecture, allowing the designer to specify how GPS signals will be monitored. In one implementation (SCINTMON), signal amplitude is recorded at 50 samples/sec, and in another implementation (PHASEMON), signal phase is recorded at 10 samples/sec. In both cases, 12 signals can be monitored simultaneously. These receivers have been distributed across South America from the magnetic equator to the equatorial anomaly. There are two principal applications of this receiver in observing ionospheric scintillations produced by equatorial spread *F*.

The first application is remote sensing of ionospheric scintillations. With a single receiver one can obtain a measure of the scintillation activity across the sky and its evolution with time. Of course, the scintillation spectrum up to 25 Hz for each satellite in view is also recorded. With multiple receivers at a single site, the scintillation drift can be measured as a proxy for ionospheric drift. Preliminary studies from Cachoeira Paulista, Brazil have demonstrated that while the nighttime ionosphere moves primarily west–to–east at about 100 m/s, there are frequent examples of much slower speeds and reversal of velocity direction. Other examples show velocity shear or, in some cases, have been confirmed with longer baseline movement of TEC. Our long–term goal with this application is to develop a regional network of GPS receivers to investigate equatorial ionospheric scintillations in South America.

The second application is an investigation of the effects of ionospheric scintillations on GPS receiver operation. Because GPS operates with a CDMA protocol and because GPS satellites move with respect to ground observers (as opposed to geostationary satellites), the conditions for successful receiver operation are somewhat different than for FDMA or TDMA receivers. Not only is the depth of a fade important, but also the length of the fade determines if the tracking loops will lose lock during the fade. Sometimes GPS satellites move so that their signal paths in the ionosphere match the ionospheric velocity, leading to increased fade times and loss of tracking during large amplitude fades. Our long–term goal with this application is to understand the effects of scintillations on GPS receivers operating in environments requiring high reliability, such as air flight.

GPS scintillations near the equatorial anomaly region over the Indian sector

S.RAY, A.DasGupta, A.Paul and P.Banerjee
Institute of Radio Physics & Electronics
University of Calcutta
92 Acharya Prafulla Chandra Road
Calcutta 700009 INDIA.
Tel. : +91–033–350–9115/9116/9413
Fax : +91–033–351–5828
e–mail : ashikp@cucc.ernet.in

National Physical Laboratory
Dr. K.S.Krishnan Road
New Delhi 110012 INDIA.

The carrier–to–noise ratio (CNO) of L_1 (1.6 GHz) transmissions from the Global Positioning System (GPS) satellites has been recorded at Calcutta(lat.:22.58°N,long.: 88.38°E;dip:32°N) since 1994. L–band microwave signal at 1.5 GHz from the geostationary INMARSAT (65°E) and VHF signal at 244 MHz from FLEETSATCOM (73°E) have also been routinely monitored at this location which is near the northern crest of the equatorial anomaly in the Indian zone. A comparison of scintillation events on the Medium Earth Orbiting (MEO) GPS satellites with those on the geostationary links observed from this station shows considerable differences in scintillation occurrence patterns. In the case of a geostationary satellite, scintillations occur when the clouds of ionospheric irregularity clouds drift across the subionospheric point of that satellite. At Calcutta, scintillations on 1.5 GHz channel of INMARSAT normally occur in between local sunset and midnight. Scintillations at 244 MHz however continue into the post–midnight hours. L–band scintillations are normally moderate to intense during high solar activity years. VHF scintillations are usually saturated and very fast in the initial stage. In the post–midnight hours, the rate of fading is appreciably reduced although the signal exhibits saturated scintillations before gradually restoring to its steady level, indicating that the smaller scale (~ 300m) irregularities causing microwave scintillations decay earlier than the medium–sized (~ 800m) irregularities responsible for VHF scintillations. In case of GPS, 6–8 satellites distributed over the sky sample different sections of the ionosphere around the station under varying look angles. As a result, scintillations appear to be more extensive. In the post–sunset hours, a number of GPS satellites often show intense scintillations simultaneously. Even in the post–midnight hours, when no scintillation activity is observed on geostationary microwave links, the L–band GPS signals experience severe fluctuations of CNO. The deep fading of GPS CNO is interpreted in terms of propagation angle of the particular satellite ray–path with respect to the geomagnetic field direction. While viewing orbiting satellites from a low latitude station in the northern hemisphere, an 'end–on' view of the satellite signal through a field tube aligned equatorial plasma bubble will introduce more intense signal level fluctuations than in the case of a geostationary satellite link which normally passes through a small section of the bubble. This paper presents a detailed study of scintillations observed with GPS, INMARSAT and FLEETSATCOM to show the difference between scintillations on GEOS and the medium earth orbiting (MEO) satellites of GPS and its effects on the accuracy of position–fixing.

The intense fluctuations of CNO of some GPS links when there were negligible or mild scintillations on the L–band signal of a geostationary satellite signal was initially puzzling. This prompted a check of the calibration of the GPS CNO fluctuations with respect to that of the geostationary satellite signal receiving system. The INMARSAT

receiver is calibrated regularly, following *Basu and Basu* [1989], at least once–a–week. The signal from a GPS satellite exhibiting moderate to intense, but not saturated scintillations, travelling near the INMARSAT subionospheric point was chosen for calibration. It has been observed on a number of occasions that there is a good correspondence of the scintillation index SI(dB) with the two satellites.

Bandyopadhyay et. al [1997] presented a case of degradation in the accuracy of position–fixing indicated by the PDOP factor during periods of scintillations on some GPS links in the equatorial region. The parameter PDOP refers to the dilution of precision in position–fixing. The GPS receiver software calculates the PDOP factor for all possible combinations of available satellites and fixes the position using the four satellites for which the PDOP value is a minimum. Normally, links with high and stable CNO are used; if the signal fades below a threshold value, 25 dB in the present case, the particular satellite is rejected and the next best possible configuration for PDOP excluding the above satellite is used. The most accurate position–fixing is obtained if three satellites are dispersed with an azimuthal separation of about 120° near the horizon and one satellite approximately near the zenith. It was observed that during periods of scintillations of some of the GPS links, the PDOP value exceeded the acceptable value of 3. The cited cases correspond to solar activity minimum epoch. With increase in solar activity, more and more GPS links are likely to be affected by scintillations in the equatorial region. Locations near the equatorial anomaly crest would show the degradation of navigation in a peculiar way. In the northern hemisphere, scintillations may simultaneously render more than one GPS satellite in the southern sky unusable for navigational purposes. In addition to the southern links, any GPS satellite near overhead will also show intense scintillations due to a higher ambient level of ionization around the crest of the anomaly. As a result, the PDOP factor may shoot up to abnormally high values. In the extreme case, three dimensional fix may not be possible at all.

The present paper shows two cases of extensive scintillations on GPS and geostationary INMARSAT links observed from Calcutta on February 22, 1999 and October 03, 1999. Figures a and b are plots of Scintillation Index SI(dB) against UTC (=Local Time – 06:00 hours) for the two dates respectively. The prominent peaks of SI(dB) for GPS are indicated with the satellite Sv number and the look angle in parentheses. It was observed on February 22 [figure a] that during 14:00–14:18 hours UTC, there is a correspondence between SI(dB) of INMARSAT (look angle : 53,224) with that of GPS Sv5 (look angle : 44,226) when sub–ionospheric points of both the satellites were close to each other. At this time, the fluctuations of both the signals were appreciably less than the saturation level (SI(dB) ~ 25). This provides a good check for calibration of GPS CNO with respect to the INMARSAT levels. From 14:30 to 15:30 hours UTC four satellites Sv 26, 13, 10 and 5 show scintillations. The satellites Sv 26 and Sv 5 with look angle (30,164) and (17,197) respectively represent cases of field–aligned propagation viewed more or less 'end–on' through equatorial bubbles. The signals from the satellites Sv 13 (look angle : 23,57) and Sv 10 (look angle : 39,28) pass through the ionosphere near the crest of a developed equatorial anomaly. The PDOP drastically fluctuates during this time interval and reaches a maximum value of 36. The bursts of scintillations observed on Sv 1 (8,221) and Sv 6 (13,178) around local midnight refer to cases when scintillations are absent in the geostationary INMARSAT link. Corresponding to these GPS events, slow and saturated scintillations were observed on the FSC VHF link. Scintillations at VHF in absence of the phenomenon at L–band with geostationary INMARSAT indicate that medium scale irregularities (~800m) are strong

enough to produce VHF scintillations but the smaller scale (~300m) ones do not have sufficient power for L–band fluctuations. However, when GPS satellites are viewed more or less along the field aligned bubbles, scintillation activity is enhanced due to the propagation geometry even with weak irregularities. Scintillations observed with Sv 1 and Sv 6 belong to this category.

The features described above are more pronounced on October 03, 1999 [figure b]. In the post–sunset period (around 14:30 hours UTC) three GPS satellites (Sv 7, 15, 18) as well as the INMARSAT exhibited intense scintillations with a corresponding high value of PDOP (maximum ~ 14). Around 16:30 hours, three GPS links (Sv 4, 13 and 27)in the southern sky and one (Sv 7) in the western sky suffered intense fading. The position accuracy factor PDOP in this interval rose to abnormally high levels (~65). During the reported events, the number of satellites tracked by the receiver was eight. There was no reduction in the number of visible satellites although different combinations were used for navigation when there were scintillations.

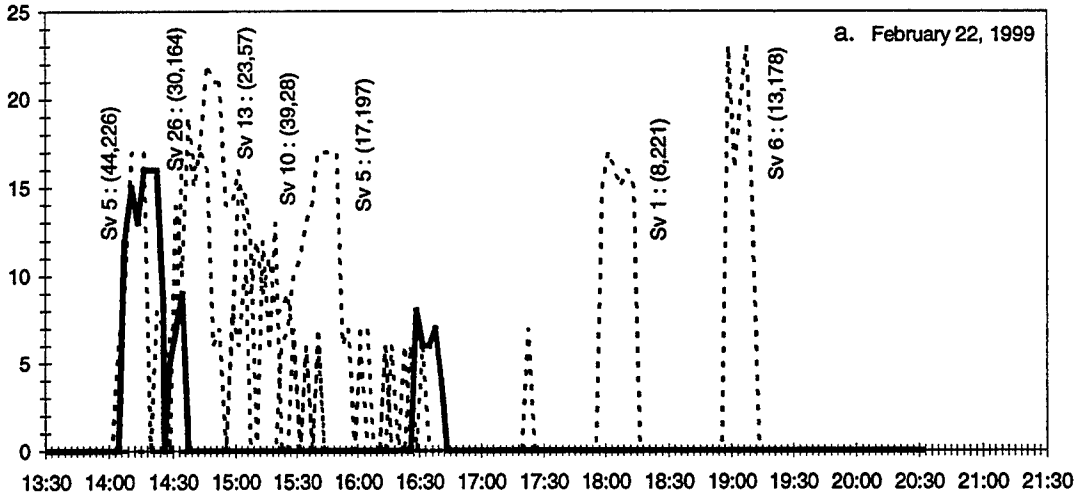
References

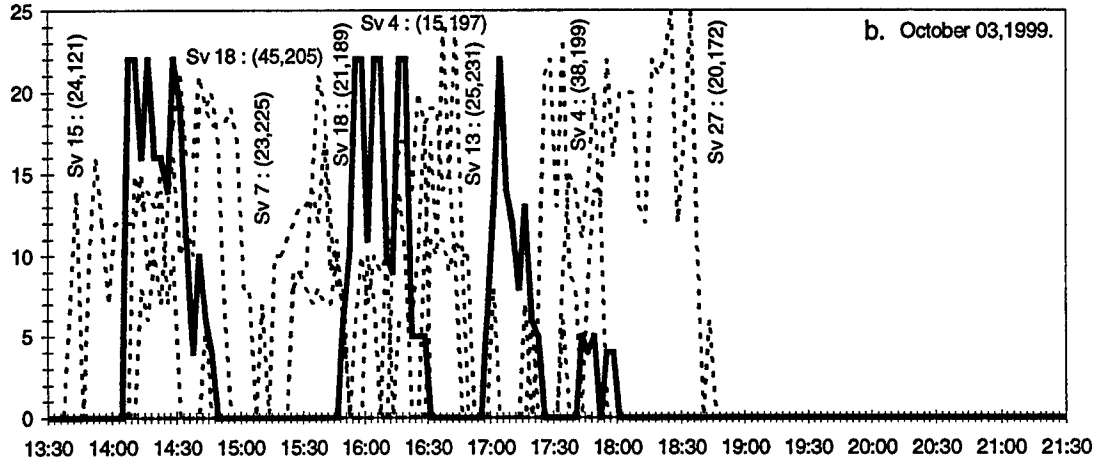
1. Bandyopadhyay T., A. Guha, A. DasGupta, P. Banerjee and A. Bose, *Electronics Letters*, **33**, 1010–1011, 1997.
2. Basu, S. and S. Basu, *World Ionospheric/Thermospheric Studies (WITS) Handbook,* **vol.2,** SCOSTEP, pp.128–130, 1989.

Figure Captions

a. Variation of Scintillation Index [SI (dB)] with UTC (Local Time – 06:00 hrs) as observed on February 22, 1999 for INMARSAT (indicated with bold line) and different GPS satellites (indicated with dotted lines).

b. Variation of Scintillation Index [SI (dB)] with UTC (Local Time – 06:00 hrs) as observed on October 03, 1999 for INMARSAT (indicated with bold line) and different GPS satellites (indicated with dotted lines).


a. February 22, 1999
Sv 5 : (44,226)
Sv 26 : (30,164)
Sv 13 : (23,57)
Sv 10 : (39,28)
Sv 5 : (17,197)
Sv 1 : (8,221)
Sv 6 : (13,178)
25
20
15
10
5
0
13:30 14:00 14:30 15:00 15:30 16:00 16:30 17:00 17:30 18:00 18:30 19:00 19:30 20:00 20:30 21:00 21:30


b. October 03,1999.
Sv 15 : (24,121)
Sv 18 : (45,205)
Sv 7 : (23,225)
Sv 18 : (21,189)
Sv 4 : (15,197)
Sv 13 : (25,231)
Sv 4 : (38,199)
Sv 27 : (20,172)
25
20
15
10
5
0
13:30 14:00 14:30 15:00 15:30 16:00 16:30 17:00 17:30 18:00 18:30 19:00 19:30 20:00 20:30 21:00 21:30

Magnetic Storm Activity, GPS/DMSP Observations, and the Equatorial Region

J. Aarons and M. MENDILLO
Department of Astronomy and Center for Space Physics
Boston University, Boston

P. Sultan
AFRL/VSBP
29 Randolph Rd.
Hanscom AFB, MA 01731

With the continued additions of GPS monitoring stations, providing data in the uniform RINEX format, it has been possible to attempt truly global studies of F–region irregularity development. Using identical data reduction methods for all latitudes, a comprehensive treatment of irregularities from auroral to equatorial regions can be achieved. At low latitudes, the number of GPS sites is sufficient to identify narrow longitude regions where the effects of geomagnetic activity differ considerably during individual storms. Several case studies have been made of storms in the years 1993, 1996, and 1998. Combining GPS–derived phase fluctuation indices with *in–situ* sampling of specific local time sectors by DMSP measurements, it has been possible to track both post–sunset and post–midnight signatures of magnetic activity upon irregularity development. In the events studied to date, geomagnetic activity does not appear to provide a subtle influence upon the well known seasonal–longitude morphology of ESF, but rather the dominant, controlling cause of complex longitudinal/ local time/ storm–time behavior.

Spread-F Dynamics from Scintillation Observations

A. BHATTACHARYYA[1](Air Force Research Laboratory, Hanscom AFB, MA.)

Information about the dynamics of equatorial spread F(ESF)from various types of observations contributes to our understanding of the roles played by various parameters of the ambient ionosphere in the day-to-day variability of the phenomenon. In recent years, L-band signals transmitted from the Global Positioning System(GPS) satellites have provided a large data base for variations in the total electron content(TEC) along the signal path in the presence of ionospheric irregularities, and intensity scintillations caused by them. Spaced receiver observations of scintillations yield estimates of irregularity drift across the signal path, and a parameter called the 'random velocity', which is a measure of the contribution of random changes to the time variation of the signal amplitude recorded at a fixed point.

Relative TEC variations derived from dual frequency GPS signals have been used to obtain a rate of change of TEC index(ROTI) which could be associated with scintillations(Pi et al, 1997). However, the ratio of the S_4-index, which is a measure of intensity scintillations, and ROTI varies considerably due to variations in the ionospheric projection of the satellite velocity and in the ionospheric irregularity drift(Basu et al., 1999). On the basis of theory it was suggested that a quantitative measure of intensity scintillations may be provided by the time derivative of the rate of change of TEC index(DROTI) (Bhattacharyya et al., 2000). The theoretical relationship yielded a dependence of the scaling factor between DROTI and S_4 on the relative drift speed between the irregularities and the signal path through the Fresnel frequency. Figure 1 shows comparisons of the S_4-index derived from the carrier-to-noise ratio of the L1 signal with S_4 computed from ROTI and DROTI with appropriate scaling factors.

The technique of estimating the motion of the ionospheric irregularities relative to the signal path, from spaced receiver measurements of amplitude scintillations has been used at a number of locations in different longitude sectors of the equatorial region. Decorrelation due to random changes in the scintillation pattern or drift speed is taken into account and quantified by the 'random velocity'. On magnetically quiet days, the drift speed shows a great deal of variability for the first couple of hours after the beginning of the scintillation event(Fig. 2). The random velocity also tends to be larger at the beginning of the scintillation event and decreases rapidly over a time scale of about 2 hours(Fig. 2). This feature of the random velocity becomes more pronounced with increasing sunspot number.In addition to this feature, in mass plots of the random velocity at the equatorial station Ancon, there exists another distinct population of points which represents much smaller random changes. This set of points has not been found in results from data recorded at Ascension Island(magnetic dip = 16 °). One possible interpretation of these observations could be that they arise due to bottomside sinusoidal (BSS) irregularities which are an equatorial phenomenon and are known to exist either by themselves or coexist with the ESF bubbles which extend over much greater altitude ranges(Valladares et al., 1983). This population is also absent in random velocities estimated from spaced receiver

[1] On leave from Indian Institute of Geomagnetism

data recorded at Guam(magnetic dip = 4.8°)(Bhattacharyya et al., 1989). VHF radar data from Kwajalein(magnetic dip = 6.5°) seems to indicate that the bottomside spread F phenomenon is infrequent in that longitude sector(Hysell et al., 1994).

Velocity structures associated with equatorial plasma depletions have been investigated in computer simulations of the temporal evolution of the bubbles(Retterer, 1999). It has been found in these simulations that depending on the background conductivity, the bubbles can rise rapidly or slowly. In either case, the ranges spanned by the extrema of the upward and eastward velocities within the bubble structure increased rapidly shortly after local sunset, peaking at a certain value and then declined more gradually over a period of one hour after which period the extrema are much closer to the ambient plasma drift. The density structures which represent the bubbles in these simulations are found to persist unchanged long after the velocity structures have been eroded. The greater variability of the irregularity drift in the early phase of bubble development is reflected in the large variations in the eastward drift of the scintillation pattern as well as in the large values of the random velocity before 22 hours LT. The other point to consider is whether the distinct population of small random velocity points represents low level turbulence associated with BSS. Huba et al.(1985) had considered a 3-mode system to describe the non-linear evolution of the R-T instability and demonstrated that in the collisional limit, this system evolves non-linearly to one of two possible fixed states with stable convection pattern. At altitudes greater than 400-500 km in the equatorial F-region ionosphere, the fixed states become unstable and the density and electric field vary in a chaotic manner. It is necessary to carry out further observations of nighttime ionospheric scintillations in different longitude zones of the equatorial region to substantiate some of the characteristics of spread F dynamics considered here and thus to pinpoint the role of various parameters in the development of ESF.

Acknowledgement

Some of the work described here was performed while A. Bhattacharyya held a National Research Council-(AFRL) Research Associateship.

References

Pi, X., A. J. Mannucci, U. J. Lindqwister, and C. M. Ho, *Geophys. Res. Lett., 24*, 2283, 1997.

Basu, S., K. M. Groves, J. M. Quinn, P. Doherty, *J. Atmos. Sol. Terr. Phys., 61*, 1219, 1999.

Bhattacharyya, A., T. L. Beach, S. Basu, and P. M. Kintner, *Radio Sc., 35*, 209, 2000.

Valladares, C. E., W. B. Hanson, J. P. McClure, and B. L. Cragin, *J. Geophys. Res., 88*, 8025, 1983.

Bhattacharyya, A., S. J. Franke, and K. C. Yeh, *J. Geophys. Res., 94*, 11959, 1989.

Hysell, D. L., M. C. Kelley, W. E. Swartz, and D. T. Farley, *J. Geophys. Res., 99*, 15,065, 1994.

Retterer, J. M., *Proceedings of Ionospheric Effects Symposium*, 688, Alexandria, Virg., 1999.

Huba, J. D., A. B. Hassam, I. B. Schwartz, and M. J. Keskinen, *Geophys. Res. Lett., 12*, 65, 1985.

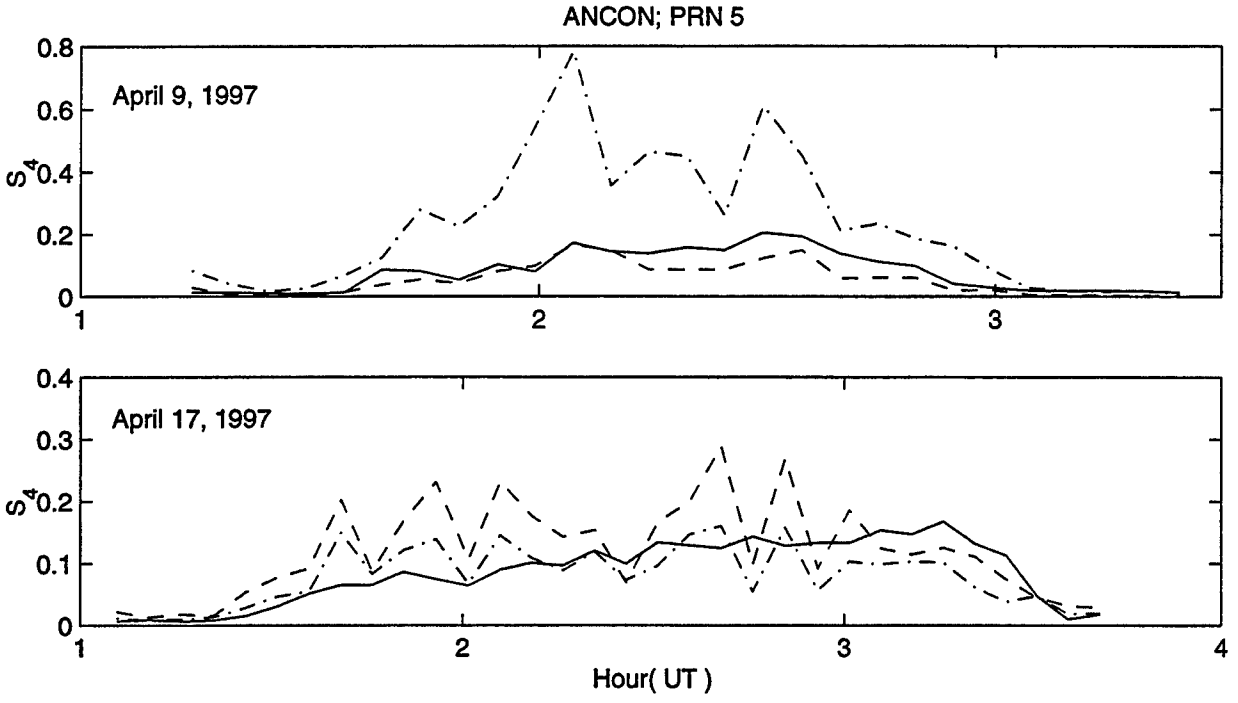


Figure 1. S_4 indices: computed from intensity scintillations on L1(solid line), derived from DROTI(TECU/min^2)=1.6 X 10^3 ν_F^2 S_4(dashed line), and derived from ROTI(TECU/min) = 2.5 S_4(dash–dotted line) for two nights with Fresnel frequencies ν_F = 0.126 Hz(top) and ν_F = 0.053 Hz(bottom).

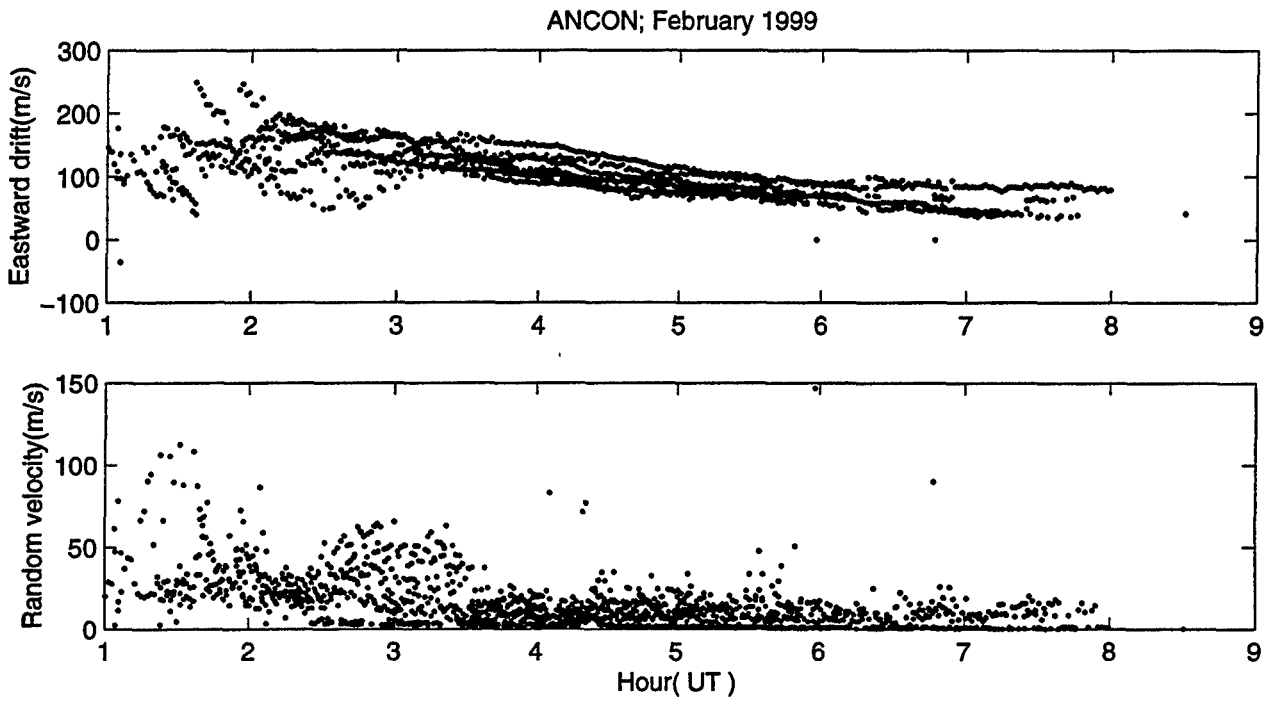


Figure 2. Eastward drift speed of the scintillation pattern on the ground and the random velocity derived from spaced receiver scintillation data recorded during eight geomagnetically quiet days($\Sigma K_p < 30$). Local time $\approx$ UT – 5 Hours.

Equatorial Bubble Development and the Source of Satellite Scintillations

G.S. SALES[1], B.W. Reinisch[1], V. Paznukhov[1] and D.L. Hysell[2]

1. Center for Atmospheric Research
University of Massachusetts Lowell
Lowell MA, 01854 USA

2. Clemson University
Clemson, SC, 29634 USA

Introduction

The relationship between equatorial plumes and satellite scintillation events has been established for a long time. Our research is aimed at developing new techniques to understand and predict the occurrence of equatorial scintillation, first by combining the Digisonde ionogram data at Jicamarca with the JULIA radar data to identify the region associated with the generation of F-layer instabilities, and then develop a method to determine the vertical plasma drift velocity associated with the upward movement of the F-layer around sunset using the ionogram data. The correlation between the presunset upward movement and the likelihood of scintillation is clearly established. The first section discusses the likelihood of scintillation occurring, given the vertical motion of the F-layer around sunset. In the next section, the JULIA radar data are combined with the Digisonde plasma frequency isodensity maps to characterize the altitude regime involved in the generation of the instabilities. The third section describes how the Digisonde is able to 'view" the generation of these bubbles and then tracks these depletion bands (bubbles) as they move eastward towards Jicamarca. Using these data, the horizontal plasma drift is determined for several nights. Finally a new vertical drift technique is introduced based on the vertical profiles derived from sequential ionograms.

Scintillation

By comparing the F-layer peak altitude, reached around sunset, with the occurrence of scintillation, in this case Fleetsat 7 and 8 (250 MHz) received at Ancon, Peru some 40 km west of Jicamarca, a close correlation has been established. For the months of February and March 1997, Digisonde ionograms and satellite scintillation data were available on 40 nights. Figure 1 shows the occurrence of scintillation with the average S4 index as a function of the F-layer peak altitude. On 20 of these nights the F-layer peak reaches an altitude greater than or equal to 400 km and on 85% of those nights scintillation occurred within 2 hours after sunset. Conversely, on the remainder of these nights when the maximum layer altitude was below 400 km, strong scintillation (S4 > 0.4) occurred only four times.

Figure 2 shows a typical example of the plasma frequency contours derived from the Digisonde soundings as they evolve through sunset and into the nighttime period on a night when scintillation occurred. The upper panel shows the scintillation index for the Fleetsat signals received at Ancon.

Using the criterion as to whether the F-layer peak altitude reaches 400 km, the prediction of satellite scintillation occurrence was found to be 85% correct with a lead-time of approximately 2 hours. This represents a beginning approach to predicting the onset of the growth of F-layer instabilities. The upward motion of the F-layer, driven by a vertically directed **ExB**, often begins before layer sunset. The altitude for the generation of these instabilities is best illustrated using the JULIA radar data from Jicamarca.

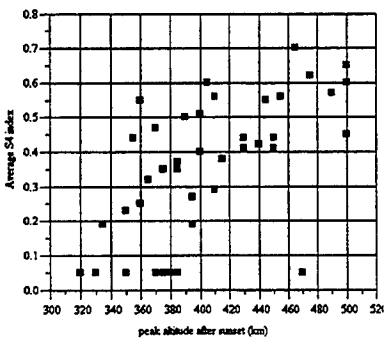


Figure 1. Ancon satellite scintillation S4 index vs. F-layer peak altitude.

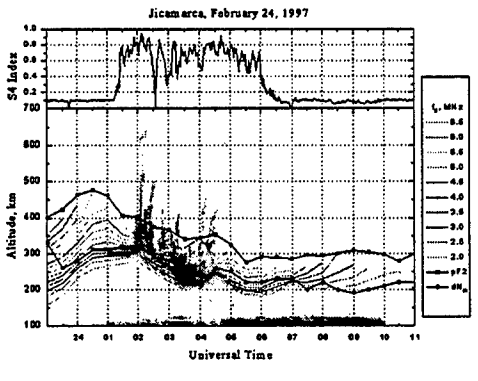


Figure 2. Jicamarca Digisonde plasma frequency contours with JULIA data superimposed.

JULIA Radar Observations

Combining the JULIA (coherent scatter) radar data with the plasma frequency contour data, the region of instability growth was made obvious. In all cases the growth maximizes well below the altitude predicted on the basis of the gravitational instability mechanism, which maximizes just below the peak of the layer. The maximum layer gradient, which enters both the gravitational and the electric field instability growth terms, is indicated as the dark line in the lower F-layer in Figure 2.

The region of maximum 3 m irregularity is, in all cases, observed in the vicinity of the bottom of the F-layer coincident with the maximum gradient and must therefore be associated with the electric field intensity component of instability growth. The JULIA radar with a narrow vertical pointing beam sees only overhead and typically does not observe the initial growth phases of the F-region instabilities. The Digisonde on the other hand with a 50° zenith beam width is able to see some 500 to 600 km west of Jicamarca and is able to observe to within 30 minutes after the passage of the solar terminator. These observations are important for understanding the conditions when the plasma becomes unstable and the motion of these "bubbles" as they travel eastward.

Digisonde Observations

The Digisonde, because of the wide antenna beam width, is able to observe the bands of irregularities associated with equatorial bubbles out to some 600 km west of the station. The sequence of Digisonde ionograms in Figure 3 taken on Feb. 24, 1997 shows the progression of the bubbles towards Jicamarca. The first indication of these irregularities was at 0000 UT at a slant range of 700 km. From the positions of these irregularities, taken once every 30 minutes at Jicamarca, and the time of arrival over Jicamarca at ≈ 0150 UT, it is possible to deduce the speed of these bands.

The observed altitude close to the peak of the layer, 390 km, is where the most intense HF scattering is expected to take place. Having estimated the altitude, the west to east speed was determined to be 95 m/s on this night. The first band arriving over Jicamarca near 0200 UT coincides with the first well-developed plume observed by the JULIA radar (see Figure 2). On other nights during the February/March 1997 period speeds up to 150 m/s were measured by this technique.

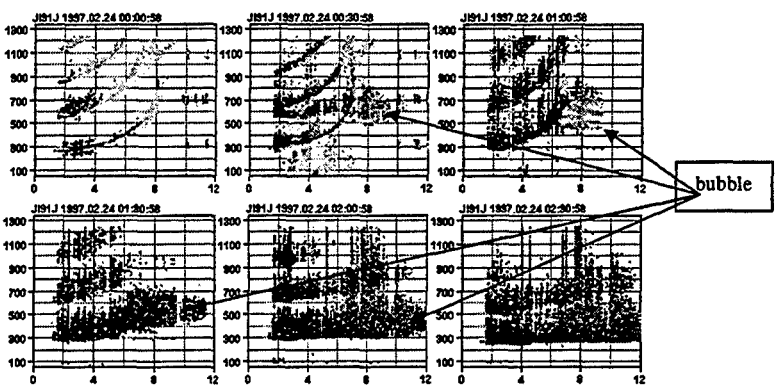


Figure 3. Jicamarca Digisonde ionogram sequence showing bubble motion on Feb. 24, 1997.

Ray tracing in an ionospheric model using PIM, adjusted using the Jicamarca sounder data, illustrates how the sounder is able to observe these extended bubbles at great distances from the site. Figure 4 shows the PIM profiles and the 3-D ray tracing results when the bubble is at distances of 300 and 500 km from Jicamarca at a frequency of 7 MHz.

Between the ionograms on Feb. 24, 1997, the Digisonde was operated in a "drift" mode at a fixed frequency of 6.9 MHz., smaller than foF2 at the observation time. Precision angle and Doppler measurements made in this mode when the depletion is relatively far away from the sounding site, the oblique rays at this low frequency cannot penetrate into the depletion and the depletion remains invisible in the drift mode until it arrives closer to the station. In future campaigns, the drift mode will be operated at frequencies above as well as below foF2 to better observe the internal structure of bubble growth at these early stages.

To determine the horizontal electric field that drives the layer upward around sunset, a new analysis technique has been developed that uses a sequence of electron density profiles to derive the vertical plasma drift.

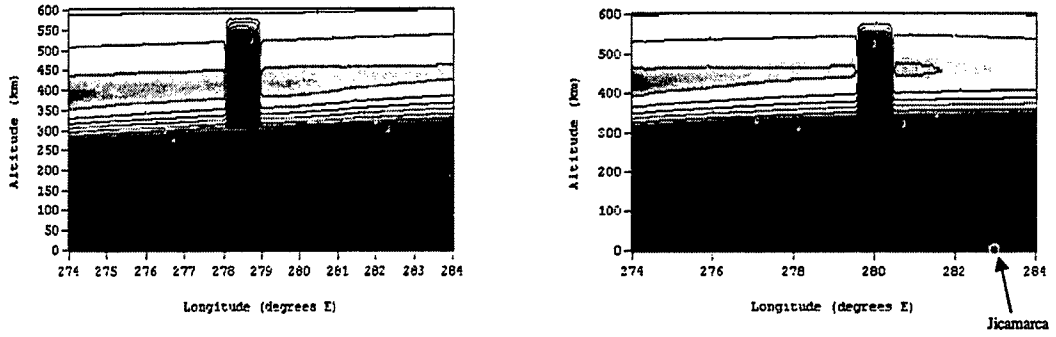


Figure 4a. Model (PIM) ionospheric profiles with superimposed bubble at 0030 and 0100 UT.

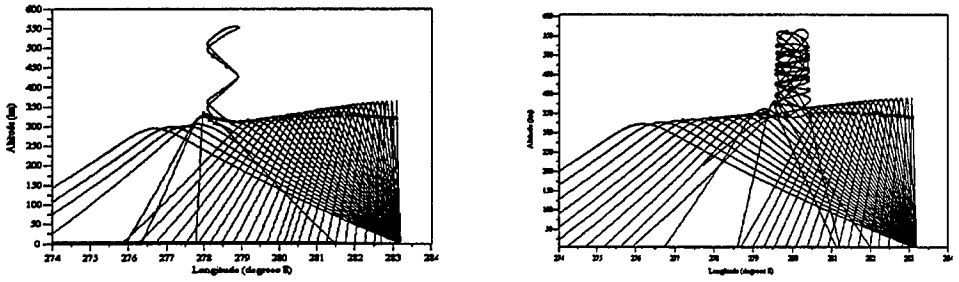


Figure 4b. Ray tracing at 7 MHz for PIM at 0030 and 0100 UT at a bearing of 273°. The dots show the location of the ray-magnetic field orthogonality.

Vertical Velocity Measurements

Using an ionosonde, it is possible to follow the movement of isodensity contours and to derive an apparent velocity by comparing sequential ionograms. However, this apparent velocity does not represent the true vertical plasma drift speed since chemical processes such as electron-ion recombination and electron production also contribute to the changing plasma density contours. To separate the plasma drift from the chemistry, this analysis begins with the continuity equation:

$$\frac{\partial n_e}{\partial t} + \nabla\cdot(n_e\,\mathbf{v}) = Q - L. \qquad (1)$$

Here n_e is the electron density, v is the plasma drift velocity, Q is the solar production rate and L is the electron-ion loss rate; all are functions of z. For the vertical component of the plasma drift velocity v_z, this equation simplifies to:

$$\frac{\partial n_e}{\partial t} + v_z\frac{\partial n_e}{\partial z} + n_e\frac{\partial v_z}{\partial z} = Q - L. \qquad (2)$$

Rearranging terms and dividing by n_e yields a linear, first order differential equation for v_z:

$$\frac{\partial v_z}{\partial z} + \left(\frac{1}{n_e}\frac{\partial n_e}{\partial z}\right)v_z = \frac{1}{n_e}\left[\frac{\partial n_e}{\partial t} - (Q-L)\right] \qquad (3)$$

or

$$\frac{\partial v_z}{\partial z} + S(z)v_z = T(z)$$

$$\text{where } S(z) = \frac{1}{n_e}\frac{\partial n_e}{\partial z} \text{ and } T(z) = \frac{1}{n_e}\left[\frac{\partial n_e}{\partial t} - (Q-L)\right]$$

This differential equation has an exact solution given as:

$$v_z = \frac{\int_0^z T(\zeta)\, n_e(\zeta)\, d\zeta}{n_e(z)} \tag{4}$$

Substituting the values for S(z) and T(z) gives for the vertical plasma drift at an altitude z:

$$v_z(z) = -\frac{1}{n_e(z)}\frac{\partial}{\partial t}[\mathrm{TEC}(z)] + \frac{1}{n_e(z)}\int_0^z [Q(\zeta) - L(\zeta)]\, d\zeta\,. \tag{5}$$

The first term on the right represents the "motion" of the isodensity contours while the second term is the contribution of the layer chemistry to the apparent vertical drift velocity. The motion of the contours at the altitude z (the time derivative) can be calculated using the total electron content up to the altitude z from sequential ionograms and the second integral is calculated using the measured profile and known reaction rates.

After sunset, the chemistry term is calculated assuming Q = 0, and using the measured electron density profiles along with standard F-layer charge exchange and recombination rates. Figure 5 shows the comparison between this technique, using a sequence of 10-minute ionograms at Jicamarca, and the vertical drift velocities measured with the collocated incoherent scatter radar (ISR). On several of the nights shown, the correspondence between the new technique and the ISR results is good.

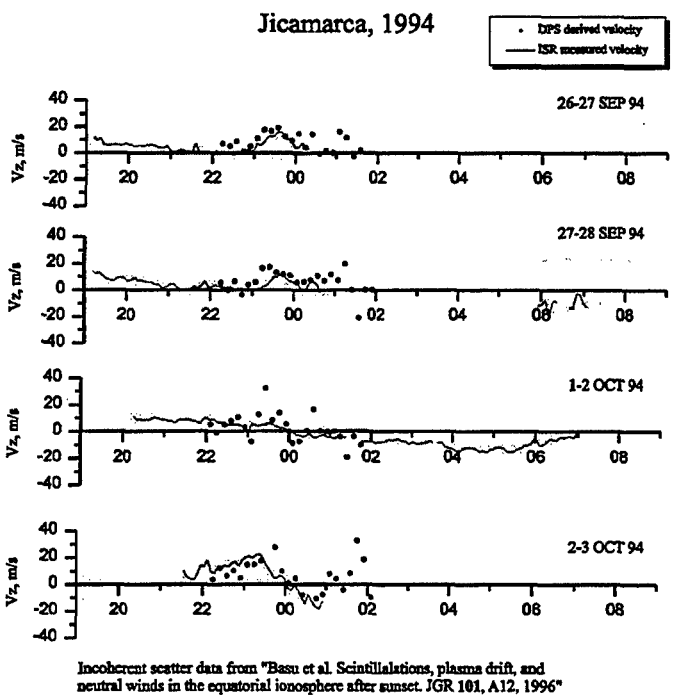


Figure 5. Comparison of Digisonde and ISR vertical plasma drift measurements at Jicamarca on four nights.

Summary

Using a fusion of ground based sensors, the Digisonde, the JULIA radar and satellite scintillation measurements, it has been possible to observe the formation and location of equatorial bubbles and then to characterize their association with scintillation events. This research has also made a good first step towards predicting the occurrence of active periods of scintillation based on the motion of the F-layer prior to sunset.

This research was supported by the USAF Research Laboratory (Hanscom AFB) under Contract F19628-96-C-0159.

Equatorial Scintillations: Current Status and Future Plans

S. Basu
Air Force Research Laboratory, VSBI
29 Randolph Road
Hanscom AFB, MA 01731
e–mail: santimay@aol.com

The earth's ionized upper atmosphere often becomes turbulent and irregularities of electron density are formed with scale–lengths ranging from tens of kilometers to tens of meters. These irregularities scatter radio waves from satellites in the frequency range of 100 MHz to 4 GHz (Basu et al., 1988; Aarons, 1993). In the presence of a relative motion between the satellite, the ionosphere and the receiver, the received signal exhibits temporal fluctuations of signal intensity and phase, called scintillations. Intensity scintillations cause signals to fade below the average level. When the depth of fading exceeds the fade margin of a receiver signal loss and cycle slips are encountered. Phase scintillations induce frequency shifts and, when this shift exceeds the phase lock loop bandwidth, the signal is lost and a receiver spends valuable time to reacquire the signal. Overall, scintillations degrade the performance of communication and navigation systems.

Scintillations are most intense in the equatorial region, moderate at high latitudes and weak at middle latitudes (Basu et al., 1988). Scintillation at all latitudes attain its maximum during the solar maximum period when the F–region ionization density increases and the irregularities of electron density occur in a background of enhanced ionization density. As such, scintillation effects, expected during the upcoming solar maximum period between 2001–2004, are of concern to systems engineers.

In the equatorial region, at the time of sunset, an enhanced eastward electric field, called the pre–reversal enhancement, generally develops at F–region heights (Farley et al. 1986; Basu et al., 1996; Eccles, 1998; Fejer et al., 1999). As a result, the ionosphere moves upward, develops steep vertical density gradient in the bottomside F–region and becomes unstable to the Rayleigh–Taylor instability (Ossakow, 1981; Kelley, 1989). Large scale plasma depletions, called plasma bubbles, that form in the bottomside F–region become populated with irregularities as the bubbles rise to great heights. The intermediate scale (tens of km to tens of m) irregularities cause intense scintillations of satellite signals during the solar maximum period along two belts of high ionization density at 15° N and 15° S magnetic latitude, called the crests of the equatorial anomaly. The pre–reversal enhancement of eastward electric field that is needed to drive the ionosphere unstable is also the cause of the equatorial anomaly during the evening hours.

Figure 1 illustrates the occurrence statistics of scintillation at 1.5 GHz in the equatorial anomaly region during the pre–midnight period (20–24 LT). The top panel refers to magnetically quiet periods (K_p= 0–3), the middle panel to active periods (K_p=3–9) and the bottom panel shows the sunspot number. The diagram indicates that there is no data during June–August, 1988 but past data indicated that these months correspond to the seasonal minimum in scintillation occurrence when scintillations are virtually absent over the American–Atlantic longitude sector. It may be noted that scintillation occurrence increases from 1987–1989 as the sunspot increases. It is interesting to note that the occurrence is much enhanced during magnetically quiet periods (top panel). It seems that during magnetically quiet periods the turbulence in the nighttime equatorial F region is driven internally and cannot be predicted by following the trail of energy from the sun.

Figure 2 shows the variation of the characteristics of equatorial scintillation as a function of latitude. The top two panels show the variation of the S4 index of intensity scintillation (defined as the normalized second central moment of signal intensity) at a frequency of 250 MHz as observed at Ancon, Peru, at the magnetic equator. The top two panels illustrate the variation observed with geostationary satellites in the west and the east and viewed respectively at a high

elevation angle of 45° and a low elevation angle of about 20°. The third and the fourth panels correspond to observations made at Antofagasta, Chile, near the crest of the equatorial anomaly, at a magnetic latitude of 11° south of the magnetic equator. A comparison of panels 1 and 2 with 3 and 4, does not indicate any difference in the magnitude of S4. This is because the S4 index of scintillation at 250 MHz attains the saturated value of unity at the magnetic equator and no further increase in S4 can occur at Antofagasta beyond the saturation value of unity. However, this difference is observed at a higher frequency (~ 1.7 GHz), as shown by panels 5 and 6. At Ancon, the S4 index at 1.7 GHz does not exceed 0.2 whereas at Antofagasta, the S4 index is 1.0. Thus the integrated strength of turbulence is at least five times higher near the crest of the anomaly as compared to its value at the magnetic equator. It may also be noted (panels 3 and 5) that scintillation observations made at high elevation angles near the anomaly region show the discrete scintillation structures. The bottom panel shows the results of the zonal irregularity drifts measured at the two stations by using spaced receiver scintillation data. It is found that zonal drifts at the two stations are equal early in the evening but later the drift measured away from the magnetic equator becomes smaller than that at the magnetic equator. This is a result of the development of the evening anomaly (indicated by strong L–band scintillations in panel 5) when the increased ion drag near the anomaly region reduces the zonal irregularity drift (Raghavarao et al., 1991)

Figure 3 shows the results of simultaneous GPS scintillation and 6300 A all–sky imager observations near the crest of the equatorial anomaly (Weber et al., 1996). The left hand panels illustrate two 6300 A all sky images at 15 minute intervals, the center of the image corresponding to the sky immediately above the station. The dark bands elongated in the magnetic north south direction represent the footprints of plasma bubbles at about 250 km altitude. The positions marked 21 and 22 correspond to the intersection points of raypaths to GPS satellites with PRNs of 21 and 22 respectively. The dark squares represent other GPS satellites. In the top image (0100 UT), the raypaths to both GPS satellites 21 and 22 intercepted the dark central band. The right hand images show that at this time 1.6 GHz signals from both satellites are scintillating (Basu et al., 2000). The dark bands or plasma bubbles move eastward due to the nighttime polarization electric field. As a result, satellite 22 emerges from the dark bands shortly after 0100 UT whereas the satellite 21 remains within the dark band till 0115 UT. The right hand panels shows that scintillations of satellite 22 cease shortly after 0100 UT but scintillations of satellite 21 continue 0115 UT. This result shows that the impact of scintillation on GPS navigation is determined by the strength of turbulence in plasma bubbles, the area covered by the footprints of plasma bubbles, and their distribution with respect to the trajectories of GPS satellites.

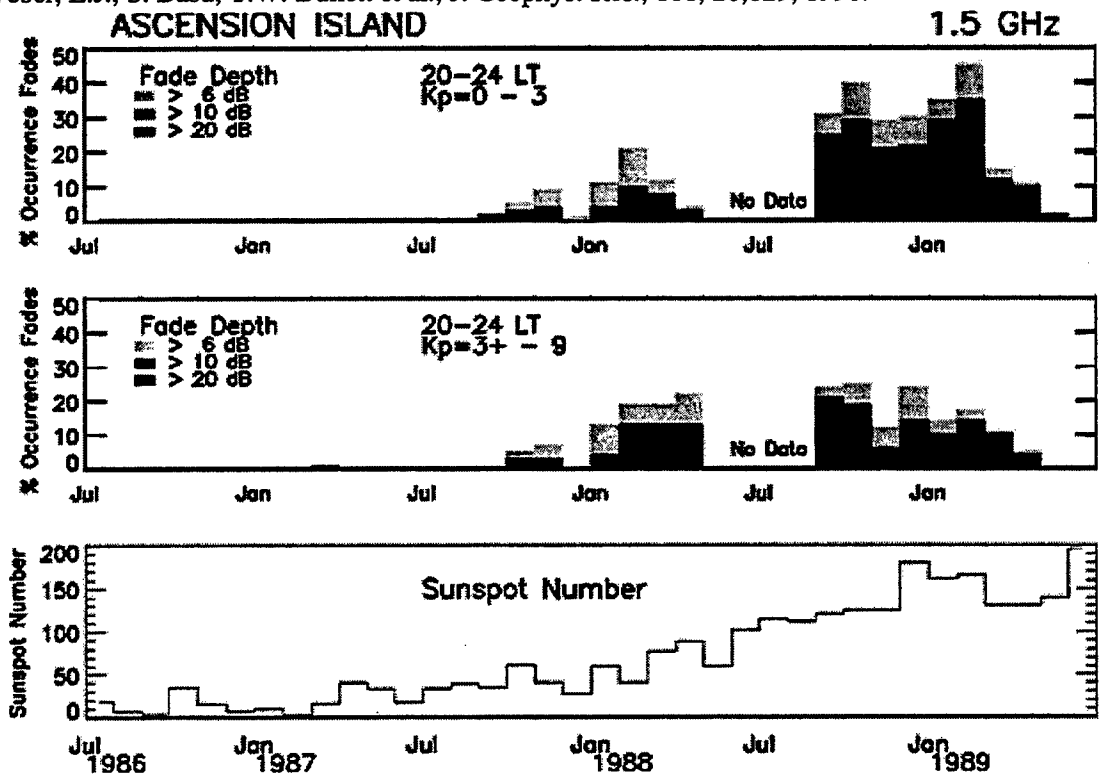
The average occurrence statistics of equatorial scintillation shown in Figure 1 are useful for planning purposes but are of limited value to users because of the extreme day–to–day variability of equatorial scintillation. The current advances that address such limitations include the development of a real–time scintillation specification system, Scintillation Network Decision Aid (SCINDA) (Groves et al., 1997). The system combines scintillation magnitude and zonal drift measurements made at two sites, one near the magnetic equator and the other near the anomaly region, by using transmissions from satellites, one to the west and the other to the east of the stations. The data is brought to the user via the internet and the data drives an equatorial scintillation model which considers upwelling and zonal motion to produce three–dimensional scintillation structures.

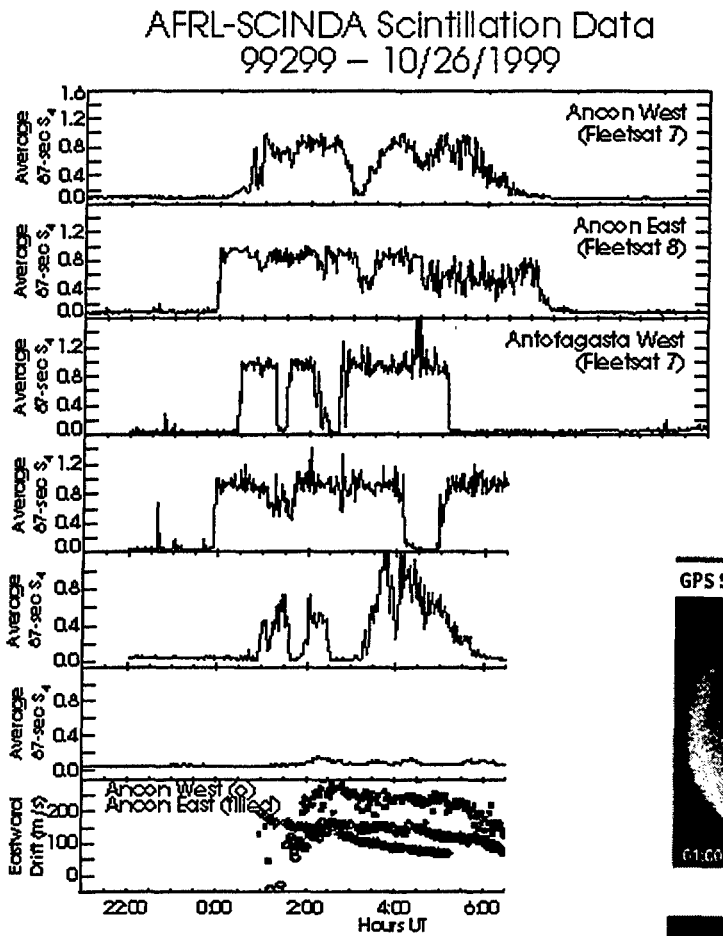
The future plans are focussed on user needs of both specification and forecasting of scintillation. Figure 4 shows the conceptual schematic of an equatorial satellite called the comunication/navigation outage forecasting system (C/NOFS). This satellite will be launched in an elliptical orbit 400 km x 700 km with an orbital inclination of 18°. The satellite in–situ sensors will include a Langmuir probe, digital ion drift meter, vector electric field and neutral wind measuring instruments. It will also include a tri–frequency (150, 400, 1067 MHz) beacon and a GPS occultation receiver. These sensors will probe the destabilizing and stabilizing forces in the ionosphere, namely, the pre–reversal enhancement of the zonal electric field as driven by the zonal neutral wind and the meridional wind respectively. Such data will drive an equatorial

ionosphere model to forecast the onset of plasma instability. Radio wave scattering theory will be used to determine the magnitudes of phase and intensity scintillation and their temporal structures. The model results will be validated by the electron density profiles determined by the GPS occultation receiver and by the measurements of scintillation at three beacon frequencies. The space–based C/NOFS and the ground–based SCINDA will be able to specify, forecast and validate scintillation products for the users.

References

Aarons, J., Space Sci. Rev., 63, 209, 1993.
Basu, S., E. MacKenzie, and Su. Basu, Radio Sci., 23, 363, 1988.
Basu, S., E. Kudeki, Su. Basu et al., J. Geophys. Res., 101, 26,795, 1996.
Basu, S., K.M. Groves, J.M. Quinn, and P. Doherty, A comparison TEC fluctuations and scintillations at Ascension Island, J. Atmos. Solar Terr. Phys., 2000 (in press).
Eccles, J.V., J. Geophys. Res., 103, 26,709, 1998.
Farley, D.T., E. Bonelli, B.G. Fejer, and M.F. Larsen, J. Geophys. Res., 91, 13,723, 1986.
Fejer, B.G., L. Scherliess, and E.R. de Paula, J. Geophys. Res., 104, 19,859, 1999.
Groves, K.M., S. Basu, E.J. Weber et al., Radio Sci., 32, 2047, 1997.
Kelley, M.C., The Earth's Ionosphere, Int. Geophys. Series, vol. 43, p.71, Academic, San Diego, Calif.
Ossakow, S.L., J. Atmos. Terr. Phys., 43, 437, 1981.
Raghavarao, R., L.E. Wharton, N.W. Spencer, et al., Geophys. Res. Lett., 18, 1193, 1991.
Weber, E.J., S. Basu, T.W. Bullett et al., J. Geophys. Res., 101, 26,829, 1996.





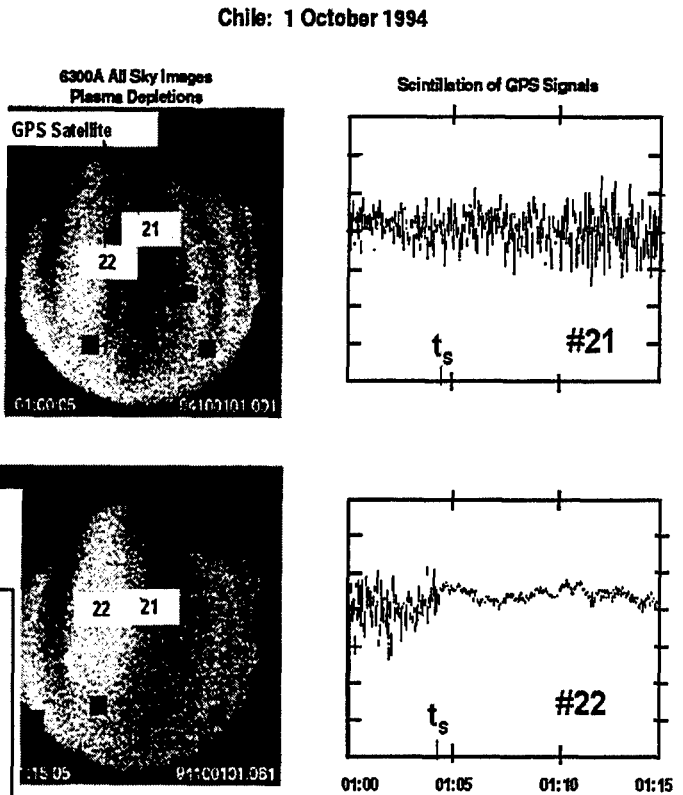


Figure 3

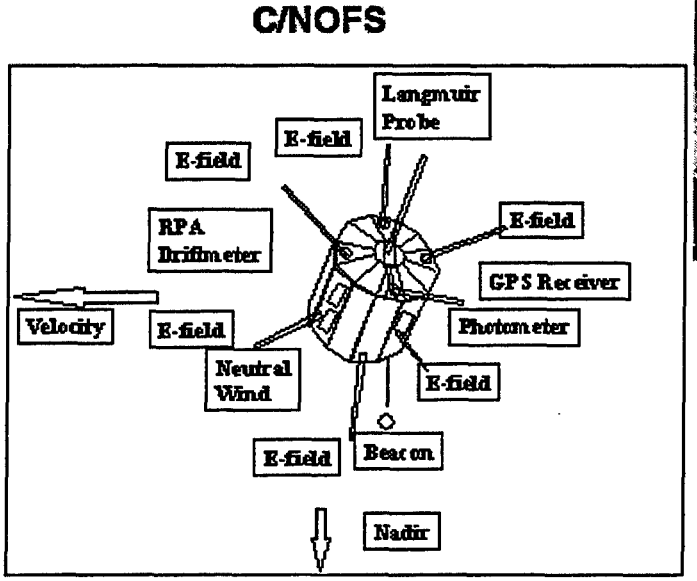


Figure 4

Spread *F* irregularities and drifts observed with the JULIA radar

D. L. HYSELL and J. D. Burcham

Dept. of Physics and Astronomy, Clemson University, Clemson, South Carolina, 29634, USA

1. Introduction

When small-scale plasma irregularities associated with spread *F* are present, the very strong field aligned radar echoes that result render the full power of the Jicamarca incoherent scatter radar unnecessary for probing the unstable layers. In this case, the low power JULIA (Jicamarca Unattended Long-term Investigations of the Ionosphere and Ionosphere) system can be used almost continuously to monitor ionospheric irregularities. The JULIA system is an independent PC based data acquisition system that uses the exciter stages of the Jicamarca radar and the main antenna array. Presently, the majority of data from Jicamarca are taken in the JULIA mode. This system routinely measures the intensity of the 3 m irregularities, their vertical and zonal drift speeds, their Doppler spectra, and their spatial structure. In addition, the JULIA radar is also able to estimate the background ionospheric zonal electric field indirectly by probing plasma irregularities in the equatorial electrojet. Since late 1996, well over 200 days of ionospheric data have been taken with the JULIA system. Most of the data can be examined through our website at `http://landau.phys.clemson.edu`.

Here, we examine three aspects of spread *F* irregularities brought to light by the unique capabilities of the JULIA radar. The first is that the irregularities come mainly in one of three varieties and include a class of waves which grow on magnetic flux tubes with *E* region dominated conductivities. These bottom-type layers occur almost universally but do not always lead to more robust irregularities. Whether violent spread *F* events occur hinges on whether bottom-type layers migrate into *F* region dynamo controlled flux tubes or instead descend and stabilize. The second involves the occurrence statistics of spread *F* irregularities revealed by an analysis of our complete database. The occurrence of irregularities depends on season, solar cycle, and magnetic activity in a manner which can be understood in terms of the climatology of the background zonal electric field. The third is the influence of the afternoon and twilight zonal ionospheric electric field on the day-to-day variability of the irregularities. The JULIA radar may be used to estimate the time history of the electric field which is predictive of the stability of the post-sunset *F* region equatorial ionosphere.

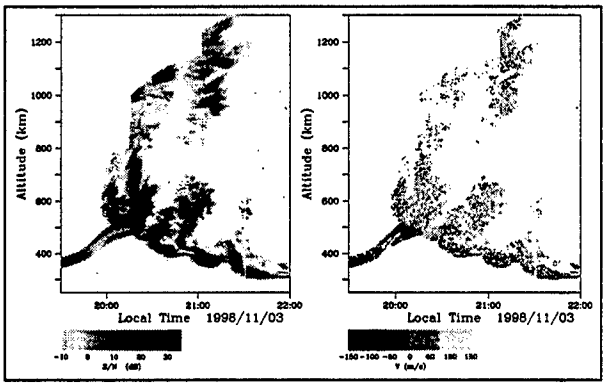


Figure 1. An ESF event observed with the Jicamarca radar. (Left) Range time intensity plot, showing the signal-to-noise ratio in dB versus altitude and local time. (Right) Zonal plasma drifts measured with radar interferometry.

2. Irregularity types

Figure 1 features a prototypical ESF event observed at Jicamarca on November 3, 1998. The left panel shows the backscatter signal-to-noise ratio in dB versus altitude and time. Intense backscatter indicates the presence of strong plasma irregularities with 3 m wavelengths. We customarily assume however that such waves are tracers for intermediate- and large-scale structures in the plasma whose boundaries are then demarcated by the backscatter. Hundreds of datasets like these have been recorded over the years at Jicamarca and elsewhere and reflect considerable variety. The morphology shown here is typical for geomagnetically quiet conditions and low to moderate solar flux levels. In particular, three distinct kinds of features are present.

Prior to 2000 LT, backscatter comes from a narrow, laminar layer rising up with the bottomside *F* region under the action of a eastward zonal electric field. Such layers were first identified by *Woodman and La Hoz* [1976] and have come to be known as bottom-type layers. Layers like this are enigmatic in that they do not demonstrate much vertical development, despite the fact that interchange instabilities function through vertical development. At about 2015 LT, a tall radar plume appears in the RTI plot. Radar plumes are evidence of deep plasma depletions rising up through

the *F* peak under the influence of well-developed instabilities and entering the topside. Plumes as high as about 1500 km have been observed, although the majority remain below 1000 km. High solar flux levels and geomagnetic activity can be conducive for the formation of very high-altitude plumes. After the plume passed over the radar, the backscatter once again became confined to a layer. Although this layer remained mainly below the bottomside, it was considerably more structured and developed than the bottom-type layer and occasionally gave rise to small plumes penetrating into the topside. Such layers are called bottomside layers.

Violent ESF episodes usually begin when bottom-type layers transform into other kinds of layers. Since bottom-type layers occur virtually every evening during equinox and December solstice over Jicamarca, forecasting irregularities mainly amounts to forecasting whether such a transformation occurs. An important clue to the nature of bottom-type layers can be found in the panel on the right of Figure 1 which shows the zonal drift speeds of the irregularities. The postsunset *F* region ionosphere mainly drifts eastward until a few hours before sunrise during magnetically quiet conditions under the influence of the eastward thermospheric wind and the the *F* region dynamo it drives. Indeed, most of the irregularities in Figure 1 drift eastward at speeds up to about 150 m/s, which is typical for the time and season in question. The drift speed altitude profile is a function of the relative *E* and *F* region flux-tube-integrated conductivities and the morphology of the irregularities. At low altitudes, the drifts slow and even reverse. This indicates that the low-altitude irregularities reside in magnetic flux tubes with integrated Pedersen conductivities dominated by the *E* region content.

If the conductivity in the *E* region is dominant, why does it not also short out the polarization fields set up by the growing plasma waves and damp the instability? The answer lies in the small scale size of the underlying primary plasma waves transverse to **B** and to the fact that the magnetic field lines are not prefect equipotentials. *Farley* [1960] first showed that the efficiency of the electrostatic coupling between ionospheric *E* and *F* regions is a function of the transverse scale size of the potential structure mapping between the two regions. *Hysell and Burcham* [1998] hypothesized that collisional interchange mode waves with wavelengths less than approximately 1 km (but greater than about 100 m so as not to suffer diffusive dissipation) would not be strongly coupled to the *E* region electrically and could exist in flux tubes controlled by the *E* region dynamo. Computer simulations suggested that such a class of waves could exist in the bottomside *F* region. Growth of the waves in the vertical direction was inhibited in these simulations by the loading effects of the *E* region conductivity.

We have performed a nonlocal computation of the growth rate of collisional interchange mode waves with finite parallel wavenumbers existing on magnetic flux tubes with apex points in the bottomside equatorial *F* region. Conducting plates lie at the feet of the field lines, representing the high flux-tube integrated *E* region conductivity. The problem is an eigenvalue problem, where the eigenvalue k_o is defined by the relationship

$$\gamma = \frac{\gamma_o}{1 + k_o^2/k^2} \quad (1)$$

and where k is the transverse wavenumber and γ_o is the usual linear, local interchange instability growth rate. Clearly growth is preferred for waves with $k \gtrsim k_o$. Boundary conditions for the problem are chosen such that 1) no interhemispheric current flows and 2) the wave amplitudes decays above the *E* region (at an altitude chosen somewhat arbitrarily to be 150 km).

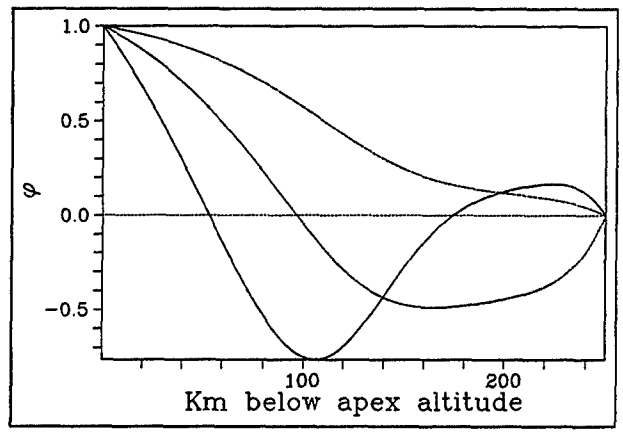


Figure 2. Mode shapes of nonlocal collisional interchange mode waves in the direction parallel to **B**. The horizontal axis represents altitude below the 400 km apex altitude of the flux tube. The three lowest order modes are shown.

Figure 2 is a plot of the mode shapes of the three lowest order collisional interchange modes for the case of bottom-type waves on a flux tube with a 400 km apex height. Dipole magnetic field lines were considered in the modeling. These mode shapes satisfy the eigenvalue problem for the stated boundary conditions. The eigenvalues for these modes are given by $2\pi/k_o$ = 1100 m, 650 m, and 400 m, respectively. These are the first three normal modes for the localized irregularities underlying bottom-type spread *F* layers.

The maximum transverse wavelength of the primary waves found in bottom-type layers should therefore be approximately 1 km, depending on the altitude of the layer. New experimental evidence involving high-resolution in-beam radar imaging seems to verify this claim [*Hysell*, 1999]. Primary waves with wavelengths longer than this cannot exist where

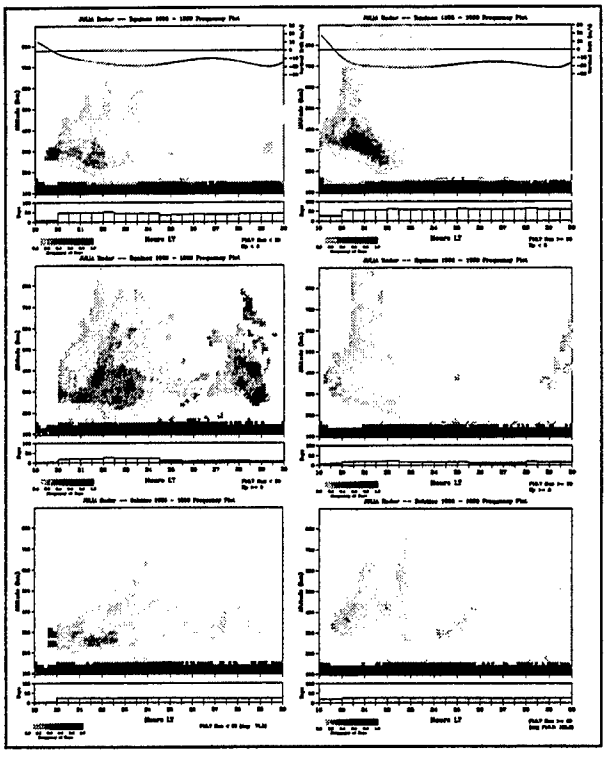


Figure 3. Occurrence statistics for spread *F* irregularities.

bottom-type layers are found. Smaller-scale primary waves meanwhile will have growth rates comparable to what would be predicted by local analysis.

3. Statistical behavior

Observations like Figure 1 reveal much about the physics underlying individual spread *F* events. Making use of the enormous database of such events accumulated with the JULIA radar, we can generalize these results and begin to gauge, at least statistically, how different geophysical forcing effects the occurrence of the different kinds of irregularities discussed above. The JULIA spread *F* database spans a widening variety of seasonal, solar flux, and geomagnetic activity conditions. We can use it establish the persistence and climatology of the irregularities and therefore establish a baseline for judging the skill of future forecast models.

Figure 3 presents the occurrence statistics for the JULIA spread *F* data sorted by season, solar flux, and geomagnetic activity. Panels to the left (right) represent low (moderate) solar flux levels. The upper two rows represent equinox data, with the first (second) row reflecting magnetically quiet (active) conditions. The third row represents December solstice data for all geomagnetic conditions. The grayscales indicate the likelihood of observing irregularities in a given altitude/local time bin. Solid lines show quiet time average vertical plasma drifts derived from incoherent scatter data.

By evaluating the occurrence phenomenology, we can recover many of the conclusions drawn recently by *Fejer and Scherliess* [1999], who demonstrated that the dependence of irregularities on seasonal, solar flux, and magnetic activity result from the corresponding effects on the zonal electric field. That is, the likelihood of observing irregularities mainly depends on the strength of the prereversal enhancement, the time of the evening reversal, and the post reversal strength of the zonal electric field, which is a destabilizing (stabilizing) influence before (after) it reverses. The climatology of the electric field meanwhile has been well established.

Under magnetically quiet equinox conditions, the effect of increasing solar flux is to cause irregularities to occur earlier and at higher altitudes and to penetrate to much higher topside altitudes on average. However, since the post reversal westward electric field grows stronger with increasing solar flux, spread *F* events tend to vanish earlier in solar maximum than in solar minimum. The late reversal time and small post-reversal electric fields associated with December solstice in particular lead to long-lived spread *F* events. Postmidnight spread *F* is likewise observed most frequently during solar minimum.

The effects of magnetic activity are most obvious in the occurrence statistics of post midnight solar minimum irregularities. During solar minimum, the small post-reversal electric fields can most easily be overcome by disturbance dynamo and prompt penetration electric fields caused by auroral zone energy deposition and changes in high-latitude convection. *Fejer and Scherliess* [1999] point out that the phasing of the disturbance dynamo electric field is such as to be mainly destabilizing in the late night sector and that the greatest effect can seen at approximately 0400 LT when prompt penetration and disturbance dynamo electric fields add constructively following a decrease in high latitude convection and drive strong upward plasma drifts. During solar maximum, strong westward disturbance dynamo electric fields mainly stabilize the ionosphere around twilight.

4. Electric field estimates

Here, we turn our attention to isolating the conditions that lead to the development of one type of irregularity or another on a given evening and to ultimately forecasting their occurrence. One of the most important forecast parameters is likely to be the afternoon and twilight time history of the zonal electric field. If the crucial forecast question revolves around whether bottom-type layers ultimately evolve

into bottomside layers or simply descend and stabilize, then the crucial parameter to measure should be the height of the *F* region and the zonal electric field that controls it. While electric fields can be measured using the usual incoherent scatter techniques, they can also be estimated using coherent scatter with accuracy satisfactory for many purposes. Since coherent scatter observations may be made routinely, the technique described below can form the basis for a spread *F* forecast strategy.

The zonal ionospheric electric field affects the stability of the *F* region ionosphere through several avenues. By driving the fountain effect throughout the day, the electric field controls the distribution of plasma density throughout magnetic flux tubes covering the entire tropical zone. The ratio of the integrated *E* and *F* region Pedersen conductivities ultimately determines where *F* region irregularities can form and of what variety. The electric field also determines the height of the *F* layer. An eastward electric field is moreover inherently destabilizing in the bottomside by virtue of the background Pedersen current it drives while a westward field is stabilizing. The intensity of the enhancement of the zonal electric field just prior to its reversal therefore would seem to set the stage for the occurrence or non-occurrence of instabilities. Other factors like gravity waves and geomagnetic activity thought to influence the growth of irregularities do so by modifying the background electric field; by concentrating on the field, we do not exclude these phenomena from our analysis.

We have estimated the zonal electric field in the afternoon and twilight hours with the JULIA radar by probing 3 m irregularities in the equatorial electrojet. One technique we have implemented was pioneered by *Balsley* [1969] and involves probing the electrojet with a broad beam so as to illuminate it over a wide sector in the equatorial plane. Coherent scatter can then be received from near zenith to much lower elevation angles. The lower the elevation angle, the greater the distance to the *E* layer, the greater the projection of the radar line-of-sight on the electron drift velocity, and the greater the mean Doppler shift of the echo. By tabulating Doppler shift versus scattering slant range, one can readily estimate the mean electron drift velocity and the polarization electric field. With some elementary modeling, the zonal ionospheric electric field can then be inferred from the electrojet polarization electric field.

Hysell and Burcham [1999] recently used a refined version of the oblique technique described above to measure the zonal ionospheric electric field over Jicamarca with the JULIA radar over a period of a few weeks in March and April of 1999. Figure 4 shows vertical plasma drift velocity estimates computed for March 7. The entire dataset shows considerable quiet time as well as storm time variability. The

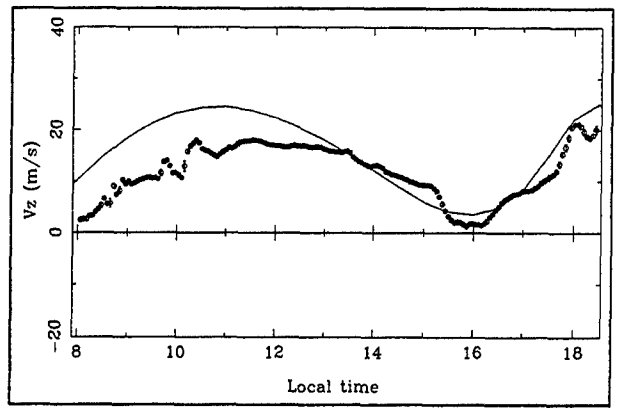


Figure 4. Vertical plasma velocity (zonal electric field) estimates inferred from oblique electrojet echoes observed with the JULIA radar on March 7, 1999 (open symbols with error bars). The solid curve represents a seasonal average computed from incoherent scatter radar data. The prereversal enhancement of the electric field is evident at 18 LT.

average of the electric field estimates for the entire period mimics closely the average measured with the incoherent scatter radar, however, and we believe the technique provides us with a good electric field measurement that can be made regularly without necessitating the full resource of the ISR.

References

Balsley, B. B., Measurement of electron drift velocities in the nighttime equatorial electrojet, *J. Atmos. Terr. Phys.*, *31*, 475, 1969.

Farley, D. T., A theory of electrostatic fields in the ionosphere at nonpolar geomagnetic latitudes, *J. Geophys. Res.*, *65*, 869, 1960.

Fejer, B. G., and L. Scherliess, Effects of the vertical plasma drift velocity on the generation and evolution of equatorial spread *F*, *J. Geophys. Res.*, *104*, 19,859, 1999.

Hysell, D. L., Imaging coherent scatter radar studies of equatorial spread *F*, *J. Atmos. Sol. Terr. Phys.*, *61*, 701, 1999.

Hysell, D. L., and J. Burcham, JULIA radar studies of equatorial spread *F*, *J. Geophys. Res.*, *103*, 29,155, 1998.

Hysell, D. L., and J. Burcham, Ionospheric electric field estimates from radar observations of the equatorial electrojet, *J. Geophys. Res.*, 1999, in press.

Woodman, R. F., and C. La Hoz, Radar observations of *F* region equatorial irregularities, *J. Geophys. Res.*, *81*, 5447, 1976.

Low-latitude ionospheric irregularities observed by the ROCSAT-1 satellite during the 22 October 1999 geomagnetic storm

H. C. YEH , S. Y. Su, L. F. Lee, S. C. Yang, and C. F. Ho (all at Institute of Space Science, National Central University, Chung-Li, Taiwan; E-mail: yeh@jupiter.ss.ncu.edu.tw);
R. A. Heelis (William B. Hanson Center for Space Sciences, The University of Texas at Dallas, Richardson, Texas, 75803, USA)

During the main phase of the 22 October 1999 magnetic storm, the ROCSAT-1 satellite flew over South America in the midnight to dawn local time. In addition to the equatorial depletions, the Ionospheric Plasma and Electrodynamics Instrument (IPEI) onboard ROCSAT-1 detected extensive ion density depletions at tropical latitudes (20° - 35°S GLAT) for more than 4 consecutive passes (~ 6 hours). Figure 1 shows the satellite trajectories for the three of these passes, along which the equatorial bubble and the tropical bubble structures are clearly separated. Preliminary analysis of these tropical latitude bubbles reveals that their spectral features do not significantly differ from those of equatorial bubbles at the medium to intermediate wavelengths (30 km - 500 m). Supersonic upward drifts were not seen in the equatorial plasma bubbles during the main phase of the storm. However, increased poleward field-aligned drifts were observed in both equatorial and tropical-latitude depletion regions. In this report, we will present a detailed comparison of the irregularities at equatorial and tropical latitudes. We will study how these low-latitude irregularities related to the storm time electrodynamics.

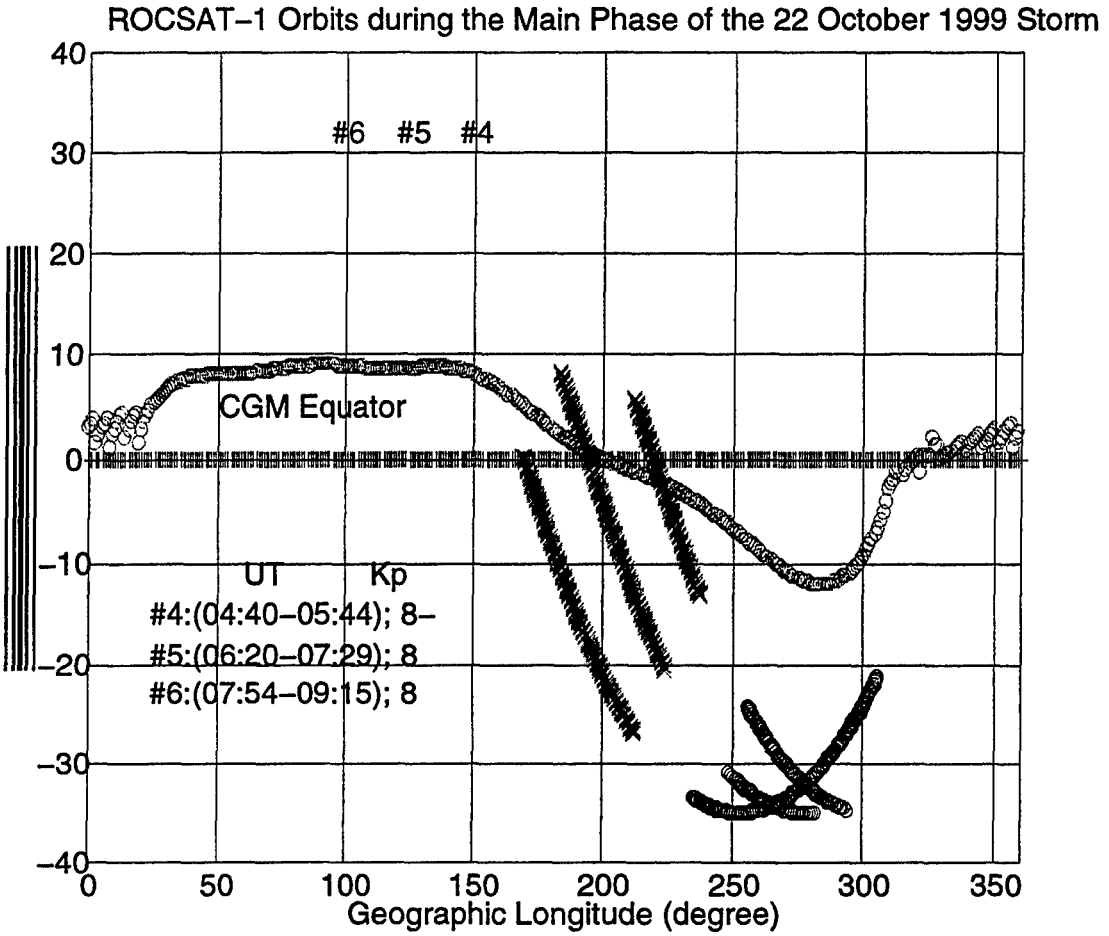


Figure 1. ROCSAT–1 orbits in geographic coordinates. Equatorial plasma bubbles were observed along the crossed segments of the orbits. Tropical latitude bubbles are along the circled segments of the orbits.

Equatorial Ionospheric Irregularity Diagnostics by the Dynasonde

J. W. Wright, NGDC/NOAA, Boulder Colorado USA 80303 and
N. A. Zabotin, Rostov State University, Rostov-on-Don, Russia

It has long been recognized that ionosonde observations contain a wide assortment of 'geophysical noise', most of which is systematically ignored in standard analyses for monitoring purposes. Modern digital research ionosondes such as the dynasonde expand the variety, resolution and dynamic range of the useful information, but also of the noise. This 'noise' is, in fact, evidence of the very essence of Space Weather in the upper atmosphere: It is a signature of the irregular and dynamic state of the region. However, because of the theoretical complexities of radiowave total-reflection in an irregular, magnetoactive, stratified medium, there have been few attempts (and fewer successes) to develop quantitative and dependable ways by which the weather could be deduced from the noise. This paper shows the experimental aspects of work underway to exploit new theoretical developments by which we use dynasonde measurements to obtain from the noise,

- Statistical parameters to quantify the prevailing small-scale ionospheric irregularities: the amplitude $(\Delta N/N)_{\mathrm{rms}}$ and the index ν of a power-law spatial spectrum usually applicable in the range of scales extending from about the radio wavelength λ to at least the radio Fresnel scale L_F (a few km);
- An outer scale L_M of the small-scale irregularities, when this can be distinguished from still larger irregularities attributable to Atmospheric Gravity Waves (AGWs);
- Local (~ ±100km) *spatial diversity* of these quantities, using the 'all-sky' view characteristic of ionosondes. This can be very important especially in equatorial and auroral regions, during conditions of intense large-scale structuring.

The technology relevant to this work is based upon the familiar classical ionosonde: ionospheric total reflection of medium- and high-frequency radiowave pulses. However, it is heavily dependent on some less familiar features of a modern digital research ionosonde, the 'dynasonde'. The central facts of the full technology, essential to our approach, are:

(1) The absolute accuracy, stability, and high resolution available for time (any microsecond) and radio frequency (any multiple of 100 Hz); these are our principal independent variables;

(2) The very high signal-to-noise levels available by total reflection (some 30 to 60 dB in the case of the dynasonde);

(3) The consequent high resolution (presently 12 bits) which can be maintained for echo complex amplitude; this is our principal 'raw' dependent variable. Resolution of the equivalent echo amplitude and phase can exceed 0.05 dB and 0.1 degree in the case of the dynasonde.

To the technological features cited in 1), 2), 3) may be added several unique properties and practical advantages of total reflection, deriving from magnetoionic radiophysics:

(4) The direct relationships obtained from classical theory between radio frequency and reflection-level plasma frequency (thus, electron density); useful redundancy arises from two independent polarizations;

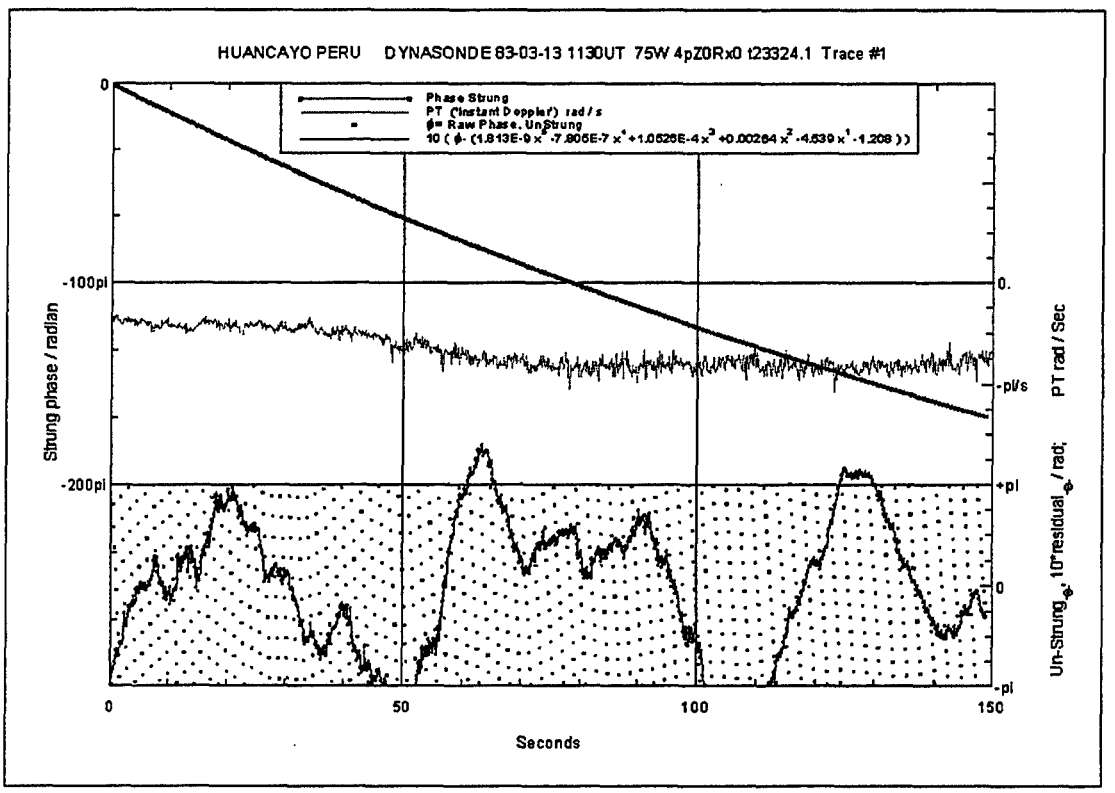
(5) The extreme sensitivity of radio echo phase and amplitude to even slight departures from an ideal, static, plane-stratified ionosphere;

(6) The particular sensitivity of echo group range ("virtual height") to variations of plasma gradient.

Finally, it is worthwhile to bear in mind that:

(7) Although ionization is a mere trace element in the mesosphere and thermosphere, it is also a sensitive and convenient tracer of nearly every photochemical, hydrodynamic, thermodynamic and electrodynamic process in these regions.

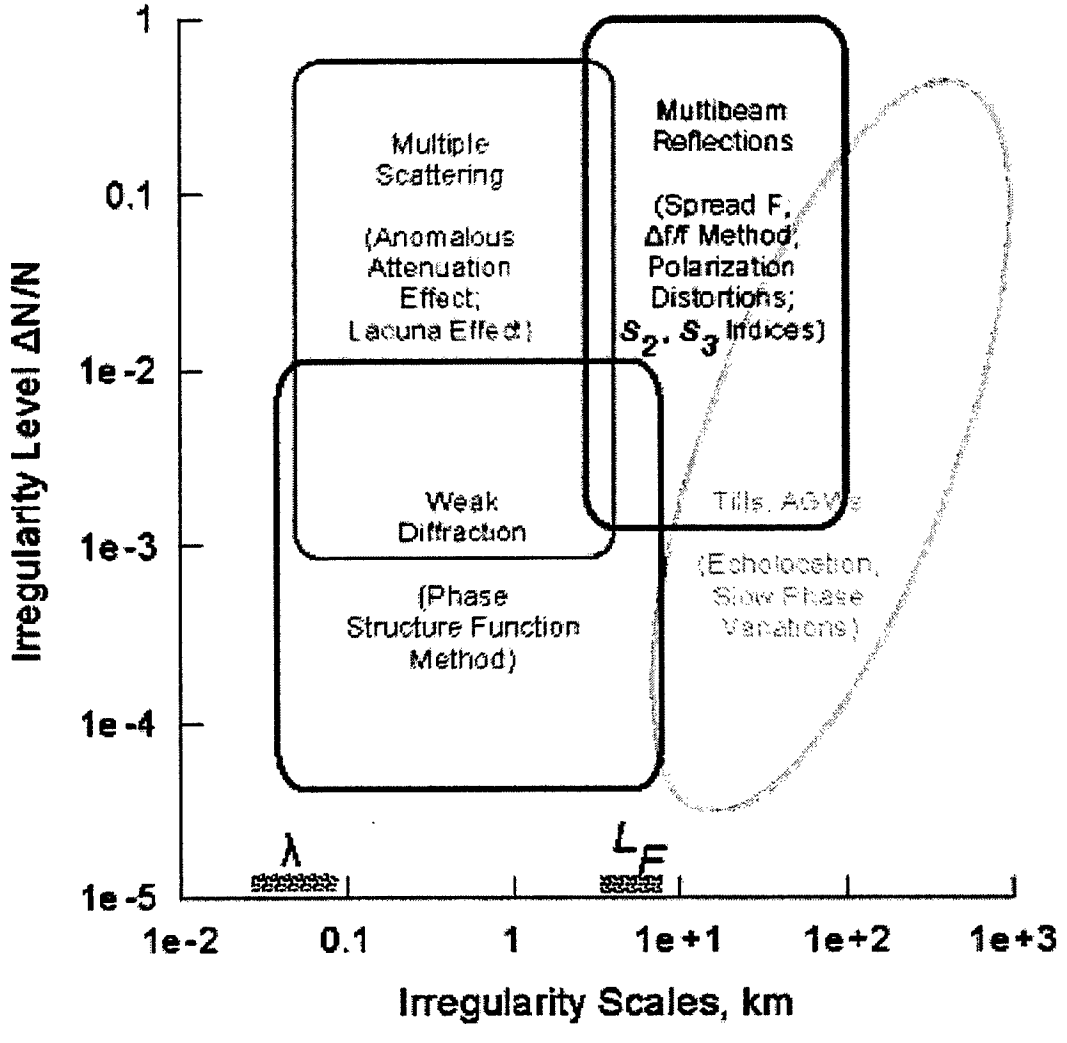
The classical analog ionosonde, and modern observatory or monitoring ionosondes, have tended to ignore items (1), (3), and (5) of our list.



An example suggesting this information content is shown here in Figure 1. This is a time series of radio echo phase angle (un-connected symbols, bottom panel) for a single sounding frequency. Phases are measured in the range $\pm\pi$. When 'strung' (by detecting $\sim|\pi|$ wraps, then adding the appropriate multiple of 2π), a sequence like the top smooth

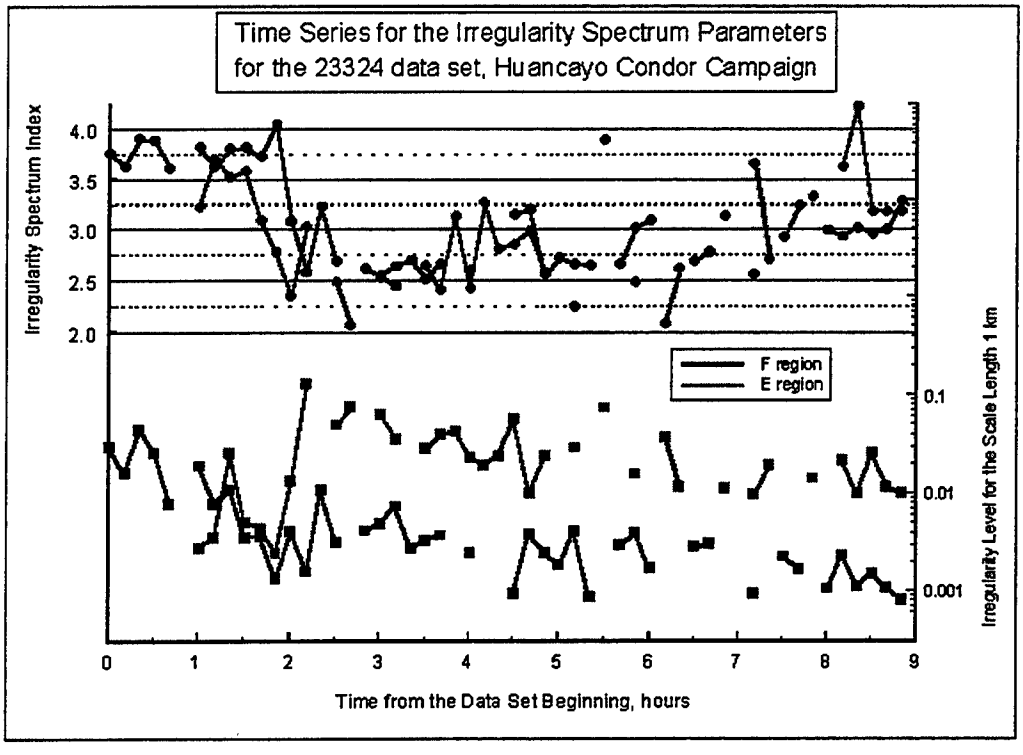
curve is obtained. The slow variation reveals ionospheric structure and motions of very large scale, which can be studied (e.g., for Atmospheric Gravity-Wave parameters) by classic methods. We seek evidence of weaker and smaller scales, and expose it by one or another method of detrending. For this example, we fit and remove a 5^{th}-order polynomial to the strung phases. The residual yields the connected data again placed in the bottom panel, but magnified here by a factor of 10 relative to the original raw phases. It contains phase fluctuations of a few 10's of seconds period, and a few tenths of radian amplitude, which are, finally, the essential input to our irregularity diagnostic methods. Meanwhile, the dynasonde also obtains a Doppler estimate over the much shorter interpulse period, here .01 second. This quantity is shown in the middle panel. Even here, the 'noise' is useful information, and serves to extend the measurable irregularity spectrum by about another order of magnitude.

Figure 2 suggests very schematically the domains of irregularity spatial scales and rms amplitudes ($\Delta N/N$) accessible by precision ionosonde methods. For completeness, the figure includes classically based deterministic measurements of large-scale 'irregularities' (tidal and solar-terminator tilts, Atmospheric Gravity Wave signatures,



etc.) It also includes the simple but powerful ability of the standard ionogram to give an estimate of $\Delta N/N$ near the radio Fresnel scale (L_F, a few km) as a direct-reading of the frequency-width $\Delta f/f$ in Spread F. Irregularity diagnostics in all of the other domains in Figure 2 are based upon our new echo amplitude- and phase-dependent methods.

During the past decade, theoretical developments by one of us (NAZ) have demonstrated new diagnostic capabilities arising mainly from items (1), (3), and (5) above. These methods adopt statistical quantities from echo amplitude and phase data, directly available as time-dependent variables, or in terms of derived quantities such as polarization ellipse parameters. Examples are the low-order moments (S_2, S_3) or "Scintillation Indices" of echo intensity, and temporal "Structure Functions", (SF), of echo phase calculated over a span of sampling lags. Theory shows how this information is related to essential parameters of the plasma-irregularity population.



An example result appears in Figure 3. This shows, separately for the E and F Regions, the spectral index (top) and $(\Delta N/N)_{rms}$ estimates during a 9-hour period starting at about local sunrise. The data of Figure 1 are contained in the first F-region result. The F-region spectral index tends to be somewhat greater than that for the E-region; it decreases with time in both regions. $(\Delta N/N)_{rms}$ is greater in the E region, especially just after the onset of 'Equatorial Sporadic E' associated with plasma waves in the electrojet. These early results are in broad agreement with those obtained by VHF and other radars, but they contain many features awaiting exploration.

OI 630.0nm dayglow measurements as a means to forecast the nighttime Equatorial Spread-F

D. PALLAMRAJU and S. Chakrabarti

Center for Space Physics, Boston University, 725 Commonwealth Avenue, Boston 02215, Massachusetts, USA.

Equatorial Spread-F (ESF) refers to the presence of irregularities in the nighttime equatorial ionosphere. The development of these irregularities is known to be a result of the electrodynamic coupling between the ionosphere-thermosphere system in the equatorial region. These irregularities span seven orders of magnitude in scale-sizes from a few centimeters to a few hundred kilometers and adversely affect trans-ionospheric communications. Results from various ground-based, rocket-, and satellite-borne instruments have enriched our knowledge on this magnificent phenomenon. These irregularities manifest themselves in different 'forms' and 'shapes' in various measurements. In ground-based ionosondes they appear as scattered echoes from the F-region; in the range-time-intensity maps derived from incoherent scatter radars they appear as 'plumes' (Woodman and La Hoz, 1976); in all-sky optical imagers they appear as airglow depletions or 'plasma bubbles' (Mendillo et al., 1992; Weber et al., 1996), and from VHF & UHF transit satellites one observes them as 'scintillations' (Aarons, 1993; Basu et al., 1996).

Although there is a broad understanding of the ESF generation mechanism and its occurrence morphology, there exists an uncertainty in its day-to-day occurrence. Even in the so-called 'ESF season' during which the ionospheric and thermospheric conditions on different days are nearly identical, ESF can not be predicted. As it is now known that varied combinations of background electron density gradient, eastward electric fields, vertical winds, eastward winds in presence of westward gradients and meridional winds play important roles in the day-to-day variability, it is a challenge to predict the ESF occurrence. At the same time, it is extremely important to be able to predict, as these irregularities are known to have a severe impact potential to radio communications and navigational geo-location. Scientifically, this is a missing element in our understanding of plasma instabilities at low latitudes.

Ground-based ionosonde measurements (Raghavarao et al., 1988; Alex et al., 1989; Jayachandran et al., 1997) indicated the existence of a precursor to the ESF in terms of the Appleton anomaly development. It was shown that the ratios in electron densities at ~270-300km altitude region between two locations (one under the anomaly crest and one between the crest and the trough) over Indian longitudes showed a steep increase starting from ~1700 LT (prior to ESF onset) on ESF 'days'. No such increase was seen on non-ESF 'days'. Since the local sunset at the dip equator for these longitudes was around half-an hour later, it was proposed that the strong development of the daytime Appleton anomaly seems to 'prepare' the ionosphere for the ESF. Nearly the same behavior was also noticed in data obtained from similar latitudes over South American longitudes (Alex et al., 1989).

The key to use this feature for predicting the ESF occurrence is to obtain the anomaly development—as it evolves, in a wide latitude region (of ~ 6° in latitude). It has been shown that thermospheric optical 630.0nm oxygen dayglow emissions can be used to obtain the evolution of the Appleton anomaly over a wide latitude range from a single location (Pallamraju et al., 1996). Such information on the development of anomaly—'as it develops' was used for obtaining precursors to the ESF occurrence (Sridharan et al., 1994) over Indian longitudes.

With the development of a new high-resolution **HiTIES** (High Throughput Imaging Echelle Spectrograph) instrument at Boston University for the investigation of OI 630.0nm dayglow, a possibility now exists to investigate the presence of such precursors from other longitude sectors. HiTIES is capable of measuring faint airglow emissions buried in the strong daytime background continuum (Chakrabarti, 1998), and it has been field-tested at Sondre Stromfjord in Greenland. Figure 1 shows the typical data obtained by HiTIES. The top panel (a) shows the 2-D solar spectral image around 630.0nm region obtained for an exposure time of 20 seconds. The x and y axes represent wavelength and spatial extent respectively. Panel (b) shows a line spectrum along a spatial region (of ~ 1° in latitude) for the same wavelength extent as in panel (a). Panel (c) shows the details ~630.0nm region for both the blue-sky spectrum (solid line) and the scaled solar spectrum (dotted line). One can notice that the blue-sky spectrum is 'filled-in' in the Fraunhofer absorption regions at ~630.03 and 630.07nm. Panel (d) shows the difference between the blue-sky and the solar spectra for different times on a given day. This 'excess' in the sky spectrum is due to the oxygen dayglow emission at 630.0nm and the so-called Ring effect (at 630.07nm) which refers to the filling-in of the Fraunhofer absorption regions in the day sky spectrum as compared to the solar spectrum. This contribution exists for all the Fraunhofer absorption regions and to take this contribution for the 630.03nm region into account, the area under the curve at 630.07nm is calculated and is subtracted from the one at 630.03nm region. The assumption here being that the two regions that are so closely separated and with nearly the same Fraunhofer depth have the same Ring effect contribution. Such dayglow intensities can be obtained from different spatial locations for a given 2-D spectral image; and such images obtained at different times would result in the time evolution of the dayglow intensities.

In the proposed presentation we will review the possible relationship between the development of the Appleton anomaly in the daytime and the occurrence of ESF in the nighttime and discuss the use of the thermospheric dayglow emission for the estimation of Appleton anomaly contribution. We would also compare the merits of using such daytime optical measurements for obtaining ESF precursors as compared to other conventional radio wave techniques.

References:

1. Aarons. J., The longitudinal morphology of equatorial F-layer irregularities relevant to their occurrence, *Space Sci. Rev., 63,* 209-243, 1993.

2. Alex, S., P. V. Koparker, and R. G. Rastogi, Spread-F and ionization anomaly belt, *J. Atmos, Solar Terr. Phys., 51,* 371-379, 1989.

3. Basu, S, E. Kudeki, Su Basu, C. E. Valladares, E. J. Weber, H. P. Zengingonul, S. Bhattacharyya, R. Sheehan, J. W. Meriwether, M. A. Biondi, H. Kuenzler and J. Espinoza, Scintillations, Plasma drifts and neutral winds in the equatorial ionosphere after sunset, *J. Geophys. Res., 101,* 26795-26809, 1996.

4. Chakrabarti, S., Ground-based spectroscopic studies of sunlit airglow and aurora, *J. Atmos. Solar Terr. Phys., 60,* 1403-1423, 1998.
5. Jayachandran, P. T., P. Sri Ram, V. V. Somayajulu and P. V. S. Ramarao, Effect of equatorial ionization anomaly on the occurrence of spread-F, *Ann. Geophys., 15,* 255-262, 1997.
6. Mendillo, M., J. Baumgardner, X. Pi, P. Sultan, and R. T. Tsunoda, Onset condition conditions for equatorial spread-F, *J. Geophys. Res., 97,* 13865-13876, 1992.
7. Pallamraju, D., R. Sridharan, S. Gurubaran and R. Raghavarao, First results from ground-based daytime optical investigation of the development of the equatorial ionization anomaly, *Ann. Geophys., 14,* 238-245, 1996.
8. Raghavarao, R., M. Nageshwararao, J. H. Sastri, G. D. Vyas and M. Sriramarao, Role of equatorial ionization anomaly in the initiation of equatorial spread-F, *J. Geophys. Res., 93,* 5959-5964, 1988
9. Sridharan, R., D. Pallamraju, R. Raghavarao and P. V. S. Ramarao, Precursor to equatorial spread-F in OI 630.0nm dayglow, *Geophys. Res. Lett., 21,* 2797-2800, 1994.
10. Weber, E. J., S. Basu, T. W. Bullet, C. Valladares, G. Bhishop, K. Groves, H. Kuenzler, P. Ning, P. J. Sultan, R. E. Sheehan and J. Araya, Equatorial plasma depletion precursor signatures and onset observed at 11° south of the magnetic equator, *J. Geophys. Res.,* 26829-26838, 1996.
11. Woodman, R. F., and C. La Hoz, Radar observations of F-region equatorial irregularities, *J. Geophys. Res., 81,* 5447-5466, 1976.

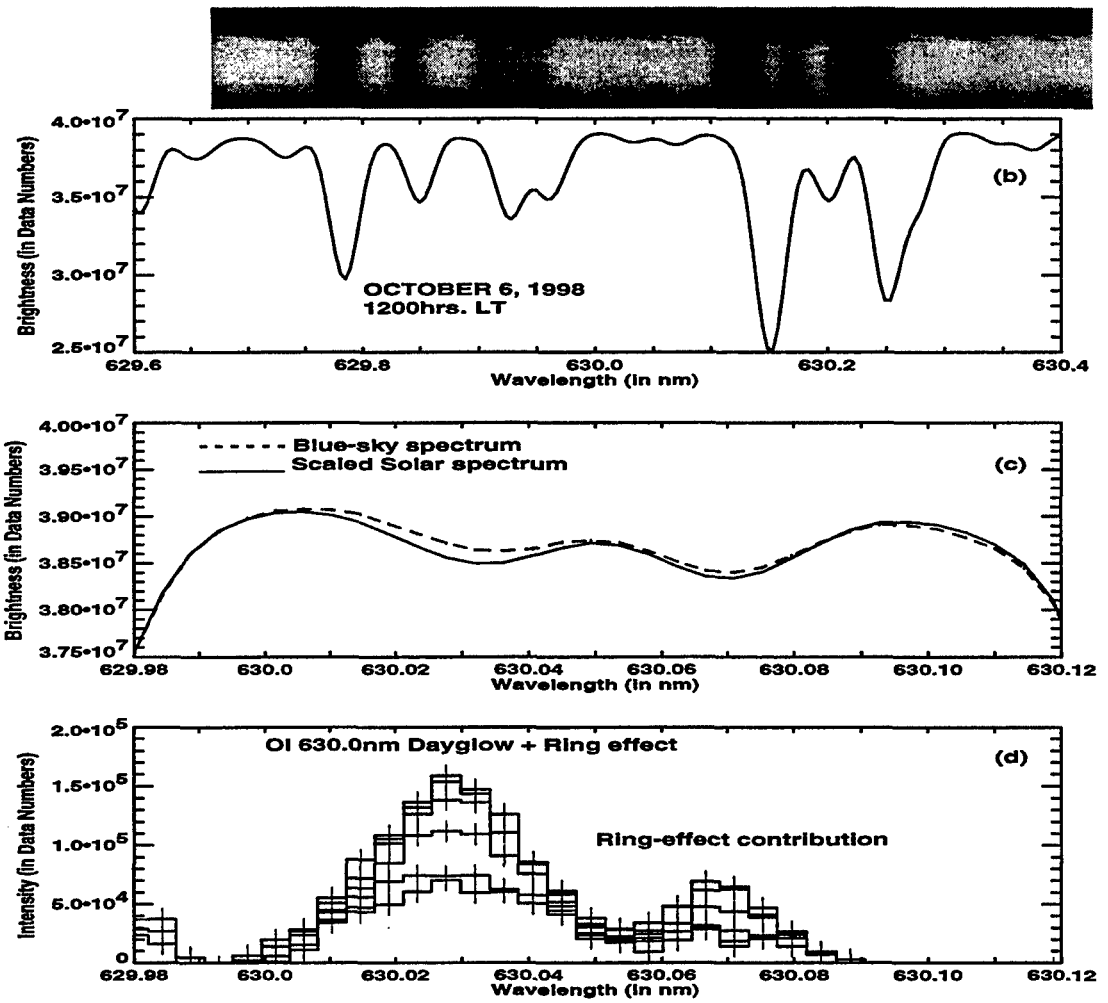


Figure 1 Top panel shows the 2-D image of the solar spectrum as obtained by HiTIES from Boston. Panel (b) shows the spectrum obtained by averaging along the y-axis of panel (a). Panel (c) shows the details of the region around the wavelength of our interest, viz., 630.03 nm. Panel (d) shows the difference between the blue-sky and scaled solar spectrum depicting the regions of dayglow emission and the Ring effect contribution, for different times on a given day.

Equatorial Spread F Variabilities and Predictive Capabilities Using Ground–Based Ionosondes

M. A. ABDU
(Instituto Nacional de Pesquisas Espaciais– INPE, São José dos Campos, Brazil)

The equatorial F–region irregularities have been the subject of investigations using a variety of diagnostic techniques depending upon the scale sizes that range from a few meters to hundreds of kilometers and the height domain that could extend from ~200 km to over 1500 km. They often are associated with plasma depleted flux tubes (plasma bubbles) of the topside ionosphere that develop from the unstable positive gradient region of the bottomside F layer. The composite effects of these irregularities on the different diagnostic techniques have received the generic name equatorial spread F (ESF). Their earliest manifestation was identified as spread in the range of F layer trace observed by ionosondes (Booker and Wells, 1938). Since then the large quantities of data sets on spread F occurrence statistics, accumulated at different longitude sectors of the earth's equatorial zone, (e.g., Abdu, et al., 2000; Chandra and Rastogi, 1972; Sastri et al., 1979) have helped establish the salient features of the medium term spread F variabilities such as those covered by seasonal and solar cycle time scales, that have corroborated also similar statistical features observed by other techniques such as scintillation and satellite born measurements (e.g., Aarons, et al., 1980; Basu et al., 1976; Kil and Heelis, 1998). Modern digital ionosondes are now widely used to investigate the dynamical characteristics of the irregularities as well.

Although the spread F instability processes, and the ambient ionospheric –thermospheric conditions conducive to their development, are considered to be reasonably known the causes of its short and medium term variabilities are far from being understood. The most enigmatic aspect concern the causes of the day–to–day variability in intensity and occurrence of ESF during its expected occurrence season over any given location, as well as how such variability could depend upon the longitude sector. The set of ionosondes now operational at equatorial and tropical sites, though limited in number, does offer opportunity to investigate this important question that has two main components: a– variability under forcing from magnetospheric processes, and b– that under magnetospherically "quiet" conditions, both of which need to be understood better if we are to achieve any progress towards improving our predictive capability of the phenomenon.

Ionosondes are sensitive to kilometer size irregularities, and when operated at, or in the immediate vicinity of, the magnetic equator, they could provide data on the variability of the F layer bottomside structures. However, observations further away from the magnetic equator (extending to within say, ±~20° in magnetic latitude) could detect the vertically extended depleted flux tubes over the equator in the form of their bottomside footprints (e.g., Abdu et al., 1983 a, b) in km scale structures. Therefore use of multi– station ionosondes that are appropriately spaced in latitude could effectively monitor the spread F variabilities of the bottom– and top–side domains.

In investigating the spread F variability based on ionosonde data it is necessary also to evaluate the ionosonde capability to diagnose the ambient ionospheric and thermospheric conditions that play key roles in the onset and development of the irregularity processes. These are: 1– linear growth rate for the generalized Rayliegh–Taylor (R–T) instability process that is dependent on the sunset (pre reversal) vertical plasma drift and associated F layer height, and the bottomside density gradients; 2– field line integrated conductivities that control the linear growth rate in (1) as well as the nonlinear bubble development that could follow; and 3– a density perturbation whose possible source could reside in gravity waves originating at lower thermospheric/atmospheric regions, or other possible mechanisms to be identified. All these items can in principle be determined/measured by ionosondes, directly or indirectly. Especially, the Item 1 is a most basic, and widely investigated aspect in spread F variability studies, (Farley, et al., 1970; Abdu, et al., 1983c; Fejer et al., 1999) and is known to involve competing actions of zonal and meridional components of thermospheric wind. The aspect of ESF variability that arises from zonal wind, through its action on the conductivity longitudinal gradient across the terminator, producing the pre reversal enhancement in zonal electric field (vertical drift), can be readily monitored by ionosondes. On the other hand the meridional/trans–equatorial wind could produce asymmetric equatorial anomaly (with response time of ~2 hours, Souza et al., 2000) that could enhance the field line integrated conductivity and modify the bottomside density gradients, (Maruyama, 1988) which in turn could contribute to inhibit the ESF development. The ESF response in this case is considerably more delayed as compared to the response to zonal wind. Thus the conditions of pre sunset meridional wind could constitute an important cause of the ESF variability. A method has recently been developed (Souza et al., 2000) that utilizes ionospheric critical parameters (peak density and height) observed by ionosondes at equatorial and low latitude sites and the SUPIM (Sheffield University Plasmasphere–Ionosphere Model) that permit unique determinations of the equatorial electric field and meridional wind at all local times.

Thus, in principle, much of the basic parameters of the ambient ionosphere and thermosphere that play roles in the ESF day–to–day variability can be determined by suitably positioned multi ionosonde systems in the equatorial–low latitude regions, that could monitor also the very characteristics of the ESF variability. This paper will address our existing knowledge of the ESF variability and predictive capability based on the available data sets and discuss how its possible improvements could be achieved through observations involving well planned experimental configuration (possibly involving also clustering of experiments) centered around ionosondes.

List of References:

Aarons, J., H.E. Whitney, E. Mackenzie, and S. Basu, Microwave equatorial scintillation intensity during the current solar maximum. Radio Sci., 16, 939 (1980).

Abdu, M. A., J. H. A. Sobral and I. S. Batista, Equatorial spread F statistics in the American longitudes: some problems relevant to ESF description in the IRI scheme, Advances in Space Res., 2000.

Abdu, M.A., R.T. de Medeiros, and Y. Nakamura, Latitudinal and magnetic flux tube extension of the equatorial spread F irregularities. J. Geophys. Res., 88, 4861 (1983a).

Abdu, M.A., R.T. de Medeiros, J.H.A. Sobral, and J.A. Bittencourt, Spread F plasma bubble vertical rise velocities determined from spaced ionosonde observations. J. Geophys. Res., 88, 9179 (1983b).

Abdu, M. A., R. T. Medeiros, J. A. Bittencourt, and I. S. Batista, Vertical ionization drift velocities and range spread F in the evening equatorial ionosphere, J. Geophys. Res., 88, 399–402, 1983c.

Basu, S., S. Basu, and B.K. Khan, Model of equatorial scintillation from in–situ measurements. Radio Sci., 11, 821 (1976).

Booker, H. G., and H. G. Wells, Scattering of radio waves in the F region of the ionosphere, Terr. Magn. Atmos. Electr., 43, 249, 1938.

Chandra, H., and R.G. Rastogi, Spread F at magnetic equatorial station Thumba. Ann. Geophys., 28, 37 (1972).

Farley, D. T., B. B. Balsley, R. F. Woodman, and J. P. McClure, Equatorial spread F, implications of VHF radar observations, J. Geophys. Res., 75, 7199– 7216, 1970.

Fejer, B. G., L. Schirliess and E. R. de Paula, Effects of plasma drift velocity on the generation and evolution of equatorial spread F, J. geophys. Res., 104, 19854–19869, 1999.

Kil, H., and R. A. Heelis, Global distribution of density irregularities in the equatorial ionosphere, J. Geophys. Res., 103, 407– 417, 1998.

Maruyama, T., A diagnostic model for equatorial spread F 1. Model description and application to electric field and neutral wind effects, J. Geophys. Res., 93, 14611–4622, 1988.

Sastri, J.H., K. Sasidharan, V. Subramanyam and M.S. Rao, Range and frequency spread–F at Kodaikanal. Ann. Geophys., 35, 153–158 (1979).

Souza, J. R., M. A. Abdu, I. S. Batista, and G. J. Bailey, Determination of vertical plasma drift and meridional wind using SUPIM and ionospheric data at equatorial and low latitude inBrazil, J. Geophys. Res., in press, 2000.

FORECASTING SCINTILLATION ACTIVITY IN THE EQUATORIAL IONOSPHERE

D. N. ANDERSON (CIRES/NOAA/SEC, Boulder, Colorado), B. Reinisch (UMLCAR, Lowell, Massachusetts)

I. Introduction

In the low latitude, ionospheric F region, the ambient ion and electron density distributions are determined through the combined physical processes of production by solar EUV radiation, loss of O+ through charge exchange with N2 and O2 and transport 1.) Along geomagnetic field lines by diffusion and neutral winds and 2.) Perpendicular to **B** by ExB drift. During the daytime, a combination of upward ExB drift at the magnetic equator and downward diffusion along the magnetic field lines creates crests of enhanced electron densities on either side of the magnetic equator at +/– 15 to 18 degrees dip latitude. This is the so–called "equatorial anomaly". Soon after sunset (between 1800 and 1930 LT) the upward ExB drift velocity can increase significantly before abruptly changing to downward drift – the so–called "pre–reversal enhancement". The likely–hood of this happening is directly correlated with the 11–year solar activity cycle, season and longitude. When enhanced upward drift does occur after sunset, it produces the ambient ionospheric conditions that are conducive for the growth of small–scale plasma density irregularities. This occurs via the Rayleigh–Taylor instability mechanism, which has been well documented and discussed in Fejer and Kelley (1980). Radio signals passing through ionospheric regions where these plasma density structures exist, experience strong amplitude fluctuations called "scintillation". The purpose of this paper is to discuss and demonstrate how certain ground–based sensors, strategically located, maybe in a position to "forecast" the probability that scintillation will occur on a night–to–night basis.

II. Sensor Observations

The objective is to be able to "forecast", just after sunset, the probability that scintillation will occur about 1 to 1 ½ hours later in local time, on a day–to–day basis. This translates to being able to observe whether or not the pre–reversal enhancement in upward ExB drift is taking place. This pre–reversal enhancement typically begins at 1800 LT and lasts until around 1930 LT. There are two possible ground–based sensors that could be used to measure or infer that the F layer is moving upward after sunset. The obvious sensor is an incoherent scatter radar (ISR) located at the magnetic equator such as the Jicamarca ISR located near Lima, Peru. This radar has been invaluable in providing the climatological vertical ExB drift measurements over the last 30 years, and was instrumental in developing the theory that connected the plasma Rayleigh–Taylor instability mechanism to the post sunset rise of the equatorial ionospheric F region. However, the operation of the Jicamarca radar is costly and that would prohibit its day–to–day use except for specific campaigns and World Days. A much less costly sensor is a digital ionospheric sounder. If one routinely observes the bottomside of the ionosphere at the magnetic equator after sunset, the increase in upward ExB drift can be inferred by measuring the change in true height of a given electron density value. For example, the 3 MHz contour represents the 1x10(5) el/cm3 bottomside density and if this true height is

observed to move from 200 km to 300 km between 1800 and 1900 LT this implies that the ExB drift is about 28 m/sec. Some of the increase is simply due to the recombination of the O+ ions after sunset but the greatest contribution is due to upward ExB drift. A drift of this magnitude would create ambient ionospheric conditions conducive to the onset of plasma instabilities and the generation of small–scale plasma irregularities.

III. Proposed Work

This paper addresses three basic questions and three tasks that are related to the day–to–day occurrence of scintillation activity and the development of small–scale plasma density irregularities in the low latitude/equatorial ionosphere. The most basic question, and one which is probably the most controversial, is whether a pre–reversal enhancement in upward ExB drift is necessary and sufficient to create the conditions required for the growth of small–scale structures in the equatorial ionosphere after sunset. It has been amply demonstrated both observationally (Basu et al., 1996) and theoretically (Haerendel et al., 1992) that an enhanced upward ExB drift velocity after sunset is required (necessary) to establish the ambient conditions conducive to the generation of small–scale structures via the Rayleigh–Taylor (R–T) instability mechanism. However, a number of papers suggest that without an appropriate "seed" mechanism, the bottom side of the ionosphere will not become unstable. The suggested seed mechanisms are horizontal perturbations in the bottom–side ionosphere generated by upward propagating gravity waves. It may be that these "seed" mechanisms are always present and what is required is simply a significant increase in vertical ExB drift to initiate the R–T instability mechanism. **The first task of this effort is to determine the relationship between the pre–reversal enhancement in upward ExB drift and the occurrence of scintillation activity as observed at UHF and L–band frequencies.** If, on a day–to–day basis, every–time scintillation activity is observed when there is a significant increase in upward drift velocity, then it can be stated that enhanced ExB drift is both necessary and sufficient for scintillation activity to occur.

The second task is to determine the relationship between the calculated linear R–T instability growth rates and the observed occurrence of scintillation activity, on a day–to–day basis. A number of investigations have theoretically calculated the linear growth rates (Haerendel et al., 1992; Maruyama, 1988) and find that the effects of vertical ExB drift and trans–equatorial horizontal neutral winds can realistically account for the climatological solar cycle, seasonal and longitudinal variability in the occurrence of scintillation activity. In order to forecast scintillation activity in a Weather sense, it is critical to know how calculated growth rates incorporating observed vertical ExB drift values are related to subsequent scintillation activity, day–to–day. Until this question is answered the Weather of scintillation activity will never progress past the "now–casting" stage.

The third task is to develop SKILL scores for forecasting scintillation activity in the equatorial region. Currently only the climatological model WBMOD is being used to forecast scintillation activity on a day–to–day basis (www.nwra.com). Since it is known that the occurrence of equatorial scintillation activity varies considerably from day–to–day for any given season, location and solar activity level, it is very important to quantify

how well the forecasting techniques proposed in tasks one and two compare with the WBMOD reference model.

IV. Progress

In Task 1, the pre–reversal enhancement in upward E X B drift will be determined from the height rise of the 4 Mhz density contour after sunset from the digital sounder at Jicamarca, Peru for the two years, 1998 and1999. There are approximately 200 days/yr of observations during this period. The following figure presents the true–height, bottom–side electron density profile on March 26, 1998 at 1830 and 1900 LT. The height rise of the 4 Mhz contour increases from 270 km to 330 km in this half–hour that corresponds to a vertical E x B drift of 30 m/sec. A network of UHF and L–band receivers at Ancon, Peru and Antofagasto, Chile, operated by the Air Force Research Lab (AFRL) at Hanscom AFB, MA, continuously observe the day–to–day occurrence of scintillation activity in the South American region. The bottom panel displays the scintillation amplitude index, S4, observed on March 26 at these two stations at both UHF and L–band frequencies. A number of examples that demonstrate the relationship between upward drift and scintillation activity will be presented.

In Task 2, the Global Theoretical Ionospheric Model (GTIM) will be used to calculate the linear Rayleigh–Taylor (R–T) instability growth rates, on a day–to–day basis, using the observed ExB drift velocities from Task 1. Details of this approach will be described in the talk.

Finally, in Task 3, the relationships that have been established in Tasks 1 and Tasks 2 between 1.) the observed vertical E x B drifts and the magnitude of the S4 index and 2.) the calculated R–T growth rates and the S4 index will be compared with the WBMOD S4 index to determine a SKILL score that will provide the "metrics" for assessing the importance of this scintillation forecasting technique compared with climatological forecasting.

V. References

Basu, S., et al., "Scintillation, plasma drifts, and neutral winds", *J. Geophys. Res., 101,* 26,795–26,809, 1996

Fejer, B. G., and M. C. Kelly, "Ionospheric irregularities", *Rev. of Geophysics, 18,* 401–450, 1980.

Haerendel, G., J. V. Eccles, S. Cakir, " Theory of modeling the equatorial evening ionosphere and the origin of the shear in horizontal plasma flow", *J. Geophys. Res., 97,* 1209–1223, 1992.

.Maruyama, Takashi, "A diagnostic model for equatorial Spread F. 1. Model description and application to electric field and neutral wind effects", *J. Geophys. Res., 93,* 14,611–14,622, 1988.

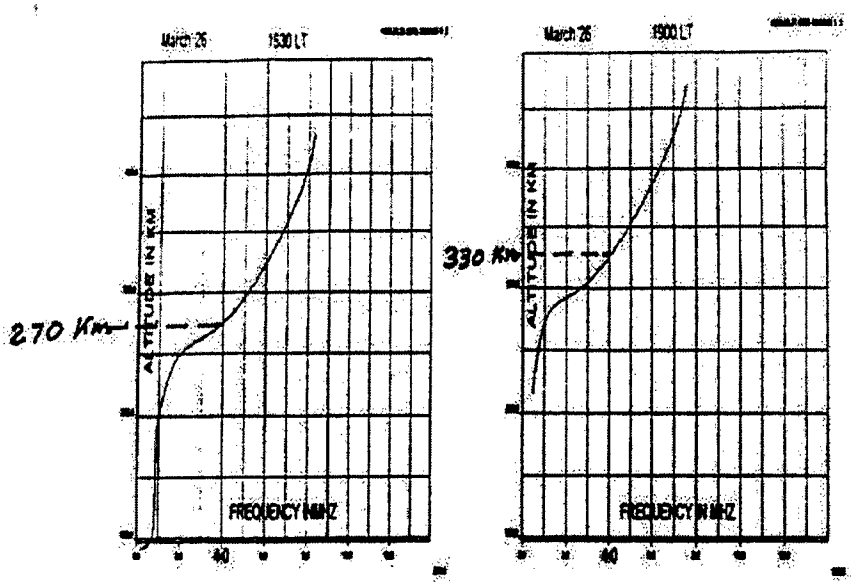


Figure 3. True height, digital sounder electron density profiles observed on March 26, 1998 between 1830 and 1900 LT at Jicamarca, Peru.

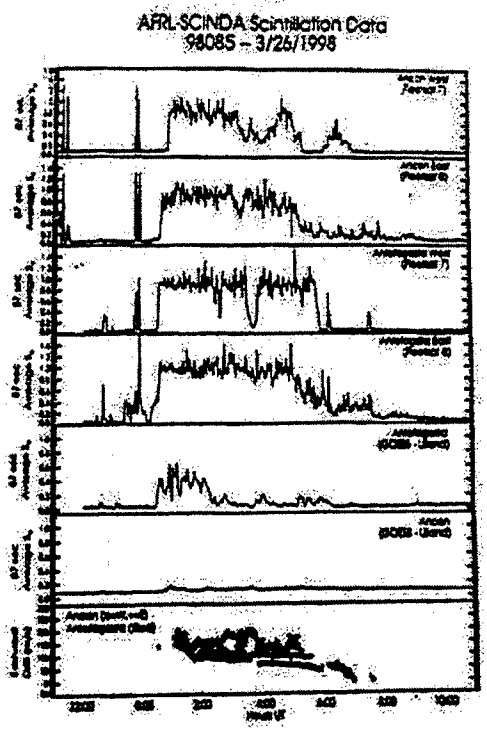


Figure 4. The S4 index observed by UHF and L –band receivers at Ancon, Peru and Antofagasta, Chile on March 26, 1998.

Satellite Instrumentation to Image Low-Latitude, Ionospheric Irregularities and Radio Wave Scintillations

P A Bernhardt and J D Huba (Beam Physics Branch, Plasma Physics Division, Naval Research Laboratory, Washington, DC 20375; Ph. 202-767-0196; Fax 202-767-0631; e-mail: bern@ppdu.nrl.navy.mil); C A Selcher (Transmission Technology Branch, Information Technology Division, Naval Research Laboratory, Washington, DC 20375; Ph. 202-767-2179; e-mail: selcher@itd.nrl.navy.mil); S. Basu and K.M. Groves, (VSBI, Air Force Research Laboratory, Hanscom AFB, MA; Ph. 781-377-3137; Fax: 781-377-3550; e-mail: basu@ppdu.nrl.navy.mil)

The equatorial and high-latitude ionosphere has long been known to be the primary source of amplitude and phase fluctuations for VHF, UHF, and L-Band radio waves. A new approach for monitoring ionospheric irregularities that affect radio propagation is being implemented using radio beacons and receivers on satellites in low-earth-orbit (LEO). These system called Monitor for Ionospheric Scintillation and Total Electron Content (MISTEC) uses three frequency radio beacons operating at VHF (150.012 MHz), UHF (400.032), and L-Band (1066.752 MHz). Receivers located on the ground and on other satellites record the phase differences between a pair of frequencies. This differential phase data is used to determine the integrated electron density along oblique and vertical paths using satellite to ground geometry and along both vertical and horizontal paths using satellite-to-satellite observations. The space-based radio beacons and receivers are scanning the ionosphere at roughly 8 km/s in LEO. This scan permits high-resolution reconstruction of electron densities using computerized ionospheric tomography (CIT). CIT has permitted reconstructions of many localized features including (1) auroral region disturbances, (2) high latitude troughs, (3) acoustic gravity waves, (4) artificial ionospheric disturbances, and (5) low latitude plasma plumes.

As radio waves propagate from satellites though regions of ionospheric disturbances, the phase front of the waves becomes distorted. The ionosphere thus acts as a phase screen for a wide range of transmissions from GPS satellites, UHF communications satellites, etc. The irregular phase front becomes highly diffracted as the signal propagates the hundreds of kilometers from the base of the ionosphere to the ground. During times of strong irregularities in both the high-latitude and equatorial ionosphere, the ground signals can show scintillations in both amplitude and phase that make navigation and communications systems inoperable. Once a large-scale irregularity has been formed in the ionosphere, it will persist for hours in the nighttime ionosphere. One basis for scintillation forecast is to monitor the drift of irregularities as they pass between satellite to ground communication links. A global network of ground receivers in a system called the Scintillation Network Decision Aid (SCINDA) has been used by the Air Force Research Laboratory (AFRL) to produce three-dimensional maps irregularity structures. Using the MISTEC system, the SCINDA technique will be extended to cover regions, such as the ocean, where ground receivers cannot be deployed. The first components of MISTEC was the radio beacons on the ARGOS and DMSP/S15 satellites that were launched in February and December 1999. Other radio beacons are scheduled for launch over the next four years on the STRV-1d, PICOsat, and C/NOFS satellites as well as the eight satellites of the COSMIC constellation. The space-based receiver is for these beacons is called SCITRIS (Scintillation and Tomography Receiver in Space). SCITRIS is currently scheduled for launch on C/NOFS and CloudSat. A program of measurements and simulations are being employed to optimize the planning for the MISTEC system.

A new algorithm for computation of digital ionograms

F. ARIKAN (Dept. of Electrical and Electronics Eng., Hacettepe University, Beytepe 06532 Ankara Turkey), O. Arikan (Dept. of Electrical and Electronics Eng., Bilkent University, Bilkent 06533 Ankara Turkey), and S. Salous (Dept. of Electrical Eng. and Electronics, UMIST, P.O. Box 88, Manchester M60 1QD U.K.)

Digital ionograms are used in a wide area from automatic scaling to automatic link establishment [1]. It is observed that these ionograms are cluttered with artificial artifacts and noise like components which complicate automatic information extraction. Standard fast Fourier Transform (with rectangular windows), which are commonly used in ionogram generation, introduce undesired spectral leakages in the form of high sidelobes [2]. Although the use of alternative windows such as Blackman window partially eliminates the speckles due to spillovers, they also widen the sharp mainlobes of rectangular windowed peridograms [2-4].

In this paper, a new ionogram algorithm which makes use of efficient signal processing tools is presented. With the new ionogram algorithm, the artificial artifacts due to hardware and processing of data are eliminated. By distortionless zooming capability, only the desired layer reflections or magnetoionic components can be observed on the ionogram. This capability facilitates the tracking of layers or modes. The data samples which are to be used in ionogram generation, are processed by both sliding Rectangular and sliding Blackman windows and two sets of periodograms are obtained by Discrete Fourier Transform (DFT). These two periodograms are then separately median filtered along the time axis to partially eliminate the speckles. The zoomed, Blackman windowed and median filtered ionogram is then passed through an edge detection filter which determines the significant and insignificant transitions of signal levels and eliminates insignificant edges. At the output of this filter, only the transitions around the desired signal components are retained. By making use of information on the significant edge locations, the peridograms which are obtained by sliding Rectangular and sliding Blackman windows are fused to form a sharp ionogram with negligible ringing. As a final step, a statistical thresholding algorithm is also used to partially eliminate noise like background. In the algorithms, various processing parameters such as the length of the data sections to be processed by periodogram, overlapping percent of sliding windows, threshold in deciding significant and insignificant edges, threshold using in fusing algorithm are to be determined.

The performance of the new ionogram algorithm is demonstrated by using a frequency modulated continuous wave (FMCW) HF chirp sounder data set collected from an oblique midlatitude path. The bistatic HF chirp sounder was developed at University of Birmingham [3]. The data set is obtained from a 273 km great circle path in the UK by a frequency sweep of 4 MHz generated in 4 seconds with a sweep separation of 10 s. The data was sampled with a 12-bit digital to analogue converter at a rate of 16384 Hz giving a total of 65536 samples per sweep. A typical sweep period is presented in Figure 1 which shows the digitized signal level versus the sweep time in seconds.

As a first step, the data samples are processed by both sliding Rectangular and sliding Blackman windows and two sets of periodograms are obtained by DFT. These periodograms are presented in Figures 2a and 2b, respectively. In the second step, both ionograms are passed through a sliding median filter which smooths the ionograms and

reduces the effect of unwanted noise like components. Figure 3 shows the Blackman windowed and median filtered ionogram which is zoomed to observe the 1F2-layer ordinary and extraordinary waves. The third step of ionogram generation is to discriminate between significant and insignificant signal transitions and eliminate the insignificant signal components. The significant edges of Blackman windowed and median filtered periodogram are determined using Canny's method of edge detection which is quite robust to noise components and is highly successful in detecting true weak edges. The advantage of using this technique is illustrated in Figure 4 which shows the difference between all edges detection (Figure 4a) and true weak edges and strong edges (Figure 4b). After determining the locations of significant signal transitions with the edge detection algorithm, median filtered Blackman and rectangular windowed spectrum estimates are fused to obtain a sharp periodogram with negligible ringing. As a final step, a statistical thresholding method is used to partially eliminate the left-over artifacts and noise-like components. Figure 5 presents a sharp and clean fused ionogram.

The success of this new ionogram algorithm is mostly determined by the proper choice of parameters such as the window length, number of overlapping samples, N-point DFT, the median filter length, and the thresholds in detemining the significant and insignificant signal transitions and statistical thresholding routine. All these parameters can be set once optimized over a specific link, and they can be adopted to automatic selection of parameters in on line analysis. Generally, once the parameters are set in an optimum or quasi-optimum manner, the ionogram algorithm is very robust to variations in the ionospheric conditions and high quality ionograms can still be generated.

In this paper, an alternative digital ionogram algorithm which is based on recent digital signal processing techniques is presented. The data samples which are multipled by both sliding Rectangular and sliding Blackman windows, are processed with chirp-z transform (zoomed in DFT) to obtain two sets spectograms. These two spectograms are separately median filtered and fused to obtain a sharp periodogram with negligible ringing. Fusing is based on an edge detection routine which automatically enhances significant transitions near desired signal components and eliminates insignificant transitions due to artifacts. A statistical thresholding algorithm is also used to eliminate remaining noise like background. The performance of this new ionogram algorithm is verified with chirp sounder data collected from an oblique midlatitude path. It is observed that the presented algorithm is highly successful in obtaining robust and sharp ionograms free of artifacts and processing noise. This algorithm can also be modified to be used in real time (online) applications.

REFERENCES

[1] J. M. Goodman, *HF Communications-Science and Technology*, New York: Van Nostrand Reinhold, 1992.

[2] S. Salous, "On the potential applicability of auto-regressive spectral estimation to HF chirp sounders," *Journal of Atmospheric and Solar-Terrestrial Physics*, vol.59, No.15, pp.1961-1972, 1997.

[3] S. Salous, "FMCW channel sounder with digital processing for measuring the coherence of wideband HF radio links," *IEE Proceedings*, vol.133, Pt. F, No.5, pp.456-462, 1986.

[4] R. L. Fante, *Signal Analysis and Estimation*, New York: John Wiley and Sons, 1988.

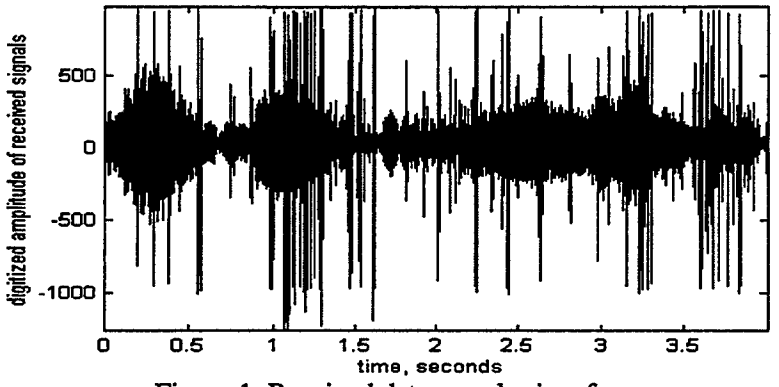


Figure 1: Received data samples in a frequency sweep

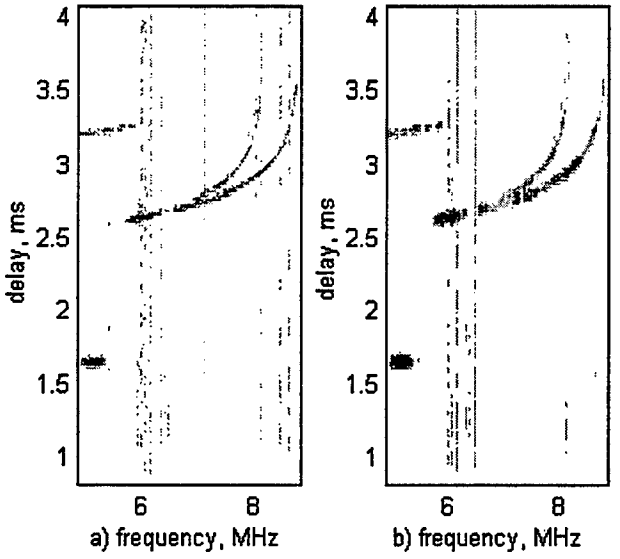


Figure 2: a) Rectangular windowed ionogram b) Blackman windowed ionogram

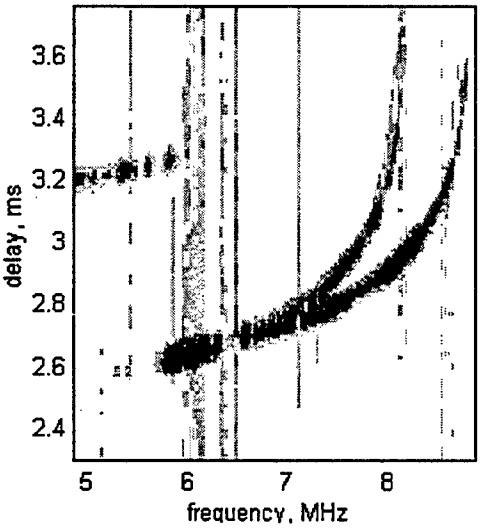


Figure 3: Blackman windowed, median filtered and zoomed ionogram

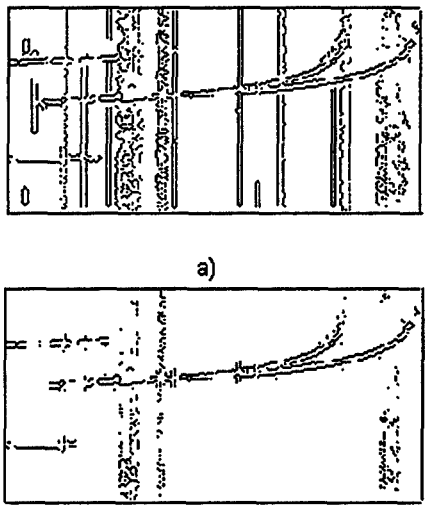


Figure 4: a) All edges b) True weak and significant edges

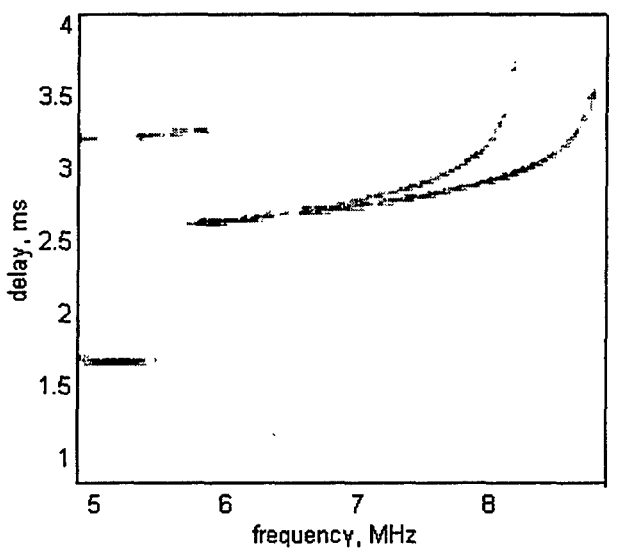


Figure 5: Fusing and statistical tresholding is applied to the ionogram

In–Situ Techniques for Aeronomy Using Ionization Gauges

J. H. CLEMMONS (The Aerospace Corporation, P. O. Box 92957, Mail Station M2/260, Los Angeles, CA 90009, USA), R. F. Pfaff (NASA/Goddard Space Flight Center, Mail Code 696, Greenbelt, MD 20771, USA), and M. F. Larsen (Department of Physics, Clemson University, Clemson, SC 29634, USA)

Ionization gauges have been used for *in–situ* aeronomy research since the late 1940s. These instruments measure the neutral gas density, and early applications yielded temperature profiles of the mesosphere/lower thermosphere. More recent applications employing modern technology have been employed to examine turbulence in the mesosphere [e.g., *Lübken et al.*, 1992]. The present work discusses the use of the ionization gauge for these measurements, as well as the extension of the technique for measurement of neutral winds. Recent rocket data in and around sporadic–E layers will be presented and discussed, and the wind measurements will be compared with those derived using the chemical release method.

TIME AND FREQUENCY DOMAIN PROPAGATION MODELS IN THE LOWER AND MIDDLE ATMOSPHERE

F. AKLEMAN[1] and L. Sevgi[2]

[1] Istanbul Technical University, Electronics and Communication Engineering Dept., 80626, Maslak – ISTANBUL, TURKEY

[2]TUBITAK–MRC Marmara Research Center Information Technologies Research Institute, Gebze – KOCAELI, TURKEY

Abstract: *Long–range communication has always been an important but complex problem to be solved. Propagation of radio waves over long distances near the earth surface shows quite different characteristics depending on the nature of the communication path. Atmospheric changes and/or ground effects including terrain variations should carefully be taken into consideration while dealing with propagation problems. Because of complexity of the problem, analytical approximate solutions can hardly be found for some idealised cases, therefore, scientists tend to use numerical modelling techniques. In this study, Split Step Propagation Equation (SSPE) and Time Domain Wave Propagator (TDWP) algorithms have been used to obtain observable numerical results for tropospheric propagation. SSPE is a frequency domain method based on the solution of a parabolic type (PE) wave equation, while TDWP, which has been recently introduced, is built by a two–dimensional (2D) Finite Difference Time Domain (FDTD) algorithm. Here, the two techniques have been tested and compared against each other through various ground wave propagation problems. Assuming azimuthal symmetry and using transverse and/or longitudinal refractivity and boundary perturbations ground wave propagation and surface and/or elevated ducts may be represented in 2D space. In this study, the results of TDWP and SSPE are compared on different ducting and anti–ducting refractivity profiles and their agreement is presented.*

I. Introduction

Long–range communication includes two typical wave types: ground and sky waves. Sky waves is mostly affected by the upper atmosphere (ionosphere), while ground wave propagation changes due to the lower and middle atmosphere (troposphere) characteristics as well as ground effects. Ground waves have three components: direct wave, ground–reflected waves and surface waves. Here, ground wave propagation is analysed with two powerful numerical methods in order to visualise the effects of troposphere. Physical characteristics of the propagation depend on many parameters such as operating frequency, medium parameters, transmitter and receiver locations and the surface geometry. As it is known, propagation beyond the horizon is possible at HF (3–30MHz) and lower frequencies since surface waves may reach ranges up to hundreds of kilometres in diffraction region, while it is limited by the line–of–sight at microwaves because at these frequencies surface waves are negligible. Analytical approximate solutions of ground wave propagation problem have been outlined in [1] together with the hybrizidation of ray and mode methods and a summary of some analytical–numerical and pure numerical techniques. Surface and/or elevated duct effects of various transverse/longitudinal refractivity profiles have been investigated either analytically [2–5] or numerically [6–8].

In this study, first time domain wave propagator (TDWP) and split step parabolic equation (SSPE) techniques are explained in Sec. II. In Sec. III, these methods are compared with their results for two different characteristics of troposphere. Finally, the conclusions are given in Sec. IV.

II. TDWP and SSPE

II.1 Time Domain Wave Propagator (TDWP) :

Time domain wave propagator (TDWP), which has been recently introduced [9], is a general technique for different kinds of propagation problems and based on a two–dimensional (2D) finite difference time domain (FDTD) algorithm where the propagation environment is assumed to have an azimuthal symmetry. In general, 3D–FDTD is based on the discretization of Maxwell' s two curl equations directly in time and spatial domains and dividing the volume of interest into very small identical blocks called Yee cells [10]). There are three electric and three magnetic field components in each Yee cell distinguished by (i,j,k) label. The time and spatial discretization steps are Δt and Δx, Δy, Δz, respectively. Although field components in each cell are labeled with the same (i,j,k) numbers (such as $E_x(i,j,k)$ or $H_z(i,j,k)$), their locations are different. There is also a $\Delta t/2$ time difference between E and H field components in Yee cell. Any object may be simulated by the medium parameters ε, μ, σ. Here, E_x, H_y (transverse) and E_z, (longitudinal) components are

calculated and a two–dimensional Yee cell available for that structure is used in order to model the classical 2D TM_z ground wave propagation.

Since the propagation region (see Fig.1a) is much larger than the FDTD computation space, the FDTD computation space covers this region like a moving computation sub–region. FDTD computation space is terminated by perfectly matched layer (PML) blocks from left ($z\rightarrow-\infty$), right ($z\rightarrow\infty$) and ($x\rightarrow\infty$) top and any boundary condition (BC) (e.g., perfectly matched layer or a lossy ground) can be simulated at x=0. Various refractivity (e.g., exponential, linear, bi–linear or tri–linear) profiles over earth's surface may be introduced via relative permittivity $\varepsilon_r=n^2(x,z)$. Initial altitude profile, which has a pulse character in time, providing broad band analysis, is injected via the necessary field components. One–way propagation is traced via a 2D rectangular window as shown in Fig.1b. This virtual propagation window moves from left to right in FDTD computation space and circulates back to the left when reaches the right most–end, which is the initial profile of the next FDTD computation space. The process and FDTD simulations repeat until the wave longitudinally propagates to a desired range in order to trace the direct, ground–reflected and surface waves in time domain. Keeping in mind the number of FDTD cells traced during the circulation of the propagation window, the transverse and/or longitudinal propagation characteristics are extracted. When time histories are accumulated at chosen observation points until all transients disappear during FDTD simulation, any vertical and/or horizontal field profile at a desired frequency can be obtained by applying off–line discrete Fourier transformation (DFT).

II.2 Split Step Parabolic Equation (SSPE):

SSPE is a frequency domain wave propagator, which is the solution of a parabolic type wave equation [6–8]. It is a one–way propagator that is valid under paraxial approximation (i.e., under weak longitudinal refractivity dependence or near axial propagation), where backscatter effects are omitted. For a scalar W(z,x) wave function the general solution of SSPE technique is given as

$$W(z,x)=\exp\left[i\frac{k_0}{2}n\Delta z\right]FFT^{-1}\left[\exp\left[-i\frac{k_x^{\,2}\Delta z}{2k_0}\right]FFT[W(z_0,x)]\right] \qquad (1)$$

where $\Delta z=z-z_0$, k_0, k_x, FFT and FFT^{-1} correspond to range step size, free–space wavenumber, transverse wavenumber, discrete (fast) Fourier and inverse discrete (fast) Fourier transforms, respectively. Since PE is an initial value problem, an initial transverse field distribution, $W(z_0,x)$ is injected then it is longitudinally propagated through a medium defined by its refractive index profile, n(z,x) and the transverse field profile $W(z_0+\Delta z,x)$, at the next range step, is obtained. By multi–moving back and forth between x and k_x domains via FFT and inverse FFT the transverse field profile at any range may be obtained [6–8].

III. Typical Applications and Numerical Results

In order compare the results of two methods, both TDWP and SSPE techniques are applied to a surface duct problem. Here, a linearly decreasing vertical refractivity profile, which results in a strongly trapping surface duct over flat earth, is used. Same transverse (spatial) Gaussian initial profile is fed into both TDWP and SSPE algorithms in which transmitter height is 25m. The TDWP is used once and broad band results are obtained. The SSPE propagator needs to be run separately for each frequency. Vertical field profiles at 500m away from the transmitter, which are obtained with both techniques are plotted in Fig. 1a using the propagation factors ($|E/E_0|$). A similar procedure is applied to calculate the propagation factor in both TDWP and SSPE techniques. Both algorithms are run twice. In the first runs, propagation over PEC ground is simulated. In the second runs, they are repeated in free–space and the propagation factors are obtained after applying off–line DFT. A good agreement between the results of time and frequency domain wave propagators is clearly seen from the figure.

A similar comparison is given in Fig. 1b for range variation of vertical electric field component at a fixed altitude. In this case, time histories of propagation at various observation ranges at 25m fixed altitude are accumulated in TDWP and off–line DFT is then applied. SSPE calculates fields at all altitudes as well as ranges, therefore, the calculation procedure does not change. The results agree quite well for both 100MHz (bottom) and 150MHz (top) frequency calculations. As seen from Fig. 2, interaction of direct and ground reflected field components increases as the frequency increases.

Guiding of waves over earth's surface is caused by a negative vertical refractivity gradient. On the other hand, it becomes a positive refractivity gradient in anti–guiding regions. While waves are trapped over surface with negative vertical refractivity gradient, energy detaches from the surface (i.e., wave divergence occurs) for positive vertical refractivity gradient. The results of TDWP and SSPE for this anti–guiding model are compared in Fig. 3. Here, vertical field profiles at three different frequencies at 500m range are shown. As clearly seen from the figure, the higher the frequency the

stronger the wave detachment from the surface. The propagation factor just above the surface at 500m range is –22dB at 100MHz and reduces to –33dB at 200MHz. This means, when the frequency increases from 100MHz to 200MHz field amplitude just above the surface at the same range reduces by 11dB.

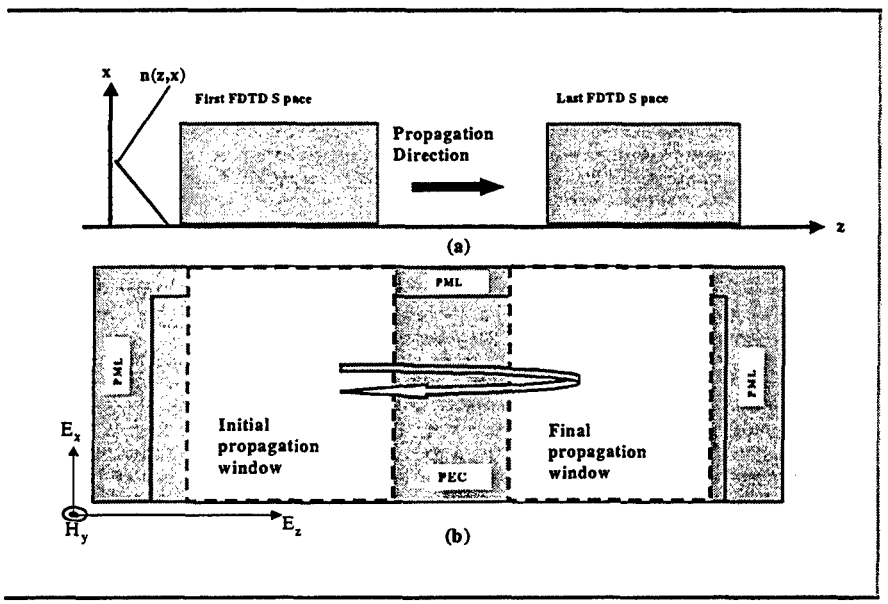


Figure 1: **(a)** The 2D propagation space. A finite–sized FDTD computation space is used as if this region is covered by multi FDTD computation spaces. **(b)** Detailed picture of one FDTD computation space. The final window of the current FDTD computation space is the initial window of the next FDTD space.

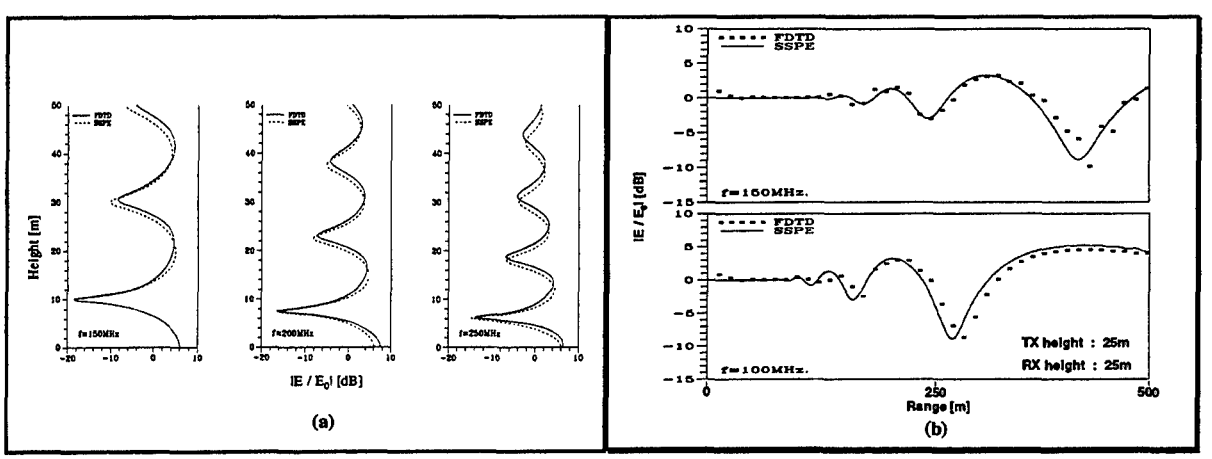


Figure 2: **(a)** Altitude field profiles at 500m away from the source (corresponding to the ranges of 250λ, 330λ, 415λ at 150MHz, 200MHz and 250MHz, respectively) The propagation region is characterized by longitudinally homogeneous, linear vertical refractive index with $dn/dx = -10^{-7}$ [n unit/m]. **(b)** Longitudinal field profiles at fixed altitude. Both the transmitter and observation altitudes are same and are equal to 25m.

IV. Conclusions

In this paper, two propagators are taken into account in order to deal with different kinds of tropospheric propagation problems. The SSPE has been in use for more than a decade and has successfully been applied to many one–way propagation problems. On the other hand, TDWP has just been introduced [9] and can be applied to various electromagnetic ducting/anti–ducting problems. A very similar FDTD based technique has also been used in analyzing VLF and LF propagation through earth – ionosphere waveguides[11]. Terrain effects and surface roughness as well as ground losses can be modeled, where any kind of transverse and/or longitudinal refractivity profiles and vertical propagation can be taken into account. Here, propagation of radio waves in troposphere has been investigated with both

techniques and their agreement has been shown. It is now possible to analyse propagation through lower and middle atmosphere for time domain characteristics with TDWP. One disadvantage of TDWP is the need of long computation times for long range propagation simulations, which may be overcomed by using some intelligent algorithmic and/or parallel processing techniques.

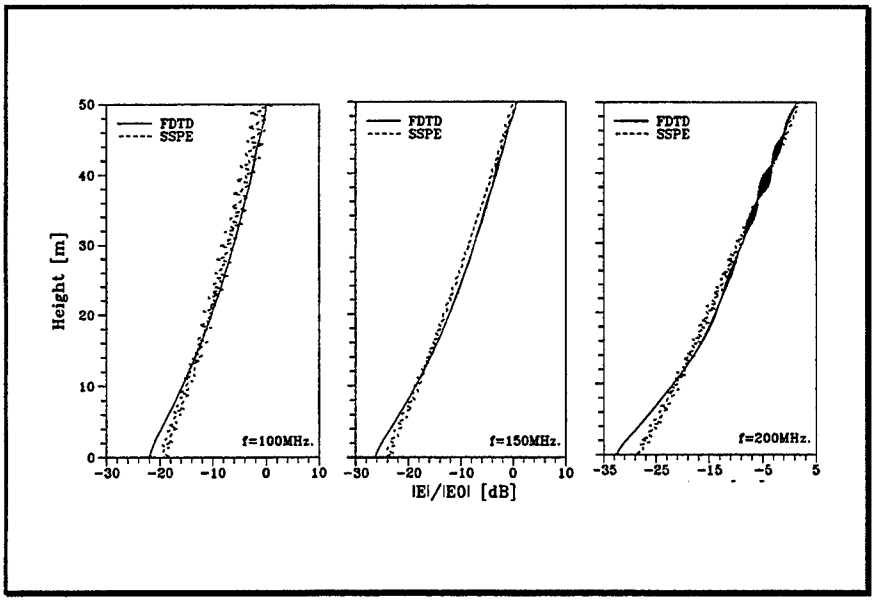


Figure 3: Altitude field profiles at 500m away from the source (corresponding to the ranges of 166λ, 250λ and 333λ at 100MHz, 150MHz and 200MHz, respectively). The propagation region is characterized by longitudinally homogeneous, linear vertical refractive index with $dn/dx = 10^{-3}$ [n unit/m].

References:

[1] L. Sevgi & L. B. Felsen, "A new Algorithm for Ground Wave Propagation Based on a Hybrid Ray–Mode Approach", Int. J. of Numerical Modeling, Vol 11, No 2, pp.87–103, 1998

[2] [2]L. B. Felsen & L. Sevgi, "Adiabatic and Intrinsic Modes for Wave Propagation in Guiding Environments with Longitudinal and Transverse Variations: Formulation and Canonical Test", IEEE Transactions on Antennas and Propagat. Vol 39 No 8, pp.1130–1136, 1991

[3] L. B. Felsen & L. Sevgi, "Adiabatic and Intrinsic Modes for Wave Propagation in Guiding Environments with Longitudinal and Transverse Variations: Continuously Refracting Media", IEEE Transactions on Antennas and Propagat. Vol.39 No.8, pp.1137–1143, 1991

[4] B. Polat, E. Topuz & L. Sevgi, "Wave Propagation Through Linearly Tapered Homogeneous Dielectric Slab Waveguides", AEU, Int. J. of Electronics and Communication, Vol.52, No.2, pp.105–108, March 1998

[5] L. Sevgi, S. Paker & E. Topuz, "Intrinsic Mode (IM) Formalism and Its Asymptotical Evaluations in 3D Non–Homogeneous Environments", AEU, Int. J. of Electronics and Communication, V.50, No.3, pp.201–207, May 1996

[6] G. D. Dockery, " Modeling Electromagnetic Wave Propagation in the Troposphere Using Parabolic Wave Equation", IEEE Transactions on Antennas and Propagat. Vol.36, pp.1464–1470, 1988

[7] A. E. Barrios, " Parabolic Equation Modeling in Horizontally inhomogeneous Environments", IEEE Transactions on Antennas and Propagat. Vol 40, pp.791–797, 1992

[8] L. Sevgi "Split Step Parabolic Equation Solutions in Surface Duct–to–Elevated Duct Transition", Turkish J. of Physics, Vol 19, No 3, pp. 541–551, 1995

[9] F. Akleman & L. Sevgi, "A Novel Finite–Difference Time–Domain Wave Propagator", (to appear) IEEE Transactions on Antennas and Propagation, March 2000

[10] K. S. Yee, "Numerical solution of initial boundary value problems involving Maxwell's equations" IEEE Transactions on Antennas and Propagat, V–14, no. 3, pp. 302–307, 1966

[11] J. P. Berenger, "Finite Difference Computation of VLF–LF Propagation in the Earth – Ionosphere Waveguide", Proc. Of URSI XXVI General Assembly, pp. 464,Toronto, 1999

DAYTIME OBSERVATIONS OF THE UPPER ATMOSPHERE AND IONOSPHERE USING PASSIVE AND LIDAR TECHNIQUES.

D. Rees[1,2]

[1]Hovemere Ltd., Hayes, Bromley, Kent, BR2 7LD, UK, and
[2]CASS, USU, Logan, Utah, USA,

ABSTRACT.

During the past five years, it has proved possible to make measurements of both passive airglow emissions and back–scattered signals from atmospheric Lidars during full daytime, by using efficient and practical narrow–band optical filters based on Fabry–Perot etalons. For example, we were able to obtain visible–light images of the aurora in the light of OI at λ630–nm wavelength during daytime in experiments with a prototype "Daytime Auroral Imager" at IRF, Kiruna, Sweden, in late spring 1999 (Rees et al., 2000). These experimental tests used an imaging spectrometer, based on a double–etalon Fabry–Perot interferometer, featuring excellent spectral resolution and out–of–band rejection and allowed us to obtain what we believe are the first such images obtained from the ground under near–daytime conditions. At the ALOMAR Observatory in Northern Norway (69°N, 16°E), the Rayleigh / Mie / Raman (RMR) Lidar has been equipped to make daytime measurements of stratospheric winds (Rees et al., 1998, Baumgarten et al., 1999), and of the Rayleigh back–scattered signal up to middle mesosphere altitudes (75 km) at 532 nm, 355 nm and 1064 nm wavelengths, at any local time throughout the summer period, when the sun is up to 43° above the horizon. Special highlights of this novel capability of the RMR Lidar include the ability to make three–colour observations of noctilucent clouds (NLCs) at all local times throughout the mid–summer NLC "season" (von Zahn et al., 1998, Rees et al., 2000). Both the passive, and the active, lidar measurements are extraordinarily difficult by day, due to the overwhelming background of atmospherically–scattered sunlight. The major design features of the double–etalon Fabry–Perot interferometers and other critical optical elements required to produce efficient daytime detection filter systems for the passive and lidar measurements will be presented and discussed. We believe these new techniques hold great promise for future ground–based studies. It is believed that certain auroral plasma processes may be unique to the sunlit ionosphere. These plasma processes, in addition to the morphology of the summer–time and daytime aurora, can now be explored in detail. There are also considerable possibilities that the techniques may be further developed as a method of imaging structures of the daytime ionosphere at equatorial and low latitudes, due to the relationship between NmF2 and the brightness of the OI λ630–nm emission

References:

Rees D., U. von Zahn, W. Singer, G. von Cossart, G. Nelke, K.H.Fricke, R. Ruster, W. Ericksen and N.D. Lloyd, *Observations of Winds in the Arctic Stratosphere by the ALOMAR Doppler Wind and Temperature System*, Proceedings of the 24th Annual European Meeting on Atmospheric by Optical Methods, ISBN 82–994583–0–7, p122–128, Sentraltrykkeriet, Bodo, Norway, (1998).

Hoffmann P., W. Singer, G.von Cossart, D. Rees, G. Schmidt, N.D. Lloyd, (1998), *Comparison of tropo––lower stratospheric winds obtained with the ALOMAR Sousy radar and the ALOMAR lidar Doppler wind system*, Proc. of the 8th Workshop on Technical and Scientific Aspects of MST radar, ed. by B. Edwards, STEP, pp. 266 –269.

Baumgarten G., D. Rees, and N. D. Lloyd, Observations of Arctic Stratospheric Winds by the ALOMAR Doppler Wind and Temperature System, ESA SP–xxx, yyy–zzz, (1999).

Rees D., M. Conde, A. Steen and U. Brandstrom, "Daytime Ground–Based Imaging of the Aurora", Geophys. Res. Lett., (2000).

Rees, D., U. von Zahn, G. von Cossart, K.H. Fricke, W. Eriksen and J.A McKay, "Daytime Lidar Measurements of the Stratosphere and Mesosphere at the ALOMAR Observatory", accepted Adv. Sp. Res. , Proceedings of the COSPAR Meeting, Nagoya, July 1998 (2000).

Submittal Information: 10th ASEA Invited Paper

Author: David Rees Presented by: David Rees
Hovemere Ltd., 56, Hayes St. Hayes, Bromley, Kent, BR2 7LD, UK.
walnut1@easynet.co.uk, fax 44–181–462–7841, phone 44–181–462–4921.

A high Resolution Imaging Spectrograph for Daytime Airglow Studies

SUPRIYA CHAKRABARTI, Jeffrey Baumgardner and D. Pallamraju

Center for Space Physics, Boston University, 725 Commonwealth Avenue, Boston 02215, Massachusetts, USA.

Ground based airglow studies has primarily been conducted during the night time and to a lesser extent at twilight due to the presence of extremely bright and complex background signal during sunlit hours. For a comprehensive understanding of the atmospheric photochemical and dynamical processes, local time or geomagnetic effects on these emission features at a given geographic site need to be studied. Unfortunately, most of the present measurement techniques require that the solar depression angle (SDA) be larger than about 18° which prohibits continuous observations of atmospheric phenomena in the visible and near–infrared.

While considerable progress has been made in instrumentation technology, round–the–clock observations over a geographic location similar to radars have, at best, remained sporadic. Auroral emissions have been observed on a continuous at high latitude during the winter months because the SDA is large even at local noon (See for example Lassen [1969]). In addition, under certain special conditions (such as a total solar eclipse), one can make airglow observations during the day (see Sharp et al., [1966]). However, these examples are not the same as observing faint airglow and auroral emissions when the Sun is above the horizon.

Recently, it has been shown that 6300Å oxygen dayglow emissions in the low to equatorial latitudes can be used to obtain the evolution of the Appleton anomaly over a wide latitude range from a single location (Pallamraju et al., 1996). Airglow observations from India at 16:00 h local time was used to demonstrate that they are precursors to the Equatorial Spread F (ESF) occurrence (Sridharan et al., 1994). These observations were conducted using a single–etalon Fabry–Perot interferometer and a photomultiplier in conjunction with a novel rotating mask (Sridharan et al., 1993). While this report has many Space Weather applications, these results need to be independently verified.

At Boston University we have developed a high–resolution imaging spectrograph called Hi–TIES (High Throughput Imaging Echelle Spectrograph) for the investigation of OI 6300Å dayglow to investigate the presence of ESF precursors from other longitude sectors. Hi–TIES is capable of measuring faint airglow emissions buried in the strong daytime background continuum (Chakrabarti, 1998), and it has been field–tested at Boston as well as at Sondre Stromfjord in Greenland.

Most imaging spectrographs use a two dimensional detector where the spectra are dispersed along one dimension (the dispersion direction) while, imaging information along the slit are recorded orthogonal to the dispersion direction. These measurements could benefit from high spectral resolution and large wavelength coverage. Due to the limitation of available number of pixels in detectors, it has been difficult to achieve both

these goals simultaneously. Hi–TIES has been designed to deliver high–resolution measurements for selected spectral features anywhere in the visible.

One technique for obtaining spectrographic data is to image the entire spectrum of interest (i.e. a large range of wavelengths). When point sources are imaged by a traditional echelle spectrograph using a cross–disperser, a wide wavelength range can be covered by a two–dimensional detector. However, for extended sources such as airglow or auroral emissions, it is not possible to fit a large spectral range (e.g., the entire visible spectrum) onto a single, finite size detector without compromising either the spectral resolution or the wavelength coverage. Long integration times are then required to obtain a high signal–to–noise ratio. However, this compromises the temporal resolution.

Our solution is based on the premise that most scientific studies require only data from specific spectral features, which are spaced widely within the visible range. Conventional long–slit imaging spectrographs must observe only a small portion of the entire spectral range at a given time. To observe all relevant features, these instruments must step through the entire range, which results in a loss of temporal resolution.

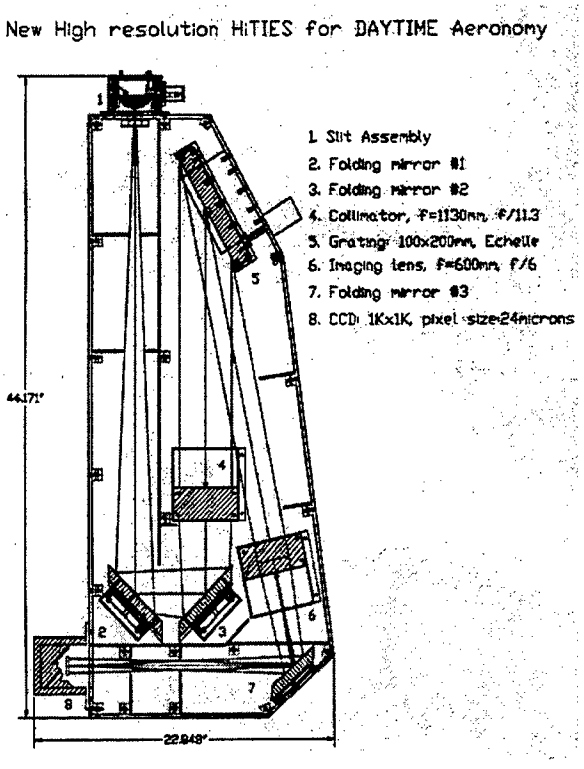


Figure 1.Schematic of the Echelle spectrograph

The Hi–TIES instrument is an echelle spectrograph with its customary cross dispersing diffraction grating replaced by an interference filter at the entrance slit. This allows only one spectral order from the echelle to be recorded. A different version of this instrument uses a mosaic of interference filters at the image plane to simultaneously record several key spectral features. A schematic of the instrument is shown in .

Hi–TIES has the ability to image several (5 to 20) user selected spectral features located anywhere in the visible spectrum (4,000 – 10,000Å), all at high dispersion (0.29Å at a wavelength of 5893Å). This resolution makes it possible to separate closely spaced features in a crowded region of the spectrum. The field of view is easily changed with a user selectable fore–optics from all–sky (180°) to a few degrees. Also, in an effort to reduce overall costs, Hi–TIES uses only off–the–shelf optical components and a single CCD detector. The entire assembly is modular so that its components (i.e. optics and grating) are easily interchangeable.

To verify the instrument performance, we first performed a ray trace computation for the instrument (). Then, we set up the spectrograph and illuminated it with a sodium lamp (). Detailed investigations have demonstrated that the two spectral lines are recorded at the same detector locations. In addition to the laboratory tests, we pointed the instrument towards the Sun. The solar spectrum recorded by the instrument is shown in .

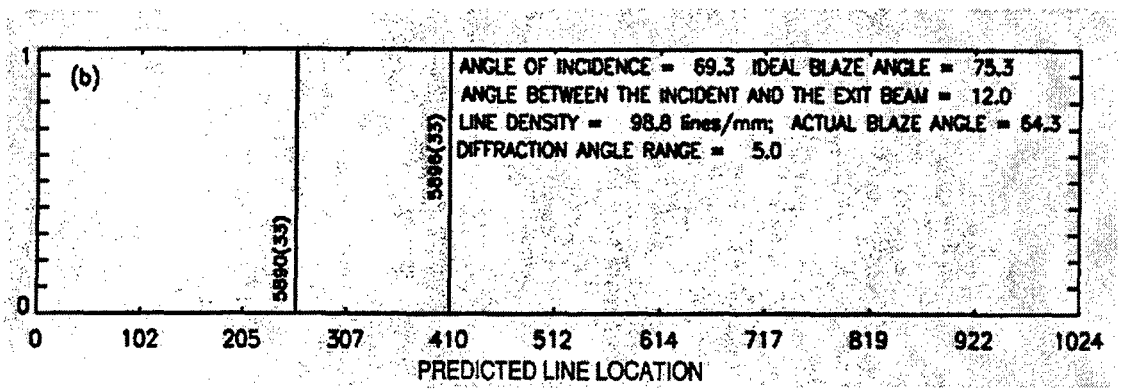


Figure 2.Ray trace calculation shows the location of the two sodium lines in detector space

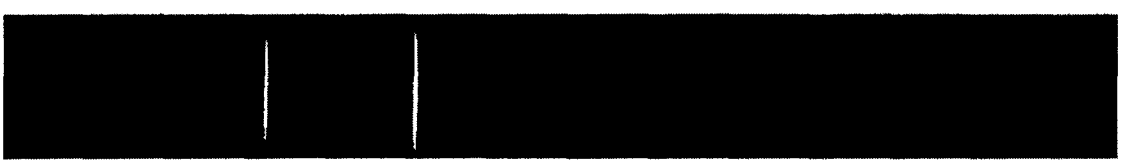


Figure 3.Emission lines from sodium as recorded by the instrument.

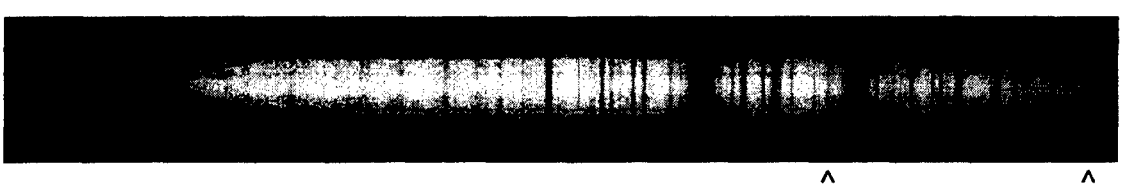


Figure 4.Solar spectrum recorded by the spectrograph. Note the locations of the sodium lines (present as absorption lines) indicated by the arrows.

In order to investigate the ability of the instrument to simultaneously observe the absorption and emission lines, we used a mirror to reflect sunlight on the instrument while it was observing the sodium lamp. The results are shown in . These data have been analyzed in detail and have demonstrated that the dispersion of the instrument is 0.004 nm/pixel. Using a 2–3–pixel slit function, the resolution of the instrument is approximately, 0.01nm.



Figure 5.Laboratory sodium doublet emissions are seen superposed on solar Fraunhofer lines.

In the presentation we will describe the instrument in detail and show airglow and auroral spectra from field observations under fully sunlit conditions.

References:

1. Chakrabarti, S., Ground–based spectroscopic studies of sunlit airglow and aurora, *J. Atmos. Solar Terr. Phys., 60,* 1403–1423, 1998.
2. Lassen, K., Polar Cap Emissions, in Atmospheric Emissions, B. McCormac and A. Ohmolt eds, Von Nostrand Reinhold Co., N.Y., pp 63, 1969.
3. Pallamraju, D., R. Sridharan, S. Gurubaran and R. Raghavarao, First results from ground–based daytime optical investigation of the development of the equatorial ionization anomaly, *Ann. Geophys., 14,* 238–245, 1996.
4. Sharp, W. E., J. Lloyd, S. Silverman, Zenith intensity and color during total solar eclipse of 20 July 1963, Appl. Opt., 5, 787, 1966.
5. Sridharan, R., R. Narayan, N. Modi and D. Pallamraju, Novel mask design for multiwavelength dayglow photometry, Appl. Opt., 32, 4178, 1993.
6. Sridharan, R., D. Pallamraju, R. Raghavarao and P. V. S. Ramarao, Precursor to equatorial spread–F in OI 630.0nm dayglow, *Geophys. Res. Lett., 21,* 2797–2800, 1994.

Simultaneous lidar and incoherent scatter radar observations of convective structures in the D- and lower E-region

M. F. Larsen
Department of Physics, Clemson University, Clemson, SC, USA

M. C. Kelley and S. Collins

School of Electrical Engineering, Cornell University, Ithaca, NY, USA

Simultaneous sodium lidar density measurements and incoherent scatter radar electron density measurements were made on approximately thirty nights at Arecibo, Puerto Rico, in support of the Coqui 2 sounding rocket campaign. The observation period covered the period from early February to the beginning of April 1998. Both the lidar and the radar provided measurements with a time resolution of a few minutes and a height resolution of a few hundred meters. The data show descending ionization layers to be a common feature of the altitude range between approximately 100 km and 85 km during the observation period. In addition, both measurements show the presence on a number of nights of structures that appear to be billows associated with shear instabilities. Chemical release sounding rocket wind measurements on two of the nights of observation show the presence of large shears within or near the top of the altitude range of interest, indicating that shear instabilities are a viable explanation for the observed structure.

LOW–LATITUDE IONOSPHERE BEHAVIOR BEFORE A FEW STRONG EARTHQUAKES

A.DEPUEVA and N. Rotanova (IZMIRAN, Troitsk Moscow Region, Russia 142092)

It is known that lithospheric phenomena of an earthquake preparation have influence on different physical processes on the Earth's surface and even at ionospheic heights. The conclusion is made that peak F–region electron density (N_m) disturbances do exist over the epicentral zone some days before the earthquake, the nocturnal effect being seen clearly [1]. As a rule, observed N_m values were increased in comparison with calculated (median or simulated) ones or those measured far from the epicenter. In the majority of available publications the ionosphere modification on the eve of earthquakes with their epicenters located at high and medium latitudes was studied. Nevertheless, some seismo–active zones are situated just at low latitudes. Here are some examples of destructive earthquakes occured over past years: 1998, magnitude M=7.1, New Guinea; 1998, M=7.1, Quito (Equador); 1999, M=8.0, Columbia.

Even in usual conditions ionospheric processes in the immediate vicinity of the magnetic equator (equatorial latitudes) and within plus and minus 20–30° of it (low–latitudes) have some specific features comparatively with those at higher latitudes. It is naturally to suppose that the responce to lithospheric processes prior to the forthcoming earthquake, if any, have to be specific as well.

The aim of the presented work is to study the equatorial and low–latitude ionosphere behavior before a several strong earthquakes.

Experimental data

Data of electron density onboard measurements of ALOUETTE–1 [2] and ISS–b [3] satellites were used. Two earthquakes were considered with their epicenters placed very close to the magnetic equator in American and East–Asian longitudinal sectors. The former of magnitude M=7.75 occurred on August 15, 1963 at 17h 25m UT, the epicenter being placed at a point with coordinates φ=–13.8°, λ=–69.3°, (I≈0°). The latter of M=5.3 occured on March 20, 1979 at 7h53m UT, the epicenter being placed at φ=7.56°, λ=126.6° (I=–0.86°). The third earthquake (M=6.88) occurred on April 13, 1963 at 2h 21m UT, the epicenter coordinates: φ=–6.3°, λ=–76.7°, (I≈+11°) have been also analysed. Hereinafter it will be named low–latitude earthquake contrary to above–mentioned equatorial ones.

In fig. 1a the average picture of F–layer critical frequencies (foF2) spatial distribution for the former event is presented based on the data collected during 20 satellite passes since July 31 till August 14. LT of measurements used was from 16h 27m to 18h 27m. Over the earthquake epicenter and within ≈10° (1000 km) from it a sufficiently deep (in average to ≈5.5 MHz, but for separate satellite passes down to 4.5 MHz) foF2 fall in comparison with the ambient background level of 8÷10 MHz is clearly seen. For the latter equatorial event the similar picture for 18–21 h LT was constructed, the zonal trough dimension being somewhat lesser, ≈500 km.

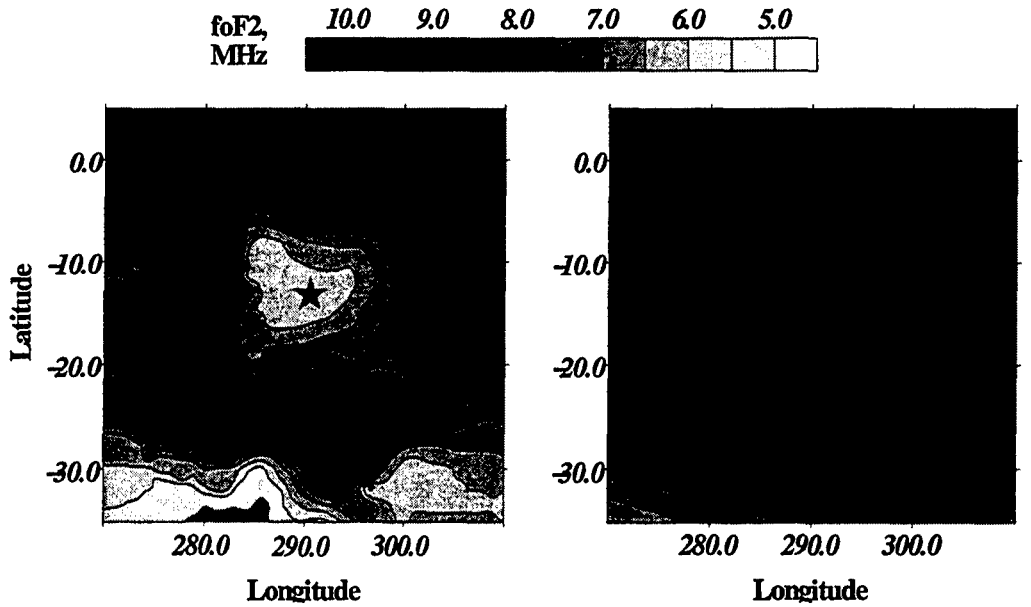


Fig.1

For the low–latitude event foF2 distribution represents a fall as well but the least values of frequencies are registered not exactly over the epicenter, as it is in fig.1a, but are biased a little in a South – West direction towards the magnetic equator. For a map construction data of 13 satellite passes, from April 2 till April 13, LT interval from 21h 01m up to 22h 26m were used.

Spectral analysis of foF2(I) variations for each satellite orbit was made. Normalized spectral density was calculated by Blackman–Tukey method [4]. Electron density inhomogeneities occurrence of 300–500 km dimension along a meridian seems a characteristic feature of ionosphere before equatorial and low–latitude earthquakes. They became more evident as closer both in time to an earthquake commencement or in distance to epicenter location. It is known that such kind of ionospheric irregularities have to lead to oblique traces, kinks, etc. on vertical sounding ionograms. These peculiarities were really observed experimentally.

Above we have considered the foF2 parameter describing electron concentration at F2 peak height level. From the analysis of N(h)–profiles calculated on the base of topside ionograms we have detected that the disturbance looking like electron density depletion envelopes even to upper heights. In fig. 2 equal electron density variations against geographic latitude are presented beginning from the main peak up to 600 km. Solid triangles designates the latitude of the epicenter position. The top panel (a) is constructed according to data obtained on August 8, the satellite being moved along the orbit displaced relatively to the epicenter by 10° to the West, 5 days before the earthquake commencement. The bottom panel (b) reflects situation of August 14, on the eve of the event, the orbit being placed immediately over the epicenter. Increased equatorial anomaly degree is clearly seen from F–layer peak up to ≈500 km. So, the modification of the ionosphere (at least, topside ionosphere) before an earthquake can be imagined as a funnel located either exactly over the epicenter or displaced by some distance from it.

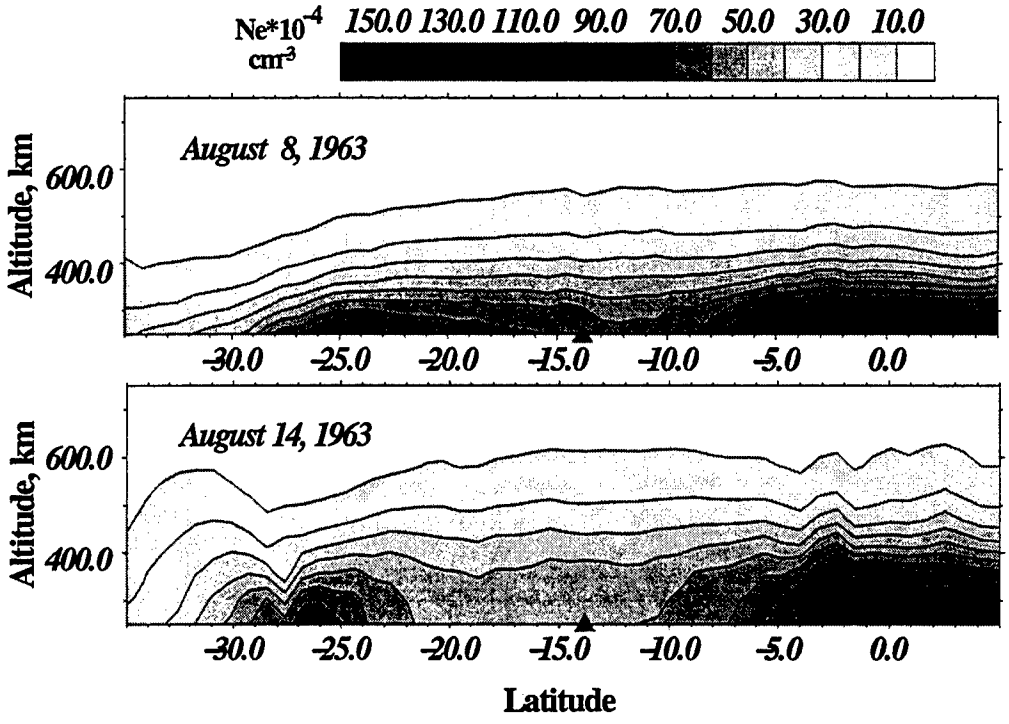


Fig. 2

Data analysis

As shown in previous section, 10–15 days before every of considered earthquakes over the area of their preparation specific modification of the foF2 spatial distribution was observed. It seems that we really observe the response of the ionosphere at F–layer peak level and somewhat higher on lithospheric processes on the eve of earthquakes as a sharp reduction of electron density. As a matter of fact the assumed seismo–ionospheric effect is exhibited as a strengthening of the equatorial anomaly of the ionosphere inside a limited space over the epicenter. Whether this fact is really a consequence of earthquake preparation processes in the Earth's lithosphere is not obvious, nevertheless in our opinion there are some arguments in favor of the affirmative answer.

1. For definite LT the disturbed area is restricted in E–W direction (see fig. 2a) whereas the picture have to be similar at all longitudes. In order to compare measured and expected foF2 spatial distributions in fig. 2b the simulated one is presented for the same conditions calculated according to CCIR model [5].
2. The effect becames more clear as approaching in time to the earthquake commencement and in space to its epicenter.
3. Before the forthcoming earthquakes the measured equatorial anomaly was far better displayed than the simulated one.

Discussion

As far as authors know the problem of ionosphere modification before equatorial earthquakes was not considered yet in the literature. As to low–latitude earthquakes,

they were mentioned in [6]. The N_m fall displaced from the epicenter towards the magnetic equator some days before the event was also observed.
The above information does not claim for a sufficient completeness but indicates an existence of a number of specific features of the equatorial and low–latitude ionosphere before some strong eartquakes. Further investigation will show whether they are essential regional properties of the ionosphere behavior during earthquake preparation processes.

Nevertheless, even at the given stage it is possible to offer a version of our result interpretation based on the supposition of electromagnetic coupling in «lithosphere–ionosphere» system taking into account a conventional model of Appleton equatorial anomaly formation. Let us suppose that electric field generated due to lithospheric processes at the magnetic equator penetrates up to E–layer height. Eastward zonal component of such a field and geomagnetic field will cause plasma upward ExB–drift. Consequently, it have to lead to the same phenomena as there were observed experimentally. The similar approach will also be valid for the low–latitude earthquake if we assume that electric field of lithospheric origin is generated not only over the epicenter, but also in the whole area of earthquake preparation. If it is really so, the zonal dimension of the seismoionospheric disturbance will be determined by earthquake magnitude (M) since the radius of preparation zone can approximately be presented as $R \approx \exp M$, the meridional dimension being determined by the assumed electric field value. The problem of transformation of lithospheric disturbance up to ionospheric dynamo–region stayes in the meantime unsolved.

Conclusions

1. Topside ionosphere vertical sounding data processing have shown that equatorial and low–latitude ionosphere behavior some days before forthcoming earthquakes have the specific feature of equatorial anomaly strenthening in a limited longitudinal sector near the epicenter. There are some reasons to suppose that the effect is connected to seismic events.
2. The possible approach to the interpretation of the observed phenomenon is offered within the framework of the supposition of the availability of electromagnetic interaction between lithosphere and ionosphere.

References

1. Liperovsky, V.A., O.A.Pokhotelov, S.L.Shalimov. Ionospheric forerunners of earthquakes. M.: Nauka. 1992. 304 p. (in rus.).
2. Alouette 1 ionospheric data ALOSYN. 1–15 April 1963, 1–15 August 1963. Ottawa, Canada.
3. Summary plots of ionospheric parameters obtained from Ionospperic Sounder Satellite b. Radio Res. Lab. Ministry of Post and Telecommunications. Japan. 1983. V. 3. 316 p.
4. Jenkins, G.M. and D.G.Watts. Spectral analysis and its applications. San Francisco: Holden–day. 1969. 316 p.

5. International Radio Consultative Committee (CCIR). CCIR Atlas of ionospheric characteristics, Rep.340–4, Int. Telecommun. Union. Geneva, 1967.
6. Pulinets, S.A. Strong earthquake prediction possibility with the help of topside sounding from satellites // Adv. Space Res. 1998. V.21. N3. P. 455–458.

Comparison of Ionosphere TEC above the Turkey during Solar Eclipse action and before two Strong Earthquakes at 1999.

Oraevsky V.N., RUZHIN Yu.Ya., I.I.Shagimuratov
IZMIRAN, Troitsk-town, Moscow region, 142190 RUSSIA
E-mail:ruzhin@izmiran.rssi.ru

1.INTRODUCTION

For today the space plasma precursors are known as electromagnetic disturbance [1,2] and as ionosphere plasma density structure [3-5] of different spatial and time scale behaviour. Possibility to use such anomalies for earthquake prediction is discussed more than 15 years (see [6] and reference therein). But up to now the main problem is limited experimental data due to complex space plasma images which varies in dependence of local time and very sensitive to geographic position [7,8]. Thus the sequence of the two Turkish earthquake of 1999 (August 17 and November 12) with magnitude more than 7.0 which occur practically at the same localisation (only 100km difference) could be as rare object of intensive investigation by involving all possible experimental data of classic seismomonitoring as well as some kind of atmosphere and ionosphere available data. Here we start to present some ionosphere or space plasma anomalies which appear as specific variation of total electron content (TEC) above the epicentre area on the eve of destructive earthquakes. This data is result of analyses of GPS data base of global net [9,10].

2.EXPERIMENTAL CONDITION.

Seismotectonic Summary

For the Turkish Earthquake of Aug. 17, 1999 (see later as EQ1) the initial preliminary magnitude, of 7.8, was based on recordings of seismic waves from a limited number of global stations that rapidly transmit data to the U.S. Geological Survey's National Earthquake Information Centre (NEIC) in Golden, Colo. The Izmit earthquake occurred at 00:01:39.80 UT (3:01 a.m. local time), and was centred at 40.702 N., 29.987 E., which places the epicentre about 11 kilometres Southeast of the city of Izmit. This location indicates that the earthquake occurred on the northernmost strand of the North Anatolian fault system. The earthquake originated at a depth of 17 kilometres and caused right-lateral strike-slip movement on the fault. Preliminary field reports confirm this type of motion on the fault, and initial field observations indicate that the earthquake produced at least 60 kilometres of surface rupture and right-lateral offsets as large as 2.7 meters. Rupture from west to east, in two rupture events. Duration of strong shaking 37 seconds; maximum fault displacement 5 meters. The 900 km-long North Anatolian fault has many characteristics [11] similar to California's San Andreas fault. These two faults are right-lateral, strike-slip faults having similar lengths and similar long-term rates of movement.

The second earthquake (EQ2) with magnitude of 7.5 occurred at November 12,1999 (16:57:19 UT) on the short distance (less of 100km) from EQ1 epicentre and was centred at 40.8N, 31.2E.

Ionosphere pre-earthquake disturbances in TEC around Ankara

As introduction of disposition geometry on FIG.1 the map of events for earthquake of 12th November (EQ2) is presented with foreshocks and aftershocks. The EQ1 of 17th august appears without foreshocks. The positions of base station Ankara of GPS ground net and epicentre of EQ1 are marked also. Let's note that more important information is received from GPS/Glonass satellites which tracks of subinosphere points are around the epicentres of both EQ. The all horizontal tracks of such satellites which intersect the epicentre area for EQ1 are shown on FIG.1 with corresponding the satellite number (GPS-3,GPS-14,GPS-15 and GPS-30). This orbit tracks are responsible for day time period when the anomalies of 'min' type (see Fig.2) or pre_earthquake plasma trough appear less than one day before the EQ1.

GPS NAVSTAR [9] is complete today and the Russian system GLONASS is nearly too. GPS consists of 24 satellites with 12-hour orbits at altitudes of 20000 km, having orbital inclinations about 55°.The number of satellites simultaneously seen in any point of the earth and in any moment of a time is more than 6, so GPS provides superior sky coverage (that enables realisation of continuous ionosphere monitoring in several space sectors simultaneously).The GPS-receiver makes measurements [12]of group delay of a signal on P- and CA-codes and phase bearing on L1 (1.575 GHz) and L2 (1.227 GHz). The system GPS permits to measure not only phase, but also group delay of signals, propagated through ionosphere. Opportunity to measure the group delay and therefore to conduct measurements of the absolute electron contents (along a ray of sounding radiowave) eliminates a problem [12] of unknown initial phase always existing for phase measurements of TRANSIT type satellite system (frequency 150/ 400 MHz).

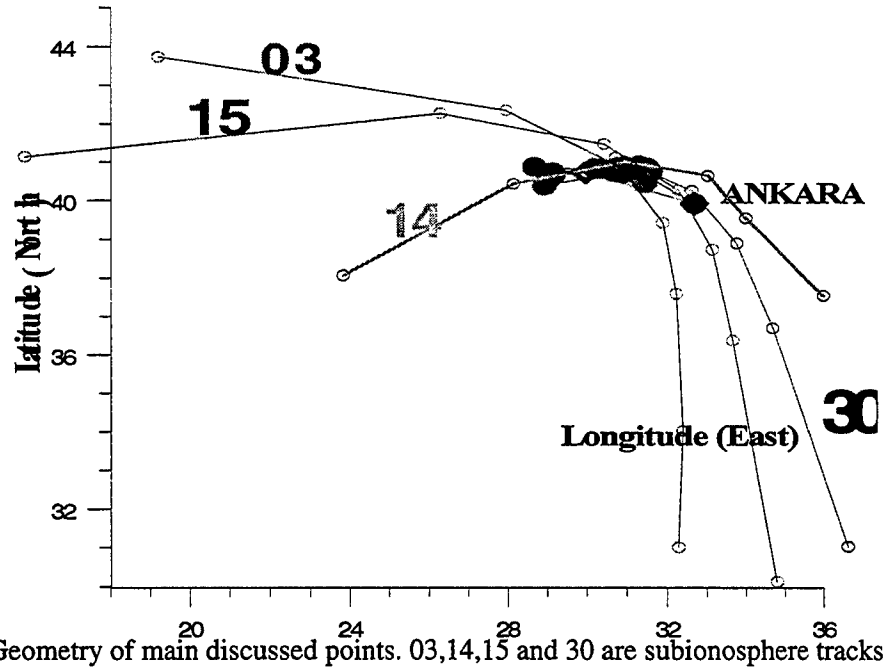


Fig.1. Geometry of main discussed points. 03,14,15 and 30 are subionosphere tracks of GPS satellites.

On Fig.2. the sequence of two plots of DTEC=TEC_{corr}- TEC_{med} over Ankara area are derived from GPS/ISG data station measurement during the ionosphere perturbation on August and November (at hours midnight- midnight UT). DTEC is measured in units of $10E16m^{-2}$ or TECU. Here TEC_{corr} is corrected value of TEC and TEC_{med} is monthly median for Ankara station of GPS measurements.

We can surely see the specifical positive-negative (or "max-min" structure) variations DTEC on eve the both earthquakes which can be as precursors of these EQs. The positive part of preseismic TEC variation as well as following negative bay begin to develop at sunrise time and are the day (sunlit time) events (see Fig.3a also). This is obvious difference of TEC precursor anomalies from preseismic plasma density or f_0F2 variations which is usually nocturnal one [3,4,5]. It is possible to characterise the ionisation of the F2-layer with a single parameters by the so-called critical frequency (maximal plasma frequency f_0F2) which is connected with the maximal electron density N_{max} that $(f_0F2)^2 = 80.6*N_{max.}$ So the main parameters of the ionosphere F2 layer displays the precursor type plasma anomalies by different ways.

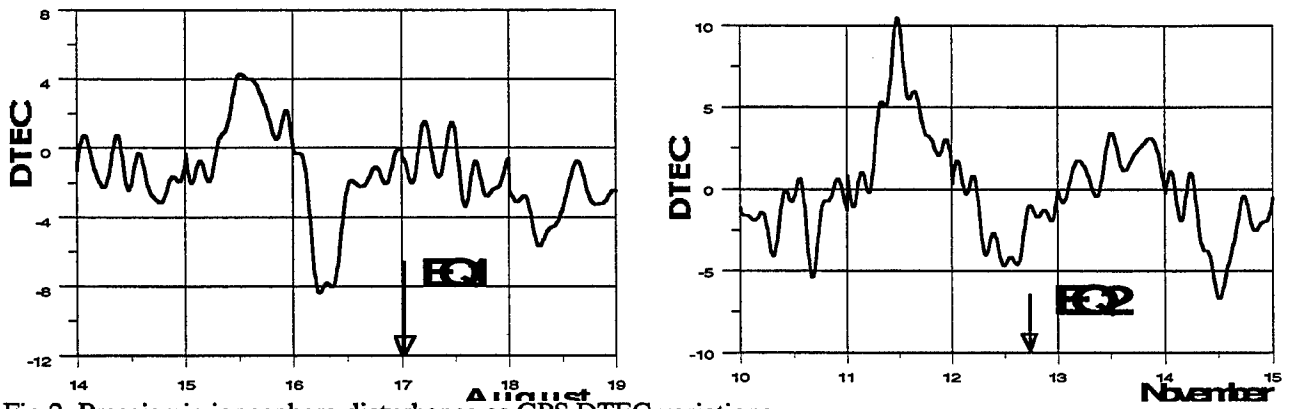


Fig.2. Preseismic ionosphere disturbance as GPS DTEC variations.

During time of EQ1 preparation appear the possibility to observe in TEC of Ankara the action of Moon shadow on earth ionosphere (August 11,1999) as known source of ionosphere ionisation. The min part of pre-EQ variations are shown in comparison with similar negative DTEC bay due to Solar eclipse action on Fig.3 for both earthquake. The deep plasma trough (a few TECU) in GPS derived DTEC data is observed which is caused by Moon shadow action on ionosphere above the Turkey area of future EQs. It is good chance to compare these TEC data for estimation of the effectivity of EQs as source of ionosphere disturbances.

DISCUSSION

The plasma anomalous structures at the ionosphere (N_{max} or maximal plasma frequency f_0F2) as

preseismic changes of the electrical parameters of the spherical condenser (capacitor) formed by the two high conductive shells: Earth's surface and lowest ionosphere boundary [3,5]. Such variations of the atmosphere electricity cause appropriate electric field at the ionospheric heights, which being added to existing natural field may both increase or decrease its action [8] on the ionospheric plasma characteristics: drifts, aeronomy, plasma chemistry, ion composition etc.

Anomalous variations appear inside whole ionosphere volume from the lowest boundary of Earth's plasma shell (80-100 km) up to 1000km and higher. Under fortunate coincidence precursor electric field can generate natural phenomena, 'fountain- effect' for example [5] leading to Appleton anomaly in the equatorial ionosphere over future earthquake position. The precursor horizontal size at ionosphere can reach value determined by a future earthquake magnitude[3,5]. Both preparation zone form in the lithosphere and natural processes in the ionosphere depended on [8] the epicentre latitude, observational place, time, season and/or gelio-geophysical activity can influence on the concentricity and final dimension of plasma anomaly in horizontal plane.

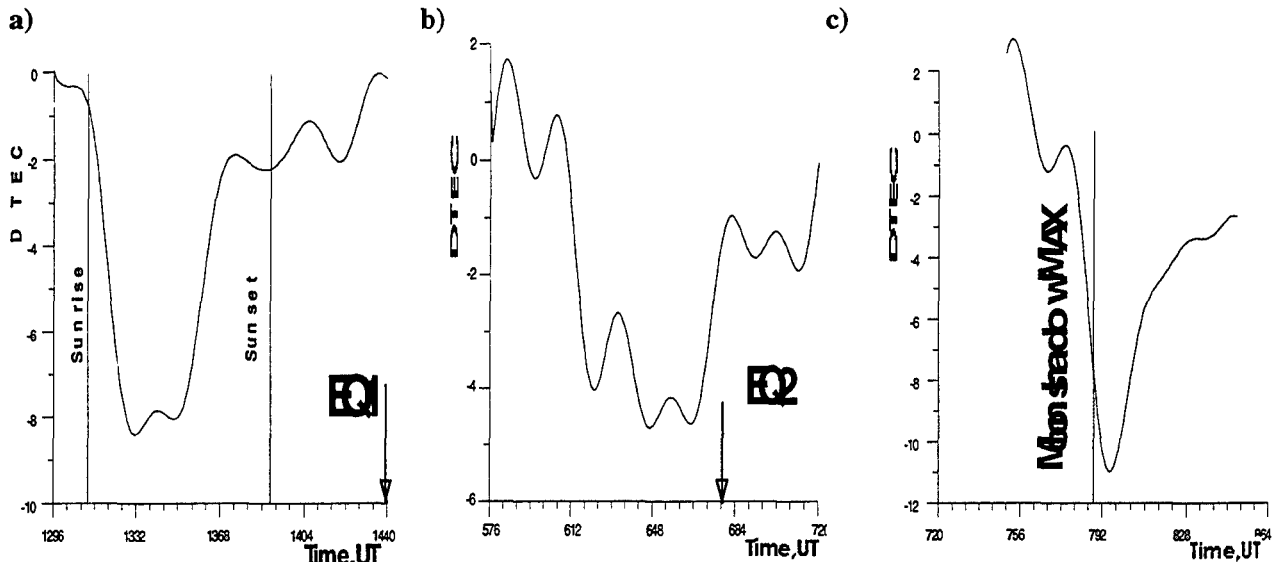


Fig.3. The three plots presents negative bays (or "min" of precursor structure) in DTEC for the EQ1-EQ2 and Solar eclipse effect in ionosphere above the Ankara. The time duration (horizontal axes) is one day or 24hrs (from midnight to midnight, Greenwich time)

The other way to characterise the ionisation of the F2-layer with a single parameters is to use the vertical total electron content (TEC) [13] which correspond to the integral of electron density over the height from the bottom to upper boundary or transmitting satellite orbit . As base of TEC measurements the radio-beacon on board of satellites have played an important role [13] in the study of the temporal and spatial structure of the ionosphere over nearly three decades. Maximum electron density and TEC are connected over equivalent slab thickness τ: $TEC= N_{max}*\tau$. Because the variability of the equivalent slab thickness is much smaller than that of TEC or that of the maximal electron density the long-term behaviour of TEC and N_{max} and also TEC and f_0F2 is often similar.

But in case of pre-earthquake anomalies it is a quiet different. The DTECU variations before the EQ (see Fig.2) occurs as combination or consequence of positive-negative variations. So it is necessary separately to examine the dependence of $TEC= N_{max}*\tau$ during such ionosphere disturbances with maximum attention. The physical mechanism of the pre_EQ TEC behaviour is not yet fully understood. Obviously that it is physically related to the lithosphere area which ivolved in preseismic activity. Since the EQ TEC is characterised by the world wide deepest ionisation level (a few TECU) it provides a good check for the quality of GPS derived TEC data. It is evident [10] that the GPS/IGS data cannot reach the spatial resolution of NNSS observations. However, the pre-EQ TEC is also well reflected in the GPS/IGS data. So its occurrence and movement may be studied by GPS techniques.

CONCLUSION

Precursors type of ionosphere total electron content anomalies for two destructive earthquakes in Turkey (at 1999) is analysed on base of TEC of GPS net.. We found the ionosphere anomalies which well pronounced one two days before the two well known Turkey earthquakes of 1999 with magnitude more than

ionosphere plasma TEC anomalies are very similar in form and dynamic. In comparison we use the TEC anomaly which is result of Sun shadowing of ionosphere by Moon in this region some days before the first destructive Turkey earthquake of 17th August of 1999. It is supported by existed in IZMIRAN classification of space plasma anomalies which appear to be as the seismoprecursors for existed system to improve the forecast of imminent earthquakes. It is proposed that the space plasma TEC anomalies could be as precursors for earthquake prediction

REFFERENCES.

1. **Larkina V.I., Migulin V.V., Nalivaiko A.V.** et al. *Observation onboard the "Intercosmos 19" satellite of VLF emissions associated with seismic activity //* Geomagn. i Aeronom. 1983. V.23, N 5. P. 842-845
2. **M.Parrot, J.Achache, J.J.Berthelier, E.Blanc, A.Deschammps, F.Lefeuvre, M.Menvielle,** et al *High-frequency seismo-electromagnetic effects,* Phys. Earth Planet. Inter., 77, 65-83, 1993
3. **Oraevsky V.N., Yu.Ya. Ruzhin, A.Kh.Depueva,** *Seismoionospheric Precursors and Atmospheric Electricity,* Tr. J.of Physics, **18.** _11. p.1229-1234, 1994
4. **Pulinets S.A., Legen'ka A.D., Alekseev V.A.** *Pre-earthquakes ionospheric effects and their possible mechanisms,* In Dusty and Dirty Plasmas, Noise and Chaos in Space and in the Laboratory: New-York: Plenum Publishing, pp.. 545-557,1994..
5. **Ruzhin Yu.Ya., Depueva A.K.**, *Seismoprecursors in space as plasma and wave anomalies*, Journal of Atmospheric Electricity, vol.16, no.3, pp.271-288. 1996
6. *Electromagnetic Phenomena Related to Earthquake Prediction,* ed.**M.Haiakawa and Y.Fujinawa**, TERRAPUB,Tokyo, pp.159-174, 1994
7. **Ruzhin Yu.Ya., V.I.Larkina, and A.Kh.Depueva** *Earthquake precursors in magnetically conjugated ionosphere regions.* Adv. Space Res.Vol.21, No.3, pp. 525-528, 1998
8. **Ruzhin Y.Y., A. Depueva**, *Regional (Local) Manifestation of Seismoprecursor Space Anomalies* Proceed.14th Wroclaw EMC Symposium (URSI) , pp.. 582-585, 1998
9. **Calais E.,and J.B.Minster**, *GPS detection of ionospheric perturbations following the January,17,1994,Northridge earthquake*, Geoph.Res.Lett.,22.1045-1048,1995
10. http://**www.grdl.noaa.gov**/cgi-bin/tecmap.p
11. **Ross S. Stein , Aykut A. Barka and James H. Dieterich** *Progressive failure on the North Anatolian fault since 1939 by earthquake stress triggering.* Geophysic. Journ. International, VOL 128, pp. 594-604, 1997
12. **Ruzhin Yu.Ya., Shagimuratov I.I., Kunitsyn V.E.,** et al. *GPS -based tomographic reconstraction of the ionosphere.* Adv.Space Res., 21, No.3, pp.521-524, 1998
13. **Evans J.V.** *Satellite Beacon Contribution to Studies of the Structures of the Ionosphere.* Rew.Geoph.&Space Phys. Vol.15, No.3, p p.325-349, 1977

Illuminating the Physics of the Upper Atmosphere
With Optical Emissions Excited by High Power HF Pump Waves

P.A. Bernhardt[1], F.T. Djuth[2], C.A. Tepley[3], M.P. Sulzer[3], V. Frolov[4], L.M. Kagan[4], M.C. Kelley[5], Francisco Garcia[5], J.A. Gardner[6], A.L. Broadfoot[7]

[1]Plasma Physics Division, Naval Research Laboratory, Washington, DC 20375
[2]Geospace Research Corporation, El Segundo, CA 90245
[3]Arecibo Observatory, Arecibo, PR 00613
[4]Radiophysical Research Institute, N. Novgorod 603600, Russia
[5]Dept. of Electrical Engineering, Cornell University, Ithaca, NY 14853
[6]Air Force Research Laboratory, VSBI, Hanscom AFB, MA 01731
[7]University of Arizona, Lunar and Planetary laboratory, Tucson, AZ 85721

Optical emissions excited by high power radio waves in the ionosphere can be used to measure a wide variety of parameters in the thermosphere. Powerful high frequency (HF) radio waves produce energetic electrons in the region where the waves reflect in the E– region, Intermediate Layers, or the F–region. These hot or suprathermal electrons collide with atomic oxygen atoms to produce localized regions of metastable $O(^1D)$ and $O(^1S)$ atoms as well as N_2 First Postive. The metastables subsequently radiate 630.0 and 557.7 nm, respectively, to produce clouds of HF Pumped Artificial Airglow (HPAA). Figure 1 illustrates the geometry for the observations in the F–region.

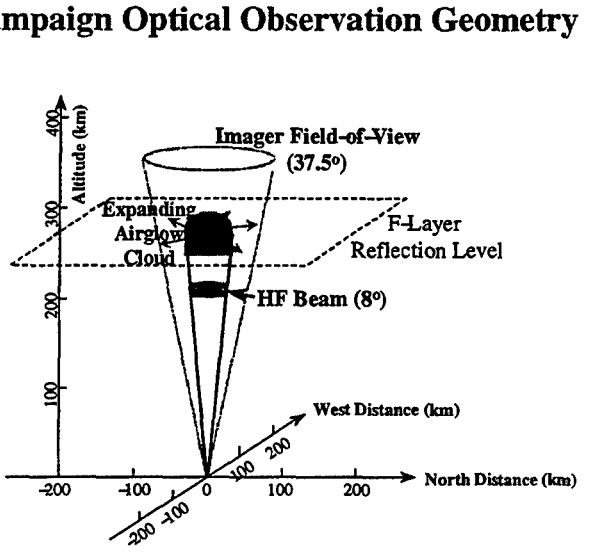


Figure 1. Observation geometry for artificial optical emissions recorded near high power radio wave facilities in SURA, Russia; and Arecibo, Puerto Rico.

Measurements of the artificial optical emissions have been reported from Platteville, Colorado [Haslet and Megill, 1974; Moore, 1983], Moskow, Russia [Adieshvili et al., 1978], Tromso, Norway [Sergienko et al., 1983; Bransdtrom et al, 1999], Arecibo, Puerto Rico [Bernhardt, et al., 1988a; Bernhardt, et al., 1988b; Bernhardt et al., 1989a, Bernhardt et al., 1989b] and from SURA, Russia [Bernhardt et al., 1991; Bernhardt et al., 2000].

Observations of the artificial airglow emissions yield information about both the structure and motion of the natural environment. In the F–region, the shapes of the HPAA clouds are determined by the structure of large–scale(> 1 km) plasma irregularities that occur naturally or that develop during ionospheric heating. When the HF wave is operated continuously, the motion of the airglow clouds follows the ExB drift of the plasma. When the HF wave is turned off, the airglow clouds decay by collisional quenching and radiation, expand by neutral diffusion, and drift in response to neutral winds. Images of HPAA clouds, obtained using both continuous and stepped radio wave transmissions, are processed to yield the electric fields, neutral wind vectors, and diffusion coefficients in the upper atmosphere. This technique is illustrated using data that were obtained in March of 1993 and 1995 at the ionospheric modification facility near Nizhny Novgorod, Russia. Analysis of HPAA clouds yields zonal plasma drifts of 70 m/s eastward at night. Based on artificial airglow from energetic electrons generated at 260 km, the zonal neutral wind speed was estimated to be 96 m/s and the $O(^1D)$ diffusion coefficient was determined to be between 0.8 and 1.4 $x10^{11}$ cm^2/s. The quenched lifetime of the $O(^1D)$ was determined to be 29.4 seconds. The diffusion and quenching rates are directly related to the atomic and molecular concentrations in the thermosphere.

Two–dimensional images of Intermediate Layers near 120 km altitude have been produced using a new technique which makes them glow when being stimulated by high power radio waves. Normally sporadic–E layers to not radiate visible emissions. Experiments on January 1998 at Arecibo Observatory in Puerto Rico have shown that the layers can be made to glow at 557.7 nm and other wavelengths by illuminating them with radio waves at 3.175 MHz with effective radiated powers of 80 megawatts. The regions of the sporadic–E layers that have electron densities greater than the critical density for reflection of the radio waves emit electrons that collide with and excite atmospheric atomic oxygen and molecular nitrogen. A charge–coupled–device (CCD) imager located on the ground is used to capture images of the glowing E–region structures. The camera exposure times were in the range of 15 to 45 seconds. The images obtained using this technique show a wide variety of structures in the sporadic–E layers. Some layers cover the 15 x 30 km region illuminated by the radio wave beam. Other layers show strong modulation of the E–region by electrodynamic instabilities or by gravity waves. Finally, other layer structures show random features that drift across the illuminated region. Consecutive images using this technique can provide (1) measurements of the lifetime of the individual Intermediate Layer patches, (2) the zonal and meridional components of the drift velocities at 120 km altitude, and (3) the temporal evolution of the spatial features. Future research should use this technique for studies of sporadic–E and Intermediate Layer structures along with complementary radar techniques of incoherent and coherent backscatter. The HPAA technique yields a large area description of the Intermediate Layer structures and the radars provide the altitudes and densities of the layers along the radar lines of sight.

Improvements in HPAA remote sensing technique may be obtained if the intensities of the artificial airglow emissions are increased. High power radio transmissions employing pulse sequences and tuning near electron cyclotron harmonics were attempted to increase the optical emissions. Both of these, however, produced reduced intensity and, consequently, continuous transmission at frequencies away from electron gyro harmonics is the preferred heating regime. Future experiments at the HF facilities Puerto Rico, Russia, Alaska, and Norway will pursue similar techniques to increase the optical intensities for use in remote sensing of the thermosphere.

References

Adieshvili, T.B. et al., Ionospheric emission caused by an intense radio wave, **Sov. J. Plasma Phys.**, **4**, 721, 1978.

Bernhardt, P.A., L.M. Duncan, and C.A. Tepley, "Artificial Airglow Excited by High–Power Radio Waves," **Science**, Volume 242, pp 1022–1027, 18 November 1988a.

Bernhardt, P.A., L.M. Duncan, C.A. Tepley, R.A. Behnke, and J.P. Sheerin, "Spatial and temporal evolution of 630.0 nm airglow enhancements during ionospheric heating experiments," **Advances in Space Research**, **8**, 271, 1988b.

Bernhardt, P. A., L. M. Duncan, and C. A. Tepley, "Heater–induced cavities as optical tracers of plasma drifts", **J. Geophys. Res.**, **94**, 7003–7010, 1989a.

Bernhardt, P. A., C. A. Tepley, and L. M. Duncan, "Airglow enhancements associated with plasma cavities formed during ionospheric heating experiments", **J. Geophys. Res.**, 94, 9071–9092, 1989b.

Bernhardt, P.A., W.A. Scales, S.M. Grach, A.N. Karashtin, D.S. Kotik, S.V. Polyakov, Excitation of artificial airglow by high power radio waves from the "SURA" ionospheric heating facility, **Geophys. Res. Lett.**, **18**, 1477–1480, 1991.

Bernhardt, P.A. Bernhardt, M. Wong, J.D. Huba, B.G. Fejer, L.S. Wagner, J.A. Goldstein, C.A. Selcher, Optical remote sensing of the thermosphere with HF pumped artificial airglow (HPAA), **J. Geophys. Res.**, in press, 2000.

Brändström, B. U. E., T. B. Leyser, Å. Steen, M. T. Rietveld, B. Gustavsson, T. Aso and M. Ejiri, Unambiguous evidence of HF pump–enhanced airglow at auroral latitudes, **Geophys. Res. Lett., 26**, 3561–3564, 1999.

Haslet, J.C. and L.R. Megill, A model of the enhance airglow excited by RF radiation, **Radio Science, 9**, 1005–1019, 1974

Henriksen, K., W. Stoffregen, B. Lybekk, and A. Steen, Photometer and Spectrometer seach of the oxygen green and redlines during artificial ionospheric heating in the auroral zone, **Annales Geophysicae, 2**, 73–76, 1984.

Moore, J.G., Airglow morphology during an inoospheric heating experiment at Platteville, Colorado, **AFGL Environ. Res. Paper No. 852**, AFTL–TR–83–0238, 1983.

Sergienko, T., I. Kornilov, E. Belova, T. Turunen, and J. Mannin, Optical effects in the aurora caused by ionospheric HF heating, **J. Atm. Solar–Terr. Phys., 59**, 2401–2407, 1997.

Sipler, D.P. and M.A. Biondi, Measurements of $O(^1D)$ quenching rates in the F–region, **J. Geophys. Res., 77**, 6202–6212, 1972

Ionospheric radiotomography by means of stochastic inversion

T. NYGREN (Department of Physical Sciences, University of Oulu, Finland), M. Lehtinen (Sodankylä Geophysical Observatory, Sodankylä, Finland), M. Markkanen (Sodankylä Geophysical Observatory, Sodankylä, Finland) and E. D. Tereshchenko (Polar Geophysical Institute, Murmansk, Russia)

We consider a chain of difference Doppler receivers on the ground level, each of them observing the phase difference of coherent radio waves at two frequencies, which are transmitted by a satellite flying above the chain (Fig. 1). The phase difference is

$$\delta\Phi \propto \int N ds + C, \tag{1}$$

where N is the electron density, C is an unknown phase constant and the integration is carried out along a ray from the satellite to the receiver. When a satellite flies above the chain and observations are made by each receiver, the integral will be determined along a great number of rays crossing each other at ionospheric heights.

The vertical plane above the receiver chain is divided into an annular grid, and the unknowns are electron densities at the grid points. Bilinear interpolation of electron density within each grid element makes the measured phase values into linear combinations of the unknown electron densities and phase constants. Collecting all measurements into a single column vector $\mathbf{m}$ and all unknowns, including the phase constants, into a column vector $\mathbf{x}$ leads to the direct theory

$$\mathbf{m} = \mathbf{A_m} \cdot \mathbf{x} + \boldsymbol{\varepsilon}_\mathbf{m}, \tag{2}$$

where $\mathbf{A_m}$ is a matrix of the linear coefficients and $\boldsymbol{\varepsilon}_\mathbf{m}$ is a column vector containing the measurement errors.

The numerical inversion of this equation is unstable and therefore a regularization method is needed. The instability is established as too strong point-to-point variations in the inversion results, which can be eliminated in the following manner. Let us consider two neighbouring grid points g_i and g_j lying either at the same altitude or straight above each other. If we assume that the difference of the electron

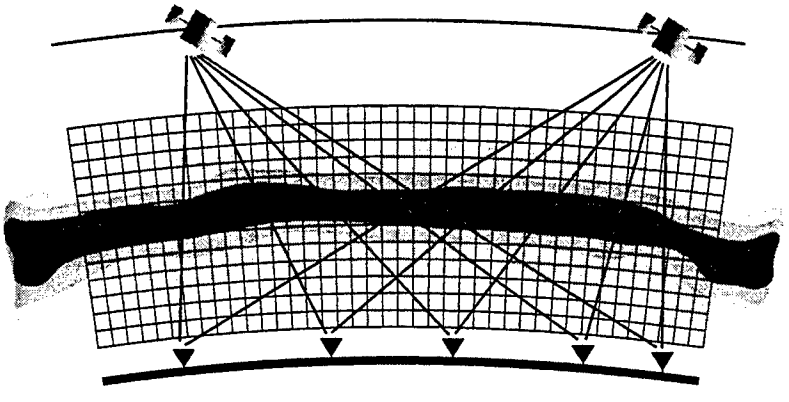


Figure 1:

densities at these points is zero, we make some error $\varepsilon_r^{(ij)}$. This can be written as

$$0 = x_i - x_j + \varepsilon_r^{(ij)}. \tag{3}$$

When this is carried out for all horizontal and vertical differences of neighboring grid points, the resulting equations make a single matrix equation

$$\mathbf{0} = \mathbf{A_r} \cdot \mathbf{x} + \boldsymbol{\varepsilon}_\mathbf{r}. \tag{4}$$

Here $\mathbf{A_r}$ is a matrix with elements $+1$, -1, and 0 in appropriate places so that each component of eq. (4) is of the form (3). Eqs. (2) and (4) can now be combined to give the direct theory of the regularized problem as a single matrix equation

$$\begin{pmatrix} \mathbf{m} \\ \mathbf{0} \end{pmatrix} = \begin{pmatrix} \mathbf{A_m} \\ \mathbf{A_r} \end{pmatrix} \cdot \mathbf{x} + \begin{pmatrix} \boldsymbol{\varepsilon}_\mathbf{m} \\ \boldsymbol{\varepsilon}_\mathbf{r} \end{pmatrix}. \tag{5}$$

In general, the purpose of stochastic inversion is to find the posterior probability density of the unknowns when their prior density and the probability density of the measurement errors are known. Priori information on the unknowns can obviously be implemented in $\boldsymbol{\varepsilon}_\mathbf{r}$ and therefore its probability density can be used as the prior density. Assuming that the measurement errors and the components of $\boldsymbol{\varepsilon}_\mathbf{r}$ are Gaussian random variables with zero mean, the posterior density is also Gaussian with a center point

$$\hat{\mathbf{x}}_\mathbf{0} = (\mathbf{A_m}^T \cdot \boldsymbol{\Sigma}_\mathbf{m}^{-1} \cdot \mathbf{A_m} + \mathbf{A_r}^T \cdot \boldsymbol{\Sigma}_\mathbf{r}^{-1} \cdot \mathbf{A_r})^{-1} \cdot \mathbf{A_m}^T \cdot \boldsymbol{\Sigma}_\mathbf{m}^{-1} \cdot \mathbf{m}, \tag{6}$$

where $\boldsymbol{\Sigma}_\mathbf{m} = < \boldsymbol{\varepsilon}_\mathbf{m} \cdot \boldsymbol{\varepsilon}_\mathbf{m}^T >$ and $\boldsymbol{\Sigma}_\mathbf{r} = < \boldsymbol{\varepsilon}_\mathbf{r} \cdot \boldsymbol{\varepsilon}_\mathbf{r}^T >$ are the covariance matrices of $\boldsymbol{\varepsilon}_\mathbf{m}$ and $\boldsymbol{\varepsilon}_\mathbf{r}$, respectively, and T indicates transpose. This center point gives the most probable solution of the inversion problem.

Contrary to the various iterative methods used in ionospheric tomography, the present one gives the result by means of a single inversion. Its second characteristic feature is that it does not have any separate procedure for the determination of the phase constants; they are just components of the unknown vector and are determined simultaneously with the unknown electron densities. Finally, it offers a controlled way of giving prior information on the electron density to the solver. At heights were small electron densities are expected, their point-to-point variations are also small and therefore small prior variances can be given to the solver. Correspondingly, within regions where the electron density is probably high, great point-to-point variations may occur so that the prior variances should also be great. In this manner the inversion result can be guided to a layer with a reasonable thickness and peak height. One should, however, notice that the prior variances by no means fix the layer thickness or peak height although they do affect the result. Also, if seriously erroneous variances are used, the results will contain clearly recognizable artefacts.

We have carried out tomographic measurements in three campaigns arranged in Scandinavia in 1993, 1995 and 1997. Four or five receivers have been used and signals from Russian navigational satellites have been observed. The sites lie approximately along the same magnetic meridian and the satellites fly at an altitude of 1000 km closely parallel to the chain. The tomographic package used in the analysis is based of a fast general-purpose linear inversion problem solver (GULIPS), originally designed for incoherent scatter analysis.

In the daytime, regular horizontal layers are usually observed. Especially in the morning sector, travelling ionospheric disturbances due to atmospheric gravity waves are often visible. In the afternoon the F layer gets weaker and a trough first appears in the north, proceeding southwards during the evening. In the morning an enhanced F region again penetrates northwards to the field of view following the rising sun and filling the trough.

During periods of high geomagnetic activity this quiet-time picture is strongly disturbed, but even in quiet or moderate geomagnetic conditions the evening-time and night-time F region often shows irregular behaviour. As examples of such cases, reconstructions of electron densities from phase curves obtained during two satellite passes are shown in Figs. 2 and 3. The inversion grid is indicated by the tic marks on the top and the right hand side of the panels and the receiver sites are shown as dots on the ground level. Both examples are from late November representing winter-time ionosphere over Scandinavia within the afternoon sector. Fig. 2 shows a large plasma cloud around 59°–63° geomagnetic latitude. A strong F layer is visible to the north of this region, but in the south the electron density is weaker. A similar plasma blob is often observed nearly in the same place over the receiver chain. Sometimes both the northern and the southern edges of the F region trough are visible and the blob lies in the middle of the trough, clearly separated from the edges.

Fig. 3 portrays an even more structured ionosphere with great variations both in the peak height and the maximum electron density. A large plasma cloud resembling to that in Fig. 2 is observed also here but, in addition, a tilted plasma enhancement covering a narrow latitude range and reaching high altitudes is visible to the north of it. This plasma finger points in the direction of the local geomagnetic field. Recordings from the IMAGE magnetometer chain suggest that this finger is associated with upward field-aligned current.

It is a well known fact that satellite tomography observations contain only little information on the layer altitude and vertical electron density profile, and therefore

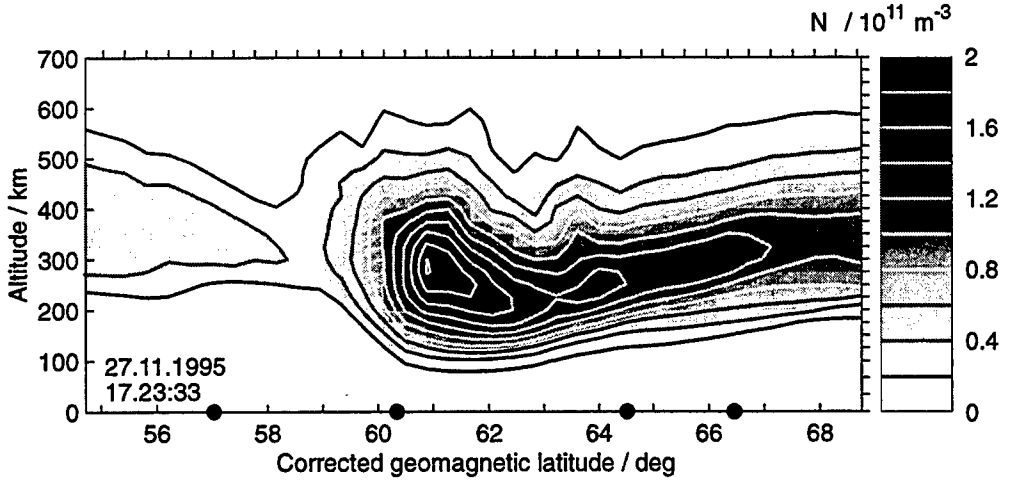


Figure 2:

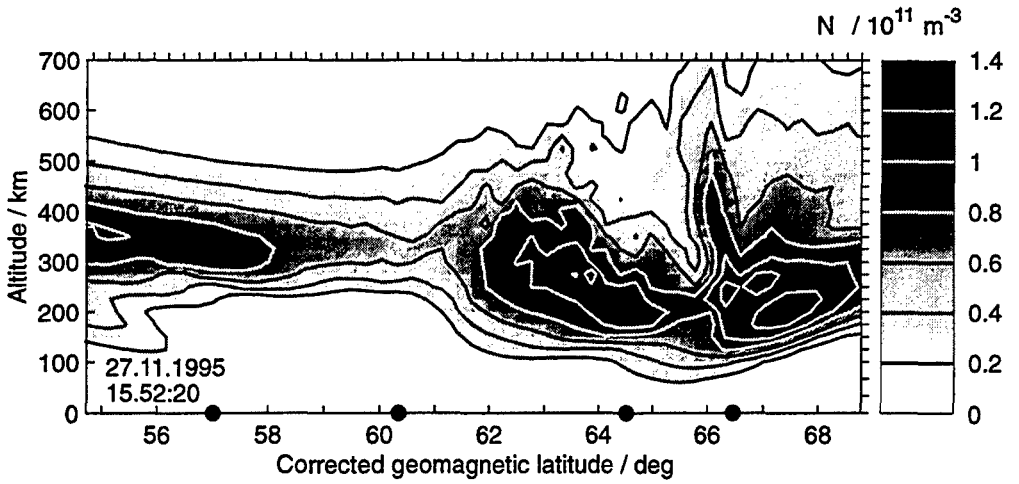


Figure 3:

some prior information is needed in the inversion. This can be fed to the solver either implicitly in terms of the start profile and the stop criteria as various iterative methods do, or explicitly e.g. in the way we do by giving the regularization variances.

We have carried out a routine tomographic analysis where the whole data set is processed several times with different height profiles of the regularization variance. Somewhat different results are obtained in each case. The reconstructions in Figs. 2 and 3 are obtained using a Chapman function as a regularization profile, with peak and scale heights of 300 km and 125 km, respectively. The broad regularization profile allows great variations in the layer height, which is well demonstrated in Figs. 2 and 3. On the other hand, it also results into a broad layer; in the shown examples the layers are most likely somewhat too broad. A more careful choice of the regularization profile might improve the results, but this would involve more laborious judgement from case to case.

In conclusion, the satellite tomographic method is not able to give unambiguous results, but they always depend on some additional information which can be based e.g. on models or other measurements. Therefore supporting instruments like ionosondes or incoherent scatter radars are valuable in estimating or improving the results. The benefit of satellite tomography is, however, that it is able to give a picture of structures within a large ionospheric region in a manner no other method can. Although the height profile or the peak height is not necessarily quite exact, the structures shown by the results are still true. Therefore the method is most valuable in ionospheric research as long as the user is aware of its limitations.

Tomographic Studies of Aeronomic Phenomena Using Radio and UV Techniques

F. KAMALABADI[1], G. Bust[2], K. Dymond[3], S. Gonzalez[4], P. Bernhardt[5], S. Chakrabarti[1], D. Cotton[1], A. Stephan[1], R. McCoy[6], S. Budzien[3], and S. Thonnard[3]

[1] Center for Space Physics, Boston University, Boston, MA 02215
[2] Applied Research Laboratories, UT Austin, Austin, TX 78758
[3] Code 7623, NRL, Washington, DC 20375
[4] Arecibo Observatory, NAIC, Arecibo, PR 00612
[5] Code 6794, NRL, Washington, DC 20375
[6] Code 321SR, ONR, Arlington, VA 22230

Tomographic characterization of ionospheric and thermospheric structures using integrated line-of-sight measurements provides a unifying paradigm for the investigation of various aeronomic phenomena. In radio tomography, measurements of the total electron content (TEC) obtained using a chain of ground receivers and a transit satellite are inverted to reconstruct a two-dimensional electron density profile. Similarly, prominent optically thin UV emissions, such as 911Å and 1356Å produced by radiative recombination of O^+, provide the means to obtain nighttime F-region electron densities from space-based spectroscopic measurements. The inherent non-ideal acquisition geometry of such remote sensing observations, however, results in limited-angle tomographic inverse problems that are both ill-posed and ill-conditioned. Furthermore, the intrinsic presence of noise, especially in the case of UV measurements, imposes severe challenges on conventional reconstruction methods. To overcome these limitations, we approach the solution of these inverse problems from a stochastic regularization standpoint. In particular, we apply regularization by incorporating appropriate edge-preserving regularizing functionals that enforce piecewise smoothness of the solution. Additionally, we present the corresponding statistical interpretation of this class of solutions in the context of Bayesian estimation. We demonstrate the performance of these techniques by analyzing both TEC and UV data. The TEC data were obtained from three receivers set up in the Caribbean by the Applied Research Laboratories. The receivers record the differences in phase between VHF and UHF radio transmissions from the TRANSIT satellite and the NRL CERTO beacon on the ARGOS satellite. TEC, with an accuracy of 0.1 percent, is proportional to the differential phase. The UV data were obtained from space-borne spectrograph measurements as part of the NRL HIRAAS experiment on-board ARGOS. These data are inverted tomographically to obtain altitude profiles and latitude gradients of ionospheric electron densities. These in turn are validated using the corresponding Arecibo incoherent scatter radar scans. Finally, we discuss unresolved scientific questions in equatorial aeronomy that can potentially be addressed by this class of techniques.

Incoherent backscatter radar measurements at Jicamarca with a beam pointed perpendicular to

Erhan Kudeki

University of Illinois at Urbana-Champaign, USA

Ronald F. Woodman

Jicamarca Radio Observatory, Lima, Peru

Abstract. Doppler spectra of 50 MHz F-region incoherent backscattered signals detected at Jicamarca will be presented. The measurements were conducted with the Jicamarca radar beams pointed perpendicular to the ambient magnetic field $\vec{B}$. Consequently, the Doppler spectra contain a sharp cusplike feature centered about the bulk $\vec{E} \times \vec{B}$ velocity of the ionospheric plasma [*Kudeki et al.* 1999]. The overall shape of the spectrum about the mean Doppler velocity represents a beam weighted superposition of incoherent scatter spectra corresponding to small magnetic aspect angles. Incoherent scatter theory based models for the measured spectra indicate that the spectral width is regulated by the electron temperature T_e. However, unless electron Coulomb collisions are included in the model, unrealistically low T_e estimates are obtained via model fitting of the measured spectra. The collisions broaden the incoherent scatter spectra at very small magnetic aspect angles (due to cross-field diffusion), but reduce the spectral width at larger aspect angles by reducing the rate of parallel diffusion as pointed out first by *Sulzer and Gonzales* [1999]. Spectral width reduction due to electron collisions is particularly important in measurements made close to perpendicularity to the ambient magnetic field. As a consequence, estimation of T_e from incoherent scatter spectra measured at small magnetic aspect angles requires the knowledge of electron collision frequency and plasma density profiles in F-region.

Recent multi-receiver (north-south antenna separation) and dual-polarization (O- and X-mode) F-region incoherent scatter measurements conducted at Jicamarca will be presented. The north-south and O-X cross-spectra of the backscattered signals provide additional information about the ionospheric plasma. Differential phase information extracted from O-X cross-spectra provides estimates of the absolute electron density profiles near the F-region peak. The normalized magnitude of the north-south cross-spectra (coherence) is sensitive to T_e/T_i. Therefore, joint inversions of the incoherent scatter self- and cross-spectra holds the potential for the estimation of all the state parameters describing the F-region plasma at low-latitudes.

References

Kudeki, E., S. Bhattacharyya, and R. F. Woodman, *J. Geophys. Res.*, *107*, 1999.

Sulzer, M. P., and S. A. Gonzales, The effect of electron coulomb collisions on the incoherent scatter spectrum in the f region at jicamarca, *J. Geophys. Res.*, *104A*, 22,535, 1999.

E. Kudeki, Department of Electrical and Computer Engineering, University of Illinois, 1308 W. Main St., Urbana, IL 61801.

R. F. Woodman, Jicamarca Radio Observatory, Lima, Peru

The Effect of Electron Coulomb Collisions on the Jicamarca Incoherent Scatter Spectrum: Review of Theory and Comparisons with Experimental Data

MICHAEL P. SULZER, Arecibo Observatory, Arecibo, PR 00612 USA
Sixto A. González, Arecibo Observatory, Arecibo, PR 00612 USA

February 15, 2000

Sulzer and González [JGR, 104A. 22,535, Oct 1999 recently described the effect of electron Coulomb collisions on the incoherent backscatter spectrum looking nearly perpendicular to the magnetic field. This paper attributes problems with modeling the width of the Jicamarca incoherent scatter spectrum as well as the electron and ion temperatures derived from it to the effects of these collisions. The fact that the effects electron Coulomb collisions need to be included is now generally accepted. However, the detailed predictions are not yet fully verified with comparisons with data. In particular, they predict a relatively slow reduction of the collisional effect as the the aspect angle moves further from perpendicular, as the electron density decreases, and as the electron temperature increases. These results, which are unexpected from experience with the predictions of simpler collisional models such as Brownian motion (Langevin's equation) and the BGK approximation, have been questioned.

The variations with these parameters are the result of the specific characteristics of Coulomb collisions, in particular the variation of the magnitudes of the diffusion coefficients with electron speed, the fact that electron-ion collisions modify the momentum strongly without significantly affecting the energy, and the fact that the electron-electron collisions affect the energy relatively slowly. We present a comparison between an analytic calculation for Brownian motion and a numerical calculation for Coulomb collisions, showing how the surprising parameter variation comes about.

In order to facilitate comparisons between data and the model, we have made a library of simulation results computed using several months of computer time. This library consists of spectra of J_e computed on a grid of input parameter values. Interpolation of these spectra gives J_e for any parameter values. The computation of an incoherent scatter spectrum proceeds by the normal analytic means except for J_e which uses these interpolated library values. This hybrid technique keeps the size of the library small since J_e does not depend upon any of the ion parameters. Figure 1 shows a block diagram of the method used to put the simulation results in a form suitable for the library.

One of the most important problems with the Jicamarca data is that T_e/T_i is too low when the beam is in the on-axis position, which is about 2° from perpendicular to the field. Data from recently and about ten years ago show apparent values of T_e/T_i of about .75 under conditions when unity is expected. One way to check the accuracy of the collisional model is to see what values of T_e/T_i would result if it is assumed correct, but analysis ignores the collisional effect. Figure 2 shows three acfs; two have no collisional effect, but different values of T_e/T_i, 1 and .765. The third one has $T_e/T_i = 1$ and includes the effects of Coulomb collisions as predicted by the simulations. This last one and the one with $T_e/T_i = .765$ are nearly identical. This shows that if the collisional effects are as we predict, then one would expect to measure the apparent values of T_e/T_i that are actually seen. Simple collisional models such as BGK would predict T_e/T_i of about .95.

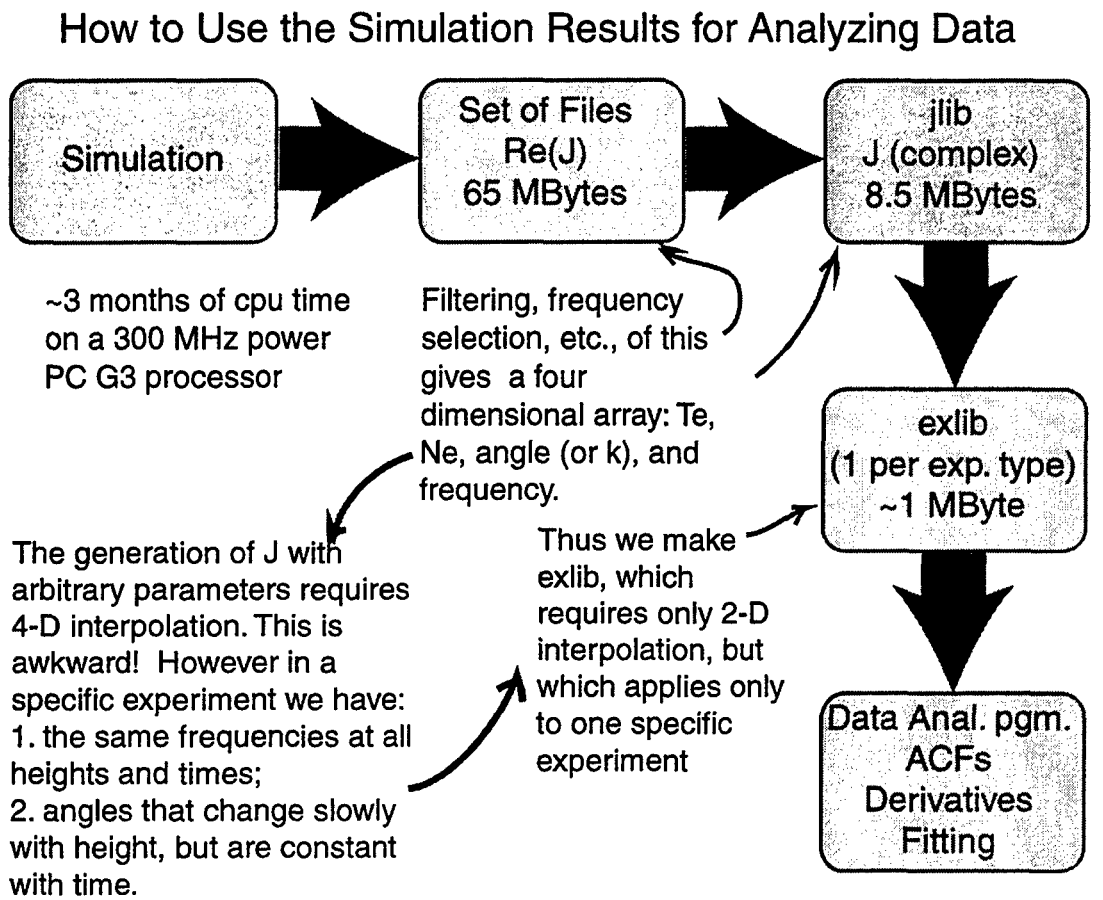


Figure 1: Block diagram for the construction of the library for making J_e

We have recently taken data at Jicamarca which also support the predictions of our model. Figure 3 shows acfs over an altitude range of almost 300 km. The plots contain the data, the model with Coulomb collisions, and a model without Coulombs with $T_e = T_i$. Two of the comparisons are magnified to make them easier to see, but it is clear that there is agreement at all heights within the limitations due to noise.

We conclude the following:

1. Coulomb collisions have an important effect on the Jicamarca incoherent backscatter spectrum in the on-axis position (near 2°) from perpendicular. The effect is not a minor one and cannot be ignored at any height where good data are obtainable.

2. The predictions of Sulzer and González [JGR, 104A. 22,535, Oct 1999] appear to be correct. The on-axis position used in the comparisons shows a strong enough effect for it to be seen easily, and the effect is clearly different enough from predictions of other collisional models so that there is no question that those predictions are incorrect.

3. Analysis of old Jicamarca data taken in the on-axis position should proceed using our model spectra.

4. Since we predict that the effect is small but still significant at angles further from perpendicular, our

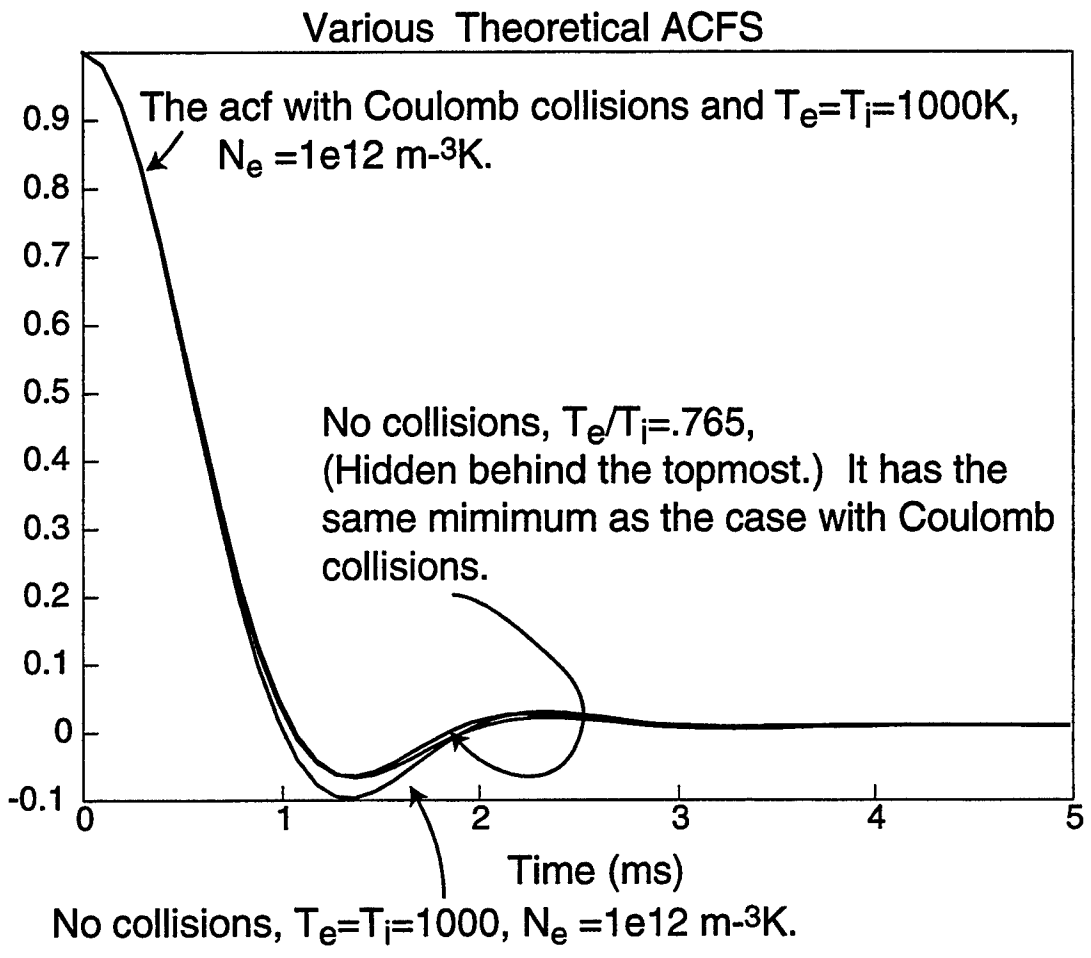


Figure 2: ACFs for no collisions with temperature ratios of 1 and .765 and Coulomb collisions with temperature ratio 1.

model should be used for analyzing data taken at the so-called 4.5° position, especially if any He^+ is present since He^+ and $T_e/T_i < 1$ produce very similar effects in the spectrum.

5. It is difficult to verify our model completely in the so-called 4.5° 6° positions. We have found no disagreement, however. Jicamarca data taken with these beam positions is not as good as on-axis data, as others have also found. Therefore we believe that Jicamarca should resume taking data in the on-axis position as standard practice as was done until a few years ago since the correct model for computing the spectra is now available.

6. Comparisons with data taken at positions closer to perpendicular should proceed, although these comparisons are not as important as the on-axis position since the different models disagree by less when the collisional effect is strong.

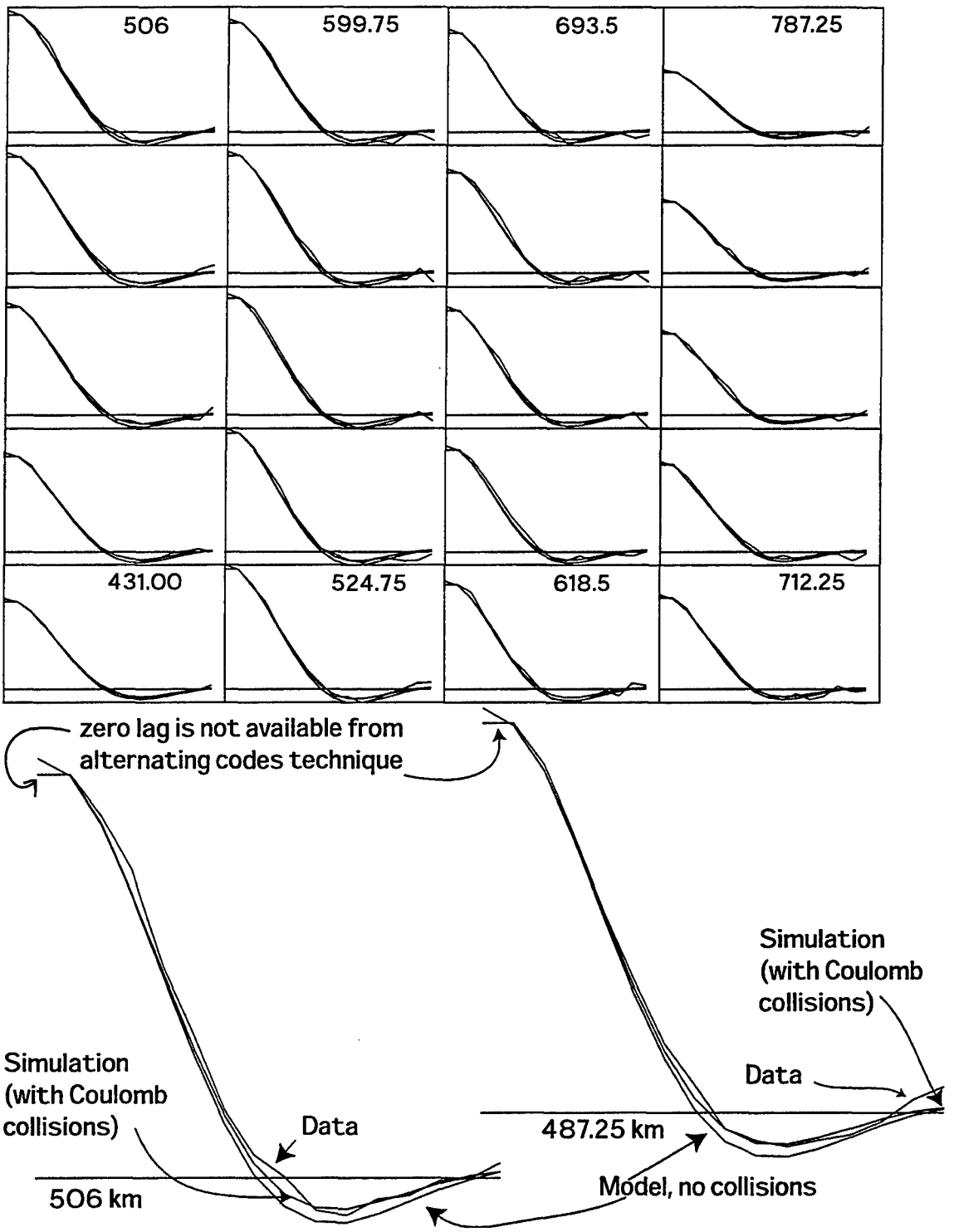


Figure 3: Data taken on November 8, 1999 at Jicamarca and model acfs using reasonable temperatures

Split-beam Studies of the Effect of Electron Collisions on ISR Spectra Near k ⊥ B

D. T. FARLEY, W. E. Swartz (both at School of Electrical Engineering, Cornell University, Ithaca, NY), J. L. Chau and R. F. Woodman (both at Jicamarca Radio Observatory, Lima, Peru)

Sulzer and Gonzales [October 1999 JGR] first pointed out that electron collisions will affect the spectrum and auto-correlation function (ACF) of incoherent scatter echoes when the beam is pointed very nearly perpendicular to the magnetic field, and that furthermore this effect, if neglected, will cause the Te/Ti ratio to be underestimated. There are various theoretical models of this effect, in particular the relatively simple BGK and Fokker-Planck models and the much more complicated numerical simulations of Sulzer and Gonzales. The Sulzer and Gonzales simulations predict larger effects than do the simpler models.

In an effort to test these models, we divided the Jicamarca radar into two beams, each with half the power and half the antenna of the full system, and ran the standard double pulse Faraday/ACF mode that gives ACFs in the F region. With split beams each beam has only one quarter of the signal-to-noise ratio of the full system, but it allows us to measure at two different aspect angles simultaneously. We have made comparisons between three pointing directions, which at an altitude of 400 km differ from normal to **B** by 4.8°, 3.4°, and 2.0°. (We compared 4.8 with 3.4 degrees and then with 2.0 degrees.) These angles all vary slightly with altitude and are significantly smaller than they were when Jicamarca was built because of the slow change in the geomagnetic field. (These beam positions once were called the 6, 4.5, and 3 degree (on axis) positions.)

The goals of the experiment were to determine (1) which collisional model (if any) best matched the data, (2) what collisional corrections, if any, are needed at the 3.4° position (the "standard" pointing direction for many ISR observations now), and (3) what corrections we might apply in a reanalysis of old ACF data taken at Jicamarca. These temperature and density data extend back more than a solar cycle into the middle 1980s and were mostly taken with the beam in the on-axis position (which was then at more like 3°).

Since we are close to solar maximum, the electron densities are now high at Jicamarca, which should enhance the effect of collisions. However, perhaps surprisingly, the high densities make it difficult to obtain high quality ACF data in the F region using the standard double-pulse technique except in a relatively limited range of altitudes. Electrojet clutter is serious at low F region altitudes and Faraday dispersion is a problem above 400 km or so in the daytime, and the situation is not much better at night. Nevertheless we obtained some usable data a few days before the abstract deadline.

We also operated for one afternoon using the alternating code mode, also with a split beam (comparing 4.8 and 2.0 degrees). In this experiment we alternated between the two beams every 15 minutes, using the full 50 MHz transmitter for one circular polarization on one beam only, and so the sensitivity of the measurement was reduced by only a factor of 2 instead of 4.

The relatively crude analysis of the data that we have been able to do so far shows no clear evidence of any collisional effects at either 3.4° or 2.0°, even during midday with electron densities somewhat above 10^{12} m^{-3} and electron temperatures between 1000 and 1500K. More specifically, our preliminary analysis has not shown any electron temperature differences between the 4.8° data and the 2.0° data that are larger than the scatter in the temperature values. However, these statements are very tentative at the time of writing. It is a bit surprising that we have seen no clear evidence of collisions even at the 2.0° position. We need to do a more thorough analysis in order to reach solid conclusions regarding the collisions. We hope to be able to report the results of this analysis at the Symposium.

Incoherent Scatter Measurements of Aurora-Like Ion Beam Distributions and Ionospheric Holes Produced by the Space Shuttle Flying over the Radars at Jicamarca, Kwajalein, and Arecibo

P.A. Bernhardt (Plasma Physics Division, Naval Research Laboratory, Washington, DC 20375)
M.P. Sulzer (Arecibo Observatory, Arecibo, PR 00613)
E. Kudeki (Electric and Computer Engineering, UIUC, Urbana IL 61801)
R.F. Woodman (Jicamarca Radio Observatory, Jicamarca, Peru)
R. Tsonuda (SRII, Menlo Park, CA 94025)

In October 1997 and July 1999 during the STS-86 and STS-93 flights of the Space Shuttle, the crew performed experiments with controlled ion injections over the incoherent scatter radar (ISR) facilities located at Arecibo, Puerto Rico; Jicamarca, Peru; and Kwajalein, Marshall Islands. Ion beams were formed by charge exchange in the ionosphere of the high velocity neutral molecules exhausted by the Orbital Maneuver Subsystem (OMS) engines on the Space Shuttle. Pick-up ions were produced with energies between 2 and 10 eV depending on the orientation of the OMS engines relative to the vehicle orbit. The ions eventually recombined with electrons yielding electron density depressions or holes.

On the STS-93 Mission, the first ISR spectra were measured by reflection from electrons in the presence of the high-speed ions. The non-equilibrium ion distributions produced atypical ion-line spectra. Bernhardt et al. [1998] predicted these spectra. Numerical fitting procedures were used to extract the ion beam parameters from the measured ISR spectra. The analysis shows relaxation from ring-beam distribution to a thermal distribution in the period of 30 seconds. The analysis of the spectra also indicates that collisional heating by the ion beams yields elevated temperatures in the background ions leading to enhanced radar echoes. Beam driven instabilities involving ions in the OMS plume may produce turbulence that yields enhanced radar backscatter. This region of enhanced turbulence was postulated by Bernhardt et al. [1995] but has not been observed in the radar data for the 2eV ion beam injections over Arecibo and Jicamarca. The 10 eV beam injections over Kwajalein may show the effects from irregularities produced by beam driven instabilities. These observations open up the possibility of conducting a new series of ion-beam instability and heating experiments using the Space Shuttle OMS engines as plasma beam generators.

One the STS-86 Mission, the Jicamarca ISR recorded the reduction in density on a modified magnetic flux tube. The refilling process occurred much more rapidly than can be duplicated with ambipolar diffusion along magnetic field lines. An electron density depression was produced at 359-km altitude on the mid-point of a magnetic field line. The experiment was scheduled when there were no zonal drifts of the plasma so the modified field-line remained fixed over the 50 MHz, Jicamarca radar. The density depression was filled in by plasma flowing along the magnetic field line with a time constant of 4.5 minutes. The density perturbation has completely vanished 20 minutes after the engine burn. The experimental measurements were compared with a model of field-aligned transport by ambipolar diffusion. The recovery time was computed to be much longer than observed. The theory of ambipolar diffusion currently used in ionospheric models is inadequate to describe these observations. Several possible sources for this discrepancy including (1) ion and electron inertia, (2) cross-field diffusion, and (3) convection of the modified plasma out of the radar beam. At this stage, no explanation has been found for the rapid refilling of the ionospheric hole.

Reaction of Equatorial Ionosphere on Forthcoming Earthquake.

RUZHIN Yu.Ya., Oraevsky V.N., and Anna Depueva
IZMIRAN, Troitsk-town, Moscow region, 142190 RUSSIA
E-mail:ruzhin@izmiran.rssi.ru

INTRODUCTION

Earthquake preparation processes in lithosphere manifest themselves not only on the Earth's surface, but also in the ionosphere, and the whole complex of various physical phenomena in near Earth environment are observable (Larkina et al.,1983; Liperovsky et al.,1992; Oraevsky et al.,1994; Ruzhin and Depueva,1996). Amongst them we have to take in mind ionospheric plasma density reaction. Particularly, in the majority of recent publications electron density at 300 -1000 km enhancement over the preparation zone of the future earthquake 1-3 days before the event is emphasized. This effect is observable at night hours and assumed as one of the seismoionospheric precursors. Changes depict not only in regular ionospheric structure but also in the irregular one.
Based on the quantitative characteristics of seismionospheric precursors and their comparison with atmospheric potential disturbances parameters and preparing zone dimension on the earth's surface it was concluded (Ruzhin and Depueva, 1994) that the anomaly of the atmospheric electric fields created by the lithosphere processes (including possible modification of atmospheric electricity redistribution due to the radioactive or/and aerosol emanations) before earthquakes may be the reason for the generation of seismo-ionospheric disturbances as space earthquake precursors even in magnetically conjugate region (Ruzhin and Larkina,1996)
The difference in earthquake preparation processes manifestation at ionospheric heights can be caused by unsimilar physical processes in low and higher latitudes. In our opinion the electric field (generated by lithosphere pre_earthquake processes in atmosphere) penetrates up to ionosphere and plays an important role anywhere. So, we have now some reasons to believe that earthquake epicenter location play an important role as to differences in electron density modification over the preparation zone or VLF anomalies observation.

PLASMA STRUCTURE OF EQUTORIAL IONOSPHERE AND LOCAL POSITION OF EPICENTER

Numerous evidences of increasing electron concentration over the epicenter some days before the future earthquake have been published in recent years (Liperovsky et al.,1992; Depuev and Zelenova, 1996). Consecutive two days before the day of earthquake F -and E- layers critical frequencies over the epicentral region increase by 1-1,5 MHz. It means that F-layer penetration frequencies (foF2) measured both by bottomside and topside ionosondes before the earthquake are greater:

- in comparison with (foF2) measured outside the preparation zone,
- in comparison with median value of (foF2) at the same location.

Nevertheless, when analyzing the ALOUETTE1 ionosphere data, we came across with the phenomenon opposite to usually observed: (foF2) values before earthquakes were less than after them, less than (foF2) measured outside the preparation zone boundary, and comparatively to median values. Example of sush situation is presented on Fig.1. In our mind the absence of correspondence between our results and usual point of view is not random. Here we have analyzed ALOUETTE topside ionospheric data

obtained some days before and during equatorial earthquake with magnitude of M=6.9 on April 13, 1963 with an epicenter 600 km to N-W of Huancayo, Peru

It is proposed (Depueva and Ruzhin, 1995) that the generation of anomalous eastward electric field at the epicenter of future earthquake together with Earth's magnetic field at ionospheric level may cause the upward vertical ionospheric plasma drift over the epicentral zone. This procesess is similar to natural one which is driven by a solar radiation and is known as 'fountain effect' or equatorial Appleton ionosphere anomaly (Appleton , 1946).

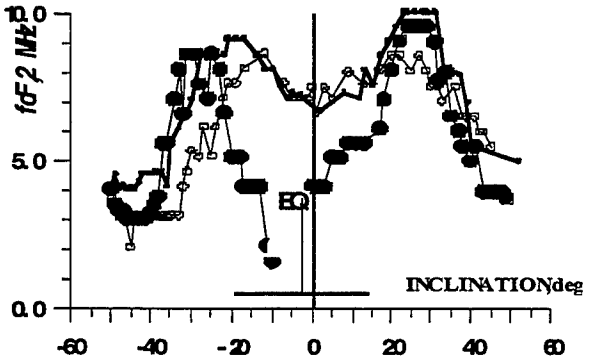


FIG.1. The plasma structure in the equatorial premidnight ionosphere one day before the pending earthquake 12.04.1963 (big black circles). The rest two lines are foF2 values more earlier and after the earthquke. Thick horizontal line is the esimated earthquake preparation zone dimension (the zone radius R=exp M is according to Ruzhin and Depueva, 1994). By EQ the epicenter position is shown.

One can conclude that the electric field of the precursor has to be less or compatible with the electric field of natural origin leading to the 'fountain- effect' and Appleton anomaly. The electric field magnitude of the precursor which is sufficient for this aim (Hanson and Moffett,1966) could be less than one mV/m at ionospheric heights.

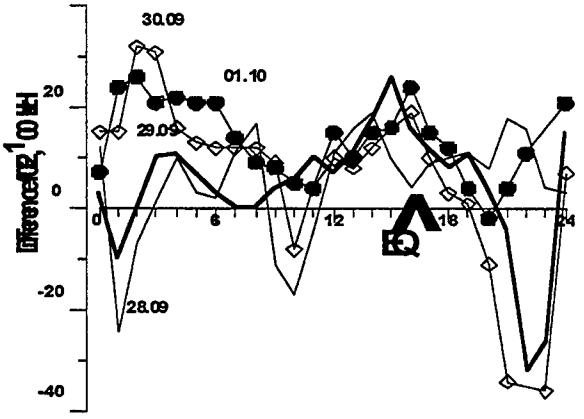


FIG.2. The differences of foF2-daily variations for four days before the earthquake. It is seen very well the premidnight MIN (deviation more than 3 MHz) for 29-30.09 and presunrise MAX for 1-2 days before. By EQ the epicenter position is shown The ALOUETTE (see Fig.1) data show plasma trough at 22LT also.

In order to decide if the originality (distinction) of our results is denoted to earthquake epicenter location near the magnetic equator we have compared ionospheric data for equatorial earthquake occurred on October 1, 1971, M=8.1 near Vanimo (New Guinea), dip=-20 ° and the second-midlatitude earthquake occurred on September 6, 1971, 05.35 UT, M=7.2 close to Wakkanai (Japan) dip=+60°. In Fig. 2 foF2 daily variations for "disturbed" (before the earthquake) four days are presented in

comparison with month median for ionosonde situated inside the preparation zone of the first earthquake.

In Fig.3 the analogous dependencies for ionosonde situated in Wakkanai before and after the second earthquake are presented. Without going into details we make a conclusion that definite effect is seen in morning and evening hours consisting in "disturbed" foF2 values relatively to month median foF2 values as to the first earthquake.It is the opposite reaction which is seen in Fig.3 (premidnight MAX/ presunrise MIN) in the case of the second earthquake: foF2 values before the event are larger than median. The same result was obtained (Depuev and Zelenova, 1986) by means of ionospheric data Milcovo situated not far from Wakkanai to North for another earthquake of the same magnitude.

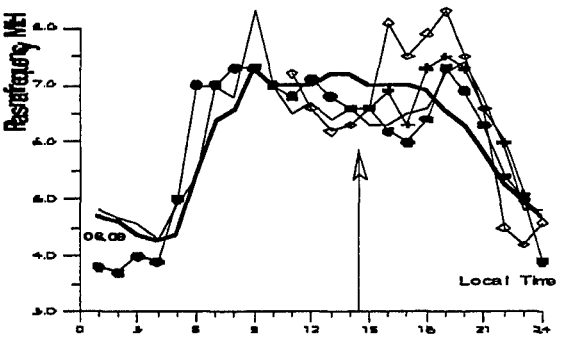


Fig.3. Daily variation and premidnight MAX/ presunrise MIN of foF2 before the midlatitude Wakkanai earthquake. Thick line is month median.

Thus, we have reasons to conclude that epicenter location and local time of observation play an important role as to differences in electron concentration modification over the preparation zone. So, one can observe the equatorial electron density reduction instead of midlatitude enhance (see Milkovo and Wakkanai events). So, such type of precursor can be very sensitive to geographic position of future earthquake epicenter and status of geomagnetic activity.

DISCUSSION

To illustrate the influence the pre-earthquake electric field on equatorial ionosphere plasma distribution during night condition we can present on Fig.4 the symmetrical electric field E distribution (directed to center) above the future earthquake epicentre. The geomagnetic field in equatorial region is horizontal and

a) **b)** **c)**

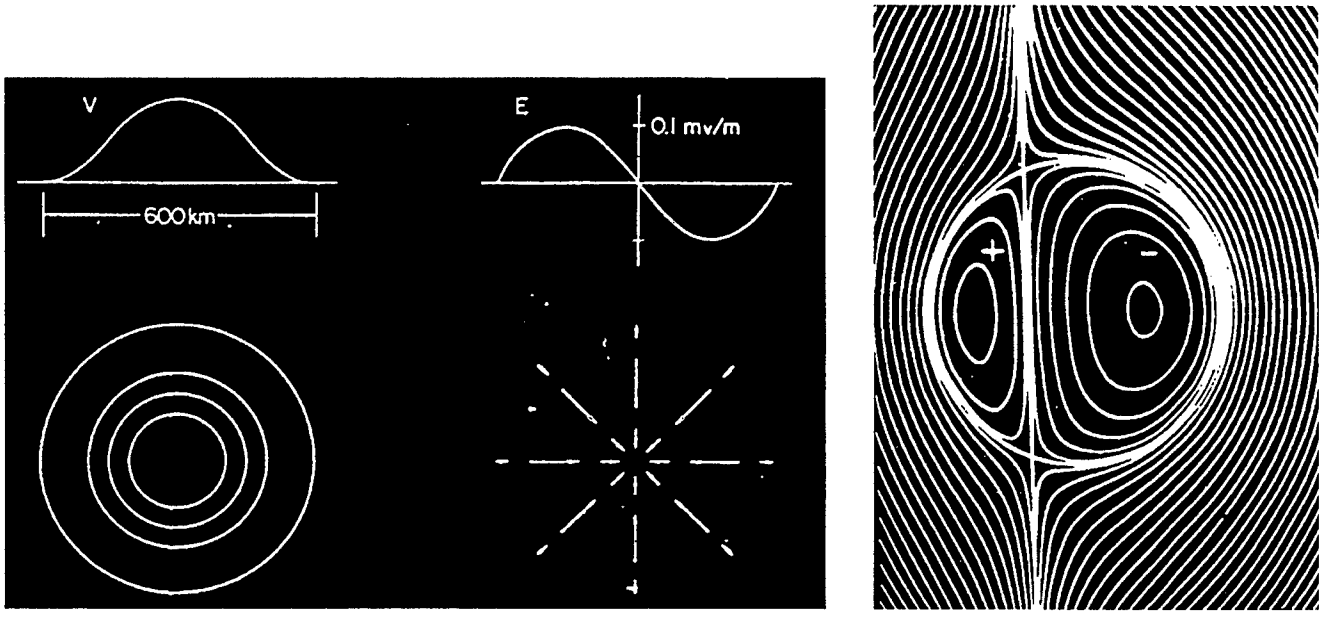


*Fig.4. This is result of some analytical speculation in seismo-electric field (**b**)) redistribution over the EQ (M=5.7) epicentral area (**a**)) and two focus drift velocity (**c**)) structure which can create the pre-earthquake Appleton anomaly (positive drift is upward plasma transportion) in equatorial ionosphere or depress it in opposite case.*

directed to North pole. So eastward electric field cause the upward plasma drift which could be reason of the precursor type Appleton anomaly or ionosphere disturbance generated by preseismic process.
In the ionosphere region where westward component of electric field exist the downward drift could be expected and so the plasma hole appear in result. In this region the appearing the natural Appleton anomaly will be depressed under convenient conditions. It is only illustration of an equatorial earthquake precursors beheviour with clear physical meaning but real picture more complex and localy procese defined.

CONCLUSIONS

Taking into account everything of above mentioned it is not surprisingly that investigations of different ionospheric plasma precursor images show the remarkable peculiarities which depend on geographical location of earthquakes epicenter (equatorial or midlatitude event) and local time of observation.
This kind of precursors are usually nocturnal ionospheric anomalies in plasma density distribution and appear over the earthquake preparation region some days before the main shock of the earthquake and can be caused by local changes of the electrical parameters of the spherical condenser (capacitor) formed by the two high conductive shells: earth's surface and lowest ionosphere plasma boundary (Ruzhin and Depueva,1996). It were shown that such variations of the atmosphere electricity cause appropriate electric field at the ionospheric heights. Anomalous variations appear inside whole ionosphere volume from the lowest boundary of Earth's plasma shell (80-100 km) up to 1000km and higher. Under fortunate coincidence precursor electric field can generate natural phenomena, 'fountain- effect' leading to Appleton anomaly in the equatorial ionosphere over future earthquake position. Estimation of electric field magnitude necessary to generate observing event was made. It was shown that the electric field less than one mV/m must be generated in the ionosphere.

REFERENCES:

Depueva A.Kh., and Yu. Ruzhin, *Seismoionospheric Fountain-Effect as Analogue of Active Space Experiment.* Adv. Space Res. V.15, N12, (12)151-(12)154, (1995).
Depuev V., and T.Zelenova, *Electron Density Profile Changes in Pre-earthquake Period,* Adv. Space Res.,V.18, (1996)
Hanson W.B. and R.J.Moffett, *Ionization Transport Effects in the Equatorial F Region,* J.Geophys.Res.,Vol.71, No.23, pp.5559-5572, (1966)
Larkina V.I., V.V Migulin, A.V. Nalivaiko et al., *Observation Onboard the "Intercosmos 19" Satellite of VLF Emissions Associated with Seismic Activity,* Geomagn. i Aeronom. V.23, N 5, PP. 842-845, (1983)
Liperovsky V., O. Pokhotelov and S. Shalimov, *Ionospheric earthquake precursors.* Nauka Publishing Co., Moscow, p.345, (1992)
Oraevsky V.N., Ruzhin Yu.Ya., Depueva A.Kh. *Seismoionospheric Precursors and Atmospheric Electricity.* Turkish J. of Physics, V. 18. N.11. P.1199-1204. (1994)
Ruzhin Yu.Ya., and A.Kh. Depueva, *Seismoprecursors in Space as Plasma and Wave Anomalies.* J.Atmosph.Electr. V.16. N3. P.251-288, (1996) .
Ruzhin Yu.Ya., and V.I. Larkina, *Magnetic Conjunction and Time Coherency of Seismoionosphere VLF Bursts and Energetic Particles.* Proceed.13th Wroclaw EMC Symposium (URSI) , PP.645-648, (1996)

Anomaly Preseismic Thunderstorm Activity as Source of HF Earthquake Precursors.

Yu.RUZHIN (1), C.Nomicos (2), F.Vallianatos (3)
1- *IZMIRAN, 142190 Troitsk-town,Moscow, Russia;* 2- *TEI of Athens, Greece;* 3- *TEI Chania branch, Crete, Greece*
E-mail:ruzhin@izmiran.rssi.ru

INTRODUCTION AND STATEMENT OF THE PROBLEM

Many electromagnetic phenomena in various ranges of frequencies are known which are connected to display of seismic activity [1-3]. The electromagnetic precursors of earthquakes (EQ) in a ULF-range registered even on satellite orbits in the ionosphere [3,4]. A number of recent papers on earthquake electromagnetic effects, together with the literature on this subject, can be found in Special Issue [5]. Here we focus interest on a new kind of electromagnetic precursors of earthquakes - precursors in high frequency (HF) range, which were registered by four stations of a network on an island Crete [6,7]. The island Crete is located in a southern part of Hellenic arch and since 1992 for research of electromagnetic precursors on an island the special network of telemetring stations is developed [6]. Among other parameters the measurements of HF noise on two frequency 41 and 53 MHz are conducted, which nature is now actively investigated. The HF signals or the candidate in precursors occurs at some days before the first displays of earthquakes occurring in Crete island vicinity. The aim of the present paper is to continue discussions on the possible relation between seismic activity and preceding HF radioemissions, started by Nomicos et al. [7].

THE ANALYSIS OF EXPERIMENTAL DATA

In the present work we carry out the analysis of the data on HF radioemission, which were received by a network of reception stations on an island Crete during three years (1992-1995) for earthquakes with magnitude M more than 5.0. In the Table the list of all earthquakes and their data for this period is given. Here h is depth of EQ center (km), OFF-station failure. The preliminary analysis of these data carried out in works [6,7] gives us such sequence of events. HF signal probably connected with EQ, occurs 1-3 days prior to event, but after signals (3 and 10 kHz) of ULF range. The long existence of signals (see Fig.1) from several hours up to one day was marked also. Let's note at once, that the island Crete is removed from industrial interference of Greece and Turkey and is an ideal place for reception seismoeffective electromagnetic HF radio emission. The amplitude of registered signals of radioemission is rather enough intensive to take in attention the astronomical radio-sources.

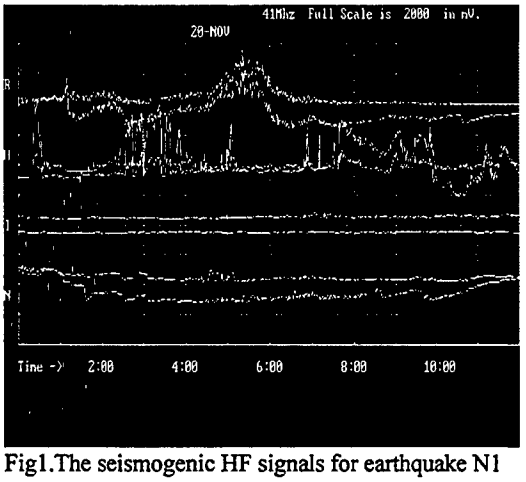


Fig1.The seismogenic HF signals for earthquake N1 of Table. N,I,H and D are the Crete stations symbol (Nipos, Heraklio, Ierapetra and Drapania)

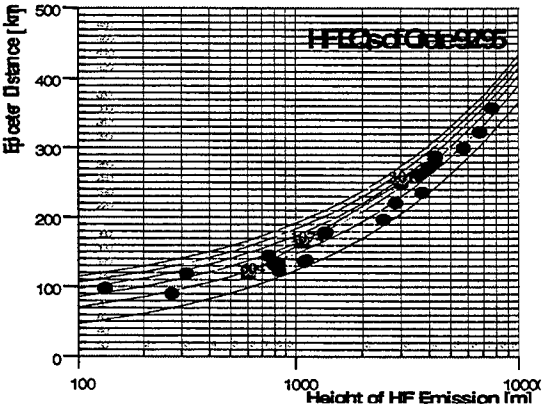


Fig.2. The minimum emitting heights

The basic relation for the analysis

For HF range on distances $R > 2\pi\lambda$ (length of a wave λ= 6-7.5m) condition of optical propagation is satisfied. As result for distances 50-300 km the reception of signals is possible, if a source of radiation or/and the reception aerial are lifted above the ground (sea level). First step in our analysis was an estimation of horizon position for each of station of measurements (see Table) on the formula: $\mathbf{R = 3.55\sqrt{h}_{ant}}$ (here R- distance up to horizon in km, and h_{ant} - height of the reception aerial in meters). This parameter R is given in the Table under the appropriate name of each station. Let's note, that the account of refraction influence on HF propagation in troposphere gives a variation of R in some percents. The distance D for each station (to epicenter) before the appropriate earthquake was calculated as length of an arch of the big circle intersected through two points. It is determined by the appropriate central angle α_i which in geographical system of coordinates calculated under the formula: $\mathbf{Cos\ \alpha_i = Sin\ \varphi_i * Sin\ \varphi_0 + Cos\ \varphi_i * Cos\ \varphi_0 * Cos\Delta\lambda}$; here φ_0 and φ_i - latitudes of earthquake and reception station and $\Delta\lambda=\lambda_i-\lambda_0$- difference of its longitudes.

Comparing the ranges up to horizon and up to epicenter for each of stations, we find out, that always D> R (see. Table) and actually all earthquakes are below the horizon. Taking into account, that the frequencies 41 and 53 MHz are not reflected from ionosphere, the superhorizon propagation is possible only if radiating and/or reception points are lifted above ground to heights H and h_{ant} accordingly. Proceeding from this geometry were calculated the minimal heights H_i of radiating points above epicenters of the future earthquakes for each station under the formula: $\mathbf{H_i=R_e/Cos(\alpha - \alpha_{ant})}$, where R_e- radius of the Earth (R_e = 6372km), and α_{ant} is determined by a ratio $Cos\alpha_{ant}=R_e/(R_e+h_{ant})$ and depends on height of the accepting aerial above a sea level.

TABLE

Earthquake (Seaquake) M≥5.0 (1992-1995)						Drapania (32.2km)		Nipos (43.4km)		Heraklio (55.6km)		Ierapetra (18.9km)	
_	Date	φ_o	λ_o	M	h	H	D	H	D	H	D	H	D
1	21.11.92	35.58	22.39	6.0	70	**590**	119	**1132**	164	**3007**	251		305
2	27.01.93	36.02	22.36	5.4	120	**821**	134	**1444**	179		265		319
3	1.06.93	34.07	26.25	5.2	1		280		237		170		116
4	29.06.93	35.39	27.07	5.5	1	**5641**	300	**3768**	263		175		135
5	18.08.93	35.15	26.11	5.2	72	**2805**	221	**1421**	178	**87**	89		43
6	1.10.93	36.64	24.01	5.4	109	**786**	132	**804**	145		181	**3692**	236
7	23.05.94	35.48	24.7	6.0	66	**262**	90	**23**	50		46		103
8	3.02.95	34.35	24.97	5.0	38		172		133		107		97
9	16.02.95	34.46	26.59	5.0	28	**OFF**	162	**3110**	243	**OFF**	161	**OFF**	103
10	7.03.95	36.90	27.67	5.0	5	**OFF**	389	**7781**	358	**4242**	288		278
11	30.03.95	34.33	24.61	5.1	1	**OFF**	152	**OFF**	120	**315**	119	**839**	122
12	5.04.95	34.53	27.88	5.0	35		207		353		264		208
13	29.07.95	34.46	27.03	5.0	1	**6667**	324	**4364**	279		196	**1111**	138
14	22.08.95	36.62	26.74	5.4	179		301	**4080**	271		205		205
15	19.09.95	34.56	26.25	5.0	148		254		209		130	**224**	72
16	30.11.95	36.60	27.14	5.3	136		333		301		230		221
17	7.12.95	34.97	24.17	5.1	22	**OFF**	73	**0**	42	**133**	97	**1090**	137
18	10.12.95	34.93	24.17	5.4	24	**OFF**	74	**12**	47	**140**	98	**1090**	137
19	18.12.95	35.54	27.73	5.1	1		356		324		236	**2485**	197

Results of the analysis.

In Table the calculated $\mathbf{H_i}$ heights of radiation are allocated with a bold font only for those cases, when at concrete station the signals for both frequencies simultaneously are found out. On FIG.2 the results of the analysis for all cases of signals reception (distance more 100km) are submitted: range (D) - height (H). It is well visible, that radiating points of the radio-frequencies 41 and 53 MHz are in a range of heights from hundred meters up to several kilometers above a sea level. This unexpected conclusion is basic for an establishment of a nature of such signals generation mechanism. The following important fact is that practically all earthquakes for which are found out HF signal- precursors are seaquakes, i.e. them epicenters are under bottom of the sea. From the Table it is visible, that for full period of observation only for 4 earthquakes (N3; N8; N12; N16) the HF signals was not registered on any of stations. It is an occasion for the further research. At the detailed analysis of absence of signals for other events by calculating azimuths of directions on appropriate epicenters by us was established, that the majority of the misses in the Table (absence of a signal at concrete station of a network) can be explained as screening (effect of a shadow) appropriate direction on a source by mountain, island or losses due to range increase. Not stopping on details, we shall note, that we could find a reasonable explanation of signal absence (proceeding from the analysis of concrete local conditions) for all events from the Table. Let's result some most obvious examples. So for earthquake N3 a signal absent only at station Heraclion. It is established that in a direction on epicenter there was a mountain of height in 2000 meters, which provided shadow of radiation heights up to 12 km above epicenter. Similarly for a case N10 and Ierapetra: the shadow of emission height reached 19 km! Absence of a signal for event N19 at three stations could be result of attenuation of a signal by longer distance or shadow from islands. It is possible to note after such analysis for all events of the Table that the source seismogenic radioemission was more often at heights more 1-3 km .

DISCUSSION

The natural radioemission in HF range is very anomalous phenomenon and sometime can be observed as result of auroral activity [8,9] or artificial beam-plasma injection [10]. More realistic source of broadband radioemission are thunderstorm [11-12] or lightning sources. First of all we examine all events of Table by this criteria (or meteorological processes) in map area and do not find any direct coincidence. More over such kind of HF range of lightning emission must eliminate the fine correlation in form and temporary behavior with ELF but it is absent for our data of analyses [6,7]. On the data of IZMIRAN station of solar storm radioemissions we have not found any event in HF range corresponded to items of our Table. The analysis of geomagnetic activity in the specified periods has shown complete absence of interrelation too. The meteoric radiopropagation could be a source of HF noise too at reception on a network of Crete stations. But practically all of monitored signals occurred irrespective of known regular meteoric flows. It s important also that the HF signals were not observed during the raised meteoric activity. Therefore, on all visibility the accepted signals on the nature are seismogenic. In this case they obviously differ from two known before cases [13,14] where the individual bursts from the super-power earthquake (M> 7.0) were registered.

To discuss the probable generation mechanism of HF radiation before earthquakes we shall present some results of radio-physical measurements of the abnormal phenomena in an atmosphere on the eve of Spitak earthquake [13]. By the authors with the help of weather radar is established, that for 1-3 days in an atmosphere above the epicenter there were charging structures similar thunderstorm, but considerably distinguished from them on duration and height of detection. The duration of existence (life time) made some hours whereas for thunderstorm activity the characteristic time does not exceed one hour. Unusual were also height and effective reflecting surface. Height made 5-30 km, and the area of reflection exceeded almost in 10 times similar for thunderstorms.

About the mechanism of generation HF radioemissions

It is known, that the optical luminescence of an atmosphere and lightning (thunder) are the usual phenomenon connected to forthcoming earthquake [15,16]. So, on the eve of powerful earthquake (M= 7.3) in China, which was successfully predicted, a many people observed a luminescence of the night sky [16] on remote distance of 100-200 kilometers from epicenter of the future earthquake. From FIG.2 follows, that height of seismogenic luminescence in this case could be as 1-2 km and above. It well supports the radar-tracking data in Spitak earthquake [13], where the anomalous charged clouds in an atmosphere are registered 1-3 days before. Proceeding from this and being based on the received above results of our analysis of a number of continuous observation on a network of Crete island we can assume, that in our case in an atmosphere above the sea on the eve of earthquake at heights of 0.1-10 km occur the charged clouds and, in a result, the conditions for the electrical discharges in an atmosphere are created which can serve a source of HF radio-emission registered on Crete.

Indirect confirmation of it can be the experimental works of the Japanese authors [17,18] in which is shown, that the source abnormal electromagnetic emission (EME) is located on a surface of the sea above a zone of the future earthquake. Let's note, that the magnitude range of these earthquakes corresponded to our : M = 5.0-6.0. As a source for such electromagnetic generator on a surface of the sea by them the model is offered [19], which basis is the injection of gases by bottom of the sea (in a zone of high pressure, arising by earthquakes preparation) which, reaching a surface of seawater, electrochemical interact with oxygen of an atmosphere with formation of positive ions (generation of charges at a surface of water) or/and them clusters.

By accepting it in attention and the assumption made by us above for an explanation of our results, we come to necessity whether to transport electrical charges from a surface of the sea (their occurrence on model of the Japanese) on height in some kilometers, whether to generate and to redistribute them at height in an atmosphere. This task is close on mechanism to generation of thunder activity in a nature [20]. One of known mechanisms of thunder electricity generation is the model of convection carry started in an atmosphere by a horizontal gradient of temperature

In our case the convective movement can be organized as follows. At the expense of increase of bottom temperature there is heating water, which rises as well as gases to a surface and creates necessary for convection a horizontal gradient of water temperature above epicenter of the future earthquake. The conditions for free thermal convection (termic) are created. Termic can arise or as separate volume - a bubble, or as a jet (fountain) . Temp of bubble lift it is possible to define [20] by balance the force of resistance F and the force of bubble buoyancy:

$F=(C_x/2)\rho' S\omega^2 = g(\rho'-\rho)V$ or, in result: $\omega=\sqrt{\{(8/3\ C_x)*g*r*(T'-T)/T}$

Where r-radius, S- section, V- volume of a bubble, Cx/2- const of air friction resistance (for sphere = 0.92), the meanings T, ρ concern to a bubble and T ', ρ' - to a neighboring atmosphere. The size of thermal convective cell is determined by the basic gradient of temperature and can vary from hundreds meters up to tens kilometers. For typical radius of convective cloudiness by size in 1km and difference of temperatures in 0,5°C the estimation gives a lifting speed equal 7,5 m/s. Thus, through thermal convection the substance / charge/cluster from a sea surface can be transported up to height of 2-2.5 km for 5 minutes.

In our model due to convective carry of charges the local conditions promoting to generation of thunder electricity are created, the occurrence and time life of which is defined by processes both in lithosphere and in an atmosphere. Thus, the occurrence of electrical charges in a surface of the sea and transportation them further on height up to 10 km in our model occurs due to energy allocated with bottom of the sea as gases and heat.

Set of processes in offered model

Let's present a sequence of key processes in our model of generation of seismogenic HF radiation:

- Gaseous injection occurring casually from the sea bottom in a zone of preparation of earthquake.
- Carry of gas from the bottom to a surface of the sea
- Oxidation of gas and formation of ions (charges) on border of sea water and air of atmosphere
- Local water heating within the limits of a zone of preparation of earthquake
- Convective transportation of electrical charges (ions) in troposphere and formation of structures of volume charges at atmosphere heights up to 10 km
- The electrical discharges in an atmosphere with radiation EME (in HF range including)

Let's note in addition, that as the small size of a nearby island results in formation of a shadow, it enables to carry out an independent estimation of the characteristic size of radiating volume in an atmosphere. That is it should be that of scale, as island (or its shadowing elements). It is well supported by the theory of convective cell [20]. So maximal height achievable by a cell, should be compared to its horizontal scale (can reach values of 5-10km), that is close to the sizes of Crete HF shadow objects.

CONCLUSION

As the monitoring preseismic HF signals was carried out continuously and long time, the material is received for all possible events which were having place almost for the three-years period of observation. It is shown, that the area of generation of a seismic - precursors (HF radioemissions) is in an atmosphere (above the sea surface) at heights of 0.1-10 km. It is offered and proved the model of generation of a high-frequency earthquakes precursor which based on reasonable assumption of formation of the charged clouds in an atmosphere above a zone of preparation of earthquake and subsequent an electrical discharges serving a source EME in HF a range. So the gaseous emission from the earth may be as main source of preseismic electromagnetic precursor of earthquake. Further detailed studies were useful for analyzing the mechanism by which electromagnetic wave radiation associated with localized volcanic and earthquake activity is generated.

REFERENCES

1. **M.B.Gohberg, V.A.Morgunov, T.Yoshino** et al *Experimental measurement of electromagnetic emissions possibly related to earthquakes in Japan.* J. Geophys. Res. 87, B9, 7824-7828, 1982
2. **A.C.Fraser-Smith, P.R.Bernardi, P.R.McGill, M.E.Ladd, B.A.Helliwell and O.G.Villard.** *Low frequency magnetic field measurements near the epicenter of the 7.1 Loma Prieta earthquake,* Geophys. Res. Lett., 17, 1465-1467, 1990
3. **M.Parrot, J.Achache, J.J.Berthelier, E.Blanc,** A.Deschammps, F.Lefeuvre, M.Menvielle, et al *High-frequency seismo-electromagnetic effects,* Phys. Earth Planet. Inter., 77, 65-83, 1993
4. **Yu.Ruzhin and A.Depueva,** *Seismoprecursors in space as plasma and waves anomalies,* Journ.Atmosph. Electricity, Vol.16, No.3, pp.271-288, 1996
5. **Special Issue:** *Seismo-Electromagnetic Phenomena.* Journal of Atmospheric Electricity,16,N3, 288pp,1996
6. **K.Nomicos, F.Vallianatos, J.Kalliakatos, S.Sideris** and M.Bakatsakis. *Latest aspects of telluric and electrmagnetic variations associated with shallow and intermediate depth earthquakes in South Aegean.* Annali di Geophysica, X1/2, 361- 375, 1995
7. F.**Vallianatos and K.Nomicos.** *Sesmogenic Radioemissions as Earthquake Precursors in Greece.* Phys.Chem.Earth, Vol. 23, No. 9-10, pp.953-957, 1998
8. **L.Harang,***Radio Noise From Aurora,* Planetary Space Sci., Vol.17,pp.869-877, 1969
9. **A.V.Dudnik, V.M.Kartashev, A.V.Lazarev** et al., *The day variations of sporadic space radioemission at middle latitudes,* Geomagnetism & Aeronomy, Vol.28, No.1, pp.82-86, 1988
10. **V.N.Oraevsky, Yu.Ya.Ruzhin and A.S.Volokitin;** *High Frequency Electromagnetic Radiation in CRRES injection,* Advance Space Research, Vol.15,No.12,pp. (12)99-(12)102,1995
11. **D.E.Proctor,** *VHF Radio Pictures of Cloud Flashes,* Journ. Geophys.Res., Vol.86, No.C5, pp.4041-4071, 1981
12. **James W. Warwick, C.O.Hayenga** and J.W.Brosnahan, *Interferometric Directions of Lightning Sources at 34 MHz,* Journ. Geophys.Res., Vol.84, No.C5, pp.2457-2467, 1979

13. **V.V.Voinov, I.L.Gufeld, V.V.Kruglikov et al.**, *Effects in the ionosphere and atmosphere before the Spitack earthquake*, News of USSR Academy, Fizika Zemli (in Russian), No.3, pp.96-101,1992
14. **Koitiro Maeda and Noritaka Tokimasa**, *Decametric Radiation at the time of the Hyogo-ken Nanbu Earthquake near Kobe in 1995*, Geoph. Research Lett., vol.23, no.18, pp.2433-2436, 1996
15. **D.Finkelstein and J.Powell,** *Earthquake lightning,* Nature, Vol.228, No.5270-5273, pp.759-760,1970
16. **Y.Zhao and F.Qian,** *Earthquake lights: a very convincing evidence for energy transfer from earth to air,* Intern.Workshop on Seismo_Electromagnetic (Abstracts), NASDA,Tokyo, p.242, 1997
17. **M.Hata and S.Yabashu;** *Observation of ELF Radiation Related to Volcanic and Earthquake Activities* in: Electromagnetic Phenomena Related to Earthquake Prediction, ed.M.Haiakawa and Y.Fujinawa , TERRAPUB,Tokyo, pp.159-174, 1994
18. **M.Hata, X.Tian,I. Takumi et al.,** *ELF Horizontal Flux Precursor of Moderate Yamashi_96 Earthquake,* Journ.Atmosph. Electricity, Vol.16, No.3, pp.199-220, 1996
19. **M.Hata, I. Takumi and S.Yabashu;** *A model of earthquake seen by electromagnetic observation - gaseous emission from the Earth as main source of pre-seismic electromagnetic precursor and trigger of followed earthquake,* Ann. Geophysicae Supplement to Vol.16 , p. C1188, 1998
20. **A.H.Hrgian**. *Physics of Atmosphere*. Moscow, MSU, 328p., 1986

Multi–Instrument Studies of Low Latitude F–Region Plasma Irregularities

Bela G. Fejer
Center for Atmospheric and Space Science
Utah State University, UMC 4405
Logan, UT 84322–4405

Equatorial and low latitude plasma irregularities have been studied for over three decades, but their understanding is still incomplete and their and forecasting remains elusive. Since this is an important component of space weather programs, a number of larger scale efforts have been proposed for improving the understanding of the physical processes involved and, especially for more accurate forecasting their occurrence and effects on communication and navigation systems. In this talk, we will describe two of these projects. The first involves the use of three nanosatellites being built at Utah State University, Virginia Polytechnic Institute, and University of Washington, and which will to be launched from the Space Shuttle. The second consists of coordinated global campaigns lasting over two months and using multi–instrument ground–based and satellite measurements.

An Overview of Low-Latitude Ionospheric Models

J.D. HUBA (Plasma Physics Division, Naval Research Laboratory, Washington, DC 20375)

Over the past two decades a number of computational models of the ionosphere have been developed. An excellent overview of the most widely used models is given in *STEP: Handbook of Ionospheric Models* [1] and in Anderson et al. (1998) [2]. In general, ionospheric models treat the global ionosphere in three parts: low-latitude, mid-latitude, and high-latitude. Low-latitude models (e.g., GTIM, FLIP, SUPIM) consider the plasma dynamics along an entire field line from hemisphere to hemisphere. Mid-latitude models (e.g., GTIM, TDIM) typically have the upper boundary < 1000 km; additional boundary conditions at the upper boundary (e.g., particle flux, heat flux) must be imposed that are generally not consistent with interhemispheric transport. Finally, high latitude models (e.g., TDIM, GTIM) also have an upper boundary typically set at 1000 km. However, an important aspect of high latitude models is that magnetospheric effects need to be included: for example, the magnetospheric electric field and auroral precipitation effects. A common feature of these models is that they use the empirical neutral atmosphere models MSIS and HWM, or observed data to specify neutral atmosphere densities and winds. There are also two global ionospheric models that solve the neutral atmosphere equations to determine the neutral atmosphere composition and dynamics, and self-consistently couple this solution to ionospheric dynamics: NCAR TIGCM, CTIM, and CTIP.

Although several of the low latitude models (GTIM, FLIP, and SUPIM) use the same basic geometry, an interhemispheric flux tube, there are considerable differences between the models. GTIM solves the ion continuity and momentum equations to determine the O^+ ion density with the ion and electron temperatures specified by an empirical model. For flux tubes with an apex altitude greater than ~ 1000 km, GTIM does not solve along the entire interhemispheric flux tube, but rather specifies an O^+ density or flux at the upper boundary. GTIM includes an electric field model which allows the plasma to $\mathbf{E} \times \mathbf{B}$ drift in the 'radial' direction. FLIP solves the ion continuity and momentum equations for H^+, O^+, He^+, and N^+, as well as the electron and ion thermal equations. H^+ and O^+ are treated as major ions, while He^+ ane and N^+ are treated as minor ions. FLIP also solves ion continuity and momentum equations to obtain the densities of the minor neutral species $N(^2D)$, $N(^4S)$, NO, and thermal balance equations for the first 6 vibrational levels of N_2. FLIP is able to model interhemispheric flux tubes that extend into the plasmasphere, i.e., the apex altitude of a flux tube can be $> 10{,}000$ km. However, FLIP does not include the $\mathbf{E} \times \mathbf{B}$ drift motion of a flux tube. SUPIM solves the continuity and momentum equations for H^+, O^+, He^+, N_2^+, O_2^+, and NO^+, and the ion temperature equations for H^+, O^+, and He^+ as well as the electron temperature equation. It models flux tubes that extend into the plasmasphere, but unlike FLIP it also includes the $\mathbf{E} \times \mathbf{B}$ drift motion of a flux tube.

Recently, a new low-latitude model of the ionosphere has been developed at the Naval Research Laboratory: SAMI2 (Sami2 is Another Model of the Ionosphere) [3, 4, 5]. It is an outgrowth of a mid-latitude ionospheric model developed at NRL in

the mid 1970's [6]. SAMI2 treats the dynamic plasma and chemical evolution of seven ion species (H^+, He^+, N^+, O^+, N_2^+, NO^+, and O_2^+). The ion continuity and momentum equations are solved for all 7 ion species. All ion species are treated the same, i.e., there are no major or minor ion species. Thermal balance equations are solved for three ion species (H^+, He^+, and O^+) and for the electrons. The neutral atmosphere is specified using the empirical codes MSIS86 and HWM93. SAMI2 models the plasma along a magnetic flux tube from hemisphere to hemisphere. It includes the $\mathbf{E} \times \mathbf{B}$ drift of a flux tube (both in altitude and in longitude), and also includes ion inertia in the ion momentum equations for plasma motion along the dipole field line. The previously discussed ionospheric models assume the ions are collisional at all altitudes and neglect ion inertia. To our knowledge, SAMI2 is the first low latitude ionospheric model to include the inertial terms in the ion momentum equations.

The purpose of this presentation will be to provide an overview of the major low-latitude ionospheric models: GTIM, FLIP, SUPIM, and SAMI2. We will compare and contrast both numerical methods and the underlying physical assumptions of each model. Representative results from the various models will be presented. Finally, we will discuss future directions in ionospheric modeling.

Acknowledgments: SAMI2 has been developed in collaboration with Drs. G. Joyce and J.A. Fedder. This research has been supported by the Office of Naval Research under the Accelerated Research Initiative "Ionospheric Specification and Forecasting".

References

[1] *STEP: Handbook of Ionospheric Models*, ed. R. Schunk (Utah State University and SCOSTEP, Logan, UT, 1996)

[2] Anderson, D.N., M.J. Buonsanto, M. Codrescu, D. Decker, C.G. Fesen, T.J. Fuller-Rowell, B.W. Reinisch, P.G. Richards, R.G. Roble, R.W. Schunk, and J.J. Sojka, Intercomparison of physical models and observations of the ionosphere, *J. Geophys. Res. 103*, 2179, 1998.

[3] Huba, J.D., G. Joyce, and J.A. Fedder, The Formation of an Electron Hole in the Topside Equatorial Ionosphere, *Geophys. Res. Lett 27*, 181, 2000a.

[4] Huba, J.D., G. Joyce, and J.A. Fedder, Ion sound waves in the topside equatorial ionosphere, submitted to *Geophys. Res. Lett*, 2000b.

[5] Huba, J.D., G. Joyce, and J.A. Fedder, SAMI2 (Sami2 is Another Model of the Ionosphere): A New Low-Latitude Ionospheric Model, submitted to *J. Geophys. Res.*, 2000c.

[6] Oran, E.S., T.R. Young, D.V. Anderson, T.P. Coffey, P.C. Kepple, A.W. Ali, and D.F. Strobel, A Numerical Model of the Mid-Latitude Ionosphere, NRL Memo Report 2839, 1974.

Future Developments in Equatorial Aeronomy

MICHAEL MENDILLO
Center for Space Physics and Department of Electrical and Computer Engineering
Boston University, Boston, MA

The first three decades of the 21st Century will mark the centennial period of the "discovery" of the ionosphere. Will there be an International Equatorial Aeronomy Symposium in 2031 to celebrate the 100th anniversary of Q = L ? For how many more years will "The Anomaly" warrant that name ? Will equatorial spread–F ever have a better name ? Should Space Weather be the major driver of low latitude aeronomy ?

The coming of a new Millennium offers, perhaps demands, some thoughtful consideration of future goals and ambitions for Equatorial Aeronomy and, indeed, for all of Space Physics. New instrumentation, improved models, and potential applications to other planets will/should sustain the field, a worthy legacy to an international community addressing global science issues of recognized importance.

"Living With a Star" and the "Tropical Coupler" Solar-Terrestrial Probe: New Programs at NASA that Explore Equatorial Ionospheric Physics

R. PFAFF, Jr., Electrodynamics Branch, Code 696, NASA/Goddard Space Flight Center
Greenbelt, MD 20771 (USA)

NASA has recently initiated a major new research program called "Living With a Star" which will address Space Weather problems and includes wide-ranging solar, heliospheric, magnetospheric, and ionospheric observations. Among the space weather problems to be addressed are scintillations and plasma structuring in the equatorial ionosphere which subsequently create an environment that may be detrimental to both navigation and communication RF systems. Initial goals of the "Ionospheric Mappers" mission within the Living with a Star program include a significantly improved understanding of equatorial Spread-F and ultimately a predictive capability of this phenomena. Concurrently, NASA's Office of Space Science's "Sun-Earth Connections Roadmap" for 2000-2025 includes a proposed Solar-Terrestrial Probe called "Tropical Coupler" that will also explore in detail the equatorial ionosphere, gathering data using a pair of satellites at two different altitudes. Initial concepts and objectives for both of these initiatives will be presented and discussed.